

Exploiting second-order nonlinear phenomena
for the generation and detection of coherent
terahertz electric fields

by

Brett Nathan Carnio

A thesis submitted in partial fulfillment of the requirements for the degree of

Doctor of Philosophy

in

Photonics and Plasmas

Department of Electrical and Computer Engineering

University of Alberta

© Brett Nathan Carnio, 2022

Abstract

This thesis explores terahertz radiation sources and detectors, where the driving physical mechanism for generation and detection is second-order nonlinear phenomena. The heart of this work considers novel crystals and waveguiding arrangements for terahertz radiation generation and/or detection to advance the field of nonlinear optics.

Experimental investigations are conducted using emerging pnictide and chalcogenide ternary crystals for both the generation and detection of terahertz radiation. While a CdSiP_2 crystal is shown to provide appreciable optical rectification phase-matching (surpassing that of a ZnGeP_2 crystal), an AgGaSe_2 crystal exhibits unprecedented optical rectification phase-matching (coherence length of $\sim 800 \mu\text{m}$ for frequencies between 0.5-2.9 THz). A BaGa_4Se_7 crystal is revealed as a highly-efficient terahertz radiation emitter (i.e. the terahertz radiation power produced by BaGa_4Se_7 is better than ZnTe in select terahertz spectral bands). Subsequently, a ZnGeP_2 crystal is shown to exhibit exceptional electro-optic phase-matching, allowing it to surpass the bandwidth of ZnTe for terahertz radiation detection.

Numerical and experimental techniques are utilized to investigate waveguiding arrangements for terahertz radiation generation. However, due to the lack of numerical methods capable of incorporating all 18 dispersive second-order nonlinear tensor elements, two separate formalisms are developed to integrate second-order nonlinear effects into finite-difference time-domain simulations. Using the developed methods and experimental terahertz time-domain spectroscopy techniques, LiNbO_3 planar waveguides are investigated for producing terahertz radiation. Key observations include ultra-broadband terahertz radiation generation spanning 0.18-106 THz, terahertz radiation generation enhancement near the phonon resonances of LiNbO_3 ,

phase-matched terahertz radiation produced in the backward direction (i.e. the direction opposite to the propagation direction of the excitation electric field), and high experimentally-realized optical-to-terahertz conversion efficiencies (i.e. $>10^{-5}$).

Interestingly, the aforementioned nonlinear finite-difference time-domain formalisms are not restricted to the terahertz frequency regime, but can accurately model second-order nonlinear processes within various other spectral regions. To make use of such an exciting outcome, this thesis briefly extends beyond the terahertz spectral regime to examine second-order nonlinear effects for the generation of radiation in the infrared and visible spectral regimes. Accordingly, an entirely new class of multi-band photonic sources is proposed, in which a single waveguiding structure concurrently satisfies phase-matching for several second-order nonlinear processes. A multi-band waveguide is experimentally-realized, which simultaneously produces phase-matched THz radiation and phase-matched radiation in the visible spectral regime.

The findings in this thesis are invaluable to the continuing development of terahertz radiation sources and detectors being driven by the physical mechanism of second-order nonlinear phenomena.

Preface

Parts of Chapter 1 consist of work submitted as invited review articles:

1. B. N. Carnio, K. T. Zawilski, P. G. Schunemann, O. Moutanabbir, and A. Y. Elezzabi, “The coming age of pnictide and chalcogenide ternary crystals in the terahertz frequency regime,” *IEEE Trans. Terahertz Sci. Technol.* **under review** (2021).
2. B. N. Carnio, O. Moutanabbir, and A. Y. Elezzabi, “Nonlinear photonic waveguides: A versatile platform for terahertz radiation generation (a review),” *Laser Photonics Rev.* **under review** (2021).

Chapter 4 describes work that has been published as:

3. B. N. Carnio, P. G. Schunemann, K. T. Zawilski, and A. Y. Elezzabi, "Generation of broadband terahertz pulses via optical rectification in a chalcopyrite CdSiP₂ crystal," *Opt. Lett.* **42**, 3920-3923 (2017).
4. B. N. Carnio, K. T. Zawilski, P. G. Schunemann, and A. Y. Elezzabi, “Optical rectification in a chalcopyrite AgGaSe₂ crystal for broadband terahertz radiation generation,” *Opt. Lett.* **44**, 2867-2870 (2019).
5. B. N. Carnio, E. Hopmann, K. T. Zawilski, P. G. Schunemann, and A. Y. Elezzabi, “Dependence on excitation polarization and crystal orientation for terahertz radiation generation in a BaGa₄Se₇ crystal,” *Opt. Express* **28**, 15016-15022 (2020).
6. B. N. Carnio, K. T. Zawilski, P. G. Schunemann, and A. Y. Elezzabi, “Generation of narrowband terahertz radiation via phonon mode enhanced nonlinearities in a BaGa₄Se₇ crystal,” *Opt. Lett.* **45**, 4722-4725 (2020).

7. B. N. Carnio, S. R. Greig, C. J. Firby, K. T. Zawilski, P. G. Schunemann, and A. Y. Elezzabi, "Terahertz electro-optic detection using a <012>-cut chalcopyrite ZnGeP₂ crystal," *Appl. Phys. Lett.* **108**, 261109 (2016).

The work presented in Chapter 5 has been published as:

8. B. N. Carnio and A. Y. Elezzabi "A modeling of dispersive tensorial second-order nonlinear effects for the finite-difference time-domain method," *Opt. Express* **27**, 23432-23445 (2019).
9. B. N. Carnio and A. Y. Elezzabi, "An extensive finite-difference time-domain formalism for second-order nonlinearities based on the Faust-Henry dispersion model: Application to terahertz generation," *J. Infrared Milli. Terahz. Waves* **41**, 291-298 (2020).

Chapter 6 reports on work published as:

10. B. N. Carnio and A. Y. Elezzabi, "Investigation of ultra-broadband terahertz generation from sub-wavelength lithium niobate waveguides excited by few-cycle femtosecond laser pulses," *Opt. Express* **25**, 20573 (2017).
11. B. N. Carnio and A. Y. Elezzabi, "Enhanced broadband terahertz radiation generation near the reststrahlen band in sub-wavelength leaky-mode LiNbO₃ waveguides," *Opt. Lett.* **43**, 1694-1697 (2018).
12. B. N. Carnio and A. Y. Elezzabi, "Backward terahertz difference frequency generation via modal phase-matching in a planar LiNbO₃ waveguide," *Opt. Lett.* **45**, 3657-3660 (2020).
13. B. N. Carnio, B. Shahriar, E. Hopmann, and A. Y. Elezzabi, "Excitation mode-dependent terahertz radiation generation from a sub-wavelength Si-SiO₂-LiNbO₃-polymer-Si planar waveguide," *IEEE Trans. Terahertz Sci. Technol.* **11**, 462-465 (2021).

The discussions in Chapter 7 are associated with works published as:

14. B. N. Carnio and A. Y. Elezzabi, "Second harmonic generation in metal-LiNbO₃-metal and LiNbO₃ hybrid-plasmonic waveguides," *Opt. Express* **26**, 26283-26291 (2018).
15. B. N. Carnio and A. Y. Elezzabi, "Second harmonic generation in CdSiP₂ nanowires in the optical frequency regime," *IEEE Photonic Tech. Lett.* **30**, 1408-1411 (2018).
16. B. N. Carnio and A. Y. Elezzabi, "Phase-matched frequency-conversion in waveguides by means of transverse wavevector projections," *J. Opt. Soc. Am. B* **37**, 1140-1143 (2020).
17. B. N. Carnio and A. Y. Elezzabi, "Off-normal incidence coupling for perfectly phase-matched second harmonic generation in a sub-micron LiNbO₃ planar waveguide," *J. Light. Technol.* **38**, 3959-3964 (2020).

The discussions in Chapter 8 are related to works published as:

18. B. N. Carnio and A. Y. Elezzabi, "Generation of mid-infrared and visible radiation in a multi-band phase-matched sub-wavelength LN waveguide," *J. Opt. Soc. Am. B* **36**, 1695-1699 (2019).
19. B. N. Carnio, E. Hopmann, B. Y. Shahriar, and A. Y. Elezzabi, "A Multi-Band Photonic Source by Means of Phase-Matched Nonlinear Generation Processes," *IEEE Photon. Technol. Lett.* **33**, 366-369 (2021).

Acknowledgements

I would like to thank my supervisor, Professor Abdul Elezzabi, for all that he has done for me. Without question, some of his finest traits include his enthusiasm toward research, the close relationship he develops with his graduate students, and his ability to motivate others. These attributes are undoubtedly correlated to any success I achieved during graduate studies, as well as any success I may find during my future. While Professor Elezzabi always recognized the importance of a strong work ethic, I am grateful he also taught me that hard work alone is not enough, but working effectively and efficiently is equally important. I appreciate Professor Elezzabi for helping me improve my writing skills, which certainly needed a lot of work. Oddly, I always enjoyed our disagreements, as they seemed to lead to productive discussions that allowed me to find clarity on the subject being debated. Thank you for shaping me into the researcher that I have become.

I am thankful for the friends I made in the lab: Dr. Curtis Firby, Dr. Shawn Greig, Dr. Nir Katchinskiy, Dr. Haizeng Li, Dr. Michael Nielsen, Dr. Shawn Sederberg, Amir Badkoobehhezaveh, Ryan Boehnke, Eric Hopmann, Aiden McDermott, Sawyer McPherson, Liam McRae, Taylor Robertson, Katherine Smith, and Wu Zhang. I enjoyed the time spent with each of you. Although I felt sadness anytime someone moved on from the lab, I was happy to see each of you achieve your goals and I was excited to watch you accept new and bigger challenges. As we all end up in different places, I hope we stay in contact.

I am lucky to have access to the Electrical and Computer Engineering Machine Shop and their wonderful staff (Herbert Dixel, Reiner Schwarze, and Terry Kugler), who were always accommodating. Additionally, I am grateful to have access to the world-class nanoFAB facility

and its amazingly knowledgeable staff. I would also like to extend a special thanks to the many other University of Alberta staff members, including Rick McGregor and Alan Lim.

I am extremely grateful to Professor Oussama Moutanabbir, who has been exceedingly kind to me. I am lucky to have met such a wonderful individual, who was willing to provide me with support and opportunities even before I completed my PhD. I am grateful for the opportunity to join your talented group, and I am eager to contribute to the research.

I would like to thank Dr. Kevin Zawilski and Dr. Peter Schunemann of BAE Systems for their collaboration partnership. Their willingness to share novel and exotic crystals with us was integral to the conducted work.

I am exceptionally grateful for the support provided by my family, my dad and his fiancée, my nonno and nonna, my mom and her husband, and my brother, his wife, and their three children. I would like to extend a special thanks to my dad, who encouraged me to pursue engineering, my nonno and nonna, who dedicated an enormous amount of their time and energy to raising me, and my mom and brother, who were there for me even before I went into engineering. I can honestly say I don't know how I would have completed this degree without so much help from family, and I am especially grateful to everyone for helping look after our three kids without hesitation.

I cannot forget our three cats, Maisie, Max, and Jenkins, whose unconditional affection was needed through the stress of graduate school.

I am overly grateful to my wife, Allison, and our three wonderful daughters, Mattea, Chiara, and Daniella. It is amazing to think that Allison and I added three members to our family during the last two years of my PhD. Although it was interesting at times, trying to complete my PhD degree while having a toddler (Mattea) and newborn twins (Chiara and Daniella), thinking of them

motivated me through the late nights. I am blessed to have their love and affection. More than anything else, I strive to be a good husband and father.

The University of Alberta is located on Treaty 6 territory, the traditional lands of First Nations and Métis people.

Table of contents

Chapter 1. Introduction.....	1
1.1. Key properties of THz radiation.....	2
1.2. Applications of THz radiation.....	4
1.3. Overview of THz sources, detectors, and measurement techniques	9
1.4. Pnictide and chalcogenide ternary crystals in the THz frequency regime	11
1.4.1. Key properties of pnictide ternary crystals.....	13
1.4.2. Linear THz radiation properties of pnictide ternary crystals.....	15
1.4.3. THz radiation generation via nonlinear frequency-conversion in pnictide ternary crystals	17
1.4.4. THz radiation detection using pnictide ternary crystals	21
1.4.5. Key properties of chalcogenide ternary crystals	21
1.4.6. Linear THz radiation properties of chalcogenide ternary crystals	25
1.4.7. THz radiation generation via nonlinear frequency-conversion in chalcogenide ternary crystals	28
1.4.8. THz radiation detection using chalcogenide ternary crystals.....	30
1.4.9. Pnictide and chalcogenide ternary crystals for high-field THz radiation generation.....	32
1.5. On-chip waveguiding platforms for THz radiation generation	34
1.5.1. Guided excitation electric fields and guided generated THz radiation	37
1.5.2. Guided excitation electric fields and free-space THz radiation emission	44
1.5.3. Free-space excitation electric fields for generating guided THz radiation.....	51

1.6. Thesis objectives	54
1.7. Thesis overview	55
Chapter 2. Second-order nonlinear phenomena: A complete prospective	58
2.1. General framework.....	62
2.1.1. Anharmonic EOM	62
2.1.2. Maxwell's equations.....	63
2.2. Monochromatic incident electric fields	66
2.2.1. Anharmonic EOM and Maxwell's equations	66
2.2.2. A quantitative example.....	77
2.2.3. Tensor representation of the second-order nonlinear polarization	85
2.3. Nonlinear second-order interaction via a broadband electric field pulse	89
2.3.1. Induced polarization and Maxwell's equations	90
2.3.2. A quantitative example.....	94
2.3.3. Tensor representation of second-order nonlinear polarization	99
2.4. Summary.....	102
Chapter 3. THz-TDS system	104
Chapter 4. THz radiation generation and detection using pnictide and chalcogenide ternary crystals	111
4.1. Generation of broadband THz radiation pulses in a CSP Crystal	112
4.1.1. Excitation arrangement.....	112
4.1.2. Linear THz radiation properties	114

4.1.3. THz-TDS measurements in the nonlinear regime	116
4.2. OR in an AGS crystal for broadband THz radiation generation	119
4.2.1. Linear THz radiation properties	120
4.2.2. THz-TDS measurements in the nonlinear regime	123
4.3. Generation of narrowband THz radiation from a BGS crystal.....	126
4.3.1. Nonlinear crystal properties	126
4.3.2. Dependence of THz radiation generation on the excitation polarization angle and crystal orientation.....	127
4.3.3. Optimal BGS crystal arrangements for THz radiation generation	133
4.4. THz EO detection using a (012)-cut ZGP crystal.....	139
4.4.1. Excitation arrangement and linear THz radiation properties	140
4.4.2. EO sampling measurements	142
4.5 Summary.....	145
Chapter 5. FDTD modeling of second-order nonlinear effects: A complete picture	147
5.1. Modeling of dispersive tensorial second-order nonlinear effects for the FDTD method: Implementing Miller's rule	148
5.1.1. Derivation of the second-order nonlinear current density	148
5.1.2. Discretization of the second-order nonlinear current density.....	151
5.1.3. Frequency-conversion in a LN crystal	158
5.2. Modeling of dispersive tensorial second-order nonlinear effects for the FDTD method: Implementing the Faust-Henry model	167

5.2.1. Nonlinear formalism.....	167
5.2.2. OR in a ZnTe Crystal	169
5.3. Summary.....	175
Chapter 6. THz radiation generation using LN waveguiding arrangements	177
6.1. Ultra-broadband THz radiation generation from sub-wavelength LN waveguides	177
6.1.1. Waveguiding structure.....	178
6.1.2. OR THz radiation generation	182
6.2. THz radiation generation near the reststrahlen band in sub-wavelength LN waveguides.....	188
6.2.1. Waveguiding arrangement.....	189
6.2.2. OR THz radiation generation	192
6.3. Backward THz DFG via modal phase-matching in a planar LN waveguide	197
6.3.1. Waveguiding structure.....	197
6.3.2. DFG THz radiation generation	199
6.4. Excitation mode-dependent THz radiation generation from a planar LN waveguide	204
6.4.1. Waveguiding structure.....	205
6.4.2. OR THz radiation generation	207
6.5. Summary.....	211
Chapter 7. Generation of radiation in the near-IR and visible spectral regions	212

7.1. SHG in Au-LN-Au and LN hybrid-plasmonic waveguides	214
7.1.1. Waveguiding structures	214
7.1.2. SHG in MLNM nanoplasmonic and LNHP waveguides	217
7.2. Optical frequency SHG in a CSP photonic waveguide	223
7.2.1. Waveguiding structure.....	223
7.2.2. SHG in CSP and LN photonic waveguides.....	225
7.3. Phase-matched frequency-conversion in waveguides by means of transverse wavevector projections	230
7.3.1. Coupling arrangement	231
7.3.2. SHG via off-normal-incidence coupling	232
7.4. Off-normal-incidence coupling for phase-matched SHG in a sub-micron LN planar waveguide	238
7.4.1. Experimental arrangement.....	238
7.4.2. Waveguide characteristics	239
7.4.3. Coupling characteristics	243
7.4.4. Experimental measurements.....	244
7.5. Summary.....	246
Chapter 8. Simultaneous generation of phase-matched radiation across multiple spectral bands	248
8.1. Generation of mid-IR and visible radiation in a multi-band planar LN waveguide	250
8.1.1. Waveguiding structure.....	250

8.1.2. SFG and DFG in a planar LN waveguide	252
8.2. A multi-band planar LN waveguide for generating THz radiation and visible light	258
8.2.1. Waveguiding structure.....	258
8.2.2. SHG visible-light generation.....	261
8.2.3. OR THz radiation generation	264
8.3. Summary.....	266
Chapter 9. Conclusion	267
9.1. Future directions.....	269
9.2. Outlook.....	271
References	272
Appendix A	299
Phase-matching in second-order nonlinear interactions.....	299

List of Tables

Table 1.1. Structural and optical properties of various pnictide ternary crystals in the THz frequency regime.	15
Table 1.2. Structural and optical properties of various chalcogenide ternary crystals in the THz frequency regime.	23

List of figures

Fig. 1.1. (a) EM spectrum showing that THz radiation lies between technologies prevalent in electronics and photonics. (b) Output power of various sources used to produce radiation within and near the THz spectral region [2]..... 2

Fig. 1.2. Absorption of THz radiation due to water vapor [8]. The spectra are obtained using an air biased coherent detection (ABCD) system and a Fourier-transform infrared (FTIR) spectroscopy system [8]..... 3

Fig. 1.3. (a) Optical arrangement showing a metallic blade concealed within an envelope [7]. (b) THz radiation image clearly identifying the concealed cutting blade [7]. (c) Spectral “fingerprint” of various explosives in the THz frequency regime [6]..... 5

Fig. 1.4. (a) Illustration of the technique used to measure the coating thickness of a pharmaceutical tablet [11]. (b) Experimental THz time-domain signal recorded after reflecting from the various interfaces of the pharmaceutical tablet [11]..... 6

Fig. 1.5. Illustration of point-to-point communication using a secure THz radiation channel for terabit-per-second (Tbps) data transfer [18]. 7

Fig. 1.6. THz radiation images of a spinach leaf undergoing a natural drying process, where dark regions correspond to a high water content [9]..... 9

Fig. 1.7. An illustration of the unit cell structure of the ZGP, CSP, CdGeP₂, and MnSiP₂ crystals. 13

Fig. 1.8. Ordinary and extraordinary (a) refractive indices and (b) extinction coefficients of ZGP crystals in the THz frequency regime [39]. 16

Fig. 1.9. (a) DFG THz radiation produced using a ZGP crystal excited at various external phase-matching angles [51]. (b) Generation of broadband THz radiation from a ZGP crystal excited using a pulse that had a duration of 100 fs and a central wavelength of 1.3 μm [53]. The inset compares the spectral distributions of the generated THz radiation for ZGP and GaAs crystals. OR phase-matching contours for ZGP crystals cut along the (c) (110) and (d) (012) crystal planes [54]. (e) THz time-domain electric field signals and (f) the associated spectra produced using (110)-cut CSP, ZGP, and CdGeP₂ crystals [28]. 20

Fig. 1.10. Temperature-dependent (a) ordinary and (b) extraordinary refractive indices of an AgGaS₂ crystal [69]. Temperature-dependent (c) ordinary and (d) extraordinary absorption coefficients of an AgGaS₂ crystal [69]. (e) Refractive indices and (f) extinction coefficients along the [100], [010], and [001] crystallographic axes of an LiInSe₂ crystal [72]. 27

Fig. 1.11. (a) THz time-domain signals and (b) the associated spectra produced using LiGaSe₂, LiGaS₂, LiInSe₂, and LiInS₂ crystals [75]. (c,d) THz time-domain signals and (e) the associated spectra produced using an LiGaS₂ crystal. In (e), the spectra centered at ~13 and 22 THz were obtained using a GaSe crystal [76]. 29

Fig. 1.12. (a) EO time-domain signal and (b) the associated spectrum obtained using an AgGaS₂ crystal [82]. (c) EO time-domain signals obtained using Zn_{1-x}Cd_xTe crystals [87]. (d) EO spectra obtained using Zn_{1-x}Mn_xTe crystals [66]. 31

Fig. 1.13. (a) DFG THz radiation spectral power produced from a GaAs planar waveguide [102]. The theoretical spectral power fits, obtained using monochromatic excitation electric fields and excitation electric fields having 100 GHz bandwidths, are shown for comparison [102]. (b) DFG THz radiation generated from a GaP planar waveguide [103]. 38

Fig. 1.14. (a) Illustration depicting THz radiation generation from a poled polymer-coated cylindrical metal wire waveguiding arrangement [94]. (b) Spectral density of OR THz radiation generated from the waveguide illustrated in (a) [94]. (c) DFG THz radiation produced by a GaP rectangular waveguide that had widths of 200, 500, and 1000 μm [106]. (d) DFG THz radiation generated by GaP ridge waveguides that had ridge widths of 200, 300, 500, and 1000 μm , where the inset illustrates a scanning electron microscope image of a GaP ridge waveguide that had a ridge width of 300 μm [107]...... 40

Fig. 1.15. (a) Scanning electron microscope image of a GaP photonic crystal waveguide that had a 300 μm -wide line defect [108]. (b) DFG THz radiation produced by the waveguide shown in (a) [108]...... 41

Fig. 1.16. (a) Cross-sectional illustration of an acrylate-poled polymer-acrylate planar waveguide embedded within a parallel plate waveguide [110]. (b) THz electric field pulses produced by the waveguiding arrangement depicted in (a) for waveguide lengths of 1, 2, and 3 mm [110]. (c) An AlGaAs-GaAs-AlGaAs ridge waveguide embedded within a metallic slit waveguide [111]. (d) A GaP ridge waveguide embedded within a rectangular Si waveguide [112]. (e,f) A waveguiding arrangement that consisted of a photonic crystal waveguide, (e), with an embedded AlGaAs ridge waveguide, (f) [114]. (g) Illustration of a Ti:LN channel waveguide embedded within a quartz-LN-HDPE waveguide [115]. (h) DFG THz radiation produced by the waveguiding arrangement depicted in (g) [115]...... 43

Fig. 1.17. (a) Illustration of a LN-MgO:LN-PET planar waveguide showing the generated THz radiation being emitted as Cherenkov waves [116]. (b) Spectra of the DFG THz radiation produced by the waveguide in (a) [116]. 45

Fig. 1.18. (a) Illustration of a Bk7-LN-Si prism leaky planar waveguide, which depicts the generated THz radiation being emitted as Cherenkov waves [118]. (b) THz electric field pulses produced by the Bk7-LN-Si prism leaky planar waveguide that had an LN thickness of 50 μm and (c) the spectra obtained from the leaky planar waveguide that had LN thicknesses of 30 and 50 μm [118]. (d) Illustration of the metal-air-LN-Si prism leaky planar waveguide, showing the generated THz radiation being emitted as Cherenkov waves [121]. (e) THz electric field pulses produced by the metal-air-LN-Si prism leaky planar waveguide that had no air gap and an infinite air gap and (f) the spectral density of the THz electric field pulses shown in (e) [121]. (g) Illustration of the Si-LN-Si leaky planar waveguide, depicting the propagation direction of the generated THz radiation [123]. (h) THz electric field pulse produced by the Si-LN-Si leaky planar waveguide and (i) the spectral density of the THz electric field pulses shown in (h) [123]..... 48

Fig. 1.19. (a) Cross-sectional image of an MgO:LN ridge waveguide and (b) a semi-cone Si lens that surrounded the ridge waveguide [124]. (c) Spectral power of the OR THz radiation produced by the MgO:LN ridge waveguide [124]. (d) Illustration of a PPMgLN ridge waveguide [126]. DFG THz radiation produced by PPMgLN ridge waveguides having grating periods of (e) 91 μm and (f) 137 μm [126]. 50

Fig. 1.20. (a) An Al-GaAs-Al parallel plate waveguide and (b) the spectral density of the OR THz radiation generated by this waveguiding structure [128]. The inset depicts the generated THz electric field pulse [128]. (c) Illustration of GaP rectangular waveguides that had cross-sectional dimensions of 600 $\mu\text{m} \times 400 \mu\text{m}$ and 1000 $\mu\text{m} \times 700 \mu\text{m}$ and (d) the spectral densities of the OR THz radiation produced by these waveguides [129]. The inset shows the generated THz electric field pulses [129]. (e-g) Illustration of a tilted wavefront excitation pulse propagating through a LN planar waveguide and the guided generated THz radiation, where (e) depicts the earliest instant

in time, (f) shows a subsequent instant in time, and (g) illustrates the latest instant in time [131]. (h) DFG THz radiation produced by a LN planar waveguide at various excitation pulse wavefront tilt angles [131]. For comparison, the dotted line represents THz radiation generation from a bulk LN crystal [131]. DFG THz radiation produced by planar and rectangular PPLN waveguides in the (i) forward direction and (j) backward direction [132]. 53

Fig. 2.1. Displacement of an electron cloud with respect to its heavier (i.e. fixed) nucleus (a) at equilibrium, (b) in the regime described by a linear restoring force, and (c) in the regime described by a nonlinear restoring force. (d) Displacement of an atom with respect to another heavier (i.e. fixed) atom. (e) Representative restoring force curve. 60

Fig. 2.2. (a) SHG, (b) SFG, and (c) DFG processes depicted as photons incident on a medium and photons exiting the medium. (d) SHG, (e) SFG, and (f) DFG processes depicted in terms of energy conservation diagrams. The photons in (f) signify that frequency components at ω_2 must initially be present in order for the DFG process to occur. 61

Fig. 2.3. (a) Time-domain and (b) frequency-domain representation of $\mathbf{E}_i^w(z, t)$ 78

Fig. 2.4. (a) Refractive index and (b) extinction coefficient of a medium described using $N=5 \times 10^{22} \text{ cm}^{-3}$, $\omega_0/(2\pi)=4000 \text{ THz}$, and $\gamma/(2\pi)=20 \text{ THz}$ 79

Fig. 2.5. (a) The bound electric charge displacement of $\mathbf{s}^{w,(2)}(z, t)$, as well as each of its contributions. (b) Fourier transform of $\mathbf{s}^{w,(2)}(z, t)$ obtained over a temporal window of 500 fs. (c) The maximum amplitudes of $\mathbf{s}_{2\omega_1}^{w,(2)}(z, t)$, $\mathbf{s}_{2\omega_2}^{w,(2)}(z, t)$, $\mathbf{s}_{\omega_1+\omega_2}^{w,(2)}(z, t)$, $\mathbf{s}_{\omega_1-\omega_2}^{w,(2)}(z, t)$, and $\mathbf{s}_0^{w,(2)}(z)$ at various positions within the medium. The vertical dotted-line at $z=70 \mu\text{m}$ corresponds to the recorded position of the time-domain bound electric charge displacements shown in (a). 80

Fig. 2.6. (a) The electric field of $\mathbf{E}_g^w(z, t)$, as well as each of its contributions. (b) Fourier transform of $\mathbf{E}_g^w(z, t)$ obtained over a temporal window of 500 fs. The Fourier transform of $\mathbf{E}_i^w(z, t)$ is shown for comparison. (c) The maximum amplitudes of $\mathbf{E}_{2\omega_1}^w(z, t)$, $\mathbf{E}_{2\omega_2}^w(z, t)$, $\mathbf{E}_{\omega_1+\omega_2}^w(z, t)$, and $\mathbf{E}_{\omega_1-\omega_2}^w(z, t)$ at various positions within the medium. The vertical dotted-line represents $z=70 \mu\text{m}$, which correspond to the recorded position of the time-domain electric fields in (a). 84

Fig. 2.7. (a) A hypothetical representation of a 2D unit cell with the atomic constituents at their equilibrium positions. The various colors represent different atomic constituents. (b) A perturbation causing the inner atomic constituents to be displaced along the x axis, where such constituents may exhibit a displacement in both the x and y axes when returning to their equilibrium positions. 86

Fig. 2.8. Frequency-domain depiction of the (a) SHG and (b) OR processes. 93

Fig. 2.9. (a) Time-domain and (b) frequency-domain representation of $\mathbf{E}_i^p(z, t)$ 94

Fig. 2.10. (a) The bound electric charge displacement of $\mathbf{s}_{OR}^{p,(2)}(z, t)$, $\mathbf{s}_{SHG}^{p,(2)}(z, t)$, and $\mathbf{s}^{p,(2)}(z, t)$. (b) Fourier transform of $\mathbf{s}^{p,(2)}(z, t)$. (c) The maximum amplitudes of $\mathbf{s}_{OR}^{p,(2)}(z, t)$ and $\mathbf{s}_{SHG}^{p,(2)}(z, t)$, where the vertical dotted-line at $z=500 \mu\text{m}$ corresponds to the recorded position of the time-domain bound electric charge displacements shown in (a). 95

Fig. 2.11. (a) The electric field of $\mathbf{E}_{OR}^p(z, t)$, $\mathbf{E}_{SHG}^p(z, t)$, and $\mathbf{E}_g^p(z, t)$. (b) Fourier transform of $\mathbf{E}_g^p(z, t)$. The Fourier transform of $\mathbf{E}_i^p(z, t)$ is shown for comparison. (c) The maximum amplitudes of $\mathbf{E}_{OR}^p(z, t)$ and $\mathbf{E}_{SHG}^p(z, t)$ at various positions within the medium, where the vertical dotted-line at $z=500 \mu\text{m}$ corresponds to the recorded position of the time-domain electric fields shown in (a). 97

Fig. 3.1. (a) Schematic of the THz-TDS system typically used to conduct experimental measurements. ‘M’ indicates planar mirrors, ‘PM’ indicates parabolic mirrors, and ‘L’ indicates lenses. (b) Photograph of the THz-TDS system. 106

Fig. 3.2. (a) Raw voltage signal obtained using the THz-TDS system and its corresponding electric field magnitude. (b) The associated spectral density (i.e. Fourier transform). 110

Fig. 4.1. Unit cell structure of the CSP crystal. The optical excitation pulse and the generated THz radiation are polarized perpendicular and parallel to the crystal’s *c*-axis, respectively. 113

Fig. 4.2. (a) Extraordinary refractive indices and (b) extraordinary extinction coefficients of the CSP and ZGP crystals. (c) Extraordinary absorption coefficients for CSP, ZGP, ZnTe, and LN crystals. The experimental data for ZnTe and LN are obtained from Refs. [147] and [148], respectively. 115

Fig. 4.3. (a) THz time-domain signals and (b) spectral densities of the electric fields generated from the CSP and ZGP crystals. 117

Fig. 4.4. The coherence lengths of the CSP and ZGP crystals. 118

Fig. 4.5. THz peak-to-peak electric field as a function of the peak intensity of the optical excitation pulse. 119

Fig. 4.6. (a) Time-domain electric field pulses transmitted through the AGS crystal, having polarizations oriented along the ordinary and extraordinary axes of the crystal. (b) Spectral density of the transmitted pulses, where the phonon resonances cause absorption at several frequencies across the measured spectra. The free-space THz radiation signal and spectrum are shown as a reference. 121

Fig. 4.7. (a) Ordinary and (b) extraordinary refractive indices and extinction coefficients of the uniaxial AGS crystal. The shaded area in (a) corresponds to the region where n_o and κ_o are not

calculated due to the spectral density vanishing. (c) OR coherence length of the AGS crystal for the scenario where the excitation pulse polarization is oriented along the ordinary crystal axis.

..... 122

Fig. 4.8. (a) THz time-domain electric field pulse generated by the AGS crystal via the process of OR. (b) Spectral density of the generated THz radiation pulse, showing absorption from the lowest-frequency B_2 mode at 1.6 THz. 124

Fig. 4.9. (a) THz peak-to-peak electric field measured upon varying the angle between the polarization of the optical excitation pulse and the crystal's c -axis. (b) Peak-to-peak THz electric field measured for various peak excitation pulse intensities in the AGS crystal. 125

Fig. 4.10. (a) Schematic showing the setup implemented to perform OR THz radiation generation experiments using the BGS crystal. x_r , y_r , and z_r define the reference coordinates. (b) An illustration of the unit cell of the BGS crystal. The near-IR excitation electric field polarization and the generated THz radiation electric field polarization are shown. 128

Fig. 4.11. (a) THz time-domain signals generated by exciting the BGS crystal along its X crystallo-physical axis (i.e. $\theta_c = \theta_p$) and (b) the corresponding spectral power. (c) Spectral powers at the frequencies of 1.97 and 2.34 THz as a function of θ_p . The inset shows an illustrative representation of the orientations of \vec{E}_{exc} and \vec{E}_{THZ} with respect to the X , Z , x_r , and z_r axes. Here, the excitation polarization and crystal orientation are fixed using the relationship of $\theta_c = \theta_p$ 130

Fig. 4.12. (a) THz time-domain signals generated by exciting the BGS crystal along its Z crystallo-physical axis (i.e. $\theta_c = \theta_p + 90^\circ$) and (b) the corresponding power spectra. (c) Spectral powers at the frequencies of 1.97 and 2.34 THz as a function of θ_p . The inset shows the illustrative representation

of the orientations of \vec{E}_{exc} and \vec{E}_{THZ} with respect to the X , Z , x_r , and z_r axes. Here, the excitation polarization and crystal orientation are fixed using the relationship of $\theta_c = \theta_p + 90^\circ$ 131

Fig. 4.13. (a) THz time-domain signals when the X crystallo-physical axis of the BGS crystal is oriented along the transmission axis of the wire-grid polarizer (i.e. $\theta_c = 90^\circ$) and (b) the corresponding power spectra. (c) Spectral powers at the frequencies of 1.97 and 2.34 THz as a function of θ_p . The inset shows the illustrative representation of the orientations of \vec{E}_{exc} and \vec{E}_{THZ} with respect to the X , Z , x_r , and z_r axes for $\theta_c = 90^\circ$ 132

Fig. 4.14. (a) THz time-domain signals when the Z crystallo-physical axis of the BGS crystal is oriented along the transmission axis of the wire-grid polarizer (i.e. $\theta_c = 0^\circ$) and (b) the corresponding power spectra. (c) Spectral powers at the frequencies of 1.97 and 2.34 THz as a function of θ_p . The inset shows the illustrative representation of the orientations of \vec{E}_{exc} and \vec{E}_{THZ} with respect to the X , Z , x_r , and z_r axes for $\theta_c = 0^\circ$ 133

Fig. 4.15. Illustration of the experimental arrangement for (a) the BGS crystal when $\vec{E}_{exc} \parallel X$, (b) the BGS crystal when $\vec{E}_{exc} \parallel Z$, and (c) the ZnTe crystal. The generated THz radiation is passed through a wire-grid polarizer to obtain the component polarized along the Z crystallo-physical axis. This THz radiation is subsequently recorded using a 500 μm -thick (110)-cut ZnTe EO sampling crystal. The (110)-cut ZnTe EO crystal orientation is optimized for maximum THz radiation generation..... 134

Fig. 4.16. (a) Time-domain signals and (b) power spectra for THz radiation produced using the $\vec{E}_{exc} \parallel X$ and $\vec{E}_{exc} \parallel Z$ BGS crystal configurations. For comparison, broadband THz radiation emission from the ZnTe crystal arrangement is shown. 136

Fig. 4.17. Spectral densities at the frequencies of (a) 1.97 THz and (b) 2.34 THz, as generated from the BGS crystal $\vec{E}_{exc} \parallel X$ configuration and the ZnTe crystal configuration. Spectral densities at the frequencies of (c) 1.97 THz and (d) 2.34 THz, as generated from the BGS crystal $\vec{E}_{exc} \parallel Z$ configuration and the ZnTe crystal configuration. 139

Fig. 4.18. (a) The unit cell and (012)-cut plane of the ZGP crystal. The illustration shows the polarization of the THz electric field in the EO detection measurements, which is rotated 110° with respect to the [100] crystallographic axis about the direction normal to the (012)-cut plane. \vec{k} is the wavevector of the THz electric field. (b) Schematic of the (012)-cut plane showing the THz polarization direction. 141

Fig. 4.19. (a) Refractive index and extinction coefficient of ZGP over the frequency range of 0.1-3.8 THz. (b) Absorption coefficient of ZGP over the frequency range of 0.1-3.8 THz. 142

Fig. 4.20. (a) THz time-domain pulses and (b) spectral density obtained using ZGP, ZnTe, and ZnSe EO crystals. Spectral densities are scaled to facilitate bandwidth comparison. 143

Fig. 4.21. The normalized amplitude of the response function for crystal thicknesses of (a) 500 μm and (b) 1080 μm 145

Fig. 5.1. An illustration of the LN crystal having a thickness ℓ and an excitation electric field polarization at the angle of θ_p with respect to the crystal's c -axis. 158

Fig. 5.2. (a) Refractive index and (b) extinction coefficient for the extraordinary LN crystal axis in the THz frequency regime. (c) Refractive index and (d) extinction coefficient for the ordinary LN crystal axis in the THz frequency regime. (e) Extraordinary and ordinary refractive indices in the optical frequency regime. The experimental data is obtained from Refs. [171,172] and the LN crystal is taken to be lossless in the optical regime. 161

Fig. 5.3. Second-order nonlinear susceptibility elements of LN for (a) $\chi_{33}^{(2)}(\Omega, \omega, \Omega - \omega)$, (b) $\chi_{31}^{(2)}(\Omega, \omega, \Omega - \omega)$, and (c) $\chi_{15}^{(2)}(\Omega, \omega, \Omega - \omega)$. The curve fits are calculated using Miller's rule with the experimental data from Refs. [98,174,175]. 162

Fig. 5.4. (a) The z -component of the spectral power obtained using the dispersive $\chi_{33}^{(2)}(\Omega, \omega, \Omega - \omega)$ and the frequency-independent $\chi_{33}^{(2)}=348$ pm/V. (b) Relative spectral power calculated when implementing the dispersive $\chi_{33}^{(2)}(\Omega, \omega, \Omega - \omega)$ and the frequency-independent $\chi_{33}^{(2)}=348$ pm/V..... 163

Fig. 5.5. (a) Coherence length for THz radiation produced in the forward direction. (b) The x -component of the spectral power recorded in free-space. (c) Coherence length for THz radiation produced in the backward direction. (d) The x -component of the spectral power recorded near the input face of the LN crystal. 165

Fig. 5.6. (a) The z -component and (b) the x -component of the spectral power at various electric field polarization angles..... 166

Fig. 5.7. (a) Magnitude and (b) phase of $\chi_{36}^{(2)}(\Omega)$ for ZnTe, as defined by the Faust-Henry model for dispersion. The Faust-Henry curve fitting parameters are obtained from Refs. [96,166]..... 170

Fig. 5.8. Illustration of the ZnTe crystal (a) perpendicular and (b) parallel to the propagation direction of the electric fields. The ZnTe crystal is excited at a polarization angle of 45° relative to the c -axis of the crystal. 171

Fig. 5.9. (a) THz time-domain electric fields and (b) spectral powers produced by OR in thin film ZnTe crystals having $\ell=0.1-1$ μm 172

Fig. 5.10. (a) THz time-domain electric fields and (b) spectral powers from ZnTe crystals having $\ell=10\text{-}40\ \mu\text{m}$. The time-domain signals and the power spectra are to scale with the data presented in Fig. 5.9. 173

Fig. 5.11. (a) THz time-domain electric fields and (b) spectral powers for THz radiation that is polarized along the x and z axes, calculated for the $\ell=1\ \mu\text{m}$ ZnTe crystal. 174

Fig. 5.12. Schematic of the $\text{SiO}_2\text{-ZnTe-air}$ planar waveguide along the (a) $y\text{-}z$ and (b) $x\text{-}y$ cross-sections, which show the Gaussian electric field pulse being coupled into the waveguide and the generated THz radiation being coupled out of the waveguide. (c) THz time-domain electric field and (d) spectral power of the generated THz radiation. 175

Fig. 6.1. Schematic showing the sub-wavelength $\text{SiO}_2\text{-LN-SiO}_2$ waveguiding geometry incorporating Si prisms. Depicted in the illustration is the waveguide width, W , length, L , and core thickness, T . The z -polarized optical excitation pulse is coupled into the $\text{SiO}_2\text{-LN-SiO}_2$ waveguide and the generated THz electric field has a polarization oriented along the z axis. 179

Fig. 6.2. (a) LN, (b) SiO_2 , and (c) Si refractive indices and extinction coefficients. The experimental data is obtained from Refs. [148,171,172] for LN, Ref. [182] for SiO_2 , and Refs. [182,183] for Si. The inset in (a) displays the LN extraordinary refractive index at frequencies of 100-500 THz. 180

Fig. 6.3. Magnitude and phase of the $\chi_{33}^{(2)}$ second-order nonlinear susceptibility element of LN. The experimental data is obtained from Refs. [30, 98, 170, 174,188–191]. 182

Fig. 6.4. (a) THz time-domain electric field generated from a $\text{SiO}_2\text{-LN-SiO}_2$ waveguide having $T=500\ \text{nm}$, $L=100\ \mu\text{m}$, and excited by a $\tau=10\ \text{fs}$, $\xi_{exc}/W=10\ \text{nJ/cm}$, 780 nm optical pulse. The time-domain signal is recorded after exiting the Si prisms. (b) NESD of the THz radiation measured after exiting the Si prisms. (c-f) Time-averaged spatial distribution of the electric field

at frequencies of 10, 20, 30, and 40 THz propagating outwards from the waveguide. The electric field values in (e) and (f) are scaled by a factor of 5. 183

Fig. 6.5. (a) NESD of the THz radiation emitted from a waveguide having $T=0.3-5 \mu\text{m}$, $L=100 \mu\text{m}$, and being excited by a $\tau=10 \text{ fs}$, $\xi_{exc}/W=10 \text{ nJ/cm}$ optical pulse. (b) The effective refractive index of the excitation mode (i.e. n_{eff}^m), as well as the effective group refractive index of the excitation mode (i.e. $n_{eff,g}^m$) at $T=0.3, 0.5$, and $5 \mu\text{m}$. (c) ξ_{OR}/W contained in the generated THz frequency components. The inset shows the intensity profiles of the modes. 185

Fig. 6.6. (a) NESD of the THz electric field emitted from a waveguide having $T=500 \text{ nm}$, $L=100 \mu\text{m}$, and excited by $\tau=7-100 \text{ fs}$, $\xi_{exc}/W=10 \text{ nJ/cm}$ optical pulses. (b) ξ_{OR}/W of the generated THz radiation. 186

Fig. 6.7. (a) NESD and (b) ξ_{OR}/W emitted from waveguides having $L=100-300 \mu\text{m}$, $T=500 \text{ nm}$, and excited by a $\tau=7 \text{ fs}$, $\xi_{exc}/W=10 \text{ nJ/cm}$ optical pulse. 187

Fig. 6.8. (a) NESD and (b) ξ_{OR}/W generated using waveguides having $L=100 \mu\text{m}$, $T=500 \text{ nm}$, and excited by $\tau=7 \text{ fs}$, $\xi_{exc}/W=2-10 \text{ nJ/cm}$ optical pulses. 188

Fig. 6.9. A schematic of the sub-wavelength planar LN waveguide used to generate THz radiation. The LN crystal's c -axis is oriented along the z axis. 189

Fig. 6.10. (a) Spatial intensity profile of the 5.6 THz mode supported by waveguides having core thicknesses of (i) 300 nm, (ii) 500 nm, (iii) 1 μm , and (iv) 5 μm . The green, red, and blue regions represent the LN crystal, the SiO_2 surrounding layers, and free-space, respectively. (b) The propagation length (i.e. L_p) and the OR coherence length (i.e. L_c^{OR}) of the waveguide mode at a frequency of 5.6 THz. The inset shows the effective refractive index of the THz mode. (c) Spatial

distribution of the electric field obtained by propagating a 5.6 THz electric field pulse along a waveguide having $L=100 \mu\text{m}$ and $T=500 \text{ nm}$ 191

Fig. 6.11. (a) Spatial distribution of the THz electric field produced by a waveguide having $T=500 \text{ nm}$ and $L=100 \mu\text{m}$. (b) THz time-domain electric field pulse generated by the planar LN waveguide and recorded in free-space. The arrow indicates the time at which the electric field distribution in (a) is recorded. (c) NESD of the THz radiation produced by the waveguide and emitted into free-space. The frequency components being considered are those emitted in the forward direction along the y axis with respect to the waveguide's end face..... 194

Fig. 6.12. NESD of THz radiation produced by waveguides having (a) $L=100 \mu\text{m}$ and $T=0.3\text{-}5 \mu\text{m}$, and (b) $T=500 \text{ nm}$ and $L=20\text{-}200 \mu\text{m}$ 195

Fig. 6.13. Conversion efficiency of waveguides having $L=100 \mu\text{m}$ and $T=0.3\text{-}5 \mu\text{m}$, as well as $T=500 \text{ nm}$ and $L=20\text{-}200 \mu\text{m}$ 196

Fig. 6.14. Illustration of the $\text{SiO}_2\text{-LN-air}$ planar waveguiding arrangement used for the phase-matched backward DFG process. 198

Fig. 6.15. The backward DFG coherence length calculated using (a) the $\text{TE}_0 \vec{E}_i$ mode for the $T=5 \mu\text{m}$ planar waveguide and (b) the $\text{TE}_2 \vec{E}_i$ mode for the $T=25 \mu\text{m}$ planar waveguide. The insets in (a) and (b) show the $\text{TE}_0 \vec{E}_i$ mode and the $\text{TE}_2 \vec{E}_i$ mode, respectively. The black areas identify the coherence lengths, where perfect phase-matching occurs along the red lines. In (a) and (b), perfect-phase matching occurs at $f_i=2.4$ and 2.6 THz , respectively. 199

Fig. 6.16. (a) THz time-domain electric field pulses and (b) the associated spectral powers generated in the $L=100\text{-}500 \mu\text{m}$ and $T=5 \mu\text{m}$ planar waveguides. The electric fields are recorded

at the planar waveguide's input. The inset shows the conversion efficiency for the $L=100-500 \mu\text{m}$ planar waveguides..... 200

Fig. 6.17. (a) THz time-domain electric field pulses and (b) the associated spectral powers produced in the $T=2-5 \mu\text{m}$ and $L=500 \mu\text{m}$ planar waveguides. The electric fields are recorded at the input of the planar waveguide. (c) The conversion efficiency (i.e. η_{DFG}) and \vec{E}_i propagation length (i.e. L_p) for the $T=2-5 \mu\text{m}$ planar waveguides. The inset shows the overlap integral values. 202

Fig. 6.18. (a) THz time-domain electric field pulses and (b) the associated spectral powers produced in the $T=15-25 \mu\text{m}$ and $L=500 \mu\text{m}$ planar waveguides. The electric fields are recorded at the input of the planar waveguide. (c) The conversion efficiency (i.e. η_{DFG}) and \vec{E}_i propagation length (i.e. L_p) for the $T=15-25 \mu\text{m}$ planar waveguides. The inset shows the overlap integral values. 204

Fig. 6.19. Schematic of the LN planar waveguide depicting the (a) TE_0 , (b) TE_1 , and (c) TE_2 excitation modes. (d) The effective group refractive indices for the TE_0 , TE_1 , and TE_2 excitation modes. 206

Fig. 6.20. (a) THz time-domain electric field generated from the TE_0 , TE_1 , and TE_2 excitation modes of a LN planar waveguide and from a $500 \mu\text{m}$ -thick bulk ZnTe crystal. The red arrows indicate pulses from reflections in the EO crystal. (b) Spectral densities obtained by isolating the individual pulses at $t=4, 10, \text{ and } 17 \text{ ps}$. The inset shows the THz spectral density of the bulk ZnTe crystal. 209

Fig. 6.21. (a) Energy and (b) conversion efficiency for the generated THz radiation. $\xi_{OR} \propto I_p^2$ and $\eta_{OR} \propto I_p$ are the theoretical equations describing this second-order nonlinear process. 210

Fig. 7.1. (a) Cross-sectional schematic of the $W=400$ nm and $T=780$ nm MLNM nanoplasmonic waveguide. (b) $\lambda_{exc}=1550$ nm and (c) $\lambda_{SHG}=775$ nm modal intensity distributions supported by the MLNM nanoplasmonic waveguide. (d) Cross-section of the $W=400$ nm and $T=100$ nm LNHP waveguide. (e) $\lambda_{exc}=1550$ nm and (f) $\lambda_{SHG}=775$ nm modal intensity distributions supported by the LNHP waveguide..... 216

Fig. 7.2. (a) Effective refractive indices of the MLNM nanoplasmonic and LNHP modes, illustrating phase-matching between $\lambda_{exc}=1550$ nm and $\lambda_{SHG}=775$ nm. (b) Coherence length for the MLNM nanoplasmonic and LNHP waveguides. (c) Propagation lengths of the excitation and SHG wavelengths for the MLNM nanoplasmonic and LNHP waveguides. 217

Fig. 7.3. Magnitude of the time-averaged spatial electric field distribution recorded at $\lambda_{SHG}=775$ nm for the (a) MLNM nanoplasmonic and (b) LNHP waveguides. (c) SHG time-domain electric field pulses and (d) SHG spectral density recorded in the waveguides near the positions of maximum electric fields..... 219

Fig. 7.4. Conversion efficiency for various lengths of the MLNM nanoplasmonic and LNHP waveguides. For comparison, the conversion efficiency is determined in a 400 nm \times 509 nm phase-matched MLN waveguide with a 100 nm thick gold layer situated on the LN, as well as a 400 nm \times 837 nm phase-matched LN photonic waveguide (see insets). 222

Fig. 7.5. Illustration of the CSP/LN photonic waveguide. A 1550 nm excitation pulse is converted to 775 nm via nonlinear effects in the photonic waveguides. The cross-sections of the photonic waveguides are cut along the (110) and (010) planes of the CSP and LN crystals, respectively. 224

Fig. 7.6. (a) The effective refractive indices of the TE_{00} excitation mode and TM_{20} SHG mode for the 600 nm \times 650 nm CSP photonic waveguide. The insets depict the transverse mode profiles at

wavelengths of $\lambda_{exc}=1550$ nm and $\lambda_{SHG}=775$ nm. (b) The effective refractive indices of the TM_{00} excitation mode and TM_{02} SHG mode for the 600 nm \times 987 nm LN photonic waveguide. The insets depict the $\lambda_{exc}=1550$ nm and $\lambda_{SHG}=775$ nm transverse mode profiles. (c) Coherence length between the excitation and SHG frequency components propagating along the CSP and LN photonic waveguides..... 226

Fig. 7.7. (a) Conversion efficiency for various photonic waveguide lengths. Time-averaged spatial electric field distribution at $\lambda_{SHG}=775$ nm on the (b) y - x and (c) x - z planes of the $W=600$ nm \times $T=650$ nm \times $L=30$ μ m CSP photonic waveguide. Time-averaged spatial electric field distribution at $\lambda_{SHG}=775$ nm on the (d) y - z and (e) x - z planes of the $W=600$ nm \times $H=987$ nm \times $L=30$ μ m LN photonic waveguide. The transverse distributions in (c) and (e) are obtained along the dotted lines in (b) and (d), respectively..... 228

Fig. 7.8. (a) SHG time-domain electric field signals and (b) their associated spectral densities. 229

Fig. 7.9. Schematic of the coupling arrangement used to angularly excite the LN waveguide, where θ_1 is the coupling angle directed towards the y - z plane and θ_2 is the coupling angle directed towards the x - y plane. 231

Fig. 7.10. (a) TM_{10} mode supported at the excitation wavelength of $\lambda_{exc}=800$ nm. (b) TM_{40} mode supported at the SHG wavelength of $\lambda_{SHG}=400$ nm. (c) Magnitude of the coupling coefficient for the TM_{10} excitation mode. 232

Fig. 7.11. (a) SHG time-domain signal produced from the $W=670$ nm, $T=800$ nm, and $L=250$ μ m waveguide at $\theta_1=40^\circ$. (b) Spectral power of the SHG signal for $\theta_1=0^\circ$ and $\theta_1=40^\circ$. Time-averaged

spatial power distributions at $\lambda_{SHG}=400$ nm along the (c) x - y plane and (d) z - y plane of the waveguide for $\theta_1=40^\circ$ 234

Fig. 7.12. (a) TM_{11} mode supported at the excitation wavelength of $\lambda_{exc}=800$ nm. (b) TM_{42} mode supported at the SHG wavelength of $\lambda_{SHG}=400$ nm. (c) Magnitude of the coupling coefficient for the TM_{11} mode. 235

Fig. 7.13. (a) SHG time-domain signal produced from the $W=600$ nm, $T=940$ nm, and $L=250$ μ m waveguide at $\theta_1=\theta_2=40^\circ$. Time-averaged spatial power distributions at $\lambda_{SHG}=400$ nm along the (b) x - y plane and (c) z - y plane of the waveguide for $\theta_1=\theta_2=40^\circ$. (d) Spectral power of the SHG signal for $\theta_1=\theta_2=0^\circ$ and $\theta_1=\theta_2=40^\circ$ 237

Fig. 7.14. Schematic of the experimental arrangement, which implements an acylindrical lens to couple the excitation pulse into the planar waveguide. The acylindrical lens is necessary to obtain the required line focus to couple the light into the planar waveguide. 238

Fig. 7.15. (a) FESEM image showing the cross-section of the SiO_2 -LN-air planar waveguide having a core thickness of 775 nm. Electric field distributions supported by the SiO_2 -LN-air planar waveguide at (b) the excitation wavelength of $\lambda_{exc}=800$ nm and (c) its SHG wavelength of $\lambda_{exc}=400$ nm. 240

Fig. 7.16. (a) Effective refractive indices of the excitation and SHG modes, where perfect phase-matching is observed at the wavelengths of $\lambda_{SHG}=395$ nm and $\lambda_{SHG}=402.4$ nm. (b) Coherence length for the TE_0 excitation and TE_3 SHG modes, as well as the TE_1 excitation and TE_4 SHG modes. 241

Fig. 7.17. (a) FDTD simulations showing the modes excited in the waveguide via coupling at the incident angles of (a) $\theta_i=0^\circ$ and (b) $\theta_i=10^\circ$. To excite the TE_1 mode necessary for phase-matched

SHG, the optical excitation pulse must be coupled in at an off-normal-incidence angle. The $y:x$ spatial aspect ratio of these images is 155:1. 243

Fig. 7.18. (a) Image showing the perfectly phase-matched SHG light produced at all positions along the 2.8 mm-long planar waveguide having a LN layer thickness of 775 nm. (b) The SHG signal measured from the planar waveguide having a thickness of 775 nm, where phase-matched SHG occurs having a central-wavelength of $\lambda_{SHG}=402.4$ nm and exhibiting the narrow linewidth of 1.5 nm. The inset shows the spectrum of the laser pulse that is exciting the planar waveguide, which encompasses wavelength components between $\lambda_{exc}=770-840$ nm. 244

Fig. 7.19. (a) Energy of the SHG pulse and (b) SHG conversion efficiency with respect to the energy of the excitation pulse. As expected, $\xi_{SHG} \propto \xi_{exc}^2$ and $\eta_{SHG} \propto \xi_{exc}$ 246

Fig. 8.1. Schematic of the multi-band generation planar waveguide producing Ω_{SFG} and Ω_{DFG} . The c -axis of the LN crystal is aligned along the z axis. 251

Fig. 8.2. (a) Intensity distribution of representative excitation modes at $\lambda_1=806$ nm and $\lambda_2=1009$ nm. (b) Intensity distribution of a representative SFG mode at $\lambda_{SFG}=448$ nm. The modal intensity distributions shown in (a) and (b) are calculated for the $T=700$ nm planar waveguide. The coherence length for the (c) $T=700$ nm and (d) $T=600$ nm planar waveguides. 253

Fig. 8.3. Time-averaged spatial distribution of the electric field at the wavelengths of (a) $\lambda_{SFG}=448$ nm and (b) $\lambda_{DFG}=4$ μ m. 254

Fig. 8.4. (a) Time-domain electric fields of the SFG and DFG radiation after exiting the planar waveguide. Power spectra of the radiation produced through (b) SFG and (c) DFG. Time-frequency spectra for the (d) SFG and (e) DFG electric fields. 256

Fig. 8.5. (a) SFG and (b) DFG spectra showing the wavelength distribution for the $T=700$ nm planar waveguide. (c) SFG and (d) DFG spectra showing the wavelength distribution for the $T=600$ nm planar waveguide. 257

Fig. 8.6. (a) Planar waveguide depicting excitation by the near-IR pulse, as well as the SHG and THz radiation generation. (b) Schematic showing the planar waveguide, prism dimensions, and LN c -axis..... 259

Fig. 8.7. (a) The effective refractive indices calculated for the excitation modes (dotted lines) and the SHG modes (solid lines) supported by the LN planar waveguide. (b) TE_0 mode electric field profile at $\lambda_{exc}=806$ nm and (c) TE_2 mode electric field profile at $\lambda_{SHG}=403$ nm. 262

Fig. 8.8. SHG spectral power generated by the LN planar waveguide. 263

Fig. 8.9. The Cherenkov angle and intensity distributions for the near-IR excitation modes at $\lambda_c^{exc}=800$ nm. 264

Fig. 8.10. (a) THz radiation pulses generated by the TE_0 and TE_1 near-IR modes and (b) their associated spectral powers. The generated THz radiation is sampled using a 500 μm -thick ZnTe EO crystal..... 265

Fig. A1. Frequency-conversion occurring within a non-centrosymmetric crystal due to second-order nonlinear interactions. The various generation events are vertically offset.300

List of Fundamental constants

$m_e=9.11\times 10^{-31}$ kg	Electron mass
$q=1.602\times 10^{-19}$ C	Elementary charge
$\mu_0=4\pi\times 10^{-7}$ H/m	Permeability free-space
$\epsilon_0=8.854\times 10^{-12}$ F/m	Permittivity of free-space
$c=2.998\times 10^8$ m/s	Speed of light in a vacuum

List of Abbreviations

AGS	AgGaSe ₂
ABCD	Air biased coherent detection
BWO	Backward wave oscillator
BGS	BaGa ₄ Se ₇
CSP	CdSiP ₂
DFG	Difference frequency generation
DC	Direct current
EL	Electroluminescence
EM	Electromagnetic
EO	Electro-optic
EOM	Equations of motion
FESEM	Field emission scanning electron microscope
FDTD	Finite-difference time-domain
FTIR	Fourier-transform infrared
FWHM	Full-width half-maximum
HDPE	High density polyethylene
HGF	Horizontal gradient freeze
IMPATT	Impact ionization avalanche transit-time
IR	Infrared
LN	LiNbO ₃
LNHP	LiNbO ₃ hybrid-plasmonic

MLN	Metal-LiNbO ₃
MLNM	Metal-LiNbO ₃ -metal
MMIC	Microwave millimeter integrated circuit
NESD	Normalized energy spectral density
NA	Numerical aperture
1D	One-dimensional
OR	Optical rectification
PPLN	Periodically-poled LiNbO ₃
PPMgLN	Periodically-poled MgO-doped LiNbO ₃
PCA	Photoconductive antenna
PET	Polyethylene terephthalate
QC	Quantum cascade
QCL	Quantum cascade laser
QWP	Quarter waveplate
RTD	Resonant tunneling diode
SHG	Second harmonic generation
SVAA	Slowly varying amplitude approximation
SPDC	Spontaneous parametric down conversion
SFG	Sum frequency generation
Tbps	Terabit-per-second
THz	Terahertz
THz-TDS	Terahertz time-domain spectroscopy

3D	Three-dimensional
TE	Transverse electric
TEM	Transverse electromagnetic
TM	Transverse magnetic
2D	Two-dimensional
VGF	Vertical gradient freeze
WP	Wollaston prism
ZGP	ZnGeP ₂

Chapter 1.

Introduction

Terahertz (THz) radiation is an electromagnetic (EM) wave that lies between microwaves (e.g. the EM waves used for Wi-Fi and microwave ovens) and infrared (IR) waves (i.e. the EM waves used for thermal imaging), as illustrated in Fig. 1.1(a) [1]. Although definitions vary, THz radiation is often defined as encompassing frequencies between ~ 0.3 -10 THz (i.e. wavelengths between ~ 0.03 -1 mm) [1]. As depicted in Fig. 1.1(b), electronic technologies such as impact ionization avalanche transit-time (IMPATT) diodes, Gunn diodes, resonant tunneling diodes (RTDs), Schottky diodes, microwave millimeter integrated circuits (MMICs), klystrons, and backward wave oscillators (BWOs) are typically utilized towards the longer-wavelength side of the EM spectrum [2]. Alternatively, photonic technologies including gas lasers, free electron lasers, quantum cascade lasers (QCLs), Si impurity lasers, and electroluminescence (EL) structures are often employed towards the shorter-wavelength side of the EM spectrum [see Fig. 1.1(b)] [2]. THz radiation lies in the transitory region of the EM spectrum, where it is unclear if electronics or photonics prevail, leading to this spectral region being denoted as the “THz gap”. In comparison to electronic and photonic technologies, far fewer technologies have been developed within the “THz gap”, with existing THz radiation technologies consisting of photomixers, photoconductive antennas (PCAs), and quantum cascade (QC) structures [see Fig. 1.1(b)] [2]. Although not depicted in Fig. 1.1(b), nonlinear frequency-conversion structures are also among the most prominent THz radiation technologies [3]. While a surplus of application potential exists for THz

radiation (see Section 1.2), further work is needed to advance THz technologies, particularly in the discovery and innovation of THz radiation sources and detectors.

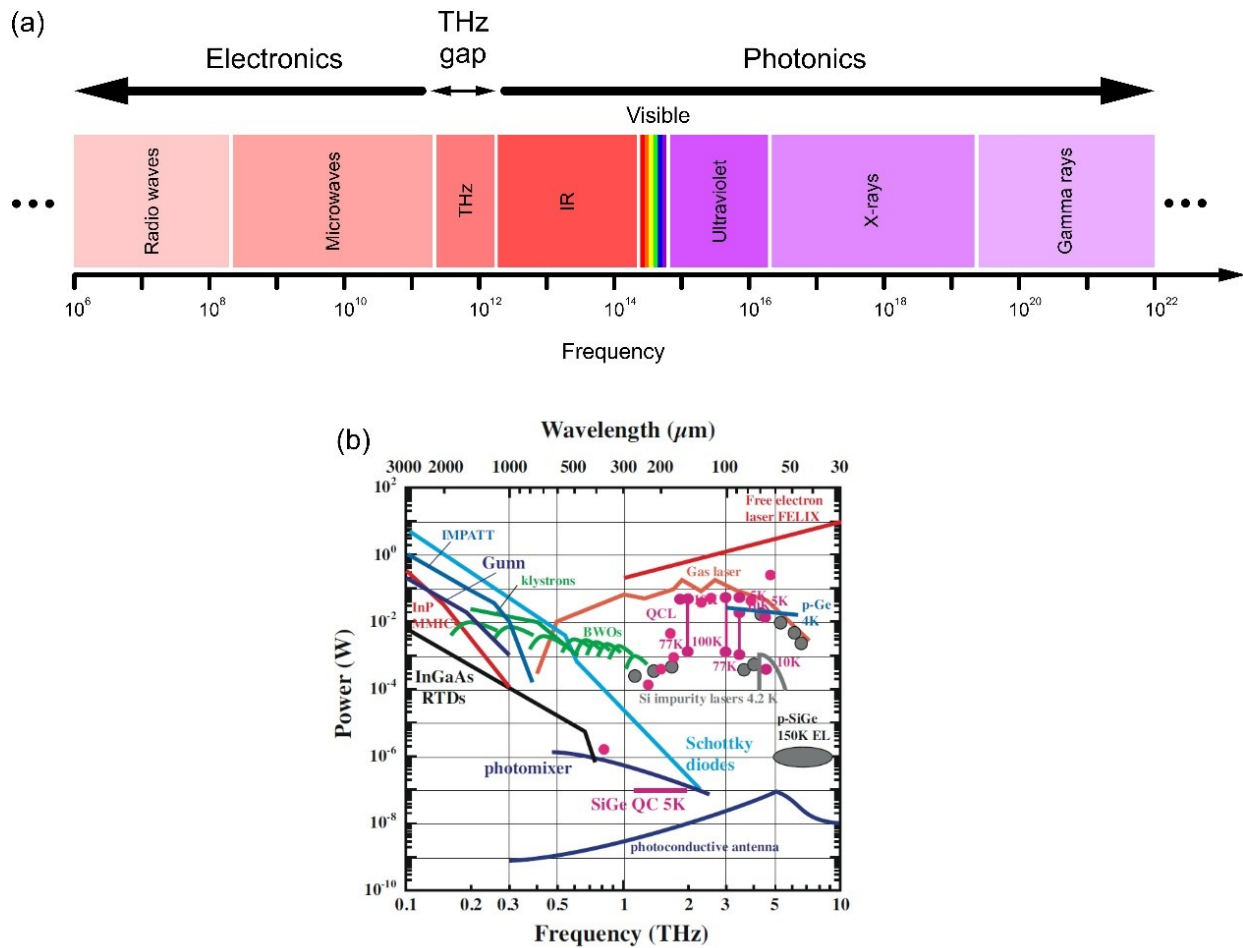


Fig. 1.1. (a) EM spectrum showing that THz radiation lies between technologies prevalent in electronics and photonics. (b) Output power of various sources used to produce radiation within and near the THz spectral region [2].

1.1. Key properties of THz radiation

THz radiation is non-ionizing [1], meaning each THz radiation photon does not contain sufficient energy to remove a valence electron from atoms or molecules. Such a property is highly beneficial, since exposure to ionizing radiation (e.g. x-rays) is linked to severe health effects, such

as cancers [4]. At low powers, THz radiation is non-destructive and non-invasive [1], such that an object interacting with THz radiation does not undergo permanent changes (i.e. after exposure to THz radiation, the object exhibits the same physical state it had prior to the interaction). Such properties allow the THz radiation to extract information about a particular object, without physically altering the object of interest. Numerous dielectric materials are transparent to THz radiation (e.g. many types of textiles, polymers, pigments, papers, clothing, cardboards, plastics, woods, and ceramics [1,5]), allowing THz radiation to image or identify an object concealed by various materials opaque to the naked eye [6,7]. Water vapor in the atmosphere absorbs THz radiation within various narrow spectral bands (see Fig. 1.2) [8]. Although such absorption is beneficial when using THz radiation to monitor the water content of an object [9], it may be a drawback in other applications (e.g. wireless communication). In applications that permit a

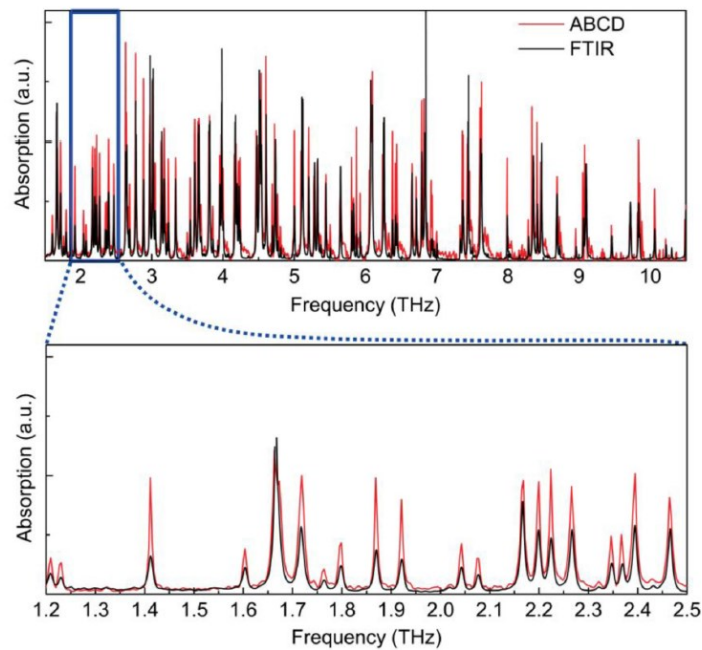


Fig. 1.2. Absorption of THz radiation due to water vapor [8]. The spectra are obtained using an air biased coherent detection (ABCD) system and a Fourier-transform infrared (FTIR) spectroscopy system [8].

controlled environment, water vapor absorption can be mitigated by operating in a nitrogen-purged chamber. It is also possible to operate within spectral bands less affected by the absorption, such as the region between 1.45-1.55 THz (see Fig. 1.2). Additionally, THz radiation used for high-altitude applications (e.g. aircraft-to-aircraft, aircraft-to-satellite, and satellite-to-satellite communication) avoids water vapor absorption, due to decreased levels of water vapor [1].

1.2. Applications of THz radiation

THz radiation is emerging as a key solution to a broad range of problems, extending across the health, safety, communication, manufacturing, security, and consumer industries. In this section, specific uses of THz radiation are discussed. In all of the applications outlined in this section (excluding communication), it is highly beneficial to create a spatial map using information extracted from the THz electric field magnitude and phase. Such spatial information could be attained using THz focal plane arrays.

Since many dielectric materials are transparent in the THz frequency range, THz radiation can be used to identify concealed metallic weapons, explosives, and hazardous chemicals. In general, THz radiation passes through the material concealing the object under investigation, interacts with the object in either a reflection or a transmission arrangement, and is subsequently detected. As shown in Fig. 1.3(a) and 1.3(b), Delgado-Notario et al. used THz radiation to identify a metallic blade concealed within an envelope [7]. When attempting to identify explosives or hazardous chemicals, the THz absorption spectra is obtained and assessed against a database containing the spectral “fingerprint” [see Fig. 1.3(c)] of known substances [6]. Such identification techniques could be used for security monitoring at airports, within postal sorting stations, and at sporting events or concerts, to name a few. Hazardous chemical gases are considered high-risk, as

they can rapidly immerse an area if not properly contained. THz radiation has been shown to identify harmful gaseous chemicals (e.g. carbon monoxide [10]), critical to ensuring a safe environment, especially in manufacturing facilities implementing processes that rely on harmful chemical gases [10].

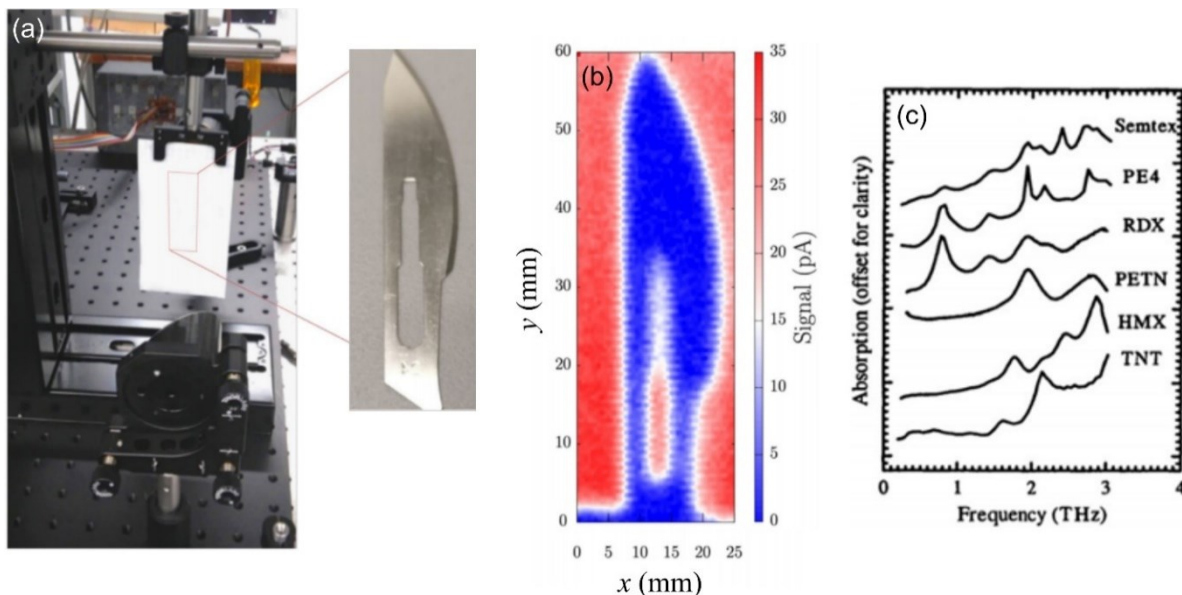


Fig. 1.3. (a) Optical arrangement showing a metallic blade concealed within an envelope [7]. (b) THz radiation image clearly identifying the concealed cutting blade [7]. (c) Spectral “fingerprint” of various explosives in the THz frequency regime [6].

When considering objects comprised of various layers, the thickness of the layers can be extracted using techniques based on pulsed THz electric fields. A portion of THz pulse is reflected from the outer interface of the object, as well as each interface within the object. The thickness of each layer is then extracted from the time delay between the resulting THz electric field pulses. By obtaining spatially-dependent measurements, the layers can be assessed for non-uniformities or cracks. Such a technique is non-destructive, such that the object under investigation retains its original integrity. Fitzgerald et al. determined the coating thickness of ibuprofen tablets [11],

where Fig. 1.4(a) and 1.4(b) show an illustration of the measurement technique and the experimental results, respectively. Given the temporal separation between the peaks, the layer thickness was determined as $314 \pm 4 \mu\text{m}$ [11]. This pulsed THz electric field technique has also been used to determine the thickness of a tooth's enamel layer, where Crawley et al. investigated numerous human incisors and measured enamel thicknesses ranging from 400-900 μm [12]. This technique was also utilized by Adam et al. to detect layers of paint hidden beneath a main painting [13], as well as Picot et al. to measure the thicknesses of various paint coatings used in the automotive sector (e.g. primer coat, external primer coat, intermediate primer coat, basecoat, and clear coat) [14].

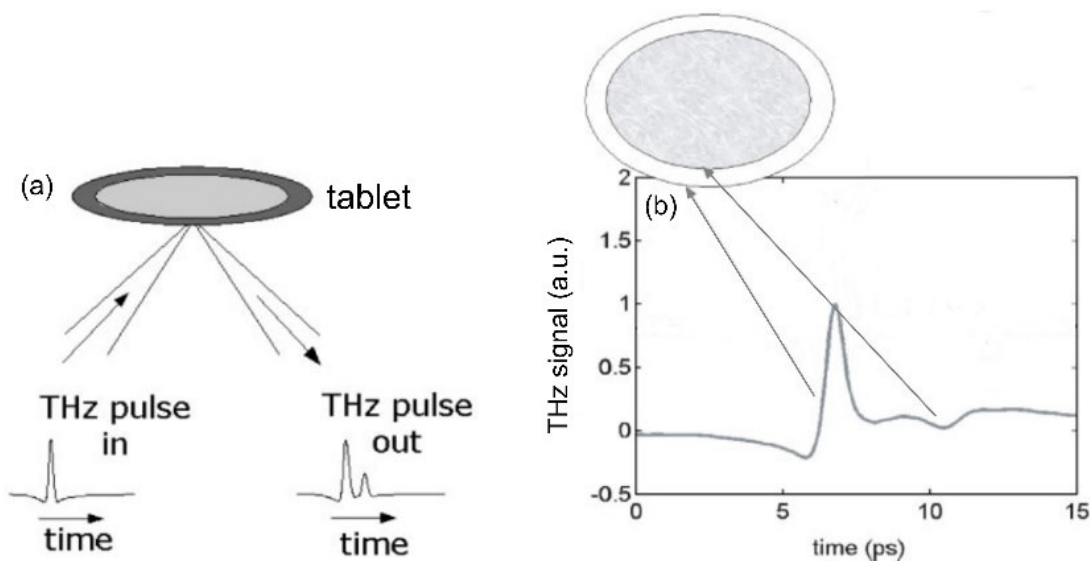


Fig. 1.4. (a) Illustration of the technique used to measure the coating thickness of a pharmaceutical tablet [11]. (b) Experimental THz time-domain signal recorded after reflecting from the various interfaces of the pharmaceutical tablet [11].

THz radiation has the ability to identify various skin conditions, critical to the health and dermatology industry. Here, THz radiation is reflected from the area of concern, and is then

detected and assessed. The technique is non-invasive, such that it does not alter the region of the skin being assessed. THz radiation techniques have been implemented to distinguish regions of healthy tissue from cancerous tissue [15,16], as well as measure the depth of skin burns [17].



Fig. 1.5. Illustration of point-to-point communication using a secure THz radiation channel for terabit-per-second (Tbps) data transfer [18].

The demand for wireless data transmission has drastically increased over the last several decades. THz radiation carrier waves permit the transfer of information over relatively short-distances (e.g. typically meters to tens of meters), beneficial for information-transfer between phones, tablets, laptops, and smart devices, to name a few. A unique opportunity for THz radiation lies in upgrading the current state of screen-mirroring technology [18]. Due to the requirement of a high-bandwidth, it is difficult to continuously play videos using the screen-mirroring technique,

which could potentially be resolved by incorporating THz radiation carrier waves. Another unique application for THz radiation lies in providing secure military communication channels [18]. As depicted in Fig. 1.5, point-to-point communication could be achieved between separate military vehicles in close proximity [18]. Since the THz radiation carrier waves are absorbed relatively rapidly by water vapor in the atmosphere, the communication channel is intrinsically secure from signal interception away from the transmitting source.

The structural integrity of a building, where supporting materials are often concealed within more aesthetically appealing materials, can be assessed using THz radiation technology [5]. In such an application, THz radiation is transmitted through the outer material and reflected from the supporting structure. By obtaining a spatial map of the concealed supporting structure, defects and weaknesses (e.g. cracks) are identified. The technique is non-destructive, such that the materials concealing the supporting material are unaffected by the testing process. As discussed by Krügener et al., THz radiation has been shown to identify defects in concrete, wood, cement, adhesives, and other construction materials [5].

THz radiation can be used to assess packaged or unpackaged foods [19], where THz radiation pulses interact with the food item (in a reflection or transmission arrangement) and are subsequently detected. Such measurements are performed without physical contact with the food, ideal for avoiding contamination. Afsah-Hejri et al. have used THz radiation to identify various items contained within foods, including glass, metals, human hair, and insects [19]. Since THz radiation is strongly-absorbed by water molecules, it is ideal for monitoring the dehydration process of foods [9]. Zhang et al. used THz radiation to monitor the water content of spinach (see Fig. 1.6) and rapeseed leaves [9].

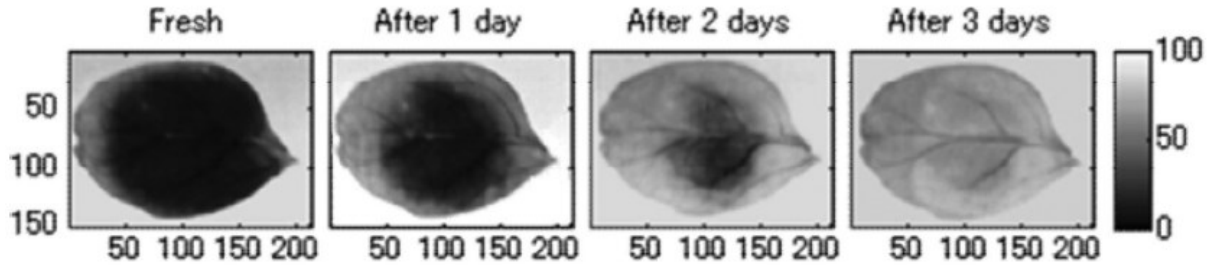


Fig. 1.6. THz radiation images of a spinach leaf undergoing a natural drying process, where dark regions correspond to a high water content [9].

1.3. Overview of THz sources, detectors, and measurement techniques

Solid-state electronics [20], spintronic emitters [21], electron-beam based oscillators [22], plasma sources [23], optically-pumped gas lasers [24], free-electron lasers [25], QCLs [26], photo-induced currents [27], and nonlinear crystals [28] have been exploited for generating coherent THz radiation. Nonetheless, nonlinear crystals stand out due to their potential for ultra-broadband generation (e.g. bandwidths in excess of 50 THz have been reported [29]). In such nonlinear crystals, the second-order nonlinear processes of difference frequency generation (DFG) and optical rectification (OR) are used to produce THz radiation. In DFG, the presence of two photons at the angular frequencies of ω_1 and ω_2 lead to a photon being produced at the angular frequency of Ω . For example, electric field frequency components at $\omega_1/(2\pi)=380$ THz and $\omega_2/(2\pi)=375$ THz can produce electric field frequency components at $\Omega/(2\pi)=5$ THz. Importantly, DFG occurs within non-centrosymmetric materials (i.e. materials that lack inversion symmetry) [30,31]. OR is the aggregate of DFG processes occurring across the bandwidth of an ultrashort electric field pulse, such that OR is strongly correlated to DFG. To better explain the OR process, we consider a broadband electric field pulse encompassing frequencies between 375-

380 THz, where $375 \text{ THz} < \omega_1/(2\pi) < 380 \text{ THz}$ and $375 \text{ THz} < \omega_2/(2\pi) < 380 \text{ THz}$. In such a scenario, DFG events occur across all of the encompassed frequencies (the process being referred to as OR) to produce $\Omega/(2\pi) \leq 5 \text{ THz}$, excluding $\Omega/(2\pi) = 0 \text{ THz}$ [i.e. the direct current (DC) component]. Such effects and associated aspects (i.e. DFG, OR, non-centrosymmetric materials, etc.) are discussed in detail in Chapter 2.

Ultrafast photo-induced currents [27] and the linear electro-optic (EO) effect (i.e. Pockel's effect) [32] are overwhelmingly utilized for the phase-resolved detection of coherent THz radiation. The linear EO effect can be used for ultra-broadband detection, where bandwidths in excess of 30 THz have been reported [32]. In a material exhibiting the linear EO effect (i.e. a non-centrosymmetric material), a birefringence is induced in the material that is proportional to the electric field. To better understand the physical mechanism driving the linear EO effect, it is beneficial to introduce a representative example: consider two separate electric field pulses encompassing frequencies between $355 \text{ THz} < \omega_1/(2\pi) < 395 \text{ THz}$ and $\omega_2/(2\pi) \leq 5 \text{ THz}$, excluding DC. The second-order nonlinear interaction of these electric fields leads to the generation of another electric field pulse encompassing frequencies between $355 \text{ THz} \lesssim \Omega/(2\pi) \lesssim 395 \text{ THz}$ (note the similarities to the OR process). If the crystal structure permits the generated electric field pulse at $\Omega/(2\pi)$ to exhibit a different polarization than the electric field pulse at $\omega_1/(2\pi)$, then the electric field at $\omega_1/(2\pi)$ undergoes a polarization change. Therefore, as the THz electric field propagates through the material, it induces an ultrafast birefringence change in the material that exists for the duration of the THz electric field pulse (often several hundreds of femtoseconds).

To measure an ultrafast birefringence, it is typical to employ a THz time-domain spectroscopy (THz-TDS) arrangement [33]. Here, a coherent THz electric field pulse is often

produced by focussing an ultrashort electric field pulse onto a material supporting the DFG or OR process. Subsequently, several off-axis parabolic mirrors are used to collect and focus the generated THz electric field pulse onto a material exhibiting the linear EO effect. The THz electric field pulse is transmitted through the material collinearly with an ultrashort optical probe electric field pulse, where the probe pulse typically exhibits a temporal duration of tens to hundreds of times less than the duration of the THz electric field pulse. In the presence of the THz electric field, the probe pulse undergoes a change in its polarization state due to the linear EO effect. Optical components [e.g. a Wollaston prism (WP) and a quarter waveplate (QWP)] are then used in conjunction with electrical devices (e.g. balanced photodetector, lock-in amplifier, etc.) to determine the induced polarization change, where this polarization change is proportional to the electric field of the THz pulse. By altering the path length between the THz electric field pulse and the ultrashort probe pulse (e.g. using a retroreflector attached to an electrically-controlled linear delay line), the polarization change can be recorded for localized regions along the THz electric field pulse, permitting a time-domain representation of the THz electric field strength to be obtained. Chapter 3 discusses the THz-TDS technique in further detail.

1.4. Pnictide and chalcogenide ternary crystals in the THz frequency regime¹

When considering second-order nonlinear processes for the generation and detection of THz radiation, key attributes (e.g. conversion efficiency, bandwidth, etc.) are highly-dependent on the material supporting the nonlinear interaction. Pnictide ternary crystals ($A_xB_yPn_z$, where $Pn=N, P,$

¹A version of this section's work is under review in *IEEE Transactions on Terahertz Science and Technology*.

As, Sb, Bi, or Mc) and chalcogenide ternary crystals ($A_xB_yCh_z$, where Ch=S, Se, Te, Po, or Lv) are gaining interest as being highly versatile THz radiation sources and detectors. Notably, ternary oxide crystals having the stoichiometric structure $A_xB_yO_z$ are excluded from the chalcogenide crystal classification (see Ref. [34]). Both pnictide and chalcogenide ternary crystals can exhibit excellent optical and THz frequency properties [e.g. high optical nonlinearity, low loss, good phase-matching (see Appendix A), etc.], such that these classes of nonlinear crystals are appealing for use in the THz frequency regime. For example, $ZnGeP_2$ (ZGP), $CdGeP_2$, and $CdSiP_2$ (CSP) crystals are recognized for their high second-order nonlinear coefficients [35,36], with CSP possessing a relatively wide bandgap of 2.45 eV [37]. While chalcogenide ternary crystals typically exhibit lower nonlinear coefficient magnitudes than that of the pnictide ternary crystals, many of the chalcogenide ternary crystals display more attractive (e.g. wider) transparency ranges in comparison to the pnictide crystals.

This section presents a detailed survey of recent developments in THz radiation generation and detection using pnictide and chalcogenide ternary crystals. Such crystals are assessed for coherent THz radiation generation via second-order nonlinear frequency-conversion techniques (i.e. OR and DFG), as well as their use in the phase-resolved detection of THz radiation via the EO effect. Additionally, we discuss phase-resolved (i.e. THz-TDS) spectroscopic investigations performed on select ternary crystals from both classes. It is envisioned that further development of the pnictide and chalcogenide ternary crystals for THz radiation generation and detection will lead to the advancements in security, medicine, communication, industry, applied research, and fundamental research.

1.4.1. Key properties of pnictide ternary crystals

In the THz frequency regime, four pnictide ternary crystals stand out: ZGP, CSP, CdGeP₂, and MnSiP₂. The structural and optical properties of these intriguing crystals are listed in Table I. Since there is no data for the second-order nonlinear coefficients in the THz frequency regime, the second harmonic generation (SHG) nonlinear coefficients are presented as a nonlinearity metric, as a high SHG nonlinear coefficient is often associated with a high THz nonlinear coefficient [38]. Interestingly, all of these crystals have a tetragonal crystal structure and exhibit the chalcopyrite atomic arrangement [35,39–41], as illustrated in Fig. 1.7 [42]. ZGP, CSP, CdGeP₂, and MnSiP₂ exhibit a point group symmetry of $\bar{4}2m$ [35,39–41]. Symmetries in the nonlinear coefficient tensor are dictated by the point group symmetry of the crystal, wherein the nonlinear coefficient tensor associated with $\bar{4}2m$ crystals is [43],

$$\bar{d}_{\bar{4}2m} = \begin{bmatrix} 0 & 0 & 0 & d_{14} & 0 & 0 \\ 0 & 0 & 0 & 0 & d_{14} & 0 \\ 0 & 0 & 0 & 0 & 0 & d_{36} \end{bmatrix}, \quad (1.1)$$

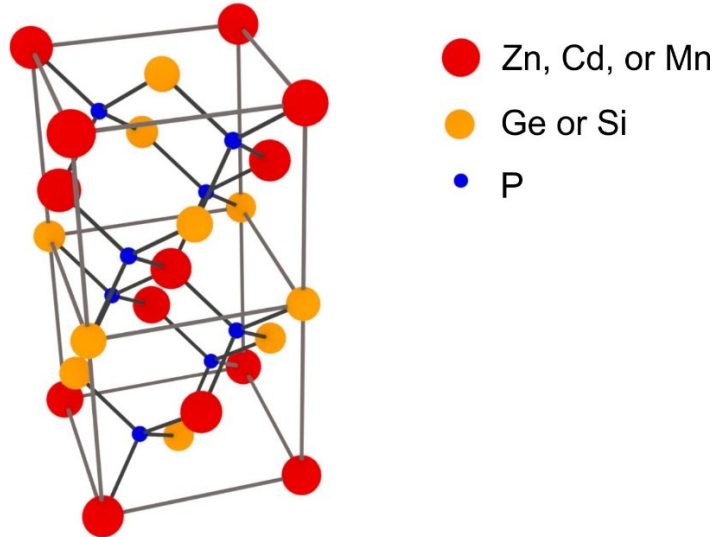


Fig. 1.7. An illustration of the unit cell structure of the ZGP, CSP, CdGeP₂, and MnSiP₂ crystals.

where d_{14} and d_{36} are the non-vanishing tensor elements. It is common to excite $\bar{4}2m$ symmetry crystals using an optical electric field polarized along the [100] crystallographic axis, $E_{[100]}$, and an electric field polarized along the [010] crystallographic axis, $E_{[010]}$, to induce a second-order nonlinear polarization along the crystal's [001] crystallographic axis, $P_{[001]}^{(2)} = 2\varepsilon_0 d_{36} E_{[100]} E_{[010]}$. In this arrangement, the induced second-order nonlinear polarization dipoles (i.e. $P_{[001]}^{(2)}$) subsequently emit [001]-polarized EM radiation. It should be noted that the EO coefficient tensor for crystals exhibiting $\bar{4}2m$ point group symmetry is closely related to $\bar{d}_{\bar{4}2m}$ in Eq. (1.1) (see Ref. [30]).

Of all the pnictide crystals, ZGP has undoubtedly been the most studied at THz frequencies. In part, this is due to the reliability in growing high-quality ZGP crystals, as well as its high nonlinear coefficient ($d_{36}=75$ pm/V at an excitation wavelength of $\lambda_{exc}=9.6$ μm [35]) and its wide wavelength transparency range of 0.74-12 μm [39]. Furthermore, ZGP exhibits a bandgap of 2 eV [44], which is higher than the energy of the excitation photons typically used for nonlinear frequency-conversion processes (e.g. ~ 0.8 -1.55 eV). Both CSP and CdGeP₂ pnictide crystals also possess high nonlinear coefficients (i.e. $d_{36}=84.5$ pm/V at $\lambda_{exc}=4.6$ μm for CSP [35] and $d_{36}=162$ pm/V at $\lambda_{exc}=10.6$ μm for CdGeP₂ [36]), which are higher than that of ZGP (i.e. $d_{36}=75$ pm/V at $\lambda_{exc}=9.6$ μm [35]). The transparency spectral range of the CSP crystals extends well into the visible spectral regime (i.e. lower cut-off wavelength of 520 nm [35]) and it has the largest bandgap of all the investigated pnictide crystal (i.e. 2.45 eV [37]). Although CdGeP₂ exhibits the highest nonlinear coefficient of the investigated pnictide crystals, this comes at the expense of a comparatively narrower bandgap (i.e. 1.72 eV [40]) and a transparency range having the lower cut-off wavelength of 900 nm [40]. While the MnSiP₂ crystal exhibits a narrow bandgap,

a poor lower cut-off wavelength for its transparency range, and a low nonlinear coefficient in comparison to the other investigated pnictide crystals, it has the benefit of offering the higher upper cut-off wavelength of 18.2 μm (i.e. 16.5 THz) [41], thus making this pnictide crystal specially-suited for high-frequency THz radiation generation and detection.

Table 1.1. Structural and optical properties of various pnictide ternary crystals in the THz frequency regime.

Crystal composition	Crystal structure	Point group symmetry	Bandgap (eV)	SHG nonlinear coefficient magnitude (pm/V)	Transparency range ($\mu\text{m}/\text{THz}$)
ZGP	Tetragonal (chalcopyrite) [39]	$\bar{4}2m$ [39]	2 [44]	$d_{36}=75$ ($\lambda_{exc}=9.6 \mu\text{m}$) [35]	0.74 – 12 μm (25 – 405 THz) [39]
CSP	Tetragonal (chalcopyrite) [35]	$\bar{4}2m$ [35]	2.45 [37]	$d_{36}=84.5$ ($\lambda_{exc}=4.6 \mu\text{m}$) [35]	0.52 – 9.5 μm (31.6 – 577 THz) [35]
CdGeP ₂	Tetragonal (chalcopyrite) [40]	$\bar{4}2m$ [40]	1.72 [40]	$d_{36}=162$ ($\lambda_{exc}=10.6 \mu\text{m}$) [36]	0.9 – 11 μm (27.3 – 333 THz) [40]
MnSiP ₂	Tetragonal (chalcopyrite) [41]	$\bar{4}2m$ [41]	1.5 [41]	$d_{36}=32.8$ ($\lambda_{exc}=2.1 \mu\text{m}$) [41]	<1.3 – 18.2 μm (16.5 – >231 THz) [41]

1.4.2. Linear THz radiation properties of pnictide ternary crystals

THz-TDS has been utilized to determine the linear THz radiation properties of pnictide ternary crystals. Within the 0.2-3.4 THz frequency range, ZGP was shown to be a positive uniaxial crystal that exhibited ordinary, n_o , and extraordinary, n_e , refractive indices that ranged from

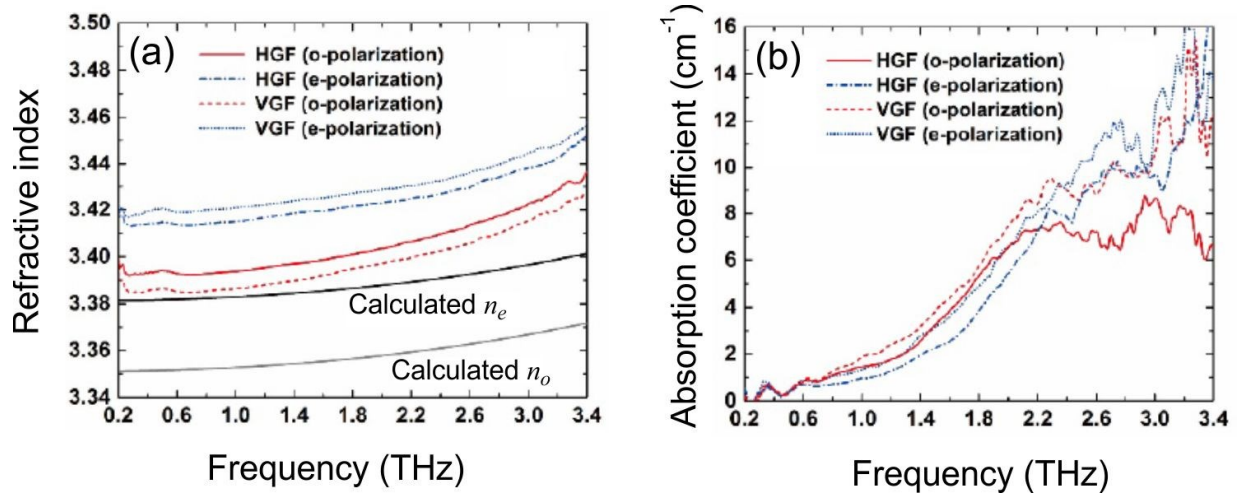


Fig. 1.8. Ordinary and extraordinary (a) refractive indices and (b) extinction coefficients of ZGP crystals in the THz frequency regime [39].

3.38-3.44 and 3.41-3.46, respectively [see Fig. 1.8(a)] [39]. Clearly, n_o and n_e varied depending on whether the ZGP crystal was grown using a horizontal gradient freeze (HGF) method or a vertical gradient freeze (VGF) method, and exhibited a birefringence of $n_e - n_o \approx 0.02$ at frequencies between 0.2-3.4 THz [39]. Due to this birefringence, the ZGP crystal could be used to construct THz waveplates for manipulating the polarization state of THz radiation electric fields [45]. In addition to the refractive indices and birefringence, it is critical to examine the THz radiation losses in these crystals. As shown in Fig. 1.8(b), the ZGP crystal exhibited the low ordinary, α_o , and extraordinary, α_e , absorption coefficients of $< 16 \text{ cm}^{-1}$ at frequencies between 0.2-3.4 THz (i.e. ordinary, κ_o , and extraordinary, κ_e , extinction coefficients of < 0.013) [39]. Although not within the aforementioned THz frequency spectral window, the IR-active B_2 phonon mode at 3.6 THz would absorb THz radiation polarized along the extraordinary crystal axis, whereas the IR-active E phonon mode at 4.26 THz would absorb ordinary-polarized THz radiation [39]. Another pnictide ternary crystal worth mentioning is MnSiP_2 . A sample that had a thickness of $340 \mu\text{m}$ was shown to exhibit an

~50% transmittance and a nearly frequency-independent refractive index of ~3.1 within the frequency range of 0.4-2 THz [41].

1.4.3. THz radiation generation via nonlinear frequency-conversion in pnictide ternary crystals

THz radiation generation in ZGP via the nonlinear DFG processes has been reported by numerous groups [46–52]. While several theoretical and numerical analyses have provided valuable information [46–48], only the experimental investigations will be discussed [49–52]. Using 1055 and 1064.2 nm excitation wavelengths in an *oe-e* DFG arrangement (i.e. one excitation wavelength as an ordinary wave, *o*, the other excitation wavelength an extraordinary wave, *e*, and the THz radiation generated as an extraordinary wave, *e*), Creeden et al. reported the generation of radiation at 2.45 THz for an external phase-matching angle of 22° [49]. It was shown that the average power of the generated THz radiation reached the high value of 2 mW when the ZGP crystal was excited at a peak excitation intensity of 300 MW/cm² [49]. Alternatively, Kumbhakar et al. investigated phase-matched DFG in a ZGP crystal for both the *oe-o* configuration (one excitation wavelength as an ordinary wave, *o*, the other excitation wavelength an extraordinary wave, *e*, and the THz radiation generated as an ordinary wave, *o*) and the *oe-e* configuration [50]. Using a fixed excitation wavelength of 1064 nm and an excitation wavelength tunable between 1064-1093 nm, the authors reported the generation of THz radiation tunable between ~1-4 THz [50]. As shown in Fig. 1.9(a), a wider frequency tunability range of 0.2-6 THz (i.e. 50-1500 μm) was demonstrated by Sirotkin et al., where these frequencies were produced using a 10 mm-thick ZGP crystal in the *oe-o* configuration [51]. The crystal was excited using mid-IR excitation wavelengths ranging from 1900-2400 nm, which were incident at external phase-matching angles

between 5° - 34° [51]. However, due to the low conversion efficiency achieved using this arrangement (i.e. $<10^{-9}$), the maximum generated THz radiation power was only a few nanowatts (e.g. ~ 4 nW at 1.6 THz) [51]. To enhance the optical-to-THz conversion efficiency, Shi et al. annealed a ZGP crystal to reduce absorption losses at excitation wavelengths near 1064 nm [52]. Conversion efficiencies as high as 2.6×10^{-4} (*oe-o* configuration) and 3.7×10^{-4} (*oe-e* configuration) were achieved for DFG radiation produced between ~ 0.2 - 3.7 THz in a 20.6 mm-thick ZGP crystal [52].

THz radiation generated via the process of OR has been demonstrated in (110)-cut ZGP crystals having lengths <1 mm [53]. As shown in Fig. 1.9(b), a THz radiation pulse (<1 ps in duration) was produced when using a 100 fs laser excitation pulse that had a central wavelength of $1.3 \mu\text{m}$ [53]. The inset of Fig. 1.9(b) shows that the frequency associated with maximum generation was higher in the ZGP crystal (i.e. ~ 1 THz) in comparison to a GaAs crystal (i.e. ~ 0.6 THz) [53]. Interestingly, the ZGP crystal did not express any evidence of phase-mismatching (i.e. no dips or nulls were observed in the generated spectrum) [53]. This is due to the fact that the (110)-cut ZGP crystal exhibited an OR coherence length ≥ 1 mm (for THz frequency generation below 2.7 THz) at the central wavelength of $1.3 \mu\text{m}$ (i.e. 0.95 eV), as depicted in Fig. 1.9(c) [54]. Nonetheless, at frequencies <3 THz, the ZGP phase-matching contour plot shows that optimal phase-matching occurred at the excitation wavelength of $\sim 1.18 \mu\text{m}$ (i.e. 1.05 eV), with phase-mismatching becoming increasingly prevalent away from $\sim 1.18 \mu\text{m}$ [54]. For example, at an excitation wavelength of 800 nm (i.e. 1.55 eV), the OR coherence length became only a few hundred microns for frequencies between ~ 2 - 3 THz [54]. Notably, a (012)-cut ZGP crystal exhibited phase-matching characteristics similar to that of a (110)-cut ZGP crystal for frequencies

<4 THz [see Fig. 1.9(d)], and (012)-cut ZGP crystals of various thicknesses have been shown to generate THz radiation at frequencies up to ~3 THz [54].

Piyathilaka et al. investigated several pnictide ternary crystals excited using various wavelengths [28]. The authors employed a 500 μm -thick (110)-cut CSP crystal excited using femtosecond pulses that had central wavelengths of 800, 1300, and 1540 nm [28]. At a peak excitation intensity of 15 GW/cm^2 , the 800 nm central-wavelength laser excitation pulse produced a 25 kV/cm peak-to-peak THz radiation electric field, while the 1300 nm and 1540 nm central-wavelength excitation pulses at the same peak intensity produced much higher peak-to-peak THz radiation electric field strengths of 290 and 170 kV/cm , respectively [28]. A similar crystal, CdGeP_2 , was also investigated by the same authors for OR THz radiation generation [28]. As shown in Fig. 1.9(e) and 1.9(f), the THz radiation electric field signal produced using this crystal is comparable to those generated from ZGP and CSP crystals [all of the crystals were cut along the (110) crystal plane, polished to a thickness of 500 μm , and excited by a femtosecond pulse that had a central wavelength of 1300 nm] [28]. Interestingly, it was also shown that the CdGeP_2 crystal exhibited nearly perfect OR phase-matching at the central wavelength of ~1550 nm, thus offering great potential for coherent THz radiation generation using wavelengths within the telecommunication band [28]. This claim was further supported by the fact that the CdGeP_2 crystal was shown to express stronger THz radiation generation than both the ZGP and CSP crystals when excited by a 1540 nm excitation pulse [28]. Specifically, a 17 GW/cm^2 peak intensity laser excitation pulse generated THz electric fields that had peak-to-peak values of 130, 190, and 220 kV/cm from 500 μm -thick ZGP, CSP, and CdGeP_2 crystals, respectively [28].

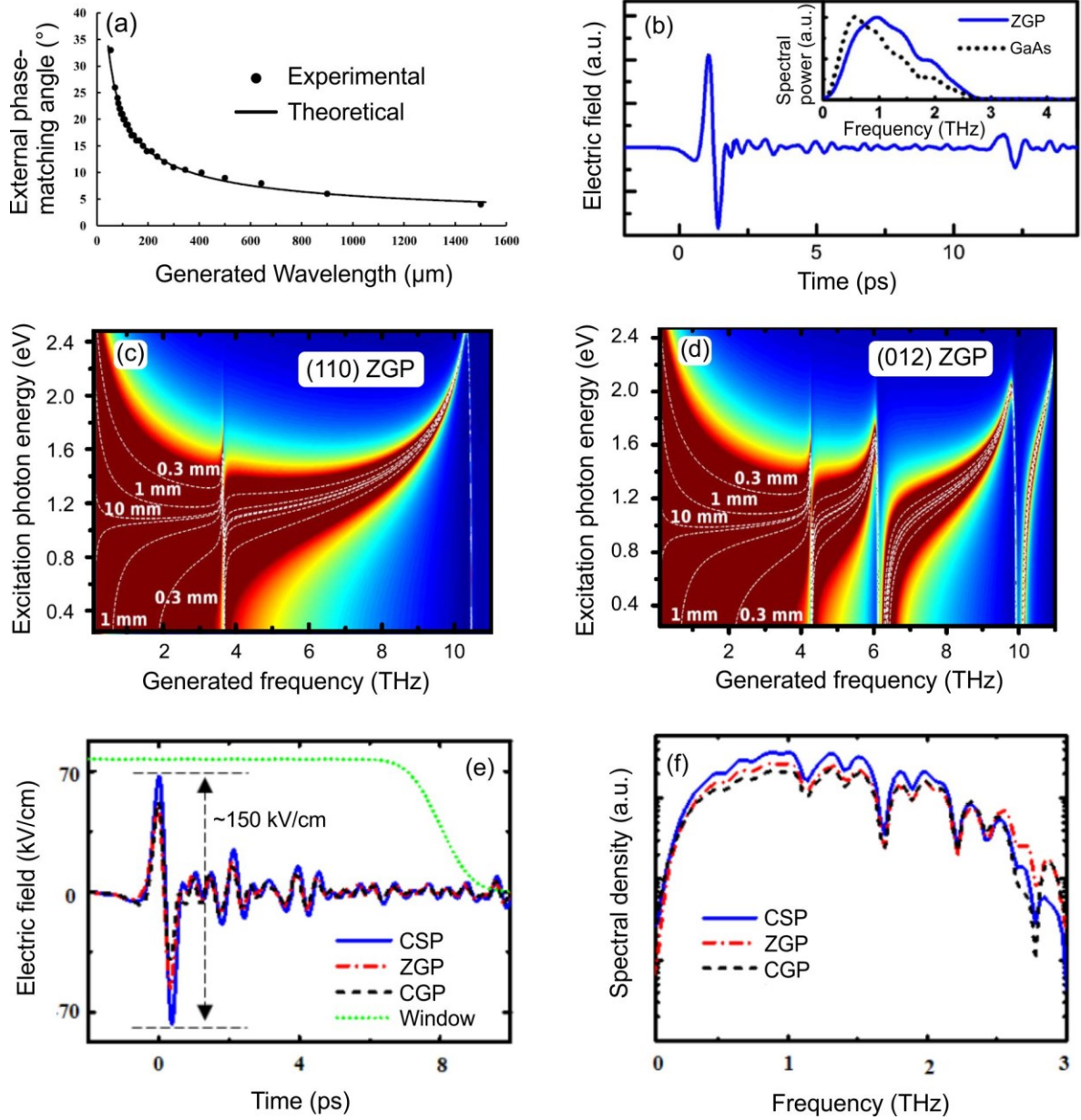


Fig. 1.9. (a) DFG THz radiation produced using a ZGP crystal excited at various external phase-matching angles [51]. (b) Generation of broadband THz radiation from a ZGP crystal excited using a pulse that had a duration of 100 fs and a central wavelength of 1.3 μm [53]. The inset compares the spectral distributions of the generated THz radiation for ZGP and GaAs crystals. OR phase-matching contours for ZGP crystals cut along the (c) (110) and (d) (012) crystal planes [54]. (e) THz time-domain electric field signals and (f) the associated spectra produced using (110)-cut CSP, ZGP, and CdGeP₂ crystals [28].

1.4.4. THz radiation detection using pnictide ternary crystals

Pnictide ternary crystals have received limited attention for their use as THz EO detectors. Such an observation is surprising, given the fact that EO sampling is a second-order nonlinear process, the same as DFG and OR.

1.4.5. Key properties of chalcogenide ternary crystals

Numerous chalcogenide ternary crystals have been investigated for use in the THz frequency regime. Among the vast number of chalcogenide ternary crystals, AgGaS₂, AgGaSe₂ (AGS), BaGa₄S₇, BaGa₄Se₇ (BGS), Cd₄SiS₆, Cd₄SiSe₆, LiGaS₂, LiGaSe₂, LiInS₂, LiInSe₂, PbGa₆Te₁₀, PbIn₆Te₁₀, Zn_{1-x}Cd_xTe, and Zn_{1-x}Mn_xTe crystals show great promise. The structural and optical properties of these chalcogenide ternary crystals are displayed in Table II. Similar to the pnictide ternary crystals, the SHG nonlinear coefficient magnitudes are presented, as there is no reported data for the nonlinear coefficients at THz frequencies.

Chalcogenide ternary crystals exhibit various structures (i.e. tetragonal, orthorhombic, monoclinic, cubic, and trigonal) and various point group symmetries (i.e. $\bar{4}2m$, $mm2$, m , $\bar{4}3m$, and 32). The nonlinear coefficient tensor associated with the $\bar{4}2m$ point group symmetry is defined in Eq. (1.1), whereas the nonlinear coefficient tensors associated with the other point group symmetries are [43]:

$$\bar{d}_{mm2} = \begin{bmatrix} 0 & 0 & 0 & 0 & d_{15} & 0 \\ 0 & 0 & 0 & d_{24} & 0 & 0 \\ d_{31} & d_{32} & d_{33} & 0 & 0 & 0 \end{bmatrix}, \quad (1.2)$$

$$\bar{d}_m = \begin{bmatrix} d_{11} & d_{12} & d_{13} & 0 & d_{15} & 0 \\ 0 & 0 & 0 & d_{24} & 0 & d_{26} \\ d_{31} & d_{32} & d_{33} & 0 & d_{35} & 0 \end{bmatrix}, \quad (1.3)$$

$$\bar{d}_{\bar{4}3m} = \begin{bmatrix} 0 & 0 & 0 & d_{14} & 0 & 0 \\ 0 & 0 & 0 & 0 & d_{14} & 0 \\ 0 & 0 & 0 & 0 & 0 & d_{14} \end{bmatrix}, \quad (1.4)$$

$$\bar{d}_{32} = \begin{bmatrix} d_{11} & -d_{11} & 0 & d_{14} & 0 & 0 \\ 0 & 0 & 0 & 0 & -d_{14} & -d_{11} \\ 0 & 0 & 0 & 0 & 0 & 0 \end{bmatrix}, \quad (1.5)$$

where d_{ij} ($i=1, 2, \text{ or } 3$ and $j=1, 2, \dots, 6$) represent the non-vanishing tensor elements. Since these crystals possess various point group symmetries and numerous non-vanishing tensor elements, they can be implemented at a variety of orientations for the generation and detection of THz radiation. The general expressions for the induced second-order nonlinear polarizations are,

$$\begin{bmatrix} P_{[100]}^{(2)} \\ P_{[010]}^{(2)} \\ P_{[001]}^{(2)} \end{bmatrix} = 2\varepsilon_0 \begin{bmatrix} d_{11} & d_{12} & d_{13} & d_{14} & d_{15} & d_{16} \\ d_{21} & d_{22} & d_{23} & d_{24} & d_{25} & d_{26} \\ d_{31} & d_{32} & d_{33} & d_{34} & d_{35} & d_{36} \end{bmatrix} \begin{bmatrix} E_{[100]}^2 \\ E_{[010]}^2 \\ E_{[001]}^2 \\ 2E_{[010]}E_{[001]} \\ 2E_{[100]}E_{[001]} \\ 2E_{[100]}E_{[010]} \end{bmatrix}, \quad (1.6)$$

where $P_{[100]}^{(2)}$, $P_{[010]}^{(2)}$, and $P_{[001]}^{(2)}$ are the second-order nonlinear polarizations induced along the [100], [010], and [001] crystallographic axes, respectively, and $E_{[100]}$, $E_{[010]}$, and $E_{[001]}$ are the excitation electric fields polarized along the [100], [010], and [001] crystallographic axes, respectively. Importantly, a time-varying second-order nonlinear polarization (e.g. a time-varying $P_{[100]}^{(2)}$, $P_{[010]}^{(2)}$, or $P_{[001]}^{(2)}$) emits EM radiation having the same polarization state. Notably, the EO coefficient tensors for crystals exhibiting $\bar{4}2m$, $mm2$, m , $\bar{4}3m$, and 32 point group symmetries are closely related to their associated second-order nonlinear coefficient tensors (see Ref. [30]).

As shown in Table II, all of the chalcogenide ternary crystals exhibit appreciable SHG nonlinear coefficient magnitudes in the pm/V range. Although the majority of the chalcogenide ternary crystals exhibit a lower transparency range cut-off wavelength of $<1 \mu\text{m}$, a few crystals (e.g. $\text{PbGa}_6\text{Te}_{10}$ and

Table 1.2. Structural and optical properties of various chalcogenide ternary crystals in the THz frequency regime.

Crystal composition	Crystal structure	Point group symmetry	Bandgap (eV)	SHG nonlinear coefficient magnitude (pm/V)	Transparency range ($\mu\text{m}/\text{THz}$)
AgGaS ₂	Tetragonal (chalcopyrite) [55]	$\bar{4}2m$ [55]	2.7 [55]	$d_{36}=12.6$ ($\lambda_{exc}=10.6 \mu\text{m}$) [55]	0.47 – 13 μm (23.1 – 638 THz) [55]
AGS	Tetragonal (chalcopyrite) [55]	$\bar{4}2m$ [55]	1.8 [55]	$d_{36}=39.5$ ($\lambda_{exc}=10.6 \mu\text{m}$) [55]	0.76 – 18 μm (16.7 – 395 THz) [55]
BaGa ₄ S ₇	Orthorhombic [55]	$mm2$ [55]	3.54 [55]	$d_{32}=5.7$ ($\lambda_{exc}=2.3 \mu\text{m}$) [55]	0.35 – 13.7 μm (21.9 – 857 THz) [55]
BGS	Monoclinic [55]	m [55]	2.64 [55]	$d_{11}=24.3$ ($\lambda_{exc}=1.064 \mu\text{m}$) $d_{13}=20.4$ ($\lambda_{exc}=1.064 \mu\text{m}$) [56]	0.47 – 18 μm (16.7 – 638 THz) [55]
Cd ₄ SiS ₆	Monoclinic [57]	m [57]	1.92 [57]	$d_{15}=3.6$ ($\lambda_{exc}=2.05 \mu\text{m}$) [57]	0.45 – 17.6 μm (17 – 667 THz) [57]
Cd ₄ SiSe ₆	Monoclinic [57]	m [57]	1.46 [57]	$d_{15}=12.2$ ($\lambda_{exc}=2.05 \mu\text{m}$) [57]	0.64 – 20.3 μm (14.8 – 469 THz) [57]
LiGaS ₂	Orthorhombic (chalcopyrite) [55]	$mm2$ [55]	4.15 [55]	$d_{31}=5.8$ ($\lambda_{exc}=2.3 \mu\text{m}$) $d_{24}=5.1$ ($\lambda_{exc}=2.3 \mu\text{m}$) [55]	0.32 – 11.6 μm (25.9 – 938 THz) [55]
LiGaSe ₂	Orthorhombic (chalcopyrite) [55]	$mm2$ [55]	3.34 [55]	$d_{31}=9.9$ ($\lambda_{exc}=2.3 \mu\text{m}$) $d_{24}=7.7$ ($\lambda_{exc}=2.3 \mu\text{m}$) [55]	0.37 – 13.2 μm (22.7 – 811 THz) [55]

Crystal composition	Crystal structure	Point group symmetry	Bandgap (eV)	SHG nonlinear coefficient magnitude (pm/V)	Transparency range ($\mu\text{m}/\text{THz}$)
LiInS ₂	Orthorhombic (chalcopyrite) [55]	<i>mm2</i> [55]	3.57 [55]	$d_{31}=7.3$ ($\lambda_{exc}=2.3 \mu\text{m}$)	0.34 – 13.2 μm
				$d_{24}=5.7$ ($\lambda_{exc}=2.3 \mu\text{m}$) [55]	(22.7 – 882 THz) [55]
LiInSe ₂	Orthorhombic (chalcopyrite) [55]	<i>mm2</i> [55]	2.86 [55]	$d_{31}=11.8$ ($\lambda_{exc}=2.3 \mu\text{m}$)	0.46 – 14
				$d_{24}=8.2$ ($\lambda_{exc}=2.3 \mu\text{m}$) [55]	(21.4 – 652 THz) [55]
PbGa ₆ Te ₁₀	Trigonal [58]	32 [58]	1.35 [59]	$d_{11}=25.5$	1.4 – 22.3 μm
				($\lambda_{exc}=10.6 \mu\text{m}$) [58]	(13.5 – 214 THz) [60]
PbIn ₆ Te ₁₀	Trigonal [58]	32 [58]	1.08 [61]	$d_{11}=48.5$	3 – 20 μm
				($\lambda_{exc}=10.6 \mu\text{m}$) [58]	(15 – 100 THz) [61]
Zn _{1-x} Cd _x Te	Cubic (zincblende) [62]	$\bar{4}3m$ [62]	1.45-	Undetermined	~ 0.7 – 30 μm
			2.25 [63]		(~ 10 – 429 THz) [64,65]
Zn _{1-x} Mn _x Te	Cubic (zincblende) [66]	$\bar{4}3m$ [66]	2.28-2.9 [67,68]	Undetermined	~ 0.53 – $>0.7 \mu\text{m}$
					($\sim <429$ – 566 THz) [67]

PbIn₆Te₁₀) do not satisfy this criteria, thus restricting their application to fewer excitation laser sources. Additionally, while the majority of the chalcogenide ternary crystals have a bandgap >1.55 eV (i.e. <800 nm), Cd₄SiSe₆, PbGa₆Te₁₀, and PbIn₆Te₁₀ possess narrower bandgaps, making them prone to single-photon absorption when excited by typical laser excitation sources (e.g. ~ 800 nm Ti:Sapphire lasers). Although PbIn₆Te₁₀ possess the highest nonlinear coefficient of the investigated chalcogenide ternary crystals (i.e. $d_{11}=48.5$ pm/V at $\lambda_{exc}=10.6 \mu\text{m}$ [58]), it suffers from a narrow bandgap of 1.08 eV

and a lower transparency range cut-off wavelength of 3 μm [61]. On the other hand, AGS exhibits the high second-order nonlinear coefficient magnitude of $d_{36}=39.5$ pm/V at $\lambda_{exc}=10.6$ μm , a bandgap of 1.8 eV, and a lower transparency range cut-off wavelength of 760 nm [55], making it a viable crystal for excitation using an ~ 800 nm femtosecond Ti:Sapphire laser source or laser sources having longer emission wavelengths. In general, the SHG nonlinear coefficient magnitudes of the chalcogenide ternary crystals (i.e. see Table II) are lower than those of the pnictide ternary crystals (i.e. see Table I) by tens of pm/V. However, many of the chalcogenide ternary crystals exhibit better lower transparency range cut-off wavelength (e.g. 470 nm for BGS [55]) in comparison to the pnictide ternary crystals, thus allowing for more flexibility in choosing excitation laser sources.

1.4.6. Linear THz radiation properties of chalcogenide ternary crystals

THz-TDS measurements have been conducted on several uniaxial and biaxial chalcogenide ternary crystals to extract their linear THz radiation properties. In the frequency range of 0.2-2.4 THz, such measurements were performed on an AgGaS₂ crystal at temperatures that ranged from 30°C-230°C [69]. At 30°C, n_o varied from 2.97-3.15, while n_e exhibited less dispersion and ranged from 2.99-3.06 [see Fig. 1.10(a) and 1.10(b), respectively] [69]. At this same temperature and across this same frequency range, the absorption coefficients were found to be $\alpha_o < 34$ cm⁻¹ and $\alpha_e < 17$ cm⁻¹ (i.e. $\kappa_o < 0.037$ and $\kappa_e < 0.017$), as shown in Fig. 1.10(c) and 1.10(d), respectively [69]. Across the investigated frequency range (i.e. 0.2-2.4 THz), both the refractive indices and the absorption coefficients typically increased with increasing temperature [69]. An E phonon mode signature at 1.03 THz and a B_2 phonon mode signature at 1.86 THz were evident in the refractive indices and the absorption coefficients [69]. Another uniaxial chalcogenide ternary

crystal, $\text{PbIn}_6\text{Te}_{10}$, has been considered in the spectral range of 0.3-1.3 THz, where n_o and n_e were found to be ~ 3.9 and ~ 4 , respectively [70].

Takeya et al. investigated LiGaS_2 , LiGaSe_2 , LiInS_2 , and LiInSe_2 biaxial crystals at frequencies between 0.4-2 THz and extracted the refractive indices along the [100] crystallographic axis, $n_{[100]}$, and the [001] crystallographic axis, $n_{[001]}$ [71]. For all of these crystals, $n_{[001]}$ was found to be higher than $n_{[100]}$ at each frequency [71]. Specifically, $n_{[001]}$ ranged between 2.76-3.04 and $n_{[100]}$ ranged between 2.61-2.74 across the investigated frequency range of 0.4-2 THz [71]. Along the [001] crystallographic axis, the THz radiation absorption coefficient, $\alpha_{[001]}$, was measured to be $< 9 \text{ cm}^{-1}$ for all of these crystals [71]. A more detailed study was performed by Liang et al. on LiInSe_2 at frequencies between 0.3-2.3 THz [72]. Here, $n_{[100]}$, the refractive index along [010] crystallographic axis ($n_{[010]}$), and $n_{[001]}$ were determined, as well as the absorption coefficient along the [100] crystallographic axis ($\alpha_{[100]}$), the absorption coefficient along the [010] crystallographic axis ($\alpha_{[010]}$), and $\alpha_{[001]}$ [72]. The values of $n_{[100]}$ and $n_{[001]}$ were quite similar, and both were higher than $n_{[010]}$ [see Fig. 1.10(e)] [72]. Similarly, $\alpha_{[100]}$ and $\alpha_{[001]}$ were similar, both of which were higher than $\alpha_{[010]}$ [see Fig. 1.10(f)] [72]. $\alpha_{[100]}$, $\alpha_{[010]}$, and $\alpha_{[001]}$ exhibited strong absorption due to phonon resonances at 1.9, 2.13, and 1.3 THz, respectively [72]. Liang et al. also reported on the temperature dependency of $n_{[100]}$, $n_{[001]}$, $\alpha_{[100]}$, and $\alpha_{[001]}$ for a LiInSe_2 crystal [73]. At frequencies between 0.3-2.3 THz, $n_{[100]}$, $n_{[001]}$, $\alpha_{[100]}$, and $\alpha_{[001]}$ typically increased as the temperature changed from 20-300 K [73]. Using THz-TDS measurements at frequencies between 0.3-2.7 THz, Yiwen et al. showed that the biaxial nature of a BGS crystal caused the THz radiation to propagate through the crystal as two elliptically-polarized eigenmodes [74]. These modes had frequency-dependent major axis directions and ellipticities, which varied by as much as $\sim 45^\circ$ and $\sim 40^\circ$ within the 0.5-2.5 THz frequency range [74].

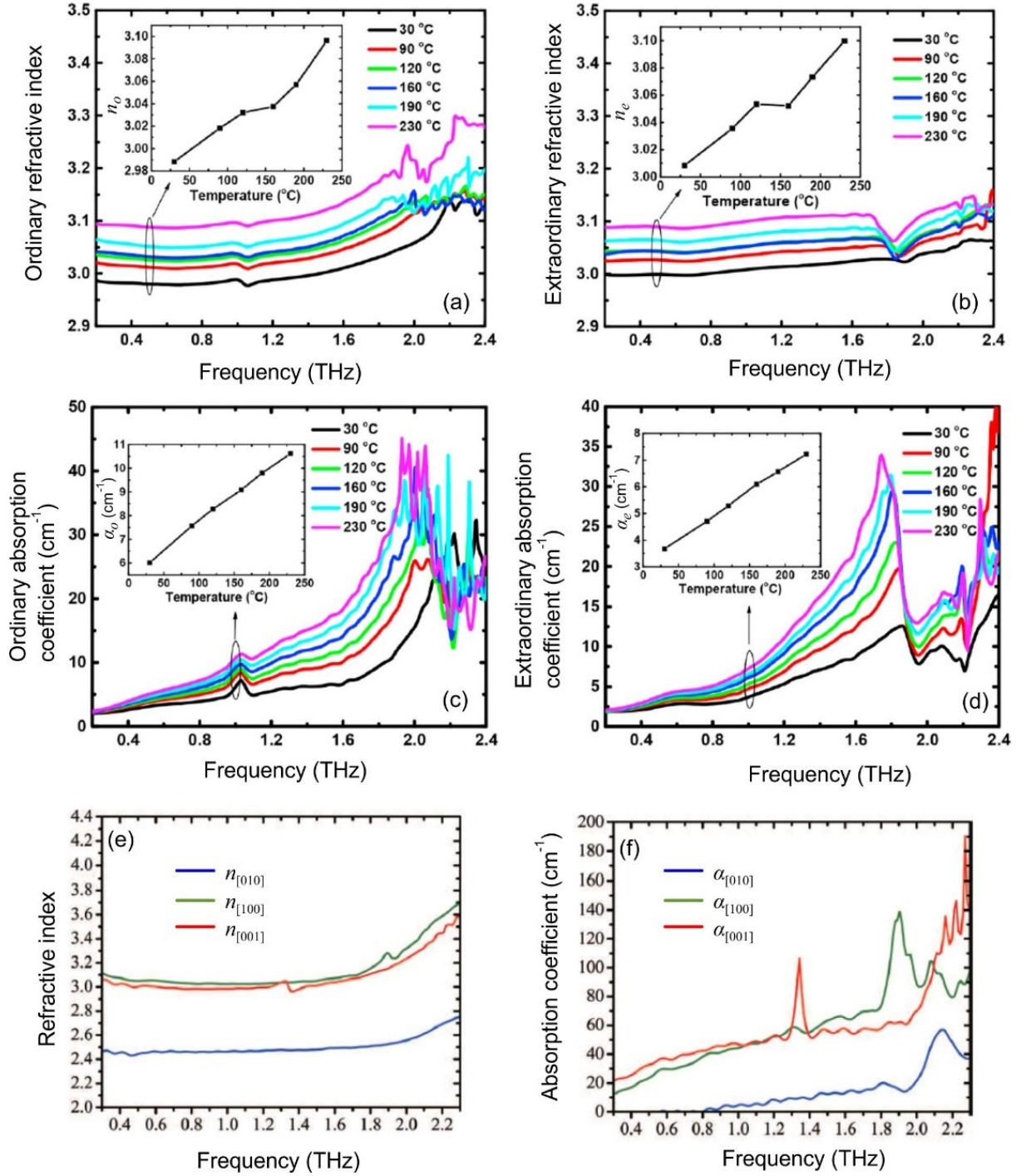


Fig. 1.10. Temperature-dependent (a) ordinary and (b) extraordinary refractive indices of an AgGaS₂ crystal [69]. Temperature-dependent (c) ordinary and (d) extraordinary absorption coefficients of an AgGaS₂ crystal [69]. (e) Refractive indices and (f) extinction coefficients along the [100], [010], and [001] crystallographic axes of an LiInSe₂ crystal [72].

1.4.7. THz radiation generation via nonlinear frequency-conversion in chalcogenide ternary crystals

THz radiation generation via OR in 2 mm-thick lithium-based chalcogenide ternary crystals (i.e. LiGaS₂, LiGaSe₂, LiInS₂, and LiInSe₂) has been reported by Takeya et al. [71,75]. THz radiation containing frequency components up to 4 THz was produced by exciting these lithium-based crystals using a 1560 nm, 63 fs laser pulse. The peak-to-peak THz electric fields generated from the LiGaSe₂ and LiInSe₂ crystals were >2.5 times higher than those produced from the LiGaS₂ and LiInS₂ crystals, as shown in Fig. 1.11(a) [75]. The long lasting (i.e. >20 ps) oscillations observed in the THz radiation electric field signal produced from the LiInSe₂ crystal were attributed to the 2.87 THz phonon resonance, as observed in Fig. 1.11(b). Similarly, phonon modes at 2.6 and 3.45 THz [see Fig. 1.11(b)] led to the beating observed in the THz radiation electric field signal produced from the LiGaSe₂ crystal [75]. More recently, Knorr et al. reported on the DFG of phase-locked THz radiation electric fields exceeding 13 MV/cm [see Fig. 1.11(c) and 1.11(d)], which were produced using a 1 mm-thick LiGaS₂ crystal in a type II phase-matching configuration [76]. The DFG spectra are displayed in Fig. 1.11(e), which exhibited central frequencies of ~30 and 42 THz, as dictated by the phase-matching angle of the crystal [76]. A similar arrangement based on DFG in a LiGaS₂ crystal was also shown to generate radiation centred at ~25 THz [77]. Notably, DFG THz radiation generation using this LiGaS₂ crystal follows the same principles outlined in detail in Refs. [32,78–80]. Liang et al. investigated another chalcogenide ternary crystal, AGS, in the THz frequency regime, where OR in this crystal exhibited a bandwidth >2 THz [81]. Using the similar crystal of AgGaS₂, Porer et al. incorporated a 780 nm, 12 fs excitation pulse to produce ultra-broadband THz radiation centered at 45 THz [82]. In order to satisfy the phase-matching requirements, the crystal was rotated by the azimuthal

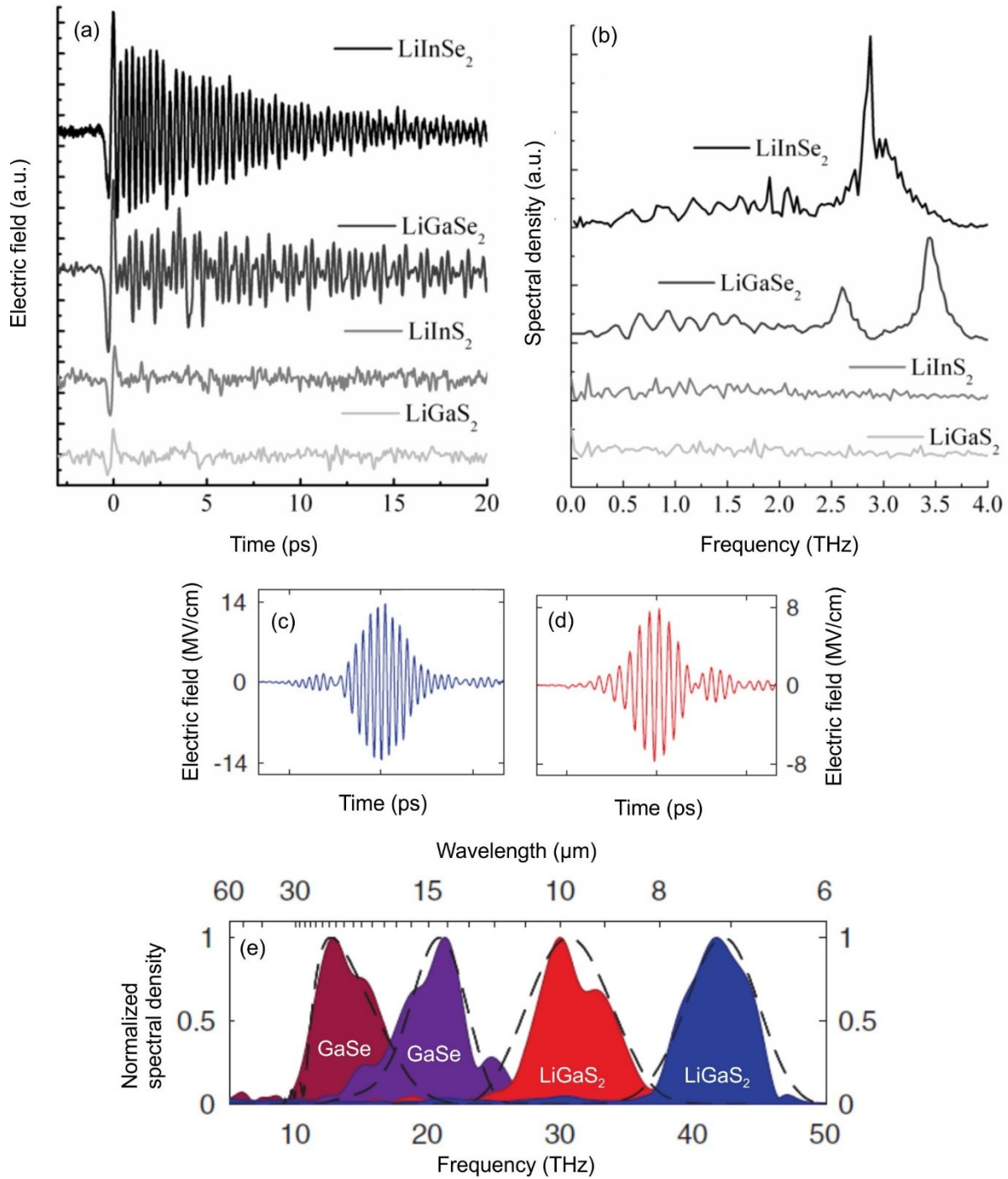


Fig. 1.11. (a) THz time-domain signals and (b) the associated spectra produced using LiGaSe₂, LiGaS₂, LiInSe₂, and LiInS₂ crystals [75]. (c,d) THz time-domain signals and (e) the associated spectra produced using an LiGaS₂ crystal. In (e), the spectra centered at ~13 and 22 THz were obtained using a GaSe crystal [76].

angle of 45° and tilted by the polar angle of 57° [82]. Interestingly, Sell et al. implemented a similar approach and crystal, but utilized a fixed laser source at $1.1 \mu\text{m}$ and a laser source tunable from $1.1\text{-}1.5 \mu\text{m}$, which produced THz radiation centred at $\sim 72 \text{ THz}$ [83]. Notably, a more detailed description of the DFG THz radiation generation arrangement implemented in Refs. [82,83] is described in Refs. [32,78–80].

Work by both Kang et al. and Liu et al. showed that a (110)-cut $\text{Zn}_{1-x}\text{Cd}_x\text{Te}$ crystal (excited using a 180 fs, 820 nm electric field pulse) produced THz radiation of varying strengths, with the highest peak-to-peak electric field value obtained from a $\text{Zn}_{0.95}\text{Cd}_{0.05}\text{Te}$ crystal [84,85]. Subsequent work by Yi et al. theoretically determined that, when utilizing an 850 nm laser excitation pulse, optimal THz radiation generation occurred from a $\text{Zn}_{0.35}\text{Cd}_{0.65}\text{Te}$ crystal [86]. THz radiation generation was also investigated using a similar crystal, (110)-cut $\text{Zn}_{0.972}\text{Mn}_{0.028}\text{Te}$, where a THz electric field pulse having a peak-to-peak value $\sim 20\%$ higher than that produced from a ZnTe crystal was generated [66]. Although no experimental THz generation measurements have been reported on $\text{PbGa}_6\text{Te}_{10}$ and $\text{PbIn}_6\text{Te}_{10}$ crystals, detailed theoretical calculations determined that the conversion efficiency of THz radiation sources based on these chalcogenide ternary crystals could be as high as 10^{-2} , with $\text{PnIn}_6\text{Te}_{10}$ being more efficient than $\text{PbGa}_6\text{Te}_{10}$ [58].

1.4.8. THz radiation detection using chalcogenide ternary crystals

In comparison to nonlinear radiation generation, significantly fewer studies have been reported on EO sampling using chalcogenide ternary crystals. EO sampling of a THz radiation pulse that contained frequencies $>60 \text{ THz}$ was achieved using a $100 \mu\text{m}$ -thick AgGaS_2 crystal [see Fig. 1.12(a) and 1.12(b)] [82]. In this arrangement, a 780 nm, 12 fs EO sampling pulse was used to detect the THz radiation when the AgGaS_2 crystals was rotated by the azimuthal angle of 45°

and tilted by the polar angle of 57° [82]. A detailed description of the principles associated with this high-frequency EO sampling arrangement can be found in Refs. [32,79]. The application of a (110)-cut $\text{Zn}_{1-x}\text{Cd}_x\text{Te}$ crystal for THz EO sampling was demonstrated by both Liu et al. and Kang et al. [85,87]. Figure 1.12(c) depicts the THz electric field pulses sampled by a 180 fs,

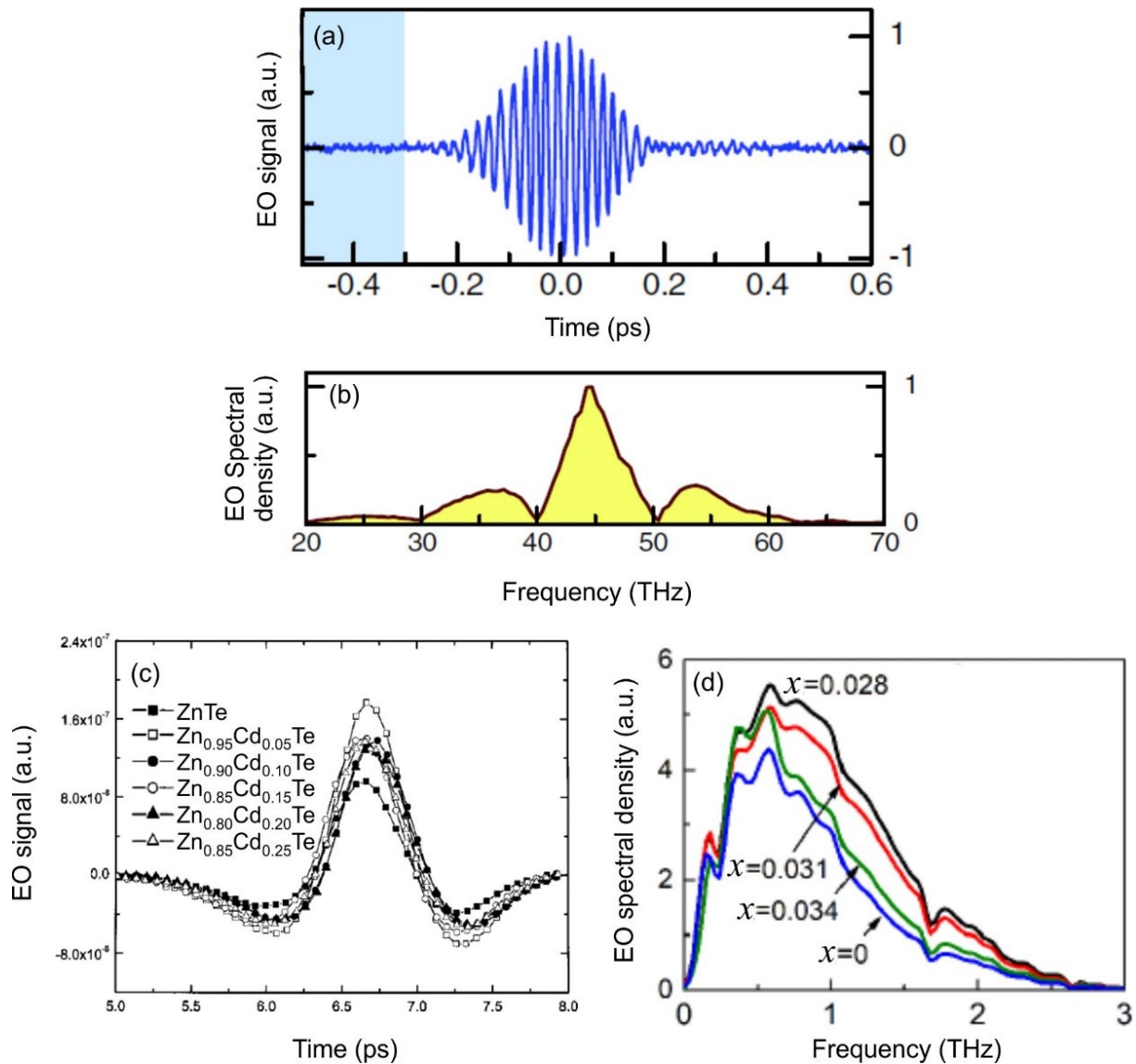


Fig. 1.12. (a) EO time-domain signal and (b) the associated spectrum obtained using an AgGaS_2 crystal [82]. (c) EO time-domain signals obtained using $\text{Zn}_{1-x}\text{Cd}_x\text{Te}$ crystals [87]. (d) EO spectra obtained using $\text{Zn}_{1-x}\text{Mn}_x\text{Te}$ crystals [66].

820 nm probe pulse in (110)-cut $\text{Zn}_{1-x}\text{Cd}_x\text{Te}$ crystals that had varying Cd molar fractions [87]. The influence of Cd on the strength of the detected THz signal was clearly apparent, where the $\text{Zn}_{0.95}\text{Cd}_{0.05}\text{Te}$ crystal exhibited a peak-to-peak amplitude $\geq 25\%$ higher than that of ZnTe or $\text{Zn}_{1-x}\text{Cd}_x\text{Te}$ with $x \geq 0.1$ [87]. An enhanced THz EO sampling response was also observed from (110)-cut $\text{Zn}_{1-x}\text{Mn}_x\text{Te}$ crystals [66,88]. As shown in Fig. 1.12(d), the sampled THz radiation spectral density depended on the crystal composition, with the $\text{Zn}_{0.972}\text{Mn}_{0.028}\text{Te}$ crystal being $>30\%$ higher than that of a ZnTe crystal [66]. This enhancement was attributed to the low density of free charge carriers that resulted from the Mn atoms tendency to substitute the Zn atoms [88].

1.4.9. Pnictide and chalcogenide ternary crystals for high-field THz radiation generation

Pnictide and chalcogenide ternary crystals provide a multitude of application potential due to their inherent properties. To achieve high-field, high-power, high-efficiency, and/or wide-bandwidth nonlinear frequency-conversion, the nonlinear media must possess several key properties. A high second-order nonlinearity permits more efficient frequency-conversion in comparison to an identical nonlinear media with a lower second-order nonlinearity. A wide bandgap is necessary to avoid free carrier generation via single-photon or multi-photon absorption, and a wide transparency range allows for flexibility in selecting the excitation wavelength. Additionally, crystals should have low absorption losses at both the excitation wavelengths and the generated THz frequencies. High absorption at the excitation wavelengths would limit the efficiency of the frequency-conversion process from occurring, while absorption at the generated THz frequencies would allow the frequency-conversion process to occur, but the generated THz frequency components would be absorbed before exiting the nonlinear crystal. A high laser

damage threshold is also beneficial, as it allows for a higher excitation intensity. Another critical property is the ability of a nonlinear crystal to exhibit phase-matching between the excitation wavelengths and the generated THz frequencies. While phase-matching is sometimes achieved in bulk crystals, more elaborate schemes can be implemented to satisfy phase-matching conditions, such as exciting the crystal at off-normal incidence angles [89], using a tilted-wavefront arrangement [90], implementing waveguiding geometries [91], etc.

Pnictide and chalcogenide ternary crystals inherently possess many of the aforementioned properties. For example, the CSP pnictide crystal exhibits a $d_{36}=84.5$ pm/V at $\lambda_{exc}=4.6$ μm [35], a wide bandgap of 2.45 eV [37], and a wide transparency range of 0.52-9.5 μm (i.e. 31.6-577 THz) [35]. Furthermore, the CSP crystal absorption is low at excitation wavelengths in the near-IR regime (e.g. absorption coefficients are $\lesssim 1$ cm^{-1} at ~ 1 μm [92]). For a femtosecond excitation pulse having a central wavelength of 800 nm, saturation of the generated THz radiation occurs at a peak intensity above 100 GW/cm^2 [28]. The damage threshold has not been determined when this crystal is excited by femtosecond electric field pulses, which could be the focus of future studies. Nonetheless, THz electric fields as high as 0.4 MV/cm have been produced using CSP crystals [28]. Alternatively, the AGS chalcogenide crystal exhibits a $d_{36}=39.5$ pm/V at $\lambda_{exc}=10.6$ μm [55], a bandgap of 1.8 eV [55], and a transparency range of 0.76-18 μm (i.e. 16.7-395 THz) [55]. The losses are low for excitation wavelengths in the near-IR regime (e.g. absorption coefficients are < 0.5 cm^{-1} at ~ 1 μm [93]). While THz electric field strengths have not been explicitly stated in literature for a AGS crystal, peak-to-peak values exceeding 13 MV/cm have been obtained using a LiGaS₂ chalcogenide crystal [76]. Since the second-order nonlinearity of AGS is > 6 times higher than that of LiGaS₂ [55], this suggests the enormous potential of AGS for high-field THz radiation generation.

1.5. On-chip waveguiding platforms for THz radiation generation²

When compared to its neighboring frequency ranges (i.e. microwave and IR), one can say that the THz frequency range has faltered in addressing practical applications. While there are numerous on-chip integrated microwave, IR, and optical sources capable of produce high powers, there is a lack of compact THz sources, thereby limiting the development of critical THz radiation technologies. Although scientific progress has broadened the scope and understanding of the intriguing THz spectral regime, these advances are calling for THz-wave technologies to evolve beyond laboratory research and into the realm of real-world applications. To enable THz radiation technology to traverse into solving real-world problems and open up doors to new applications, the first step is to realize THz sources that are compact, broadband, and highly efficient.

As waveguides are compatible with on-chip fabrication techniques and can exhibit small footprints, they provide an optimal platform for on-chip THz radiation generation via nonlinear frequency-conversion processes [e.g. DFG and OR]. Notably, since the cross-sectional dimensions of a waveguide are directly related to the effective refractive indices of the guided excitation mode and the guided THz mode, waveguides provide added versatility in satisfying the conditions for phase-matching (see Appendix A). Not to mention, diffraction is advantageously avoided in waveguides, since the excitation electric field remains confined along the entire length of the waveguide, thus permitting high peak intensities (e.g. $>GW/cm^2$) beneficial to nonlinear frequency-conversion processes. In this respect, it is important to consider the advantages of specific waveguiding geometries (e.g. planar dielectric waveguides, parallel plate waveguides,

²A version of this section's work is under review in *Laser & Photonics Reviews*.

rectangular dielectric waveguides, metallic slit waveguides, ridge waveguides, photonic crystal waveguides, etc.) for guiding the optical excitation electric fields and the generated THz radiation. Parallel plate and metallic slit waveguides allow the generated THz radiation to be guided as a transverse electromagnetic (TEM) mode, such that there is no cut-off frequency. Rectangular dielectric waveguides, ridge waveguides, and metallic slit waveguides are ideal for achieving high optical-to-THz conversion efficiencies. In such waveguiding structures, the excitation electric field can be confined to a small cross-sectional area, which aids in achieving a high peak intensity and thus a high conversion efficiency. Planar waveguides are specially-suited for handling very high excitation electric field energies (e.g. millijoules to joules). Specifically, in DFG and OR, THz radiation generation saturates at peak excitation intensities higher than the threshold for multi-photon absorption, such that the excitation electric field can be spread along the planar waveguide to ensure its peak intensity remains below the multi-photon absorption threshold. Photonic crystal waveguides allow for the design of transmission bands and stop bands, which provide control of the frequencies supported by the waveguide. As such, the optimal choice of waveguide depends on several factors, including the excitation pulse energy, the excitation pulse peak intensity, the generated THz frequencies, and the intended application.

Nonlinear frequency-conversion for THz radiation generation in a waveguide is governed by the orientation and the atomic or molecular asymmetry of the nonlinear waveguiding layer. Naturally, this layer is composed of either a nonlinear crystalline material [30], or a polymer whose chromophores are aligned through a poling process [94,95]. Some common nonlinear crystals used for THz radiation generation in waveguides are GaP, GaAs, and LiNbO₃ (LN). GaP, and GaAs crystals exhibit a $\bar{4}3m$ point group symmetry [96,97], with the second-order nonlinear coefficient

tensor given in Eq. (1.4). Withal, a LN crystal exhibits a $3m$ point group symmetry [30], with a second-order nonlinear coefficient tensor of [30,43],

$$\bar{d}_{3m} = \begin{bmatrix} 0 & 0 & 0 & 0 & d_{15} & -d_{22} \\ -d_{22} & d_{22} & 0 & d_{15} & 0 & 0 \\ d_{31} & d_{31} & d_{33} & 0 & 0 & 0 \end{bmatrix}, \quad (1.7)$$

where d_{15} , d_{22} , d_{31} , and d_{33} are non-vanishing tensor elements. For $\bar{4}3m$ crystals, a typical arrangement employs electric fields polarized along the $[100]$ crystallographic axis, $E_{[100]}$, and the $[010]$ crystallographic axis, $E_{[010]}$, to produce a second-order nonlinear polarization along the $[001]$ crystallographic axis, $P_{[001]}^{(2)} = 4\varepsilon_0 d_{36} E_{[100]} E_{[010]}$. Similarly, for crystals belonging to the $3m$ symmetry group, it is common to excite them using an electric field polarized along the $[001]$ crystallographic axis, $E_{[001]}$, which produces a second-order nonlinear polarization along the crystal's $[001]$ crystallographic axis, $P_{[001]}^{(2)} = 2\varepsilon_0 d_{33} E_{[001]}^2$. These excitation arrangements can be realized using $\bar{4}3m$ crystals cut along the (110) crystallographic plane or $3m$ crystals cut along the (100) or (010) crystallographic planes. In these scenarios, d_{36} and d_{33} become the primary tensor element influencing the second-order nonlinear frequency-conversion process in the $\bar{4}3m$ and $3m$ crystals, respectively. Interestingly, such second-order nonlinear tensor elements can be very high for nonlinear interactions occurring at THz frequencies, since significant enhancement occurs near phonon mode resonances (i.e. the atoms and ions of the crystal respond strongly near these resonances) [38]. For THz radiation generated by near-IR excitation wavelengths, $d_{36} \approx 50$ and 25 pm/V for GaAs and GaP, respectively, and $d_{33} \approx 180$ pm/V for LN [96,98,99]. Nonetheless, in addition to the crystal's nonlinearity, the efficiency of THz radiation generation within a nonlinear waveguide is highly-dependent on other factors, including the spatial pattern of the mode,

confinement of the mode to the nonlinear medium, mode parity, waveguide dispersion, excitation angle, etc.

In this section, we survey past and recent progress in nonlinear frequency-conversion for the generation of THz radiation in waveguides. Such THz radiation waveguiding sources provide an ideal platform for integration with photonic chips, primarily due to the waveguide's compatibility with nanofabrication techniques and the added benefit of a small footprint. The second-order nonlinear interactions of DFG and OR are considered in the most widely used nonlinear materials, which include GaP, GaAs, LN, and poled-polymers. A comprehensive discussion of recent developments is presented for a variety of waveguiding arrangements, emphasizing their inherent characteristics and potential. Herein, such arrangements are categorized as those that confine both the optical excitation and the generated THz electric fields, those that confine the optical excitation electric field but not the generated THz radiation, and those that confine the generated THz radiation but not the optical excitation electric field. Within each of these categories, a broad assortment of waveguiding platforms are considered, including planar dielectric waveguides, leaky planar waveguides, parallel plate waveguides, metallic slit waveguides, rectangular waveguides, ridge waveguides, wire waveguides, photonic crystal waveguides, poled waveguides, and multiple waveguides embedded within each other.

1.5.1. Guided excitation electric fields and guided generated THz radiation

Exploiting the modal confinement properties of waveguides is an effective approach to achieving nonlinear THz radiation generation over long distances (e.g. up to millimeters or centimeters). As such, for both OR and DFG nonlinear processes, it is common for both the optical

excitation electric fields and generated THz radiation to be guided along a waveguiding structure. It should be noted to the reader that, in the following discussions, we differentiate between THz radiation frequencies produced by OR and DFG as f_{OR} and f_{DFG} , respectively. Owing in part to their fabrication simplicity, planar dielectric waveguides have emerged as a prominent platform to guide both the excitation electric fields and the generated THz radiation. Yang et al. reported a theoretical analysis to determine the OR coherence length in planar dielectric waveguides [100]. At an excitation wavelength of 1550 nm, a ZGP-GaAs-ZGP planar waveguide (that had a 60 μm -thick GaAs layer) exhibited the long coherence length of 4 mm [100]. Pálfalvi et al. proposed another waveguiding geometry, which reduced THz loss by ensuring that the majority of the THz radiation energy was guided in the low-loss cladding layers of the waveguide [101]. To allow for phase-matching, the proposed arrangement required an excitation pulse that had a tilted wavefront [101]. Vodopyanov and Avetisyan investigated a 7.5 mm-long, 61 μm -thick GaAs planar waveguide [102]. When excited at wavelengths near 2128 nm, the waveguide produced THz radiation at the frequency of 2.07 THz [see Fig. 1.13(a)] [102]. A 290 μm -thick,

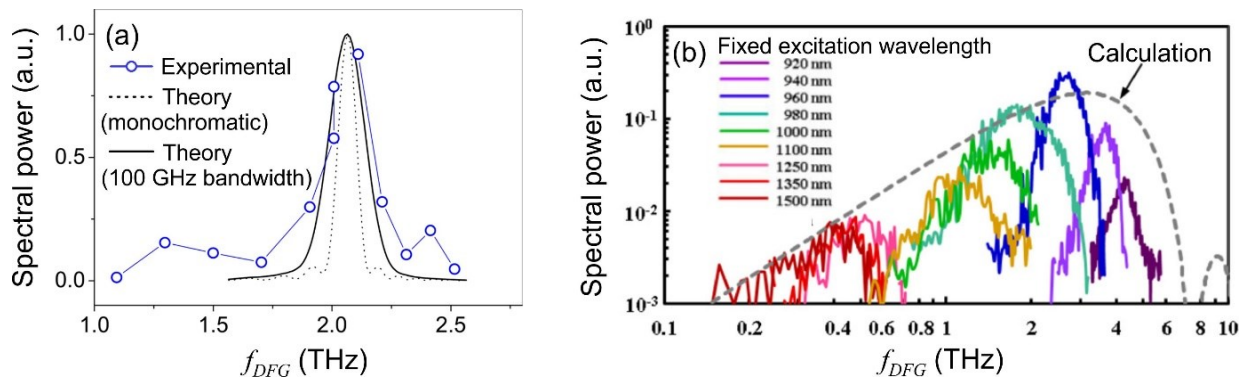


Fig. 1.13. (a) DFG THz radiation spectral power produced from a GaAs planar waveguide [102]. The theoretical spectral power fits, obtained using monochromatic excitation electric fields and excitation electric fields having 100 GHz bandwidths, are shown for comparison [102]. (b) DFG THz radiation generated from a GaP planar waveguide [103].

10 mm-long, (100) GaP planar waveguide was also investigated for DFG THz radiation generation, where the waveguide was excited using a fixed wavelength (chosen within the range of 920-1500 nm) and a wavelength tuned across the range of 920-1500 nm [103]. As shown in Fig. 1.13(b), THz radiation was produced up to ~ 5 THz and followed the trend expected by theoretical calculations [103]. A similar GaP planar waveguide configuration was investigated by Saito et al.; however, elliptically-polarized THz radiation was produced by adjusting the polarization of the excitation pulses and the length of the GaP waveguide [104].

Generally, in comparison to planar waveguides, three-dimensional (3D) waveguides are more versatile for on-chip light guiding beyond a single plane. Excitation electric fields guided along various 3D platforms (i.e. rectangular dielectric waveguides, ridge waveguides, and cylindrical metal wire waveguides) have been realized for producing guided THz radiation via OR and DFG. A unique structure that consisted of a cylindrical metal wire, partially coated with a poled polymer that had a second-order nonlinearity, was experimentally investigated by Zhu et al. [94]. As depicted in Fig. 1.14(a), when the excitation pulse was guided along the polymer coated wire, it produced OR THz radiation that was also guided along the wire's metallic surface [94]. Using an 820 nm femtosecond excitation pulse, the authors demonstrated the generation of guided THz radiation having a bandwidth that extended up to 1 THz [see Fig. 1.14(b)] [94]. Using a LN rectangular (i.e. 9.4 μm thickness, 126 μm width, and 1 mm length) waveguide excited near 1060 nm, Takushima et al. numerically demonstrated THz radiation generation at the frequencies of 1 and 1.45 THz, which corresponded to DFG phase-matching for a TE_{11} (i.e. transverse electric) THz mode and a TE_{31} THz mode, respectively [105]. THz radiation generation via DFG was also observed using a (110) GaP rectangular waveguide, where a fixed wavelength of 1064 nm and a tunable wavelength between 1048-1063 nm were simultaneously used to excite the

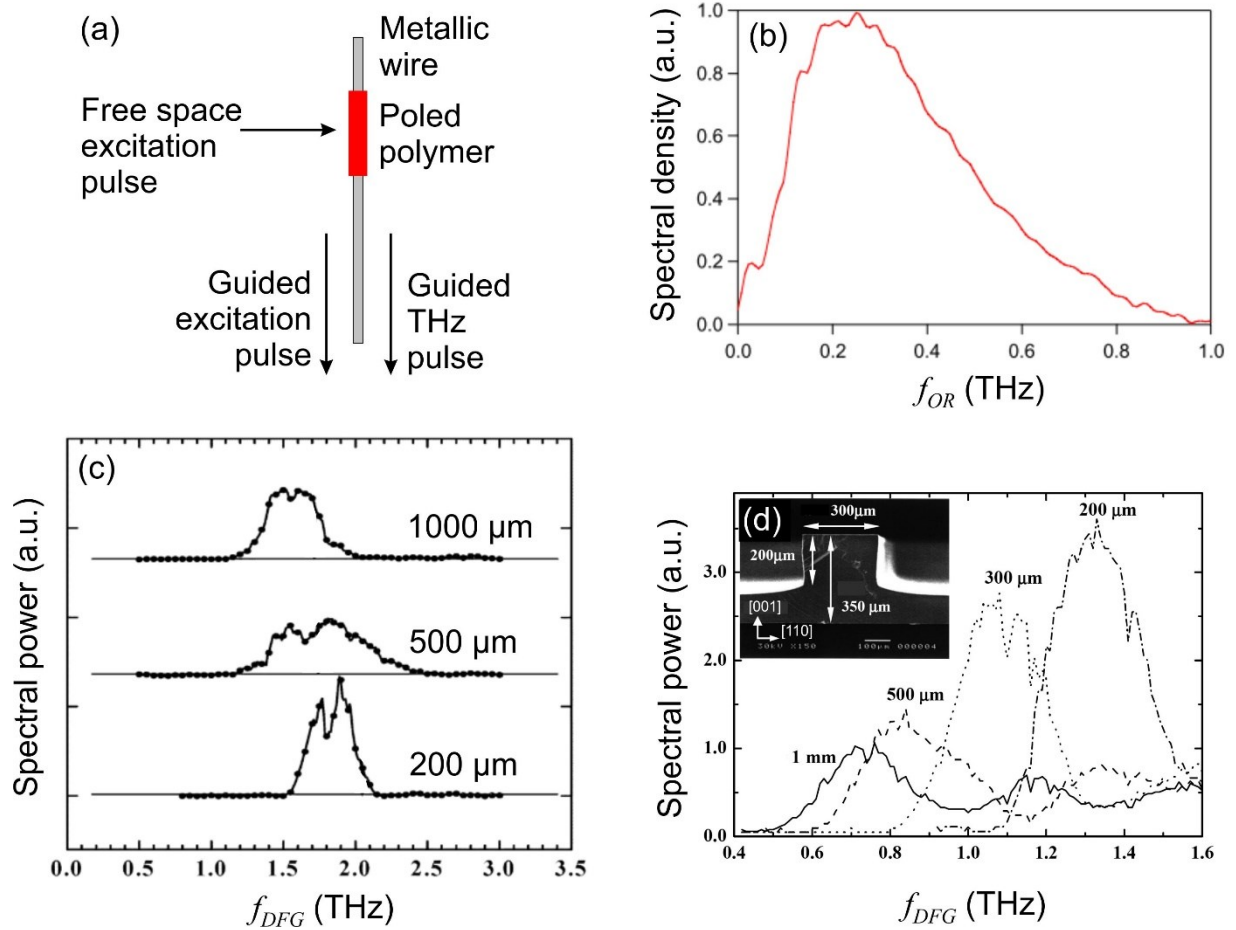


Fig. 1.14. (a) Illustration depicting THz radiation generation from a poled polymer-coated cylindrical metal wire waveguiding arrangement [94]. (b) Spectral density of OR THz radiation generated from the waveguide illustrated in (a) [94]. (c) DFG THz radiation produced by GaP rectangular waveguides that had widths of 200, 500, and 1000 μm [106]. (d) DFG THz radiation generated by GaP ridge waveguides that had ridge widths of 200, 300, 500, and 1000 μm , where the inset illustrates a scanning electron microscope image of a GaP ridge waveguide that had a ridge width of 300 μm [107].

waveguide [106]. 5 mm-long, 160 μm -thick waveguides that had widths of 200, 500, and 1000 μm exhibited THz radiation emission at ~ 1.6 -2.1 THz, ~ 1.2 -2.3 THz, and ~ 1.2 -2 THz, respectively [see Fig. 1.14(c)] [106]. Similar experiments were performed using a 200 μm thick, (110) GaP ridge waveguide that was fabricated on a 150 μm -thick GaP slab, as shown in the inset of

Fig. 1.14(d) [107]. This structure was excited using a wavelength fixed at 1064 nm and a wavelength tunable from 1058-1063 nm [107]. As shown in Fig. 1.14(d), the generated THz radiation exhibited peak emission at the frequencies of 1.3, 1.05, 0.8, and 0.7 THz for ridge widths of 200, 300, 500, and 1000 μm , respectively [107].

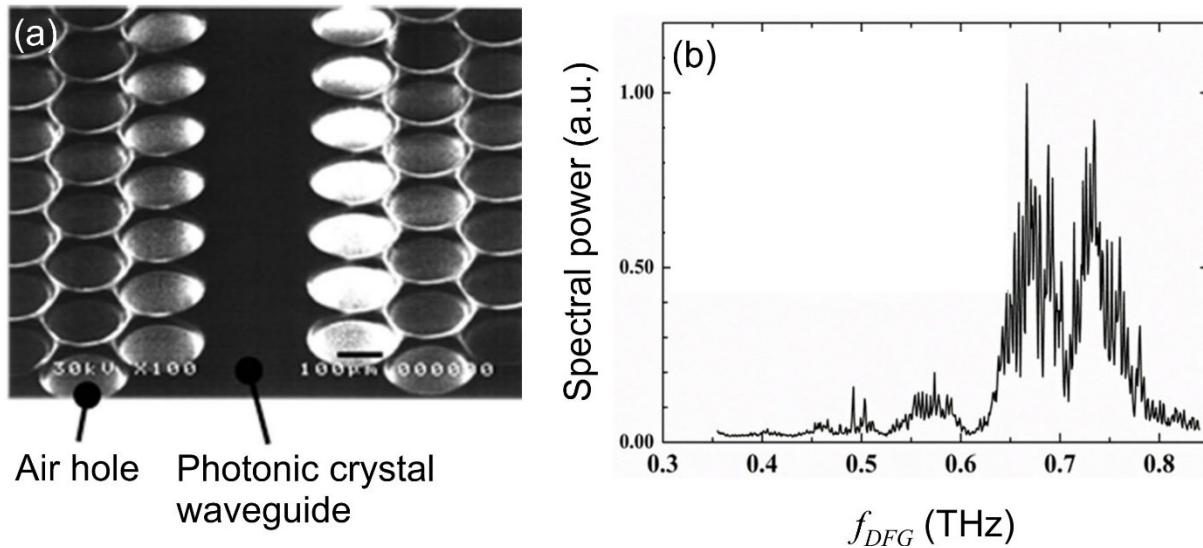


Fig. 1.15. (a) Scanning electron microscope image of a GaP photonic crystal waveguide that had a 300 μm -wide line defect [108]. (b) DFG THz radiation produced by the waveguide shown in (a) [108].

Photonic crystal waveguides have been utilized for guiding both the excitation electric field and the generated THz radiation. A GaP photonic crystal fiber, comprised of a solid GaP central section surrounded by circular air regions, was proposed by Li et al. for producing OR THz radiation [109]. Their theoretical analysis showed that THz radiation generation near 1 THz was possible when the photonic crystal fiber was excited by a 1040 nm, 100 fs laser pulse [109]. Saito et al. reported on THz radiation generation from a 60 μm -thick, 10 mm-long, (110) GaP photonic crystal waveguiding arrangement that had a 300 μm wide line defect [see Fig. 1.15(a)] [108]. When the photonic crystal waveguide was simultaneously excited at a fixed wavelength of

1216 nm and a wavelength tunable between 1217-1221 nm, a \sim 0.6-0.8 THz DFG signal was obtained [see Fig. 1.15(b)] [108].

Since the optical excitation wavelength is much shorter in comparison to the generated THz wavelength, it has become typical to embed the waveguide guiding the excitation electric field within the waveguide that guides the generated THz radiation. Such embedded waveguiding configurations have been used in both OR and DFG processes for producing THz radiation. An acrylate-poled polymer-acrylate planar waveguide embedded within a parallel plate waveguide [see Fig. 1.16(a)] was experimentally investigated by Cao et al. for OR THz radiation generation [110]. An 820 nm, 100 fs excitation pulse was guided along the acrylate-poled polymer-acrylate planar waveguide and produced THz radiation that coupled into the parallel plate waveguide [110]. THz electric field pulses having \lesssim 1 ps durations were measured from waveguides that had lengths of 1, 2, and 3 mm, the results of which are shown in Fig. 1.16(b) [110]. The embedded waveguiding configuration illustrated in Fig. 1.16(c) was proposed by Marandi et al., where 1.5 and 1.6 μ m excitation wavelengths were guided along the AlGaAs-GaAs-AlGaAs ridge waveguide and produced DFG THz radiation at 3.5 THz, which propagated along the metallic slit waveguide [111]. Another arrangement for DFG THz radiation generation implemented a GaP ridge waveguide embedded within a rectangular Si waveguide [see Fig. 1.16(d)], where the former and latter mentioned waveguides were used to guide the excitation wavelengths and the generated THz radiation, respectively [112]. Using numerical methods, this arrangement was shown to produce radiation at 5.93 THz (conversion efficiency of $6.6 \times 10^{-4} \text{ W}^{-1}$) when excited using wavelengths near 1550 nm [112]. Chen et al. proposed a hybrid waveguiding platform that consisted of a Ti-diffused LN channel waveguide embedded within a photonic crystal waveguide [113]. The proposed structure guided two excitation wavelengths (i.e. 1542 and 1550 nm) in the

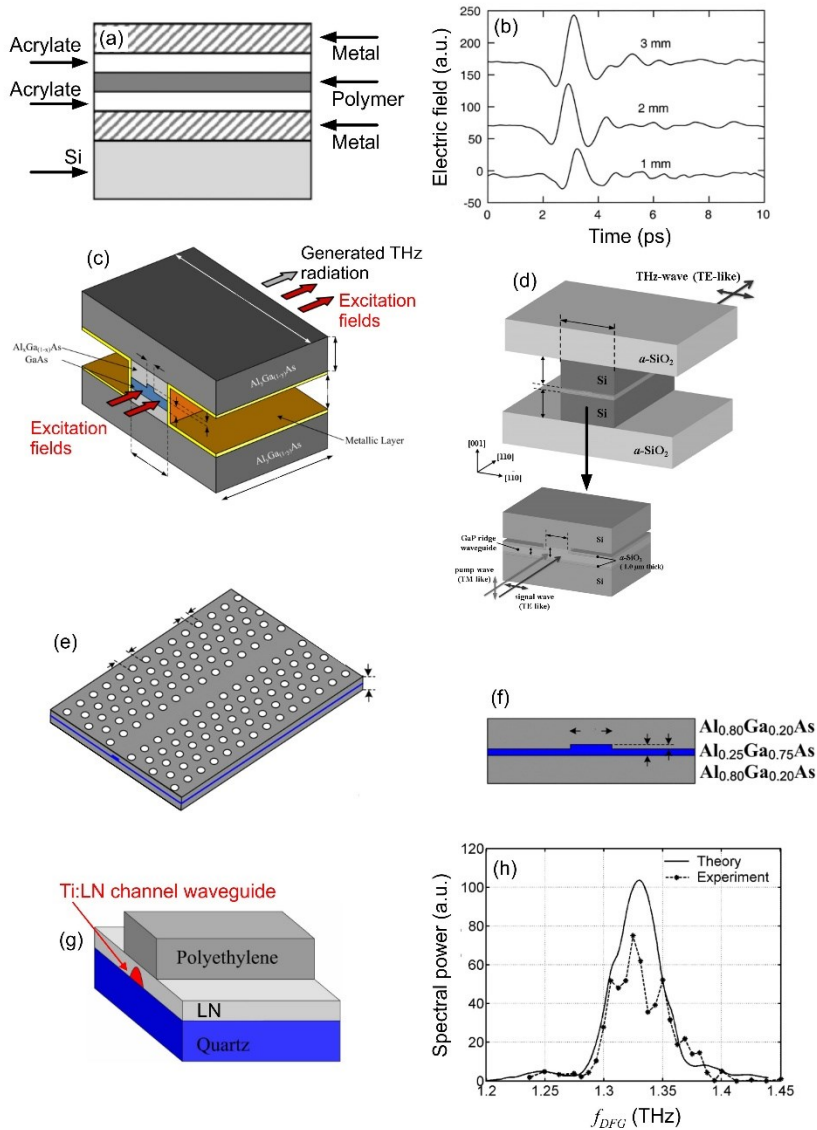


Fig. 1.16. (a) Cross-sectional illustration of an acrylate-poled polymer-acrylate planar waveguide embedded within a parallel plate waveguide [110]. (b) THz electric field pulses produced by the waveguiding arrangement depicted in (a) for waveguide lengths of 1, 2, and 3 mm [110]. (c) An AlGaAs-GaAs-AlGaAs ridge waveguide embedded within a metallic slit waveguide [111]. (d) A GaP ridge waveguide embedded within a rectangular Si waveguide [112]. (e,f) A waveguiding arrangement that consisted of a photonic crystal waveguide, (e), with an embedded AlGaAs ridge waveguide, (f) [114]. (g) Illustration of a Ti:LN channel waveguide embedded within a quartz-LN-HDPE waveguide [115]. (h) DFG THz radiation produced by the waveguiding arrangement depicted in (g) [115].

Ti-diffused LN channel waveguide, and confined the DFG THz wave within the photonic crystal waveguide [113]. For a channel length of 12 mm, the authors calculated a maximum conversion efficiency of $1.5 \times 10^{-5} \text{ W}^{-1}$ at 1 THz [113]. Another similar geometry was proposed by Chen et al., where a THz electric field produced via DFG was guided by an AlGaAs photonic crystal waveguide [see Fig. 1.16(e)] and the excitation wavelengths at 1565 and 1590 nm were guided by an embedded AlGaAs ridge waveguide [see Fig. 1.16(f)] [114]. The conversion efficiency of the proposed 12 mm long waveguiding structure was calculated to be $7.6 \times 10^{-5} \text{ W}^{-1}$ for generation at 3 THz [114]. Experimentally, DFG THz radiation generation was observed in a Ti:LN channel waveguide embedded in a waveguide comprised of a quartz cladding layer, a LN core layer, and a high density polyethylene (HDPE) ridge [see Fig. 1.16(g)] [115]. The excitation electric fields (a fixed wavelength of 1555 nm and a wavelength tunable between 1530-1610 nm) were confined to propagate in the Ti:LN layer, whereas the generated THz radiation was guided by the quartz-LN-HDPE waveguide [115]. As shown in Fig. 1.16(h), 1.33 THz radiation was produced using an 11 mm-long waveguide that had a LN thickness of 14 μm , a $500 \mu\text{m} \times 500 \mu\text{m}$ HDPE ridge cross-section, and a $100 \text{ nm} \times 9 \mu\text{m}$ a Ti:LN channel cross-section [115].

1.5.2. Guided excitation electric fields and free-space THz radiation emission

Various configurations have been reported that employ waveguides to confine the excitation electric field, while allowing the generated THz electric field to propagate unguided into free-space. Although the investigations are limited, planar dielectric waveguides that confine the excitation electric fields have been implemented as a platform for producing THz radiation. DFG THz radiation was produced using an LN-MgO:LN-polyethylene terephthalate (PET) planar

waveguide with a Si prism array contacted to its surface [shown in Fig. 1.17(a)], where the generated THz radiation was emitted as Cherenkov waves [116,117]. A 70 mm-long waveguide that had an MgO:LN thickness of $3.8\ \mu\text{m}$ produced free-space radiation tunable between 0.2-7.8 THz [see Fig. 1.17(b)], where the generated radiation exhibited a maximum energy of $\sim 3.2\ \text{pJ}$ and a maximum conversion efficiency of 10^{-7} [116,117]. Since the THz frequency components propagated through an array of Si prisms (opposed to a single larger prism), this arrangement was optimal for extracting narrowband THz radiation [116,117]. While no studies have been performed on planar dielectric waveguides for the generation of OR THz radiation, we envision such investigations being conducted going forward, due to the advantages associated with both planar waveguides and the OR process (e.g. ease of fabricating planar waveguides, the ability of planar waveguides to support large excitation energies, OR producing broadband THz radiation, etc.).

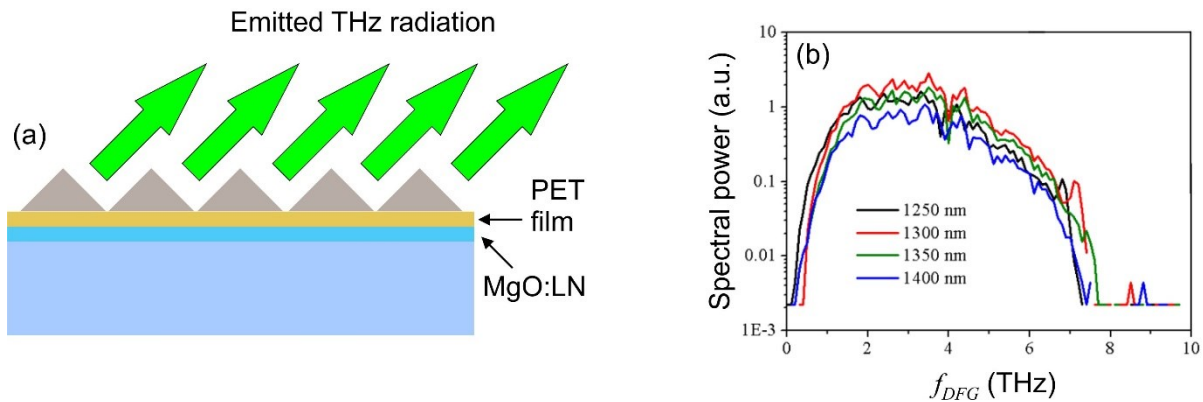


Fig. 1.17. (a) Illustration of a LN-MgO:LN-PET planar waveguide showing the generated THz radiation being emitted as Cherenkov waves [116]. (b) Spectra of the DFG THz radiation produced by the waveguide in (a) [116].

Leaky planar waveguides have been utilized to weakly confine optical excitation electric fields and generate OR THz radiation emitted as free-space Cherenkov waves. Typically, leaky

waveguides consist of a low index dielectric core and higher index dielectric cladding layer(s) [91]. As long as the dielectric core layer is sufficiently thick, the majority of the optical excitation electric field is guided, while radiating weakly into free-space (e.g. a Si-LN-Si waveguide having an LN layer thickness of a few tens of micrometers exhibits radiative losses of only a few percent when excited at the wavelength of 800 nm) [91]. Notably, all the forthcoming leaky planar waveguide investigations have been conducted for an optical excitation electric field polarization oriented along the LN layer's [001] crystallographic axis. OR THz radiation generation was numerically investigated for a Si-LN-Si leaky planar waveguide that had LN thicknesses of 20 and 40 μm [91]. When excited by an 800 nm, 100 fs pulse, the generated THz radiation bandwidth extended past 4 THz [91]. Bodrov et al. reported on a similar leaky planar waveguide that consisted of Bk7-LN-Si layers [see Fig. 1.18(a)] [118]. By coupling a high-energy (i.e. microjoule) 780 nm, 50 fs excitation pulse into a leaky planar waveguide that had a LN layer thicknesses of 50 μm , an ~ 1 ps-long OR THz electric field pulse was produced [see Fig. 1.18(b)] [118]. As shown in Fig. 1.18(c), frequency components >3 THz were obtained using waveguides that had LN layer thicknesses of 30 and 50 μm [118]. The dependence of the generated OR THz radiation on the excitation electric field wavelength was further studied by Bodrov et al. [119]. Using excitation pulses that had a duration of ~ 50 fs and central wavelengths of 800, 1300, 1500, 2000, and 2100 nm, OR THz radiation was produced from a 9 mm-long air-LN-Si leaky planar waveguide that had an LN thickness of 40 μm [119]. The authors showed that the conversion efficiency could be improved by a factor of three when the excitation wavelength was increased from 800 nm to 2.1 μm [119]. While the previously mentioned experiments were conducted with optical excitation pulses at energies in the microjoule range, Bakunov et al. reported on Cherenkov THz radiation generation from an air-LN-Si waveguide excited by ultrashort laser pulses at

nanojoule energies [120]. A 10 mm-long air-LN-Si leaky planar waveguiding arrangement that had an LN thickness of 35 μm was excited by an 8 nJ, 800 nm, 100 fs pulse [120]. THz radiation was produced up to ~ 4.5 THz at a conversion efficiency of 8×10^{-5} , where this latter value is two orders of magnitude higher than that of free-space THz radiation generation arrangements impinging a bulk ZnTe crystal [120]. A variation of the leaky planar waveguide, comprised of metal-air-LN-Si layers [see Fig. 1.18(d)], exhibited a good THz radiation conversion efficiency of 2.5×10^{-3} when excited at an energy of ~ 20 μJ [121,122]. The metal substrate layer reflected the THz radiation generated at the Cherenkov angle of $-|\theta_c|$, which combined with the THz radiation generated at the Cherenkov angle of $+|\theta_c|$ [121,122]. Controlling the thickness of the air layer allowed the Cherenkov THz radiation waves to interfere constructively at specific frequencies [121,122]. Figure 1.18(e) illustrates the THz electric field pulses produced by a leaky planar waveguide that had an LN thickness of 35 μm and no air gap or an infinite air gap [121]. As shown in Fig. 1.18(f), the corresponding spectra exhibited different spectral shapes due to the interfering THz radiation [121]. Bakunov et al. reversed the orientation of the Si prisms (with respect to the propagation direction of the excitation beam) in a Si-LN-Si waveguiding structure, as shown in Fig. 1.18(g) [123]. Consequently, the generated THz electric fields (emitted at the Cherenkov angle) propagated within the Si prism and experienced total internal reflection from the hypotenuse side of the Si prism [123]. The THz radiation pulses subsequently emerged into free-space as two laterally displaced beams, which propagated parallel to the propagation direction of the excitation laser pulse [123]. Figures 1.18(h) and 1.18(i) depict the generated THz time-domain electric field pulse and its corresponding spectral density, respectively, obtained using a 55 μm -thick LN layer and a 10 μJ , 35 fs, 800 nm laser pulse [123]. The majority of the generated THz frequency

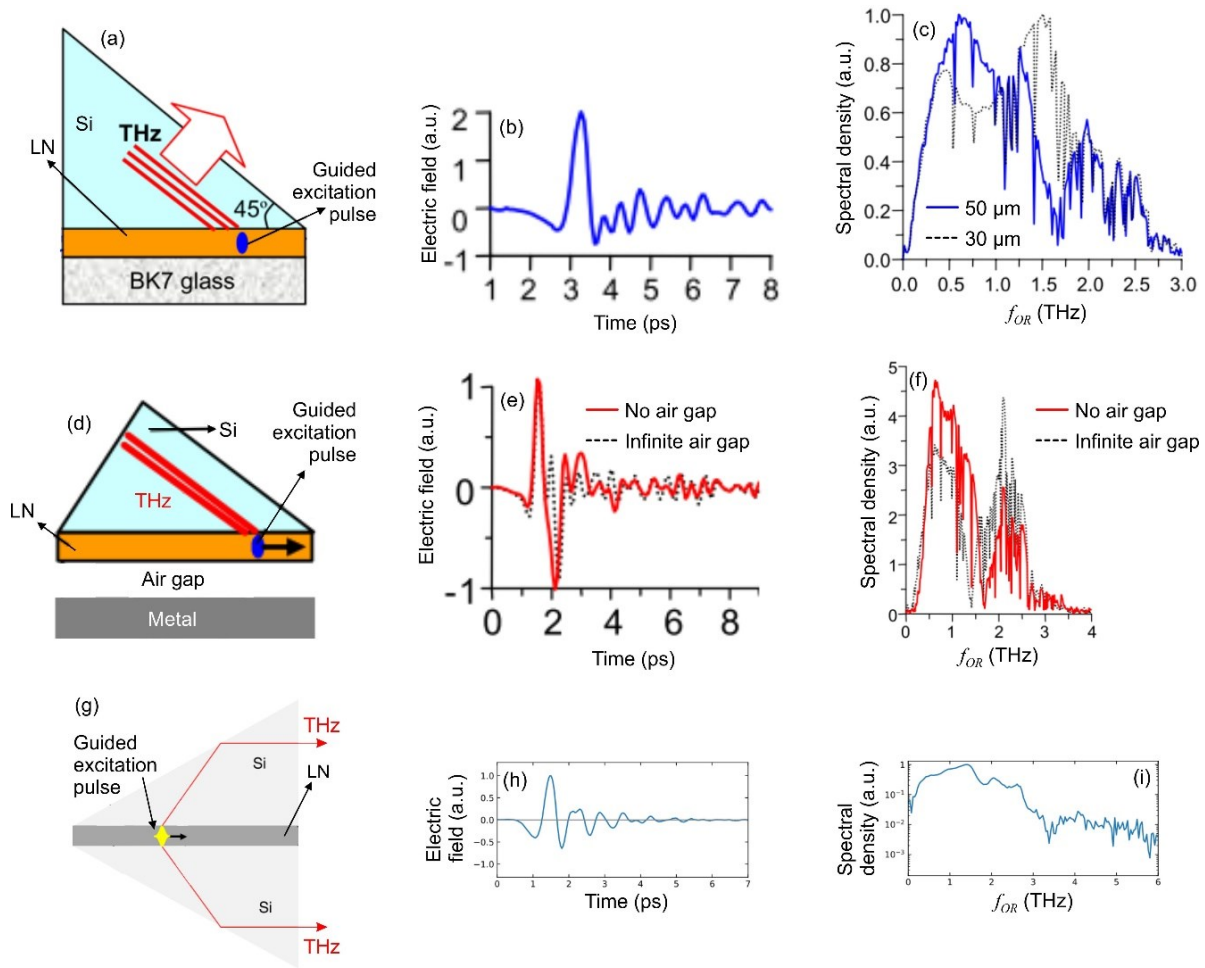


Fig. 1.18. (a) Illustration of a Bk7-LN-Si prism leaky planar waveguide, which depicts the generated THz radiation being emitted as Cherenkov waves [118]. (b) THz electric field pulses produced by the Bk7-LN-Si prism leaky planar waveguide that had an LN thickness of $50\ \mu\text{m}$ and (c) the spectra obtained from the leaky planar waveguide that had LN thicknesses of 30 and $50\ \mu\text{m}$ [118]. (d) Illustration of the metal-air-LN-Si prism leaky planar waveguide, showing the generated THz radiation being emitted as Cherenkov waves [121]. (e) THz electric field pulses produced by the metal-air-LN-Si prism leaky planar waveguide that had no air gap and an infinite air gap and (f) the spectral density of the THz electric field pulses shown in (e) [121]. (g) Illustration of the Si-LN-Si leaky planar waveguide, depicting the propagation direction of the generated THz radiation [123]. (h) THz electric field pulse produced by the Si-LN-Si leaky planar waveguide and (i) the spectral density of the THz electric field pulses shown in (h) [123].

components were observed <3 THz and a high conversion efficiency of 3.5×10^{-3} was realized when producing the OR THz electric field [123].

3D Cherenkov waveguiding arrangements and poled waveguides have been employed to confine and guide the optical excitation electric field and generate free-space THz radiation. Fan et al. reported on the generation of OR THz radiation emitted as Cherenkov waves from a $3.8 \mu\text{m} \times 5 \mu\text{m} \times 10 \text{mm}$ MgO:LN ridge waveguide [124]. Figure 1.19(a) shows a cross-sectional view of the ridge waveguide, where the (100) crystallographic plane of the MgO:LN layer was set normal to the propagation direction of the excitation electric field [124]. The MgO:LN layer was coated with a $3.5 \mu\text{m}$ -thick PET film that exhibited a refractive index lower than that of the MgO:LN, which confined the 1560nm excitation pulse within the ridge waveguide but allowed the generated THz radiation to escape [124]. A 40° apex angle semi-cone Si lens was used to out-couple the generated Cherenkov THz radiation from the arrangement and into free-space [see Fig. 1.19(b)] [124]. The MgO:LN ridge waveguide was excited using either a 20 or 60 fs pulse, which generated THz radiation having a bandwidth that extended past 6 THz, as shown in Fig. 1.19(c) [124]. Similarly, a $3 \mu\text{m} \times 7 \mu\text{m} \times 10 \text{mm}$ MgO:LN ridge waveguiding arrangement that utilized a half-cone Si lens was investigated by Takeya et al. [125]. When excited using a 1560nm , 48 fs pulse, OR THz radiation was produced up to ~ 5 THz [125]. Schulz et al. numerically investigated DFG THz radiation from a folded Si rectangular waveguide coated with a cladding material that had a second-order nonlinearity [95]. Tunable THz radiation generation was shown to be possible across the spectral range of 1-10 THz, and conversion efficiencies on the order of 10^{-4} were achieved for milliwatt optical excitation powers [95]. DFG in quasi-phase-matched crystals is another promising method for generating tunable, highly coherent THz radiation. Avetisyan et al. analyzed phase-matched DFG THz radiation emitted normal to the

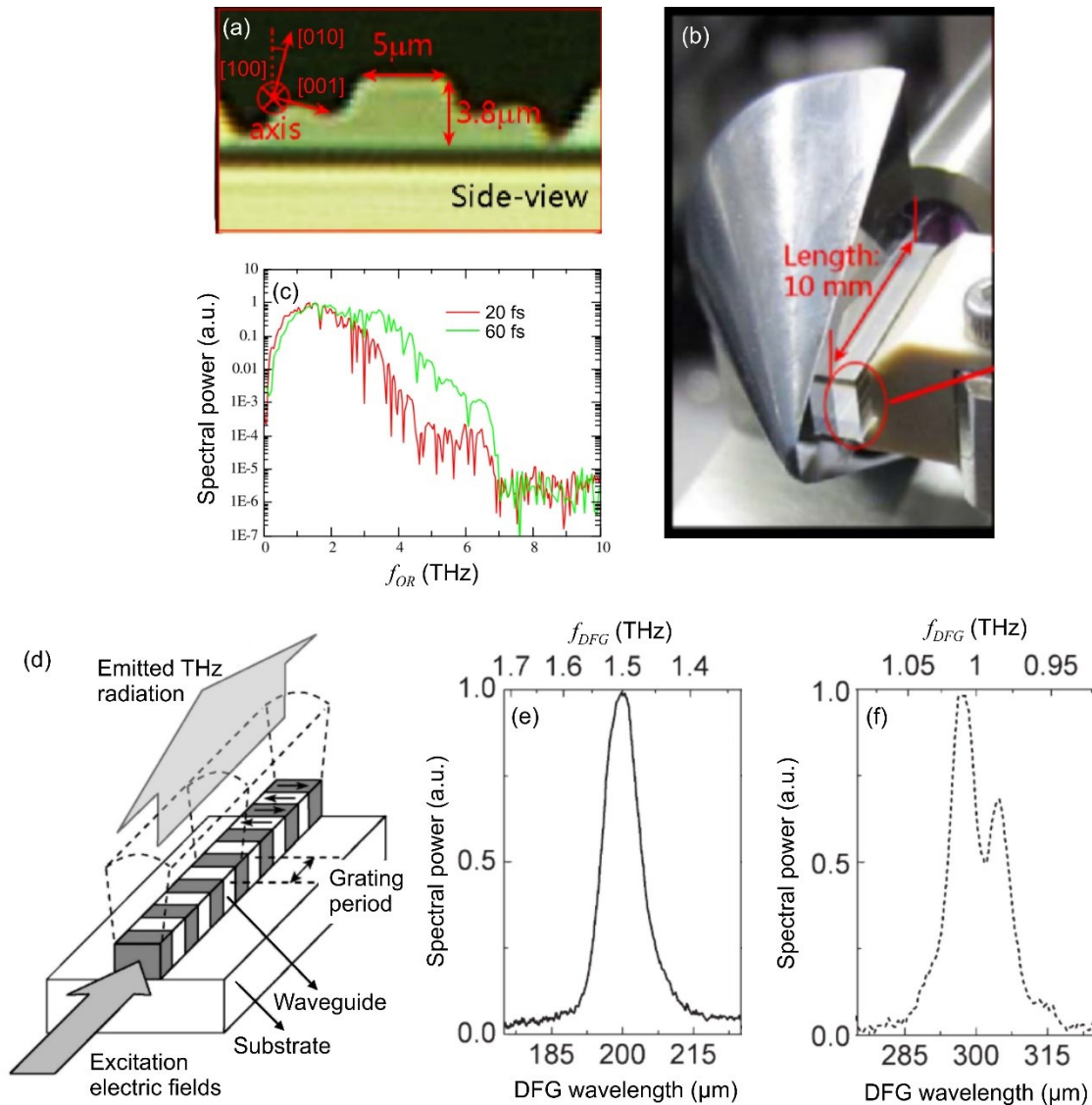


Fig. 1.19. (a) Cross-sectional image of an MgO:LN ridge waveguide and (b) a semi-cone Si lens that surrounded the ridge waveguide [124]. (c) Spectral power of the OR THz radiation produced by the MgO:LN ridge waveguide [124]. (d) Illustration of a PPMgLN ridge waveguide [126]. DFG THz radiation produced by PPMgLN ridge waveguides having grating periods of (e) 91 μm and (f) 137 μm [126].

surface of a periodically-poled LN (PPLN) waveguide [127]. When a 6 mm-long, 300 μm -thick planar PPLN waveguide was excited at 600 W, it was estimated that 2 mW of THz radiation would be generated at 2 THz [127]. Experimental realization of DFG THz radiation from a periodically-

poled MgO-doped LN (PPMgLN) ridge waveguide was reported by Sasaki et al., where the THz wave was emitted normal to the surface of the PPMgLN ridge waveguide [see Fig. 1.19(d)] [126]. A fixed excitation wavelength of 1554 nm and a tunable wavelength between 1560-1578 nm were employed to excite the PPMgLN ridge waveguide [126]. DFG THz radiation at 1.5 THz [see Fig. 1.19(e)] and 1 THz [see Fig. 1.19(f)] was observed from PPMgLN ridge waveguides that had grating periods of 91 and 137 μm , respectively [126].

1.5.3. Free-space excitation electric fields for generating guided THz radiation

To date, only a few investigations have been reported using a free-space excitation electric field to generate guided OR or DFG THz radiation. Coleman and Grischkowsky investigated OR THz radiation generated from an Al-GaAs-Al parallel plate waveguide [see Fig. 1.20(a)] that had a length of 860 μm and a 120 μm -thick GaAs layer [128]. Here, the excitation electric field propagated through the waveguide (i.e. the lateral beam dimension was less than the GaAs layer thickness), while the generated THz radiation was guided by the parallel plate waveguide and emitted into free-space [128]. When the Al-GaAs-Al parallel plate waveguide was excited using an 810 nm femtosecond laser pulse, a <1 ps-long THz electric field pulse was produced [see inset of Fig. 1.20(b)] that encompassed frequency components $\lesssim 3$ THz [see Fig. 1.20(b)] [128]. Due to the absence of a cut-off frequency in the THz spectrum, it was inferred that the OR THz radiation was guided along the waveguide as the TEM mode [128]. Figure 1.20(c) illustrates waveguides investigated by Chang et al., where these waveguides had cross-sectional dimensions of 600 $\mu\text{m} \times 400 \mu\text{m}$ and 1000 $\mu\text{m} \times 700 \mu\text{m}$ [129]. In these arrangements, the excitation electric fields had lateral beam dimensions less than the GaP rectangular regions, such that they were not

guided or confined by the GaP layers [129]. However, the generated THz radiation was guided by the rectangular GaP waveguide, since the wavelengths were comparable to the cross-sectional dimensions of the waveguides [129]. Figure 1.20(d) presents the THz time-domain electric field pulses, and their associated spectra, obtained using 6 mm-long, (110) GaP rectangular waveguides excited by 1064 nm, 110 fs laser pulses [129]. The waveguide that had the smaller and larger cross-sections exhibited peak generation at the frequencies of ~ 0.7 THz and ~ 0.4 THz, respectively [129]. This difference was attributed to the cross-sectional dimensions of the waveguides, which influenced the effective refractive index of the THz mode and thus modified the OR phase-matching condition [129]. Interestingly, modifying the shape of the excitation optical beam can enhance the OR THz radiation generation process. Xu et al. excited a similar GaP rectangular waveguide (cross-sectional dimensions of 1 mm \times 0.7 mm) using a 1040 nm-wavelength non-diffracting Bessel beam [130]. In comparison to a Gaussian beam that had the same power as the central spot of the Bessel beam and the same central beam size, the Bessel beam provided a THz radiation power enhancement of 3.5 and 3.3 for a 6 mm-long and 10 mm-long GaP waveguide, respectively [130]. A 33 μm -thick LN planar waveguide was experimentally investigated by Lin et al. for OR THz radiation generation [131]. As illustrated in Fig. 1.20(e)-1.20(g), an 800 nm, 70 fs excitation pulse that had a tilted wavefront produced phase-matched THz radiation that was guided along the planar waveguide [131]. The generated THz radiation spectra were centered at the frequencies of 0.2, 0.4, 0.65, and 0.95 THz and increased for steeper excitation pulse tilt angles [see Fig. 1.20(h)] [131]. Huang et al. observed forward and backward DFG THz radiation in a 500 μm -thick and 25 mm-long PPLN planar waveguide, as well as a 25 mm-long PPLN rectangular waveguide that had a thickness of 500 μm and a width of 600 μm [132]. The excitation electric fields had beam dimensions less than the PPLN waveguiding regions,

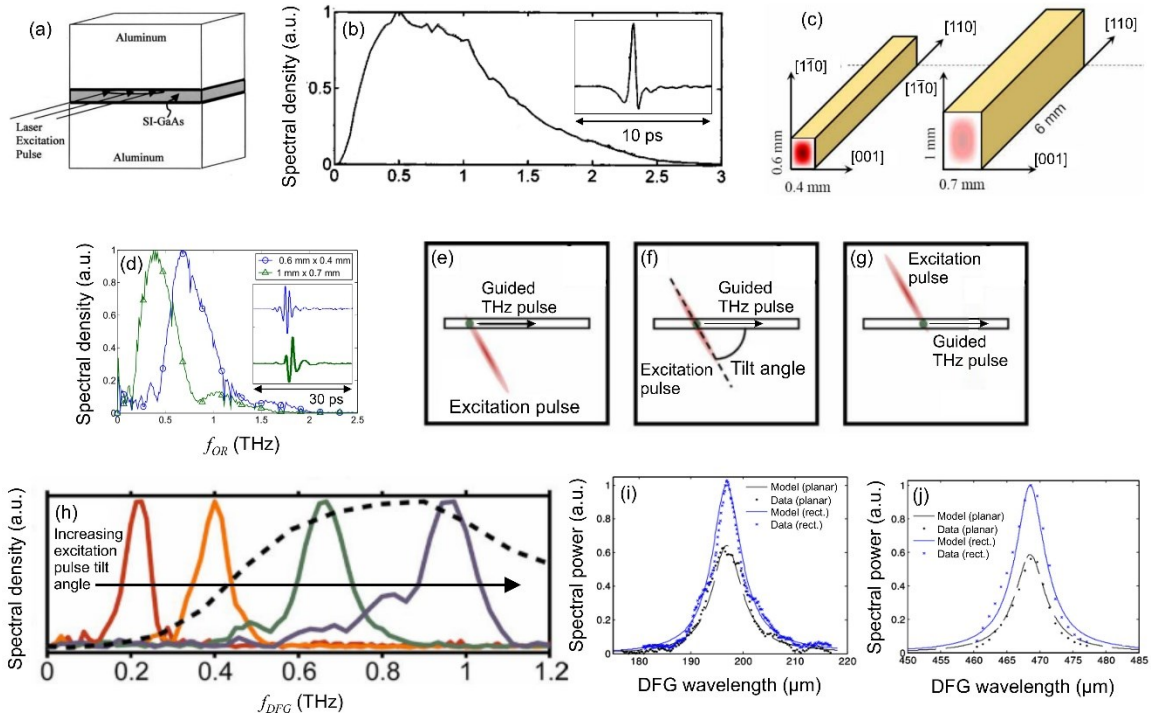


Fig. 1.20. (a) An Al-GaAs-Al parallel plate waveguide and (b) the spectral density of the OR THz radiation generated by this waveguiding structure [128]. The inset depicts the generated THz electric field pulse [128]. (c) Illustration of GaP rectangular waveguides that had cross-sectional dimensions of $600\ \mu\text{m} \times 400\ \mu\text{m}$ and $1000\ \mu\text{m} \times 700\ \mu\text{m}$ and (d) the spectral densities of the OR THz radiation produced by these waveguides [129]. The inset shows the generated THz electric field pulses [129]. (e-g) Illustration of a tilted wavefront excitation pulse propagating through a LN planar waveguide and the guided generated THz radiation, where (e) depicts the earliest instant in time, (f) shows a subsequent instant in time, and (g) illustrates the latest instant in time [131]. (h) DFG THz radiation produced by a LN planar waveguide at various excitation pulse wavefront tilt angles [131]. For comparison, the dotted line represents THz radiation generation from a bulk LN crystal [131]. DFG THz radiation produced by planar and rectangular PPLN waveguides in the (i) forward direction and (j) backward direction [132].

whereas the generated THz radiation was guided by the waveguiding regions [132]. For excitation wavelengths near 1540 nm, phase-matched THz radiation generation was observed at a frequency of 1.5 THz in the forwards direction [see Fig. 1.20(i)] and 0.6 THz in the backwards direction [see

Fig. 1.20(j)) [132]. In comparison to the planar waveguide, the rectangular waveguide exhibited a THz power enhancement of 1.6 and 1.8 for the forward and backward generated THz radiation, respectively [132].

1.6. Thesis objectives

The main objective of this work is to explore and discover second-order nonlinear THz radiation sources and detectors using novel crystals and/or unique waveguiding geometries.

The primary goals of this work are to:

1. Explore emerging pnictide and chalcogenide ternary crystals for the generation and detection of THz radiation via second-order nonlinear effects.
2. Develop a comprehensive numerical technique to model second-order nonlinear frequency-conversion, which incorporates all 18 elements of the nonlinear tensor and dispersion for each element.
3. Explore novel waveguiding arrangements for the generation of THz radiation occurring through second-order nonlinear processes.
4. Provide a fundamental physical understanding of second-order nonlinear optical effects.

This is necessary because, when considering second-order nonlinear interactions, there is a lack of intuitive and comprehensive discussions that consider both the incident and resulting electric fields, as well as the behavior of the induced dipoles in the medium.

5. Offer a clear and comprehensive understanding of the current-state of THz radiation sources and detectors that operate on the physics driving second-order nonlinear interactions.

The physical principles driving second-order nonlinear interactions persist into the spectral regions neighboring the THz frequency regime. As such, the work presented in this thesis briefly delves beyond the THz frequency regime to consider second-order nonlinear generation within the IR and visible spectral regions.

In relation to such work, the main goals are to:

6. Investigate waveguiding geometries for the generation of radiation in the IR and visible regions of the EM spectrum.
7. Develop a new class of multi-band photonic sources, in which a single waveguiding structure concurrently satisfies the phase-matching requirements of several second-order nonlinear processes.

1.7. Thesis overview

The nine chapters presented in this thesis provide novel theoretical, numerical, and experimental investigations pertaining to second-order nonlinear phenomena for the generation and detection of radiation, mainly within the THz spectral regime. Emerging crystals are investigated for THz radiation generation and detection, and unique waveguiding arrangements are considered for THz radiation generation. The novel THz radiation sources and detectors presented in this thesis (exhibiting key properties such as high-field THz radiation generation, high conversion efficiency, wide generation and detection bandwidths, etc.) are key to advancing the field of nonlinear optics. This thesis is organized as follows:

Chapter 2 provides a comprehensive study of second-order nonlinear effects for the generation of radiation. While such an investigation relies on derivations pertaining to the equations of motion (EOM) and Maxwell's Equations, emphasis is placed on interpreting the

resulting equation to provide an intuitive description of the physics driving the nonlinear interactions. Second-order nonlinear frequency-conversion is considered for the representative scenarios of monochromatic incident electric fields and a pulsed incident electric field.

Chapter 3 provides a detailed description of the THz-TDS system used to characterize the investigated THz radiation sources and detectors. This discussion considers the optical components incorporated within the THz-TDS system, as well the electrical equipment needed to modulate and process the optical signals.

Chapter 4 presents experimental investigations on pnictide ternary crystals (e.g. ZGP and CSP) and chalcogenide ternary crystals (e.g. AGS and BGS) for THz radiation generation and/or detection. Broadband THz radiation generation is observed from the CSP and AGS crystals, while narrowband THz radiation generation is observed from the BGS crystal. The ZGP crystals is investigated for phase-resolved THz radiation detection via the linear EO effect.

Chapter 5 presents two separate numerical formalisms for modeling second-order nonlinear effects in finite-difference time-domain (FDTD) simulations. The novel methods incorporate all 18 elements of the second-order nonlinear tensor, and allow for dispersion of each element. The developed methods are applied to evaluate nonlinear frequency-conversion from a $3m$ point group symmetry crystal (i.e. LN) and a $\bar{4}3m$ point group symmetry crystal (i.e. ZnTe).

Chapter 6 provides numerical and experimental investigations of LN planar waveguides for the generation of THz radiation. Using the methods developed in Chapter 5, such waveguides are shown to exhibit ultra-broadband Cherenkov THz radiation generation (i.e. bandwidth >100 THz), enhanced THz radiation generation near the LN phonon resonances, and phase-matched THz radiation generation occurring in the backward direction (i.e. the direction opposite to the propagation direction of the excitation electric field pulse). A planar LN waveguide is

experimentally realized, which produces THz radiation emitted as Cherenkov waves. Upon scaling the length of the waveguide, we envision it being integrated as on-chip sources of THz radiation.

Chapter 7 expands on the knowledge-base created in the previous chapters to show that the theoretical, numerical, and experimental approaches can go beyond the THz spectral regime. The numerical methods developed in Chapter 5 are implemented to investigate LN plasmonic waveguides and a CSP photonic waveguide, both of which show conversion efficiency enhancement in comparison to LN photonic waveguides of comparable dimensions. Subsequently, LN waveguides are used as a platform to study off-normal-incident coupling arrangements and the impact of these coupling arrangements on SHG. Phase-matched SHG is experimentally-realize using a planar LN waveguide excited via an off-normal-incident coupling arrangement.

Chapter 8 presents an entirely new class of multi-band photonic sources, where a single waveguiding structure simultaneously satisfies phase-matching for several second-order nonlinear processes. The methods developed in Chapter 5 are used to investigate concurrent phase-matched sum frequency generation (SFG) and phase-matched DFG for a planar LN waveguide. Subsequently, a planar LN waveguide is experimentally-realized for the simultaneous generation of radiation via the phase-matched second-order nonlinear processes of SHG and OR.

Chapter 9 summarizes the theoretical, numerical, and experimental investigations conducted within this thesis, as well as key outcomes and observations. Future studies are proposed that pertain to this work.

Chapter 2.

Second-order nonlinear phenomena: A complete prospective

At its basic level, optics can be viewed as the behavior of EM waves as they interact with matter comprised of atoms and electrons. An EM wave incident on a medium induces a displacement of positive and negative electrical charges, resulting in electric dipole moments [133]. Interestingly, the electric dipoles arise from electron clouds being displaced with respect to their corresponding nuclei, as well as the displacement of atomic constituents in IR-active lattice vibrations. It is important to note that we use expressions such as “bound charge displacement” or “bound electric charge displacement” when referring to both of the aforementioned situations. Figure 2.1(a)-2.1(c) illustrate an atom (i.e. nucleus and electron cloud) that is part of a broader unit cell (not shown). At equilibrium, the electron cloud is displaced from its much heavier (i.e. fixed) nucleus [see Fig. 2.1(a)] due to forces exerted on it from other atomic constituents within the unit cell. When an EM wave is incident on a medium, it is often appropriate to assume the electron cloud oscillates in response to the perturbation by following the oscillations of the EM wave [133]. Figure 2.1(b) represents this scenario, where the electron cloud is displaced with respect to equilibrium. Here, the incident electric field exerts a force on the electric dipole, displacing the electron cloud and causing it to experience a restoring force in an effort to return to its equilibrium position. As shown in Fig. 2.1(e), the restoring force, F , is analogous to that of a linear spring undergoing a small displacement (i.e. $F \approx -k^{(1)}\Delta s$, where $k^{(1)}$ is the first-order spring constant and Δs is the spring’s displacement from its equilibrium position) [134]. Here, the electron cloud

returns to its equilibrium position at the same frequencies present in the incident electric field [43], and the interaction is denoted as occurring within the linear optical regime. Such behavior is only observed for sufficiently weak EM waves, while more involved electron cloud displacement occurs for stronger EM waves. Figure 2.1(c) represents this latter scenario, where the electron cloud is again displaced with respect to equilibrium, experiencing a restoring force in an effort to return to its equilibrium position. However, as shown in Fig. 2.1(e), the restoring force is analogous to that of a spring undergoing a large displacement (i.e. $F = -k^s(\Delta s)\Delta s = -k^{(1)}\Delta s - k^{(2)}\Delta s^2 - k^{(3)}\Delta s^3 - \dots$, where k^s is the overall spring constant, $k^{(2)}$ is the second-order spring constant, $k^{(3)}$ is the third-order spring constant, etc.) [134]. In such a situation, the electron cloud returns to its equilibrium position at the same frequencies present in the incident electric field, as well as frequencies not present in the incident electric field [43]. The new frequencies arise due to the spring's stiffness changing as the spring is either elongated or compressed, which occurs since the spring constant depends on displacement [i.e. $k^s(\Delta s)$]. Such an interaction is defined as occurring within the nonlinear optical regime. The aforementioned picture can also be applied to lattice vibrations within the unit cell. Figure 2.1(d) depicts the displacement of an atom with respect to another heavier (i.e. fixed) atom, which exhibits a linear restoring force for $\Delta s < \Delta s_0$ and a nonlinear restoring force for $\Delta s > \Delta s_0$ [see Fig. 2.1(e)]. In general, the intensity of the incident EM wave and various properties of the material itself are key characteristics distinguishing whether the interaction occurs in the linear or nonlinear optical regime [30,133].

Despite the development of detailed mathematical models and ground-breaking experimental works in the second-order nonlinear optical regime [90,135–138], the area lacks comprehensive intuitive discussions pertaining to the physics driving the various nonlinear processes. For example, Fig. 2.2 shows illustrations typically used to describe the second-order

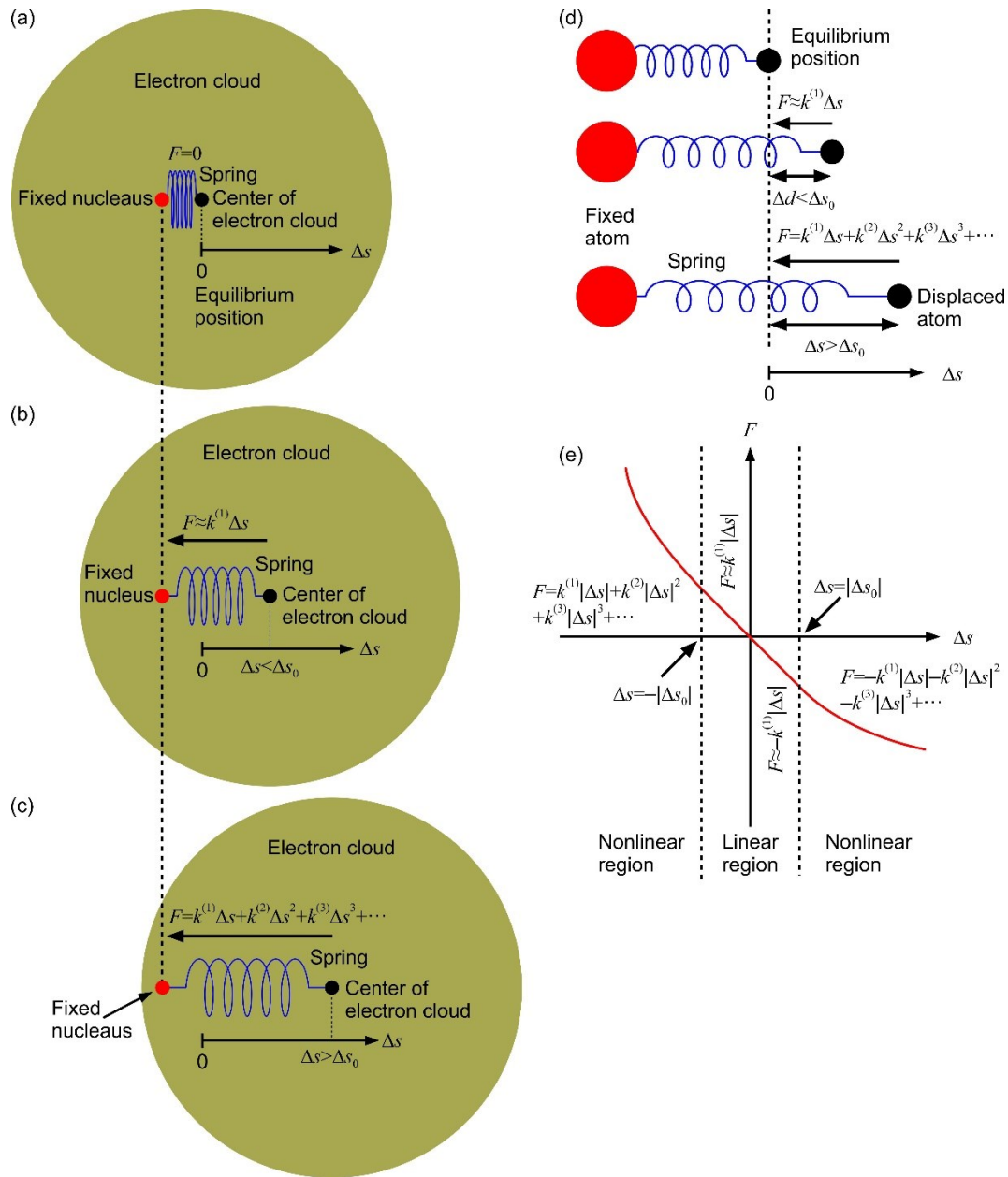


Fig. 2.1. Displacement of an electron cloud with respect to its heavier (i.e. fixed) nucleus (a) at equilibrium, (b) in the regime described by a linear restoring force, and (c) in the regime described by a nonlinear restoring force. (d) Displacement of an atom with respect to another heavier (i.e. fixed) atom. (e) Representative restoring force curve.

nonlinear processes of SHG, SFG, and DFG. As shown in Fig. 2.2(a)-2.2(c), photons at the angular frequencies of ω_1 and ω_2 produce photons at the angular frequencies of $2\omega_1$ via SHG, $\omega_1 + \omega_2$

via SFG, and $\omega_1 - \omega_2$ via DFG, respectively. Alternatively, Fig. 2.2(d)-2.2(f) depict these second-order nonlinear processes though their need to satisfy energy conservation. While such pictorials are important and informative, they are incomplete in describing the entire nature of the physical processes. Specifically, the medium in which the frequency-conversion occurs is depicted as a “black box”, with only the incident and resulting photons being illustrated. To obtain a complete understanding of second-order nonlinear phenomena, it is necessary to consider the response occurring within the nonlinear medium.

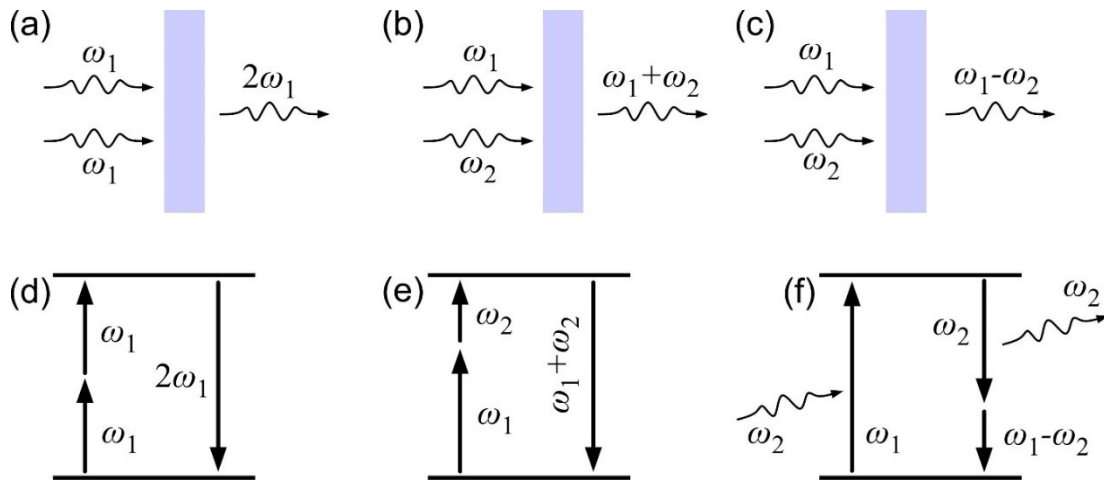


Fig. 2.2. (a) SHG, (b) SFG, and (c) DFG processes depicted as photons incident on a medium and photons exiting the medium. (d) SHG, (e) SFG, and (f) DFG processes depicted in terms of energy conservation diagrams. The photons in (f) signify that frequency components at ω_2 must initially be present in order for the DFG process to occur.

In this section, we introduce second-order nonlinear interactions occurring within a non-centrosymmetric material by considering key representative scenarios (i.e. monochromatic incident electric fields and a pulsed incident electric field). To provide a complete picture, we consider the relationship between the electric field incident on the medium, the induced

displacement of the bound electric charges in the medium, and the resulting electric field. Detailed mathematical derivations are presented along with intuitive physical interpretations.

2.1. General framework

It is critical to have a comprehensive understanding of the anharmonic EOM, which describes the displacement of the bound electric charges in a medium, as well as Maxwell's equations, which describe the EM waves resulting from the motion of the bound electric charges.

2.1.1. Anharmonic EOM

When first-order and second-order nonlinear effect are considered, the bound electric charge displacement in a medium is described by the anharmonic EOM [30],

$$m_e \frac{\partial^2 \mathbf{s}(\mathbf{r}, t)}{\partial t^2} + m_e \gamma \frac{\partial \mathbf{s}(\mathbf{r}, t)}{\partial t} + m_e \omega_0^2 \mathbf{s}(\mathbf{r}, t) + \mathfrak{S} m_e \mathbf{s}^2(\mathbf{r}, t) = -q \mathbf{E}(\mathbf{r}, t), \quad (2.1)$$

where $\mathbf{s}(\mathbf{r}, t)$ is the displacement of the bound electric charges, ω_0 is the resonant frequency associated with the bound electric charge displacement in the medium, γ is the damping term associated with the bound electric charge displacement in the medium, \mathfrak{S} represents the nonlinearity of the medium, $\mathbf{E}(\mathbf{r}, t)$ represents the electric field in the medium, t is the time, $\mathbf{r} = (x, y, z)$, and x , y , and z are the axes of the Cartesian coordinate system. Notably, while \mathfrak{S} can be approximated using ω_0 and the lattice constant defining a material's unit cell (see Ref. [30]), the nonlinearity of a medium is typically determined empirically. Equation (2.1) is solved using perturbation theory [30], which allows $\mathbf{s}(\mathbf{r}, t)$ and $\mathbf{E}(\mathbf{r}, t)$ to be expressed as:

$$\mathbf{s}(\mathbf{r}, t) \rightarrow \mathfrak{S} \mathbf{s}^{(1)}(\mathbf{r}, t) + \mathfrak{S}^2 \mathbf{s}^{(2)}(\mathbf{r}, t) + \dots, \quad (2.2)$$

$$\mathbf{E}(\mathbf{r}, t) \rightarrow \mathfrak{S} \mathbf{E}(\mathbf{r}, t), \quad (2.3)$$

respectively, where \mathfrak{H} is the expansion parameter. Substituting Eqs. (2.2) and (2.3) into Eq. (2.1) and rearranging based on the order of \mathfrak{H} gives,

$$\begin{aligned} & \mathfrak{H} \left\{ m_e \frac{\partial^2 \mathbf{s}^{(1)}(\mathbf{r}, t)}{\partial t^2} + m_e \gamma \frac{\partial \mathbf{s}^{(1)}(\mathbf{r}, t)}{\partial t} + m_e \omega_0^2 \mathbf{s}^{(1)}(\mathbf{r}, t) + q \mathbf{E}(\mathbf{r}, t) \right\} \\ & + \mathfrak{H}^2 \left\{ m_e \frac{\partial^2 \mathbf{s}^{(2)}(\mathbf{r}, t)}{\partial t^2} + m_e \gamma \frac{\partial \mathbf{s}^{(2)}(\mathbf{r}, t)}{\partial t} + m_e \omega_0^2 \mathbf{s}^{(2)}(\mathbf{r}, t) \right. \\ & \left. + \mathfrak{S} m_e [\mathbf{s}^{(1)}(\mathbf{r}, t)]^2 \right\} + \dots = 0. \end{aligned} \quad (2.4)$$

Invoking the fact that each order of \mathfrak{H} is independent [30], we can write,

$$m_e \frac{\partial^2 \mathbf{s}^{(1)}(\mathbf{r}, t)}{\partial t^2} + m_e \gamma \frac{\partial \mathbf{s}^{(1)}(\mathbf{r}, t)}{\partial t} + m_e \omega_0^2 \mathbf{s}^{(1)}(\mathbf{r}, t) = -q \mathbf{E}(\mathbf{r}, t), \quad (2.5)$$

$$\frac{\partial^2 \mathbf{s}^{(2)}(\mathbf{r}, t)}{\partial t^2} + \gamma \frac{\partial \mathbf{s}^{(2)}(\mathbf{r}, t)}{\partial t} + \omega_0^2 \mathbf{s}^{(2)}(\mathbf{r}, t) + \mathfrak{S} [\mathbf{s}^{(1)}(\mathbf{r}, t)]^2 = 0. \quad (2.6)$$

Perturbation theory further dictates that the bound electric charge displacement is obtained by setting $\mathfrak{H}=1$ [30], such that $\mathbf{s}(\mathbf{r}, t) = \mathbf{s}^{(1)}(\mathbf{r}, t) + \mathbf{s}^{(2)}(\mathbf{r}, t)$. The emission of EM waves in response to this time-varying $\mathbf{s}(\mathbf{r}, t)$ is discussed in the following section.

2.1.2. Maxwell's equations

In the time-domain, Maxwell's equations are expressed in differential form as [30,133]:

$$\nabla \cdot \mathbf{D}(\mathbf{r}, t) = \rho_f(\mathbf{r}, t), \quad (2.7)$$

$$\nabla \cdot \mathbf{B}(\mathbf{r}, t) = 0, \quad (2.8)$$

$$\nabla \times \mathbf{E}(\mathbf{r}, t) = -\frac{\partial \mathbf{B}(\mathbf{r}, t)}{\partial t}, \quad (2.9)$$

$$\nabla \times \mathbf{H}(\mathbf{r}, t) = \mathbf{J}_f(\mathbf{r}, t) + \frac{\partial \mathbf{D}(\mathbf{r}, t)}{\partial t}, \quad (2.10)$$

where $\mathbf{H}(\mathbf{r}, t)$ is the magnetic field, $\mathbf{D}(\mathbf{r}, t)$ is the electric displacement field, $\mathbf{B}(\mathbf{r}, t)$ is the magnetic flux density, $\rho_f(\mathbf{r}, t)$ is the free charge volume density in the medium, and $\mathbf{J}_f(\mathbf{r}, t)$ is the free current density in the medium. The constitutive relations further describe the interaction of EM waves with a given medium, which, in a non-magnetic medium, are expressed as [30,133]:

$$\mathbf{D}(\mathbf{r}, t) = \varepsilon_0 \mathbf{E}(\mathbf{r}, t) + \mathbf{P}(\mathbf{r}, t), \quad (2.11)$$

$$\mathbf{B}(\mathbf{r}, t) = \mu_0 \mathbf{H}(\mathbf{r}, t), \quad (2.12)$$

where $\mathbf{P}(\mathbf{r}, t)$ is the polarization induced in the medium, given as [30,133],

$$\mathbf{P}(\mathbf{r}, t) = \mathbf{P}^{(1)}(\mathbf{r}, t) + \mathbf{P}^{(2)}(\mathbf{r}, t) + \mathbf{P}^{(3)}(\mathbf{r}, t) + \dots, \quad (2.13)$$

where $\mathbf{P}^{(1)}(\mathbf{r}, t)$ represents the first-order contribution, $\mathbf{P}^{(2)}(\mathbf{r}, t)$ represents the second-order contribution, $\mathbf{P}^{(3)}(\mathbf{r}, t)$ represents the third-order contribution, and so on. While Eqs. (2.7)-(2.13) describe the interaction of an EM wave with a general non-magnetic medium, several assumptions can be introduced to simplify the complexity of the equations. Specifically, only the first-order and second-order polarization terms are considered [i.e. $\mathbf{P}(\mathbf{r}, t) = \mathbf{P}^{(1)}(\mathbf{r}, t) + \mathbf{P}^{(2)}(\mathbf{r}, t)$] and the medium is assumed to be absent of free charges and free currents [i.e. $\rho_f(\mathbf{r}, t)=0$ and $\mathbf{J}_f(\mathbf{r}, t)=0$].

This results in Eqs. (2.7)-(2.13) simplifying to:

$$\nabla \cdot \mathbf{D}(\mathbf{r}, t) = 0, \quad (2.14)$$

$$\nabla \cdot \mathbf{B}(\mathbf{r}, t) = 0, \quad (2.15)$$

$$\nabla \times \mathbf{E}(\mathbf{r}, t) = -\frac{\partial \mathbf{B}(\mathbf{r}, t)}{\partial t}, \quad (2.16)$$

$$\nabla \times \mathbf{H}(\mathbf{r}, t) = \frac{\partial \mathbf{D}(\mathbf{r}, t)}{\partial t}, \quad (2.17)$$

$$\mathbf{D}(\mathbf{r}, t) = \varepsilon_0 \mathbf{E}(\mathbf{r}, t) + \mathbf{P}(\mathbf{r}, t), \quad (2.18)$$

$$\mathbf{B}(\mathbf{r}, t) = \mu_0 \mathbf{H}(\mathbf{r}, t), \quad (2.19)$$

$$\mathbf{P}(\mathbf{r}, t) = \mathbf{P}^{(1)}(\mathbf{r}, t) + \mathbf{P}^{(2)}(\mathbf{r}, t). \quad (2.20)$$

Importantly, a medium exhibiting second-order nonlinear effects [i.e. $\mathbf{P}^{(2)}(\mathbf{r}, t) \neq 0$] must be non-centrosymmetric, while a centrosymmetric medium always exhibits $\mathbf{P}^{(2)}(\mathbf{r}, t) = 0$ [30,31]. In a centrosymmetric medium, inverting the atomic constituents about the center of the unit cell leads to an indistinguishable arrangement of the basic atomic structure. Therefore, when a centrosymmetric medium is perturbed by an EM wave, any displacement incurred by the bound electric charges in one direction is exactly cancelled by their displacement in the opposite direction as the EM wave reverses its polarization orientation. The wave equation can be derived from Eqs. (2.16)-(2.20). Using the vector identity $\nabla \times (\nabla \times \mathbf{A}) = \nabla(\nabla \cdot \mathbf{A}) - \nabla^2 \mathbf{A}$, where \mathbf{A} is a vector, Eq. (2.16) is manipulated to obtain,

$$\nabla[\nabla \cdot \mathbf{E}(\mathbf{r}, t)] - \nabla^2 \mathbf{E}(\mathbf{r}, t) = -\frac{\partial[\nabla \times \mathbf{B}(\mathbf{r}, t)]}{\partial t}. \quad (2.21)$$

Subsequently, Eqs. (2.17)-(2.19) and the relationship $c = (\epsilon_0 \mu_0)^{-1/2}$ are used to simplify Eq. (2.21), giving,

$$-\nabla[\nabla \cdot \mathbf{E}(\mathbf{r}, t)] + \nabla^2 \mathbf{E}(\mathbf{r}, t) - \frac{1}{c^2} \frac{\partial^2 \mathbf{E}(\mathbf{r}, t)}{\partial t^2} = \frac{1}{c^2 \epsilon_0} \frac{\partial^2 \mathbf{P}(\mathbf{r}, t)}{\partial t^2}. \quad (2.22)$$

In general, $\nabla[\nabla \cdot \mathbf{E}(\mathbf{r}, t)]$ is non-zero [30]; however, it can be shown that $\nabla[\nabla \cdot \mathbf{E}(\mathbf{r}, t)] = 0$ for a plane wave. In such a scenario, Eq. (2.20) is used to show that Eq. (2.22) becomes,

$$\nabla^2 \mathbf{E}(\mathbf{r}, t) - \frac{1}{c^2} \frac{\partial^2}{\partial t^2} \left[\mathbf{E}(\mathbf{r}, t) + \frac{1}{\epsilon_0} \mathbf{P}^{(1)}(\mathbf{r}, t) \right] = \frac{1}{c^2 \epsilon_0} \frac{\partial^2 \mathbf{P}^{(2)}(\mathbf{r}, t)}{\partial t^2}. \quad (2.23)$$

Using this wave equation, the electric field can be calculated for a given second-order nonlinear polarization.

2.2. Monochromatic incident electric fields

An informative scenario to consider is an electric field comprised of two monochromatic EM waves interacting within a one-dimensional (1D) isotropic and uniform dielectric medium. The EM waves induce bound electric charge oscillations (described by the anharmonic EOM), leading to the emission of EM waves (described by Maxwell's equations). Prior to investigating this scenario, it is imperative to clarify certain points. Dispersion and absorption loss are considered in the medium. The monochromatic EM waves are assumed to propagate along the z Cartesian coordinate and exist in the spatial region of $z \geq 0$. We investigate the scenario where frequency-conversion is restricted to less than a few percent, such that depletion of the two incident monochromatic EM waves is not considered [30,31]. Additionally, cascading effects (i.e. electric field frequency components produced by second-order nonlinear effects subsequently producing other electric field frequency components via second-order nonlinear effects) are ignored [30,31].

2.2.1. Anharmonic EOM and Maxwell's equations

Consider two monochromatic EM waves incident on the medium and exhibiting an electric field of,

$$\begin{aligned} \mathbf{E}_t^w(z, t) &= \mathbf{E}_{\omega_1}^w(z, t) + \mathbf{E}_{\omega_2}^w(z, t) \\ &= A_1 e^{-k_0(\omega_1)\kappa(\omega_1)z} \cos[\omega_1 t - k_0(\omega_1)n(\omega_1)z - \vartheta_1] \hat{\mathbf{x}} \\ &\quad + A_2 e^{-k_0(\omega_2)\kappa(\omega_2)z} \cos[\omega_2 t - k_0(\omega_2)n(\omega_2)z - \vartheta_2] \hat{\mathbf{x}}, \end{aligned} \quad (2.24)$$

where the superscript 'w' indicates that the corresponding variable is associated with monochromatic EM waves, A_1 represents the amplitude of the first monochromatic EM wave, A_2 represents the amplitude of the second monochromatic EM wave, ω_1 is the angular frequency of

the first monochromatic EM wave, ω_2 is the angular frequency of the second monochromatic EM wave, ϑ_1 is the phase shift of the first monochromatic EM wave, ϑ_2 is the phase shift of the second monochromatic EM wave, $k_0(\omega)$ represents the free-space wavenumber at the angular frequency of ω , $n(\omega)$ represents the refractive index of the medium at the angular frequency of ω , $\kappa(\omega)$ represents the extinction coefficient of the medium at the angular frequency of ω , $\mathbf{E}_{\omega_1}^w(z, t)$ is the electric field component related to ω_1 , and $\mathbf{E}_{\omega_2}^w(z, t)$ is the electric field component related to ω_2 . The mathematical analysis is drastically simplified by expressing Eq. (2.24) as complex exponentials,

$$\begin{aligned} \mathbf{E}_i^w(z, t) &= \tilde{\mathbf{E}}_{\omega_1}^w(z, t)\hat{\mathbf{x}} + \tilde{\mathbf{E}}_{\omega_2}^w(z, t)\hat{\mathbf{x}} + \text{CC} \\ &= \frac{\tilde{A}_1}{2} e^{-i[\omega_1 t - \tilde{k}(\omega_1)z]}\hat{\mathbf{x}} + \frac{\tilde{A}_2}{2} e^{-i[\omega_2 t - \tilde{k}(\omega_2)z]}\hat{\mathbf{x}} + \text{CC}, \end{aligned} \quad (2.25)$$

where $\tilde{A}_1 = A_1 e^{i\vartheta_1}$, $\tilde{A}_2 = A_2 e^{i\vartheta_2}$, CC indicates the complex conjugate, $\tilde{k}(\omega)$ is the complex wavenumber [= $\omega \tilde{n}(\omega)/c$] in the medium at the angular frequency ω , $\tilde{n}(\omega)$ is the complex refractive index [= $n(\omega) + i\kappa(\omega)$] of the medium at the angular frequency ω , $\tilde{\mathbf{E}}_{\omega_1}^w(z, t)$ is the complex electric field component related to ω_1 , and $\tilde{\mathbf{E}}_{\omega_2}^w(z, t)$ is the complex electric field component related to ω_2 . Notably, although several variables in Eq. (2.25) are complex [i.e. \tilde{A}_1 , \tilde{A}_2 , $\tilde{k}(\omega_1)$, and $\tilde{k}(\omega_2)$], the imaginary parts ultimately cancel out due to the presence of the complex conjugate (i.e. CC), resulting in a real-valued $\mathbf{E}_i^w(z, t)$. For this scenario, Eqs. (2.5), (2.6), and (2.23) reduce to:

$$m_e \frac{\partial^2 \mathbf{s}^{w,(1)}(z, t)}{\partial t^2} + m_e \gamma \frac{\partial \mathbf{s}^{w,(1)}(z, t)}{\partial t} + m_e \omega_0^2 \mathbf{s}^{w,(1)}(z, t) = -q \mathbf{E}^w(z, t), \quad (2.26)$$

$$\frac{\partial^2 \mathbf{s}^{w,(2)}(z, t)}{\partial t^2} + \gamma \frac{\partial \mathbf{s}^{w,(2)}(z, t)}{\partial t} + \omega_0^2 \mathbf{s}^{w,(2)}(z, t) + \mathfrak{S}[\mathbf{s}^{w,(1)}(z, t)]^2 = 0, \quad (2.27)$$

$$\frac{\partial^2 \mathbf{E}^w(z, t)}{\partial z^2} - \frac{1}{c^2} \frac{\partial^2}{\partial t^2} \left[\mathbf{E}^w(z, t) + \frac{1}{\epsilon_0} \mathbf{P}^{w,(1)}(z, t) \right] = \frac{1}{c^2 \epsilon_0} \frac{\partial^2 \mathbf{P}^{w,(2)}(z, t)}{\partial t^2}, \quad (2.28)$$

respectively, where $\mathbf{E}^w(z, t)$ is the electric field in the medium, $\mathbf{s}^{w,(1)}(z, t)$ is the first-order bound electric charge displacement in the medium, $\mathbf{s}^{w,(2)}(z, t)$ is the second-order bound electric charge displacement in the medium, $\mathbf{P}^{w,(1)}(z, t)$ is the first-order polarization in the medium, and $\mathbf{P}^{w,(2)}(z, t)$ is the second-order polarization in the medium. $\mathbf{E}^w(z, t)$ consists of contributions at: (i) the angular frequencies present in Eq. (2.24) [i.e. $\mathbf{E}_{\omega_1}^w(z, t)$ and $\mathbf{E}_{\omega_2}^w(z, t)$] and (ii) angular frequencies arising from the second-order nonlinear interactions [i.e. $\mathbf{E}_{2\omega_1}^w(z, t)$, $\mathbf{E}_{2\omega_2}^w(z, t)$, $\mathbf{E}_{\omega_1+\omega_2}^w(z, t)$, and $\mathbf{E}_{\omega_1-\omega_2}^w(z, t)$]. The latter contribution occurs because of the $[\mathbf{s}^{w,(1)}(z, t)]^2$ term in Eq. (2.27). $\mathbf{E}^w(z, t)$ is expressed as the superposition of the various contributions, such that,

$$\begin{aligned} \mathbf{E}^w(z, t) &= \mathbf{E}_i^w(z, t) + \mathbf{E}_g^w(z, t) \\ &= \mathbf{E}_{\omega_1}^w(z, t) + \mathbf{E}_{\omega_2}^w(z, t) + \mathbf{E}_{2\omega_1}^w(z, t) + \mathbf{E}_{2\omega_2}^w(z, t) + \mathbf{E}_{\omega_1+\omega_2}^w(z, t) \\ &\quad + \mathbf{E}_{\omega_1-\omega_2}^w(z, t), \end{aligned} \quad (2.29)$$

where $\mathbf{E}_g^w(z, t)$ represents the electric field containing angular frequencies not present in $\mathbf{E}_i^w(z, t)$ [i.e. $\mathbf{E}_g^w(z, t) = \mathbf{E}_{2\omega_1}^w(z, t) + \mathbf{E}_{2\omega_2}^w(z, t) + \mathbf{E}_{\omega_1+\omega_2}^w(z, t) + \mathbf{E}_{\omega_1-\omega_2}^w(z, t)$]. Equation (2.29) can be written in its complex form,

$$\begin{aligned} \mathbf{E}^w(z, t) &= \tilde{E}_{\omega_1}^w(z, t) \hat{\mathbf{x}} + \tilde{E}_{\omega_2}^w(z, t) \hat{\mathbf{x}} + \tilde{E}_{2\omega_1}^w(z, t) \hat{\mathbf{x}} + \tilde{E}_{2\omega_2}^w(z, t) \hat{\mathbf{x}} + \tilde{E}_{\omega_1+\omega_2}^w(z, t) \hat{\mathbf{x}} \\ &\quad + \tilde{E}_{\omega_1-\omega_2}^w(z, t) \hat{\mathbf{x}} + \text{CC}, \end{aligned} \quad (2.30)$$

where $\tilde{E}_{\zeta}^w(z, t)$ represents the complex electric field contribution at the angular frequency of ζ [$= \omega_1, \omega_2, 2\omega_1, 2\omega_2, \omega_1 + \omega_2$, or $\omega_1 - \omega_2$] and exhibits the form of a plane wave [i.e. $\tilde{E}_{\zeta}^w(z, t) \propto e^{-i[\zeta t - \tilde{k}(\zeta)z]}$]. Similar to $\mathbf{E}^w(z, t)$, $\mathbf{s}^{w,(1)}(z, t)$ consists of contributions at: (i) the angular frequencies present in Eq. (2.24) [i.e. $\mathbf{s}_{\omega_1}^{w,(1)}(z, t)$ and $\mathbf{s}_{\omega_2}^{w,(1)}(z, t)$] and (ii) angular

frequencies arising from the second-order nonlinear interactions [i.e. $\mathbf{s}_{2\omega_1}^{w,(1)}(z, t)$, $\mathbf{s}_{2\omega_2}^{w,(1)}(z, t)$, $\mathbf{s}_{\omega_1+\omega_2}^{w,(1)}(z, t)$, and $\mathbf{s}_{\omega_1-\omega_2}^{w,(1)}(z, t)$]. $\mathbf{s}^{w,(1)}(z, t)$ is expressed as the superposition of the various contributions,

$$\begin{aligned} \mathbf{s}^{w,(1)}(z, t) = & \mathbf{s}_{\omega_1}^{w,(1)}(z, t) + \mathbf{s}_{\omega_2}^{w,(1)}(z, t) + \mathbf{s}_{2\omega_1}^{w,(1)}(z, t) + \mathbf{s}_{2\omega_2}^{w,(1)}(z, t) + \mathbf{s}_{\omega_1+\omega_2}^{w,(1)}(z, t) \\ & + \mathbf{s}_{\omega_1-\omega_2}^{w,(1)}(z, t), \end{aligned} \quad (2.31)$$

which in complex form is,

$$\begin{aligned} \mathbf{s}^{w,(1)}(z, t) = & \tilde{s}_{\omega_1}^{w,(1)}(z, t)\hat{\mathbf{x}} + \tilde{s}_{\omega_2}^{w,(1)}(z, t)\hat{\mathbf{x}} + \tilde{s}_{2\omega_1}^{w,(1)}(z, t)\hat{\mathbf{x}} + \tilde{s}_{2\omega_2}^{w,(1)}(z, t)\hat{\mathbf{x}} \\ & + \tilde{s}_{\omega_1+\omega_2}^{w,(1)}(z, t)\hat{\mathbf{x}} + \tilde{s}_{\omega_1-\omega_2}^{w,(1)}(z, t)\hat{\mathbf{x}} + \text{CC}, \end{aligned} \quad (2.32)$$

where $\tilde{s}_{\zeta}^{w,(1)}(z, t)$ represents the complex first-order bound charge displacement contribution at the angular frequency of ζ and exhibits the form of a plane wave [i.e. $\tilde{s}_{\zeta}^{w,(1)}(z, t) \propto e^{-i[\zeta t - \bar{k}(\zeta)z]}$].

Inserting Eqs. (2.30) and (2.32) into Eq. (2.26) and rearranging gives six independent equations for each frequency (recall $\zeta = \omega_1, \omega_2, 2\omega_1, 2\omega_2, \omega_1 + \omega_2$, or $\omega_1 - \omega_2$),

$$m_e \frac{\partial^2 \tilde{s}_{\zeta}^{w,(1)}(z, t)}{\partial t^2} + m_e \gamma \frac{\partial \tilde{s}_{\zeta}^{w,(1)}(z, t)}{\partial t} + m_e \omega_0^2 \tilde{s}_{\zeta}^{w,(1)}(z, t) = -q \tilde{E}_{\zeta}^w(z, t). \quad (2.33)$$

Solving Eq. (2.33) permits [30]:

$$\mathbf{s}_{\zeta}^{w,(1)}(z, t) = \tilde{s}_{\zeta}^{w,(1)}(z, t)\hat{\mathbf{x}} + \text{CC} = -\frac{\varepsilon_0}{Nq} \tilde{\chi}^{(1)}(\zeta) \tilde{E}_{\zeta}^w(z, t)\hat{\mathbf{x}} + \text{CC}, \quad (2.34)$$

with,

$$\tilde{\chi}^{(1)}(\zeta) = \frac{Nq^2}{\varepsilon_0 m_e \omega_0^2 - \zeta^2 - i\gamma\zeta}, \quad (2.35)$$

where N is the density of electric dipoles in the medium and $\tilde{\chi}^{(1)}(\zeta)$ is the first-order susceptibility of the medium at the angular frequency of ζ . The amplitude of $\mathbf{s}_{2\omega_1}^{w,(1)}(z, t)$, $\mathbf{s}_{2\omega_2}^{w,(1)}(z, t)$,

$\mathbf{s}_{\omega_1+\omega_2}^{w,(1)}(z, t)$, and $\mathbf{s}_{\omega_1-\omega_2}^{w,(1)}(z, t)$ are typically much less than those of $\mathbf{s}_{\omega_1}^{w,(1)}(z, t)$ and $\mathbf{s}_{\omega_2}^{w,(1)}(z, t)$, such that $\mathbf{s}^{w,(1)}(z, t) \approx \mathbf{s}_{\omega_1}^{w,(1)}(z, t)\hat{\mathbf{x}} + \mathbf{s}_{\omega_2}^{w,(1)}(z, t)\hat{\mathbf{x}}$. Using this approximation and considering Eq. (2.27), it can be inferred that $\mathbf{s}^{w,(2)}(z, t)$ exhibits contributions at the angular frequencies of $2\omega_1$, $2\omega_2$, $\omega_1 + \omega_2$, $\omega_1 - \omega_2$, and DC [i.e. $\mathbf{s}_{2\omega_1}^{w,(2)}(z, t)$, $\mathbf{s}_{2\omega_2}^{w,(2)}(z, t)$, $\mathbf{s}_{\omega_1+\omega_2}^{w,(2)}(z, t)$, $\mathbf{s}_{\omega_1-\omega_2}^{w,(2)}(z, t)$, and $\mathbf{s}_0^{w,(2)}(z)$, respectively]. Therefore,

$$\mathbf{s}^{w,(2)}(z, t) = \mathbf{s}_{2\omega_1}^{w,(2)}(z, t) + \mathbf{s}_{2\omega_2}^{w,(2)}(z, t) + \mathbf{s}_{\omega_1+\omega_2}^{w,(2)}(z, t) + \mathbf{s}_{\omega_1-\omega_2}^{w,(2)}(z, t) + \mathbf{s}_0^{w,(2)}(z), \quad (2.36)$$

which in complex form is,

$$\begin{aligned} \mathbf{s}^{w,(2)}(z, t) = & \left\{ \tilde{\mathbf{s}}_{2\omega_1}^{w,(2)}(z, t)\hat{\mathbf{x}} + \tilde{\mathbf{s}}_{2\omega_2}^{w,(2)}(z, t)\hat{\mathbf{x}} + \tilde{\mathbf{s}}_{\omega_1+\omega_2}^{w,(2)}(z, t)\hat{\mathbf{x}} + \tilde{\mathbf{s}}_{\omega_1-\omega_2}^{w,(2)}(z, t)\hat{\mathbf{x}} + \text{CC} \right\} \\ & + \mathbf{s}_0^{w,(2)}(z)\hat{\mathbf{x}}, \end{aligned} \quad (2.37)$$

where $\mathbf{s}_0^{w,(2)}(z)$ represents the real-valued second-order bound electric charge displacement contribution at the angular frequency of zero (i.e. DC) and $\tilde{\mathbf{s}}_{2\omega_1}^{w,(2)}(z, t)$, $\tilde{\mathbf{s}}_{2\omega_2}^{w,(2)}(z, t)$, $\tilde{\mathbf{s}}_{\omega_1+\omega_2}^{w,(2)}(z, t)$, and $\tilde{\mathbf{s}}_{\omega_1-\omega_2}^{w,(2)}(z, t)$ represent the complex second-order bound electric charge displacement contributions at the angular frequencies of $2\omega_1$, $2\omega_2$, $\omega_1 + \omega_2$, and $\omega_1 - \omega_2$, respectively. Notably, we have assumed that the displacement of $\mathbf{s}^{w,(2)}(z, t)$ occurs along the same direction as the polarization of $\mathbf{E}_i^w(z, t)$, although this can differ for the general case that implements the second-order nonlinear tensor (see Section 2.2.3). Using $\mathbf{s}^{w,(1)}(z, t) \approx \mathbf{s}_{\omega_1}^{w,(1)}(z, t)\hat{\mathbf{x}} + \mathbf{s}_{\omega_2}^{w,(1)}(z, t)\hat{\mathbf{x}}$ and Eq. (2.37) allows the following five independent equations to be obtained from Eq. (2.27):

$$\begin{aligned} \frac{\partial^2 \tilde{s}_{2\omega_1}^{w,(2)}(z,t)}{\partial t^2} + \gamma \frac{\partial \tilde{s}_{2\omega_1}^{w,(2)}(z,t)}{\partial t} + \omega_0^2 \tilde{s}_{2\omega_1}^{w,(2)}(z,t) \\ + \frac{\mathfrak{S}\varepsilon_0^2}{4N^2q^2} [\tilde{A}_1 \tilde{\chi}^{(1)}(\omega_1)]^2 e^{-i[2\omega_1 t - 2\tilde{k}(\omega_1)z]} = 0, \end{aligned} \quad (2.38)$$

$$\begin{aligned} \frac{\partial^2 \tilde{s}_{2\omega_2}^{w,(2)}(z,t)}{\partial t^2} + \gamma \frac{\partial \tilde{s}_{2\omega_2}^{w,(2)}(z,t)}{\partial t} + \omega_0^2 \tilde{s}_{2\omega_2}^{w,(2)}(z,t) \\ + \frac{\mathfrak{S}\varepsilon_0^2}{4N^2q^2} [\tilde{A}_2 \tilde{\chi}^{(1)}(\omega_2)]^2 e^{-i[2\omega_2 t - 2\tilde{k}(\omega_2)z]} = 0, \end{aligned} \quad (2.39)$$

$$\begin{aligned} \frac{\partial^2 \tilde{s}_{\omega_1+\omega_2}^{w,(2)}(z,t)}{\partial t^2} + \gamma \frac{\partial \tilde{s}_{\omega_1+\omega_2}^{w,(2)}(z,t)}{\partial t} + \omega_0^2 \tilde{s}_{\omega_1+\omega_2}^{w,(2)}(z,t) \\ + \frac{\mathfrak{S}\varepsilon_0^2}{2N^2q^2} \tilde{A}_1 \tilde{\chi}^{(1)}(\omega_1) \tilde{A}_2 \tilde{\chi}^{(1)}(\omega_2) e^{-i\{(\omega_1+\omega_2)t - [\tilde{k}(\omega_1) + \tilde{k}(\omega_2)]z\}} = 0, \end{aligned} \quad (2.40)$$

$$\begin{aligned} \frac{\partial^2 \tilde{s}_{\omega_1-\omega_2}^{w,(2)}(z,t)}{\partial t^2} + \gamma \frac{\partial \tilde{s}_{\omega_1-\omega_2}^{w,(2)}(z,t)}{\partial t} + \omega_0^2 \tilde{s}_{\omega_1-\omega_2}^{w,(2)}(z,t) \\ + \frac{\mathfrak{S}\varepsilon_0^2}{2N^2q^2} \tilde{A}_1 \tilde{\chi}^{(1)}(\omega_1) [\tilde{A}_2 \tilde{\chi}^{(1)}(\omega_2)]^* e^{-i\{(\omega_1-\omega_2)t - [\tilde{k}(\omega_1) - \tilde{k}^*(\omega_2)]z\}} \\ = 0, \end{aligned} \quad (2.41)$$

$$\begin{aligned} \omega_0^2 s_0^{w,(2)}(z) + \frac{\mathfrak{S}\varepsilon_0^2}{2N^2q^2} \tilde{A}_1 \tilde{\chi}^{(1)}(\omega_1) [\tilde{A}_1 \tilde{\chi}^{(1)}(\omega_1)]^* e^{-2k_0(\omega_1)\kappa(\omega_1)z} \\ + \frac{\mathfrak{S}\varepsilon_0^2}{2N^2q^2} \tilde{A}_2 \tilde{\chi}^{(1)}(\omega_2) [\tilde{A}_2 \tilde{\chi}^{(1)}(\omega_2)]^* e^{-2k_0(\omega_2)\kappa(\omega_2)z} = 0. \end{aligned} \quad (2.42)$$

By solving Eqs. (2.38)-(2.42), we obtain [30]:

$$\begin{aligned} \mathbf{s}_{2\omega_1}^{w,(2)}(z,t) &= \tilde{s}_{2\omega_1}^{w,(2)}(z,t) \hat{\mathbf{x}} + \text{CC} \\ &= -\frac{\varepsilon_0}{4Nq} \tilde{A}_1^2 \tilde{\chi}^{(2)}(2\omega_1; \omega_1, \omega_1) e^{-i[2\omega_1 t - 2\tilde{k}(\omega_1)z]} \hat{\mathbf{x}} + \text{CC}, \end{aligned} \quad (2.43)$$

$$\begin{aligned}
\mathbf{s}_{2\omega_2}^{w,(2)}(z, t) &= \tilde{s}_{2\omega_2}^{w,(2)}(z, t)\hat{\mathbf{x}} + \text{CC} \\
&= -\frac{\varepsilon_0}{4Nq}\tilde{A}_2^2\tilde{\chi}^{(2)}(2\omega_2: \omega_2, \omega_2)e^{-i[2\omega_2 t - 2\tilde{k}(\omega_2)z]}\hat{\mathbf{x}} + \text{CC},
\end{aligned} \tag{2.44}$$

$$\begin{aligned}
\mathbf{s}_{\omega_1+\omega_2}^{w,(2)}(z, t) &= \tilde{s}_{\omega_1+\omega_2}^{w,(2)}(z, t)\hat{\mathbf{x}} + \text{CC} \\
&= -\frac{\varepsilon_0}{2Nq}\tilde{A}_1\tilde{A}_2\tilde{\chi}^{(2)}(\omega_1 + \omega_2: \omega_1, \omega_2)e^{-i\{(\omega_1+\omega_2)t - [\tilde{k}(\omega_1) + \tilde{k}(\omega_2)]z\}}\hat{\mathbf{x}} \\
&\quad + \text{CC},
\end{aligned} \tag{2.45}$$

$$\begin{aligned}
\mathbf{s}_{\omega_1-\omega_2}^{w,(2)}(z, t) &= \tilde{s}_{\omega_1-\omega_2}^{w,(2)}(z, t)\hat{\mathbf{x}} + \text{CC} \\
&= -\frac{\varepsilon_0}{2Nq}\tilde{A}_1\tilde{A}_2^*\tilde{\chi}^{(2)}(\omega_1 - \omega_2: \omega_1, -\omega_2)e^{-i\{(\omega_1-\omega_2)t - [\tilde{k}(\omega_1) - \tilde{k}^*(\omega_2)]z\}}\hat{\mathbf{x}} \\
&\quad + \text{CC},
\end{aligned} \tag{2.46}$$

$$\begin{aligned}
\mathbf{s}_0^{w,(2)}(z) &= s_0^{w,(2)}(z)\hat{\mathbf{x}} \\
&= -\frac{\varepsilon_0}{2Nq}\tilde{A}_1\tilde{A}_1^*\chi^{(2)}(0: \omega_1, -\omega_1)e^{-2k_0(\omega_1)\kappa(\omega_1)z}\hat{\mathbf{x}} \\
&\quad - \frac{\varepsilon_0}{2Nq}\tilde{A}_2\tilde{A}_2^*\chi^{(2)}(0: \omega_2, -\omega_2)e^{-2k_0(\omega_2)\kappa(\omega_2)z}\hat{\mathbf{x}},
\end{aligned} \tag{2.47}$$

with,

$$\tilde{\chi}^{(2)}(2\omega_1: \omega_1, \omega_1) = \frac{\Im m_e \varepsilon_0^2}{N^2 q^3} \tilde{\chi}^{(1)}(2\omega_1)\tilde{\chi}^{(1)}(\omega_1)\tilde{\chi}^{(1)}(\omega_1), \tag{2.48}$$

$$\tilde{\chi}^{(2)}(2\omega_2: \omega_2, \omega_2) = \frac{\Im m_e \varepsilon_0^2}{N^2 q^3} \tilde{\chi}^{(1)}(2\omega_2)\tilde{\chi}^{(1)}(\omega_2)\tilde{\chi}^{(1)}(\omega_2), \tag{2.49}$$

$$\tilde{\chi}^{(2)}(\omega_1 + \omega_2: \omega_1, \omega_2) = \frac{\Im m_e \varepsilon_0^2}{N^2 q^3} \tilde{\chi}^{(1)}(\omega_1 + \omega_2)\tilde{\chi}^{(1)}(\omega_1)\tilde{\chi}^{(1)}(\omega_2), \tag{2.50}$$

$$\tilde{\chi}^{(2)}(\omega_1 - \omega_2: \omega_1, -\omega_2) = \frac{\Im m_e \varepsilon_0^2}{N^2 q^3} \tilde{\chi}^{(1)}(\omega_1 - \omega_2)\tilde{\chi}^{(1)}(\omega_1)\tilde{\chi}^{(1)}(-\omega_2), \tag{2.51}$$

$$\chi^{(2)}(0: \omega_1, -\omega_1) = \frac{\Im N q^3}{\varepsilon_0 m_e^2 \omega_0^2} \frac{1}{(\omega_0^2 - \omega_1^2)^2 + (\gamma \omega_1)^2}, \quad (2.52)$$

$$\chi^{(2)}(0: \omega_2, -\omega_2) = \frac{\Im N q^3}{\varepsilon_0 m_e^2 \omega_0^2} \frac{1}{(\omega_0^2 - \omega_2^2)^2 + (\gamma \omega_2)^2}, \quad (2.53)$$

where the $\tilde{\chi}^{(2)}$ terms represent the second-order nonlinear susceptibility of the medium, with $\chi^{(2)}(0: \omega_1, -\omega_1)$ and $\chi^{(2)}(0: \omega_2, -\omega_2)$ being real-valued. Notably, $\tilde{\chi}^{(2)}(\omega_1 + \omega_2: \omega_1, \omega_2)$ is interpreted as the second-order nonlinear susceptibility of the medium at the angular frequency of $\omega_1 + \omega_2$, due to an incident electric field containing angular frequency components at ω_1 and ω_2 (with the other $\tilde{\chi}^{(2)}$ definitions being interpreted in a similar fashion). Additionally, as seen from Eqs. (2.45) and (2.46), the sum of ω_1 and ω_2 leads to $\omega_1 + \omega_2$ and the difference between ω_1 and ω_2 leads to $\omega_1 - \omega_2$, respectively. However, the resulting angular frequency of $\omega_1 - \omega_2$ can instead be interpreted as the sum of ω_1 and $-\omega_2$, where the latter is a negative frequency. Such an approach mathematically links the various second-order nonlinear processes, allowing certain portions of the derivations to be simplified. Importantly, no physical differences arise by treating the $\omega_1 - \omega_2$ process as the sum of ω_1 and $-\omega_2$, opposed to the difference between ω_1 and ω_2 . The total bound electric charge displacement is,

$$\begin{aligned} \mathbf{s}^w(\mathbf{z}, t) &= \mathbf{s}^{w,(1)}(\mathbf{z}, t) + \mathbf{s}^{w,(2)}(\mathbf{z}, t) \\ &= \mathbf{s}_{\omega_1}^{w,(1)}(\mathbf{z}, t) + \mathbf{s}_{\omega_2}^{w,(1)}(\mathbf{z}, t) + \mathbf{s}_{2\omega_1}^{w,(1)}(\mathbf{z}, t) + \mathbf{s}_{2\omega_2}^{w,(1)}(\mathbf{z}, t) \\ &\quad + \mathbf{s}_{\omega_1+\omega_2}^{w,(1)}(\mathbf{z}, t) + \mathbf{s}_{\omega_1-\omega_2}^{w,(1)}(\mathbf{z}, t) + \mathbf{s}_{2\omega_1}^{w,(2)}(\mathbf{z}, t) + \mathbf{s}_{2\omega_2}^{w,(2)}(\mathbf{z}, t) \\ &\quad + \mathbf{s}_{\omega_1+\omega_2}^{w,(2)}(\mathbf{z}, t) + \mathbf{s}_{\omega_1-\omega_2}^{w,(2)}(\mathbf{z}, t) + \mathbf{s}_0^{w,(2)}(\mathbf{z}). \end{aligned} \quad (2.54)$$

Recall that a time-dependent second-order nonlinear polarization produces an electric field [i.e. see Eq. (2.28)]. $\mathbf{s}^{w,(1)}(z, t)$ and $\mathbf{s}^{w,(2)}(z, t)$ are directly related to the polarization in the medium via the expressions $\mathbf{P}^{w,(1)}(z, t) = -Nq\mathbf{s}^{w,(1)}(z, t)$ and $\mathbf{P}^{w,(2)}(z, t) = -Nq\mathbf{s}^{w,(2)}(z, t)$, such that:

$$\begin{aligned}
\mathbf{P}^{w,(1)}(z, t) &= \mathbf{P}_{\omega_1}^{w,(1)}(z, t) + \mathbf{P}_{\omega_2}^{w,(1)}(z, t) + \mathbf{P}_{2\omega_1}^{w,(1)}(z, t) + \mathbf{P}_{2\omega_2}^{w,(1)}(z, t) \\
&\quad + \mathbf{P}_{\omega_1+\omega_2}^{w,(1)}(z, t) + \mathbf{P}_{\omega_1-\omega_2}^{w,(1)}(z, t) \\
&= \tilde{\mathbf{P}}_{\omega_1}^{w,(1)}(z, t)\hat{\mathbf{x}} + \tilde{\mathbf{P}}_{\omega_2}^{w,(1)}(z, t)\hat{\mathbf{x}} + \tilde{\mathbf{P}}_{2\omega_1}^{w,(1)}(z, t)\hat{\mathbf{x}} + \tilde{\mathbf{P}}_{2\omega_2}^{w,(1)}(z, t)\hat{\mathbf{x}} \\
&\quad + \tilde{\mathbf{P}}_{\omega_1+\omega_2}^{w,(1)}(z, t)\hat{\mathbf{x}} + \tilde{\mathbf{P}}_{\omega_1-\omega_2}^{w,(1)}(z, t)\hat{\mathbf{x}} + \text{CC} .
\end{aligned} \tag{2.55}$$

with,

$$\mathbf{P}_{\zeta}^{w,(1)}(z, t) = \tilde{\mathbf{P}}_{\zeta}^{w,(1)}(z, t)\hat{\mathbf{x}} + \text{CC} = \varepsilon_0\tilde{\chi}^{(1)}(\zeta)\tilde{\mathbf{E}}_{\zeta}^w(z, t)\hat{\mathbf{x}} + \text{CC} , \tag{2.56}$$

and,

$$\begin{aligned}
\mathbf{P}^{w,(2)}(z, t) &= \mathbf{P}_{2\omega_1}^{w,(2)}(z, t) + \mathbf{P}_{2\omega_2}^{w,(2)}(z, t) + \mathbf{P}_{\omega_1+\omega_2}^{w,(2)}(z, t) + \mathbf{P}_{\omega_1-\omega_2}^{w,(2)}(z, t) \\
&\quad + \mathbf{P}_0^{w,(2)}(z, t) \\
&= \left\{ \tilde{\mathbf{P}}_{2\omega_1}^{w,(2)}(z, t)\hat{\mathbf{x}} + \tilde{\mathbf{P}}_{2\omega_2}^{w,(2)}(z, t)\hat{\mathbf{x}} + \tilde{\mathbf{P}}_{\omega_1+\omega_2}^{w,(2)}(z, t)\hat{\mathbf{x}} + \tilde{\mathbf{P}}_{\omega_1-\omega_2}^{w,(2)}(z, t)\hat{\mathbf{x}} \right. \\
&\quad \left. + \text{CC} \right\} + P_0^{w,(2)}(z)\hat{\mathbf{x}} ,
\end{aligned} \tag{2.57}$$

with,

$$\begin{aligned}
\mathbf{P}_{2\omega_1}^{w,(2)}(z, t) &= \tilde{\mathbf{P}}_{2\omega_1}^{w,(2)}(z, t)\hat{\mathbf{x}} + \text{CC} \\
&= \frac{\varepsilon_0}{4}\tilde{A}_1^2\tilde{\chi}^{(2)}(2\omega_1: \omega_1, \omega_1)e^{-i[2\omega_1 t - 2\tilde{k}(\omega_1)z]}\hat{\mathbf{x}} + \text{CC} ,
\end{aligned} \tag{2.58}$$

$$\begin{aligned}
\mathbf{P}_{2\omega_2}^{w,(2)}(z, t) &= \tilde{\mathbf{P}}_{2\omega_2}^{w,(2)}(z, t)\hat{\mathbf{x}} + \text{CC} \\
&= \frac{\varepsilon_0}{4}\tilde{A}_2^2\tilde{\chi}^{(2)}(2\omega_2: \omega_2, \omega_2)e^{-i[2\omega_2 t - 2\tilde{k}(\omega_2)z]}\hat{\mathbf{x}} + \text{CC} ,
\end{aligned} \tag{2.59}$$

$$\begin{aligned}
\mathbf{P}_{\omega_1+\omega_2}^{w,(2)}(z,t) &= \tilde{\mathbf{P}}_{\omega_1+\omega_2}^{w,(2)}(z,t)\hat{\mathbf{x}} + \text{CC} \\
&= \frac{\varepsilon_0}{2}\tilde{A}_1\tilde{A}_2\tilde{\chi}^{(2)}(\omega_1+\omega_2;\omega_1,\omega_2)e^{-i\{(\omega_1+\omega_2)t-[\tilde{k}(\omega_1)+\tilde{k}(\omega_2)]z\}}\hat{\mathbf{x}} + \text{CC},
\end{aligned} \tag{2.60}$$

$$\begin{aligned}
\mathbf{P}_{\omega_1-\omega_2}^{w,(2)}(z,t) &= \tilde{\mathbf{P}}_{\omega_1-\omega_2}^{w,(2)}(z,t)\hat{\mathbf{x}} + \text{CC} \\
&= \frac{\varepsilon_0}{2}\tilde{A}_1\tilde{A}_2^*\tilde{\chi}^{(2)}(\omega_1-\omega_2;\omega_1,-\omega_2)e^{-i\{(\omega_1-\omega_2)t-[\tilde{k}(\omega_1)-\tilde{k}^*(\omega_2)]z\}}\hat{\mathbf{x}} \\
&+ \text{CC},
\end{aligned} \tag{2.61}$$

$$\begin{aligned}
\mathbf{P}_0^{w,(2)}(z) &= P_0^{w,(2)}(z)\hat{\mathbf{x}} \\
&= \frac{\varepsilon_0}{2}\tilde{A}_1\tilde{A}_1^*\chi^{(2)}(0;\omega_1,-\omega_1)e^{-2k_0(\omega_1)\kappa(\omega_1)z}\hat{\mathbf{x}} \\
&+ \frac{\varepsilon_0}{2}\tilde{A}_2\tilde{A}_2^*\chi^{(2)}(0;\omega_2,-\omega_2)e^{-2k_0(\omega_2)\kappa(\omega_2)z}\hat{\mathbf{x}},
\end{aligned} \tag{2.62}$$

where $\tilde{\mathbf{P}}_{\zeta}^{w,(1)}(z,t)$ represents the complex first-order polarization contributions at the angular frequency of ζ , $P_0^{w,(2)}(z,t)$ represents the real-valued second-order polarization contribution at the angular frequency of zero (i.e. DC), and $\tilde{\mathbf{P}}_{2\omega_1}^{w,(2)}(z,t)$, $\tilde{\mathbf{P}}_{2\omega_2}^{w,(2)}(z,t)$, $\tilde{\mathbf{P}}_{\omega_1+\omega_2}^{w,(2)}(z,t)$, and $\tilde{\mathbf{P}}_{\omega_1-\omega_2}^{w,(2)}(z,t)$ represent the complex second-order polarization contributions at the angular frequencies of $2\omega_1$, $2\omega_2$, $\omega_1 + \omega_2$, and $\omega_1 - \omega_2$, respectively. Inserting Eq. (2.30), (2.55), and (2.57) into Eq. (2.28) and simplifying yields six independent equations, represented as:

$$\frac{\partial^2 \tilde{E}_{\zeta}^w(z,t)}{\partial z^2} - \frac{\tilde{n}^2(\zeta)}{c^2} \frac{\partial^2 \tilde{E}_{\zeta}^w(z,t)}{\partial t^2} = \frac{1}{c^2 \varepsilon_0} \frac{\partial^2 \tilde{\mathbf{P}}_{\zeta}^{w,(2)}(z,t)}{\partial t^2}, \tag{2.63}$$

where $\tilde{n}(\zeta) = \sqrt{1 + \tilde{\chi}^{(1)}(\zeta)}$ and $\tilde{\mathbf{P}}_{\omega_1}^{w,(2)}(z,t) = \tilde{\mathbf{P}}_{\omega_2}^{w,(2)}(z,t) = 0$ [i.e. ω_1 and ω_2 are the angular frequencies present in $\mathbf{E}_i^w(z,t)$, such that second-order nonlinear polarizations are not induced at these angular frequencies]. Notably, since a time-independent charge cannot produce propagating

EM waves, there is no electric field contribution from the $\mathbf{P}_0^{w,(2)}(z)$ polarization term. Solving Eq. (2.63) for the electric field contributions at $2\omega_1$, $2\omega_2$, $\omega_1 + \omega_2$, and $\omega_1 - \omega_2$ yields [30]:

$$\begin{aligned} \mathbf{E}_{2\omega_1}^w(z, t) &= \tilde{E}_{2\omega_1}^w(z, t)\hat{\mathbf{x}} + \text{CC} \\ &= \frac{\omega_1 \tilde{A}_1^2 \tilde{\chi}^{(2)}(2\omega_1: \omega_1, \omega_1)}{4\tilde{n}(2\omega_1)c} \frac{e^{i[2\tilde{k}(\omega_1) - \tilde{k}(2\omega_1)]z} - 1}{2\tilde{k}(\omega_1) - \tilde{k}(2\omega_1)} e^{-i[2\omega_1 t - \tilde{k}(2\omega_1)z]}\hat{\mathbf{x}} \\ &\quad + \text{CC}, \end{aligned} \quad (2.64)$$

$$\begin{aligned} \mathbf{E}_{2\omega_2}^w(z, t) &= \tilde{E}_{2\omega_2}^w(z, t)\hat{\mathbf{x}} + \text{CC} \\ &= \frac{\omega_2 \tilde{A}_2^2 \tilde{\chi}^{(2)}(2\omega_2: \omega_2, \omega_2)}{4\tilde{n}(2\omega_2)c} \frac{e^{i[2\tilde{k}(\omega_2) - \tilde{k}(2\omega_2)]z} - 1}{2\tilde{k}(\omega_2) - \tilde{k}(2\omega_2)} e^{-i[2\omega_2 t - \tilde{k}(2\omega_2)z]}\hat{\mathbf{x}} \\ &\quad + \text{CC}, \end{aligned} \quad (2.65)$$

$$\begin{aligned} \mathbf{E}_{\omega_1 + \omega_2}^w(z, t) &= \tilde{E}_{\omega_1 + \omega_2}^w(z, t)\hat{\mathbf{x}} + \text{CC} \\ &= \frac{(\omega_1 + \omega_2) \tilde{A}_1 \tilde{A}_2 \tilde{\chi}^{(2)}(\omega_1 + \omega_2: \omega_1, \omega_2)}{4\tilde{n}(\omega_1 + \omega_2)c} \frac{e^{i[\tilde{k}(\omega_1) + \tilde{k}(\omega_2) - \tilde{k}(\omega_1 + \omega_2)]z} - 1}{\tilde{k}(\omega_1) + \tilde{k}(\omega_2) - \tilde{k}(\omega_1 + \omega_2)} \\ &\quad \times e^{-i[(\omega_1 + \omega_2)t - \tilde{k}(\omega_1 + \omega_2)z]}\hat{\mathbf{x}} + \text{CC}, \end{aligned} \quad (2.66)$$

$$\begin{aligned} \mathbf{E}_{\omega_1 - \omega_2}^w(z, t) &= \tilde{E}_{\omega_1 - \omega_2}^w(z, t)\hat{\mathbf{x}} + \text{CC} \\ &= \frac{(\omega_1 - \omega_2) \tilde{A}_1 \tilde{A}_2^* \tilde{\chi}^{(2)}(\omega_1 - \omega_2: \omega_1, -\omega_2)}{4\tilde{n}(\omega_1 - \omega_2)c} \frac{e^{i[\tilde{k}(\omega_1) - \tilde{k}^*(\omega_2) - \tilde{k}(\omega_1 - \omega_2)]z} - 1}{\tilde{k}(\omega_1) - \tilde{k}^*(\omega_2) - \tilde{k}(\omega_1 - \omega_2)} \\ &\quad \times e^{-i[(\omega_1 - \omega_2)t - \tilde{k}(\omega_1 - \omega_2)z]}\hat{\mathbf{x}} + \text{CC}, \end{aligned} \quad (2.67)$$

respectively, where several approximations are utilized. Specifically, the slowly varying amplitude approximation (SVAA) is implemented, such that Eqs. (2.64)-(2.67) are valid for:

$$|2\tilde{k}(\omega_1) - \tilde{k}(2\omega_1)| \ll 2|\tilde{k}(2\omega_1)|, \quad (2.68)$$

$$|2\tilde{k}(\omega_2) - \tilde{k}(2\omega_2)| \ll 2|\tilde{k}(2\omega_2)|, \quad (2.69)$$

$$|\tilde{k}(\omega_1) + \tilde{k}(\omega_2) - \tilde{k}(\omega_1 + \omega_2)| \ll 2|\tilde{k}(\omega_1 + \omega_2)|, \quad (2.70)$$

$$|\tilde{k}(\omega_1) - \tilde{k}^*(\omega_2) - \tilde{k}(\omega_1 - \omega_2)| \ll 2|\tilde{k}(\omega_1 - \omega_2)|, \quad (2.71)$$

respectively. The left-hand side of these approximations represent the degree of phase-matching (see Appendix A), or phase-mismatching, of the second-order nonlinear interactions. Phase-mismatching occurs when the generated electric fields (having angular frequencies of $2\omega_1$, $2\omega_2$, $\omega_1 + \omega_2$, and $\omega_1 - \omega_2$) propagate through the medium with a different refractive index than the incident electric fields (having angular frequencies of ω_1 and ω_2). Consequently, the electric field generated at a given position in the medium may not constructively interfere with the electric field generated from a previous position. If phase-mismatching is severe, the amplitude of the generated electric fields changes rapidly, thereby causing the terms on the left-hand side to be large and the SVAA to be invalid. Additionally, in the second-order nonlinear process described by Eq. (2.67), a photon is destroyed at the angular frequency of ω_1 to produce photons at both $\omega_1 - \omega_2$ and ω_2 . However, in this analysis, a sufficiently large electric field is assumed at both ω_1 and ω_2 , such that the angular frequency components destroyed at ω_1 and generated at ω_2 are negligible. Moreover, we assume no frequency components are initially present at ω_1 , ω_2 , $\omega_1 + \omega_2$, and $\omega_1 - \omega_2$. Such assumptions simplify the mathematical analysis and facilitate a more intuitive investigation. To briefly summarize this section, Eqs. (2.64)-(2.67) describe the electric fields resulting from $\mathbf{E}_i^w(z, t)$ [see Eq. (2.24)] when considering first-order and second-order nonlinear effects in a dispersive and lossy 1D medium, but ignoring depletion of $\mathbf{E}_i^w(z, t)$ and cascading effects.

2.2.2. A quantitative example

To illustrate the bound electric charge displacement in a given medium and the resulting electric field, the equations derived in Section 2.2.1 are evaluated using specific parameter values.

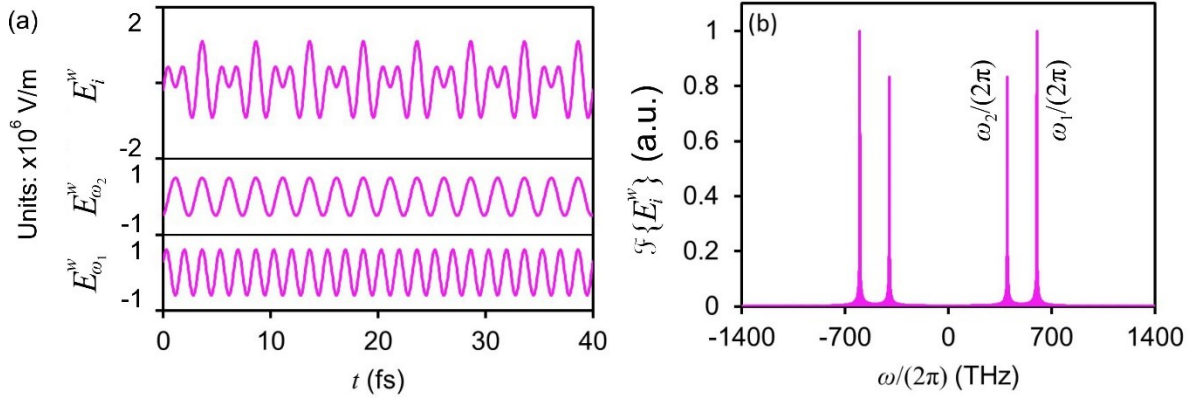


Fig. 2.3. (a) Time-domain and (b) frequency-domain representation of $\mathbf{E}_i^w(z, t)$.

$\mathbf{E}_i^w(z, t)$ is described using $A_1=6$ kV/cm, $A_2=5$ kV/cm, $\omega_1/(2\pi)=600$ THz, $\omega_2/(2\pi)=400$ THz, $\vartheta_1=60^\circ$, and $\vartheta_2=160^\circ$. The time and frequency domain representations of $\mathbf{E}_i^w(z, t)$ are shown in Fig. 2.3(a) and 2.3(b), respectively, where it is clear that angular frequencies exist at $\omega_1/(2\pi)=600$ THz and $\omega_2/(2\pi)=400$ THz. The medium is described using $N=5 \times 10^{22}$ cm $^{-3}$, $\omega_0/(2\pi)=4000$ THz, $\gamma/(2\pi)=20$ THz, and $\mathfrak{S}=2 \times 10^{44}$ m $^{-1}$ s $^{-2}$. n and κ of this medium [extracted from Eq. (2.35)] are shown in Fig. 2.4(a) and 2.4(b), respectively. Clearly, $\tilde{n}(\omega_1)=1.1215+8.8 \times 10^{-5}i$, $\tilde{n}(\omega_2)=1.12+5.7 \times 10^{-5}i$, $\tilde{n}(2\omega_1)=1.1299+20.2 \times 10^{-5}i$, $\tilde{n}(2\omega_2)=1.1235+12.2 \times 10^{-5}i$, $\tilde{n}(\omega_1 + \omega_2)=1.1263+15.9 \times 10^{-5}i$, and $\tilde{n}(\omega_1 - \omega_2)=1.1192+2.8 \times 10^{-5}i$. As can be inferred from Eqs. (2.43)-(2.46), the magnitude of the $\tilde{\chi}^{(2)}$ terms (i.e. $|\tilde{\chi}^{(2)}|$) influences the strength of the bound electric charge displacement, while the phase of the $\tilde{\chi}^{(2)}$ terms (i.e. $\phi\{\tilde{\chi}^{(2)}\}$) influences the phase of the bound electric charge displacement. Similarly, $|\tilde{\chi}^{(2)}|$ and $\phi\{\tilde{\chi}^{(2)}\}$ influence the strength and phase of the resulting electric field, respectively [see Eqs. (2.64)-(2.67)]. From Eqs. (2.48)-(2.53), it is determined that $|\tilde{\chi}^{(2)}(2\omega_1; \omega_1, \omega_1)|=25.5$ pm/V, $|\tilde{\chi}^{(2)}(2\omega_2; \omega_2, \omega_2)|=23.6$ pm/V, $|\tilde{\chi}^{(2)}(\omega_1 +$

$\omega_2: \omega_1, \omega_2) = 24.5$ pm/V, $|\tilde{\chi}^{(2)}(\omega_1 - \omega_2: \omega_1, -\omega_2)| = 23$ pm/V, $|\tilde{\chi}^{(2)}(0: \omega_1, -\omega_1)| = 23.2$ pm/V, $|\tilde{\chi}^{(2)}(0: \omega_2, -\omega_2)| = 22.7$ pm/V, and $\phi\{\tilde{\chi}^{(2)}\} \lesssim 3.2$ mrad for all of the processes.

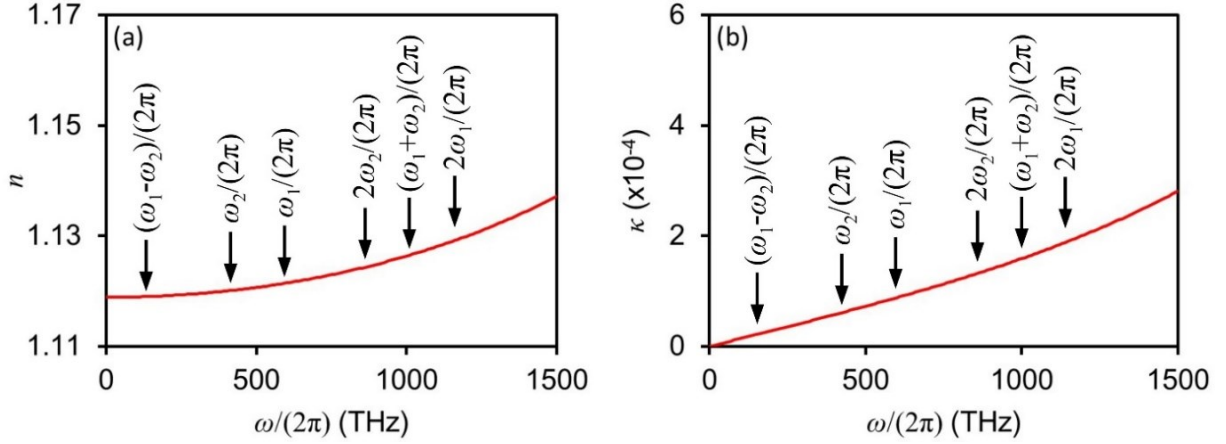


Fig. 2.4. (a) Refractive index and (b) extinction coefficient of a medium described using $N=5 \times 10^{22}$ cm⁻³, $\omega_0/(2\pi)=4000$ THz, and $\gamma/(2\pi)=20$ THz.

The bound electric charge displacement is considered at a position of $z=70$ μm . Figure 2.5(a) displays $\mathbf{s}^{w,(2)}(z, t)$, as well as each of its contributions [i.e. $\mathbf{s}_{2\omega_1}^{w,(2)}(z, t)$, $\mathbf{s}_{2\omega_2}^{w,(2)}(z, t)$, $\mathbf{s}_{\omega_1+\omega_2}^{w,(2)}(z, t)$, $\mathbf{s}_{\omega_1-\omega_2}^{w,(2)}(z, t)$, and $\mathbf{s}_0^{w,(2)}(z)$]. As this displacement is the motion of the electric charges that result from the incident electric field [i.e. Eq. (2.24)], the time-domain displacements presented in Fig. 2.5(a) provide an intuitive representation of the events occurring within the medium. It is worth noting that the maximum displacement of the bound electric charge is on the order of 10^{-20} m, which is much smaller than the typical size of an atom (e.g. angstroms) [133]. The Fourier transform of $\mathbf{s}^{w,(2)}(z, t)$ is shown in Fig. 2.5(b). As expected, bound electric charge displacement is induced at the frequencies of $2\omega_1/(2\pi)=1200$ THz, $2\omega_2/(2\pi)=800$ THz, $(\omega_1 + \omega_2)/(2\pi)=1000$ THz, $(\omega_1 - \omega_2)/(2\pi)=200$ THz, and 0 THz (i.e. DC). Figure 2.5(c) shows the maximum amplitudes of $\mathbf{s}_{2\omega_1}^{w,(2)}(z, t)$, $\mathbf{s}_{2\omega_2}^{w,(2)}(z, t)$, $\mathbf{s}_{\omega_1+\omega_2}^{w,(2)}(z, t)$, $\mathbf{s}_{\omega_1-\omega_2}^{w,(2)}(z, t)$, and

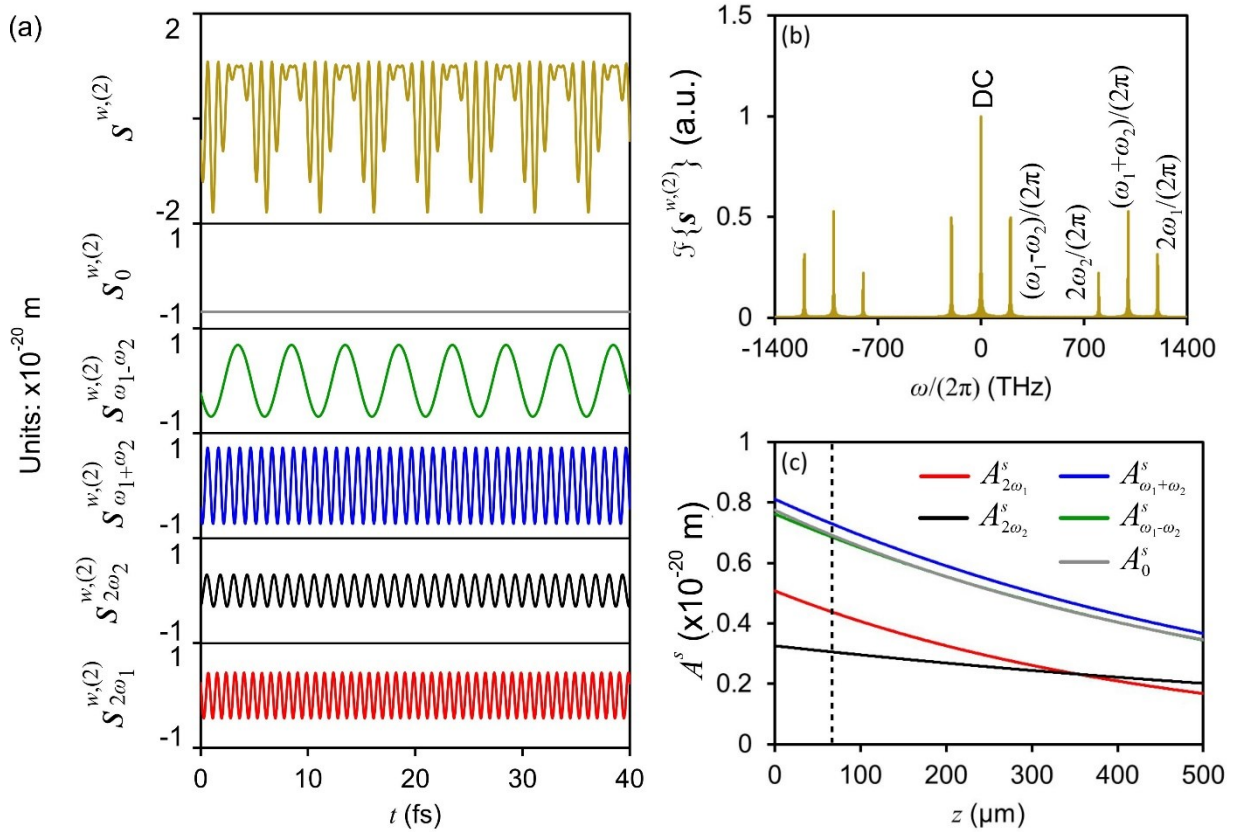


Fig. 2.5. (a) The bound electric charge displacement of $\mathbf{s}^{w,(2)}(z, t)$, as well as each of its contributions. (b) Fourier transform of $\mathbf{s}^{w,(2)}(z, t)$ obtained over a temporal window of 500 fs. (c) The maximum amplitudes of $\mathbf{s}_{2\omega_1}^{w,(2)}(z, t)$, $\mathbf{s}_{2\omega_2}^{w,(2)}(z, t)$, $\mathbf{s}_{\omega_1+\omega_2}^{w,(2)}(z, t)$, $\mathbf{s}_{\omega_1-\omega_2}^{w,(2)}(z, t)$, and $\mathbf{s}_0^{w,(2)}(z)$ at various positions within the medium. The vertical dotted-line at $z=70 \mu\text{m}$ corresponds to the recorded position of the time-domain bound electric charge displacements shown in (a).

$\mathbf{s}_0^{w,(2)}(z)$ for a given position within the medium, which are denoted as $A_{2\omega_1}^s(z)$, $A_{2\omega_2}^s(z)$, $A_{\omega_1+\omega_2}^s(z)$, $A_{\omega_1-\omega_2}^s(z)$, and $A_0^s(z)$, respectively. These amplitudes decrease with increasing z , due to absorption loss at ω_1 and ω_2 (i.e. the amplitude of the incident electric fields are reduced as they propagate within the medium, thereby limiting the strength at which they can induce bound electric charge displacement).

The electric field resulting from the displacement of the bound electric charges is evaluated at a position of $z=70 \mu\text{m}$. Figure 2.6(a) displays $\mathbf{E}_g^w(z, t)$, as well as each of its contributions [i.e. $\mathbf{E}_{2\omega_1}^w(z, t)$, $\mathbf{E}_{2\omega_2}^w(z, t)$, $\mathbf{E}_{\omega_1+\omega_2}^w(z, t)$, and $\mathbf{E}_{\omega_1-\omega_2}^w(z, t)$]. The maximum amplitudes of $\mathbf{E}_{2\omega_1}^w(z, t)$, $\mathbf{E}_{2\omega_2}^w(z, t)$, $\mathbf{E}_{\omega_1+\omega_2}^w(z, t)$, and $\mathbf{E}_{\omega_1-\omega_2}^w(z, t)$ for a given position within the medium are denoted as $A_{2\omega_1}(z)$, $A_{2\omega_2}(z)$, $A_{\omega_1+\omega_2}(z)$, and $A_{\omega_1-\omega_2}(z)$, respectively. Therefore, for $z=70 \mu\text{m}$, $A_{2\omega_1}(z)=346 \text{ V/m}$, $A_{2\omega_2}(z)=584 \text{ V/m}$, $A_{\omega_1+\omega_2}(z)=768 \text{ V/m}$, and $A_{\omega_1-\omega_2}(z)=771 \text{ V/m}$. The conversion efficiencies for each of these processes are obtained from the relationships:

$$\eta_{2\omega_1}(z) = \frac{A_{2\omega_1}^2(z)n(2\omega_1)}{A_1^2n(\omega_1) + A_2^2n(\omega_2)}, \quad (2.72)$$

$$\eta_{2\omega_2}(z) = \frac{A_{2\omega_2}^2(z)n(2\omega_2)}{A_1^2n(\omega_1) + A_2^2n(\omega_2)}, \quad (2.73)$$

$$\eta_{\omega_1+\omega_2}(z) = \frac{A_{\omega_1+\omega_2}^2(z)n(\omega_1 + \omega_2)}{A_1^2n(\omega_1) + A_2^2n(\omega_2)}, \quad (2.74)$$

$$\eta_{\omega_1-\omega_2}(z) = \frac{A_{\omega_1-\omega_2}^2(z)n(\omega_1 - \omega_2)}{A_1^2n(\omega_1) + A_2^2n(\omega_2)}, \quad (2.75)$$

where we have utilized the condition $n(\zeta) \gg \kappa(\zeta)$, which is typically valid when the angular frequencies are far from any resonances in the medium. $\eta_{2\omega_1}=2 \times 10^{-7}$, $\eta_{2\omega_2}=5.6 \times 10^{-7}$, $\eta_{\omega_1+\omega_2}=9.7 \times 10^{-7}$, and $\eta_{\omega_1-\omega_2}=9.7 \times 10^{-7}$ at $z=70 \mu\text{m}$. The Fourier transform of $\mathbf{E}_g^w(z, t)$ is shown in Fig. 2.6(b), along with the Fourier transform of $\mathbf{E}_i^w(z, t)$. While $\mathbf{E}_i^w(z, t)$ oscillates at the angular frequencies of $\omega_1/(2\pi)=600 \text{ THz}$ and $\omega_2/(2\pi)=400 \text{ THz}$, $\mathbf{E}_g^w(z, t)$ oscillates at the angular frequencies of $2\omega_1/(2\pi)=1200 \text{ THz}$, $2\omega_2/(2\pi)=800 \text{ THz}$, $(\omega_1 + \omega_2)/(2\pi)=1000 \text{ THz}$, and $(\omega_1 - \omega_2)/(2\pi)=200 \text{ THz}$, as expected. It is important to understand the terminology associated with each of the frequency-conversion processes. Generation at the angular frequency of $2\omega_1$, as

well as generation at $2\omega_2$, is referred to as SHG. Additionally, generation at the angular frequency of $\omega_1 + \omega_2$ is referred to as SFG, whereas generation at $\omega_1 - \omega_2$ is referred to as DFG. Figure 2.6(c) shows $A_{2\omega_1}(z)$, $A_{2\omega_2}(z)$, $A_{\omega_1+\omega_2}(z)$, and $A_{\omega_1-\omega_2}(z)$ for various positions within the medium. Notably, the left-hand sides of the SVAA [see Eqs. (2.68)-(2.71)] are more than two orders of magnitude smaller than the corresponding right-hand sides, such that the observed amplitudes vary sufficiently slowly to satisfy the SVAA. As seen from Fig. 2.6(c), the maximum amplitudes exhibit a quasi-periodic behavior with respect to position in the medium, which is related to phase-mismatching effects. $\mathbf{E}_{2\omega_1}^w$, $\mathbf{E}_{2\omega_2}^w$, $\mathbf{E}_{\omega_1+\omega_2}^w$, and $\mathbf{E}_{\omega_1-\omega_2}^w$ are the aggregate of second-order nonlinear generation at the current position of $z = z_0$, as well as generation at previous positions of $z < z_0$ (i.e. angular frequency components previously produced within the medium that continue to propagate). To better understand this phenomenon, we consider $\mathbf{E}_{2\omega_1}^w(z, t)$ produced from $\mathbf{E}_{\omega_1}^w(z, t)$. In the ideal situation, $\mathbf{E}_{\omega_1}^w(z, t)$ propagates through the medium while experiencing the same refractive index as $\mathbf{E}_{2\omega_1}^w(z, t)$. As such, newly-generated $\mathbf{E}_{2\omega_1}^w(z, t)$ components produced at $z = z_0$ constructively interfere with previously-generated $\mathbf{E}_{2\omega_1}^w(z, t)$ components from $z < z_0$, resulting in an electric field that grows linearly with z . However, in other scenarios, $\mathbf{E}_{\omega_1}^w(z, t)$ propagates through the medium with a different refractive index than $\mathbf{E}_{2\omega_1}^w(z, t)$. Therefore, previously-generated $\mathbf{E}_{2\omega_1}^w(z, t)$ components from $z < z_0$ and newly-generated $\mathbf{E}_{2\omega_1}^w(z, t)$ components at $z = z_0$ interfere constructively at certain positions within the crystal but destructively at others, thus leading to the quasi-periodic behavior seen in Fig. 2.6(c). To quantify such effects, it is customary to use the coherence length, defined as the length at which the generated electric field ceases to combine constructively and begins to

destructively interfere, thus producing a local maximum [i.e. the first maximum in Fig. 2.6(c)].

From Eq. (2.64), it is determined that the position of the first maximum occurs at,

$$L_c^{2\omega_1} = \frac{\pi c}{2\omega_1 |n(\omega_1) - n(2\omega_1)|}, \quad (2.76)$$

where we have utilized the conditions of $n(\omega_1) \gg \kappa(\omega_1)$ and $n(2\omega_1) \gg \kappa(2\omega_1)$. $L_c^{2\omega_1} = 15 \mu\text{m}$, in agreement with the position of the first maximum in Fig. 2.6(c). When observing Fig. 2.6(c), it is interesting to notice that the magnitudes of the minimums increase with increasing z and the magnitudes of the maximums decrease with increasing z , which are related to loss in the medium. Specifically, at the minimums, $\mathbf{E}_{2\omega_1}^w(z, t)$ components produced over the last half of the cycle are unable to fully compensate for $\mathbf{E}_{2\omega_1}^w(z, t)$ components produced over the first half of the cycle, since absorption loss causes generation to weaken with increasing z . At the maximums, $\mathbf{E}_{2\omega_1}^w(z, t)$ components produced over the first half of the current cycle are less than $\mathbf{E}_{2\omega_1}^w(z, t)$ components produced over the first half of the previous cycle, again due to absorption loss causing generation to weaken with increasing z . Another interesting observation is that the maximum $A_{2\omega_2}(z)$ is greater than the maximum $A_{2\omega_1}(z)$ [see Fig. 2.6(c)], despite the fact that $A_{2\omega_1}^s(z) \approx A_{2\omega_2}^s(z)$ [see Fig. 2.5(c)]. This is due to phase-matching between $\mathbf{E}_{\omega_2}^w(z, t)$ and $\mathbf{E}_{2\omega_2}^w(z, t)$ being better in comparison to phase-matching between $\mathbf{E}_{\omega_1}^w(z, t)$ and $\mathbf{E}_{2\omega_1}^w(z, t)$. $\mathbf{E}_{2\omega_2}^w$, $\mathbf{E}_{\omega_1+\omega_2}^w$, and $\mathbf{E}_{\omega_1-\omega_2}^w$ can be interpreted in a similar manner to $\mathbf{E}_{2\omega_1}^w$, with their corresponding coherence lengths being obtained from Eqs. (2.65)-(2.67) as:

$$L_c^{2\omega_2} = \frac{\pi c}{2\omega_2 |n(\omega_2) - n(2\omega_2)|}, \quad (2.77)$$

$$L_c^{\omega_1+\omega_2} = \frac{\pi c}{|\omega_1 n(\omega_1) + \omega_2 n(\omega_2) - (\omega_1 + \omega_2) n(\omega_1 + \omega_2)|}, \quad (2.78)$$

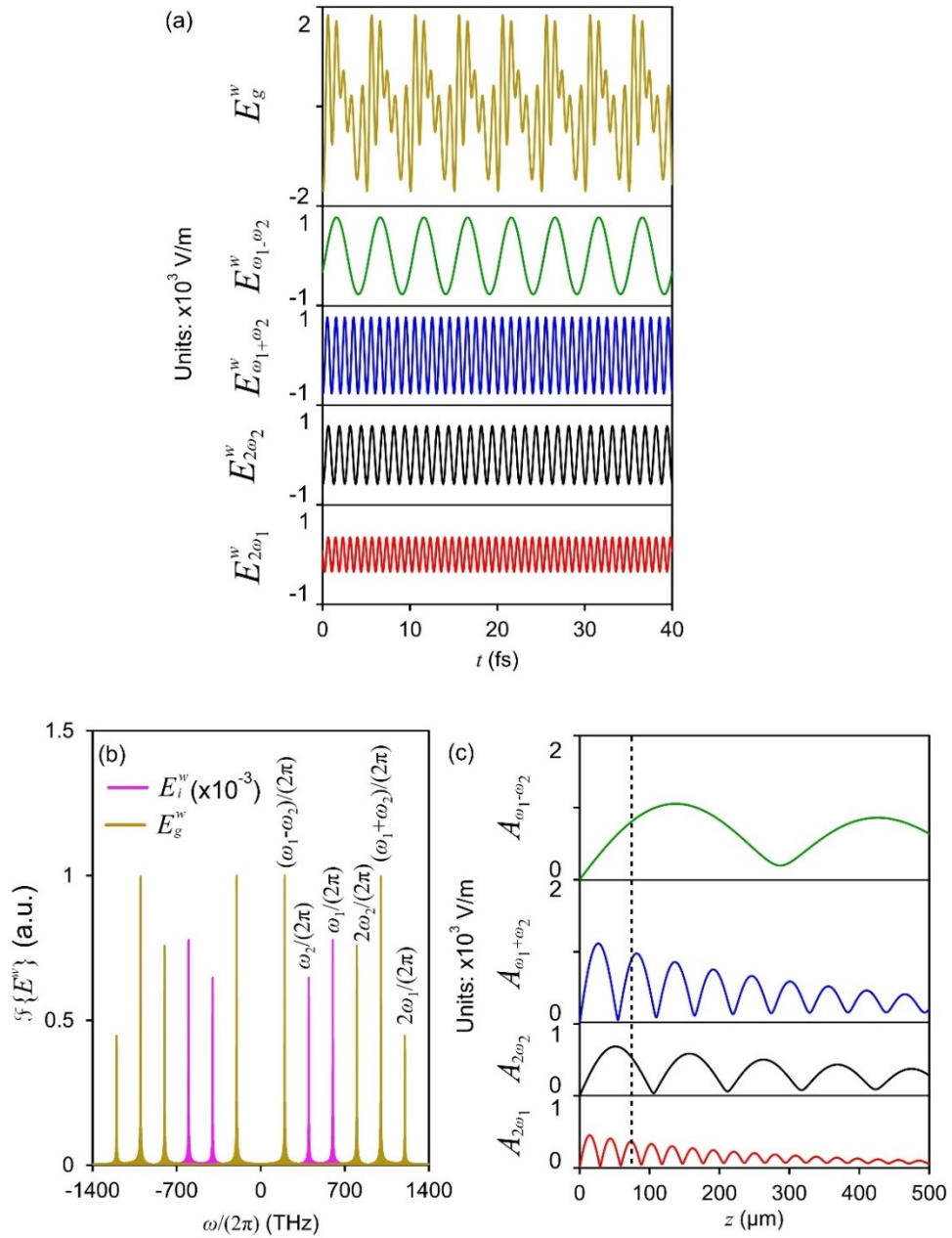


Fig. 2.6. (a) The electric field of $\mathbf{E}_g^w(z, t)$, as well as each of its contributions. (b) Fourier transform of $\mathbf{E}_g^w(z, t)$ obtained over a temporal window of 500 fs. The Fourier transform of $\mathbf{E}_i^w(z, t)$ is shown for comparison. (c) The maximum amplitudes of $\mathbf{E}_{2\omega_1}^w(z, t)$, $\mathbf{E}_{2\omega_2}^w(z, t)$, $\mathbf{E}_{\omega_1+\omega_2}^w(z, t)$, and $\mathbf{E}_{\omega_1-\omega_2}^w(z, t)$ at various positions within the medium. The vertical dotted-line represents $z = 70 \mu\text{m}$, which correspond to the recorded position of the time-domain electric fields in (a).

$$L_c^{\omega_1-\omega_2} = \frac{\pi c}{|\omega_1 n(\omega_1) - \omega_2 n(\omega_2) - (\omega_1 - \omega_2)n(\omega_1 - \omega_2)|}, \quad (2.79)$$

respectively, where we have utilized the condition of $n(\zeta) \gg \kappa(\zeta)$. $L_c^{2\omega_2}=54 \mu\text{m}$, $L_c^{\omega_1+\omega_2}=28 \mu\text{m}$, and $L_c^{\omega_1-\omega_2}=142 \mu\text{m}$, in agreement with the first maximums observed in Fig. 2.6(c).

2.2.3. Tensor representation of the second-order nonlinear polarization

Sections 2.2.1 and 2.2.2 consider an isotropic medium, such that each second-order nonlinear process was described by a single $\tilde{\chi}^{(2)}$. For an anisotropic medium, the second-order nonlinear polarizations [i.e. Eqs. (2.58)-(2.62)] become more cumbersome as bound electric charge oscillations can couple with perturbations in different directions. To aid in understanding second-order nonlinear effects in anisotropic materials, it is helpful to consider the hypothetical two-dimensional (2D) unit cell depicted in Fig. 2.7. Figure 2.7(a) illustrates the equilibrium positions of the atomic constituents, where such constituents are coupled by the forces they exhibit on each other, as depicted by the springs. Consider a perturbation causing the inner atomic constituents to be displaced along the x axis [see Fig. 2.7(b)], where the corner (i.e. gold colored) atomic constituents are assumed to be heavier and remain fixed. Due to the anisotropy of the unit cell, the inner atomic constituents may exhibit a displacement in both the x and y axes when returning to their equilibrium positions. When bound electric charge displacement occurs along both axes, electric fields can be produced having polarization components along both axes, despite the initial perturbation being along one axis (i.e. the x axis). Notably, while we have illustrated the displacement of the atomic constituents within a unit cell, an analogous interpretation can be made for the anisotropic displacement of electron clouds relative to their corresponding nuclei. Additionally, while a 2D representation is presented for simplicity, this same reasoning applies to

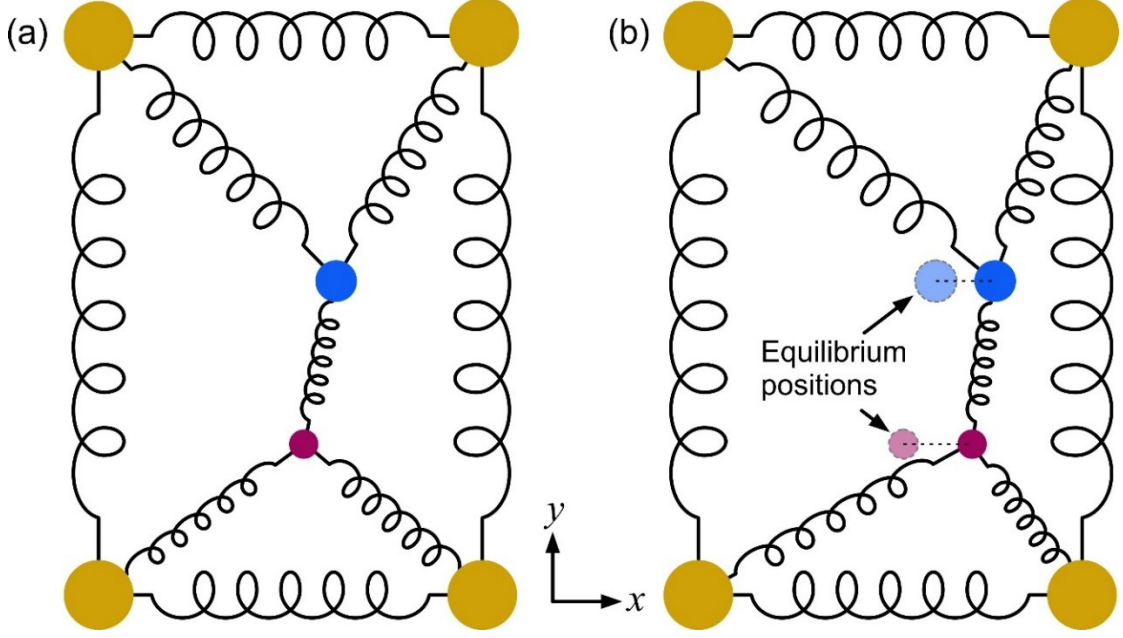


Fig. 2.7. (a) A hypothetical representation of a 2D unit cell with the atomic constituents at their equilibrium positions. The various colors represent different atomic constituents. (b) A perturbation causing the inner atomic constituents to be displaced along the x axis, where such constituents may exhibit a displacement in both the x and y axes when returning to their equilibrium positions.

the 3D scenario, where an incident perturbation along one direction can induce bound electric charge displacement along any direction in the 3D unit cell. The frequency-domain expression for the second-order nonlinear polarization in an anisotropic medium is [30],

$$\begin{aligned}
\tilde{P}_{\psi}^{(2)}(\Omega) = & \varepsilon_0 \tilde{\chi}_{\psi xx}^{(2)}(\Lambda) \tilde{E}_x(\omega_1) \tilde{E}_x(\omega_2) + \varepsilon_0 \tilde{\chi}_{\psi yy}^{(2)}(\Lambda) \tilde{E}_y(\omega_1) \tilde{E}_y(\omega_2) \\
& + \varepsilon_0 \tilde{\chi}_{\psi zz}^{(2)}(\Lambda) \tilde{E}_z(\omega_1) \tilde{E}_z(\omega_2) + \varepsilon_0 \tilde{\chi}_{\psi yz}^{(2)}(\Lambda) \tilde{E}_y(\omega_1) \tilde{E}_z(\omega_2) \\
& + \varepsilon_0 \tilde{\chi}_{\psi zy}^{(2)}(\Lambda) \tilde{E}_z(\omega_1) \tilde{E}_y(\omega_2) + \varepsilon_0 \tilde{\chi}_{\psi xz}^{(2)}(\Lambda) \tilde{E}_x(\omega_1) \tilde{E}_z(\omega_2) \\
& + \varepsilon_0 \tilde{\chi}_{\psi zx}^{(2)}(\Lambda) \tilde{E}_z(\omega_1) \tilde{E}_x(\omega_2) + \varepsilon_0 \tilde{\chi}_{\psi xy}^{(2)}(\Lambda) \tilde{E}_x(\omega_1) \tilde{E}_y(\omega_2) \\
& + \varepsilon_0 \tilde{\chi}_{\psi yx}^{(2)}(\Lambda) \tilde{E}_y(\omega_1) \tilde{E}_x(\omega_2) ,
\end{aligned} \tag{2.80}$$

where Λ denotes ' $\Omega: \omega_1, \omega_2$ ', Ω represents the generated angular frequency ($=\omega_1+\omega_2$), $\psi = x, y$, or z , $\tilde{P}_\psi^{(2)}(\Omega)$ is the second-order nonlinear polarization induced along the ψ axis, \tilde{E}_x , \tilde{E}_y and \tilde{E}_z are the incident electric field components polarized along the x, y , and z axes, respectively, and $\tilde{\chi}_{\psi\rho\zeta}^{(2)}$ is the second-order nonlinear susceptibility associated with the induced polarization along the ψ axis due to \tilde{E}_ρ and \tilde{E}_ζ ($\rho = x, y$, or z and $\zeta = x, y$, or z). Importantly, Eq. (2.80) gives $\Omega = 2\omega_1$ (when $\omega_1 \rightarrow \omega_1$ and $\omega_2 \rightarrow \omega_1$), $\Omega = 2\omega_2$ (when $\omega_1 \rightarrow \omega_2$ and $\omega_2 \rightarrow \omega_2$), $\Omega = \omega_1 + \omega_2$ (when $\omega_1 \rightarrow \omega_1$ and $\omega_2 \rightarrow \omega_2$), $\Omega = \omega_1 - \omega_2$ (when $\omega_1 \rightarrow \omega_1$ and $\omega_2 \rightarrow -\omega_2$), and $\Omega = 0$ (when $\omega_1 \rightarrow \omega_1$ and $\omega_2 \rightarrow -\omega_1$ or $\omega_1 \rightarrow \omega_2$ and $\omega_2 \rightarrow -\omega_2$). Additionally, it does not matter which frequency component is defined as ω_1 and ω_2 (i.e. it is equivalent to substitute $\omega_1 \rightarrow \omega_2$ and $\omega_2 \rightarrow \omega_1$), such that:

$$\begin{aligned}\tilde{\chi}_{\psi zy}^{(2)}(\Omega: \omega_1, \omega_2)\tilde{E}_z(\omega_1)\tilde{E}_y(\omega_2) &= \tilde{\chi}_{\psi zy}^{(2)}(\Omega: \omega_2, \omega_1)\tilde{E}_z(\omega_2)\tilde{E}_y(\omega_1) \\ &= \tilde{\chi}_{\psi yz}^{(2)}(\Omega: \omega_1, \omega_2)\tilde{E}_y(\omega_1)\tilde{E}_z(\omega_2),\end{aligned}\tag{2.81}$$

$$\begin{aligned}\tilde{\chi}_{\psi zx}^{(2)}(\Omega: \omega_1, \omega_2)\tilde{E}_z(\omega_1)\tilde{E}_x(\omega_2) &= \tilde{\chi}_{\psi zx}^{(2)}(\Omega: \omega_2, \omega_1)\tilde{E}_z(\omega_2)\tilde{E}_x(\omega_1) \\ &= \tilde{\chi}_{\psi xz}^{(2)}(\Omega: \omega_1, \omega_2)\tilde{E}_x(\omega_1)\tilde{E}_z(\omega_2),\end{aligned}\tag{2.82}$$

$$\begin{aligned}\tilde{\chi}_{\psi yx}^{(2)}(\Omega: \omega_1, \omega_2)\tilde{E}_y(\omega_1)\tilde{E}_x(\omega_2) &= \tilde{\chi}_{\psi yx}^{(2)}(\Omega: \omega_2, \omega_1)\tilde{E}_y(\omega_2)\tilde{E}_x(\omega_1) \\ &= \tilde{\chi}_{\psi xy}^{(2)}(\Omega: \omega_1, \omega_2)\tilde{E}_x(\omega_1)\tilde{E}_y(\omega_2),\end{aligned}\tag{2.83}$$

where $\tilde{\chi}_{\psi zy}^{(2)}(\Omega: \omega_2, \omega_1) = \tilde{\chi}_{\psi yz}^{(2)}(\Omega: \omega_1, \omega_2)$, $\tilde{\chi}_{\psi zx}^{(2)}(\Omega: \omega_2, \omega_1) = \tilde{\chi}_{\psi xz}^{(2)}(\Omega: \omega_1, \omega_2)$, and

$\tilde{\chi}_{\psi yx}^{(2)}(\Omega: \omega_2, \omega_1) = \tilde{\chi}_{\psi xy}^{(2)}(\Omega: \omega_1, \omega_2)$ is evident from Eqs. (2.48)-(2.53). Clearly, Eqs. (2.81)-(2.83) permit Eq. (2.80) to be written as,

$$\begin{aligned}
\tilde{P}_\psi^{(2)}(\Omega) &= \varepsilon_0 \tilde{\chi}_{\psi xx}^{(2)}(\Lambda) \tilde{E}_x(\omega_1) \tilde{E}_x(\omega_2) + \varepsilon_0 \tilde{\chi}_{\psi yy}^{(2)}(\Lambda) \tilde{E}_y(\omega_1) \tilde{E}_y(\omega_2) \\
&+ \varepsilon_0 \tilde{\chi}_{\psi zz}^{(2)}(\Lambda) \tilde{E}_z(\omega_1) \tilde{E}_z(\omega_2) + 2\varepsilon_0 \tilde{\chi}_{\psi yz}^{(2)}(\Lambda) \tilde{E}_y(\omega_1) \tilde{E}_z(\omega_2) \\
&+ 2\varepsilon_0 \tilde{\chi}_{\psi xz}^{(2)}(\Lambda) \tilde{E}_x(\omega_1) \tilde{E}_z(\omega_2) + 2\varepsilon_0 \tilde{\chi}_{\psi xy}^{(2)}(\Lambda) \tilde{E}_x(\omega_1) \tilde{E}_y(\omega_2),
\end{aligned} \tag{2.84}$$

which can be recast in the form of matrix notation as,

$$\begin{aligned}
\begin{bmatrix} \tilde{P}_x^{(2)}(\Omega) \\ \tilde{P}_y^{(2)}(\Omega) \\ \tilde{P}_z^{(2)}(\Omega) \end{bmatrix} &= \varepsilon_0 \begin{bmatrix} \tilde{\chi}_{xxx}^{(2)}(\Lambda) & \tilde{\chi}_{xyy}^{(2)}(\Lambda) & \tilde{\chi}_{xzz}^{(2)}(\Lambda) & \tilde{\chi}_{xyz}^{(2)}(\Lambda) & \tilde{\chi}_{xxz}^{(2)}(\Lambda) & \tilde{\chi}_{xxy}^{(2)}(\Lambda) \\ \tilde{\chi}_{yxx}^{(2)}(\Lambda) & \tilde{\chi}_{yyy}^{(2)}(\Lambda) & \tilde{\chi}_{yzz}^{(2)}(\Lambda) & \tilde{\chi}_{yyz}^{(2)}(\Lambda) & \tilde{\chi}_{yxz}^{(2)}(\Lambda) & \tilde{\chi}_{yyx}^{(2)}(\Lambda) \\ \tilde{\chi}_{zxx}^{(2)}(\Lambda) & \tilde{\chi}_{zyy}^{(2)}(\Lambda) & \tilde{\chi}_{zzz}^{(2)}(\Lambda) & \tilde{\chi}_{zyz}^{(2)}(\Lambda) & \tilde{\chi}_{zxx}^{(2)}(\Lambda) & \tilde{\chi}_{zxy}^{(2)}(\Lambda) \end{bmatrix} \\
&\times \begin{bmatrix} \tilde{E}_x^2(\omega_1) \\ \tilde{E}_y^2(\omega_1) \\ \tilde{E}_z^2(\omega_1) \\ 2\tilde{E}_y(\omega_1)\tilde{E}_z(\omega_2) \\ 2\tilde{E}_x(\omega_1)\tilde{E}_z(\omega_2) \\ 2\tilde{E}_x(\omega_1)\tilde{E}_y(\omega_2) \end{bmatrix}.
\end{aligned} \tag{2.85}$$

Equation (2.85) is often depicted using condensed notation, where the first subscript position of the $\tilde{\chi}^{(2)}$ terms are represented as $x \rightarrow 1$, $y \rightarrow 2$, and $z \rightarrow 3$, and the second and third subscript positions are represented as $xx \rightarrow 1$, $yy \rightarrow 2$, $zz \rightarrow 3$, $yz \rightarrow 4$, $xz \rightarrow 5$, and $xy \rightarrow 6$ [43], such that,

$$\begin{aligned}
\begin{bmatrix} \tilde{P}_x^{(2)}(\Omega) \\ \tilde{P}_y^{(2)}(\Omega) \\ \tilde{P}_z^{(2)}(\Omega) \end{bmatrix} &= \varepsilon_0 \begin{bmatrix} \tilde{\chi}_{11}^{(2)}(\Lambda) & \tilde{\chi}_{12}^{(2)}(\Lambda) & \tilde{\chi}_{13}^{(2)}(\Lambda) & \tilde{\chi}_{14}^{(2)}(\Lambda) & \tilde{\chi}_{15}^{(2)}(\Lambda) & \tilde{\chi}_{16}^{(2)}(\Lambda) \\ \tilde{\chi}_{21}^{(2)}(\Lambda) & \tilde{\chi}_{22}^{(2)}(\Lambda) & \tilde{\chi}_{23}^{(2)}(\Lambda) & \tilde{\chi}_{24}^{(2)}(\Lambda) & \tilde{\chi}_{25}^{(2)}(\Lambda) & \tilde{\chi}_{26}^{(2)}(\Lambda) \\ \tilde{\chi}_{31}^{(2)}(\Lambda) & \tilde{\chi}_{32}^{(2)}(\Lambda) & \tilde{\chi}_{33}^{(2)}(\Lambda) & \tilde{\chi}_{34}^{(2)}(\Lambda) & \tilde{\chi}_{35}^{(2)}(\Lambda) & \tilde{\chi}_{36}^{(2)}(\Lambda) \end{bmatrix} \\
&\times \begin{bmatrix} \tilde{E}_x^2(\omega_1) \\ \tilde{E}_y^2(\omega_1) \\ \tilde{E}_z^2(\omega_1) \\ 2\tilde{E}_y(\omega_1)\tilde{E}_z(\omega_2) \\ 2\tilde{E}_x(\omega_1)\tilde{E}_z(\omega_2) \\ 2\tilde{E}_x(\omega_1)\tilde{E}_y(\omega_2) \end{bmatrix}.
\end{aligned} \tag{2.86}$$

Alternatively, the following convention for Eq. (2.86) is also used,

$$\begin{bmatrix} \tilde{P}_x^{(2)}(\Omega) \\ \tilde{P}_y^{(2)}(\Omega) \\ \tilde{P}_z^{(2)}(\Omega) \end{bmatrix} = 2\varepsilon_0 \begin{bmatrix} \tilde{d}_{11}(\Lambda) & \tilde{d}_{12}(\Lambda) & \tilde{d}_{13}(\Lambda) & \tilde{d}_{14}(\Lambda) & \tilde{d}_{15}(\Lambda) & \tilde{d}_{16}(\Lambda) \\ \tilde{d}_{21}(\Lambda) & \tilde{d}_{22}(\Lambda) & \tilde{d}_{23}(\Lambda) & \tilde{d}_{24}(\Lambda) & \tilde{d}_{25}(\Lambda) & \tilde{d}_{26}(\Lambda) \\ \tilde{d}_{31}(\Lambda) & \tilde{d}_{32}(\Lambda) & \tilde{d}_{33}(\Lambda) & \tilde{d}_{34}(\Lambda) & \tilde{d}_{35}(\Lambda) & \tilde{d}_{36}(\Lambda) \end{bmatrix} \\
 \times \begin{bmatrix} \tilde{E}_x^2(\omega_1) \\ \tilde{E}_y^2(\omega_1) \\ \tilde{E}_z^2(\omega_1) \\ 2\tilde{E}_y(\omega_1)\tilde{E}_z(\omega_2) \\ 2\tilde{E}_x(\omega_1)\tilde{E}_z(\omega_2) \\ 2\tilde{E}_x(\omega_1)\tilde{E}_y(\omega_2) \end{bmatrix}, \tag{2.87}$$

where $\tilde{\chi}_{ij}^{(2)}(\Lambda) = 2\tilde{d}_{ij}(\Lambda)$ ($i=1, 2, \text{ or } 3$ and $j=1, 2, 3, 4, 5, \text{ or } 6$).

2.3. Nonlinear second-order interaction via a broadband electric field pulse

The previous discussion considered an electric field oscillating at monochromatic frequencies. Such a description is valid for continuous wave excitation of a nonlinear medium. However, since the efficiency of second-order nonlinear interactions is proportional to the incident radiation intensity, it is often desirable to access this nonlinearity via pulsed electric fields. It is important to consider a broadband electric field pulse incident on a nonlinear medium, since subtle differences arise in both the frequency-conversion process and the terminology, when compared to monochromatic incident electric fields (see Section 2.2). For this discussion, a 1D isotropic, uniform, dispersionless, and lossless medium is considered. Furthermore, cascading effects and depletion effects are ignored [30,31]. Such assumptions simplify the mathematical analysis, which in turn allows for a more intuitive interpretation of the nonlinear frequency-conversion process. Again, the electric fields are assumed to propagate along the z axis and exist for $z \geq 0$.

2.3.1. Induced polarization and Maxwell's equations

A transform-limited Gaussian electric field pulse is incident on the medium, where this electric field has the form,

$$\mathbf{E}_i^p(z, t) = E_i^p(z, t)\hat{\mathbf{x}} = Ae^{-(t-zn/c)^2/\sigma^2} \cos[\omega_c t - k(\omega_c)z - \vartheta] \hat{\mathbf{x}}, \quad (2.88)$$

where the superscript 'p' indicates that the corresponding variable is associated with the pulsed Gaussian electric field, A is the amplitude of the electric field pulse, ω_c is the central angular frequency, ϑ is the phase shift, σ describes the duration of the Gaussian envelope, $k(\omega_c)$ is the wavenumber [= $\omega_c n/c$] at the angular frequency of ω_c , and n is the frequency-independent refractive index. The frequency-domain representation of such an electric field pulse is depicted in Fig. 2.8. Figure 2.8(a) shows an angular frequency of ω_1 combining with an angular frequency of ω_2 to produce an angular frequency of $\Omega = \omega_1 + \omega_2$. This process occurs over the entire spectrum, resulting in generation across a spectral band centered at $2\omega_c$. Although such a process involves an infinite number of both SHG and SFG events, this process is often referred to as SHG. Figure 2.8(b) shows an angular frequency of ω_1 combining with an angular frequency of $-\omega_2$ to produce an angular frequency of $\Omega = \omega_1 - \omega_2$. Again, this process occurs over the entire spectrum, resulting in generation across a spectral band near DC. Although such a process is comprised of an infinite number of DFG events, it is often referred to as OR. By considering the SHG process as the sum of ω_1 and ω_2 to obtain $\Omega = \omega_1 + \omega_2$ and the OR process as the sum of ω_1 and $-\omega_2$ (i.e. a negative frequency) to obtain $\Omega = \omega_1 - \omega_2$, the induced second-order nonlinear polarizations for SHG and OR are described by the same integral equation, which in the frequency-domain is [139],

$$\mathbf{P}^{p,(2)}(z, \Omega) = \varepsilon_0 \int_{-\infty}^{\infty} \tilde{\chi}^{(2)}(\Omega: \omega_1, \Omega - \omega_1) E_i^p(z, \omega_1) E_i^p(z, \Omega - \omega_1) d\omega_1 \hat{\mathbf{x}}, \quad (2.89)$$

where we have assumed that the polarization of $\mathbf{P}^{p,(2)}(z, \Omega)$ and $\mathbf{E}_i^p(z, t)$ are the same, although they can differ for the general case of a second-order nonlinear tensor (see Section 2.3.3). Additionally, by using $E_i^p(z, \omega_1)$ and $E_i^p(z, \Omega - \omega_1)$ in Eq. (2.89), cascading effects have been ignored. Introducing the assumption of a dispersionless and lossless second-order nonlinear susceptibility [i.e. $\tilde{\chi}^{(2)}(\Omega: \omega_1, \Omega - \omega_1) = \chi^{(2)}$] permits Eq. (2.89) to be written as,

$$\mathbf{P}^{p,(2)}(z, \Omega) = \varepsilon_0 \chi^{(2)} \int_{-\infty}^{\infty} E_i^p(z, \omega_1) E_i^p(z, \Omega - \omega_1) d\omega_1 = \varepsilon_0 \chi^{(2)} \{E_i^p * E_i^p\}(z, \Omega) \hat{\mathbf{x}}, \quad (2.90)$$

where $\{E_i^p * E_i^p\}(z, \Omega)$ represents the convolution operation. Applying the inverse Fourier transform allows Eq. (2.90) to be expressed in the time-domain as,

$$\mathbf{P}^{p,(2)}(z, t) = \varepsilon_0 \chi^{(2)} [E_i^p(z, t)]^2 \hat{\mathbf{x}}. \quad (2.91)$$

Substituting Eq. (2.88) into Eq. (2.91) and simplifying yields:

$$\mathbf{P}^{p,(2)}(z, t) = \mathbf{P}_{OR}^{p,(2)}(z, t) + \mathbf{P}_{SHG}^{p,(2)}(z, t), \quad (2.92)$$

with,

$$\mathbf{P}_{OR}^{p,(2)}(z, t) = \frac{\varepsilon_0 \chi^{(2)} A^2}{2} e^{-2(t-zn/c)^2/\sigma^2} \hat{\mathbf{x}}, \quad (2.93)$$

$$\mathbf{P}_{SHG}^{p,(2)}(z, t) = \frac{\varepsilon_0 \chi^{(2)} A^2}{2} e^{-2(t-zn/c)^2/\sigma^2} \cos[2\omega_c t - 2k(\omega_c)z - 2\vartheta] \hat{\mathbf{x}}. \quad (2.94)$$

Here, $\mathbf{P}_{OR}^{p,(2)}(z, t)$ is the second-order nonlinear polarization related to OR and $\mathbf{P}_{SHG}^{p,(2)}(z, t)$ is the second-order nonlinear polarization related to SHG. The electric field in the medium can be expressed as,

$$\mathbf{E}^p(z, t) = \mathbf{E}_i^p(z, t) + \mathbf{E}_g^p(z, t) = \mathbf{E}_i^p(z, t) + \mathbf{E}_{OR}^p(z, t) + \mathbf{E}_{SHG}^p(z, t), \quad (2.95)$$

where $\mathbf{E}_g^p(z, t)$ represents the electric field containing angular frequencies not present in $\mathbf{E}_i^p(z, t)$ [i.e. $\mathbf{E}_g^p(z, t) = \mathbf{E}_{OR}^p(z, t) + \mathbf{E}_{SHG}^p(z, t)$]. Since the medium is dispersionless, the first-order polarization is simply:

$$\mathbf{P}^{p,(1)}(z, t) = \mathbf{P}_i^{p,(1)}(z, t) + \mathbf{P}_{OR}^{p,(1)}(z, t) + \mathbf{P}_{SHG}^{p,(1)}(z, t), \quad (2.96)$$

with,

$$\mathbf{P}_i^{p,(1)}(z, t) = \varepsilon_0 \chi^{(1)} \mathbf{E}^p(z, t), \quad (2.97)$$

$$\mathbf{P}_{OR}^{p,(1)}(z, t) = \varepsilon_0 \chi^{(1)} \mathbf{E}_{OR}^p(z, t), \quad (2.98)$$

$$\mathbf{P}_{SHG}^{p,(1)}(z, t) = \varepsilon_0 \chi^{(1)} \mathbf{E}_{SHG}^p(z, t), \quad (2.99)$$

where $\mathbf{P}_i^{p,(1)}(z, t)$ is the first-order polarization related to the incident electric field, $\mathbf{P}_{OR}^{p,(1)}(z, t)$ is the first-order polarization related to OR, and $\mathbf{P}_{SHG}^{p,(1)}(z, t)$ is the first-order polarization related to SHG. For this scenario, Eq. (2.23) reduces to,

$$\frac{\partial^2 \mathbf{E}^p(z, t)}{\partial z^2} - \frac{1}{c^2} \frac{\partial^2}{\partial t^2} \left[\mathbf{E}^p(z, t) + \frac{1}{\varepsilon_0} \mathbf{P}^{p,(1)}(z, t) \right] = \frac{1}{c^2 \varepsilon_0} \frac{\partial^2 \mathbf{P}^{p,(2)}(z, t)}{\partial t^2}. \quad (2.100)$$

Inserting Eqs. (2.92), (2.95), and (2.96) into Eq. (2.100) and simplifying yields three independent equations:

$$\frac{\partial^2 \mathbf{E}_i^p(z, t)}{\partial z^2} - \frac{n^2}{c^2} \frac{\partial^2 \mathbf{E}_i^p(z, t)}{\partial t^2} = 0, \quad (2.101)$$

$$\frac{\partial^2 \mathbf{E}_{OR}^p(z, t)}{\partial z^2} - \frac{n^2}{c^2} \frac{\partial^2 \mathbf{E}_{OR}^p(z, t)}{\partial t^2} = \frac{1}{c^2 \varepsilon_0} \frac{\partial^2 \mathbf{P}_{OR}^{p,(2)}(z, t)}{\partial t^2}, \quad (2.102)$$

$$\frac{\partial^2 \mathbf{E}_{SHG}^p(z, t)}{\partial z^2} - \frac{n^2}{c^2} \frac{\partial^2 \mathbf{E}_{SHG}^p(z, t)}{\partial t^2} = \frac{1}{c^2 \varepsilon_0} \frac{\partial^2 \mathbf{P}_{SHG}^{p,(2)}(z, t)}{\partial t^2}, \quad (2.103)$$

where we used the relationship $n = \sqrt{1 + \chi^{(1)}}$. Solving Eqs. (2.102) and (2.103) give:

$$\mathbf{E}_{OR}^p(z, t) = \frac{\chi^{(2)} A^2 z}{\sigma^2 c n} \left(t - \frac{zn}{c} \right) e^{-2(t-zn/c)^2/\sigma^2} \hat{\mathbf{x}}, \quad (2.104)$$

$$\mathbf{E}_{SHG}^p(z, t) = \frac{\chi^{(2)} A^2 \omega_c z}{2cn} e^{-2(t-zn/c)^2/\sigma^2} \sin[2\omega_c t - k(2\omega_c)z - 2\vartheta] \hat{\mathbf{x}}, \quad (2.105)$$

respectively, where the assumption of $\sigma^2 \omega_c \gg 2|t - zn/c|$ is utilized to obtain $\mathbf{E}_{SHG}^p(z, t)$. By restricting the analysis to times between $t = zn/c \pm 2\sigma$, the aforementioned assumption reduces to $\sigma \omega_c \gg 4$, which requires $\mathbf{E}_i^p(z, t)$ to exhibit several cycles within its envelope. As seen from Eq. (2.105), the envelope of $\mathbf{E}_{SHG}^p(z, t)$ at $t = zn/c \pm 2\sigma$ is given as $e^{-2(t-zn/c)^2/\sigma^2} = e^{-8}$, meaning $\mathbf{E}_{SHG}^p(z, t)$ is 0.03% of its maximum value at these times. Additionally, we assume no frequency components are initially present at the OR angular frequencies or the SHG angular frequencies, and the SVAA was not required when solving for $\mathbf{E}_{OR}^p(z, t)$ or $\mathbf{E}_{SHG}^p(z, t)$, since a dispersionless medium implies perfect phase-matching. To briefly summarize this section, Eqs. (2.104) and (2.105) describe the electric fields resulting from $\mathbf{E}_i^p(z, t)$ [see Eq. (2.88)] when considering first-order and second-order nonlinear effects in a 1D medium, but ignoring dispersion and loss in the medium, dispersion of the second-order nonlinear susceptibility, depletion of $\mathbf{E}_i^p(z, t)$, and cascading effects.

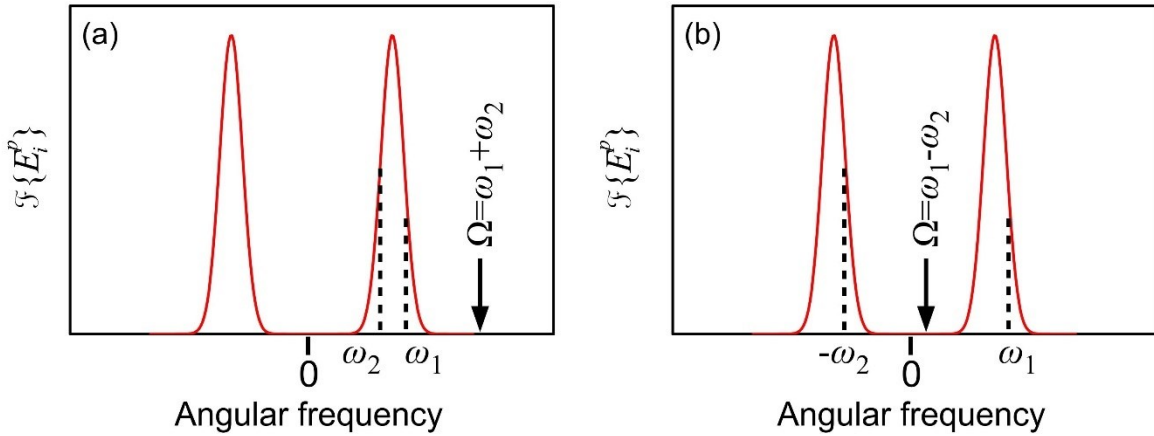


Fig. 2.8. Frequency-domain depiction of the (a) SHG and (b) OR processes.

2.3.2. A quantitative example

To illustrate the displacement of the bound electric charges due to $\mathbf{E}_i^p(z, t)$ and the resulting electric field, the equations derived in Section 2.3.1 are evaluated using specific parameter values. $\mathbf{E}_i^p(z, t)$ is described using $A=1$ kV/cm, $\omega_c/(2\pi)=600$ THz, $\vartheta=60^\circ$, and $\sigma=\sqrt{2/\ln(2)}\times 10$ fs. Figure 2.9(a) and 2.9(b) show the time and frequency domain representation of this $\mathbf{E}_i^p(z, t)$, respectively, where it is clear that the central frequency of the spectrum is located at $\omega_c/(2\pi)=600$ THz. As seen from Eqs. (2.35) and (2.48)-(2.53), for a lossless medium (i.e. $\gamma=0$), dispersionless $\chi^{(1)}$ and $\chi^{(2)}$ occur when $\omega_0 \gg \omega_1$, $\omega_0 \gg \omega_2$ and $\omega_0 \gg \Omega$, resulting in a medium described by,

$$\chi^{(1)} \approx \frac{Nq^2}{\epsilon_0 m_e \omega_0^2}, \quad (2.106)$$

and

$$\chi^{(2)} \approx \frac{\Xi Nq^3}{\epsilon_0 m_e^2 \omega_0^6}. \quad (2.107)$$

Although the parameter values of $N=10^{26}$ cm⁻³, $\omega_0/(2\pi)=60000$ THz, and $\Xi=1.6\times 10^{48}$ m⁻¹s⁻² are

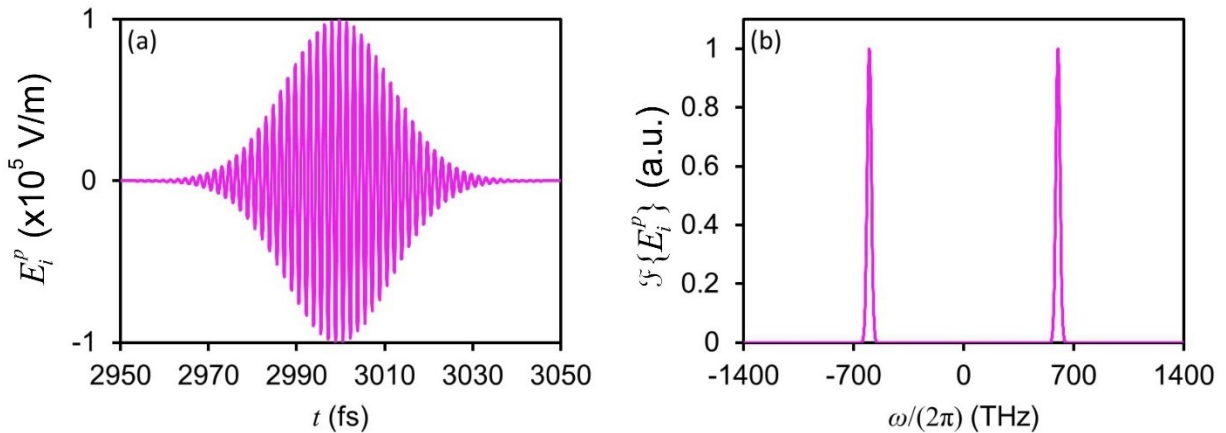


Fig. 2.9. (a) Time-domain and (b) frequency-domain representation of $\mathbf{E}_i^p(z, t)$.

unphysical, they are utilized as they provide the practical parameter values of $\chi^{(1)}=2.24$ (i.e. $n=1.8$) and $\chi^{(2)}=31.2$ pm/V.

The displacement of the bound electric charges is considered at a position of $z=500$ μm . The relationships $\mathbf{s}_{OR}^{p,(2)}(z, t) = -\mathbf{P}_{OR}^{p,(2)}(z, t)/(Nq)$, $\mathbf{s}_{SHG}^{p,(2)}(z, t) = -\mathbf{P}_{SHG}^{p,(2)}(z, t)/(Nq)$, and $\mathbf{s}^{p,(2)}(z, t) = -\mathbf{P}^{p,(2)}(z, t)/(Nq)$ are used to obtain the bound electric charges displacements, which are shown in Fig. 2.10(a). $\mathbf{s}_{OR}^{p,(2)}(z, t)$ simply exhibits the square of the envelope of $\mathbf{E}_i^p(z, t)$ [i.e. $e^{-2(t-zn/c)^2/\sigma^2}$]. Alternatively, $\mathbf{s}_{SHG}^{p,(2)}(z, t)$ exhibits oscillations at $2\omega_c$, which are contained

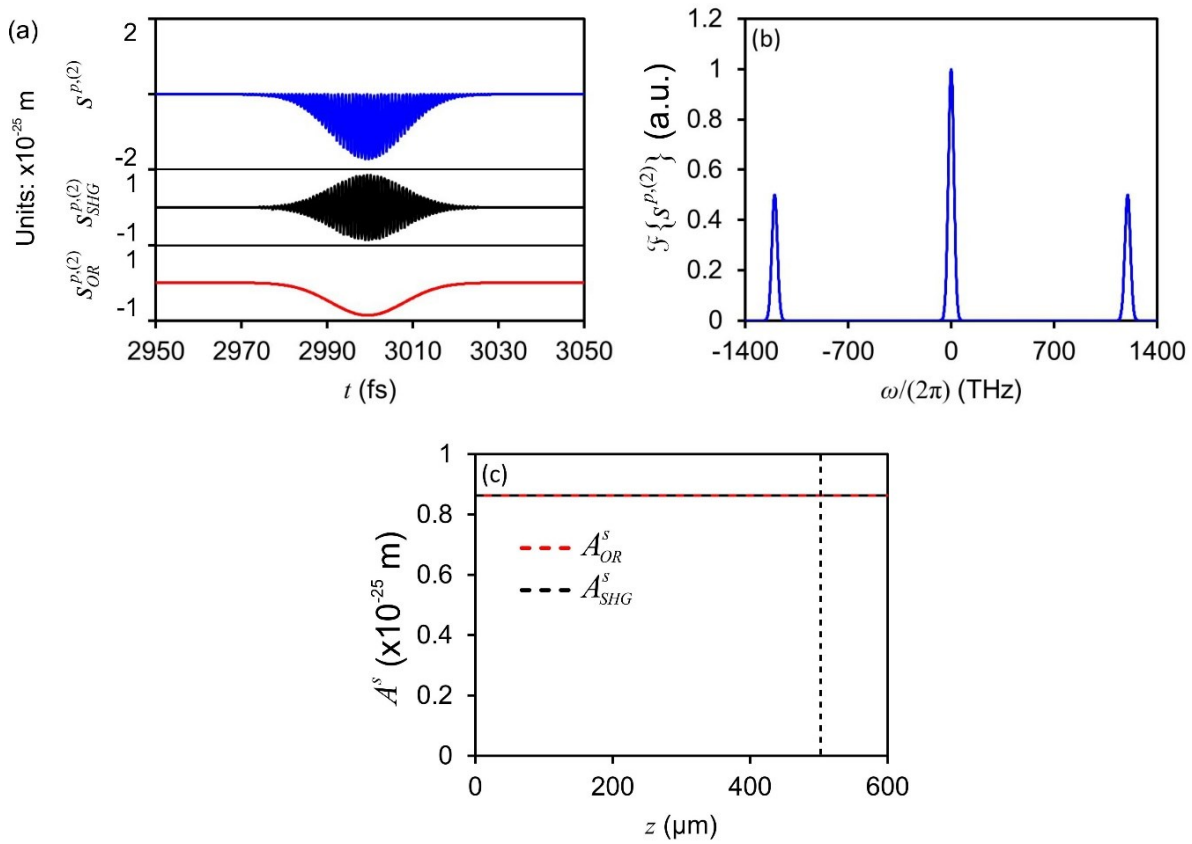


Fig. 2.10. (a) The bound electric charge displacement of $\mathbf{s}_{OR}^{p,(2)}(z, t)$, $\mathbf{s}_{SHG}^{p,(2)}(z, t)$, and $\mathbf{s}^{p,(2)}(z, t)$. (b) Fourier transform of $\mathbf{s}^{p,(2)}(z, t)$. (c) The maximum amplitudes of $\mathbf{s}_{OR}^{p,(2)}(z, t)$ and $\mathbf{s}_{SHG}^{p,(2)}(z, t)$, where the vertical dotted-line at $z=500$ μm corresponds to the recorded position of the time-domain bound electric charge displacements shown in (a).

within a Gaussian envelope described by $e^{-2(t-zn/c)^2/\sigma^2}$. $\mathbf{s}^{p,(2)}(z, t)$ is the superposition of these contributions, and exhibits a maximum displacement amplitude of 1.7×10^{-25} m. Figure 2.10(b) shows the Fourier transform of $\mathbf{s}^{p,(2)}(t)$, where frequencies are observed at $\omega/(2\pi) \lesssim 50$ THz and $\omega/(2\pi) \approx 1100$ -1300 THz. Figure 2.10(c) shows the maximum amplitudes of $\mathbf{s}_{OR}^{p,(2)}(z, t)$ and $\mathbf{s}_{SHG}^{p,(2)}(z, t)$ for a given position within the medium, which are denoted as $A_{OR}^s(z)$ and $A_{SHG}^s(z)$, respectively. The maximum bound charge displacement amplitudes are independent of z , since there is no absorption loss in the medium. If loss was considered, the maximum charge displacement amplitudes would decrease with increasing z .

The electric field resulting from displacement of the bound electric charges is considered at $z=500 \mu\text{m}$, where $\mathbf{E}_{OR}^p(z, t)$, $\mathbf{E}_{SHG}^p(z, t)$, and $\mathbf{E}_g^p(z, t)$ are shown in Fig. 2.11(a). Notably, $\sigma\omega_c=64$ (i.e. $\sigma\omega_c \gg 4$), such that Eq. (2.105) is valid in describing $\mathbf{E}_{SHG}^p(z, t)$. Similar to $\mathbf{s}_{SHG}^{p,(2)}(z, t)$, $\mathbf{E}_{SHG}^p(z, t)$ exhibits oscillations at $2\omega_c$, which are contained within a Gaussian envelope described by $e^{-2(t-zn/c)^2/\sigma^2}$. While $\mathbf{E}_{OR}^p(z, t)$ exhibits a bipolar electric field pulse that is also contained within a Gaussian envelope of $e^{-2(t-zn/c)^2/\sigma^2}$, it is difficult to distinguish the envelope shape. Electric field generation is highly correlated with acceleration and deceleration of the bound electric charges. For example, $\mathbf{E}_{OR}^p(z, t)=0$ [see Fig. 2.11(a)] when the bound electric charges change direction and exhibits an acceleration of zero, corresponding to maximum $\mathbf{s}_{OR}^{p,(2)}(z, t)$ [see Fig. 2.10(a)]. Furthermore, when the bound electric charges exhibit maximum acceleration or deceleration [i.e. at the inflection points of $\mathbf{s}_{OR}^{p,(2)}(z, t)$], the amplitude of $\mathbf{E}_{OR}^p(z, t)$ is maximum. The maximum amplitudes of $\mathbf{E}_{OR}^p(z, t)$ and $\mathbf{E}_{SHG}^p(z, t)$ for a given position within the medium are denoted as $A_{OR}(z)$ and $A_{SHG}(z)$, respectively. $A_{OR}(z)=5.2$ V/m and $A_{SHG}(z)=543$ V/m at

$z=500 \mu\text{m}$, such that $\mathbf{E}_g^p(z, t)$ is indistinguishable from $\mathbf{E}_{SHG}^p(z, t)$ [see Fig. 2.11(a)]. The conversion efficiencies for the OR and SHG processes are obtained from the relationships of,

$$\eta_{OR}(z) = \frac{\int_{-\infty}^{\infty} [\mathbf{E}_{OR}^p(z, t)]^2 dt}{\int_{-\infty}^{\infty} [\mathbf{E}_i^p(z, t)]^2 dt}, \quad (2.108)$$

and

$$\eta_{SHG}(z) = \frac{\int_{-\infty}^{\infty} [\mathbf{E}_{SHG}^p(z, t)]^2 dt}{\int_{-\infty}^{\infty} [\mathbf{E}_i^p(z, t)]^2 dt}, \quad (2.109)$$

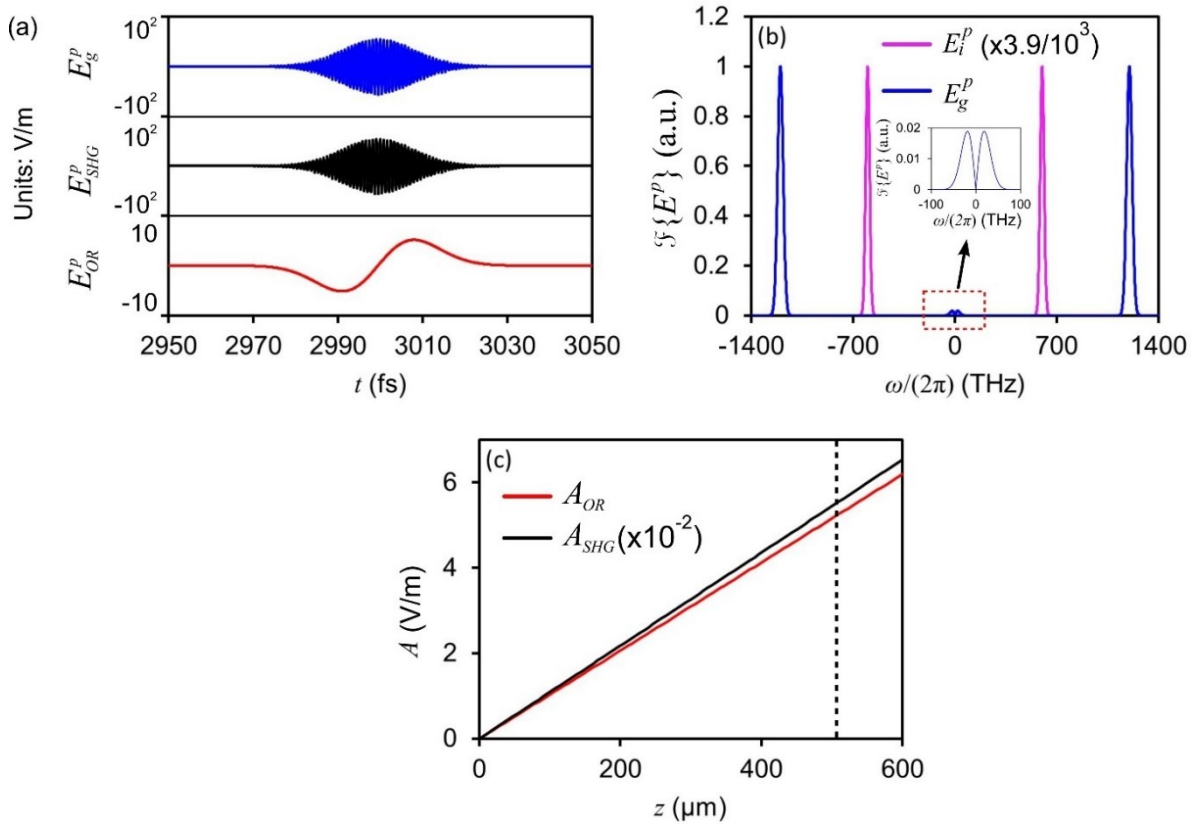


Fig. 2.11. (a) The electric field of $\mathbf{E}_{OR}^p(z, t)$, $\mathbf{E}_{SHG}^p(z, t)$, and $\mathbf{E}_g^p(z, t)$. (b) Fourier transform of $\mathbf{E}_g^p(z, t)$. The Fourier transform of $\mathbf{E}_i^p(z, t)$ is shown for comparison. (c) The maximum amplitudes of $\mathbf{E}_{OR}^p(z, t)$ and $\mathbf{E}_{SHG}^p(z, t)$ at various positions within the medium, where the vertical dotted-line at $z=500 \mu\text{m}$ corresponds to the recorded position of the time-domain electric fields shown in (a).

respectively, such that $\eta_{OR}=5.1\times 10^{-9}$ and $\eta_{SHG}=2.1\times 10^{-5}$ at $z=500\ \mu\text{m}$. This difference in A_{OR} and A_{SHG} , as well as η_{OR} and η_{SHG} , is due to the fact that a rapidly-oscillating bound electric charge is more efficient at producing EM radiation than a slowly-oscillating bound electric charge, as can be inferred from the $\partial^2 \mathbf{P}^{p,(2)}(z,t)/\partial t^2$ term in Eq. (2.100). The Fourier transform of $\mathbf{E}_g^p(z,t)$ is shown in Fig. 2.11(b), where no generation occurs at DC, as expected. Figure 2.11(c) shows $A_{OR}(z)$ and $A_{SHG}(z)$ for various positions within the medium. Since the medium is dispersionless, any newly-generated $\mathbf{E}_{OR}^p(z,t)$ [or $\mathbf{E}_{SHG}^p(z,t)$] components constructively interfere with previously-generated $\mathbf{E}_{OR}^p(z,t)$ [or $\mathbf{E}_{SHG}^p(z,t)$] components, resulting in an electric field that grows linearly with z .

Although a dispersive medium is not directly considered for $\mathbf{E}_i^p(z,t)$, it is nonetheless important to discuss this scenario. If phase-mismatching ensued in such a dispersive medium, $A_{OR}(z)$ and $A_{SHG}(z)$ would exhibit a quasi-periodic behavior, analogous to that observed in Fig. 2.6(c). Importantly, the coherence lengths of the OR process, L_c^{OR} , and the SHG process, L_c^{SHG} , are described by the expressions [140,141]:

$$L_c^{OR}(\Omega_{OR}) = \frac{\pi c}{\Omega_{OR} |n_d^g(\omega_c) - n_d(\Omega_{OR})|}, \quad (2.110)$$

$$L_c^{SHG}(\Omega_{SHG}) = \frac{\pi c}{|\omega_1 n_d(\omega_1) + \omega_2 n_d(\omega_2) - \Omega_{SHG} n_d(\Omega_{SHG})|}, \quad (2.111)$$

respectively, where n_d is the refractive index of the dispersive medium, n_d^g is the group refractive index of the dispersive medium, Ω_{OR} represents the angular frequency components produced through the OR process, and Ω_{SHG} represents the angular frequency components produced through the SHG process. To better understand L_c^{OR} , we refer to $\mathbf{s}_{OR}^{p,(2)}(z,t)$ [i.e. see Fig. 2.10(a)], despite it representing the dispersionless scenario. $\mathbf{s}_{OR}^{p,(2)}(z,t)$ exhibits a displacement in accordance with

the envelope of $\mathbf{E}_i^p(z, t)$, independent of the events occur within the envelope, such that L_c^{OR} depends on the group refractive index of the envelope, opposed to the phase refractive index of the wave within the envelope. In general, L_c^{SHG} must be calculated for all of the various SFG events associated with the spectral components of $\mathbf{E}_i^p(z, t)$, such that L_c^{SHG} exhibits the same form as $L_c^{\omega_1+\omega_2}$ [see Eq. (2.78)]. However, implementing $\omega_1 = \omega_2 \approx \Omega_{SHG}/2$ permits the L_c^{SHG} to be approximated as,

$$L_c^{SHG}(\Omega_{SHG}) \approx \frac{\pi c}{\Omega_{SHG} |n_d(\Omega_{SHG}/2) - n_d(\Omega_{SHG})|}, \quad (2.112)$$

which exhibits a form similar to $L_{2\omega_1}^{coh}$ [see Eq. (2.76)] and $L_{2\omega_2}^{coh}$ [see Eq. (2.77)].

2.3.3. Tensor representation of second-order nonlinear polarization

Sections 2.3.1 and 2.3.2 consider an isotropic medium that is both dispersionless and lossless, such that each second-order nonlinear process was described by a single $\chi^{(2)}$ value. For a dispersive, lossy, and anisotropic medium, the second-order nonlinear polarizations [i.e. Eqs. (2.93)-(2.94)] become more cumbersome. The frequency-domain expression representing each of the second-order nonlinear processes is,

$$\begin{aligned}
\tilde{P}_\psi^{(2)}(\Omega) = & \varepsilon_0 \int_{-\infty}^{\infty} \tilde{\chi}_{\psi xx}^{(2)}(\Omega: \omega_1, \Omega - \omega_1) \tilde{E}_x(\omega_1) \tilde{E}_x(\Omega - \omega_1) d\omega_1 \\
& + \varepsilon_0 \int_{-\infty}^{\infty} \tilde{\chi}_{\psi yy}^{(2)}(\Omega: \omega_1, \Omega - \omega_1) \tilde{E}_y(\omega_1) \tilde{E}_y(\Omega - \omega_1) d\omega_1 \\
& + \varepsilon_0 \int_{-\infty}^{\infty} \tilde{\chi}_{\psi zz}^{(2)}(\Omega: \omega_1, \Omega - \omega_1) \tilde{E}_z(\omega_1) \tilde{E}_z(\Omega - \omega_1) d\omega_1 \\
& + 2\varepsilon_0 \int_{-\infty}^{\infty} \tilde{\chi}_{\psi yz}^{(2)}(\Omega: \omega_1, \Omega - \omega_1) \tilde{E}_y(\omega_1) \tilde{E}_z(\Omega - \omega_1) d\omega_1 \\
& + 2\varepsilon_0 \int_{-\infty}^{\infty} \tilde{\chi}_{\psi xz}^{(2)}(\Omega: \omega_1, \Omega - \omega_1) \tilde{E}_x(\omega_1) \tilde{E}_z(\Omega - \omega_1) d\omega_1 \\
& + 2\varepsilon_0 \int_{-\infty}^{\infty} \tilde{\chi}_{\psi xy}^{(2)}(\Omega: \omega_1, \Omega - \omega_1) \tilde{E}_x(\omega_1) \tilde{E}_y(\Omega - \omega_1) d\omega_1 .
\end{aligned} \tag{2.113}$$

However, the second-order nonlinear susceptibilities are often considered to be independent of the angular frequencies present in the incident electric field [i.e. $\tilde{\chi}_{\psi \rho\sigma}^{(2)}(\Omega: \omega_1, \Omega - \omega_1) = \tilde{\chi}_{\psi \rho\sigma}^{(2)}(\Omega)$], such that Eq. (2.113) simplifies to,

$$\begin{bmatrix} \tilde{P}_x^{(2)}(\Omega) \\ \tilde{P}_y^{(2)}(\Omega) \\ \tilde{P}_z^{(2)}(\Omega) \end{bmatrix} = \varepsilon_0 \begin{bmatrix} \tilde{\chi}_{xxx}^{(2)}(\Omega) & \tilde{\chi}_{xyy}^{(2)}(\Omega) & \tilde{\chi}_{xzz}^{(2)}(\Omega) & \tilde{\chi}_{xyz}^{(2)}(\Omega) & \tilde{\chi}_{xxz}^{(2)}(\Omega) & \tilde{\chi}_{xxy}^{(2)}(\Omega) \\ \tilde{\chi}_{yxx}^{(2)}(\Omega) & \tilde{\chi}_{yyy}^{(2)}(\Omega) & \tilde{\chi}_{yzz}^{(2)}(\Omega) & \tilde{\chi}_{yyz}^{(2)}(\Omega) & \tilde{\chi}_{yxz}^{(2)}(\Omega) & \tilde{\chi}_{yyx}^{(2)}(\Omega) \\ \tilde{\chi}_{zxx}^{(2)}(\Omega) & \tilde{\chi}_{zyy}^{(2)}(\Omega) & \tilde{\chi}_{zzz}^{(2)}(\Omega) & \tilde{\chi}_{zyz}^{(2)}(\Omega) & \tilde{\chi}_{zxx}^{(2)}(\Omega) & \tilde{\chi}_{zxy}^{(2)}(\Omega) \end{bmatrix}$$

$$\times \begin{bmatrix} \int_{-\infty}^{\infty} \tilde{E}_x(\omega_1) \tilde{E}_x(\Omega - \omega_1) d\omega_1 \\ \int_{-\infty}^{\infty} \tilde{E}_y(\omega_1) \tilde{E}_y(\Omega - \omega_1) d\omega_1 \\ \int_{-\infty}^{\infty} \tilde{E}_z(\omega_1) \tilde{E}_z(\Omega - \omega_1) d\omega_1 \\ 2 \int_{-\infty}^{\infty} \tilde{E}_y(\omega_1) \tilde{E}_z(\Omega - \omega_1) d\omega_1 \\ 2 \int_{-\infty}^{\infty} \tilde{E}_x(\omega_1) \tilde{E}_z(\Omega - \omega_1) d\omega_1 \\ 2 \int_{-\infty}^{\infty} \tilde{E}_x(\omega_1) \tilde{E}_y(\Omega - \omega_1) d\omega_1 \end{bmatrix}. \quad (2.114)$$

In contracted notation, Eq. (2.114) becomes,

$$\begin{bmatrix} \tilde{P}_x^{(2)}(\Omega) \\ \tilde{P}_y^{(2)}(\Omega) \\ \tilde{P}_z^{(2)}(\Omega) \end{bmatrix} = \varepsilon_0 \begin{bmatrix} \tilde{\chi}_{11}^{(2)}(\Omega) & \tilde{\chi}_{12}^{(2)}(\Omega) & \tilde{\chi}_{13}^{(2)}(\Omega) & \tilde{\chi}_{14}^{(2)}(\Omega) & \tilde{\chi}_{15}^{(2)}(\Omega) & \tilde{\chi}_{16}^{(2)}(\Omega) \\ \tilde{\chi}_{21}^{(2)}(\Omega) & \tilde{\chi}_{22}^{(2)}(\Omega) & \tilde{\chi}_{23}^{(2)}(\Omega) & \tilde{\chi}_{24}^{(2)}(\Omega) & \tilde{\chi}_{25}^{(2)}(\Omega) & \tilde{\chi}_{26}^{(2)}(\Omega) \\ \tilde{\chi}_{31}^{(2)}(\Omega) & \tilde{\chi}_{32}^{(2)}(\Omega) & \tilde{\chi}_{33}^{(2)}(\Omega) & \tilde{\chi}_{34}^{(2)}(\Omega) & \tilde{\chi}_{35}^{(2)}(\Omega) & \tilde{\chi}_{36}^{(2)}(\Omega) \end{bmatrix}$$

$$\times \begin{bmatrix} \int_{-\infty}^{\infty} \tilde{E}_x(\omega_1) \tilde{E}_x(\Omega - \omega_1) d\omega_1 \\ \int_{-\infty}^{\infty} \tilde{E}_y(\omega_1) \tilde{E}_y(\Omega - \omega_1) d\omega_1 \\ \int_{-\infty}^{\infty} \tilde{E}_z(\omega_1) \tilde{E}_z(\Omega - \omega_1) d\omega_1 \\ 2 \int_{-\infty}^{\infty} \tilde{E}_y(\omega_1) \tilde{E}_z(\Omega - \omega_1) d\omega_1 \\ 2 \int_{-\infty}^{\infty} \tilde{E}_x(\omega_1) \tilde{E}_z(\Omega - \omega_1) d\omega_1 \\ 2 \int_{-\infty}^{\infty} \tilde{E}_x(\omega_1) \tilde{E}_y(\Omega - \omega_1) d\omega_1 \end{bmatrix}. \quad (2.115)$$

Expressed in terms of the second-order nonlinear coefficients, Eq. (2.115) is,

$$\begin{bmatrix} \tilde{P}_x^{(2)}(\Omega) \\ \tilde{P}_y^{(2)}(\Omega) \\ \tilde{P}_z^{(2)}(\Omega) \end{bmatrix} = 2\varepsilon_0 \begin{bmatrix} \tilde{d}_{11}(\Omega) & \tilde{d}_{12}(\Omega) & \tilde{d}_{13}(\Omega) & \tilde{d}_{14}(\Omega) & \tilde{d}_{15}(\Omega) & \tilde{d}_{16}(\Omega) \\ \tilde{d}_{21}(\Omega) & \tilde{d}_{22}(\Omega) & \tilde{d}_{23}(\Omega) & \tilde{d}_{24}(\Omega) & \tilde{d}_{25}(\Omega) & \tilde{d}_{26}(\Omega) \\ \tilde{d}_{31}(\Omega) & \tilde{d}_{32}(\Omega) & \tilde{d}_{33}(\Omega) & \tilde{d}_{34}(\Omega) & \tilde{d}_{35}(\Omega) & \tilde{d}_{36}(\Omega) \end{bmatrix}$$

$$\times \begin{bmatrix} \int_{-\infty}^{\infty} \tilde{E}_x(\omega_1) \tilde{E}_x(\Omega - \omega_1) d\omega_1 \\ \int_{-\infty}^{\infty} \tilde{E}_y(\omega_1) \tilde{E}_y(\Omega - \omega_1) d\omega_1 \\ \int_{-\infty}^{\infty} \tilde{E}_z(\omega_1) \tilde{E}_z(\Omega - \omega_1) d\omega_1 \\ 2 \int_{-\infty}^{\infty} \tilde{E}_y(\omega_1) \tilde{E}_z(\Omega - \omega_1) d\omega_1 \\ 2 \int_{-\infty}^{\infty} \tilde{E}_x(\omega_1) \tilde{E}_z(\Omega - \omega_1) d\omega_1 \\ 2 \int_{-\infty}^{\infty} \tilde{E}_x(\omega_1) \tilde{E}_y(\Omega - \omega_1) d\omega_1 \end{bmatrix}. \tag{2.116}$$

2.4. Summary

While second-order nonlinear interactions have been known for over 50 years, this chapters presented a more comprehensive picture of these phenomena, citing and explaining the differences between monochromatic and broadband incident electric fields. The detailed investigations presented in this chapter extended beyond other nonlinear optics discussions, accomplished by addressing the relationship between the incident electric field, the induced displacement of the bound electric charge in the medium, and the electric field resulting from the induced dipoles. We have provided a detailed mathematical approach, as well as an intuitive interpretation of the derived equations, which is crucial to understanding the physics driving the second-order nonlinear processes. The anharmonic EOM and Maxwell's Equations were derived for second-order nonlinear interactions, and subsequently used to investigate key representative scenarios (i.e. an

incident electric field composed of two monochromatic waves and an incident transform-limited Gaussian electric field pulse). Notably, while this section explicitly distinguished complex variable through the use of the ‘ \sim ’ accent (e.g. $\tilde{\chi}$, \tilde{d} , \tilde{E} , \tilde{P} , etc.), the ‘ \sim ’ accent is typically omitted in discussions pertaining to second-order nonlinear effects. Additionally, when discussing OR in a general context, it is typical to refer to the polarization matrices in Eq. (2.86) or (2.87), despite the fact that the polarization matrices in Eq. (2.115) or (2.116) provides a more complete picture of the OR process.

Chapter 3.

THz-TDS system

THz-TDS is a method of measuring the time-domain electric field of a THz radiation pulse, thereby providing both frequency-domain magnitude and phase information. While this section discusses the general THz-TDS system used to conduct the measurements presented in the forthcoming chapters, variations are frequently made to the THz radiation source, THz radiation detector, and the excitation laser. Figure 3.1(a) depicts a schematic of the primary THz-TDS system used to conduct the measurements, and Fig. 3.2(b) shows a photograph of this THz-TDS system. The main Ti:Sapphire oscillator used for the system provides a train of electric field pulses at a repetition rate of 5.1 MHz, where each pulse is horizontally-polarized (i.e. parallel to the surface of the optical table), exhibits a central wavelength near 800 nm, and has a duration of 50 fs. The pulse train beam passes through a 70:30 beam splitter, resulting in two independent beams having different powers. The higher-power pulse train beam (i.e. denoted as the pump or excitation beam) is used to generate THz radiation and the lower-power pulse train beam (i.e. denoted as the probe beam) is used to detect the THz radiation. To achieve THz radiation generation, the pump beam is focused onto a THz source, which can be a nonlinear crystal, a PCA, or a spintronic emitter, to name a few. In the current THz-TDS system, a (110)-cut ZnTe crystal having a thickness of 500 μm is frequently used to produce the THz electric field pulses. Typically, a 10 cm focal-length lens (L1) focuses the pump laser beam onto the ZnTe crystal, providing a beam waist diameter of $\sim 38 \mu\text{m}$ and a peak excitation intensity of $\sim 1 \text{ GW}/\text{cm}^2$. Second-order nonlinear dipoles are induced in the ZnTe crystal, subsequently emitting EM radiation at frequencies between $\sim 0.1-$

3 THz via OR. Since the pump pulse beam is modulated by a mechanical chopping wheel at the reference frequency of f_R (see Fig. 3.1), the generated THz radiation beam is also modulated at this same f_R . Due to the spot size of the pump laser beam being much smaller than the wavelength of the generated THz radiation, the nonlinear dipoles appear as point source THz emitters, resulting in diverging THz radiation that is collimated by PM1 (i.e. a 50.8 mm focal-length off-axis parabolic mirror). Subsequently, a set of 101.6 mm focal-length parabolic mirrors (PM2 and PM3) are used to focus and re-collimate the THz radiation, where samples are often placed at the focus of PM2. PM4 (50.8 mm focal-length) focusses the THz radiation onto a crystal [typically 500 μm -thick (110)-cut ZnTe] that acts as an EO detector for the THz electric field. Notably, the THz radiation exhibits a beam waist diameter of a few hundreds of microns. The ZnTe EO crystal is key to sensing the THz time-domain electric field; however, it is also necessary to have the THz electric field pulse simultaneously (i.e. temporally and spatially) coincide with the probe pulse within the EO crystal. To realize spatial overlap between the THz radiation beam and the probe beam, a 2 mm hole is formed through PM4. Since the THz radiation beam fills the reflective face of the parabolic mirror, the hole has minimal impact on the radiation. A 15 cm focal-length lens (L2) is typically used to focus the probe beam through the hole in PM4 and onto the same position of the EO crystal as the focused THz radiation. The focused probe beam has a beam waist diameter of $\sim 57 \mu\text{m}$. Temporal overlap is achieved by ensuring the pump pulse/THz radiation path length is identical to the path length traversed by the probe pulse. Coarse adjustment is made to the temporal overlap by the placement of the various optical components, while fine adjustments are made by a stepper motor controlled retroreflector.

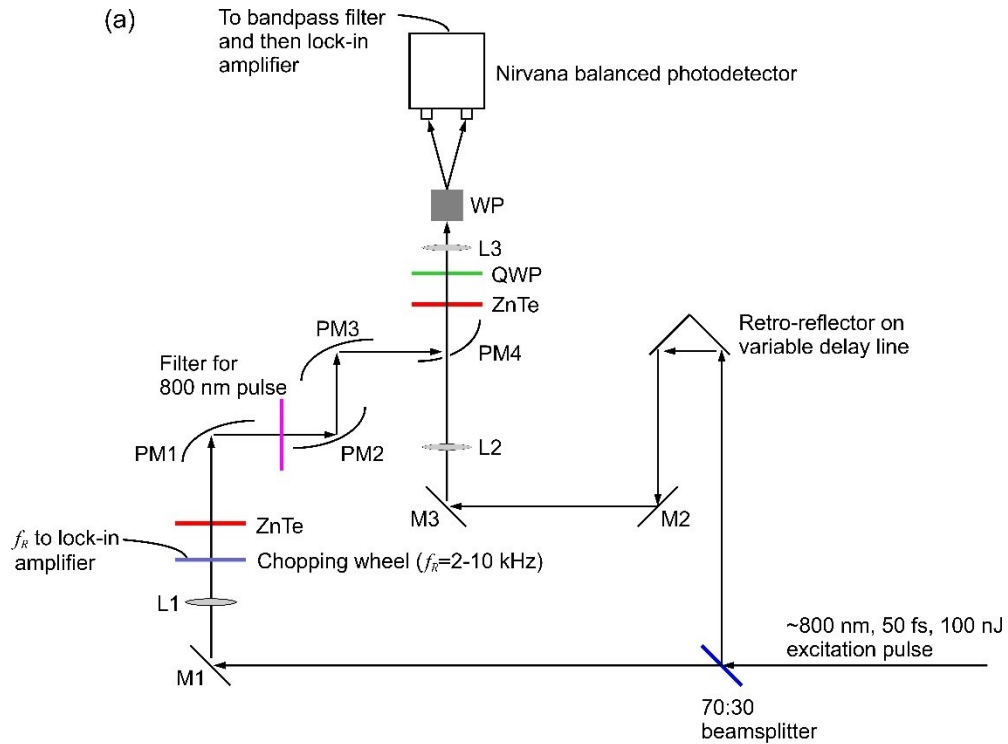


Fig. 3.1. (a) Schematic of the THz-TDS system typically used to conduct experimental measurements. ‘M’ indicates planar mirrors, ‘PM’ indicates parabolic mirrors, and ‘L’ indicates lenses. (b) Photograph of the THz-TDS system.

As the probe pulse propagates through the ZnTe EO crystal, it experiences a phase-retardation induced by the THz electric field, which is expressed as [142],

$$\Gamma = \frac{2\pi n_p^3 r_{41} \ell E_{THz}}{\lambda_p}, \quad (3.1)$$

where λ_p is the central wavelength of the probe pulse, n_p is the refractive index of the EO crystal at λ_p , r_{41} is the EO coefficient of the EO crystal, ℓ is the thickness of the EO crystal, and E_{THz} is the value of the THz electric field. To extract Γ , and subsequently E_{THz} , from the laser beam probe pulse, we utilize a QWP, WP, and Nirvana 2017 balanced photodetector set up for common-mode rejection. Here, the photocurrent difference measured by the balanced photodetector is described as [142],

$$\frac{\Delta I}{I_1 + I_2} = \sin(\Gamma) \approx \frac{2\pi n_p^3 r_{41} \ell E_{THz}}{\lambda_p}, \quad (3.2)$$

where ΔI is the current difference measured between the photodiodes of the balanced photodetector, I_1 is the current measured by one of the photodiodes of the balanced photodetector, and I_2 is the current measured by the other photodiode of the balanced photodetector. In the absence of a THz electric field (i.e. $E_{THz}=0$), the horizontally-polarized probe beam is converted to circularly-polarized light by the QWP. Since the horizontal and vertical polarization components are equal in amplitude, the WP splits the laser probe beam into two orthogonally polarized beams of equal power, thereby inducing no current difference in the balanced photodetector (i.e. $\Delta I=0$, since the photodetector is balanced). In the presence of a positive THz electric field (i.e. $E_{THz}>0$), the horizontally-polarized probe beam experiences a positive phase retardation (i.e. $\Gamma>0$) resulting in a right-handed elliptically-polarized probe laser beam emerging from the EO crystal. After passing through the QWP, the probe beam exhibits a right-handed ellipticity wherein the vertical polarization component is greater than the horizontal polarization component. As such, passing this beam through the WP results in two beams of different average powers, thereby inducing a

positive current difference in the balanced photodetector (i.e. $\Delta I > 0$). Similarly, for a negative THz electric field (i.e. $E_{THz} < 0$), the horizontally-polarized probe laser beam experiences a negative phase retardation (i.e. $\Gamma < 0$), resulting in a left-handed elliptically-polarized probe beam emerging from the EO crystal. After passing through the QWP, the probe pulse exhibits a right-handed ellipticity wherein the horizontal polarization component is greater than the vertical polarization component. Therefore, passing this beam through the WP results in two beams of different average powers, thereby inducing a negative current difference in the balanced photodetector (i.e. $\Delta I < 0$).

While the pump pulse/THz radiation path length is fixed, the stepper motor is used to adjust the path length traversed by the probe beam, thus permitting discrete points of the THz electric field pulse to be sampled. Typically, the THz electric field pulse is recorded every 42 fs, such that the probe path length is altered by 12.6 μm each step. Discrete data measurements are collected to obtain ΔI across the entire duration of the THz electric field pulse, thus allowing the THz signal to be reconstructed point-by-point. Notably, each measurement processes a train of probe pulses having a repetition rate of 5.1 MHz, modulated at the chopping frequency of f_R . However, due to the long rise time of the balanced photodetector (i.e. 3 μs for the Nirvana 2007 balanced photodetector), the resulting ΔI is a square wave of frequency f_R . The balanced photodetector converts ΔI to a voltage signal, which is then sent to a Stanford SR560 preamplifier and processed using a bandpass filter having cut-off frequencies of 1 and 30 kHz. The filtered voltage signal (along with f_R from the mechanical chopper) is then sent to a Stanford SR830 lock-in amplifier. The lock-in amplifier transforms the filtered square wave voltage signal at f_R to DC, and passes it through a low-pass filter having a time constant of \mathcal{T} [corresponding to a cut-off frequency of $f_c = (2\pi\mathcal{T})^{-1}$]. Given a low-pass filter with a sharp roll-off, this process effectively removes the noise outside of f_c , permitting the extraction of signals submerged in high-noise backgrounds. While a

low-pass filter having a long time constant (i.e. low cut-off frequency) and a sharp roll-off permits more noise to be removed, this requires long processing times. We empirically determine that time constants of 100-300 ms and roll-offs of 6-12 dB provide a good compromise between noise reduction and time utilization efficiency. Using a time constant of 100 ms and a roll off-of 6 dB dictates that the lock-in amplifier requires 500 ms to reach 99% of the final signal value. As a typical THz electric field signal recording extends ~10 ps and the detection process is performed at discrete points separated by $\Delta t=42$ fs, this corresponds to 238 recorded points for a total time of ~2 minutes. Notably, this is the time required by the lock-in amplifier to properly process the input signal, and does not include other factors that increase the overall measurement time (e.g. the time required by the stepper motor to physically move the retroreflector or reading the lock-in amplifier's output to the computer). The voltage signal output by the lock-in amplifier is described by the equation,

$$\Delta V(\rho\Delta t) = \frac{2\pi n_p^3 r_{41} \ell E_{THz}(\rho\Delta t) 2\mathbb{I} \mathcal{G}_t \mathcal{G}_A 0.64}{\sqrt{2}\lambda_p}, \quad (3.3)$$

where ρ is a non-negative integer ($=0, 1, 2, \dots$), $\mathbb{I}_1 \approx \mathbb{I}_2 = \mathbb{I}$, \mathcal{G}_t is the transimpedance gain of the balanced photodetector, and \mathcal{G}_A is the gain of the preamplifier. The factor of 0.64 arises from the lock-in amplifier extracting the first harmonic of the square wave, while the factor of $1/\sqrt{2}$ arises from the lock-in amplifier outputting the root-mean-square voltage. Clearly, the peak ΔV (i.e. ΔV^p) is recorded when E_{THz} is at its peak (i.e. E_{THz}^p). Figure 3.2(a) shows a typical voltage signal measured using the THz-TDS system and output by the lock-in amplifier ($\mathcal{T}=300$ ms, a 6 dB roll-off, $\mathbb{I}=500$ μA , $\mathcal{G}_t=10^5$, and $\mathcal{G}_A=1$). Equation (3.3) permits this voltage signal to be expressed in terms of the electric field, as displayed in Fig. 3.2(a). At a time of $t=4$ ps, $\Delta V^p=25$ mV, corresponding to $E_{THz}^p=1585$ V/m. The spectral density (i.e. Fourier transform) of the THz time-

domain signal is depicted in Fig. 3.2(b), showing the presence of frequency components $\lesssim 3$ THz. Notably, when conducting the measurements, the THz-TDS system is purged with dry nitrogen gas to minimize absorption of the THz radiation by water vapor.

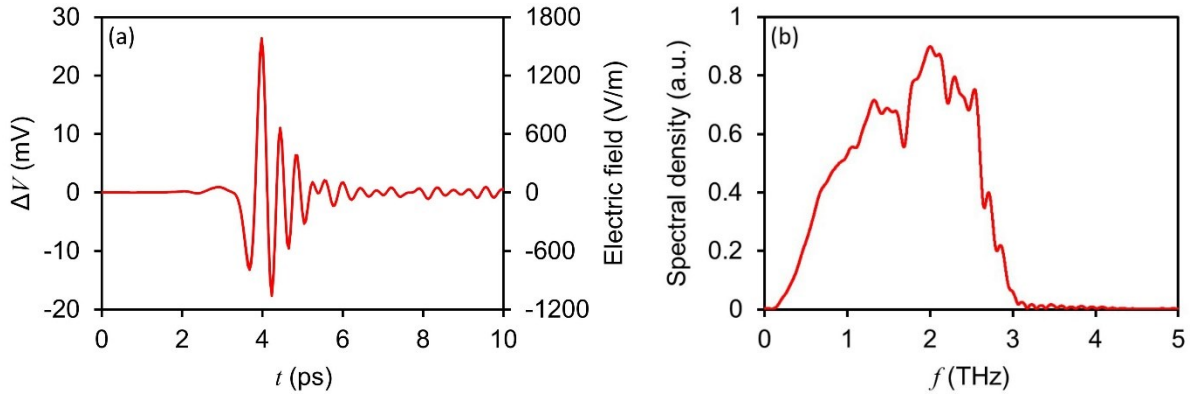


Fig. 3.2. (a) Raw voltage signal obtained using the THz-TDS system and its corresponding electric field magnitude. (b) The associated spectral density (i.e. Fourier transform).

Chapter 4.

THz radiation generation and detection using pnictide and chalcogenide ternary crystals

The emergence of THz radiation sources and detectors has opened up a wealth of real-world applications, spanning the fields of physics, chemistry, biology, medicine, non-destructive testing, material characterization, security, short range point-to-point wireless communication, and inter-satellite communication links, to name a few [5,6, 15, 18,143–145]. OR and DFG conversion efficiencies strongly depend on the material's second-order nonlinear coefficient magnitude, linear optical absorption, threshold for multi-photon absorption, THz radiation absorption, optical and THz dispersion, and optical-to-THz phase-matching conditions. Likewise, these same properties influence the linear EO effect (i.e. Pockel's effect), which is the counterpart of OR and is commonly used for the detection of ultrashort THz radiation pulses. As the aforementioned properties are mainly influenced by the nonlinear crystal itself, exploring and identifying novel classes of nonlinear crystals will open the door to a new frontier of THz radiation applications. In Section 1.4, we argued that both pnictide and chalcogenide ternary crystals constitute emerging classes of nonlinear crystals with the potential to advance THz radiation sources and detectors. In this chapter, we investigate THz radiation generation using a pnictide crystal (i.e. CSP) and chalcogenide crystals (i.e. AGS and BGS), as well as THz radiation detection using a pnictide crystal (i.e. ZGP).

4.1. Generation of broadband THz radiation pulses in a CSP Crystal³

As seen from Table 1.1, CSP exhibits a wide bandgap of 2.45 eV [37], a high second-order nonlinear coefficient (i.e. $d_{36}=84.5$ pm/V at an excitation wavelength of 4.6 μm [35]), and a wide transparency range of 0.52-9.5 μm [35]. While such properties suggest CSP has the potential to be an excellent source of THz radiation, generation in the THz frequency regime is influenced by other factors (e.g. phase-matching). In this section, OR from a CSP crystal is experimentally investigated for the generation of THz radiation, which allows the OR phase-matching condition to be quantified. Of all pnictide crystals, ZGP has overwhelmingly received the majority of interest for nonlinear frequency-conversion (see Section 1.4). As such, OR THz radiation generation from the CSP crystal is compared to that from a ZGP crystal.

4.1.1. Excitation arrangement

For the excitation arrangement depicted in Fig. 4.1, the second-order nonlinear polarization matrix defining the CSP crystal is given as [43],

$$\begin{bmatrix} P_x^{(2)} \\ P_y^{(2)} \\ P_z^{(2)} \end{bmatrix} = 2\epsilon_0 \begin{bmatrix} 0 & 0 & 0 & d_{14} & 0 & 0 \\ 0 & 0 & 0 & 0 & d_{14} & 0 \\ 0 & 0 & 0 & 0 & 0 & d_{36} \end{bmatrix} \begin{bmatrix} E_x^2 \\ E_y^2 \\ E_z^2 \\ 2E_xE_z \\ 2E_yE_z \\ 2E_xE_y \end{bmatrix}, \quad (4.1)$$

³A version of this section's work is published as B. N. Carnio, P. G. Schunemann, K. T. Zawilski, and A. Y. Elezzabi, "Generation of broadband terahertz pulses via optical rectification in a chalcopyrite CdSiP₂ crystal," *Opt. Lett.* **42**, 3920-3923 (2017).

where d_{14} and d_{36} are non-vanishing second-order nonlinear coefficients, $E_{x,y,z}$ represent the excitation electric fields polarized along the x , y , and z axes, respectively, and $P_{x,y,z}^{(2)}$ represent the second-order nonlinear polarizations oriented along the x , y , and z axes, respectively. A 780 nm, 50 fs laser excitation pulse, having a polarization oriented perpendicular to the crystal's c -axis (i.e. its [001] crystallographic axis), is directed towards the (110)-cut CSP crystal at normal incidence. In this arrangement, the nonlinear polarization equation [see Eq. (4.1)] reduces to $P_z^{(2)} = 4\epsilon_0 d_{36} E_x E_y$, where the optical electric field polarization is split equally along the x and y axes and THz radiation generation occurs along the c -axis (i.e. z axis) of the crystal. The CSP crystal employed in the experiments is grown using the HGF method described in Ref. [146] and a 980 μm -thick crystal is cut from the high-quality boule along the (110) plane. Importantly, the growth technique has been shown to influence the THz radiation properties (see section 1.4.2). The linear THz radiation properties and the nonlinear frequency-conversion properties of the CSP

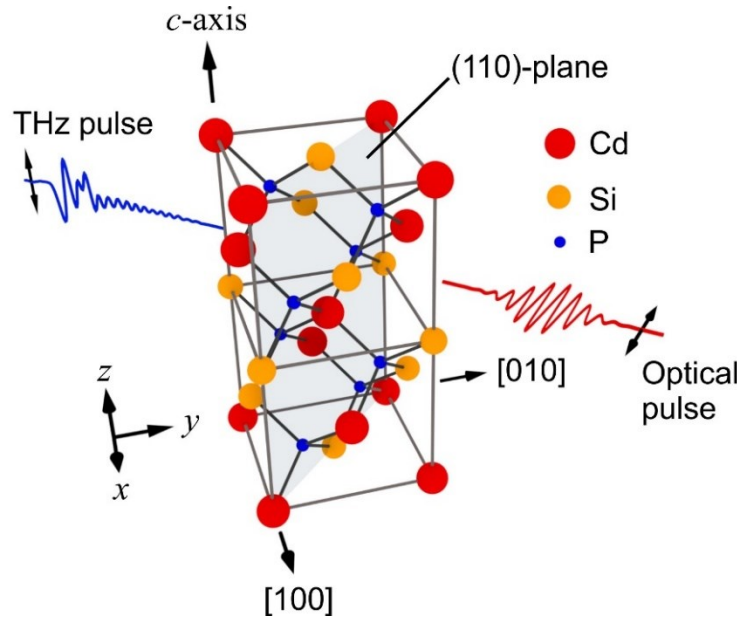


Fig. 4.1. Unit cell structure of the CSP crystal. The optical excitation pulse and the generated THz radiation are polarized perpendicular and parallel to the crystal's c -axis, respectively.

crystal will be compared against an established crystal. Specifically, a (110)-cut, 990 μm -thick ZGP crystal is employed in the experiments, also grown using the HGF method [146].

4.1.2. Linear THz radiation properties

The linear THz radiation properties (i.e. the refractive index, n , and extinction coefficient, κ) of a crystal influence OR THz radiation generation via phase-matching. The complex refractive index, $\tilde{n} = n + i\kappa$, of a bulk crystal can be determined by measuring THz radiation transmission through the sample and using the following Fresnel equation,

$$\frac{\tilde{E}_{sample}}{\tilde{E}_{ref}} = \frac{4\tilde{n}}{(1 + \tilde{n})^2} e^{ik_0(\tilde{n}-1)\ell}, \quad (4.2)$$

where \tilde{E}_{sample} represents the experimentally measured THz electric field pulse transmitted through the sample, \tilde{E}_{ref} represents the reference THz electric field pulse transmitted through free-space, k_0 is the free-space wavevector, and ℓ is the thickness of the sample. \tilde{E}_{sample} polarized along the c -axis of the CSP crystal and \tilde{E}_{ref} are obtained using the THz-TDS system (see Chapter 3) incorporating a 500 μm -thick ZnTe OR crystal and a 500 μm -thick ZnTe EO crystal. Using Eq. (4.2), along with the measured \tilde{E}_{sample} and \tilde{E}_{ref} , the complex extraordinary refractive index of the CSP crystal is determined in the frequency range of 0.6-2.9 THz. As shown in Fig. 4.2(a), the extraordinary CSP refractive index, n_e , has values between 3.34-3.48 and exhibits positive dispersion ($|dn_e/df| \lesssim 0.3 \text{ THz}^{-1}$) within the investigated frequency range (i.e. 0.6-2.9 THz). This dispersion is a result of THz radiation polarized along the c -axis of the CSP crystal coupling to the crystal's B_2 phonon modes. Figure 4.2(b) presents the extraordinary CSP extinction coefficient, κ_e , which shows that the material exhibits extremely low loss ($\kappa_e \leq 0.016$)

over the same investigated frequency range. This finding is a very appealing for OR, since the generated THz radiation in the CSP crystal will experience minimal absorption. For comparison, n_e and κ_e for the (110)-cut ZGP crystal are presented in Fig. 4.2. While the ZGP crystal exhibits very low dispersion ($|dn_e/df| \lesssim 0.02 \text{ THz}^{-1}$) and small losses ($\kappa_e \leq 0.018$), we will later show that phase-mismatching between the optical excitation pulse and the generated THz radiation is significantly better in the CSP crystal opposed to the ZGP crystal. Figure 4.2(c) compares the extraordinary absorption coefficient, α_e , of CSP to those of ZGP, ZnTe, and LN [147,148]. Clearly, the CSP α_e is less than α_e for both the ZnTe and LN crystals over the entire frequency

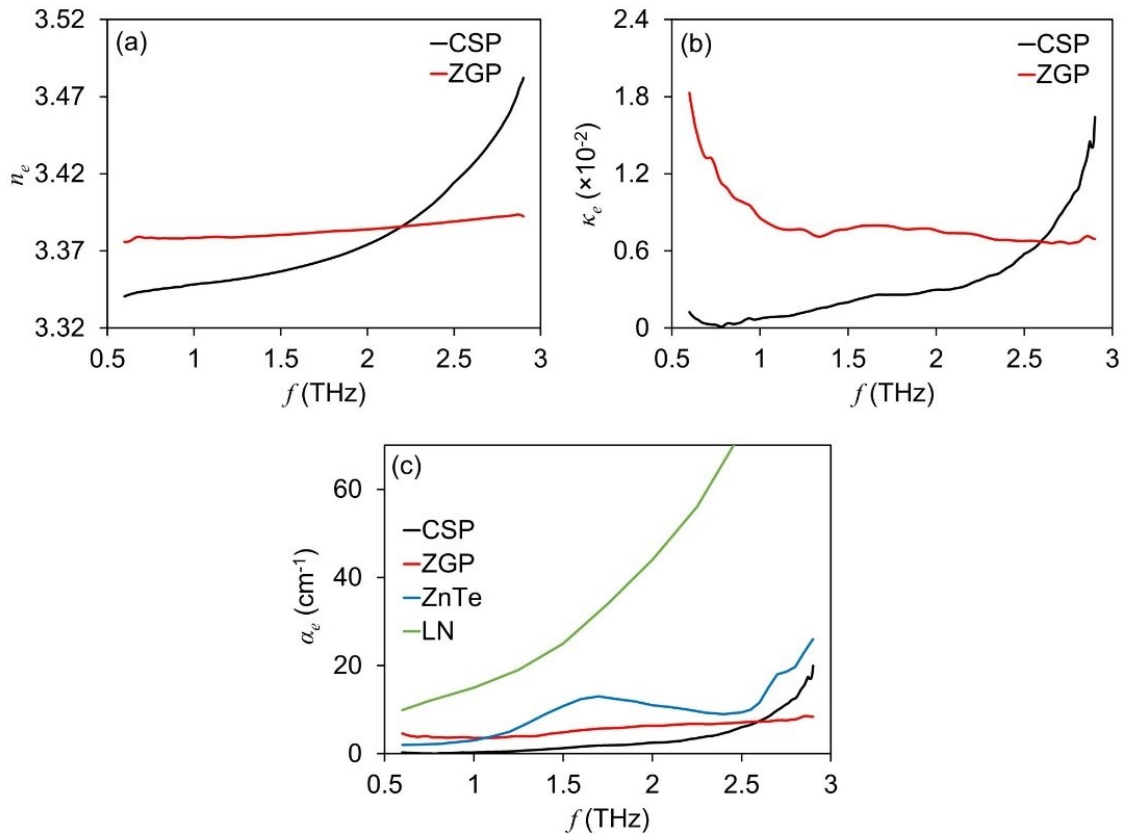


Fig. 4.2. (a) Extraordinary refractive indices and (b) extraordinary extinction coefficients of the CSP and ZGP crystals. (c) Extraordinary absorption coefficients for CSP, ZGP, ZnTe, and LN crystals. The experimental data for ZnTe and LN are obtained from Refs. [147] and [148], respectively.

range of 0.6-2.9 THz, while the α_e for CSP is less than that for ZGP at frequencies between 0.6-2.6 THz. When considering the frequency range of 1-2 THz, α_e is more than 4.4 times higher for ZnTe opposed to CSP and more than 17.6 times higher for LN in comparison to CSP, emphasizing the benefit of the CSP crystal's low loss.

4.1.3. THz-TDS measurements in the nonlinear regime

To investigate OR, the CSP crystal is incorporated as the THz radiation source in the THz-TDS system. Broadband THz radiation generation is obtained by focusing 118 nJ, 780 nm, 50 fs optical excitation pulses onto the CSP crystal. As shown in Fig. 4.3(a), the THz radiation signal is comprised of a main pulse having a duration of ~ 2 ps, followed by a series of oscillations having a peak-to-peak signal strength $\leq 13\%$ of the main pulse. These oscillations have a frequency of 3 THz and originate from phonon-polariton coupling, where the ordinary group refractive index of the excitation pulse, $n_{o,g}^{exc}$, and n_e of the THz radiation become equal [149]. From the EO signal, the conversion efficiency of the OR process is estimated to be 10^{-6} [150]. However, this can be enhanced by spatially confining the optical excitation pulse or using an amplifier to increase the energy of the excitation pulse. In comparison to the THz radiation signal generated from the 990 μm -thick, (110)-cut ZGP crystal, the peak-to-peak THz amplitude generated from the CSP crystals is 1.6 times higher [see Fig. 4.3(a)].

The spectral density (i.e. Fourier transform) of the THz radiation signals generated from the CSP and ZGP crystals are displayed in Fig. 4.3(b), where both crystals generate a similar THz radiation spectrum extending past 3 THz. Since we are using a 50 fs excitation pulse, the generated bandwidth could exceed 8.8 THz [i.e. the full-width half-maximum (FWHM) bandwidth of the excitation pulse]. As such, the sharp decrease in spectral density at ~ 3 THz is attributed to the

bandwidth limitation of the 500 μm -thick ZnTe EO sampling crystal employed in the THz-TDS system.

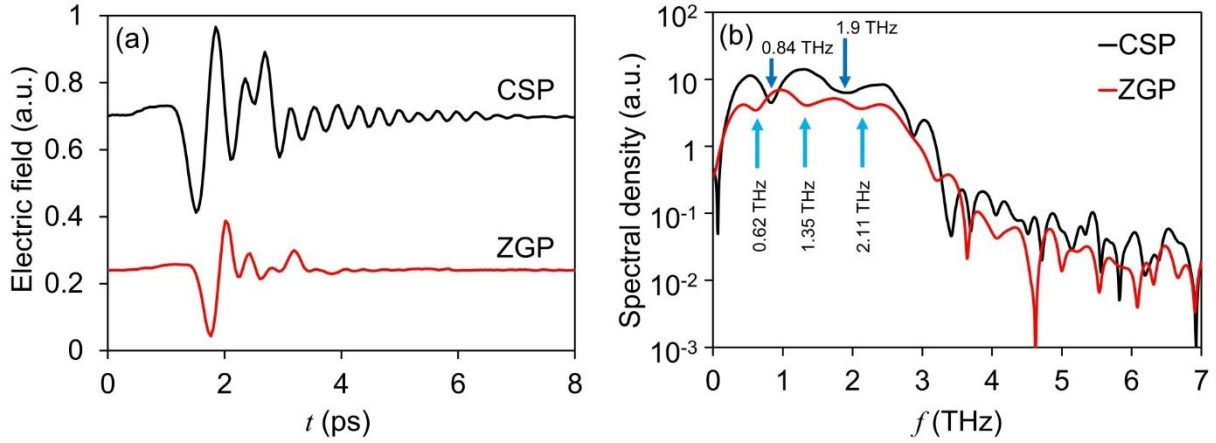


Fig. 4.3. (a) THz time-domain signals and (b) spectral densities of the electric fields generated from the CSP and ZGP crystals.

Examining the spectrum of the CSP crystal in the frequency range below 3 THz reveals three dips at 0.84, 1.90, and 2.89 THz. While the minimum at 2.89 THz is due to the phonon-polariton effect discussed previously, the dips at the frequencies of $f_d=0.84$ and 1.9 THz are attributed to phase-mismatching between the optical excitation pulse and the generated THz radiation. Theoretically, $n_{o,g}^{exc}$ can be obtained from the equation [151],

$$n_{o,g}^{exc} = n_e(f_d) + \frac{c\rho}{f_d \ell}, \quad (4.3)$$

where ρ is a positive integer and $n_e(f_d)$ is the extraordinary refractive index at the frequency f_d . Using the aforementioned f_d values of 0.84 and 1.9 THz, along with Eq. (4.3), $n_{o,g}^{exc}$ is found to be 3.70. Although dispersive effects cause the optical excitation pulse to spatially separate during propagation, the excitation pulse travels through the CSP crystal having this effective group refractive index of $n_{o,g}^{exc}=3.70$. Also seen in Fig. 4.3(b) are three phase-mismatching frequency dips

at $f_d=0.62, 1.35,$ and 2.11 THz in the spectrum associated with the ZGP crystal. Using Eq. (4.3), we calculate $n_{o,g}^{exc}$ for the ZGP crystal to be 3.84.

Phase-matching in the OR process is quantified by calculating the coherence length (see Section 2.3.2), given as,

$$L_c^{OR}(f) = \frac{c}{2f|n_{o,g}^{exc} - n_e(f)|}. \quad (4.4)$$

Figure 4.4 illustrates L_c^{OR} for the CSP and ZGP crystals in the frequency range of 0.6-2.9 THz. As expected, both CSP and ZGP have an L_c^{OR} less than their thicknesses, which is consistent with the observation of phase-mismatching dips in Fig. 4.3(b). Importantly, L_c^{OR} indicates that phase-matching could be satisfied using CSP and ZGP crystals having thicknesses $\lesssim 200 \mu\text{m}$ and $\lesssim 100 \mu\text{m}$, respectively.

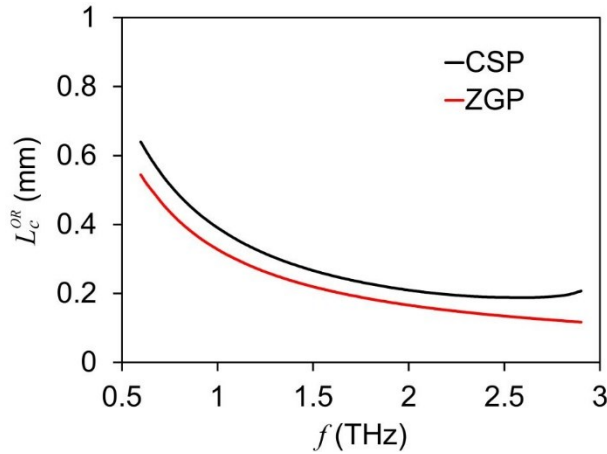


Fig. 4.4. The coherence lengths of the CSP and ZGP crystals.

In the regime where the optical excitation intensity is below the threshold for the onset of multi-photon absorption, the THz electric field generated in the CSP crystal is proportional to the peak intensity of the excitation pulse, I_p . Figure 4.5 shows this expected THz radiation generation characteristic (i.e. the generated THz electric field increases linearly with I_p). Such an observation

suggests that the CSP crystal can produce higher-strength THz radiation amplitudes by increasing the excitation pulse peak intensity. This can be easily realized by spatially confining the excitation electric field to a waveguiding structure [118].

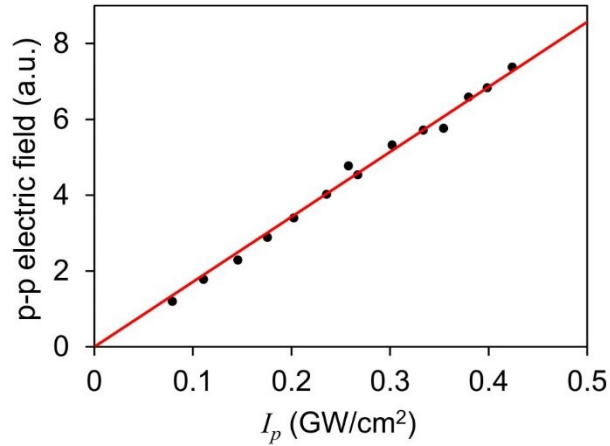


Fig. 4.5. THz peak-to-peak electric field as a function of the peak intensity of the optical excitation pulse.

4.2. OR in an AGS crystal for broadband THz radiation generation⁴

AGS exhibits a bandgap of 1.8 eV [55], a high second-order nonlinear coefficient of $d_{36}=39.5$ pm/V (at an excitation wavelength of 4.6 μm) [55], and a transparency range of 0.76-18 μm [55] (see Table 1.2). While such properties are important for OR THz radiation generation, they do not indicate the degree of OR phase-matching in the AGS crystal. Here, we investigate OR phase-matching for the AGS crystal, and show phase-matched OR THz radiation generation.

⁴A version of this section’s work is published as B. N. Carnio, K. T. Zawilski, P. G. Schunemann, and A. Y. Elezzabi, “Optical rectification in a chalcopyrite AgGaSe₂ crystal for broadband terahertz radiation generation,” *Opt. Lett.* **44**, 2867-2870 (2019).

4.2.1. Linear THz radiation properties

The linear THz radiation properties of the AGS crystal are investigated by performing THz-TDS experiments. The AGS crystal used in this study was grown via the HGF method using low axial temperature gradients and Ar-overpressure, as described by Schunemann et al. [152]. A 485 μm -thick, (110) plate (measuring 5 mm \times 10 mm) was cut from an AGS crystal boule and the large faces were polished. In the THz-TDS system [see Chapter 3], the THz electric field pulses are generated from a 500 μm -thick ZnTe OR crystal excited using 800 nm, 50 fs laser pulses. Subsequently, the THz electric field pulses are detected using a 500 μm -thick ZnTe EO crystal and 800 nm, 50 fs laser pulses. Figure 4.6(a) shows the THz electric field pulses transmitted through the AGS crystal at normal incidence, where the electric fields are polarized along the ordinary and extraordinary crystal axes. Oscillations are observed following the main pulses, which are due to the THz radiation coupling to the phonon modes of the AGS crystal and propagating as phonon-polaritons [153]. The spectral densities of the transmitted signals are shown in Fig. 4.6(b). The ordinary-polarized THz radiation shows weak absorption at 0.74 THz, which originates from the lowest-frequency E mode of the AGS crystal. Much stronger absorption is witnessed across the spectral range of 2.1-2.5 THz, which is attributed to the higher-frequency E modes. Notably, THz radiation near the lowest-frequency phonon resonance (i.e. 0.74 THz) only propagates a few wavelengths within the crystal, resulting in much lower absorption in comparison to THz radiation near the higher-frequency phonon mode. When considering the spectral density of the extraordinary-polarized THz radiation, absorption is witnessed at a frequency of 1.68 THz, which corresponds to the lowest-frequency B_2 mode of the AGS crystal. Although the other B_2 modes have central frequencies located outside of the THz spectrum, the off-resonant spectral

wings are wide enough to cause a reduction in the spectral density at frequencies between ~ 2.5 - 2.9 THz.

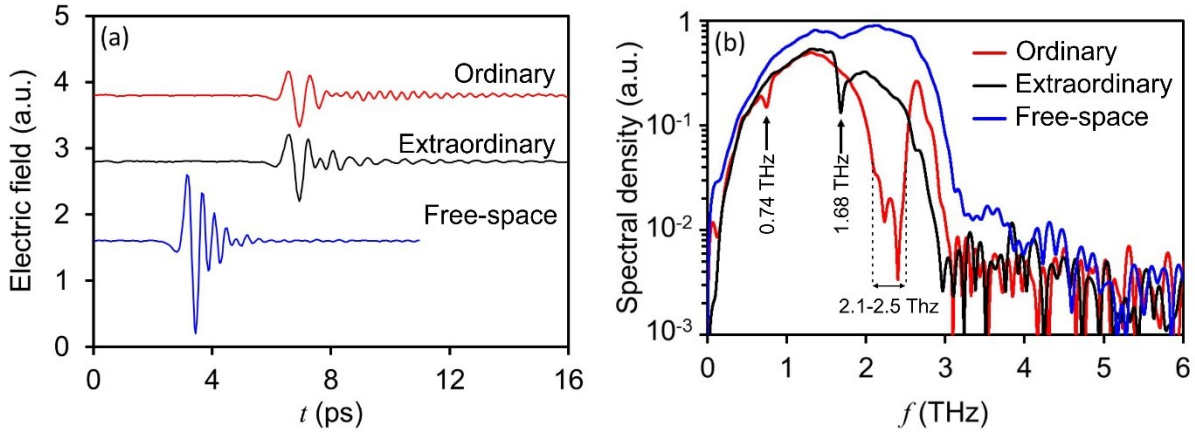


Fig. 4.6. (a) Time-domain electric field pulses transmitted through the AGS crystal, having polarizations oriented along the ordinary and extraordinary axes of the crystal. (b) Spectral density of the transmitted pulses, where the phonon resonances cause absorption at several frequencies across the measured spectra. The free-space THz radiation signal and spectrum are shown as a reference.

The linear THz radiation properties are determined for the uniaxial AGS crystal. The ordinary, n_o , and extraordinary, n_e , refractive indices, as well as the ordinary, κ_o , and extraordinary, κ_e , extinction coefficients, are obtained from the experimental transmission measurements (see Fig. 4.6) and Eq. (4.2). Due to the vanishing spectral content between ~ 2.1 - 2.5 THz, n_o and κ_o are only calculated within the 0.5-2 THz frequency range [see Fig. 4.7(a)], whereas n_e and κ_e are calculated for all frequencies between 0.5-2.9 THz [see Fig. 4.7(b)]. As seen in Fig. 4.7(a), the signature of the lowest-frequency E mode appears at 0.74 THz, where n_o varies from 3.07-3.15 and κ_o reaches values as large as 0.08. At frequencies between 1-2 THz, n_o increases at the fast rate of ~ 0.14 THz $^{-1}$ and κ_o monotonically increases up to a value of 0.09, due to the influence of higher-frequency E modes. n_e and κ_e are influenced by the lowest-frequency B_2 mode at 1.68 THz,

where n_e and κ_e reach a maximum value of 3.19 and 0.08, respectively [see Fig. 4.7(b)]. Away from this resonance, higher-frequency B_2 modes cause n_e to increase at a rate of $\sim 0.14 \text{ THz}^{-1}$ and κ_e to increase to a value of 0.09. As such, along both crystal axes, a fast rate of increase in the refractive index is accompanied by a large increase in the extinction coefficient, both of which are inherent signatures of a phonon resonance.

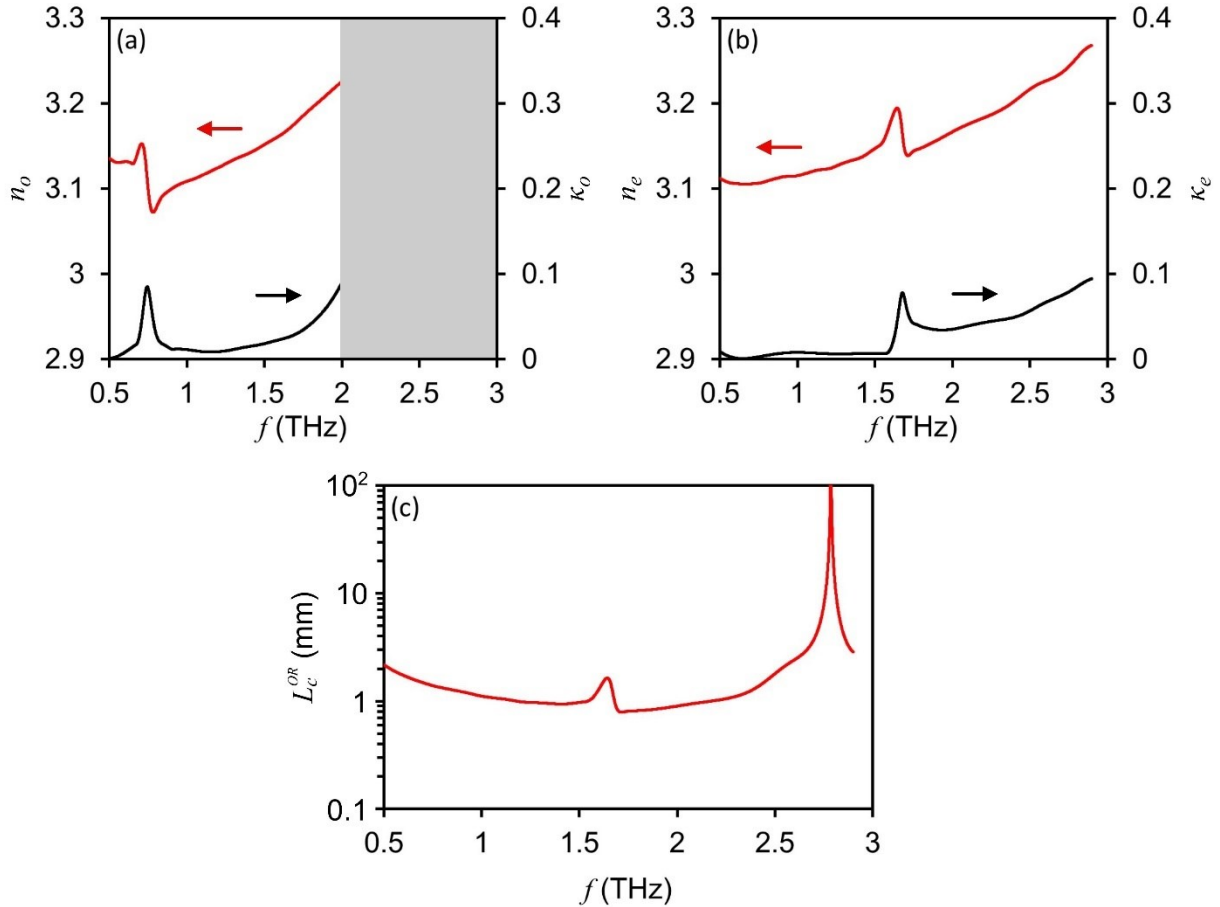


Fig. 4.7. (a) Ordinary and (b) extraordinary refractive indices and extinction coefficients of the uniaxial AGS crystal. The shaded area in (a) corresponds to the region where n_o and κ_o are not calculated due to the spectral density vanishing. (c) OR coherence length of the AGS crystal for the scenario where the excitation pulse polarization is oriented along the ordinary crystal axis.

When investigating OR in a nonlinear crystal, it is necessary to consider phase-matching, which is accomplished by calculating the OR coherence length [see Eq. (4.4)]. Using the experimental data from Ref. [154], $n_{o,g}^{exc}=3.25$ at a wavelength of 800 nm for the AGS crystal. The minimum coherence length for the AGS crystal, L_c^{OR} , is ~ 800 μm over the investigated frequency range of 0.5-2.9 THz, as depicted in Fig. 4.7(c). Notably, over a similar frequency range, the CSP and ZGP crystals exhibit the comparatively shorter coherence lengths of $\lesssim 200$ μm (see Fig. 4.4). As such, the AGS crystal serves as an excellent candidate for THz radiation generation via OR.

4.2.2. THz-TDS measurements in the nonlinear regime

The nonlinear properties of the crystal are investigated by utilizing the (110)-cut AGS crystal as the THz radiation source in the THz-TDS system. The crystal is excited using an 800 nm, 50 fs Ti:Sapphire oscillator and the generated THz radiation is measured using a 500 μm -thick ZnTe EO crystal. AGS exhibits the same second-order nonlinear polarization matrix as CSP [see Eq. (4.1)]. As such, the polarization of the optical excitation pulse is oriented along the ordinary axis of the crystal to generate THz radiation having a polarization along the crystal's c -axis (coinciding with the extraordinary crystal axis). As shown in Fig. 4.8(a), the generated THz electric field pulse is followed by low-amplitude oscillations. Here, the optical excitation signal generates localized nonlinear dipoles near the lowest-frequency B_2 phonon resonance of the AGS crystal, which oscillate and emit THz radiation for the lifetime of the phonon resonance. For an excitation pulse energy of 8.2 nJ, the energy of the generated THz radiation pulse is 4.1 fJ, corresponding to a conversion efficiency of 6×10^{-7} . Obviously, this conversion efficiency could be improved by using higher energy excitation pulses or spatially confining the excitation pulse, where the latter could be achieved through the use of a waveguide comprised of the AGS crystal.

The generated THz spectral density is shown in Fig. 4.8(b), which has a dynamic range of more than 40 dB and a bandwidth extending up to ~ 4 THz. Notably, this bandwidth is limited by the 500 μm -thick ZnTe EO detection crystal and not the AGS crystal itself. Due to absorption from the lowest-frequency B_2 phonon mode, a strong null is observed in the spectrum at a frequency of 1.6 THz. Although enhancement of both the nonlinear coefficient and absorption loss occur near this phonon resonance [38], absorption dominates due to the bulk nature of the crystal. However, by implementing the AGS crystal in a waveguiding geometry, such as that proposed in Ref. [124], phonon mode enhancement of the nonlinear coefficient could be made to dominate over phonon mode absorption, thereby permitting enhanced THz radiation generation. The spectral density also provides important information for phase-matching. The only null in the spectral density is due to the lowest-frequency B_2 mode, meaning phase-matching is satisfied within the 485 μm -thick AGS crystal, in agreement with the calculated coherence length [see Fig. 4.7(c)].

THz radiation generation is investigated for various excitation polarization angles and excitation intensities. Figure 4.9(a) shows THz radiation produced by varying the angle, θ_p ,

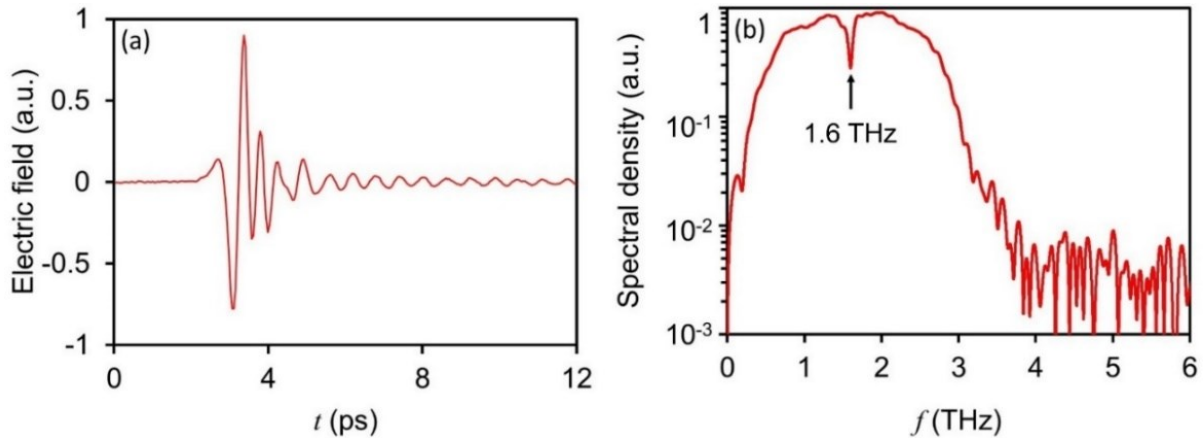


Fig. 4.8. (a) THz time-domain electric field pulse generated by the AGS crystal via the process of OR. (b) Spectral density of the generated THz radiation pulse, showing absorption from the lowest-frequency B_2 mode at 1.6 THz.

between the polarization of the excitation pulse and the c -axis of the crystal. Here, a THz wire-grid polarizer is placed behind the AGS crystal and oriented to only pass THz electric fields that are polarized perpendicular to the optical excitation pulse polarization. As expected, there is no THz radiation generation when the polarization of the optical excitation pulse is directed along the c -axis (e.g. $\theta_p=0^\circ$), whereas THz radiation generation is maximum when the polarization of the excitation pulse is set perpendicular to the c -axis (e.g. $\theta_p=90^\circ$). For all the angles, THz electric field generation is in good agreement with the theoretical equation, $E_{THz} = \sin^2(\theta_p)$ [150]. Figure 4.9(b) shows the intensity scaling of the THz electric field produced using the AGS crystal. As the peak intensity of the excitation signal in the crystal, I_p , is increased up to ~ 0.07 GW/cm², the peak-to-peak value of the generated THz electric field shows the onset of saturation. A simple saturation curve $[\propto I_p/(1 + 4I_p)]$ is fit to the experimental data. By extrapolating this curve, THz radiation generation saturation is estimated to occur at $I_p \approx 0.3$ GW/cm². Due to the bandgap of AGS being 1.8 eV [55], this saturation is likely due to two-photon absorption.

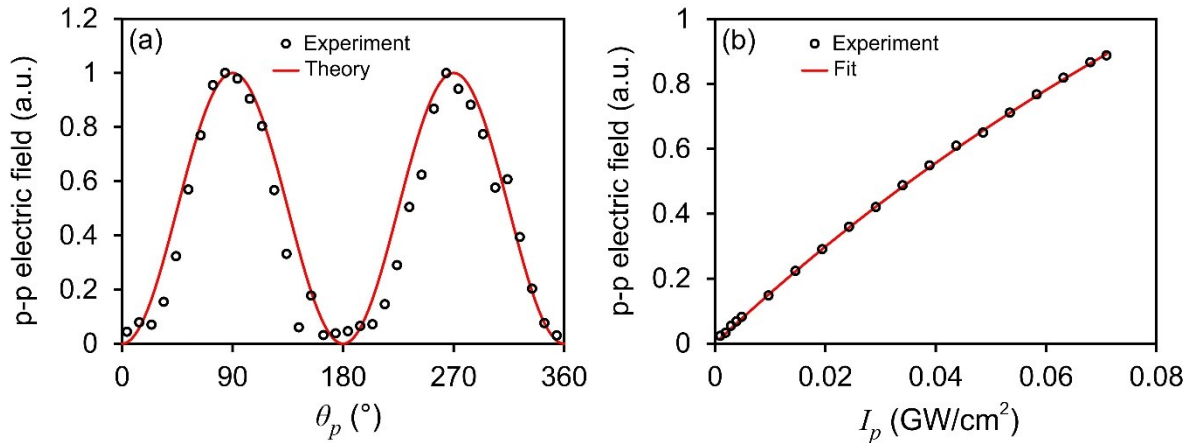


Fig. 4.9. (a) THz peak-to-peak electric field measured upon varying the angle between the polarization of the optical excitation pulse and the crystal's c -axis. (b) Peak-to-peak THz electric field measured for various peak excitation pulse intensities in the AGS crystal.

4.3. Generation of narrowband THz radiation from a BGS crystal⁵

BGS exhibits the key properties of a wide bandgap (i.e. 2.64 eV [55]), a reasonable second-order nonlinear coefficient (i.e. $d_{11}=24.3$ pm/V at an excitation wavelength of 1064 nm [56]), and a wide transparency range of 0.47-18 μm [55] [see Table 1.2]. Since BGS is biaxial and optically complex, a complete investigation must be performed to characterize the THz radiation generation properties of this crystal. Here, a systematic experimental investigation is conducted to determine the optimal near-IR excitation polarization angles and crystal orientations for OR THz radiation generation in the crystal. Subsequently, THz radiation generation using the optimal BGS crystal arrangements are compared to that from a ZnTe crystal.

4.3.1. Nonlinear crystal properties

The BGS crystal was grown using the HGF method [155] and exhibits the following second-order nonlinear polarization tensor [56],

$$\begin{bmatrix} P_X^{(2)} \\ P_Y^{(2)} \\ P_Z^{(2)} \end{bmatrix} = 2\epsilon_0 \begin{bmatrix} d_{11} & d_{12} & d_{13} & 0 & d_{15} & 0 \\ 0 & 0 & 0 & d_{24} & 0 & d_{26} \\ d_{31} & d_{32} & d_{33} & 0 & d_{35} & 0 \end{bmatrix} \begin{bmatrix} E_X^2 \\ E_Y^2 \\ E_Z^2 \\ 2E_Y E_Z \\ 2E_X E_Z \\ 2E_X E_Y \end{bmatrix}, \quad (4.5)$$

⁵A version of this section's work is published as B. N. Carnio, E. Hopmann, K. T. Zawilski, P. G. Schunemann, and A. Y. Elezzabi, "Dependence on excitation polarization and crystal orientation for terahertz radiation generation in a BaGa₄Se₇ crystal," *Opt. Express* **28**, 15016-15022 (2020) and B. N. Carnio, K. T. Zawilski, P. G. Schunemann, and A. Y. Elezzabi, "Generation of narrowband terahertz radiation via phonon mode enhanced nonlinearities in a BaGa₄Se₇ crystal," *Opt. Lett.* **45**, 4722-4725 (2020).

where X , Y , and Z are the crystallo-physical axes of the crystal [156], d_{11} , d_{12} , d_{13} , d_{15} , d_{24} , d_{26} , d_{31} , d_{32} , d_{33} , and d_{35} are non-vanishing tensor elements, $E_{X,Y,Z}^{(2)}$ are the excitation electric fields oriented along the X , Y , and Z crystallo-physical axes, respectively, and $P_{X,Y,Z}^{(2)}$ are the second-order nonlinear polarizations oriented along the X , Y , and Z crystallo-physical axes, respectively. It is important to note that the crystallo-physical axes (i.e. X , Y , and Z) are defined with respect to the crystal itself, and differ from the Cartesian coordinate system. For a bulk BGS crystal cut along the (010) crystal plane, $E_Y=0$ V/m and THz radiation can only be produced along the X and Z crystallo-physical axes, allowing the tensor formalism in Eq. (4.5) to be simplified to two equations:

$$P_X^{(2)} = 2\varepsilon_0 d_{11} E_X^2 + 2\varepsilon_0 d_{13} E_Z^2 + 4\varepsilon_0 d_{15} E_X E_Z, \quad (4.6)$$

$$P_Z^{(2)} = 2\varepsilon_0 d_{31} E_X^2 + 2\varepsilon_0 d_{33} E_Z^2 + 4\varepsilon_0 d_{35} E_X E_Z. \quad (4.7)$$

Equations (4.6) and (4.7) show that the BGS crystal can support THz radiation generation having a polarization along either the X or Z crystallo-physical axes, regardless of the polarization of the excitation radiation. Nonetheless, the strength of the generated THz radiation also depends on the magnitude of the nonlinear coefficients and phase-matching.

4.3.2. Dependence of THz radiation generation on the excitation polarization angle and crystal orientation

Figure 4.10(a) shows a schematic of the experimental arrangement used to excite the BGS crystal, as defined with respect to the reference coordinates x_r , y_r , and z_r . Here, the near-IR excitation electric field, \vec{E}_{exc} , has a linear-polarization defined by the angle θ_p and the BGS crystal's angular orientation is denoted as θ_c . A THz wire-grid polarizer, used to select the polarization component of the generated THz radiation, is set to have its transmission axis fixed

along the z_r axis. This arrangement ensures that well-defined linearly-polarized THz radiation, \vec{E}_{THz} , is incident on a fixed-orientation 500 μm -thick ZnTe EO crystal. The polarizations of \vec{E}_{exc} and \vec{E}_{THz} are depicted relative to the unit cell of the BGS crystal [see Fig. 4.10(b)], described using the crystallographic coordinate system (i.e. [100], [010], and [001]) [156,157].

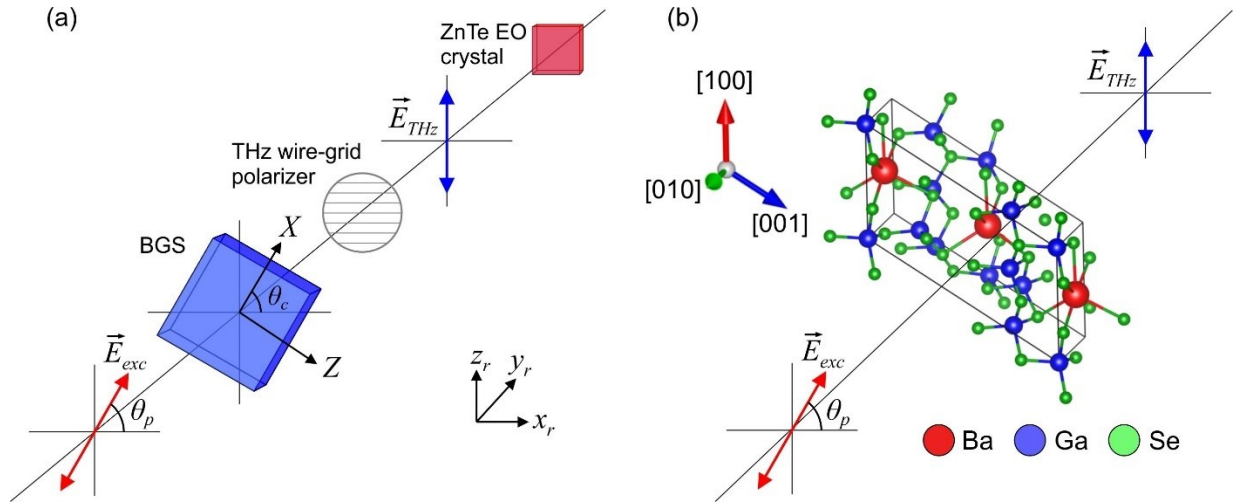


Fig. 4.10. (a) Schematic showing the setup implemented to perform OR THz radiation generation experiments using the BGS crystal. x_r , y_r , and z_r define the reference coordinates. (b) An illustration of the unit cell of the BGS crystal. The near-IR excitation electric field polarization and the generated THz radiation electric field polarization are shown.

OR experiments are conducted by focusing Ti:Sapphire laser pulses onto the BGS crystal, where this crystal is integrated as the THz radiation source of the THz-TDS system [see chapter 3]. The excitation pulses each have a duration of 50 fs, a central wavelength of 800 nm, and an average power of 24 mW. At the input face of the BGS crystal, the laser beam spot size is 590 μm , corresponding to a peak intensity of 34 MW/cm^2 . Since the OR process strongly depends on the polarization of \vec{E}_{exc} and the crystal orientation, this nonlinear phenomenon is investigated for various angles of θ_p and θ_c [see Fig. 4.10(a)]. OR measurements are performed for an \vec{E}_{exc}

oriented along the X axis of the BGS crystal (i.e. $\theta_c=\theta_p$) [see Fig. 4.11(c)]. As displayed in Fig. 4.11(a), the maximum \vec{E}_{THZ} is measured when the crystal's Z axis is aligned with the transmission axis of the wire-grid polarizer (i.e. $\theta_p=0^\circ$) and \vec{E}_{THZ} is nearly zero when the crystal's X axis is aligned along the transmission axis (i.e. $\theta_p=90^\circ$). A close examination of the \vec{E}_{THZ} time-domain signals indicate evidence of frequency beating. As shown from the power spectra in Fig. 4.11(b), this is as a result of narrowband (i.e. 50 GHz linewidth) generation at 1.97 and 2.34 THz. The generated frequencies can be used to calculate the beating period of the time-domain signal as $|2.34 \text{ THz}-1.97 \text{ THz}|^{-1}=2.7 \text{ ps}$, which agrees with the beating period seen in Fig. 4.11(a). Additionally, the spectral power generated along the Z crystallo-physical axis (i.e. $\theta_p=0^\circ$) is ~ 14 times higher than the spectral power produced along the X crystallo-physical axis (i.e. $\theta_p=90^\circ$), such that the generated THz radiation has a polarization ratio of 14:1. The peak spectral powers (i.e. square of the Fourier transform) at 1.97 and 2.34 THz are displayed in Fig. 4.11(c) for the various excitation angles. When $\theta_p \approx 90^\circ$, THz radiation generation is influenced by a combination of the d_{11} nonlinear coefficient [see Eq. (4.6)] and phase-matching between the X -polarized \vec{E}_{exc} pulse and the X -polarized \vec{E}_{THZ} pulse. However, when $\theta_p \approx 0^\circ$, THz radiation generation is influenced by a combination of the d_{31} nonlinear coefficient [see Eq. (4.7)] and phase-matching between the X -polarized \vec{E}_{exc} pulse and the Z -polarized \vec{E}_{THZ} pulse. Clearly, the latter combination proves to be optimal, since the highest spectral powers are measured at $\theta_p=0^\circ$ and 22.5° . At these excitation angles, generation at 2.34 THz is $>20\%$ higher than generation at 1.97 THz.

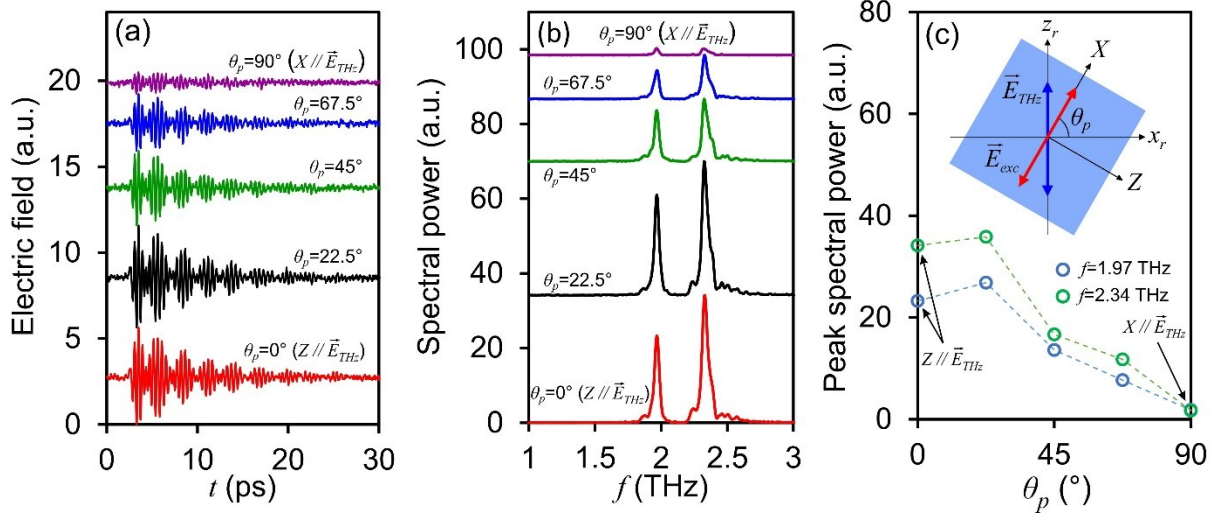


Fig. 4.11. (a) THz time-domain signals generated by exciting the BGS crystal along its X crystallo-physical axis (i.e. $\theta_c = \theta_p$) and (b) the corresponding spectral power. (c) Spectral powers at the frequencies of 1.97 and 2.34 THz as a function of θ_p . The inset shows an illustrative representation of the orientations of \vec{E}_{exc} and \vec{E}_{THz} with respect to the X , Z , x_r , and z_r axes. Here, the excitation polarization and crystal orientation are fixed using the relationship of $\theta_c = \theta_p$.

OR is investigated for \vec{E}_{exc} polarized along the Z axis of the BGS crystal (i.e. $\theta_c = \theta_p + 90^\circ$), as illustrated in the inset in Fig. 4.12(c). The generated THz time-domain signals are shown in Fig. 4.12(a), whereas the associated power spectra are presented in Fig. 4.12(b). The THz time-domain pulses exhibit a nearly monotonic decay with a characteristic time of approximately 10 ps. The peak spectral powers at various angles show a strong narrowband (i.e. 50 GHz linewidth) frequency component at 1.97 THz and a weak one at 2.34 THz, such that narrowband generation occurs mainly at the frequency of 1.97 THz. As expected, the measured decay time agrees with the measured linewidth via the theoretical relationship [i.e. $(2 \times 10 \text{ ps})^{-1} \approx 50 \text{ GHz}$]. The spectral power generated along the Z crystallo-physical axis (i.e. $\theta_p = 90^\circ$) is ~ 15 times higher than the

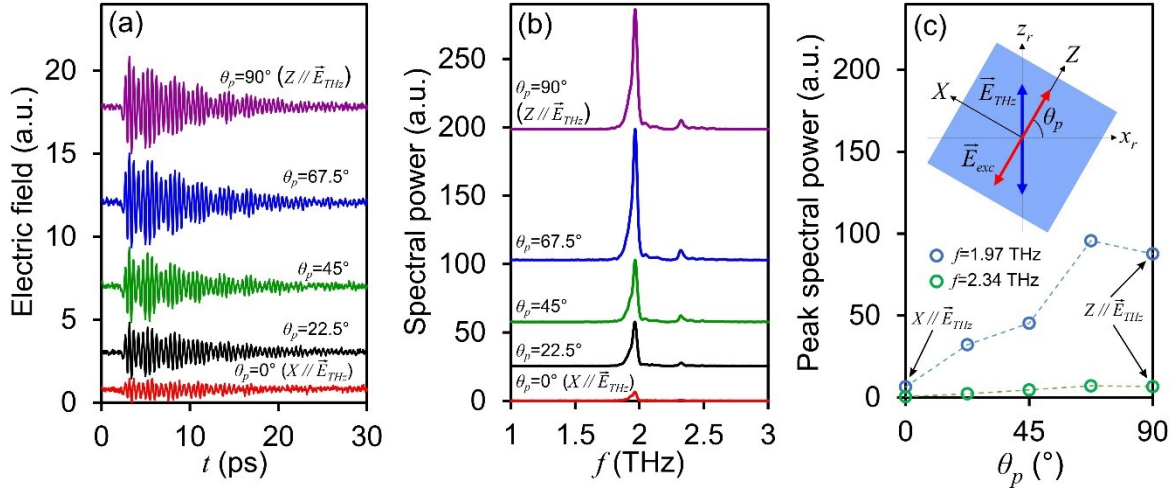


Fig. 4.12. (a) THz time-domain signals generated by exciting the BGS crystal along its Z crystallo-physical axis (i.e. $\theta_c = \theta_p + 90^\circ$) and (b) the corresponding power spectra. (c) Spectral powers at the frequencies of 1.97 and 2.34 THz as a function of θ_p . The inset shows the illustrative representation of the orientations of \vec{E}_{exc} and \vec{E}_{THz} with respect to the X, Z, x_r , and z_r axes. Here, the excitation polarization and crystal orientation are fixed using the relationship of $\theta_c = \theta_p + 90^\circ$.

spectral power produced along the X crystallo-physical axis (i.e. $\theta_p = 0^\circ$), such that the generated THz radiation has a polarization ratio of 15:1. Figure 4.12(c) shows the peak spectral powers for the various excitation angles at the frequencies of 1.97 and 2.34 THz. When $\theta_p \approx 0^\circ$, THz radiation generation is influenced by a combination of the d_{13} nonlinear coefficient [see Eq. (4.6)] and phase-matching between the Z -polarized \vec{E}_{exc} pulse and the X -polarized \vec{E}_{THz} pulse. However, when $\theta_p \approx 90^\circ$, THz radiation generation is influenced by a combination of the d_{33} nonlinear coefficient [see Eq. (4.7)] and phase-matching between the Z -polarized \vec{E}_{exc} pulse and the Z -polarized \vec{E}_{THz} pulse. The latter of these is the optimal combination, since the highest spectral powers are measured at $\theta_p = 67.5^\circ$ and 90° . For these angles, the generated radiation at 1.97 THz is 13 times greater than that at 2.34 THz.

OR experiments are performed to investigate THz radiation generation when the crystal's X axis is oriented along the wire-grid polarizer's transmission axis (i.e. $\theta_c=90^\circ$), as shown in the inset of Fig. 4.13(c). The time-domain signals, power spectra, and peak spectral powers at 1.97 and 2.34 THz are displayed in Fig. 4.13(a), 4.13(b), and 4.13(c), respectively. Clearly, THz radiation generation is weak, where the highest spectral power in Fig. 4.13(c) is 0.17 and 0.04 times the highest spectral power in Fig. 4.11(c) and 4.12(c), respectively.

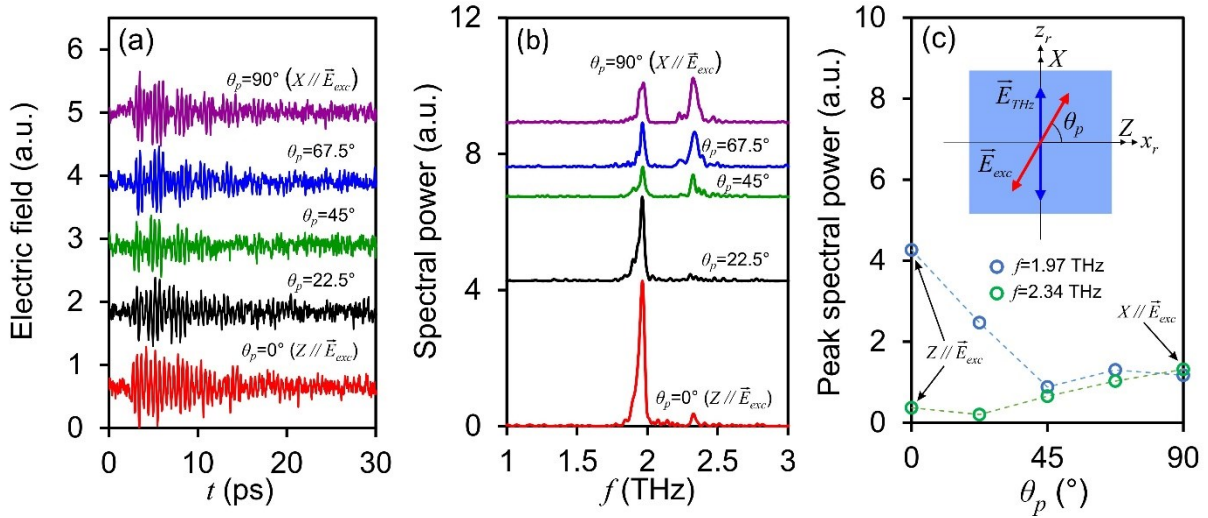


Fig. 4.13. (a) THz time-domain signals when the X crystallo-physical axis of the BGS crystal is oriented along the transmission axis of the wire-grid polarizer (i.e. $\theta_c=90^\circ$) and (b) the corresponding power spectra. (c) Spectral powers at the frequencies of 1.97 and 2.34 THz as a function of θ_p . The inset shows the illustrative representation of the orientations of \vec{E}_{exc} and \vec{E}_{THz} with respect to the X , Z , x_r , and z_r axes for $\theta_c=90^\circ$.

OR is investigated when the crystal's Z axis is oriented along the wire-grid polarizer's transmission axis (i.e. $\theta_c=0^\circ$), as depicted in the inset of Fig. 4.14(c). The generated THz time-domain signals are shown in Fig. 4.14(a) and the associated power spectra are presented in Fig. 4.14(b). Interestingly, \vec{E}_{exc} can be used as a means to control the relative strength between the

narrowband peaks at 1.97 and 2.34 THz. Here, when \vec{E}_{exc} is oriented along the crystal's Z axis (i.e. $\theta_p=90^\circ$), narrowband generation occurs primarily at 1.97 THz, since the spectral power at this frequency is 15 times higher than that at 2.34 THz. By altering θ_p , the peak spectral power at 2.34 THz increases at the expense of the peak spectral power observed at 1.97 THz. When \vec{E}_{exc} is oriented along the X axis of the crystal (i.e. $\theta_p=0^\circ$), the peak spectral power at 2.34 THz is 1.5 times higher than the peak spectral power at 1.97 THz. Figure 4.14(c) shows the peak spectral powers at 1.97 and 2.34 THz, depicting this dependence on the polarization angle.

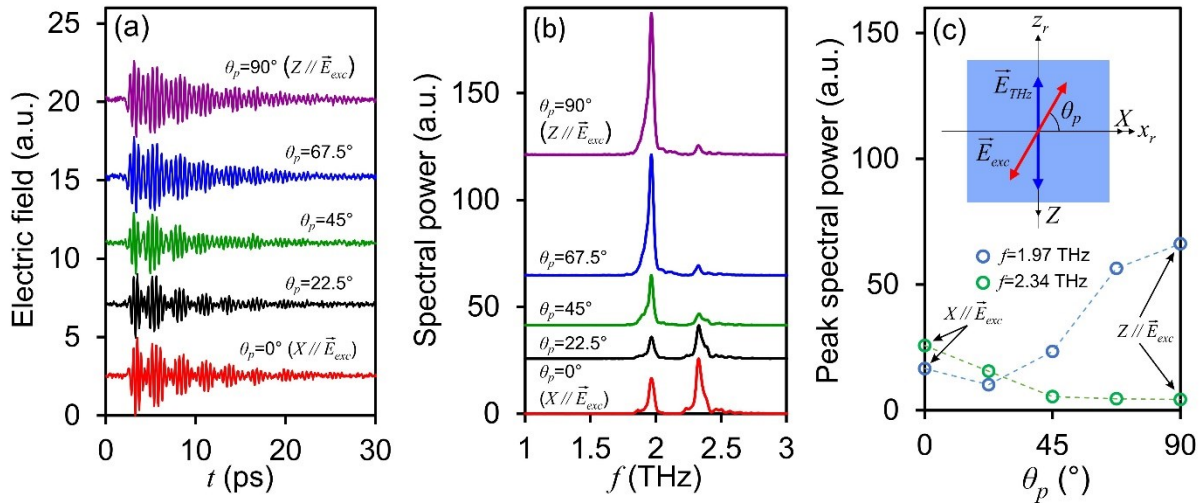


Fig. 4.14. (a) THz time-domain signals when the Z crystallo-physical axis of the BGS crystal is oriented along the transmission axis of the wire-grid polarizer (i.e. $\theta_c=0^\circ$) and (b) the corresponding power spectra. (c) Spectral powers at the frequencies of 1.97 and 2.34 THz as a function of θ_p . The inset shows the illustrative representation of the orientations of \vec{E}_{exc} and \vec{E}_{THz} with respect to the X , Z , x_r , and z_r axes for $\theta_c=0^\circ$.

4.3.3. Optimal BGS crystal arrangements for THz radiation generation

As determined in Section 4.3.2, optimal THz radiation generation is achieved from the BGS crystal when: (i) $\vec{E}_{exc} \parallel X$ and $\vec{E}_{THz} \parallel Z$, and (ii) $\vec{E}_{exc} \parallel Z$ and $\vec{E}_{THz} \parallel Z$. The former arrangement

is depicted in Fig. 4.15(a) and corresponds to $\theta_c=0^\circ/\theta_p=0^\circ$ in Fig. 4.10(a), while the latter arrangement is depicted in Fig. 4.15(b) and corresponds to $\theta_c=0^\circ/\theta_p=90^\circ$ in Fig. 4.10(a). For comparison, THz radiation generation is measured from the 500 μm -thick, (110)-cut ZnTe crystal arrangement presented in Fig. 4.15(c).

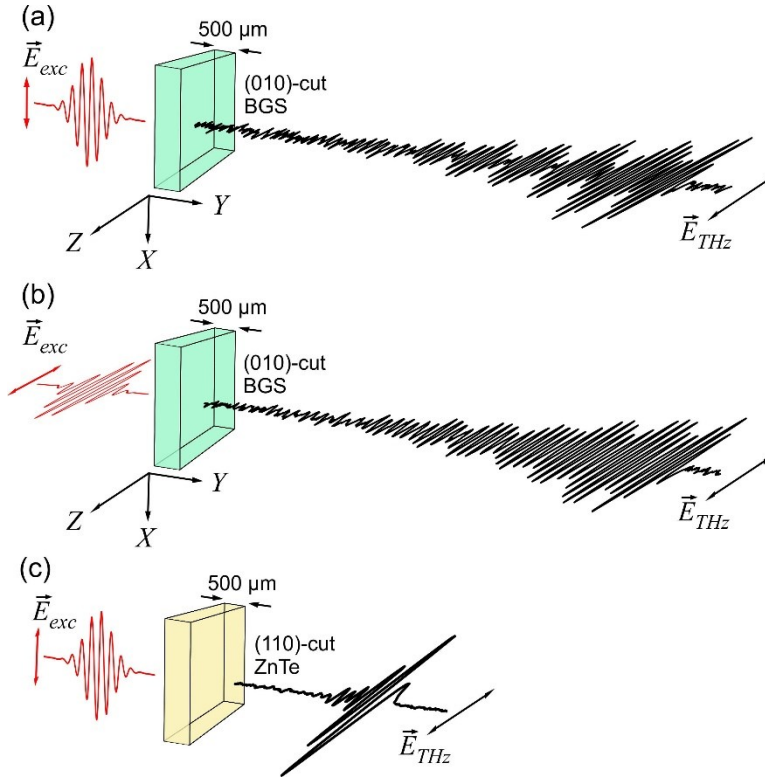


Fig. 4.15. Illustration of the experimental arrangement for (a) the BGS crystal when $\vec{E}_{exc} \parallel X$, (b) the BGS crystal when $\vec{E}_{exc} \parallel Z$, and (c) the ZnTe crystal. The generated THz radiation is passed through a wire-grid polarizer to obtain the component polarized along the Z crystallo-physical axis. This THz radiation is subsequently recorded using a 500 μm -thick (110)-cut ZnTe EO sampling crystal. The (110)-cut ZnTe EO crystal orientation is optimized for maximum THz radiation generation.

OR experiments are conducted using a laser beam having a spot size of 54 μm and a peak intensity of 4.1 GW/cm^2 . Figure 4.16(a) shows the THz time-domain signals produced by the BGS

crystal arrangements [i.e. see Fig. 4.15(a) and 4.15(b)], along with the THz time-domain signal obtained from the ZnTe crystal arrangement [i.e. see Fig. 4.15(c)]. The peak-to-peak amplitude of the ZnTe THz electric field signal is >4 times higher than those from the BGS crystal, while the durations of the BGS THz electric field signals are >5 time longer than that from the ZnTe crystal. Figure 4.16(b) depicts the THz spectral powers associated with the BGS and ZnTe crystals. Unlike the broadband THz radiation emission obtained from the ZnTe crystal, the THz radiation produced from the BGS crystal shows two narrow [i.e. 50 GHz linewidth] spectral bands centered at 1.97 and 2.34 THz. Interestingly, for the $\vec{E}_{exc} \parallel X$ BGS crystal arrangement, the spectral power at 2.34 THz exceeds that of ZnTe by 63%. More impressively, for the $\vec{E}_{exc} \parallel Z$ BGS crystal arrangement, the spectral power at 1.97 THz is 4.5 times higher than that from the ZnTe crystal. Clearly, by choosing suitable orientations for \vec{E}_{exc} , the BGS crystal strongly outperforms ZnTe for THz radiation generation at both 1.97 and 2.34 THz. Therefore, the BGS crystal has the potential to be used in a wide range of applications, since it is uncommon for a bulk crystal to surpass ZnTe for THz radiation generation.

The BGS spectral powers in Fig. 4.16(b) are dramatically influenced by the numerous phonon modes supported by this crystal. The total number of optical phonon modes in the BGS crystal is 69, which are both Raman-active and IR-active [158]. Interestingly, the heaviest atom (i.e. Ba) does not vibrate at frequencies above the phonon gap, but vibrates at frequencies below the phonon gap [158]. As such, the low THz frequency regime we investigate is associated with a vibrating Ba atom. An A' phonon mode is supported at 2.1 THz [158], which separates the generation bands observed in the spectra. A combination of numerous other A' and A'' phonon modes absorb the THz radiation produced at frequencies below the 1.97 THz spectral peak and above the 2.34 THz spectral peak [158]. However, only select phonon modes influence the

narrowband THz radiation generation process in the (010)-cut BGS crystal. For example, although a phonon mode exists at the wavenumber of 78.7 cm^{-1} (i.e. 2.36 THz) [158], it does not influence THz radiation generation due to the implemented crystal orientation and excitation polarization angles.

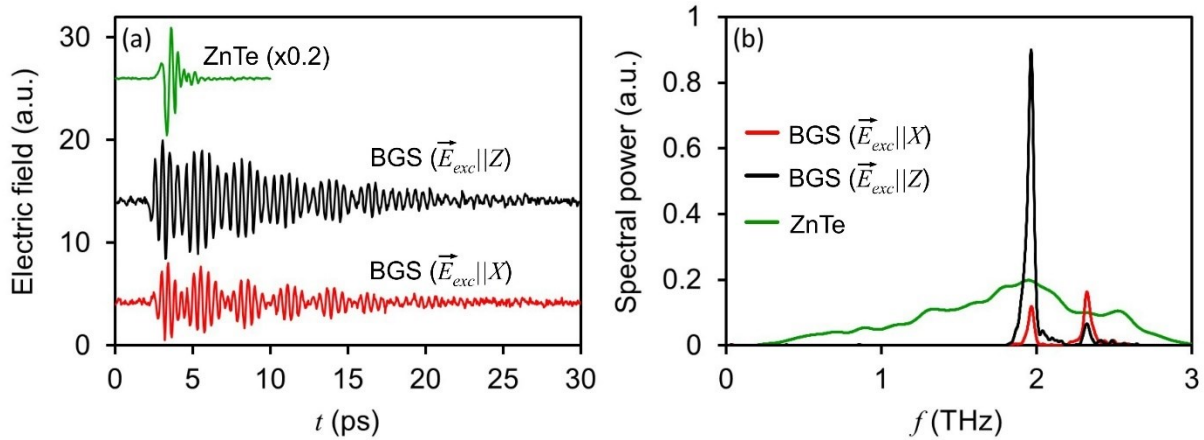


Fig. 4.16. (a) Time-domain signals and (b) power spectra for THz radiation produced using the $\vec{E}_{exc} \parallel X$ and $\vec{E}_{exc} \parallel Z$ BGS crystal configurations. For comparison, broadband THz radiation emission from the ZnTe crystal arrangement is shown.

Due to the biaxial nature of the BGS crystal, along with its non-negligible THz loss, the generated THz radiation (i.e. see Fig. 4.16) propagates through this crystal as two elliptically-polarized eigenmodes [74]. As determined in Ref. [74], one of the elliptically-polarized eigenmodes exhibits the low extinction coefficient of <0.02 at the frequencies of 1.97 and 2.34 THz, which are separated by the much higher extinction coefficient value of 0.2 at 2.1 THz. Clearly, these absorption loss values are in strong agreement with the $\vec{E}_{exc} \parallel X$ and $\vec{E}_{exc} \parallel Z$ THz radiation spectra displayed in Fig. 4.16(b). The other elliptically-polarized eigenmode discussed in Ref. [74] shows less agreement with the spectra depicted in Fig. 4.16(b), suggesting that the generated THz radiation mainly propagates as the former elliptically-polarized eigenmode. It is

also necessary to consider phase-matching for the OR process. For both THz elliptically-polarized eigenmodes, the refractive indices are ~ 10 at 1.97 and 2.34 THz [74]. Although such a refractive index is high, it may be the result of the dense phonon mode distribution of the BGS crystal. The high THz refractive indices of ~ 10 and the much lower group refractive index of the excitation pulse (i.e. ~ 2.8 at 800 nm [156]) suggest that THz radiation generation is only occurring over the last few tens of micrometres in the BGS crystal, due to phase-mismatching effects. Nonetheless, THz radiation generation from these few tens of micrometres is much higher than THz radiation generation from the 500 μm -thick ZnTe crystal (i.e. 4.5 times higher at 1.97 THz).

It is crucial to determine the energy of the generated THz radiation and its conversion efficiency. When the \vec{E}_{exc} laser pulse energy is 4.2 nJ, the measured THz radiation energy is found to be 0.09 and 0.28 fJ for the $\vec{E}_{exc} \parallel X$ and $\vec{E}_{exc} \parallel Z$ BGS crystal arrangements, respectively. This corresponds to a conversion efficiency of 2.2×10^{-8} for the $\vec{E}_{exc} \parallel X$ configuration and 6.3×10^{-8} for the $\vec{E}_{exc} \parallel Z$ configuration. Notably, these conversion efficiencies could be increased by using higher energy laser pulses or confining the excitation electric field to waveguides comprised of the BGS crystal. It is also informative to determine the energy encompassed within each of the generated spectral bands. For the frequency band centered at 2.34 THz, the encompassed energy is 0.06 and 0.02 fJ for the $\vec{E}_{exc} \parallel X$ and $\vec{E}_{exc} \parallel Z$ configurations, respectively. For the frequency band centered at 1.97 THz, the encompassed energy is 0.03 fJ for the $\vec{E}_{exc} \parallel X$ configuration and 0.26 fJ for the $\vec{E}_{exc} \parallel Z$ configuration.

The THz spectral density is investigated for its dependence on the peak laser excitation intensity, I_p . The excitation laser beam is focused on the BGS crystal to achieve a spot size of 54 μm and its peak intensity is varied using an adjustable neutral density filter. The spectral density

is calculated by integrating over the FWHM bandwidth of the generated THz radiation bands. At the frequency of 1.97 THz, the ZnTe crystal configuration exhibits higher spectral densities in comparison to the BGS crystal $\vec{E}_{exc} \parallel X$ configuration [Fig. 4.17(a)]. However, for all investigated I_p , the BGS crystal provides superior generation at the frequency of 2.34 THz [Fig. 4.17(b)]. At the highest peak intensity of $I_p=3.2 \text{ GW/cm}^2$, the BGS crystal shows an enhancement of 32% in comparison to the ZnTe crystal. The THz spectral density dependence on I_p is also investigated for the BGS crystal $\vec{E}_{exc} \parallel Z$ configuration. At the frequency of 2.34 THz [Fig. 4.17(d)], the spectral densities of the ZnTe crystal are higher than that from the BGS crystal. However, at the frequency of 1.97 THz, the BGS crystal provides superior generation for all investigated I_p [Fig. 4.17(c)]. At $I_p=3.2 \text{ GW/cm}^2$, the BGS crystal shows an improvement of 2 times relative to the ZnTe crystal.

It is necessary to consider the influence of multi-photon absorption on the intensity-dependent THz spectral densities shown in Fig. 4.17. The band gap of the BGS crystal is 2.64 eV [156], such that the 800 nm excitation pulse has the potential to induce the two-photon absorption process, provided it exhibits a sufficiently high intensity. This process produces electron-hole pairs by exciting electrons from the valence band to the conduction band, where these free carriers subsequently absorb THz radiation produced by the OR process. Notably, the two-photon absorption process is independent of the polarization of \vec{E}_{exc} , such that this process should be similar for both the $\vec{E}_{exc} \parallel X$ and $\vec{E}_{exc} \parallel Z$ excitation configurations. As seen from Fig. 4.17, minimal or no saturation of the BGS spectral densities are observed with increasing I_p . Alternatively, spectral density saturation is clearly evident for the ZnTe crystal. Therefore, the threshold for multi-photon absorption effects is higher for BGS in comparison to ZnTe, which is another beneficial property for THz radiation generation in the BGS crystal.

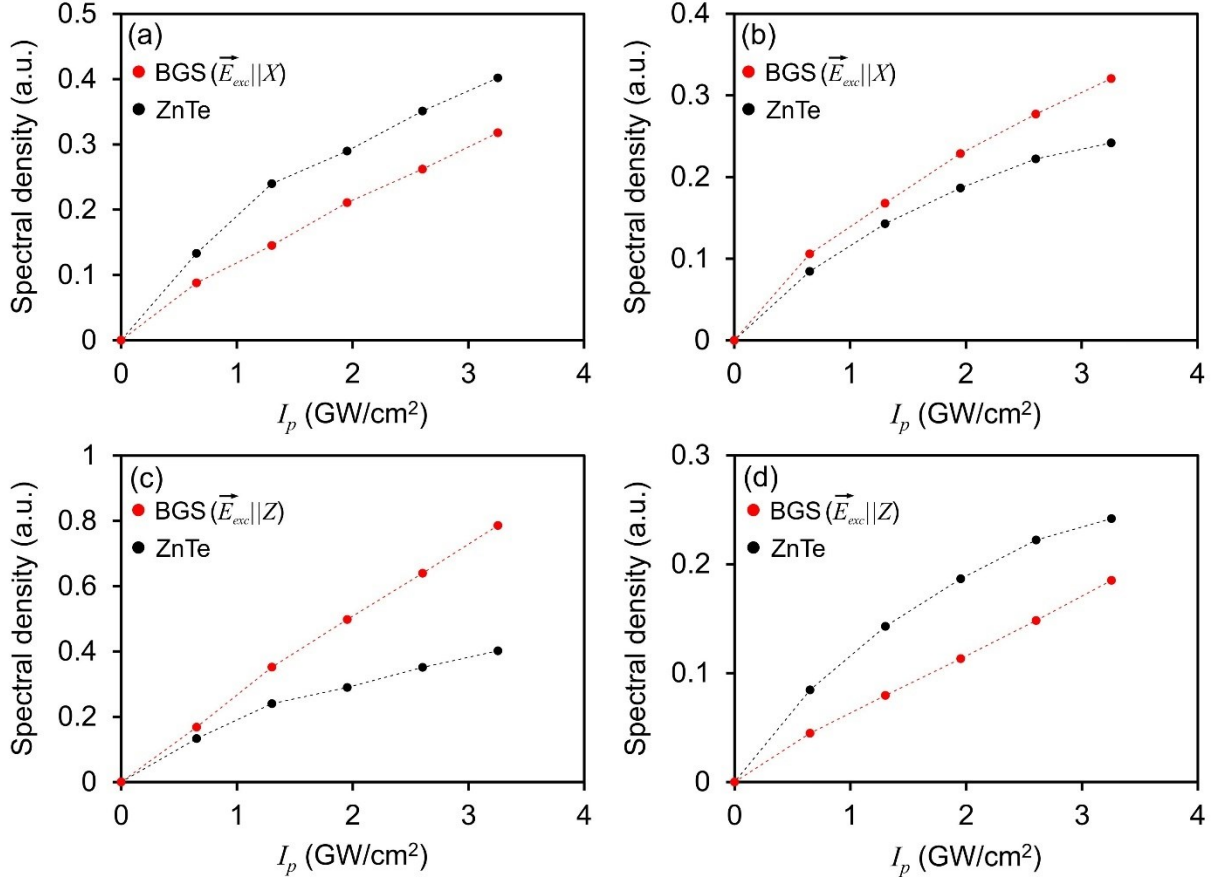


Fig. 4.17. Spectral densities at the frequencies of (a) 1.97 THz and (b) 2.34 THz, as generated from the BGS crystal $\vec{E}_{exc} \parallel X$ configuration and the ZnTe crystal configuration. Spectral densities at the frequencies of (c) 1.97 THz and (d) 2.34 THz, as generated from the BGS crystal $\vec{E}_{exc} \parallel Z$ configuration and the ZnTe crystal configuration.

4.4. THZ EO detection using a (012)-cut ZGP crystal⁶

ZGP exhibits a reasonable bandgap (i.e. 2 eV [44]) and transparency range (i.e. 0.74-12 μm [39]), as stated in Table 1.1, as well as an EO coefficient of $r_{41}=1.6 \text{ pm/V}$ [159]. In addition to

⁶A version of this section's work is published as B. N. Carnio, S. R. Greig, C. J. Firby, K. T. Zawilski, P. G. Schunemann, and A. Y. Elezzabi, "Terahertz electro-optic detection using a <012>-cut chalcopyrite ZnGeP₂ crystal," *Appl. Phys. Lett.* **108**, 261109 (2016).

these properties, phase-matching is crucial to the EO THz radiation detection process. In this section, a ZGP crystal is used to detect THz radiation via the linear EO effect and its phase-matching properties are compared against other crystals.

4.4.1. Excitation arrangement and linear THz radiation properties

The ZGP crystal was grown from a melt using the HGF method, as described in Ref. [160]. A 20 mm × 15 mm (012)-cut ZGP crystal having a thickness of 1080 μm was cut from a 240 g-sized single crystal boule. The ZGP unit cell and (012)-cut plane are illustrated in Fig. 4.18. The linear THz radiation properties of the ZGP crystal are determined using the THz-TDS system outlined in Chapter 3, but incorporating a GaAs PCA as the THz source, a 100 μm-thick, (110)-cut ZnTe EO crystal as the THz detector, and a 80 MHz, 10 fs, 780 nm Ti:Sapphire excitation laser. The generated THz radiation pulses are linearly polarized, have a center frequency at 1.2 THz, and have a bandwidth extending up to 3.8 THz. The complex refractive index of the ZGP crystal in the THz frequency regime is extracted using normal-incidence experimental transmission measurements and Eq. (4.2). Importantly, the THz electric field has polarization components along both the ordinary and extraordinary axes of the ZGP crystal, such that the calculated complex refractive index can be interpreted as an effective value influenced by both the ordinary and extraordinary complex refractive indices. This leads to effective values for the refractive index, n , extinction coefficient, κ , and absorption coefficient, α , of the ZGP crystal. As shown in Fig. 4.19(a), n varies between 3.35-3.45 over the investigated frequency range of 0.1-3.8 THz, which corresponds to a percent difference of only 3%. The increase in n above 2.6 THz is due to the interaction of the THz radiation pulse with the wing of the 4.26 THz phonon resonance. Over the frequency range of 0.1-3.8 THz, the ZGP crystal exhibits low THz loss (i.e. κ varies between

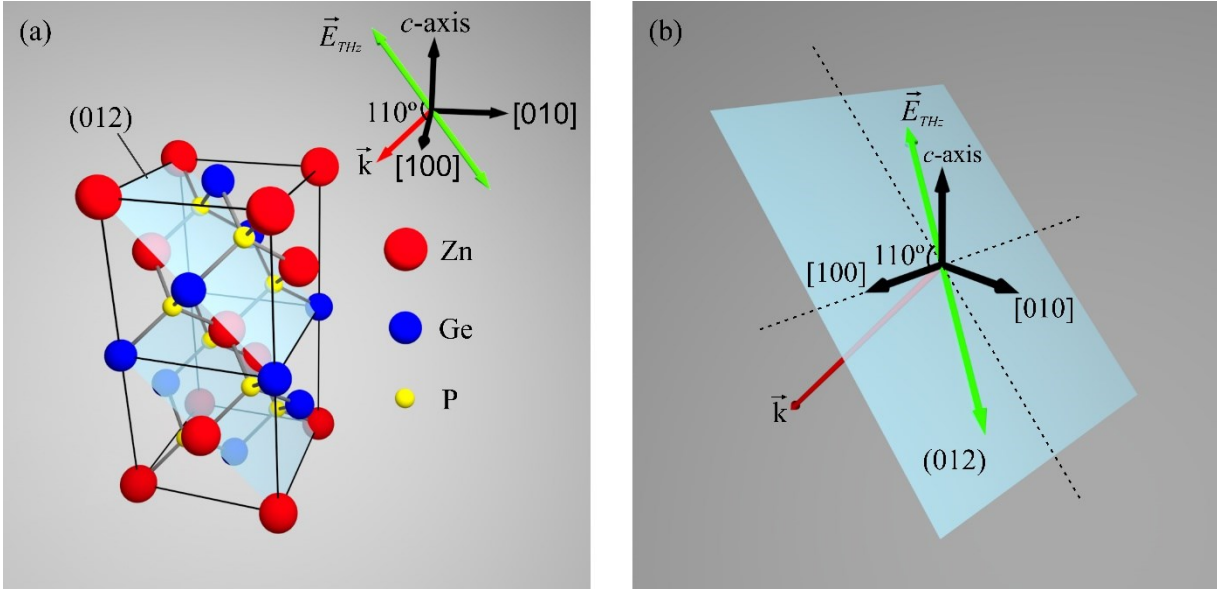


Fig. 4.18. (a) The unit cell and (012)-cut plane of the ZGP crystal. The illustration shows the polarization of the THz electric field in the EO detection measurements, which is rotated 110° with respect to the [100] crystallographic axis about the direction normal to the (012)-cut plane. \vec{k} is the wavevector of the THz electric field. (b) Schematic of the (012)-cut plane showing the THz polarization direction.

0.002-0.018), as shown in Fig. 4.19(a). With such small variation in n and a low κ , the ZGP crystal is expected to exhibit a flat EO response over this frequency range, provided that phase-matching is achieved between the THz radiation and the optical sampling probe pulse. Figure 4.19(b) shows α of the ZGP crystal, which is similar to that of ZnTe at frequencies between 0.1-2.6 THz [147]. At frequencies between 3-3.8 THz, the α of ZGP is 46% lower than that of ZnTe, due to the fact that a two-phonon process occurring in ZnTe causes significant absorption in the vicinity of 3.7 THz [161,162].

In the experimental transmission arrangement, a component of the THz electric field polarization is perpendicular to the c -axis of the crystal, such that all E phonon modes have the potential to be excited [42]. Nonetheless, no phonon features are evident at ~ 2.8 THz [see Fig.

4.19], corresponding to ZGP's lowest-frequency E phonon mode [163]. Interestingly, the absence of this mode is consistent with the IR reflection and transmission experiments reported in earlier studies [42,164], which measure all IR-active phonons except this particular mode. Such an observation is further supported by the data provided in Ref. [165], which shows what appears to be an extremely weak influence of this resonance in the measured reflectance data.

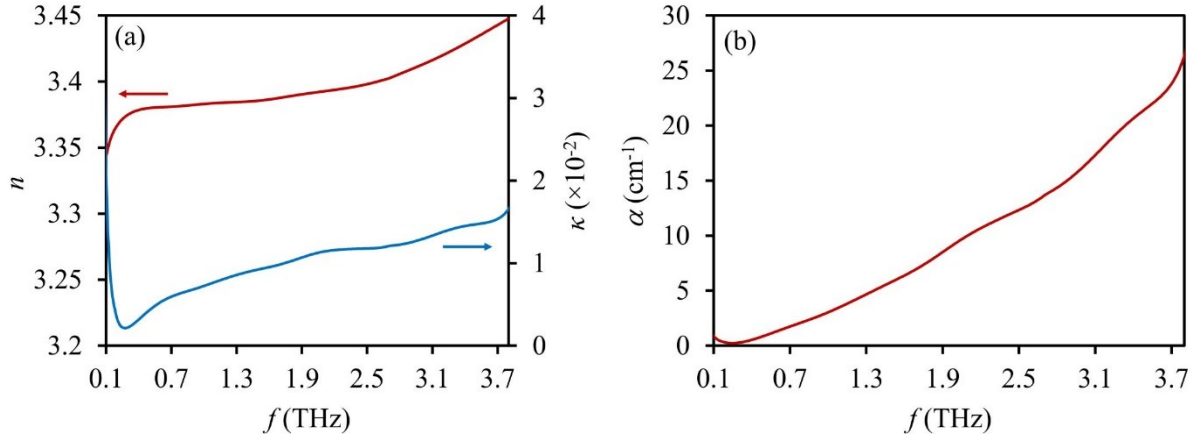


Fig. 4.19. (a) Refractive index and extinction coefficient of ZGP over the frequency range of 0.1-3.8 THz. (b) Absorption coefficient of ZGP over the frequency range of 0.1-3.8 THz.

4.4.2. EO sampling measurements

The EO detection properties of the ZGP crystal are compared to those of a 100 μm -thick ZnTe crystal and a 500 μm -thick ZnSe crystal. These crystals are integrated into the THz-TDS system [i.e. see Chapter 3] as THz detectors. In the ZGP crystal EO sampling measurements, the THz polarization is set at an angle of 110° with respect to its [100] crystallographic axis (see Fig. 4.18). As shown in Fig. 4.20(a), the EO signals of the ZnTe and ZnSe crystals are higher than that of the ZGP crystal by a factor of 4 and 27, respectively. The strength of an EO signal detected by a nonlinear crystal depends on numerous factors, including the crystal's point group symmetry and cut plane, as well as the polarization direction of the THz radiation and optical probe pulse.

The weaker EO strength measured by the ZGP crystal, in comparison to the ZnTe and ZnSe crystals, is likely due to a combination of such factors. Both the ZnTe and ZGP EO signals show pulse durations of ~ 0.8 ps, while the ZnSe crystal exhibits the longer pulse duration of ~ 1.4 ps. This suggests the ZnSe crystal does not possess the bandwidth necessary to detect the high-frequency THz radiation components emitted from the GaAs PCA. Figure 4.20(b) displays the spectral density measured by the three EO sampling crystals. Both the ZGP and ZnTe crystals show similar frequency responses up to the ~ 3.8 THz bandwidth limit of the GaAs PCA. Alternatively, the ZnSe crystal has a bandwidth extending up to ~ 1.7 THz, due to poor phase-matching between the THz radiation and the optical probe pulse.

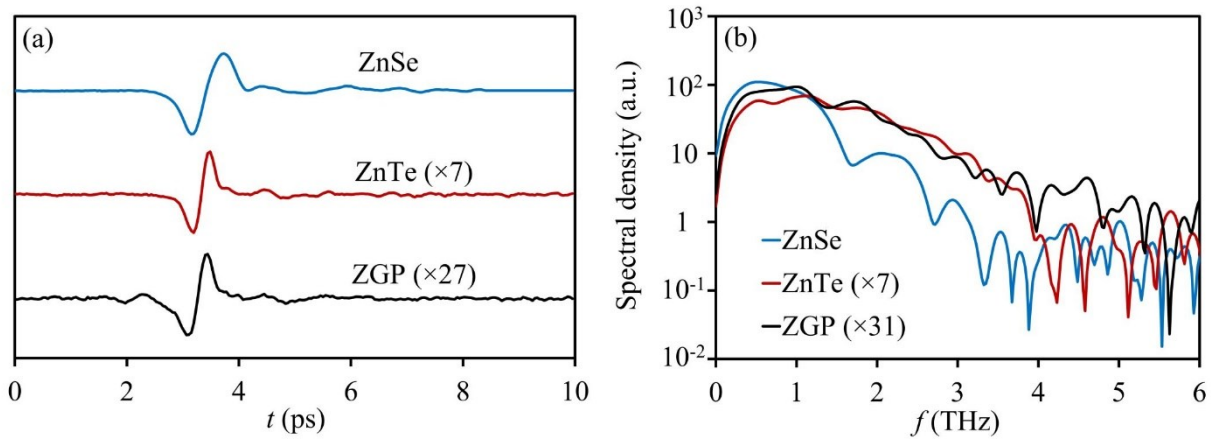


Fig. 4.20. (a) THz time-domain pulses and (b) spectral density obtained using ZGP, ZnTe, and ZnSe EO crystals. Spectral densities are scaled to facilitate bandwidth comparison.

The EO detection bandwidths of ZGP, ZnTe, ZnSe, and GaP crystals are investigated by computing the complex EO response function, given as [166],

$$\tilde{G}(\omega) = \frac{c}{i\omega\ell} \frac{e^{i\ell\omega[\tilde{n}(\omega) - n_g^p]/c} - 1}{\tilde{n}(\omega) - n_g^p}, \quad (4.8)$$

where ω is the angular frequency ($=2\pi f$), $\tilde{n}(\omega)$ is the complex refractive index [$= n(\omega) + i\kappa(\omega)$] at the angular frequency of ω , ℓ is the crystal thickness, and n_g^p is the group refractive index of the optical probe pulse. Notably, n_g^p for ZGP is experimentally determined by placing the crystal in the optical probe beam path of the THz-TDS system and measuring the time delay of the THz radiation pulse induced by the resulting time delay of the probe pulse. The normalized amplitude of the response function, $|\tilde{G}_{norm}(\omega)|$, is calculated for ZGP, ZnTe, ZnSe, and GaP crystals having thicknesses of 500 μm [see Fig. 4.21(a)] and 1080 μm [see Fig 4.21(b)]. For a thickness of 500 μm [i.e. Fig. 4.21(a)], the ZnSe detection bandwidth is severely limited by the low responses occurring at 1.64, 2.72, and 3.41 THz. When this response is compared with the ZnSe spectral power presented in Fig. 4.20(b), these frequencies are clearly identifiable, suggesting that Eq. (4.8) very accurately models the EO detection properties of the ZnSe crystal. The poor bandwidth response of ZnSe is a result of the large difference between the THz refractive index ($n > 3$ at the investigated THz frequencies [167]) and the optical group refractive index ($n_g^p = 2.75$ at 780 nm) [168]. Similarly, the GaP crystal exhibits a very limited detection bandwidth of < 1.7 THz, due to the large THz-optical index mismatch of 13% (i.e. $n \approx 3.2$ at frequencies between 0.1-3.8 THz and $n_g^p = 3.6$) [166]. The 500 μm -thick ZnTe crystal has a low response at frequencies > 3.3 THz, again due to the poor index matching (i.e. $n > 3.4$ at frequencies > 3.3 THz and $n_g^p = 3.28$) [147,166]. However, the ZGP crystal is capable of detecting all frequencies emitted from the GaAs PCA (i.e. 0.1-3.8 THz) as a result of its excellent phase-matching properties (i.e. $n = 3.35$ -3.45 at these THz frequencies, while $n_g^p = 3.43$). As such, the ZGP crystal has an EO detection bandwidth that is 1.2 times larger than that of ZnTe (i.e. < 3.3 THz) and more than twice as large as the bandwidth of the ZnSe and GaP crystals (i.e. $\lesssim 1.7$ THz).

For a crystal thickness of 1080 μm [i.e. Fig. 4.21(b)], both the ZnSe and GaP crystals exhibit bandwidths up to ~ 0.8 THz, while the ZnTe bandwidth ranges up to ~ 3 THz. As such, increasing the crystal thickness from 500 μm to 1080 μm reduces the EO detection bandwidths by 53% for ZnSe and GaP and 9% for ZnTe. Alternatively, as the crystal thickness increases, the ZGP crystal maintains its frequency response of 0.1-3.8 THz. At a thickness of 1080 μm , the ZGP crystal has an EO detection bandwidth that is 1.3 times larger than that of the ZnTe crystal and 4.8 times larger than that of the ZnSe and GaP crystals. Clearly, over the investigated frequency range, both the 500 and 1080 μm -thick ZGP crystals exhibit the most uniform EO frequency response of all the studied crystals.

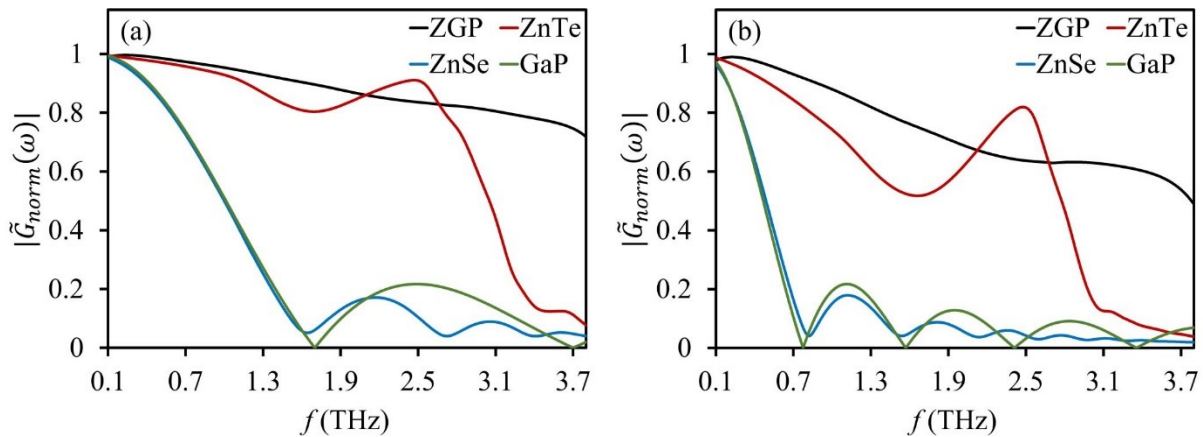


Fig. 4.21. The normalized amplitude of the response function for crystal thicknesses of (a) 500 μm and (b) 1080 μm .

4.5 Summary

OR THz radiation generation is experimentally investigated using the pnictide ternary crystal of CSP, as well as the chalcogenide ternary crystals of AGS and BGS. By using a CSP crystal having a thickness on the order of the coherence length (i.e. ~ 200 μm), the generated THz spectrum is expected to exhibit a uniform spectral distribution. While OR in the AGS crystal produced

phase-matched THz radiation generation over the entire crystal thickness of 485 μm , phase-matching is expected to be satisfied for crystal thicknesses up to ~ 800 nm (considering frequencies between 0.5-2.9 THz). OR in the BGS crystal produced narrowband (i.e. 50 GHz linewidth) THz radiation centered at the frequencies of 1.97 and 2.34 THz, where the spectral power at 1.97 THz was shown to be 4.5 times higher than that from a ZnTe crystal. This chapter also considered the phase-resolved detection of THz radiation using the pnictide ternary crystal of ZGP, where detection occurred via the linear EO effect. It was shown that ZGP exhibited a wider THz EO detection bandwidth than the conventional EO sensing crystals of ZnTe, ZnSe, and GaP. Such investigations are critical to advancing THz radiation generation and detection using the emerging pnictide and chalcogenide ternary crystal classes.

Chapter 5.

FDTD modeling of second-order nonlinear effects: A complete picture

The finite difference time domain (FDTD) technique has evolved to become one of the most powerful numerical methods for modeling EM phenomena and optical devices. In part, this is due to the simplicity of the numerical algorithm in calculating the evolution of the electric and magnetic fields in real time. While the FDTD technique would be ideal for modeling on-chip devices based on optical nonlinearities, the exploration of intricate and complex nonlinear interactions in on-chip structures have been constrained by inadequacies of nonlinear FDTD methods. To date, no complete second-order nonlinear optical formalism is available, not even by leading commercial software packages. In this Chapter, we develop methods capable of describing the complete second-order nonlinear picture (i.e. OR, DFG, SHG, SFG, and cascading interactions involving these processes) within FDTD simulations. The methods are capable of describing frequency-conversion from all 18 elements of the second-order nonlinear tensor, where dispersion of each tensor element is included. While such methods are capable of modeling arbitrary geometries, they are ideal for compact on-chip structures, such as waveguiding arrangements (see Section 1.5). Notably, to simplify the presentation of the equations derived in this chapter, the ‘ \sim ’ accent typically used to denote complex variables has been omitted.

5.1. Modeling of dispersive tensorial second-order nonlinear effects for the FDTD method: Implementing Miller's rule⁷

In general, the second-order nonlinear susceptibility is influenced by dispersion at the frequencies of the incident electric field, as well as dispersion at the frequencies of the generated electric field (see Chapter 2). Herein, we present a generalized FDTD formalism for modeling frequency-conversion from all 18 elements of the second-order nonlinear tensor, where dispersion of each tensor element is included at both the excitation and generated frequencies.

5.1.1. Derivation of the second-order nonlinear current density

Light interacting with a non-centrosymmetric material can be described by the current density, $J = J^{(1)} + J^{(2)}$, where $J^{(1)}$ and $J^{(2)}$ are the linear (i.e. first-order) and second-order current densities, respectively. Although $J^{(1)}$ and its implementation into an FDTD formalism has been well-established [169], a generalized FDTD formalism needs to be developed for nonlinear light interactions involving $J^{(2)}$. When a non-centrosymmetric material is excited using optical electric fields having frequencies of ω and $\Omega - \omega$, a $J^{(2)}$ is induced at the frequency Ω . The second-order nonlinear susceptibility tensor associated with such an interaction (utilizing contracted notation for the tensor elements) is written as,

$$\bar{\chi}^{(2)}(\Lambda) = \begin{bmatrix} \chi_{11}^{(2)}(\Lambda) & \chi_{12}^{(2)}(\Lambda) & \chi_{13}^{(2)}(\Lambda) & \chi_{14}^{(2)}(\Lambda) & \chi_{15}^{(2)}(\Lambda) & \chi_{16}^{(2)}(\Lambda) \\ \chi_{21}^{(2)}(\Lambda) & \chi_{22}^{(2)}(\Lambda) & \chi_{23}^{(2)}(\Lambda) & \chi_{24}^{(2)}(\Lambda) & \chi_{25}^{(2)}(\Lambda) & \chi_{26}^{(2)}(\Lambda) \\ \chi_{31}^{(2)}(\Lambda) & \chi_{32}^{(2)}(\Lambda) & \chi_{33}^{(2)}(\Lambda) & \chi_{34}^{(2)}(\Lambda) & \chi_{35}^{(2)}(\Lambda) & \chi_{36}^{(2)}(\Lambda) \end{bmatrix}, \quad (5.1)$$

⁷A version of this section's work is published as B. N. Carnio and A. Y. Elezzabi "A modeling of dispersive tensorial second-order nonlinear effects for the finite-difference time-domain method," *Opt. Express* **27**, 23432-23445 (2019).

where Λ represents ‘ $\Omega:\omega,\Omega-\omega$ ’. The tensor in Eq. (5.1), expressed using its non-contracted tensor element representation, is,

$$\bar{\chi}^{(2)}(\Lambda) = \begin{bmatrix} \chi_{xxx}^{(2)}(\Lambda) & \chi_{xyy}^{(2)}(\Lambda) & \chi_{xzz}^{(2)}(\Lambda) & \chi_{xyz}^{(2)}(\Lambda) & \chi_{xxz}^{(2)}(\Lambda) & \chi_{xxy}^{(2)}(\Lambda) \\ \chi_{yxx}^{(2)}(\Lambda) & \chi_{yyy}^{(2)}(\Lambda) & \chi_{yzz}^{(2)}(\Lambda) & \chi_{yyz}^{(2)}(\Lambda) & \chi_{yxz}^{(2)}(\Lambda) & \chi_{yyx}^{(2)}(\Lambda) \\ \chi_{zxx}^{(2)}(\Lambda) & \chi_{zyy}^{(2)}(\Lambda) & \chi_{zzz}^{(2)}(\Lambda) & \chi_{zyz}^{(2)}(\Lambda) & \chi_{zxx}^{(2)}(\Lambda) & \chi_{zxy}^{(2)}(\Lambda) \end{bmatrix}, \quad (5.2)$$

where $\chi_{hjk}^{(2)}$ is the second-order nonlinear susceptibility representing generation along the h axis due to excitations along the j and k axes. Notably, the subscripts h, j , and k are either x, y or z . Each individual element in the nonlinear tensor produces a second-order nonlinear polarization according to the following equation [139],

$$P_{h:j,k}^{(2)}(\Omega) = \varepsilon_0 \int_{-\infty}^{\infty} \chi_{hjk}^{(2)}(\Omega: \omega, \Omega - \omega) E_j(\omega) E_k(\Omega - \omega) d\omega, \quad (5.3)$$

where $E_{j,k}$ are the optical excitation electric fields having polarizations along the j and k axes, respectively. Moreover, the subscript $h:j,k$ signifies that excitation frequencies oriented along the j and k axes produce a second-order nonlinear polarization along the h axis. To incorporate second-order nonlinear dispersive effects, the FDTD model implements $\chi_{hjk}^{(2)}$ coefficients according to Miller’s rule [38],

$$\chi_{hjk}^{(2)}(\Omega: \omega, \Omega - \omega) = \delta_{hjk} \chi_h(\Omega) \chi_j(\omega) \chi_k(\Omega - \omega), \quad (5.4)$$

where δ_{hjk} is Miller’s proportionality constant and $\chi_{h,j,k}$ are the linear susceptibilities along the h, j , and k axes, respectively. It should be noted that Miller’s formalism inherently links the nonlinear dispersion of an optical material to the linear material dispersion, at both the excitation frequencies (i.e. ω and $\Omega-\omega$) and the generation frequency (i.e. Ω). It is interesting to note the similarities between Eq. (5.4) and Eqs. (2.48)-(2.53). Using the definition in Eq. (5.4) for $\chi_{hjk}^{(2)}$, Eq. (5.3) becomes,

$$P_{h:j,k}^{(2)}(\Omega) = \varepsilon_0 \delta_{hjk} \chi_h(\Omega) \int_{-\infty}^{\infty} S_j(\omega) S_k(\Omega - \omega) d\omega, \quad (5.5)$$

where,

$$S_{j,k}(\omega) = \chi_{j,k}(\omega) E_{j,k}(\omega). \quad (5.6)$$

The integral in Eq. (5.5) is the convolution operation, such that this equation can be recast in a more compact form,

$$P_{h:j,k}^{(2)}(\Omega) = \varepsilon_0 \delta_{hjk} \chi_h(\Omega) \{S_j * S_k\}(\Omega). \quad (5.7)$$

By transforming $P_{h:j,k}^{(2)}$ to the time-domain, we obtain,

$$P_{h:j,k}^{(2)}(t) = \varepsilon_0 \delta_{hjk} \{\chi_h * (S_j S_k)\}(t), \quad (5.8)$$

where t is time. Using Eq. (5.8), the complete set of second-order nonlinear polarizations along the x , y , and z axes are [170]:

$$P_x^{(2)}(t) = P_{x:x,x}^{(2)}(t) + P_{x:y,y}^{(2)}(t) + P_{x:z,z}^{(2)}(t) + 2P_{x:y,z}^{(2)}(t) + 2P_{x:x,z}^{(2)}(t) + 2P_{x:x,y}^{(2)}(t), \quad (5.9)$$

$$P_y^{(2)}(t) = P_{y:x,x}^{(2)}(t) + P_{y:y,y}^{(2)}(t) + P_{y:z,z}^{(2)}(t) + 2P_{y:y,z}^{(2)}(t) + 2P_{y:x,z}^{(2)}(t) + 2P_{y:x,y}^{(2)}(t), \quad (5.10)$$

$$P_z^{(2)}(t) = P_{z:x,x}^{(2)}(t) + P_{z:y,y}^{(2)}(t) + P_{z:z,z}^{(2)}(t) + 2P_{z:y,z}^{(2)}(t) + 2P_{z:x,z}^{(2)}(t) + 2P_{z:x,y}^{(2)}(t). \quad (5.11)$$

The second-order nonlinear polarizations are related to the second-order nonlinear current densities through:

$$J_x^{(2)}(t) = \frac{dP_x^{(2)}(t)}{dt}, \quad (5.12)$$

$$J_y^{(2)}(t) = \frac{dP_y^{(2)}(t)}{dt}, \quad (5.13)$$

$$J_z^{(2)}(t) = \frac{dP_z^{(2)}(t)}{dt}. \quad (5.14)$$

Equations (5.12)-(5.14) allow the full, dispersive second-order nonlinear susceptibility tensor to be implemented in the FDTD algorithm. Nonetheless, an accurate representation of the linear susceptibility is still required. Since most physical processes permit the linear susceptibility (i.e. $\chi_{h,j,k}$) to be represented by a frequency-independent term and a summation of Lorentzian oscillators, the linear susceptibility along the x , y , and z axes is,

$$\chi_{x,y,z}(\omega) = \chi_s^{x,y,z} + \sum_{m=1}^{Q^{x,y,z}} \frac{(\omega_m^{x,y,z})^2 \chi_m^{x,y,z}}{(\omega_m^{x,y,z})^2 - i\gamma_m^{x,y,z} \omega - \omega^2}, \quad (5.15)$$

where $\chi_s^{x,y,z}$ is the frequency-independent linear susceptibility, $\chi_m^{x,y,z}$ is the Lorentz susceptibility of the m^{th} Lorentzian oscillator, $\omega_m^{x,y,z}$ is the resonant angular frequency of the m^{th} Lorentzian oscillator, $\gamma_m^{x,y,z}$ is the damping factor of the m^{th} Lorentzian oscillator, and $Q^{x,y,z}$ is the number of Lorentzian oscillators used to describe the linear susceptibility.

5.1.2. Discretization of the second-order nonlinear current density

To discretize the $J_h^{(2)}$ terms in Eqs. (5.12)-(5.14), we must first discretize the $S_{j,k}$ and $P_{h;j,k}^{(2)}$ terms in Eq. (5.6) and Eq. (5.7), respectively. Using Eq. (5.15), $S_{j,k}$ is written as,

$$S_{j,k}(\omega) = G_s^{j,k}(\omega) + \sum_{m=1}^{Q^{j,k}} G_m^{j,k}(\omega), \quad (5.16)$$

where:

$$G_s^{j,k}(\omega) = \chi_s^{j,k} E_{j,k}(\omega), \quad (5.17)$$

$$G_m^{j,k}(\omega) = \frac{(\omega_m^{j,k})^2 \chi_m^{j,k}}{(\omega_m^{j,k})^2 - i\gamma_m^{j,k} \omega - \omega^2} E_{j,k}(\omega) \quad \text{for } m = 1, 2, \dots, Q^{j,k}. \quad (5.18)$$

To solve the term in Eq. (5.17), it is first transformed to the time-domain,

$$G_s^{j,k}(t) = \chi_s^{j,k} E_{j,k}(t). \quad (5.19)$$

Using temporal averaging of the $G_s^{j,k}$ term, Eq. (5.19) is then discretized for the time iteration of ρ to obtain,

$$G_s^{j,k}(\rho + 1) = 2\chi_s^{j,k} E_{j,k}(\rho) - G_s^{j,k}(\rho - 1), \quad (5.20)$$

where ρ is related to the time step, Δt , via the relationship $t = \rho \Delta t$. To solve Eq. (5.18), the terms are first rearranged to,

$$\begin{aligned} (\omega_m^{j,k})^2 G_m^{j,k}(\omega) - i\gamma_m^{j,k} \omega G_m^{j,k}(\omega) - \omega^2 G_m^{j,k}(\omega) \\ = (\omega_m^{j,k})^2 \chi_m^{j,k} E_{j,k}(\omega) \quad \text{for } m = 1, 2, \dots, Q^{j,k}. \end{aligned} \quad (5.21)$$

Next, using the fact that $-i\omega G_m^{j,k}(\omega) \Leftrightarrow \frac{dG_m^{j,k}(t)}{dt}$ and $-\omega^2 G_m^{j,k}(\omega) \Leftrightarrow \frac{d^2 G_m^{j,k}(t)}{dt^2}$, Eq. (5.21) is transformed to its time-domain form,

$$\begin{aligned} (\omega_m^{j,k})^2 G_m^{j,k}(t) + \gamma_m^{j,k} \frac{dG_m^{j,k}(t)}{dt} + \frac{d^2 G_m^{j,k}(t)}{dt^2} \\ = (\omega_m^{j,k})^2 \chi_m^{j,k} E_{j,k}(t) \quad \text{for } m = 1, 2, \dots, Q^{j,k}. \end{aligned} \quad (5.22)$$

Using central-differencing techniques, this equation is discretized for the time iteration ρ to obtain,

$$\begin{aligned} G_m^{j,k}(\rho + 1) = \frac{2\Delta t^2 (\omega_m^{j,k})^2 \chi_m^{j,k}}{\gamma_m^{j,k} \Delta t + 2} E_{j,k}(\rho) + \frac{4 - 2\Delta t^2 (\omega_m^{j,k})^2}{\gamma_m^{j,k} \Delta t + 2} G_m^{j,k}(\rho) \\ + \frac{\gamma_m^{j,k} \Delta t - 2}{\gamma_m^{j,k} \Delta t + 2} G_m^{j,k}(\rho - 1) \quad \text{for } m = 1, 2, \dots, Q^{j,k}. \end{aligned} \quad (5.23)$$

Now that both $G_s^{j,k}$ and $G_m^{j,k}$ have been retrieved in their discretized form, a solution for $S_{j,k}$ is obtained by converting Eq. (5.16) to the time-domain and discretizing it for the time iteration of $\rho+1$,

$$S_{j,k}(\rho + 1) = G_s^{j,k}(\rho + 1) + \sum_{m=1}^{Q^{j,k}} G_m^{j,k}(\rho + 1). \quad (5.24)$$

Importantly, $S_{j,k}(\rho)$ must also be obtained, which leads to the following equations:

$$G_s^{j,k}(\rho) = \chi_s^{j,k} E_{j,k}(\rho), \quad (5.25)$$

$$G_m^{j,k}(\rho) = \frac{2\Delta t^2 (\omega_m^{j,k})^2 \chi_m^{j,k}}{\gamma_m^{j,k} \Delta t + 2} E_{j,k}(\rho - 1) + \frac{4 - 2\Delta t^2 (\omega_m^{j,k})^2}{\gamma_m^{j,k} \Delta t + 2} G_m^{j,k}(\rho - 1) \\ + \frac{\gamma_m^{j,k} \Delta t - 2}{\gamma_m^{j,k} \Delta t + 2} G_m^{j,k}(\rho - 2) \quad \text{for } m = 1, 2, \dots, Q^{j,k}, \quad (5.26)$$

$$S_{j,k}(\rho) = G_s^{j,k}(\rho) + \sum_{m=1}^{Q^{j,k}} G_m^{j,k}(\rho). \quad (5.27)$$

Alternatively, $G_s^{j,k}(\rho)$ and $G_m^{j,k}(\rho)$ can instead be obtained from Eq. (5.20) and (5.23), which is achieved by using the results from the current time iteration at the next time iteration. Next, using Eq. (5.15), $P_{h:j,k}^{(2)}$ in Eq. (5.7) is recast as,

$$P_{h:j,k}^{(2)}(\Omega) = K_s^{hjk}(\Omega) + \sum_{m=1}^{Q^h} K_m^{hjk}(\Omega), \quad (5.28)$$

where:

$$K_s^{hjk}(\Omega) = \varepsilon_0 \delta_{hjk} \chi_s^h \{S_j * S_k\}(\Omega), \quad (5.29)$$

$$K_m^{hjk}(\Omega) = \varepsilon_0 \delta_{hjk} \frac{(\omega_m^h)^2 \chi_m^h}{(\omega_m^h)^2 - i\gamma_m^h \Omega - \Omega^2} \{S_j * S_k\}(\Omega) \quad \text{for } m = 1, 2, \dots, Q^h. \quad (5.30)$$

Equation (5.29) is solved by first converting it to the time-domain,

$$K_s^{hjk}(t) = \varepsilon_0 \delta_{hjk} \chi_s^h S_j(t) S_k(t), \quad (5.31)$$

and then discretizing it for the time iteration of $\rho+1$ to obtain,

$$K_s^{hjk}(\rho + 1) = \varepsilon_0 \delta_{hjk} \chi_s^h S_j(\rho + 1) S_k(\rho + 1). \quad (5.32)$$

Clearly, this depends on the solution to $S_{j,k}$, which is presented in Eq. (5.24). Equation (5.30) is solved by first rearranged it into the form,

$$\begin{aligned} (\omega_m^h)^2 K_m^{hjk}(\Omega) - i\gamma_m^h \Omega K_m^{hjk}(\Omega) - \Omega^2 K_m^{hjk}(\Omega) \\ = \varepsilon_0 \delta_{hjk} (\omega_m^h)^2 \chi_m^h \{S_j * S_k\}(\Omega) \quad \text{for } m = 1, 2, \dots, Q^h. \end{aligned} \quad (5.33)$$

Utilizing $-i\Omega K_m^{hjk}(\Omega) \Leftrightarrow \frac{dK_m^{hjk}(t)}{dt}$ and $-\Omega^2 K_m^{hjk}(\Omega) \Leftrightarrow \frac{d^2 K_m^{hjk}(t)}{dt^2}$ with Eq. (5.33), we obtain the time-domain equation,

$$\begin{aligned} (\omega_m^h)^2 K_m^{hjk}(t) + \gamma_m^h \frac{dK_m^{hjk}(t)}{dt} + \frac{d^2 K_m^{hjk}(t)}{dt^2} \\ = \varepsilon_0 \delta_{hjk} (\omega_m^h)^2 \chi_m^h S_j(t) S_k(t) \quad \text{for } m = 1, 2, \dots, Q^h. \end{aligned} \quad (5.34)$$

Using central-differencing techniques, Eq. (5.34) is discretized for the time iteration of ρ ,

$$\begin{aligned} K_m^{hjk}(\rho + 1) = \varepsilon_0 \delta_{hjk} \frac{2\Delta t^2 (\omega_m^h)^2 \chi_m^h}{\gamma_m^h \Delta t + 2} S_j(\rho) S_k(\rho) + \frac{4 - 2\Delta t^2 (\omega_m^h)^2}{\gamma_m^h \Delta t + 2} K_m^{hjk}(\rho) \\ + \frac{\gamma_m^h \Delta t - 2}{\gamma_m^h \Delta t + 2} K_m^{hjk}(\rho - 1) \quad \text{for } m = 1, 2, \dots, Q^h, \end{aligned} \quad (5.35)$$

where Eq. (5.35) depends on the $S_{j,k}$ solution in Eq. (5.27). Now that K_s^{hjk} and K_m^{hjk} are obtained in their discretized form, a discretized solution is attained for $P_{h:j,k}^{(2)}$ by converting Eq. (5.28) to the time-domain and discretizing it for the time iteration of $\rho+1$,

$$P_{h:j,k}^{(2)}(\rho + 1) = K_s^{hjk}(\rho + 1) + \sum_{m=1}^{Q^h} K_m^{hjk}(\rho + 1). \quad (5.36)$$

The above equation is the final, discretized form for $P_{h:j,k}^{(2)}$, where K_s^{hjk} and K_m^{hjk} are given in Eqs. (5.32) and (5.35), respectively. Finally, the discretization of $P_h^{(2)}$ [Eqs. (5.9)-(5.11)] for the time iteration of $\rho+1$ is straightforward and results in:

$$P_x^{(2)}(\rho + 1) = P_{x:x,x}^{(2)}(\rho + 1) + P_{x:y,y}^{(2)}(\rho + 1) + P_{x:z,z}^{(2)}(\rho + 1) + 2P_{x:y,z}^{(2)}(\rho + 1) + 2P_{x:x,z}^{(2)}(\rho + 1) + 2P_{x:x,y}^{(2)}(\rho + 1), \quad (5.37)$$

$$P_y^{(2)}(\rho + 1) = P_{y:x,x}^{(2)}(\rho + 1) + P_{y:y,y}^{(2)}(\rho + 1) + P_{y:z,z}^{(2)}(\rho + 1) + 2P_{y:y,z}^{(2)}(\rho + 1) + 2P_{y:x,z}^{(2)}(\rho + 1) + 2P_{y:x,y}^{(2)}(\rho + 1), \quad (5.38)$$

$$P_z^{(2)}(\rho + 1) = P_{z:x,x}^{(2)}(\rho + 1) + P_{z:y,y}^{(2)}(\rho + 1) + P_{z:z,z}^{(2)}(\rho + 1) + 2P_{z:y,z}^{(2)}(\rho + 1) + 2P_{z:x,z}^{(2)}(\rho + 1) + 2P_{z:x,y}^{(2)}(\rho + 1), \quad (5.39)$$

whereas the discretization of $J_h^{(2)}$ [Eqs. (5.12)-(5.14)] for the time iteration of $\rho+1/2$ provides:

$$J_x^{(2)}(\rho + 1/2) = \frac{P_x^{(2)}(\rho + 1) - P_x^{(2)}(\rho)}{\Delta t}, \quad (5.40)$$

$$J_y^{(2)}(\rho + 1/2) = \frac{P_y^{(2)}(\rho + 1) - P_y^{(2)}(\rho)}{\Delta t}, \quad (5.41)$$

$$J_z^{(2)}(\rho + 1/2) = \frac{P_z^{(2)}(\rho + 1) - P_z^{(2)}(\rho)}{\Delta t}. \quad (5.42)$$

To include second-order nonlinear effects in the FDTD formalism, these $J^{(2)}$ terms are incorporated in the update equations:

$$\begin{aligned}
E_x^{p-1/2,r,s}(\rho+1) &= E_x^{p-1/2,r,s}(\rho) - \frac{\Delta t}{\varepsilon_0 \varepsilon_{rx}} J_x^{(1)p-1/2,r,s} \left(\rho + \frac{1}{2} \right) \\
&\quad - \frac{\Delta t}{\varepsilon_0 \varepsilon_{rx}} J_x^{(2)p-1/2,r,s} \left(\rho + \frac{1}{2} \right)
\end{aligned} \tag{5.43}$$

$$\begin{aligned}
&+ \frac{\Delta t}{\varepsilon_0 \varepsilon_{rx} \Delta y} \left[H_z^{p-1/2,r+1/2,s} \left(\rho + \frac{1}{2} \right) - H_z^{p-1/2,r-1/2,s} \left(\rho + \frac{1}{2} \right) \right] \\
&- \frac{\Delta t}{\varepsilon_0 \varepsilon_{rx} \Delta z} \left[H_y^{p-1/2,r,s+1/2} \left(\rho + \frac{1}{2} \right) - H_y^{p-1/2,r,s-1/2} \left(\rho + \frac{1}{2} \right) \right],
\end{aligned}$$

$$\begin{aligned}
E_y^{p,r-1/2,s}(\rho+1) &= E_y^{p,r-1/2,s}(\rho) - \frac{\Delta t}{\varepsilon_0 \varepsilon_{ry}} J_y^{(1)p,r-1/2,s} \left(\rho + \frac{1}{2} \right) \\
&\quad - \frac{\Delta t}{\varepsilon_0 \varepsilon_{ry}} J_y^{(2)p,r-1/2,s} \left(\rho + \frac{1}{2} \right)
\end{aligned} \tag{5.44}$$

$$\begin{aligned}
&+ \frac{\Delta t}{\varepsilon_0 \varepsilon_{ry} \Delta z} \left[H_x^{p,r-1/2,s+1/2} \left(\rho + \frac{1}{2} \right) - H_x^{p,r-1/2,s-1/2} \left(\rho + \frac{1}{2} \right) \right] \\
&- \frac{\Delta t}{\varepsilon_0 \varepsilon_{ry} \Delta x} \left[H_z^{p+1/2,r-1/2,s} \left(\rho + \frac{1}{2} \right) - H_z^{p-1/2,r-1/2,s} \left(\rho + \frac{1}{2} \right) \right],
\end{aligned}$$

$$\begin{aligned}
E_z^{p,r,s-1/2}(\rho+1) &= E_z^{p,r,s-1/2}(\rho) - \frac{\Delta t}{\varepsilon_0 \varepsilon_{rz}} J_z^{(1)p,r,s-1/2} \left(\rho + \frac{1}{2} \right) \\
&\quad - \frac{\Delta t}{\varepsilon_0 \varepsilon_{rz}} J_z^{(2)p,r,s-1/2} \left(\rho + \frac{1}{2} \right)
\end{aligned} \tag{5.45}$$

$$\begin{aligned}
&+ \frac{\Delta t}{\varepsilon_0 \varepsilon_{rz} \Delta x} \left[H_y^{p+1/2,r,s-1/2} \left(\rho + \frac{1}{2} \right) - H_y^{p-1/2,r,s-1/2} \left(\rho + \frac{1}{2} \right) \right] \\
&- \frac{\Delta t}{\varepsilon_0 \varepsilon_{rz} \Delta y} \left[H_x^{p,r+1/2,s-1/2} \left(\rho + \frac{1}{2} \right) - H_x^{p,r-1/2,s-1/2} \left(\rho + \frac{1}{2} \right) \right],
\end{aligned}$$

$$\begin{aligned}
H_x^{p,r-1/2,s-1/2} \left(\rho + \frac{1}{2} \right) &= H_x^{p,r-1/2,s-1/2} \left(\rho - \frac{1}{2} \right) \\
+ \frac{\Delta t}{\mu_0 \Delta z} [E_y^{p,r-1/2,s}(\rho) - E_y^{p,r-1/2,s-1}(\rho)] & \\
- \frac{\Delta t}{\mu_0 \Delta y} [E_z^{p,r,s-1/2}(\rho) - E_z^{p,r-1,s-1/2}(\rho)], & \tag{5.46}
\end{aligned}$$

$$\begin{aligned}
H_y^{p-1/2,r,s-1/2} \left(\rho + \frac{1}{2} \right) &= H_y^{p-1/2,r,s-1/2} \left(\rho - \frac{1}{2} \right) \\
+ \frac{\Delta t}{\mu_0 \Delta x} [E_z^{p,r,s-1/2}(\rho) - E_z^{p-1,r,s-1/2}(\rho)] & \\
- \frac{\Delta t}{\mu_0 \Delta z} [E_x^{p-1/2,r,s}(\rho) - E_x^{p-1/2,r,s-1}(\rho)], & \tag{5.47}
\end{aligned}$$

$$\begin{aligned}
H_z^{p-1/2,r-1/2,s} \left(\rho + \frac{1}{2} \right) &= H_z^{p-1/2,r-1/2,s} \left(\rho - \frac{1}{2} \right) \\
+ \frac{\Delta t}{\mu_0 \Delta y} [E_x^{p-1/2,r,s}(\rho) - E_x^{p-1/2,r-1,s}(\rho)] & \\
- \frac{\Delta t}{\mu_0 \Delta x} [E_y^{p,r-1/2,s}(\rho) - E_y^{p-1,r-1/2,s}(\rho)], & \tag{5.48}
\end{aligned}$$

where p , r , and s are the spatial indices of the field components along the x , y , and z axes, respectively, Δx , Δy , and Δz are the mesh steps along the x , y , and z axes, respectively, H_x , H_y , and H_z are the magnetic field components along the x , y , and z axes, respectively, ϵ_{rx} , ϵ_{ry} , and ϵ_{rz} are the relative permittivities along the x , y , and z axes, respectively, and $J_x^{(1)}$, $J_y^{(1)}$, and $J_z^{(1)}$ are the dispersive parts of the linear components of the current densities along the x , y , and z axes, respectively.

5.1.3. Frequency-conversion in a LN crystal

The derived FDTD method is evaluated by simulating the representative effects of OR and DFG. These nonlinear effects are investigated using an LN crystal layer having a thickness ℓ , as illustrated in Fig. 5.1. LN serves as a prime material to evaluate the generalized second-order nonlinear method, since it exhibits strong nonlinear dispersion in the THz frequency regime, contains a nonlinear tensor with numerous non-vanishing elements, and has sufficient nonlinear experimental data available. The LN layer is excited using an electric field pulse having a central-wavelength of 1550 nm, a duration of 80 fs, and a polarization angle of θ_p with respect to the crystal's c -axis (see Fig. 5.1). Here, it is assumed that an index-matched layer and free-space are positioned at the input and output faces of the LN layer, respectively. The c -axis of the crystal is oriented along the z axis, the $[100]$ crystallographic axis is aligned with the x axis, and the y axis is defined as the direction of propagation. Since a bulk crystal is being simulated, periodic boundary conditions are implemented for the boundaries normal to the x and z axes, whereas

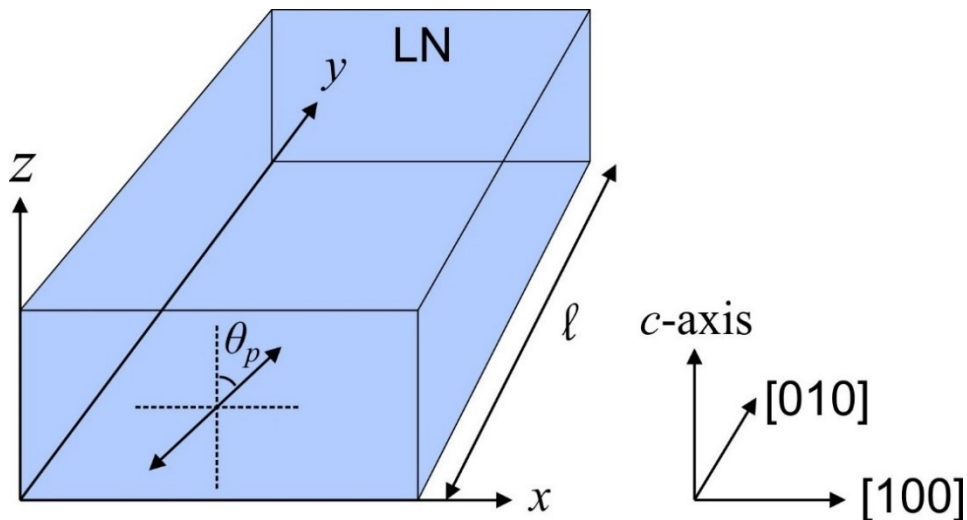


Fig. 5.1. An illustration of the LN crystal having a thickness ℓ and an excitation electric field polarization at the angle of θ_p with respect to the crystal's c -axis.

perfectly matched layers are used for the boundaries normal to the propagation direction (i.e. y axis). A mesh size of 40 nm is used, which is sufficiently small for both the excitation and generated frequency components.

It is critical to determine the frequency-dependence of the LN refractive indices, extinction coefficients, and second-order nonlinear susceptibilities. The extraordinary, n_e , and ordinary, n_o , refractive indices are shown in Fig. 5.2(a), 5.2(c), and 5.2(e) for the frequency ranges of interest. Furthermore, the extraordinary, κ_e , and ordinary, κ_o , extinction coefficients are shown in Fig. 5.2(b) and 5.2(d), respectively. The experimental data is obtained from Refs. [171,172] and the curve fits are achieved using a superposition of Lorentzian oscillators. Clearly, the fitted curves match the experimental data very well. Both n_e and κ_e show a phonon resonance at 7.6 THz, corresponding to the lowest-frequency A_1 mode of LN, whereas three E mode phonon resonances (located at 4.6, 7.9, and 9.7 THz) are observed in n_o and κ_o [171]. Since nonlinear dispersion is directly related to linear dispersion via Miller's rule, the $\chi^{(2)}$ elements of the LN crystal cannot be taken as constants. The LN crystal belongs to the $3m$ point group symmetry class, such that its second-order nonlinear susceptibility tensor is written as [173],

$$\bar{\chi}^{(2)}(\Lambda) = \begin{bmatrix} 0 & 0 & 0 & 0 & \chi_{15}^{(2)}(\Lambda) & -\chi_{22}^{(2)}(\Lambda) \\ -\chi_{22}^{(2)}(\Lambda) & \chi_{22}^{(2)}(\Lambda) & 0 & \chi_{15}^{(2)}(\Lambda) & 0 & 0 \\ \chi_{31}^{(2)}(\Lambda) & \chi_{31}^{(2)}(\Lambda) & \chi_{33}^{(2)}(\Lambda) & 0 & 0 & 0 \end{bmatrix}, \quad (5.49)$$

where Λ represents ' $\Omega, \omega, \Omega - \omega$ ' and $\chi_{15}^{(2)}(\Omega, \omega, \Omega - \omega)$, $\chi_{22}^{(2)}(\Omega, \omega, \Omega - \omega)$, $\chi_{31}^{(2)}(\Omega, \omega, \Omega - \omega)$, and $\chi_{33}^{(2)}(\Omega, \omega, \Omega - \omega)$ are the non-vanishing tensor elements. Notably, since the THz region exhibits significant dispersion, the Kleinman symmetry condition is invalid and the $\chi_{15}^{(2)}(\Omega, \omega, \Omega - \omega)$ element differs from the $\chi_{31}^{(2)}(\Omega, \omega, \Omega - \omega)$ element [31]. It may be important to note that contracted notation is being used in Eq. (5.49), where $\chi_{15}^{(2)}(\Omega, \omega, \Omega - \omega)$,

$\chi_{22}^{(2)}(\Omega, \omega, \Omega - \omega)$, $\chi_{31}^{(2)}(\Omega, \omega, \Omega - \omega)$, and $\chi_{33}^{(2)}(\Omega, \omega, \Omega - \omega)$ correspond to $\chi_{xxz}^{(2)}(\Omega, \omega, \Omega - \omega)$, $\chi_{yyy}^{(2)}(\Omega, \omega, \Omega - \omega)$, $\chi_{zxx}^{(2)}(\Omega, \omega, \Omega - \omega)$, and $\chi_{zzz}^{(2)}(\Omega, \omega, \Omega - \omega)$, respectively. From Eq. (5.3), (5.9), (5.11), (5.49), and the fact that propagation is along the y axis, it is determined that the second-order nonlinear polarizations occurring along the x and z axes are,

$$P_x^{(2)}(\Omega) = 2\varepsilon_0 \int_{-\infty}^{\infty} \chi_{15}^{(2)}(\Omega, \omega, \Omega - \omega) E_x(\omega) E_z(\Omega - \omega) d\omega, \quad (5.50)$$

and,

$$P_z^{(2)}(\Omega) = \varepsilon_0 \int_{-\infty}^{\infty} \chi_{31}^{(2)}(\Omega, \omega, \Omega - \omega) E_x(\omega) E_x(\Omega - \omega) d\omega \\ + \varepsilon_0 \int_{-\infty}^{\infty} \chi_{33}^{(2)}(\Omega, \omega, \Omega - \omega) E_z(\omega) E_z(\Omega - \omega) d\omega, \quad (5.51)$$

such that it is necessary to consider dispersion for the $\chi_{15}^{(2)}(\Omega, \omega, \Omega - \omega)$, $\chi_{31}^{(2)}(\Omega, \omega, \Omega - \omega)$, and $\chi_{33}^{(2)}(\Omega, \omega, \Omega - \omega)$ tensor elements. Figure 5.3(a) illustrates the highly-dispersive $\chi_{33}^{(2)}(\Omega, \omega, \Omega - \omega)$ element, which is calculated using Miller's rule [Eq. (5.4)], a proportionality constant of $\delta_{zzz}=1.3$ pm/V, and the experimental data from Refs. [98,174]. Similarly, the $\chi_{31}^{(2)}(\Omega, \omega, \Omega - \omega)$ element [see Fig. 5.3(b)] is obtained using a proportionality constant of $\delta_{zxx}=0.21$ pm/V and the experimental data from Ref. [175], whereas $\chi_{15}^{(2)}(\Omega, \omega, \Omega - \omega)$ [see Fig. 5.3(c)] is described using $\delta_{xxz}=0.71$ pm/V and the experimental data from Ref. [175]. Importantly, in comparison to the low-frequency (i.e. $\lesssim 1$ THz) nonlinear susceptibility values, all three of the nonlinear elements exhibit an enhancement of >7 times at their lowest-frequency phonon resonance.

To illustrate the implication of a dispersive second-order nonlinear susceptibility on the nonlinear frequency-conversion process, simulations are performed using $\ell=150$ μm and $\theta_p=0^\circ$,

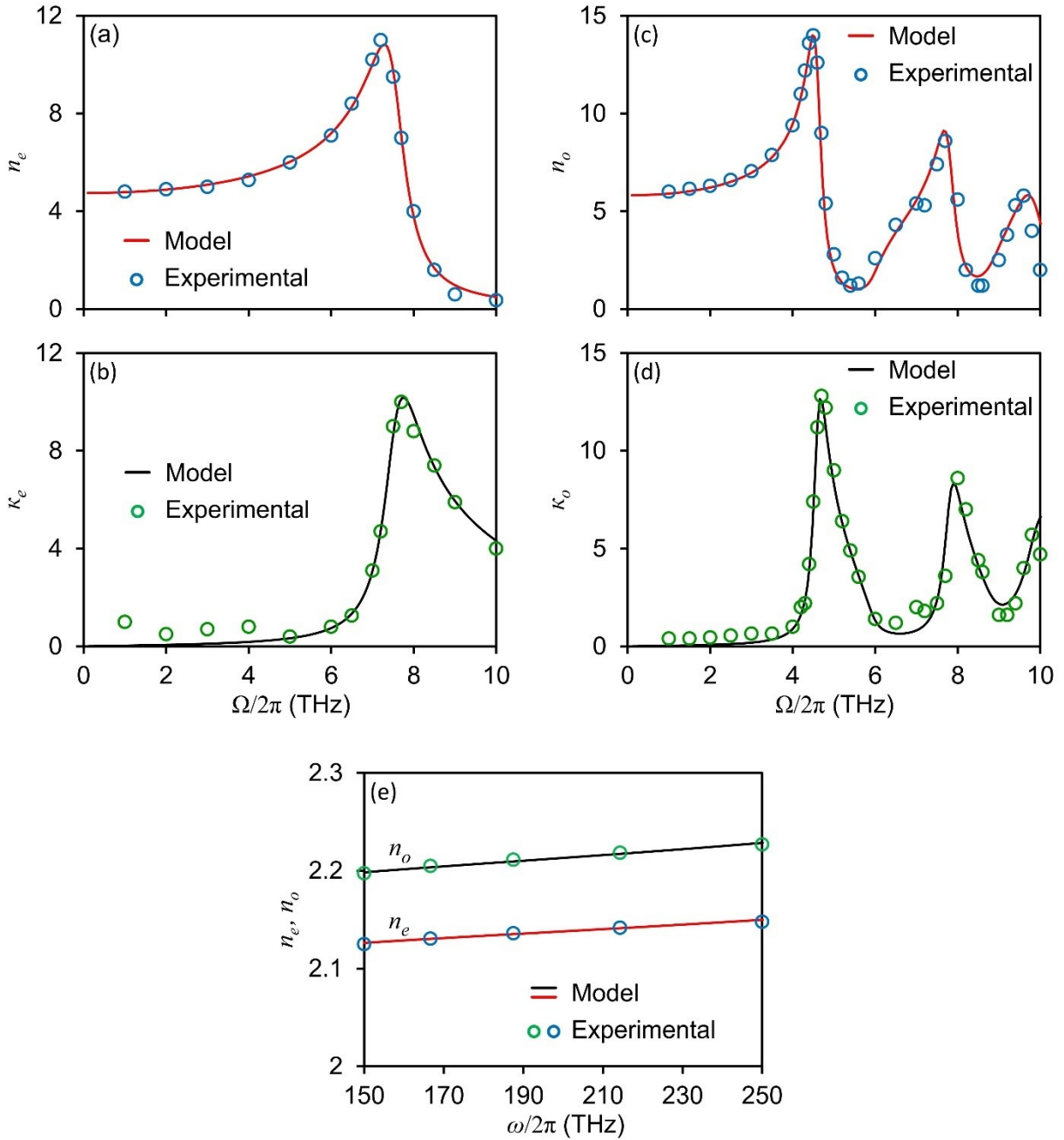


Fig. 5.2. (a) Refractive index and (b) extinction coefficient for the extraordinary LN crystal axis in the THz frequency regime. (c) Refractive index and (d) extinction coefficient for the ordinary LN crystal axis in the THz frequency regime. (e) Extraordinary and ordinary refractive indices in the optical frequency regime. The experimental data is obtained from Refs. [171,172] and the LN crystal is taken to be lossless in the optical regime.

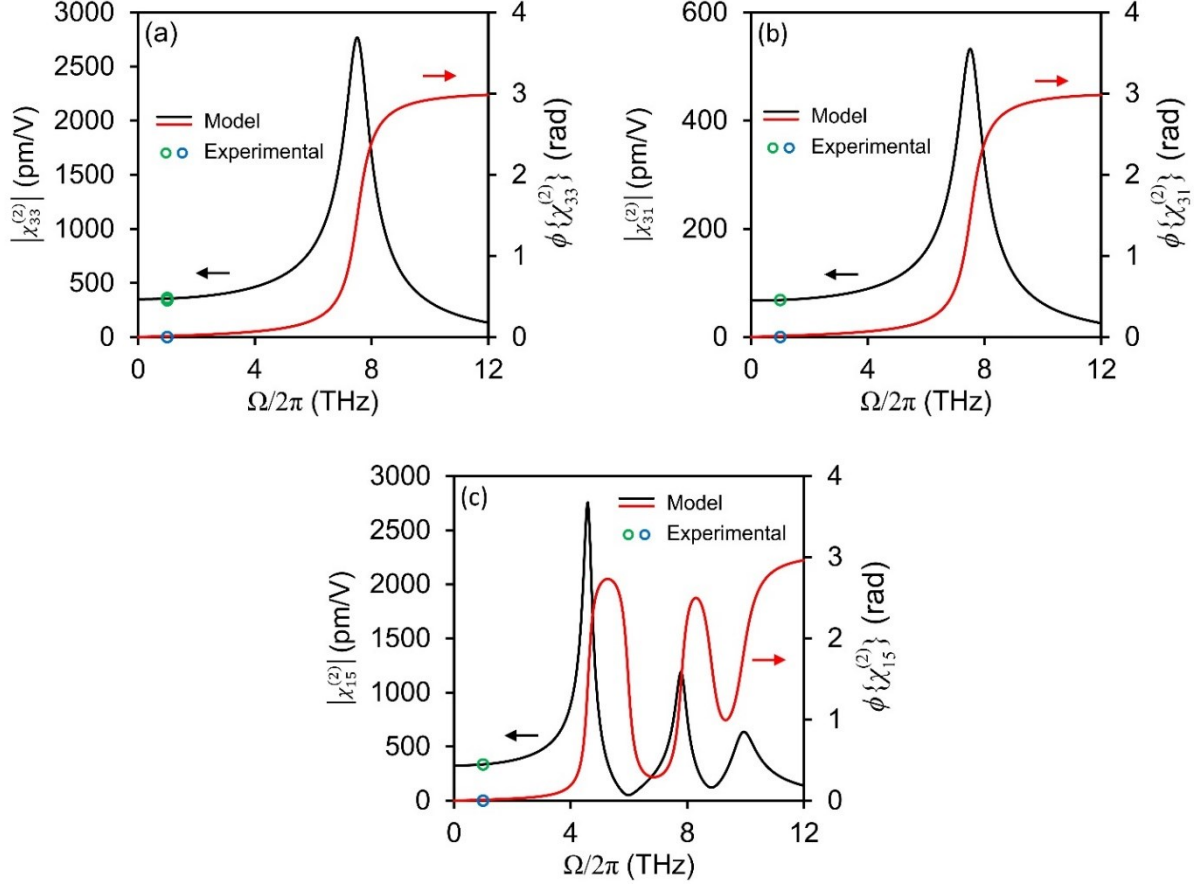


Fig. 5.3. Second-order nonlinear susceptibility elements of LN for (a) $\chi_{33}^{(2)}(\Omega, \omega, \Omega - \omega)$, (b) $\chi_{31}^{(2)}(\Omega, \omega, \Omega - \omega)$, and (c) $\chi_{15}^{(2)}(\Omega, \omega, \Omega - \omega)$. The curve fits are calculated using Miller's rule with the experimental data from Refs. [98,174,175].

such that the 1550 nm excitation pulse is polarized along the crystal's c -axis. Here, the only contributing nonlinear element is $\chi_{33}^{(2)}(\Omega, \omega, \Omega - \omega)$. The simulations are conducted using the fully-dispersive $\chi_{33}^{(2)}(\Omega, \omega, \Omega - \omega)$ element [see Fig. 5.3(a)], as well as the frequency-independent $\chi_{33}^{(2)}=348$ pm/V. Figure 5.4(a) depicts the spectral power generated along the z axis, \mathcal{SP}_z , where the phase-mismatching effects appear as dips in the spectral power (e.g. $f_d=0.8$ THz, 1.5 THz, etc.), in agreement with those predicted by the theoretical formula,

$$f_d = \frac{c\rho}{\ell |n_{e,g}^{exc} - n_e(f_d)|}, \quad (5.52)$$

where ρ is a positive integer, $n_{e,g}^{exc}$ is the extraordinary group refractive index at the excitation wavelength of 1550 nm, and $n_e(f_d)$ is the extraordinary refractive index at the frequency of f_d .

When comparing \mathcal{SP}_z obtained using the dispersive $\chi_{33}^{(2)}(\Omega, \omega, \Omega - \omega)$ and the frequency-independent $\chi_{33}^{(2)}=348$ pm/V, significant disagreement is evident, especially at frequencies near the 7.6 THz phonon resonance of the LN crystal. Figure 5.4(b) shows the relative spectral power, which is defined as \mathcal{SP}_z obtained using the dispersive $\chi_{33}^{(2)}(\Omega, \omega, \Omega - \omega)$ divided by \mathcal{SP}_z obtained using the frequency-independent $\chi_{33}^{(2)}=348$ pm/V. While the discrepancy in the relative spectral power is moderate at frequencies <6 THz, it is more than 60 times higher at frequencies near 7.6 THz. Therefore, a dispersive nonlinear element is critical to accurately modeling frequency-conversion near the phonon resonance of a crystal.

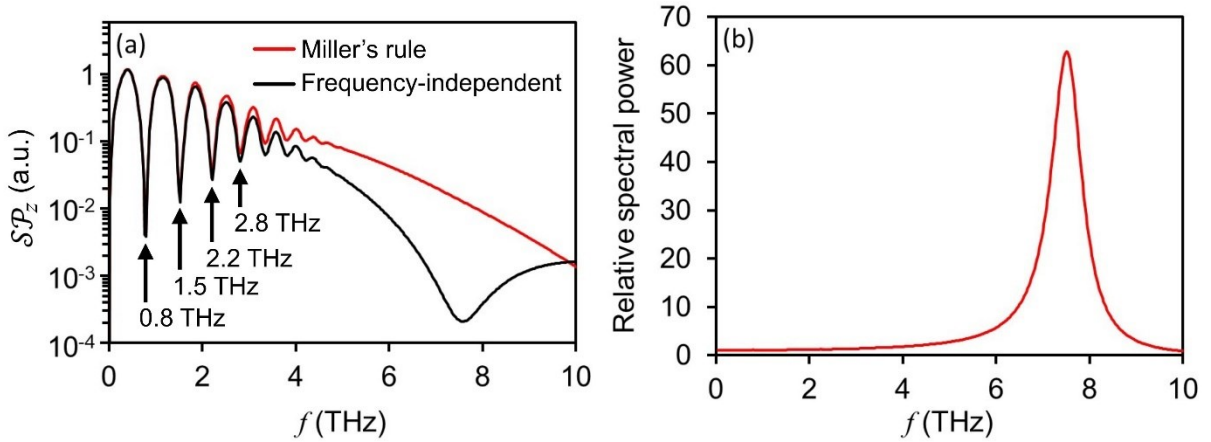


Fig. 5.4. (a) The z -component of the spectral power obtained using the dispersive $\chi_{33}^{(2)}(\Omega, \omega, \Omega - \omega)$ and the frequency-independent $\chi_{33}^{(2)}=348$ pm/V. (b) Relative spectral power calculated when implementing the dispersive $\chi_{33}^{(2)}(\Omega, \omega, \Omega - \omega)$ and the frequency-independent $\chi_{33}^{(2)}=348$ pm/V.

The nonlinear algorithm is also used to model DFG THz radiation generation in a LN crystal having $\ell=50\text{-}150\ \mu\text{m}$ and an excitation electric field pulse at $\theta_p=45^\circ$. In DFG, phase-matching can occur between the pump frequency, f_p , the signal frequency, f_s , and either the forward, f_i^+ , or backward, f_i^- , propagating idler frequencies. The forward propagation DFG coherence length, $L_c^{DFG,+}$, is,

$$L_c^{DFG,+} = \frac{c}{2} |n_p f_p - n_s f_s - n_i f_i^+|^{-1}, \quad (5.53)$$

and the backward propagation DFG coherence length, $L_c^{DFG,-}$, is,

$$L_c^{DFG,-} = \frac{c}{2} |n_p f_p - n_s f_s + n_i f_i^-|^{-1}, \quad (5.54)$$

where n_p , n_s , and n_i are the pump, signal, and idler refractive indices, respectively, and $f_i = |f_p - f_s|$. Since the excitation angle is $\theta_p=45^\circ$, the electric fields at f_p, f_s , and f_i^+ or f_i^- are polarized along the ordinary, extraordinary, and ordinary crystal axes, respectively. When considering THz radiation generation in the forward direction [i.e. Eq. (5.53)], phase-matching occurs at $f_i^+=3\ \text{THz}$ [see Fig. 5.5(a)]. This agrees with the FDTD model, where the x -component of the spectral power, \mathcal{SP}_x , exhibits THz radiation generation at $f_i^+=3\ \text{THz}$, as seen in Fig. 5.5(b). Similarly, $L_c^{DFG,-}$ from Eq. (5.54) is displayed in Fig. 5.5(c), which shows that phase-matching occurs at the idler frequency of $f_i^-=1.8\ \text{THz}$. By performing FDTD simulations and recording \mathcal{SP}_x near the input facet of the LN layer, we confirm that $f_i^-=1.8\ \text{THz}$ [see Fig. 5.5(d)]. Clearly, the versatility of this nonlinear FDTD approach arises from its ability in modeling excitation electric fields at arbitrary polarization states, along with the dispersive second-order nonlinear susceptibilities.

Next, by using $\ell=150\ \mu\text{m}$ and $\theta_p=0^\circ\text{-}90^\circ$, we examine the two simultaneous nonlinear frequency-conversion processes of DFG and OR in the THz frequency regime. These two

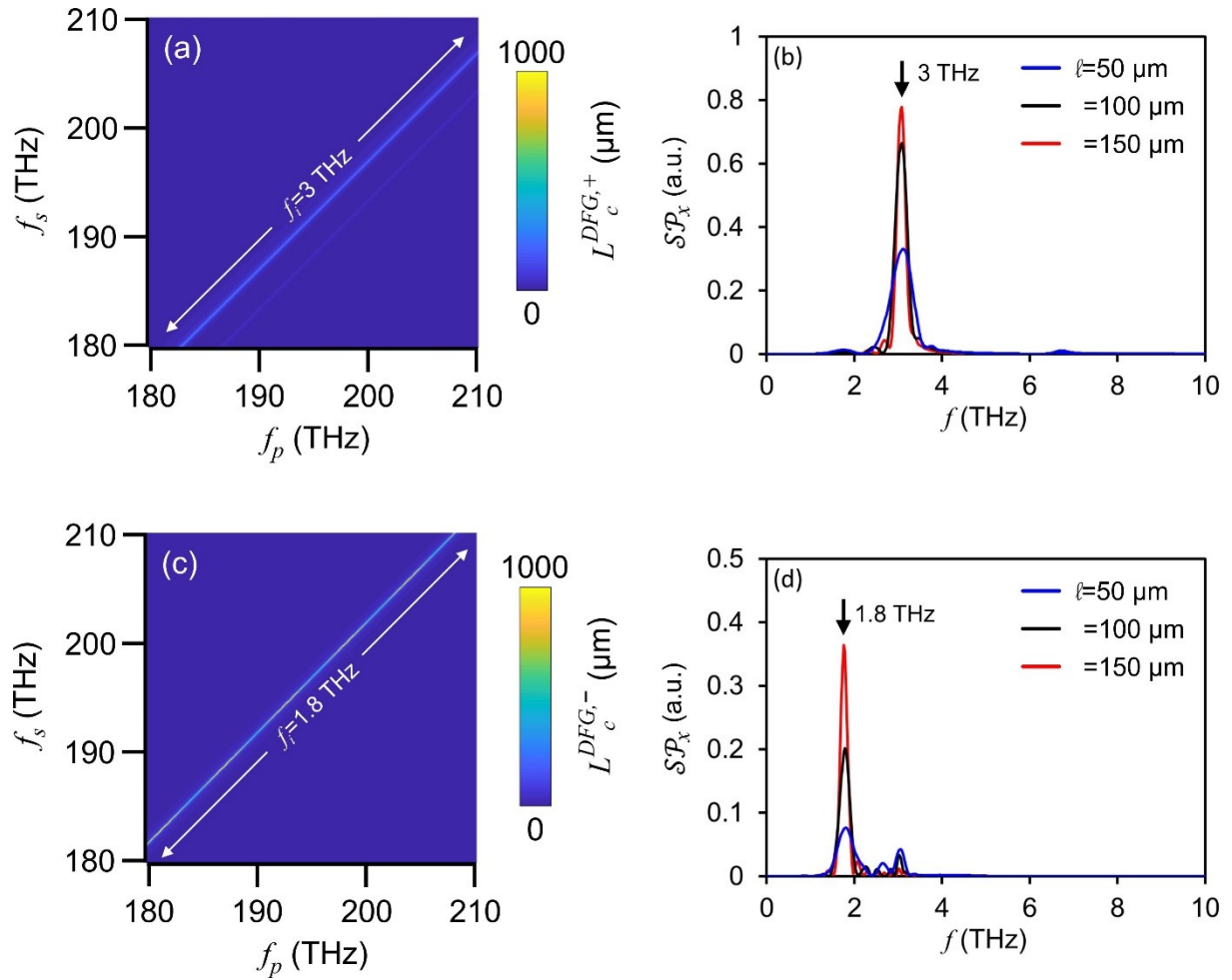


Fig. 5.5. (a) Coherence length for THz radiation produced in the forward direction. (b) The x -component of the spectral power recorded in free-space. (c) Coherence length for THz radiation produced in the backward direction. (d) The x -component of the spectral power recorded near the input face of the LN crystal.

processes depend on the polarization state of both the excitation electric field and the generated THz radiation. Broadband THz radiation polarized along the z axis is produced via OR, whereas narrowband THz radiation produced via DFG is polarized along the x axis. Figure 5.6(a) depicts $S P_z$, where THz radiation generation is highest when the excitation pulse is oriented along the crystal's c -axis (i.e. $\theta_p=0^\circ$), since $P_z^{(2)}$ is maximum and the only contribution is from the

$\chi_{33}^{(2)}(\Omega, \omega, \Omega - \omega)$ term [see Eq. (5.51)]. THz radiation generation decreases as θ_p increases, since the contribution from $\chi_{33}^{(2)}(\Omega, \omega, \Omega - \omega)$ is reduced; nonetheless, the weaker $\chi_{31}^{(2)}(\Omega, \omega, \Omega - \omega)$ coefficient now contributes to $P_z^{(2)}$. At $\theta_p=90^\circ$, THz radiation generation is lowest, since $P_z^{(2)}$ is only influenced by $\chi_{31}^{(2)}(\Omega, \omega, \Omega - \omega)$. Figure 5.6(b) depicts $\mathcal{S}\mathcal{P}_x$, where THz radiation generation vanishes at both $\theta_p=0^\circ$ and 90° , since $P_x^{(2)}=0$ [see Eq. (5.50)]. The power spectra are similar in magnitude at the intermediate angles of $\theta_p=22.5^\circ$ and 67.5° , whereas THz radiation generation is highest when $\theta_p=45^\circ$. As such, the presented generalized FDTD method is capable of modeling dispersive second-order nonlinear frequency-conversion processes that depend on the excitation polarization state and the generated electric field polarization.

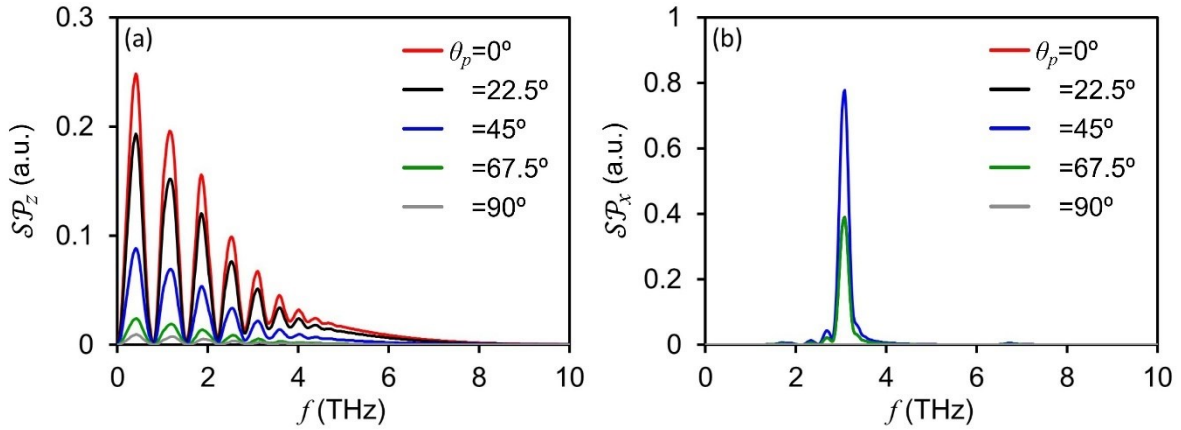


Fig. 5.6. (a) The z-component and (b) the x-component of the spectral power at various electric field polarization angles.

5.2. Modeling of dispersive tensorial second-order nonlinear effects for the FDTD method: Implementing the Faust-Henry model⁸

In the THz frequency regime, Miller’s rule can accurately describe crystals belonging to $3m$ symmetry group (e.g. LN and LiTaO₃), but is incapable of modeling $\bar{4}3m$ crystals (e.g. ZnTe, GaAs, GaP) [166,176–179]. This is due to the fact that, in $\bar{4}3m$ crystals, the ionic displacement and the excitation electric fields are out-of-phase at frequencies below the lattice resonance and are in-phase above it, such that the second-order nonlinear susceptibility dispersion does not follow the linear susceptibility dispersion [176]. Since crystals exhibiting $\bar{4}3m$ point group symmetry are frequently employed for THz radiation generation, it is crucial to develop an FDTD formalism to describe nonlinear frequency-conversion in this class of crystals. Here, we develop a nonlinear FDTD technique that utilizes the Faust-Henry model to describe dispersion of all 18 elements of the second-order nonlinear tensor. Unlike the formalism developed in Section 5.1, the Faust-Henry nonlinear FDTD technique is capable of modeling frequency-conversion near a phonon resonance in $\bar{4}3m$ crystals.

5.2.1. Nonlinear formalism

When the frequencies of ω and $\Omega-\omega$ are present in a non-centrosymmetric crystal, a second-order nonlinear polarization, $P_h^{(2)}$, is generated at the angular frequency of Ω ,

⁸A version of this section’s work is published as B. N. Carnio and A. Y. Elezzabi, “An extensive finite-difference time-domain formalism for second-order nonlinearities based on the Faust-Henry dispersion model: application to terahertz generation,” *J. Infrared Milli. Terahz. Waves* **41**, 291-298 (2020).

$$P_h^{(2)}(\Omega) = \sum_{j=x,y,z} \sum_{k=x,y,z} P_{h:j,k}^{(2)}(\Omega), \quad (5.55)$$

where h, j , and k represent the axes of x, y , or z . Each term in Eq. (5.55) is expressed as [139],

$$P_{h:j,k}^{(2)}(\Omega) = \varepsilon_0 \chi_{hjk}^{(2)}(\Omega) \{E_j * E_k\}(\Omega), \quad (5.56)$$

where $\chi_{hjk}^{(2)}$ are the second-order nonlinear susceptibility elements, E_j is the electric field along the j axis, E_k is the electric field along the k axis, and,

$$\{E_j * E_k\}(\Omega) = \int_{-\infty}^{\infty} E_j(\omega) E_k(\Omega - \omega) d\omega, \quad (5.57)$$

represents the convolution operation. The Faust-Henry model for $\chi_{hjk}^{(2)}$ is described by [176],

$$\chi_{hjk}^{(2)}(\Omega) = \chi_E^{hjk} + \sum_{m=1}^{Q^{hjk}} \frac{(\Omega_m^{hjk})^2 \chi_E^{hjk} C_m^{hjk}}{(\Omega_m^{hjk})^2 - i\gamma_m^{hjk} \Omega - \Omega^2}, \quad (5.58)$$

where χ_E^{hjk} is the electronic component of the second-order nonlinear susceptibility, C_m^{hjk} is the Faust-Henry coefficient, Ω_m^{hjk} is the resonant angular frequency, γ_m^{hjk} is the damping factor, and Q^{hjk} is the number of Lorentzian oscillators. Using Eq. (5.58), Eq. (5.56) is written as,

$$P_{h:j,k}^{(2)}(\Omega) = \varepsilon_0 \chi_E^{hjk} \{E_j * E_k\}(\Omega) + \sum_{m=1}^{Q^{hjk}} \frac{(\Omega_m^{hjk})^2 \varepsilon_0 \chi_E^{hjk} C_m^{hjk}}{(\Omega_m^{hjk})^2 - i\gamma_m^{hjk} \Omega - \Omega^2} \{E_j * E_k\}(\Omega). \quad (5.59)$$

By defining the time as $t = \rho \Delta t$, where Δt is the time step at an increment ρ , Eq. (5.59) can be transformed to the time-domain and discretized according to the techniques discussed in Section 5.1, such that,

$$P_{h:j,k}^{(2)}(\rho + 1) = P_s^{(2)}(\rho + 1) + \sum_{m=1}^{Q^{hjk}} P_m^{(2)}(\rho + 1), \quad (5.60)$$

where:

$$P_s^{(2)}(\rho + 1) = 2\varepsilon_0\chi_E^{hjk} E_j(\rho)E_k(\rho) - P_s^{(2)}(\rho - 1), \quad (5.61)$$

$$P_m^{(2)}(\rho + 1) = \frac{2(\Omega_m^{hjk})^2 \varepsilon_0 \Delta t^2 \chi_E^{hjk} C_m^{hjk}}{\gamma_m^{hjk} \Delta t + 2} E_j(\rho)E_k(\rho) + \frac{4 - 2(\Omega_m^{hjk})^2 \Delta t^2}{\gamma_m^{hjk} \Delta t + 2} P_m^{(2)}(\rho) \\ + \frac{\gamma_m^{hjk} \Delta t - 2}{\gamma_m^{hjk} \Delta t + 2} P_m^{(2)}(\rho - 1). \quad (5.62)$$

The discretized second-order nonlinear polarization equation is,

$$P_h^{(2)}(\rho + 1) = \sum_{j=x,y,z} \sum_{k=x,y,z} P_{h:j,k}^{(2)}(\rho + 1). \quad (5.63)$$

This $P_h^{(2)}$ term can be used to obtain the second-order nonlinear current density,

$$J_h^{(2)}\left(\rho + \frac{1}{2}\right) = \frac{P_h^{(2)}(\rho + 1) - P_h^{(2)}(\rho)}{\Delta t}, \quad (5.64)$$

which is included in the FDTD update equations [see Eqs. (5.43)-(5.48)].

5.2.2. OR in a ZnTe Crystal

The developed FDTD formalism is used to study OR near the phonon resonance of a ZnTe crystal, such that it is necessary to define the dispersive second-order nonlinear susceptibility coefficient, $\chi_{36}^{(2)}(\Omega)$ [i.e. $\chi_{zxy}^{(2)}(\Omega)$ in non-contracted notation]. Figure 5.7 shows $\chi_{36}^{(2)}(\Omega)$ calculated using the Faust-Henry dispersion model, where the parameters [$\chi_E^{zxy}=139$ pm/V, $C_1^{zxy}=-0.07$ pm/V, $\Omega_1^{zxy}/(2\pi)=5.3$ THz, $\gamma_1^{zxy}/(2\pi)=0.09$ THz, and $Q^{zxy}=1$] are determined using Refs. [96,166]. At the frequency of 5.1 THz, $|\chi_{36}^{(2)}(\Omega)|$ experiences a minimum, whereas $|\chi_{36}^{(2)}(\Omega)|$ is maximum at 5.3 THz. This is opposite to the behavior of the refractive index near a phonon resonance (i.e. as the frequency increases, the refractive index exhibits a maximum value followed by a minimum value). Notably, this difference between the linear and nonlinear THz radiation

properties is responsible for the inability of Miller's rule to describe $\chi_{36}^{(2)}(\Omega)$, and the need to implement the Faust-Henry dispersion model.

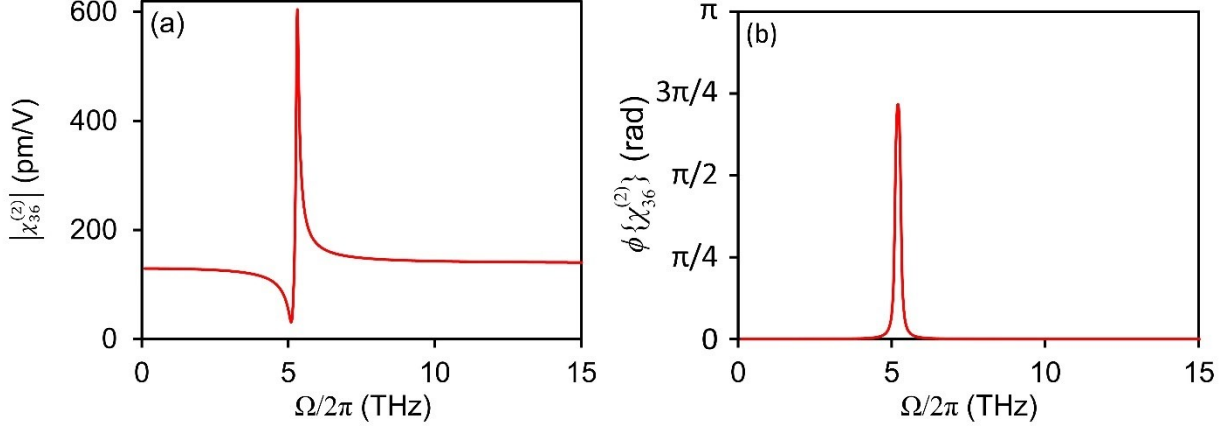


Fig. 5.7. (a) Magnitude and (b) phase of $\chi_{36}^{(2)}(\Omega)$ for ZnTe, as defined by the Faust-Henry model for dispersion. The Faust-Henry curve fitting parameters are obtained from Refs. [96,166].

A schematic of the ZnTe crystal and excitation arrangement is shown in Fig. 5.8. The (110)-cut ZnTe crystal of thickness ℓ is excited using an electric field pulse having a duration of 80 fs, a central-wavelength of 800 nm, and polarized at an angle of 45° relative to the crystal's c -axis (i.e. z axis). Since SiO₂ is a commonly-used substrate material, the ZnTe crystal is surrounded by a SiO₂ layer at the input face and free-space at the output face. Along the coordinate system defined in Fig. 5.8, the $\chi_{36}^{(2)}(\Omega)$ coefficient for the (110)-cut ZnTe crystal is related to the second-order nonlinear polarizations via,

$$\begin{bmatrix} P_x^{(2)}(\Omega) \\ P_y^{(2)}(\Omega) \\ P_z^{(2)}(\Omega) \end{bmatrix} = \epsilon_0 \begin{bmatrix} 0 & 0 & 0 & 0 & -\chi_{36}^{(2)}(\Omega) & 0 \\ 0 & 0 & 0 & \chi_{36}^{(2)}(\Omega) & 0 & 0 \\ -\chi_{36}^{(2)}(\Omega) & \chi_{36}^{(2)}(\Omega) & 0 & 0 & 0 & 0 \end{bmatrix} \begin{bmatrix} \{E_x * E_x\}(\Omega) \\ \{E_y * E_y\}(\Omega) \\ \{E_z * E_z\}(\Omega) \\ 2\{E_y * E_z\}(\Omega) \\ 2\{E_x * E_z\}(\Omega) \\ 2\{E_x * E_y\}(\Omega) \end{bmatrix}. \quad (5.65)$$

Therefore, exciting the ZnTe crystal using electric fields polarized along the x and z axes induce both $P_x^{(2)}$ and $P_z^{(2)}$.

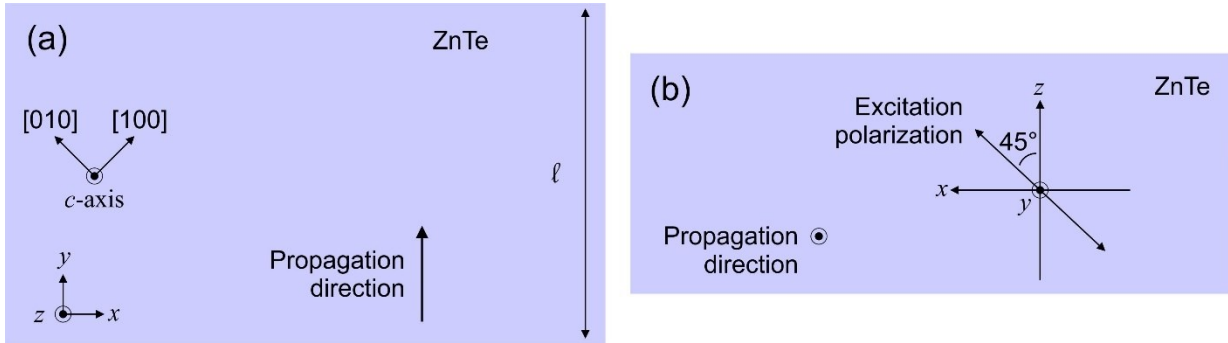


Fig. 5.8. Illustration of the ZnTe crystal (a) perpendicular and (b) parallel to the propagation direction of the electric fields. The ZnTe crystal is excited at a polarization angle of 45° relative to the c -axis of the crystal.

OR is investigated in thin film ZnTe crystals, which have the potential for enhanced THz radiation generation near the phonon resonance. Notably, when investigating OR in the isotropic ZnTe crystal, the generated THz radiation polarized along the x and z axes are identical except for a constant scaling factor. Figure 5.9(a) depicts the THz time-domain electric field pulses generated in $\ell=0.1-1 \mu\text{m}$ ZnTe crystals and emitted into free-space. The oscillations following the main pulses have a frequency of 5.3 THz and are due to the phonon resonance. The spectral power of the generated radiation, \mathcal{SP} , is shown in Fig. 5.9(b). For $\ell=0.1-0.2 \mu\text{m}$, reduced generation is observed at the frequency of 5.1 THz and enhanced generation occurs at the frequency of 5.3 THz, in good agreement with $|\chi_{36}^{(2)}(\Omega)|$ [see Fig. 5.7(a)]. In the $\ell=0.5-1 \mu\text{m}$ crystals, phonon loss becomes appreciable and the enhanced THz radiation generation at 5.3 THz is less evident. Clearly, the Faust-Henry FDTD formalism is capable of modeling frequency-conversion processes in the ZnTe crystal, even across spectral regions that exhibit high $\chi_{36}^{(2)}(\Omega)$ dispersion.

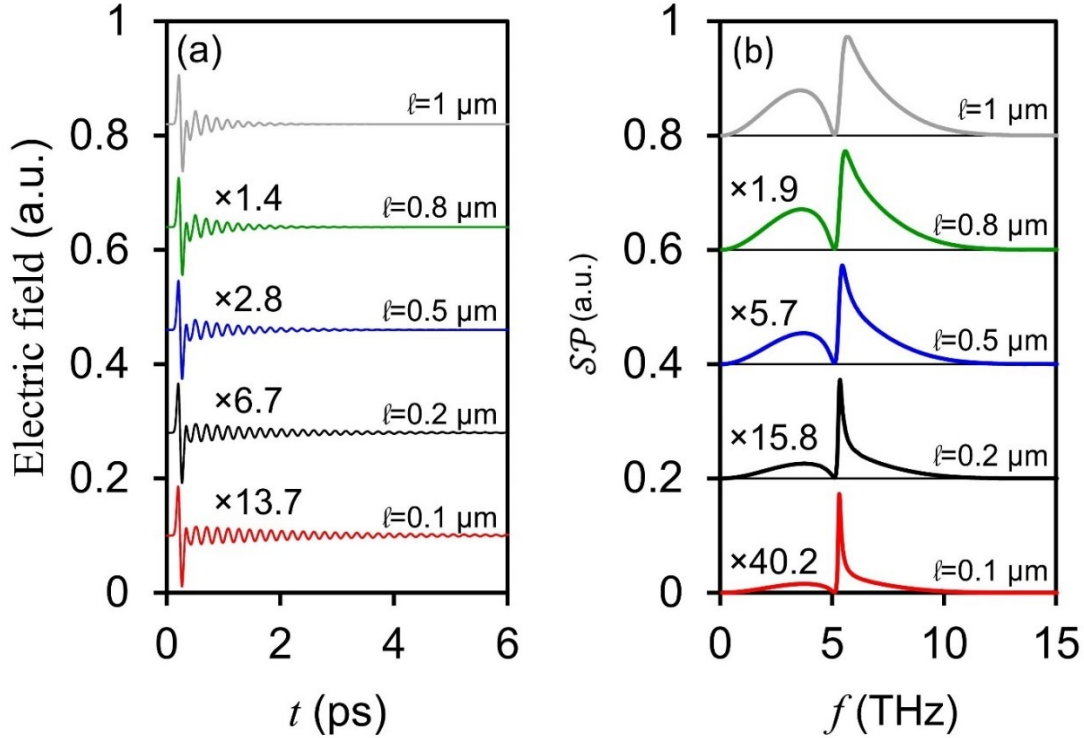


Fig. 5.9. (a) THz time-domain electric fields and (b) spectral powers produced by OR in thin film ZnTe crystals having $\ell=0.1\text{-}1 \mu\text{m}$.

Although THz radiation generation has been demonstrated at the phonon resonance of very thin (i.e. $\ell=0.1\text{-}1 \mu\text{m}$) ZnTe crystals, the shape of the THz radiation spectrum varies significantly for thicker crystals, due to phase-mismatching effects, multiple reflections occurring within the crystal, and strong phonon mode absorption loss. Figure 5.10(a) illustrates THz radiation generation from ZnTe crystals having thicknesses of $\ell=10\text{-}40 \mu\text{m}$. The time-domain electric field signals are obviously shorter in comparison to the signals obtained from the thin film ZnTe crystals [see Fig. 5.9(a)] and exhibit lower-amplitude phonon oscillations. By examining Fig. 5.10(b), it is clear that the S_P vanishes at frequencies within the range of $\sim 5\text{-}6$ THz, which spans the phonon absorption linewidth. Notably, multiple peaks are evident in the spectra, which are due to phase-mismatching effects and multiple reflections in the crystal.

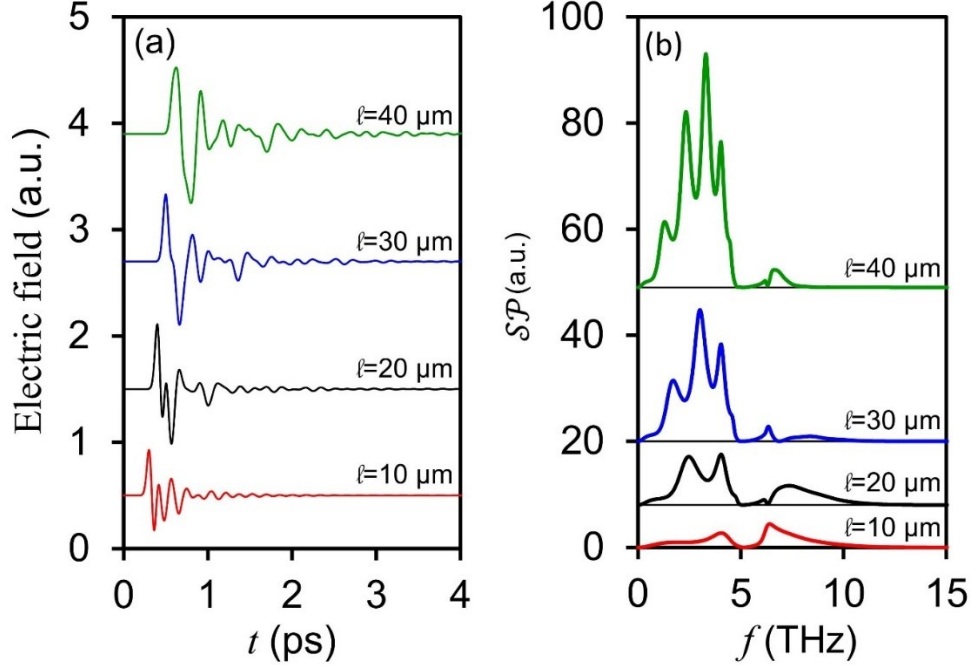


Fig. 5.10. (a) THz time-domain electric fields and (b) spectral powers from ZnTe crystals having $l=10\text{-}40\ \mu\text{m}$. The time-domain signals and the power spectra are to scale with the data presented in Fig. 5.9.

To illustrate that the nonlinear formalism is capable of modeling THz radiation generation from arbitrary elements of the nonlinear tensor [see Eq. (5.65)], we investigate THz radiation generation along the x axis [i.e. $P_x^{(2)}(\Omega) = -2\chi_{36}^{(2)}(\Omega)\{E_x * E_z\}(\Omega)$] and z axis [i.e. $P_z^{(2)}(\Omega) = -\chi_{36}^{(2)}(\Omega)\{E_x * E_x\}(\Omega)$]. When considering the $l=1\ \mu\text{m}$ ZnTe crystals, the x and z -polarized time-domain signals [Fig. 5.11(a)] have the same shape, but their amplitudes differ by a factor of two. This is in agreement with the theoretical formulas,

$$E_x(\Omega) \propto \sin(2\theta_p), \quad (5.66)$$

and

$$E_z(\Omega) \propto \sin^2(\theta_p), \quad (5.67)$$

where $\theta_p (=45^\circ)$ is the angle between the z axis and the excitation polarization direction, such that $E_x=2E_z$. Similarly, the corresponding spectra [Fig. 5.11(b)] have the same shape and differ in magnitude by a factor of four.

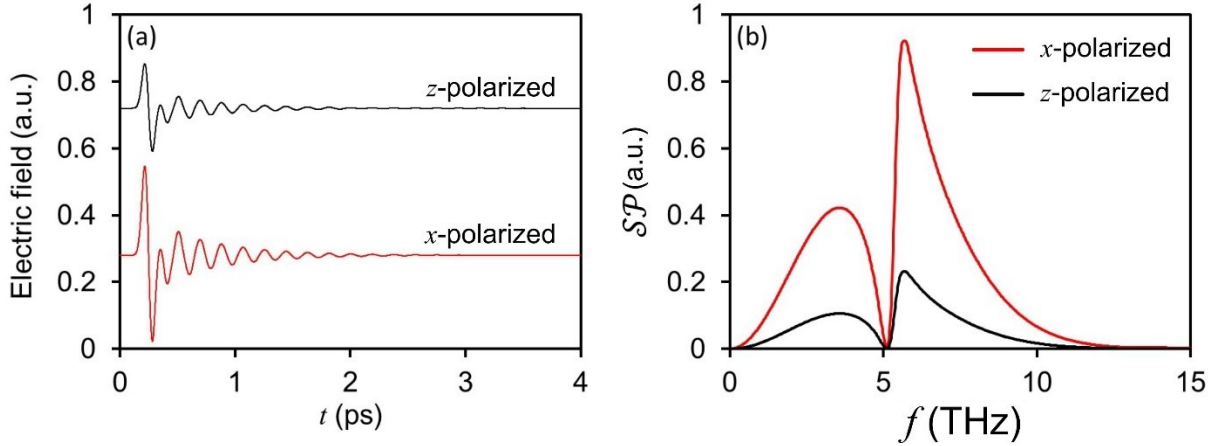


Fig. 5.11. (a) THz time-domain electric fields and (b) spectral powers for THz radiation that is polarized along the x and z axes, calculated for the $\ell=1 \mu\text{m}$ ZnTe crystal.

The versatility of our approach is further demonstrated by investigating THz radiation generation in the 2D arrangement depicted in Fig. 5.12(a) and 5.12(b), where a free-space pulse exhibiting a Gaussian spatial distribution is coupled into a SiO_2 -ZnTe-air planar waveguide having a thickness of $4 \mu\text{m}$ and a length of $100 \mu\text{m}$. The electric field pulse has a duration of 80 fs, a central-wavelength of 800 nm, and a beam waist of $4 \mu\text{m}$. By exciting the waveguide using an electric field pulse polarized perpendicular to the c -axis, the majority of the energy couples into the transverse magnetic (TM) mode. Through the process of OR, THz radiation is generated having a polarization along the c -axis. The majority of this THz energy couples into the TE mode, which propagates towards the waveguide output and is emitted into free-space. The generated time-domain pulse consists of oscillations having a duration of ~ 10 ps [see Fig. 5.12(c)] and the associated spectral power shows the highest generation at 4.8 THz [see Fig. 5.12(d)]. At this

frequency, the effective refractive index of the THz mode is equal to the effective group refractive index of the excitation mode (i.e. both are 3.25), allowing for phase-matched THz radiation generation.

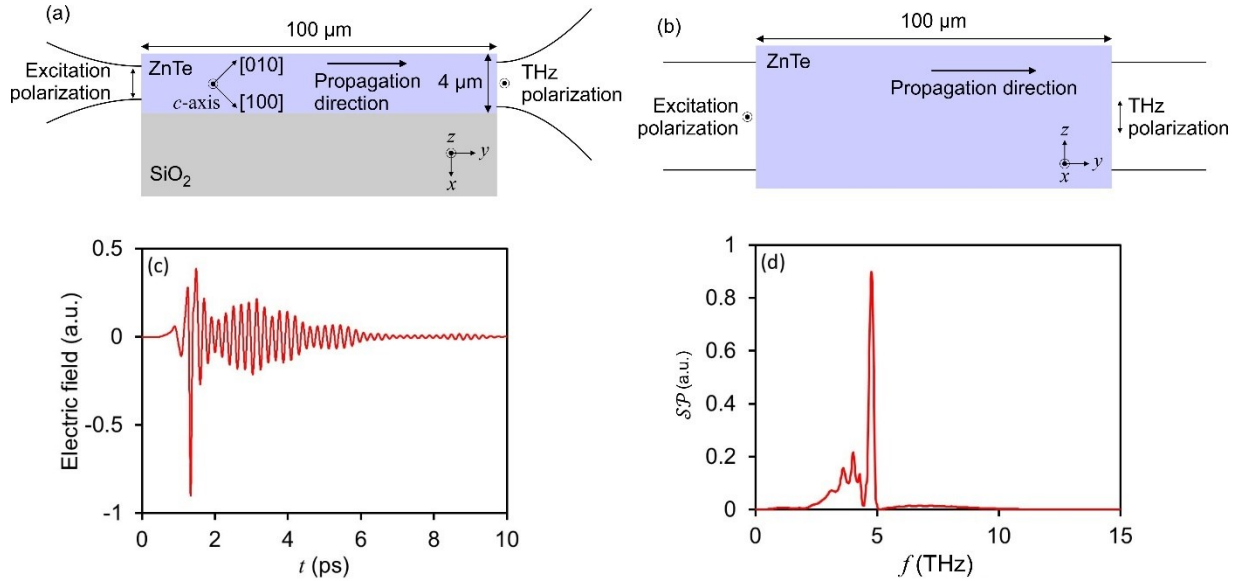


Fig. 5.12. Schematic of the SiO₂-ZnTe-air planar waveguide along the (a) y - z and (b) x - y cross-sections, which show the Gaussian electric field pulse being coupled into the waveguide and the generated THz radiation being coupled out of the waveguide. (c) THz time-domain electric field and (d) spectral power of the generated THz radiation.

5.3. Summary

FDTD formalisms are developed to describe nonlinear frequency-conversion from all 18 dispersive elements of the second-order nonlinear susceptibility tensor. A method based on Miller's rule is developed, which applies to many crystal classes (e.g. those exhibiting $3m$ point group symmetry), but not $\bar{4}3m$ point group symmetry crystals. To address this concern, a method based on the Faust-Henry model is developed to describe second-order nonlinear frequency-conversion in $\bar{4}3m$ crystals, where many crystals within this class are critical to THz radiation

generation (e.g. ZnTe, GaAs, GaP, etc). Importantly, the developed methods describe all second-order nonlinear processes, including OR, DFG, SHG, and SFG. Additionally, these formalisms describe second-order nonlinear cascading effects, permitting the modeling of arrangements such as that in Ref. [180]. While the formalisms developed in this chapter were not applied to quasi-phase-matched structures or the tilted pulse front technique for THz radiation generation, they are nonetheless capable of modeling such processes. Interestingly, since confining an excitation pulse having a tilted pulse front to a planar waveguide beneficially impacts the conversion efficiency (see Ref. [101]), this arrangement should be explored further. Although the developed nonlinear methods permit modeling of second-order nonlinearities in arbitrary geometries, they are envisioned to have the most dramatic impact in developing nonlinear frequency-conversion structures for on-chip applications, such as waveguides.

Chapter 6.

THz radiation generation using LN waveguiding arrangements

An important advantage of waveguides is their ability to confine an optical excitation pulse as it propagates, thus permitting high peak intensities (e.g. $>GW/cm^2$), critical to boosting nonlinear frequency-conversion efficiencies. Other key advantages of waveguiding geometries are their compatibility with nanofabrication techniques and ability to realize a small footprint, making them ideal for integration onto photonic chips. Herein, the numerical FDTD methods previously developed [see Chapter 5] are implemented to model THz radiation generation in planar LN waveguides. Subsequently, THz radiation produced from a planar LN waveguide is observed experimentally. Such investigations push beyond previous works (see Section 1.5) to develop novel THz waveguiding sources. In this chapter, we omit the ‘ \sim ’ accent typically used to denote complex variables related to a material’s nonlinearity.

6.1. Ultra-broadband THz radiation generation from sub-wavelength LN waveguides⁹

When considering OR THz radiation generation in a bulk LN crystal, generation is limited to less than a few THz, due to the large refractive index mismatch between the excitation pulse

⁹A version of this section’s work is published as B. N. Carnio and A. Y. Elezzabi, "Investigation of ultra-broadband terahertz generation from sub-wavelength lithium niobate waveguides excited by few-cycle femtosecond laser pulses," *Opt. Express* **25**, 20573 (2017).

and the generated THz radiation. In this section, we show that ultra-broadband Cherenkov THz radiation can be produced by implementing the LN crystal in a sub-wavelength waveguiding arrangement.

6.1.1. Waveguiding structure

Figure 6.1 depicts a schematic of the LN waveguide, where the LN layer (having its c -axis oriented along the z axis) can have a sub-wavelength thickness, T , with respect to the 780 nm central-wavelength optical excitation pulse. In order to confine the optical excitation beam, the LN layer is sandwiched between two 500 nm-thick SiO_2 cladding layers. SiO_2 is chosen for these layers because extensive work has been performed to perfect the bonding process between this material and thin film LN [181]. This bonding technique produces high-quality, single-crystal LN thin films that exhibit refractive index values matching that of bulk LN [181]. As a result of the LN thickness being sub-wavelength with respect to the THz radiation (i.e. $T \ll \lambda_{\text{THz}}$, where λ_{THz} is the THz radiation wavelength), the SiO_2 -LN- SiO_2 waveguide can be inserted between two high-index dielectric layers to allow the generated THz radiation to be emitted as Cherenkov waves. 47° -cut high-resistivity Si prisms are implemented on the waveguide structure, where the angle is chosen to allow the generated THz radiation to be directed towards the Si-air interface at normal incidence. Since the waveguide width, W , is much larger than the THz wavelengths (i.e. $W \gg \lambda_{\text{THz}}$), 2D FDTD simulations are sufficient to model the structure. In the forthcoming discussions, both the optical excitation pulse energy, ξ_{exc} , and the generated OR THz energy, ξ_{OR} , are presented per waveguide width (i.e. W).

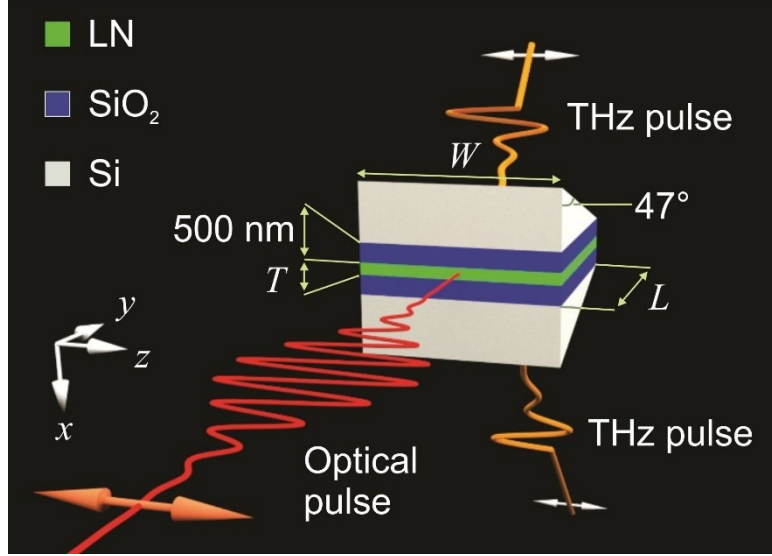


Fig. 6.1. Schematic showing the sub-wavelength SiO₂-LN-SiO₂ waveguiding geometry incorporating Si prisms. Depicted in the illustration is the waveguide width, W , length, L , and core thickness, T . The z -polarized optical excitation pulse is coupled into the SiO₂-LN-SiO₂ waveguide and the generated THz electric field has a polarization oriented along the z axis.

To obtain a realistic picture of OR in the sub-wavelength SiO₂-LN-SiO₂ waveguide, it is essential to accurately model the refractive index, n , and extinction coefficient, κ , of LN, SiO₂, and Si. Since both the optical excitation pulse and the generated THz radiation are polarized along the c -axis of the LN crystal (i.e. z axis), only the extraordinary refractive index, n_e , and extinction coefficient, κ_e , need to be defined. Figure 6.2(a) shows n_e and κ_e for the LN crystal, where the curves are obtained using a double Lorentzian model,

$$(n_e + i\kappa_e)^2 = \varepsilon_\infty + \frac{D_1^2}{D_1^2 - \omega^2} + \sum_{m=1}^2 \frac{\chi_m \omega_m^2}{\omega_m^2 - i\gamma_m \omega - \omega^2}, \quad (6.1)$$

where ε_∞ is the frequency-independent relative permittivity, D_1 and D_2 are optical dispersion coefficients, χ_m is the Lorentzian susceptibility, ω_m is the angular frequency of the phonon resonance, γ_m is the damping term associated with each resonance, and ω is the angular frequency.

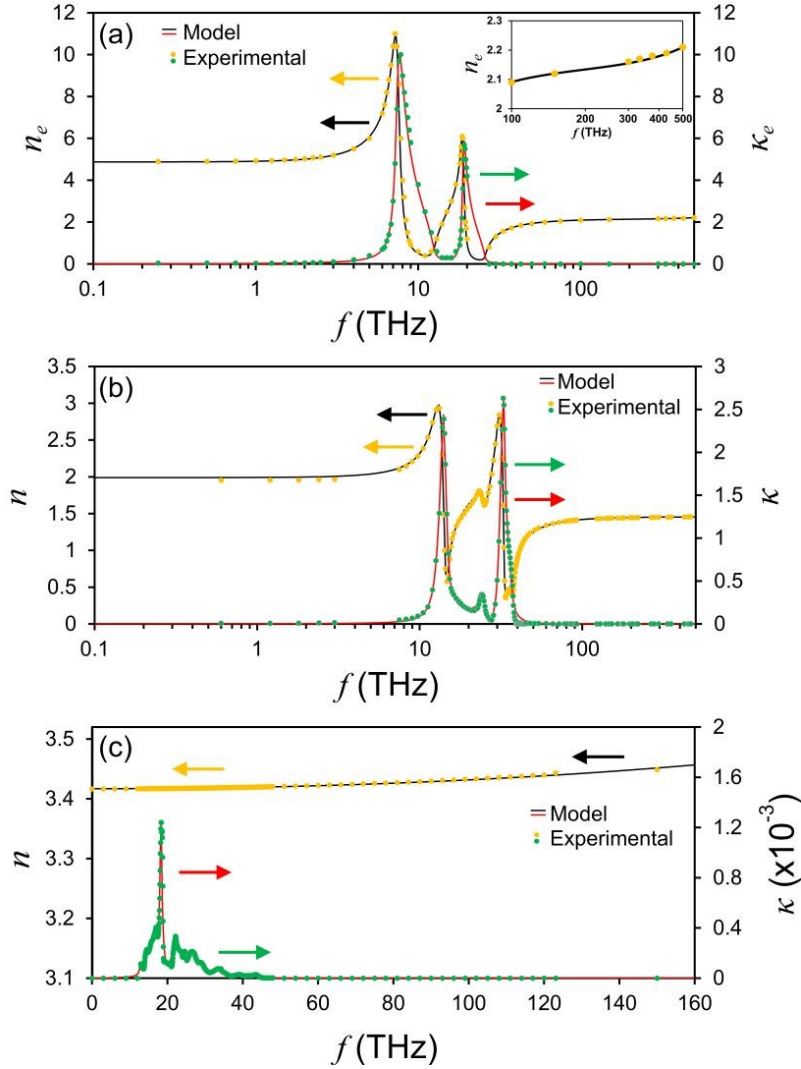


Fig. 6.2. (a) LN, (b) SiO₂, and (c) Si refractive indices and extinction coefficients. The experimental data is obtained from Refs. [148,171,172] for LN, Ref. [182] for SiO₂, and Refs. [182,183] for Si. The inset in (a) displays the LN extraordinary refractive index at frequencies of 100-500 THz.

An excellent fit to the combined experimental data from Refs. [148,171,172] is achieved using the parameters $\epsilon_{\infty}=0.95$, $D_1/(2\pi)=3226$ THz, $D_2/(2\pi)=1700$ THz, $\chi_1=16.6$, $\chi_2=2.6$, $\omega_1/(2\pi)=7.5$ THz, $\omega_2/(2\pi)=18.9$ THz, $\gamma_1/(2\pi)=0.73$ THz, and $\gamma_2/(2\pi)=0.89$ THz. Clearly, the strong phonon absorption bands centered at 7.6 and 19 THz, as well as the optical dispersion [see inset of

Fig. 6.2(a)], are well-represented by this model. The use of the bulk refractive index values represent the actual index of the LN thin films, permitted the films are grown using highly-optimized techniques, such as those discussed in Ref. [181]. Using a multi-coefficient fitting routine [184], n and κ for SiO₂ exhibit an excellent fit to the experimental data provided in Ref. [182] [see Fig. 6.2(b)]. Importantly, the strong phonon resonance features at 14.1 and 32.7 THz, as well as the weaker mode at 23.7 THz, are fitted with a high degree of precision. As discussed in Ref. [185], bulk refractive index values well-describe those for SiO₂ layers having thicknesses larger than 20 nm. As shown in Fig. 6.2(c), n and κ for Si (including the region between 10 and 50 THz) are both very accurately modelled, where the experimental data is obtained from Refs. [182,183]. Notably, multi-photon absorption, self phase modulation, and Raman effects in LN occur at peak excitation intensities >100 GW/cm² [186], while the optical damage threshold of LN is ~ 10 TW/cm² [187]. Peak excitation pulse intensities in our simulations are restricted to values <100 GW/cm² to avoid these effects.

The LN crystal is excited along its c -axis, such that the $\chi_{33}^{(2)}$ second-order nonlinear susceptibility element drives the frequency-conversion process. Since dispersion of the LN $\chi_{33}^{(2)}$ element is negligible at the excitation wavelengths, $\chi_{33}^{(2)}$ can be described using the Faust-Henry model (Section 5.2) opposed to Miller's rule (Section 5.1). This permits improved computational speed, since the FDTD method based on Miller's rule is more involved in comparison to the Faust-Henry FDTD method. The LN $\chi_{33}^{(2)}$ element (i.e. the $\chi_{zzz}^{(2)}$ element in non-contracted notation) is described by Eq. (5.58) with the parameters $\chi_E^{zzz} = -51.8$ pm/V, $\Omega_1^{zzz}/(2\pi) = 7.5$ THz, $\Omega_2^{zzz}/(2\pi) = 18.9$ THz, $\gamma_1^{zzz}/(2\pi) = 0.73$ THz, $\gamma_2^{zzz}/(2\pi) = 0.89$ THz, $C_1^{zzz} = 5$, $C_2^{zzz} = 0.78$, and $Q_{zzz} = 2$. Figure 6.3 shows the modelled $\chi_{33}^{(2)}$, along with experimental data for the LN nonlinear

susceptibility [30, 98, 170, 174,188–191]. Due to the lack of explicit frequency information, the low-frequency measurements are plotted at 150 GHz, where $\chi_{33}^{(2)}$ dispersion is negligible.

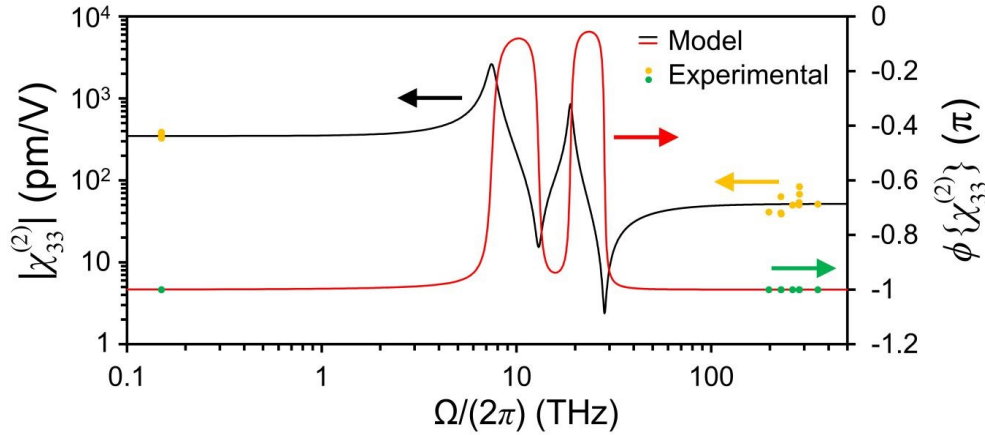


Fig. 6.3. Magnitude and phase of the $\chi_{33}^{(2)}$ second-order nonlinear susceptibility element of LN. The experimental data is obtained from Refs. [30, 98, 170, 174,188–191].

6.1.2. OR THz radiation generation

THz radiation generation is demonstrated for an $L=100\ \mu\text{m}$ LN waveguide that has $T=500\ \text{nm}$. The waveguide is excited by an optical excitation pulse having a duration, τ , of 10 fs, a central-wavelength of 780 nm, and an $\xi_{exc}/W=10\ \text{nJ/cm}$. Figure 6.4(a) displays the generated THz time-domain electric field pulse, which has a bipolar shape and a short duration of $<1\ \text{ps}$. At this ξ_{exc}/W , the THz radiation pulse has a peak-to-peak electric field strength of 1.6 kV/cm, which is a considerably high electric field value obtained from a sub-wavelength waveguide.

Of great interest is the spectral content of the THz radiation pulse. Figure 6.4(b) shows the THz energy spectral density normalized to the device width (i.e. W), denoted as the normalized energy spectral density (NESD). Remarkably, the spectrum is ultra-broad, extending from 0.18-81 THz when using a 40 dB dynamic range (which is chosen as a conservative estimate

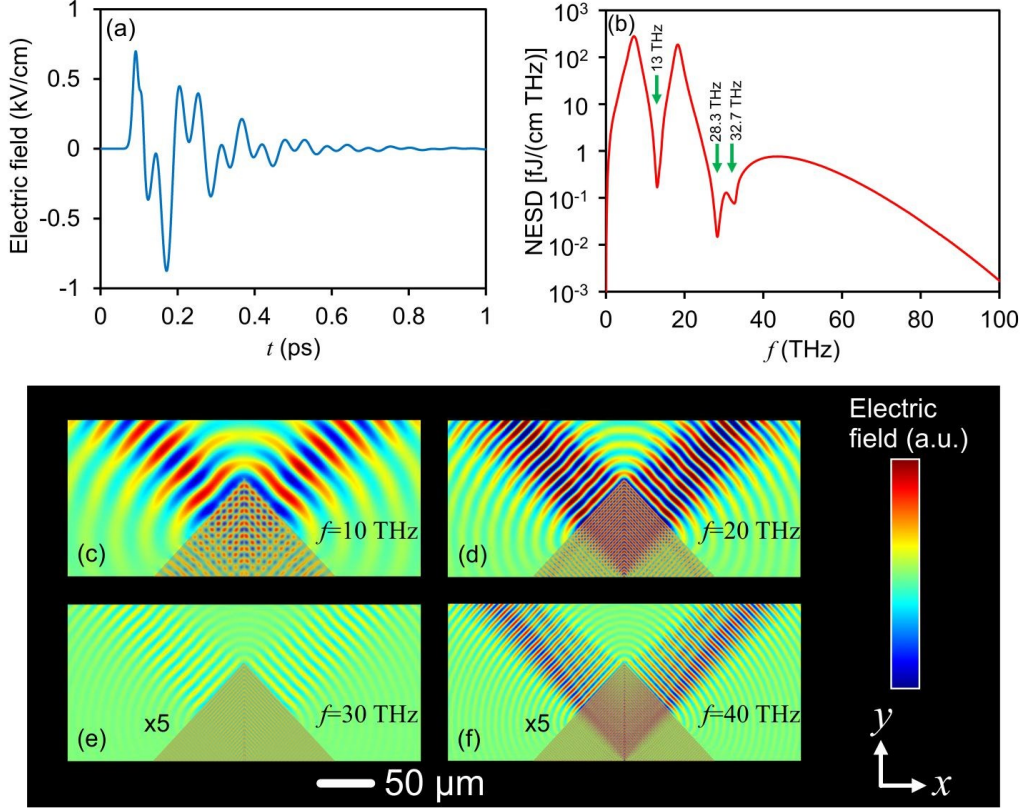


Fig. 6.4. (a) THz time-domain electric field generated from a SiO₂-LN-SiO₂ waveguide having $T=500$ nm, $L=100$ μm , and excited by a $\tau=10$ fs, $\xi_{exc}/W=10$ nJ/cm, 780 nm optical pulse. The time-domain signal is recorded after exiting the Si prisms. (b) NESD of the THz radiation measured after exiting the Si prisms. (c-f) Time-averaged spatial distribution of the electric field at frequencies of 10, 20, 30, and 40 THz propagating outwards from the waveguide. The electric field values in (e) and (f) are scaled by a factor of 5.

based on the 50 dB range achieved in Ref. [124]). Over this bandwidth, the generated THz radiation signal has an $\xi_{OR}/W=1.35$ pJ/cm, such that the conversion efficiency for this $L=100$ μm structure is 1.35×10^{-4} . There is reduced generation at the frequencies of 13 and 28.3 THz, where $|\chi_{33}^{(2)}|$ exhibits minimums (see Fig. 6.3). Such minimums correspond to spectral regions where the electric and ionic contributions of the second-order susceptibility destructively interfere [176]. The minimum at 28.3 THz causes the NESD to fall below the 40 dB dynamic range, leading to a null

within the generation spectrum when using this bandwidth definition. Also observed in the frequency spectrum is the strongest phonon resonance of the SiO₂ layer occurring at 32.7 THz.

When exciting the SiO₂-LN-SiO₂ waveguide with an optical pulse, the induced nonlinear dipoles emit THz radiation that experiences an effective refractive index, n_{eff}^{THz} , dominated by the Si layers. The equation describing the Cherenkov emission angle of the THz radiation is,

$$\theta_c(f) = \cos^{-1} \left[\frac{n_{eff,g}^m}{n_{eff}^{THz}(f)} \right], \quad (6.2)$$

where $n_{eff,g}^m$ is the effective group refractive index of the excitation mode. Since the refractive index of the Si prisms varies by only 0.009 within the frequency range of 0.18-81 THz (i.e. the bandwidth of the generated THz radiation), $\theta_c=47.2^\circ$ - 47.4° over this frequency interval (i.e. $n_{eff,g}^m=2.32$ and $n_{eff}^{THz}=3.417$ - 3.426). Figures 6.4(c)-6.4(f) show this nearly constant THz radiation emission angle at the representative frequencies of 10, 20, 30, and 40 THz.

For a constant excitation pulse energy, the peak intensity of the excitation mode, and therefore the THz signal strength, depends on T . Figure 6.5(a) shows the NESD for a waveguide having $T=0.3$ - 5 - μm , $L=100$ μm , and excited by a $\tau=10$ fs, $\xi_{exc}/W=10$ nJ/cm optical pulse. The reststrahlen bands at 7.6 and 19 THz clearly exhibit stronger absorption with increasing T . This is a result of the generated THz radiation needing to propagate larger distances in the LN core before exiting the LN. Group velocity dispersion of the excitation mode causes a reduction in the length over which the high-frequency and low-frequency components in the optical excitation pulse exhibit the spatial overlap necessary to generate THz radiation. The effective refractive index of the excitation mode, n_{eff}^m , and $n_{eff,g}^m$ are shown in Fig. 6.5(b) for $T=0.3$, 0.5 and 5 μm . Dispersion of the optical excitation mode in the $T=5$ μm waveguide is determined mainly by the LN refractive index, since the excitation mode primarily occupies the LN layer. However, the optical excitation

mode begins to leak into the SiO₂ cladding regions for $T=300$ and 500 nm, such that dispersion of the excitation mode is influenced by both the LN and SiO₂ refractive indices. Importantly, at the optical excitation pulse central-frequency of 385 THz (i.e. wavelength of 780 nm), sub-wavelength effects cause $n_{eff,g}^m$ to increase from 2.28 ($T=5$ μm waveguide) to 2.32 ($T=500$ nm waveguide). As shown in Fig. 6.5(c), reducing T from 5 μm to 300 nm results in a 22 times improvement to ξ_{OR}/W . This is due to better confinement of the excitation pulse to the LN layer and lower absorption of the generated THz frequencies within the LN reststrahlen bands. The spatial intensity profiles displayed in the inset of Fig. 6.5(c) show that the optical mode is mainly confined to the

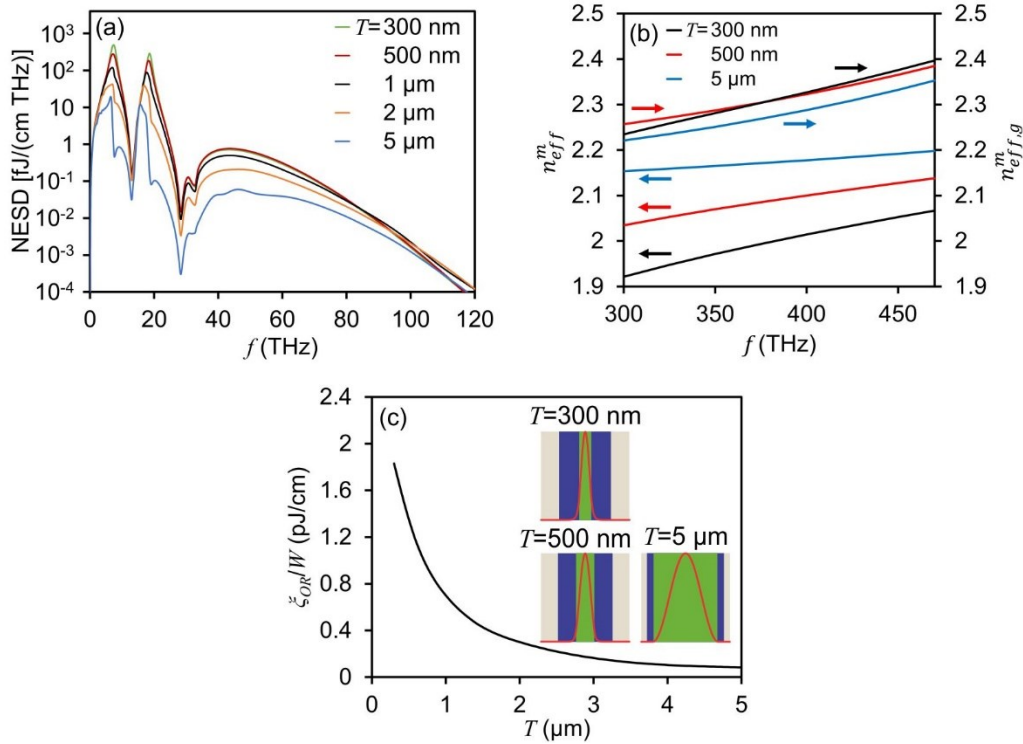


Fig. 6.5. (a) NESD of the THz radiation emitted from a waveguide having $T=0.3$ - 5 μm , $L=100$ μm , and being excited by a $\tau=10$ fs, $\xi_{exc}/W=10$ nJ/cm optical pulse. (b) The effective refractive index of the excitation mode (i.e. n_{eff}^m), as well as the effective group refractive index of the excitation mode (i.e. $n_{eff,g}^m$) at $T=0.3$, 0.5 , and 5 μm . (c) ξ_{OR}/W contained in the generated THz frequency components. The inset shows the intensity profiles of the modes.

LN and SiO₂ layers, and negligibly intensity values exist in the Si layers. Here, $T=500$ nm is chosen as a compromise between a large ξ_{OR}/W and a dimension that would be easily fabricated.

The NESD dependence on τ is shown in Fig. 6.6(a) for a SiO₂-LN-SiO₂ waveguide having $L=100$ μm , $T=500$ nm, and excited at $\tau=7$ -100 fs and $\xi_{exc}/W=10$ nJ/cm. Here, the $\tau=7$ fs curve exhibits the largest THz bandwidth, producing frequency components between 0.18-106 THz when considering a dynamic range of 40 dB. Alternatively, the radiation produced by the $\tau=10$, 20, 50, and 100 fs optical excitation pulses have bandwidths that extend up to 81, 42, 21, and 11 THz, respectively. Therefore, to achieve an ultra-wide spectrum that produces THz radiation well above the LN phonon mode at 19 THz, it is best to excite the waveguide with $\lesssim 20$ fs optical pulses. Interestingly, as shown in Fig. 6.6(b), reducing τ from 100 fs to 7 fs allows for a 2300% improvement in the generated THz energy. This is due to the increase in the peak excitation mode intensity that arises from shortening the optical pulse (while retaining the optical energy) and the additional high-frequency THz radiation generation that results from the shorter duration pulse.

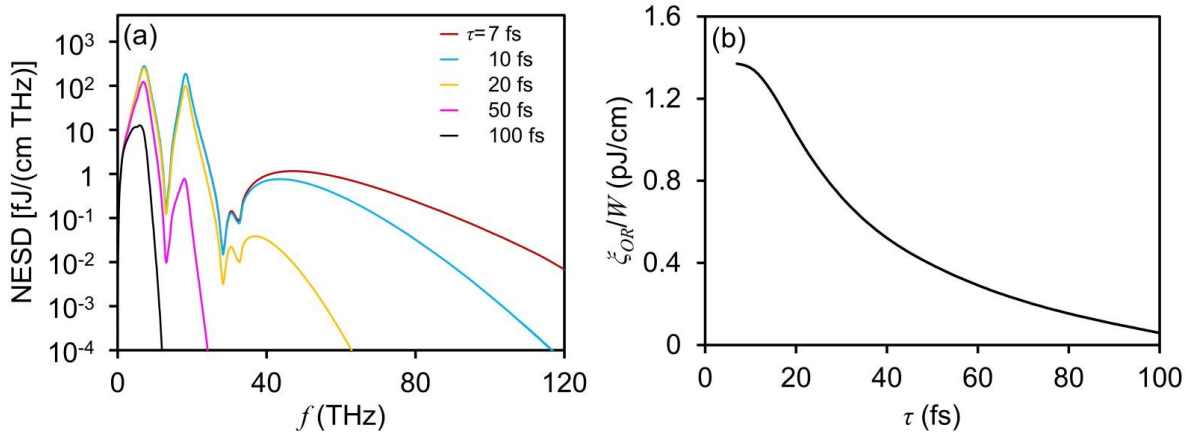


Fig. 6.6. (a) NESD of the THz electric field emitted from a waveguide having $T=500$ nm, $L=100$ μm , and excited by $\tau=7$ -100 fs, $\xi_{exc}/W=10$ nJ/cm optical pulses. (b) ξ_{OR}/W of the generated THz radiation.

In this waveguide configuration, it is essential to understand the relationship by which the THz NESD changes with L . Figure 6.7(a) shows the THz NESD for waveguides having $L=100-300 \mu\text{m}$, $T=500 \text{ nm}$, and driven by a $\tau=7 \text{ fs}$ optical excitation pulse at $\xi_{exc}/W=10 \text{ nJ/cm}$. NESD values at frequencies $\lesssim 13 \text{ THz}$ continually improve by increasing L up to $300 \mu\text{m}$, while higher-frequency components experience little or no benefit from increasing L . Group velocity dispersion of the optical excitation mode causes the encompassed frequency components to spatially separate during propagation, therefore negating high-frequency THz radiation generation. This reduced generation causes ξ_{OR}/W to saturate with increasing L , as shown in Fig. 6.7(b), with the energy improvement mainly arising from additional generation at frequencies $\lesssim 13 \text{ THz}$.

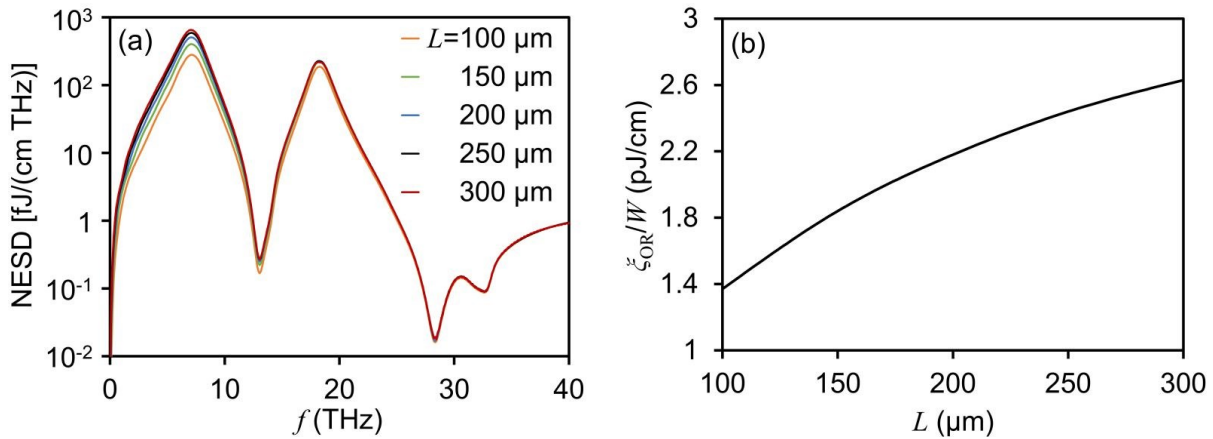


Fig. 6.7. (a) NESD and (b) ξ_{OR}/W emitted from waveguides having $L=100-300 \mu\text{m}$, $T=500 \text{ nm}$, and excited by a $\tau=7 \text{ fs}$, $\xi_{exc}/W=10 \text{ nJ/cm}$ optical pulse.

As in all nonlinear frequency-conversion devices, it is necessary to understand the impact of the excitation pulse energies. The THz NESD and ξ_{OR}/W are shown in Fig. 6.8(a) and 6.8(b), respectively, for waveguides having $L=100 \mu\text{m}$, $T=500 \text{ nm}$, and excited by a $\tau=7 \text{ fs}$ optical pulse at $\xi_{exc}/W=2-10 \text{ nJ/cm}$. Both the spectrum and ξ_{OR}/W show the expected second-order improvement with increasing ξ_{exc}/W . This is witnessed by the 25 times enhancement in ξ_{OR}/W

that occurs when ξ_{exc}/W is increased from 2 nJ/cm to 10 nJ/cm. This second-order increase in the generated THz energy occurs because the optical excitation pulse energy is restricted to values below the threshold for multi-photon absorption, self phase modulation, and Raman effects.

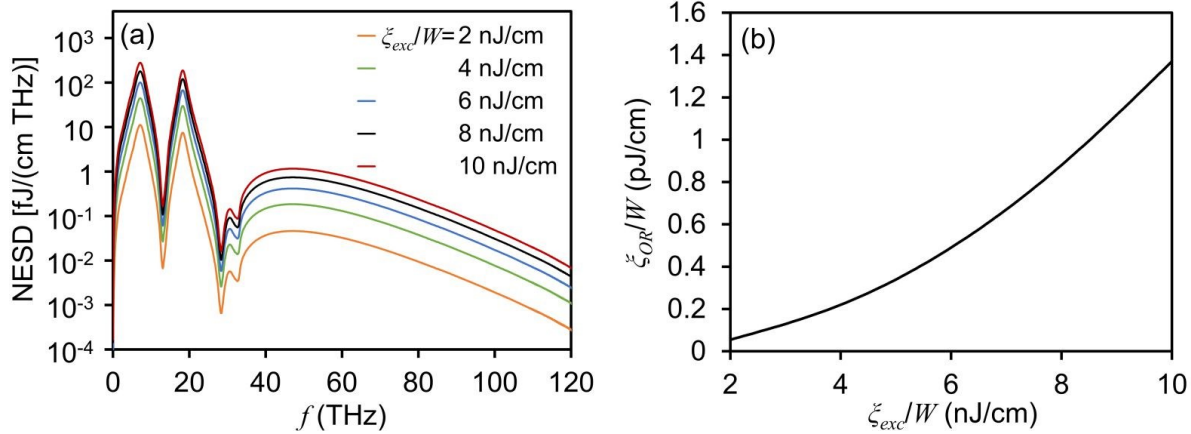


Fig. 6.8. (a) NESD and (b) ξ_{OR}/W generated using waveguides having $L=100 \mu\text{m}$, $T=500 \text{ nm}$, and excited by $\tau=7 \text{ fs}$, $\xi_{exc}/W=2\text{-}10 \text{ nJ/cm}$ optical pulses.

6.2. THz radiation generation near the reststrahlen band in sub-wavelength LN waveguides¹⁰

Near the phonon resonance of a material, enhancement of the second-order nonlinear susceptibility occurs in conjunction with an increase in reststrahlen band absorption [38]. As such, although this resonance enhancement leads to a high portion of the excitation photons being converted to THz photons, the majority of the THz photons are absorbed within the bulk crystal. Interestingly, to exploit the nonlinear susceptibility enhancement and minimize the reststrahlen band absorption, the crystal can be made extremely thin (e.g. hundreds of nanometers). In this

¹⁰A version of this section's work is published as B. N. Carnio and A. Y. Elezzabi, "Enhanced broadband terahertz radiation generation near the reststrahlen band in sub-wavelength leaky-mode LiNbO₃ waveguides," *Opt. Lett* **43**, 1694-1697 (2018).

section, we investigate the generation of THz electric field pulses from a planar LN waveguide supporting THz modes, where sub-wavelength core thicknesses are necessary for producing coherent radiation in the frequency band exhibiting nonlinear susceptibility enhancement.

6.2.1. Waveguiding arrangement

Figure 6.9 shows a schematic of the sub-wavelength waveguide consisting of a LN core having thickness T , length L , width W , and whose crystal c -axis is oriented along the z axis. The optical excitation mode is confined to the LN core by two SiO_2 cladding layers having thicknesses of $10\ \mu\text{m}$. The excitation electric field pulse exhibits a polarization oriented along the c -axis of the LN crystal, such that its $\chi_{33}^{(2)}$ second-order nonlinear susceptibility permits the generation of OR THz radiation polarized along the LN c -axis. Due to the planar nature of the structure, and since the waveguide's width (i.e. W) is larger than the THz electric field wavelength, it is sufficient to employ 2D simulations to investigate THz radiation generation and propagating within the

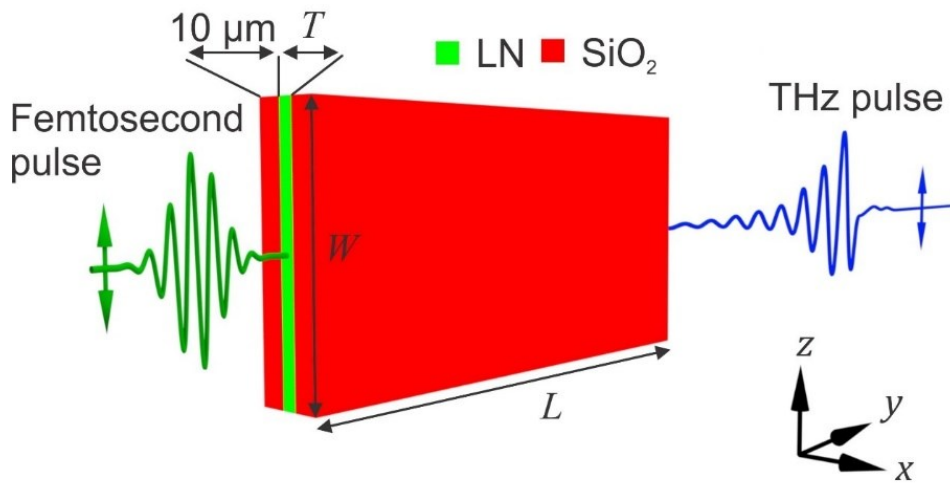


Fig. 6.9. A schematic of the sub-wavelength planar LN waveguide used to generate THz radiation. The LN crystal's c -axis is oriented along the z axis.

waveguide. Notably, the forthcoming simulations are performed using 50 fs, 780 nm excitation pulses having a peak electric field amplitude of 0.4 V/nm (i.e. peak intensities of ~ 90 GW/cm² in the LN crystal). This peak intensity value is below the threshold intensity for multi-photon absorption, Raman effects, self-phase modulation, and optical laser damage [186,187]. The refractive indices and extinction coefficients provided in Fig. 6.2(a) and 6.2(b) are used for LN and SiO₂, respectively. Similarly, the $\chi_{33}^{(2)}$ second-order nonlinear susceptibility of LN is obtained from Fig. 6.3, where enhancement occurs near the LN phonon resonance frequencies. From this model, we obtain a low-frequency (i.e. $\lesssim 1$ THz) $|\chi_{33}^{(2)}| \approx 350$ pm/V. Alternatively, $|\chi_{33}^{(2)}| = 660$ pm/V at 5.6 THz and $|\chi_{33}^{(2)}| = 881$ pm/V at 6 THz, corresponding to an enhancement of 1.9 and 2.5, respectively.

The nonlinear conversion efficiency relies on the propagation and confinement characteristics of the THz modes supported by the waveguide. Figure 6.10(a) shows the spatial intensity profiles of representative THz modes at 5.6 THz (i.e. a frequency within the region of $\chi_{33}^{(2)}$ enhancement) for waveguides having LN core thicknesses between $T=0.3$ -5 μm . As seen from the $T=5$ μm intensity profile, waveguides having sufficiently large thicknesses confine the 5.6 THz mode to the LN core. However, such confinement is undesirable at 5.6 THz and other frequencies near the LN resonance, since it results in significant reststrahlen band absorption of the generated THz radiation. On the contrary, for small waveguide thicknesses (i.e. $T \leq 1$ μm), the modes leak into the surrounding SiO₂ cladding material and free-space. Due to the low-loss of SiO₂ at frequencies $\lesssim 7$ THz, the THz modes propagate with minimal absorption. Importantly, although leakage of the mode results in an inherent increase in the electric field radiated from the waveguide, the majority of the electric field remains guided along the waveguide.

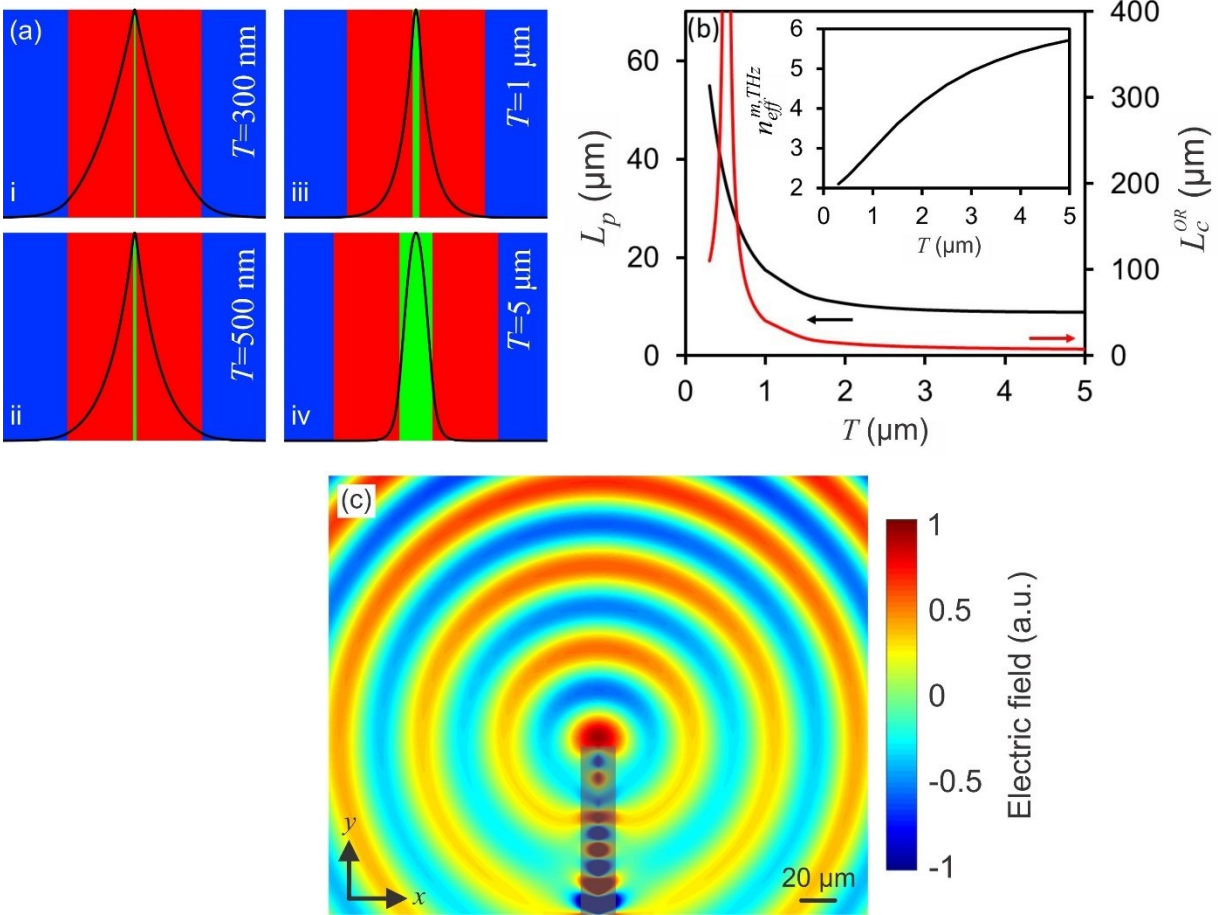


Fig. 6.10. (a) Spatial intensity profile of the 5.6 THz mode supported by waveguides having core thicknesses of (i) 300 nm, (ii) 500 nm, (iii) 1 μm , and (iv) 5 μm . The green, red, and blue regions represent the LN crystal, the SiO₂ surrounding layers, and free-space, respectively. (b) The propagation length (i.e. L_p) and the OR coherence length (i.e. L_c^{OR}) of the waveguide mode at a frequency of 5.6 THz. The inset shows the effective refractive index of the THz mode. (c) Spatial distribution of the electric field obtained by propagating a 5.6 THz electric field pulse along a waveguide having $L = 100$ μm and $T = 500$ nm.

The propagation length, L_p , associated with the 5.6 THz mode is presented in Fig. 6.10(b) for waveguides having thicknesses ranging from $T = 0.3$ – 5 μm . $L_p \approx 9$ μm for large thicknesses of $T > 2$ μm , where L_p is limited by LN reststrahlen band loss, since the modes are mainly confined to the LN core. Alternatively, for waveguides having small core thicknesses, there is a drastic

increase in L_p , reaching values as high as 35 μm at $T=500$ nm and 55 μm at $T=300$ nm. Evidently, waveguides having $T < 2$ μm are necessary to minimize LN reststrahlen band absorption loss and achieve THz radiation generation from the frequency region exhibiting $\chi_{33}^{(2)}$ enhancement. As shown in the inset of Fig. 6.10(b), the effective refractive index of the THz mode, $n_{eff}^{m,THz}$, at 5.6 THz increases with increasing LN core thicknesses (varying from 2.1-5.7 as T is increases from 300 nm-5 μm). Notably, the THz modes at $T < 2$ μm have an $n_{eff}^{m,THz}$ that is a strongly influenced by both the low refractive index of the surrounding SiO_2 materials and the high refractive index of LN. $n_{eff}^{m,THz}$ (in conjunction with the effective group refractive index of the excitation mode, $n_{eff,g}^m$) allows the OR coherence length to be calculated as $L_c^{OR}(f) = cf^{-1}|n_{eff,g}^m - n_{eff}^{m,THz}(f)|^{-1}/2$ [see Fig. 6.10(b)]. For a waveguide having $T=500$ nm, the 5.6 THz mode propagates in-phase with the optical pulse for a distance >1 mm. This is drastically different from waveguides having $T > 2$ μm , where $L_c^{OR} < 14.4$ μm . Clearly, THz modes supported by sub-wavelength waveguides have the added benefit of better phase-matching and larger propagation distances in the frequency region exhibiting LN nonlinearity enhancement. Figure 6.10(c) shows the spatial electric field distribution of a 5.6 THz electric field pulse after propagating along a $T=500$ nm and $L=100$ μm waveguide and being emitted from the waveguide's end facet. The THz radiation is emitted as cylindrical waves, meaning the THz mode exhibits sufficient confinement for the waveguide's output to act as a point emission source.

6.2.2. OR THz radiation generation

THz electric field generation is investigated for a planar LN waveguide having dimensions of $T=500$ nm and $L=100$ μm . As shown in Fig. 6.11(a), the excitation pulse generates THz

radiation along the waveguide, which is emitted as cylindrical waves at the waveguide's output (spatial electric field is recorded at a time of 2.4 ps after exciting the waveguide). Notably, these cylindrical waves could be collimated by implementing a cylindrical lens or a planar parabolic reflector. An off-axis parabolic reflector would be inefficient at collecting the highly-divergent generated THz radiation (estimated at less than a few tens of percent), such that an on-axis parabolic reflector is likely the better option. The THz time-domain electric field signal recorded in free-space, at a distance of 80 μm from the waveguide's output, is shown in Fig. 6.11(b). Interestingly, for the waveguide length of $L=100 \mu\text{m}$, the electric field reaches a high peak-to-peak value of 3.4 kV/cm. The decaying tail of the THz time-domain signal is composed of frequencies near the LN phonon resonance, where the second-order nonlinear susceptibility of LN experiences enhancement. At these near-resonance frequencies, the optical excitation pulse excites strong nonlinear dipoles in the LN crystal, which continue to oscillate and emit THz radiation even after the excitation pulse passes the spatial location.

The NESD, calculated from the THz electric field emitted into free-space, is shown in Fig. 6.11(c). Although the LN nonlinearity is strongest at a frequency of 7.5 THz [see Fig. 6.3], LN reststrahlen band loss strongly absorbs the generated photons before they can be emitted from the waveguide. As such, the peak NESD instead occurs at the lower frequency of 5.6 THz, where $\chi_{33}^{(2)}$ exhibits enhancement but LN reststrahlen band loss is sufficiently low to allow for extraction of the THz radiation from the waveguide. An important metric for frequency-conversion structures is the conversion efficiency, which is calculated as 2.5×10^{-4} for this 100 μm -long waveguide. The planar LN waveguide also has the property of broadband THz radiation generation. When using a 40 dB dynamic range (which is less than the dynamic range values often obtained experimentally [124]), this waveguide is able to produce frequency components between 0.2-11.6 THz.

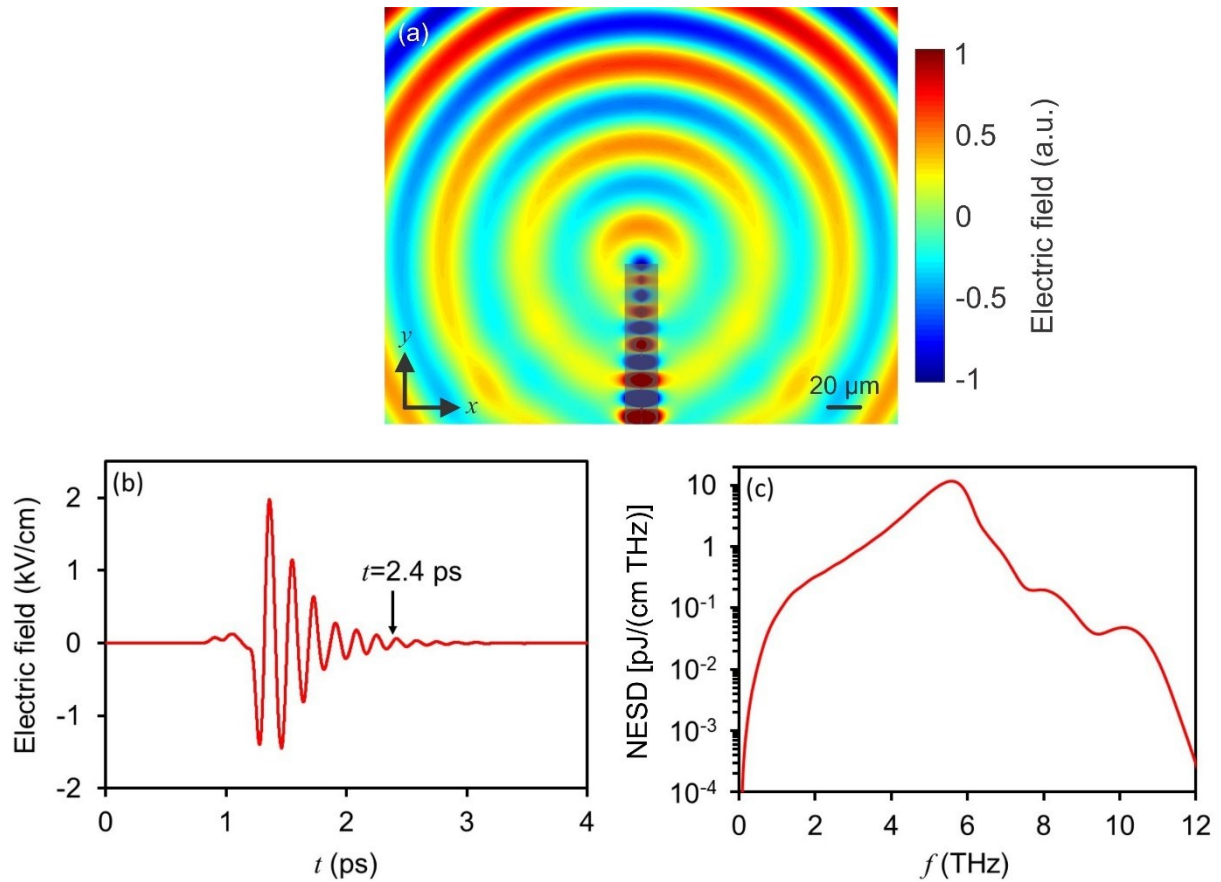


Fig. 6.11. (a) Spatial distribution of the THz electric field produced by a waveguide having $T=500$ nm and $L=100$ μm. (b) THz time-domain electric field pulse generated by the planar LN waveguide and recorded in free-space. The arrow indicates the time at which the electric field distribution in (a) is recorded. (c) NESD of the THz radiation produced by the waveguide and emitted into free-space. The frequency components being considered are those emitted in the forward direction along the y axis with respect to the waveguide's end face.

THz radiation generation depends on the waveguide thickness, since this property affects absorption of the THz radiation produced in the LN core, influences the energy of the excitation pulse in the LN core, and impacts the bandwidth of the emitted THz radiation. Planar LN waveguides are studied having a length of $L=100$ μm and thicknesses ranging from $T=0.3$ -5 μm. The NESD of the generated THz radiation is shown in Fig. 6.12(a), where it is clear that the peak

NESD value increases with T . This effect is from the peak electric field in the LN remaining constant with varying waveguide thicknesses, such that waveguides having larger thicknesses are excited by higher energy optical pulses. When considering the high-frequency region (i.e. ~ 4 -7 THz), the NESD is highest for waveguides having smaller core thicknesses. As was discussed in the waveguide analysis [see Fig. 6.10(b)], this high-frequency NESD improvement is from the $T \leq 1 \mu\text{m}$ waveguide modes having lower THz loss (i.e. longer L_p) and better OR phase-matching (i.e. longer L_c^{OR}) than the modes supported by waveguides having larger thicknesses. Notably, the phase-mismatching effects associated with the large-thickness waveguides (i.e. $T > 2 \mu\text{m}$) are evident from the low-amplitude oscillation seen in the NESD curves at frequencies between 2.6-5 THz.

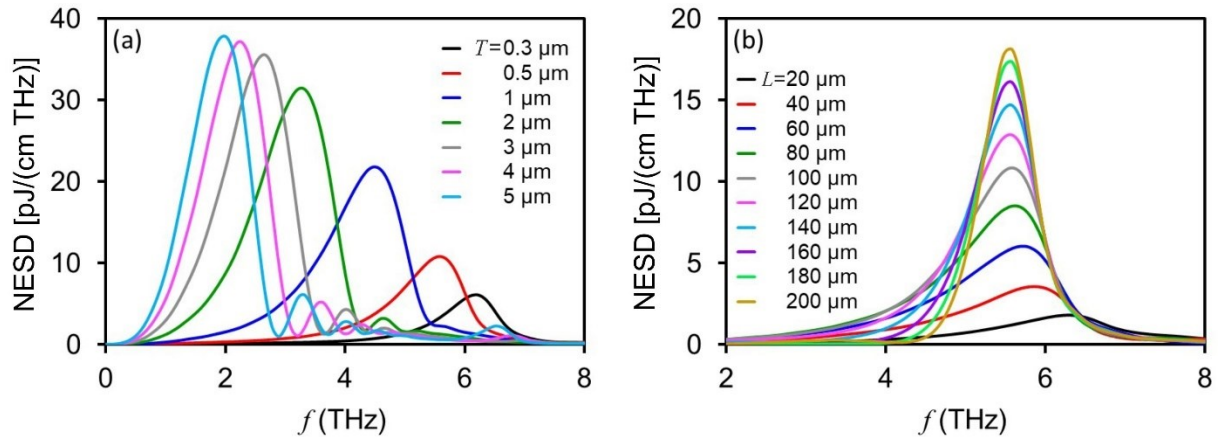


Fig. 6.12. NESD of THz radiation produced by waveguides having (a) $L=100 \mu\text{m}$ and $T=0.3$ -5 μm , and (b) $T=500 \text{ nm}$ and $L=20$ -200 μm .

The THz electric field strength and bandwidth are also influenced by the length of the waveguides, such that waveguides are investigated for $L=20$ -200 μm and $T=500 \text{ nm}$. As shown in Fig. 6.12(b), the NESD peak value increases with increasing L . Interestingly, for frequencies in the spectral region of the NESD maximum, phase-mismatching effects are not observed (indicated

by the absence of phase-mismatching oscillations in the NESD), which is due to $L_p < L_c^{OR}$ [see Fig. 6.10(b)]. The NESD at frequencies $\lesssim 5$ THz decreases for waveguides having $L > 100 \mu\text{m}$, which is a result of the phase-mismatching effects occurring within this spectral region. For a waveguide length of $L = 100 \mu\text{m}$, a large NESD value is achieved for frequencies near 5.6 THz (i.e. in the region exhibiting LN nonlinearity enhancement) and THz radiation generation occurs at frequencies $\lesssim 5$ THz, since this waveguide length is sufficiently short to avoid phase-mismatching effects. As such, the optimal spectrum is produced by this $L = 100 \mu\text{m}$ planar LN waveguide.

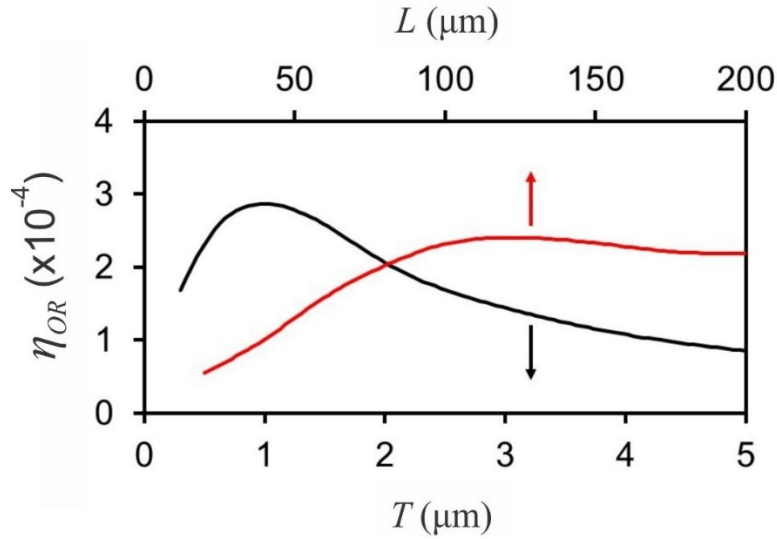


Fig. 6.13. Conversion efficiency of waveguides having $L = 100 \mu\text{m}$ and $T = 0.3\text{--}5 \mu\text{m}$, as well as $T = 500 \text{ nm}$ and $L = 20\text{--}200 \mu\text{m}$.

The OR conversion efficiency, η_{OR} , is an important property for designing the planar LN waveguides. Waveguides having $T = 0.3\text{--}2 \mu\text{m}$ have high η_{OR} (i.e. $\geq 1.7 \times 10^{-4}$), as shown in Fig. 6.13. Although the maximum η_{OR} is 2.9×10^{-4} and occurs for a waveguide core thickness of $T = 1 \mu\text{m}$, the NESD of frequencies ≥ 5.5 THz is low [i.e. $\leq 2.5 \text{ pJ}/(\text{cm THz})$]. As such, the waveguide having $T = 500 \text{ nm}$ is optimal when designing a frequency-conversion structure having

both a high conversion efficiency (i.e. $\eta_{OR}=2.5\times 10^{-4}$) and strong high-frequency generation [e.g. NESD=10.9 pJ/(cm THz) at 5.6 THz]. Waveguides having $L>100\ \mu\text{m}$ provide the largest conversion efficiencies (i.e. $\eta_{OR}>2\times 10^{-4}$), where η_{OR} is seen to level off and decreases slightly. This is caused by phase-mismatching effects decreasing the NESD at frequencies $\lesssim 5$ THz and the waveguide length approaching the propagation length of frequencies near the LN resonance.

6.3. Backward THz DFG via modal phase-matching in a planar LN waveguide¹¹

In typical (i.e. forward) DFG geometries, the pump, signal, and idler waves propagate in the same direction. On the other hand, the backward DFG arrangement permits the idler wave to propagate in the direction opposite to the pump and signal waves. Due to forward and backward DFG arrangements providing different phase-matching requirements, the backward DFG geometry provides an added degree-of-freedom for generating phase-matched THz radiation. In this section, narrowband phase-matched THz radiation is produced via the backward DFG process in a SiO₂-LN-air planar waveguide.

6.3.1. Waveguiding structure

Figure 6.14 shows the SiO₂-LN-air planar waveguide having a LN layer thickness of T and a length of L . The planar waveguide is excited using an electric field having a central-wavelength of 1550 nm and a pulse duration of 100 fs. Both the TM₀ pump electric field mode, \vec{E}_p , and the

¹¹A version of this section's work is published as B. N. Carnio and A. Y. Elezzabi, "Backward terahertz difference frequency generation via modal phase-matching in a planar LiNbO₃ waveguide," *Opt. Lett.* **45**, 3657-3660 (2020).

TE₀ signal electric field mode, \vec{E}_s , are excited at a peak electric field amplitude of 10^8 V/m. Due to the $\chi_{15}^{(2)}$ second-order nonlinear susceptibility element of the LN crystal, the TE₀ and TE₂ idler electric field modes, \vec{E}_i , are produced through the backward DFG process. Importantly, \vec{E}_p at the pump frequency of f_p interacts with \vec{E}_s at the signal frequency of f_s to produce \vec{E}_i at the idler frequency of $f_i = f_p - f_s$. Unlike a PPLN waveguide (or the LN waveguides discussed in Sections 6.1 and 6.2) that depends on the $\chi_{33}^{(2)}$ nonlinear susceptibility element for THz radiation generation [192–197], the modal phase-matched LN waveguiding arrangement illustrated in Fig. 6.14 relies on the $\chi_{15}^{(2)}$ nonlinear susceptibility element to generate THz radiation. The values of this dispersive $\chi_{15}^{(2)}$ element are obtained from Fig. 5.3(c), the refractive indices and extinction coefficients of the

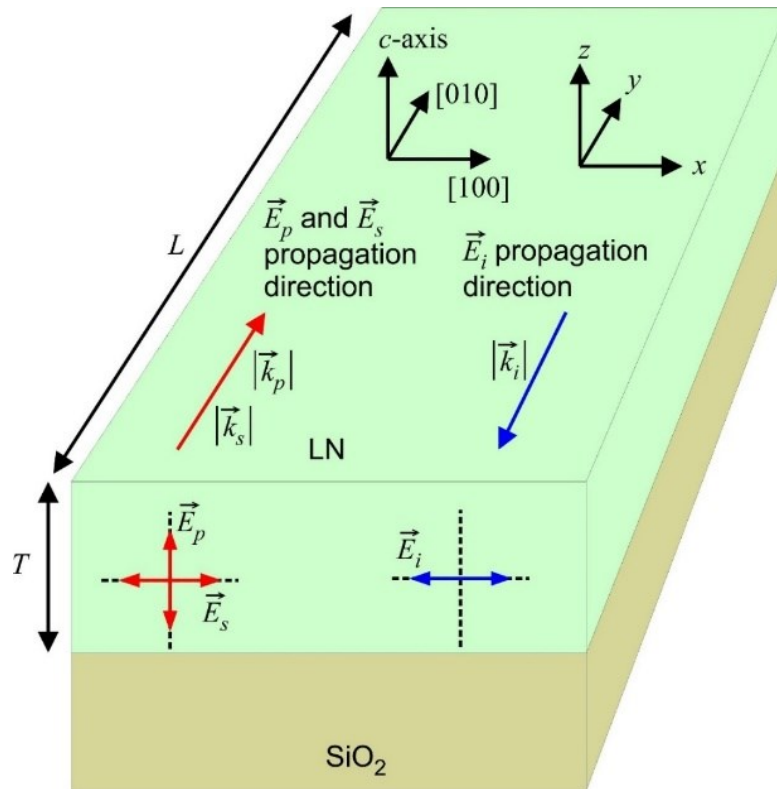


Fig. 6.14. Illustration of the SiO₂-LN-air planar waveguiding arrangement used for the phase-matched backward DFG process.

LN crystal are provided in Fig. 5.2, and the refractive index and extinction coefficient of the SiO₂ substrate are taken from Ref. [182].

6.3.2. DFG THz radiation generation

Phase-matching is investigated between \vec{E}_p (i.e. the TM₀ pump mode), \vec{E}_s (i.e. the TE₀ signal mode), and \vec{E}_i (i.e. the TE₀ and TE₂ idler modes). The coherence length for the backward DFG process is given as, $L_c^{DFG,-} = c|f_p n_{eff}^{m,p} - f_s n_{eff}^{m,s} + f_i n_{eff}^{m,i}|^{-1}/2$, where $n_{eff}^{m,p}$, $n_{eff}^{m,s}$, and $n_{eff}^{m,i}$ are the effective modal phase refractive indices of \vec{E}_p , \vec{E}_s , and \vec{E}_i , respectively. The inset of Fig. 6.15(a) depicts the TE₀ \vec{E}_i mode for the $T=5 \mu\text{m}$ planar waveguide. Figure 6.15(a) shows that perfect phase-matching occurs at $f_i=2.4$ THz, determined using the relationship of $f_i = f_p - f_s$. The inset of Fig. 6.15(b) depicts the TE₂ \vec{E}_i mode for the $T=25 \mu\text{m}$ planar waveguide, and Fig. 6.15(b) shows

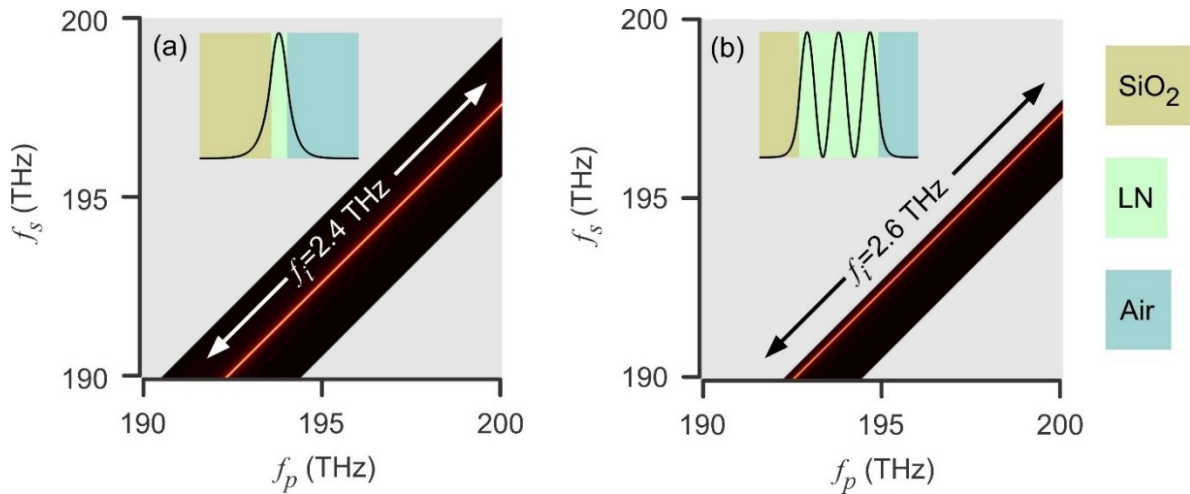


Fig. 6.15. The backward DFG coherence length calculated using (a) the TE₀ \vec{E}_i mode for the $T=5 \mu\text{m}$ planar waveguide and (b) the TE₂ \vec{E}_i mode for the $T=25 \mu\text{m}$ planar waveguide. The insets in (a) and (b) show the TE₀ \vec{E}_i mode and the TE₂ \vec{E}_i mode, respectively. The black areas identify the coherence lengths, where perfect phase-matching occurs along the red lines. In (a) and (b), perfect-phase matching occurs at $f_i=2.4$ and 2.6 THz, respectively.

that perfect phase-matching occurs at $f_i=2.6$ THz. Importantly, although the $T=5$ μm planar waveguides supports 11 TM modes and 11 TE modes, the $\text{TM}_0 \vec{E}_p$ mode and $\text{TE}_0 \vec{E}_s$ mode can be selectively excited using the coupling approach outlined in Ref. [91]. FDTD simulations show that a Gaussian beam waist diameter of 4 μm allows the power coupled into the TM_0 and TE_0 modes to be >500 higher than the power coupled into the higher-order (i.e. $\rho=1-10$) TM_ρ and TE_ρ modes. Similar reasoning holds for waveguides having other T .

The backward DFG process is investigated for planar waveguides having $L=100-500$ μm and $T=5$ μm , where \vec{E}_i is phase-matched using the TE_0 mode [see Fig. 6.15(a)]. The generated THz time-domain electric fields are shown in Fig. 6.16(a), where the $L=100$ μm planar waveguide produces an electric field pulse having a short duration of ~ 4 ps. In comparison, the $L=400-500$ μm planar waveguides have durations of >10 ps, since the phase-matched backward DFG process is occurring over larger distances. The monotonically decaying nature of the time-domain electric fields suggest that generation occurs at a single frequency. Figure 6.16(b) shows the power spectra

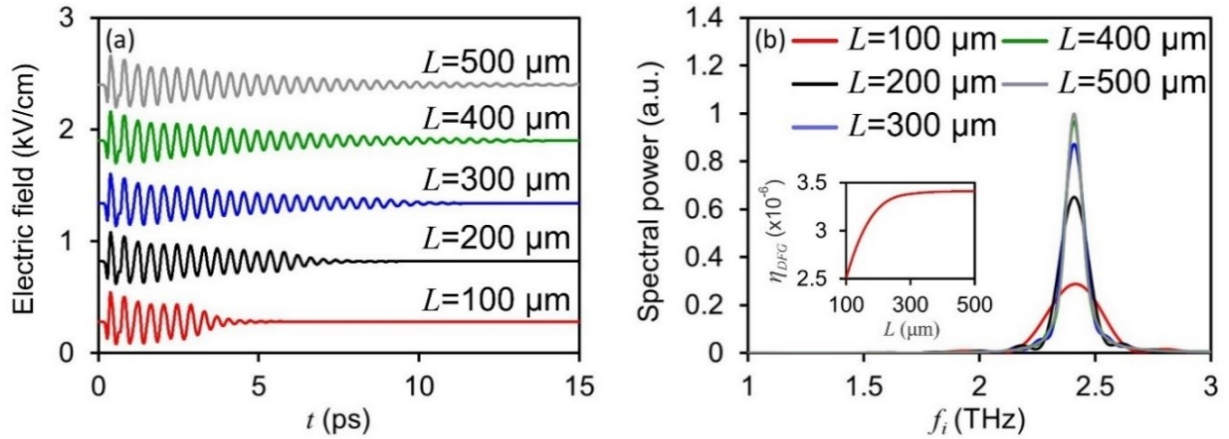


Fig. 6.16. (a) THz time-domain electric field pulses and (b) the associated spectral powers generated in the $L=100-500$ μm and $T=5$ μm planar waveguides. The electric fields are recorded at the planar waveguide's input. The inset shows the conversion efficiency for the $L=100-500$ μm planar waveguides.

of the generated THz radiation, confirming this single-frequency generation at the idler frequency of $f_i=2.4$ THz, as predicted from $L_c^{DFG,-}$ in Fig. 6.15(a). A FWHM linewidth of 260 GHz is obtained for the shortest planar waveguide length of $L=100$ μm ; however, much narrower FWHM linewidths of <100 GHz are achieved for $L=400\text{-}500$ μm . Interestingly the $L=100, 200,$ and 300 μm spectral powers vary greatly, whereas the $L=400$ and 500 μm spectra are nearly identical. We must determine whether this is due to separation of \vec{E}_s and \vec{E}_p , or due to absorption of the THz radiation. The distance at which \vec{E}_s lags \vec{E}_p by a time of Δt is given by the equation, $L_s = c\Delta t / |n_{eff,g}^{m,p} - n_{eff,g}^{m,s}|$, where $n_{eff,g}^{m,p}$ is the effective group modal refractive index of \vec{E}_p and $n_{eff,g}^{m,s}$ is the effective group modal refractive index of \vec{E}_s . $L_s=353$ μm when using $\Delta t=100$ fs (i.e. the duration of the pump and signal pulses). However, the propagation length due to absorption losses at 2.4 THz is $L_p=203$ μm , such that THz radiation absorption is the effect preventing further generation at $L>300$ μm . The DFG conversion efficiency, η_{DFG} , of the narrowband THz radiation produced by the backward DFG process is shown in the inset of Fig. 6.16(b). η_{DFG} increases linearly for $L=100\text{-}200$ μm and plateaus at the value of $\eta_{DFG}=3.4\times 10^{-6}$ for $L>300$ μm , since $L_p=203$ μm . It is important to determine if η_{DFG} is limited by the spatial modal overlap of $\vec{E}_p, \vec{E}_s,$ and \vec{E}_i , which is investigated by calculating the DFG overlap integral normalized to T ,

$$\mathbb{S} = \frac{\sqrt{T}}{\sqrt{2}} \frac{|\int_{-\infty}^{\infty} E_p(x)E_s(x)E_i(x) dx|}{\sqrt{\int_{-\infty}^{\infty} E_p^2(x) dx} \sqrt{\int_{-\infty}^{\infty} E_s^2(x) dx} \sqrt{\int_{-\infty}^{\infty} E_i^2(x) dx}}. \quad (6.3)$$

\mathbb{S} exhibits the high value of 0.65 for the $T=5$ μm planar waveguide, such that \mathbb{S} does not significantly suppress η_{DFG} . Notably, since THz radiation in the planar waveguide is confined below its diffraction limit, it would be emitted from the waveguide in the form of diverging

cylindrical waves. Similar to the discussion in Section 6.2.2, an on-axis planar parabolic reflector may be a good choice to collimate the generated THz radiation.

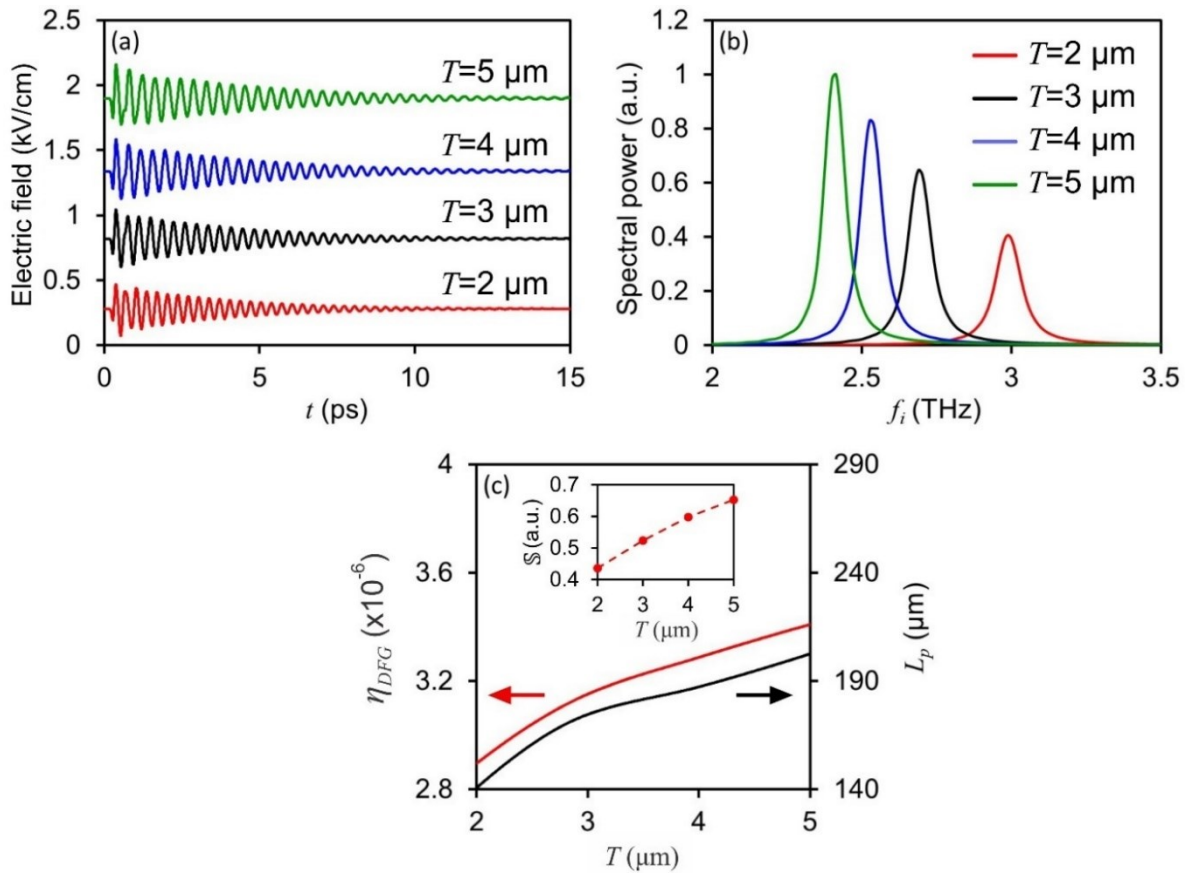


Fig. 6.17. (a) THz time-domain electric field pulses and (b) the associated spectral powers produced in the $T=2-5 \mu\text{m}$ and $L=500 \mu\text{m}$ planar waveguides. The electric fields are recorded at the input of the planar waveguide. (c) The conversion efficiency (i.e. η_{DFG}) and \vec{E}_i propagation length (i.e. L_p) for the $T=2-5 \mu\text{m}$ planar waveguides. The inset shows the overlap integral values.

The backward DFG process is further investigate for the $T=2-5 \mu\text{m}$ and $L=500 \mu\text{m}$ planar waveguides. As shown in Fig. 6.17(a), the generated THz time-domain electric fields have durations >10 ps and are monotonically decreasing in time. Narrowband THz radiation generation is achieved [see Fig. 6.17(b)], where the central frequency of the spectra is tunable within the range of 2.4-3 THz for $T=2-5 \mu\text{m}$. η_{DFG} is shown in Fig. 6.17(c), where the highest conversion efficiency

of $\eta_{DFG}=3.4\times 10^{-6}$ is observed for $T=5\ \mu\text{m}$ and reduces to the value of $\eta_{DFG}=2.9\times 10^{-6}$ for $T=2\ \mu\text{m}$. Since $S=0.43-0.65$ for the $T=2-5\ \mu\text{m}$ waveguides [inset of Fig. 6.17(c)], η_{DFG} is not limited by S . L_p is shown in Fig. 6.17(c), where $L_p=140-203\ \mu\text{m}$ for the $T=2-5\ \mu\text{m}$ planar waveguides. As such, waveguides longer than this provide diminishing benefits.

Interestingly, modal phase-matching can be applied to higher-order \vec{E}_i modes, which allows for added tunability of the generated f_i . The backward DFG process is investigated for planar waveguides having $T=15-25\ \mu\text{m}$ and $L=500\ \mu\text{m}$, where \vec{E}_i is phase-matched using the TE_2 mode [see Fig. 6.15(b)]. Figure 6.18(a) shows the generated THz time-domain electric fields, which have time durations $>10\ \text{ps}$, due to the long length of the planar waveguide (i.e. $L=500\ \mu\text{m}$). It can be inferred that several frequencies are contributing to the modulated (i.e. beating) shape of the time-domain electric fields. From the power spectra shown in Fig. 6.18(b), it is evident that two narrowband spectral regions are associated with THz radiation generation in each waveguide. The lower-frequency and higher-frequency spectral regions occur because \vec{E}_i is phase-matched via the TE_0 and TE_2 modes, respectively. For the $T=25\ \mu\text{m}$ planar waveguide, THz radiation generation occurs at $f_i=2.6\ \text{THz}$, in agreement with $L_c^{DFG,-}$ in Fig. 6.15(b). The center of the high-frequency spectra is tunable between 2.6-3.2 THz by using $T=15-25\ \mu\text{m}$ waveguides. $S\approx 0.36$ for all waveguides having $T=15-25\ \mu\text{m}$ [see inset of Fig. 6.18(c)], such that the $\text{TE}_2\ \vec{E}_i$ modal distribution still allows for an appreciable spatial overlap. Figure 6.18(c) shows that $\eta_{DFG}=4.15\times 10^{-6}-4.55\times 10^{-6}$ for the $T=15-25\ \mu\text{m}$ waveguides, which considers both the low-frequency and high-frequency spectral bands. As shown in Fig. 6.18(c), $L_p=63-145\ \mu\text{m}$ for the $T=15-25\ \mu\text{m}$ waveguides, such that waveguides longer than this provide diminishing benefits for THz radiation generation within the high-frequency spectral bands.

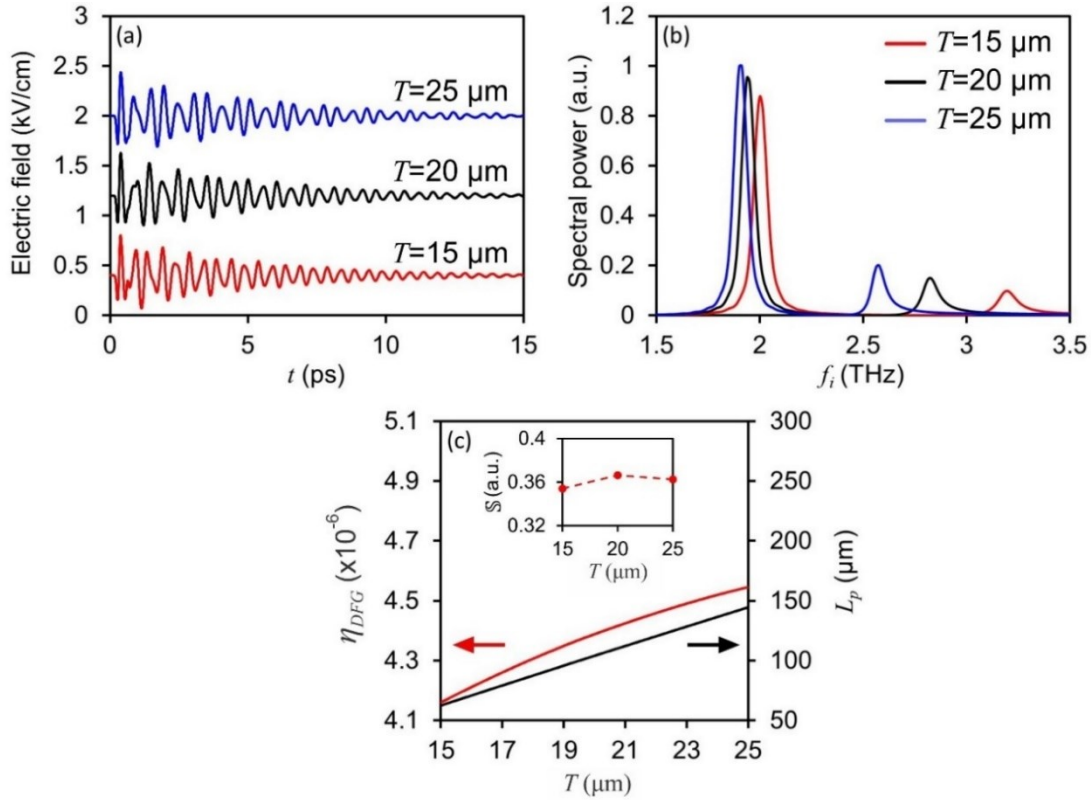


Fig. 6.18. (a) THz time-domain electric field pulses and (b) the associated spectral powers produced in the $T=15\text{-}25 \mu\text{m}$ and $L=500 \mu\text{m}$ planar waveguides. The electric fields are recorded at the input of the planar waveguide. (c) The conversion efficiency (i.e. η_{DFG}) and \vec{E}_i propagation length (i.e. L_p) for the $T=15\text{-}25 \mu\text{m}$ planar waveguides. The inset shows the overlap integral values.

6.4. Excitation mode-dependent THz radiation generation from a planar LN waveguide¹²

THz radiation generation in waveguides only supporting a few optical modes is highly dependent on the relative coupling strength of the excitation pulse into each of these modes. In

¹²A version of this section's work is published as B. N. Carnio, B. Shahriar, E. Hopmann, and A. Y. Elezzabi, "Excitation mode-dependent terahertz radiation generation from a sub-wavelength Si-SiO₂-LiNbO₃-polymer-Si planar waveguide," *IEEE Trans. Terahertz Sci. Technol.* **11**, 462-465 (2021).

particular, each mode exhibits a different effective group refractive index, and thus different OR phase-matching requirements. When considering the generation of Cherenkov THz radiation, this difference in the effective group refractive index manifests as the generated THz radiation being emitted at different Cherenkov angles. Herein, we investigate OR THz radiation produced in a SiO₂-LN-polymer planar waveguiding arrangement, which supports three TE modes (i.e. the TE₀, TE₁, and TE₂ modes) at the optical excitation wavelengths.

6.4.1. Waveguiding structure

Figure's 6.19(a)-6.19(c) depict the SiO₂-LN-polymer planar waveguiding arrangement used for THz radiation generation. The LN layer is 530 nm thick, which is sandwiched between a 2 μm-thick SiO₂ layer and a 1.2 μm-thick polymer layer (i.e. AZ 1512 photoresist). Notably, the SiO₂ and polymer layers are crucial to confine the excitation modes to the LN region. An excitation pulse having a central wavelength of 800 nm, a pulse duration of 50 fs, and a polarization along the *c*-axis of the LN crystal [i.e. *z* axis in Fig. 6.19(a)-6.19(c)] is coupled into the TE₀, TE₁, and TE₂ modes supported by the SiO₂-LN-polymer waveguiding region. The incident excitation beam has a diameter of 2.7 mm, which remains collimated along the *z* axis, but is focused to a width of 4 μm along the *x* axis [using an acylindrical lens having a numerical aperture (NA) of 0.49]. Clearly, since the beam waist along the focused dimension is larger than the thickness of the LN region, the excitation beam does not fully couple into the waveguide. This coupling arrangement can be further improved by incorporating a higher NA acylindrical lens or by implementing a more complex coupling configuration [198]. Since the LN crystal has a non-vanishing $\chi_{33}^{(2)}$ second-order nonlinear coefficient [see Fig. 5.3(a)], the TE₀, TE₁, and TE₂ modes induce *z*-polarized second-

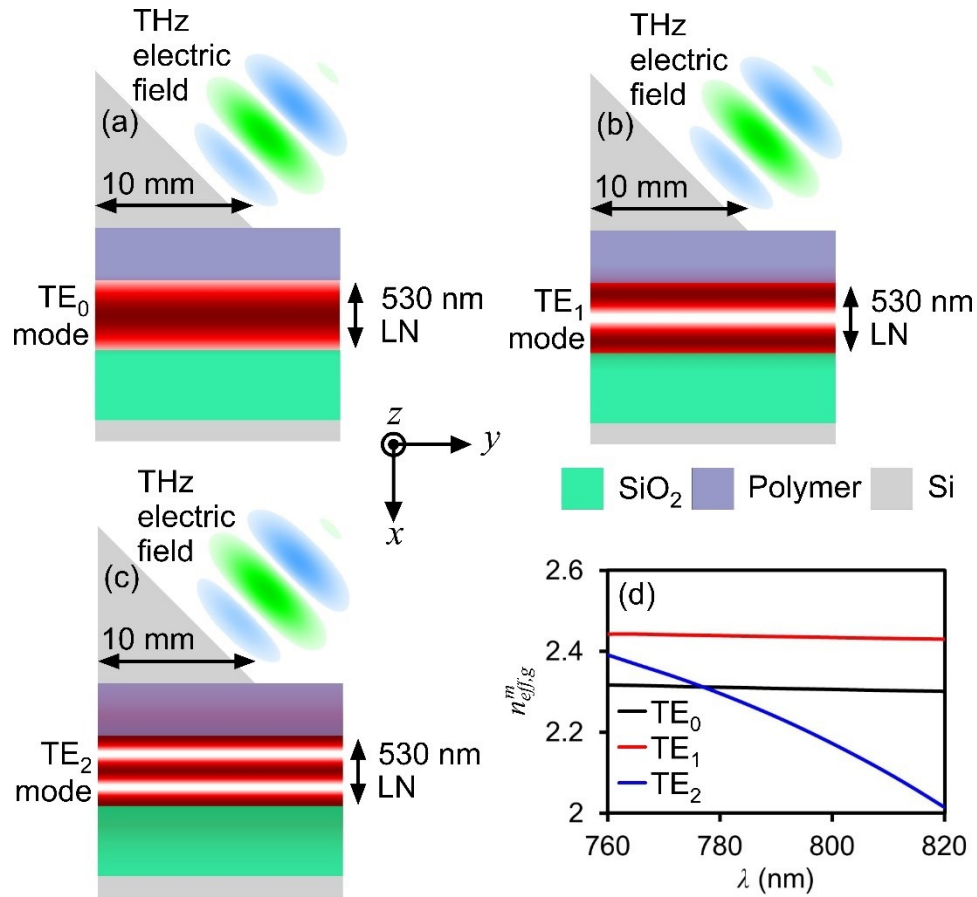


Fig. 6.19. Schematic of the LN planar waveguide depicting the (a) TE₀, (b) TE₁, and (c) TE₂ excitation modes. (d) The effective group refractive indices for the TE₀, TE₁, and TE₂ excitation modes.

order nonlinear dipoles. Subsequently, these oscillating bound charges produce THz radiation that form Cherenkov waves in the Si prism. The 45°-cut Si prism allows the generated THz radiation to avoid total internal reflection at the Si-air interface, permitting the THz radiation to be coupled out into free-space. Importantly, due to the planar nature of the Si-SiO₂-LN-polymer-Si arrangement and the THz radiation being emitted as Cherenkov waves, the generated THz radiation has a planar wavefront [91,120]. Figure 6.19(d) shows the effective group refractive indices, $n_{eff,g}^m$, of the TE₀, TE₁, and TE₂ modes. For this Cherenkov generation scheme, the

emission angle of the generated THz radiation can be calculated using Eq. (6.2) (which depends on $n_{eff,g}^m$ and the effective refractive index of the generated THz radiation, n_{eff}^{THz}). Since the LN thickness (i.e. 530 nm) is sub-wavelength with respect to the generated THz radiation wavelengths, n_{eff}^{THz} is simply the THz refractive index of the Si prism (i.e. ~ 3.42 for frequencies < 4 THz [199]). At the central excitation wavelength of 800 nm, $\theta_c = 47.6^\circ$, 44.6° , and 50.6° for the TE₀, TE₁, and TE₂ modes, respectively. Therefore, the TE₀, TE₁, and TE₂ modes will each produce their own angle-dependent Cherenkov THz radiation pulse.

6.4.2. OR THz radiation generation

THz radiation generation is experimentally investigated from the SiO₂-LN-polymer planar waveguide, as well as from a 500 μm -thick, (110)-cut bulk ZnTe crystal for comparison. To measure THz radiation generation, the waveguiding structure and the bulk ZnTe crystal are separately utilized as the THz source in the THz-TDS system [see Chapter 3]. Figure 6.20(a) shows the THz time-domain signal produced by the planar waveguiding arrangement and the THz time-domain signal obtained from the bulk ZnTe crystal. Three temporally-separated THz radiation pulses are produced by the TE₀, TE₁, and TE₂ modes supported by the planar waveguide. Despite these THz radiation pulses being emitted at various θ_c , they are collected and measured by the THz-TDS system, as it incorporates parabolic coupling and focusing mirrors to direct all of the beams to a 500 μm -thick ZnTe EO sampling crystal. However, the different θ_c cause the three THz radiation pulses to traverse different paths through the THz-TDS system, manifesting as a path length difference due to inexactness in the positions of the mirrors, inexactness in the angles of the mirrors, deformities in the surfaces of the parabolic mirrors, etc. Since the THz radiation pulses propagate > 40 cm and the path length difference between the THz radiation pulses at $t = 4$ ps

and $t=17$ ps is only 3.9 mm, it is challenging to determine with high certainty at which positions in the system the path length difference manifests. Nonetheless, we expect that the lowest-amplitude THz radiation pulse observed at $t=17$ ps is being generated by the TE₂ mode. The low-amplitude of this THz radiation pulse is due to the dispersion of $n_{eff,g}^m$ [i.e. see Fig. 6.19(d)], which varies from 2-2.4 over the wavelength range of 760-820 nm. The frequency components in the TE₂ mode spatially-separate after a much shorter distance than the frequency components in the TE₀ or TE₁ modes. This, in turn, lowers the peak intensity of the TE₂ mode and its efficiency to generate THz radiation. Despite the TE₁ mode having an odd spatial distribution, this mode is excited due to non-idealities in the waveguide and coupling arrangement (e.g. roughness of the waveguide's input facet, the excitation beam deviating from normal incidence, etc.). However, since the Gaussian excitation beam has a spatial profile that is similar to the TE₀ mode, the TE₀ mode is expected to exhibit a higher coupling efficiency than the TE₁ mode. Therefore, it is possible that the highest-amplitude THz radiation pulse at $t=4$ ps is produced by the TE₀ mode and the THz radiation pulse at $t=10$ ps is produced by the TE₁ mode. It should be noted that the THz radiation pulses indicated by the red arrows occur from reflections in the 500 μm -thick EO crystal. This observation is supported by comparing the THz time-domain signal from the waveguiding arrangement to that from the bulk ZnTe crystal, indicating that these pulses are not from the generation arrangements but are artifacts of the THz-TDS system. To further verify that the three THz radiation electric field pulses in Fig. 6.20(a) are from the TE₀, TE₁, and TE₂ modes of the sub-wavelength LN planar waveguide, we consider THz radiation generation from a LN planar waveguide having a thickness much larger than the wavelength of the excitation electric field. For such waveguides, numerous of the lowest-order excitation modes exhibit the same $n_{eff,g}^m$, and therefore the same θ_c , such that there is no temporal separation between the THz radiation pulses

produced by the various excitation modes. This is supported by many publications [91, 116, 118–121,123], where only a single THz radiation pulse is observed. Additionally, we conduct an experimental analysis on a 5 μm -thick LN planar waveguide that is otherwise similar to the sub-wavelength 530 nm-thick LN planar waveguide. For such a waveguide, many of the lowest-order excitation modes (i.e. the TE_0 , TE_1 , TE_2 , TE_3 , and TE_4 modes) exhibit the same $n_{eff,g}^m \approx 2.28$, and therefore the same $\theta_c \approx 48^\circ$. Our measurements confirm the generation of only a single THz radiation pulse.

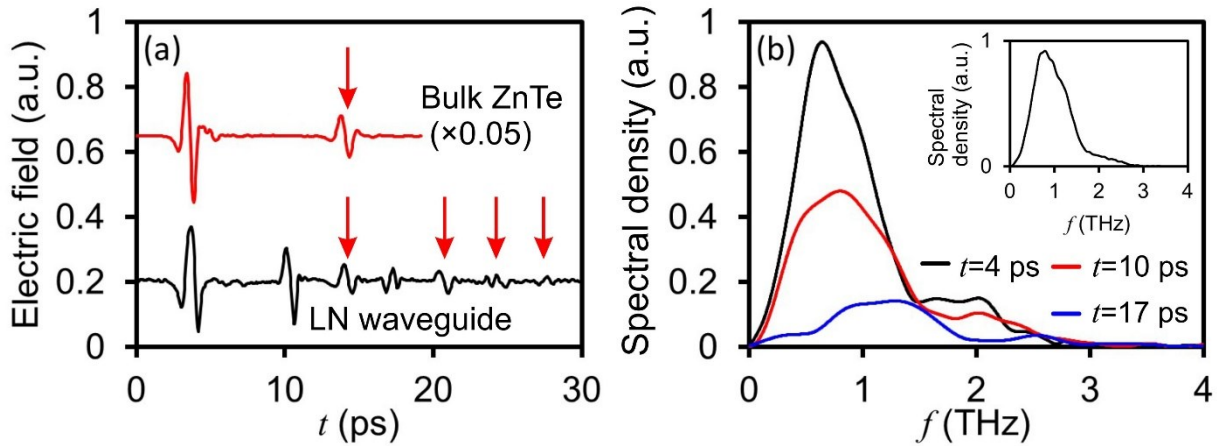


Fig. 6.20. (a) THz time-domain electric field generated from the TE_0 , TE_1 , and TE_2 excitation modes of a LN planar waveguide and from a 500 μm -thick bulk ZnTe crystal. The red arrows indicate pulses from reflections in the EO crystal. (b) Spectral densities obtained by isolating the individual pulses at $t=4$, 10, and 17 ps. The inset shows the THz spectral density of the bulk ZnTe crystal.

Figure 6.20(b) shows the spectral densities of the THz radiation electric field pulses produced by the TE_0 , TE_1 , and TE_2 modes, and the inset of Fig. 6.20(b) depicts the spectral density of the THz radiation electric field pulse produced by the bulk ZnTe crystal. Notably, these spectral densities are obtained by isolating each of the THz radiation pulses, thus avoiding the EO reflection

artifacts. Clearly, the THz radiation pulses produced by the planar waveguide and the THz radiation pulse produced by the bulk ZnTe crystal have similar bandwidths, encompassing frequencies up to ~ 3 THz.

It is imperative to determine the OR THz radiation energy, ξ_{OR} , and OR conversion efficiency, η_{OR} , at various excitation pulse peak intensities in the planar waveguide, I_p . Figure 6.21(a) shows that $\xi_{OR} \propto I_p^2$, as expected, and ξ_{OR} exhibits a maximum value of 22 fJ at $I_p=4$ GW/cm². Additionally, Fig. 6.21(b) shows the expected relationship of $\eta_{OR} \propto I_p$ and η_{OR} exhibits a maximum value of 1.1×10^{-5} at $I_p=4$ GW/cm². The out-coupling Si prism has an extinction coefficient of 0.006 in the THz frequency regime, corresponding to an absorption coefficient of 2.5 cm⁻¹ at the frequency of 1 THz. Since the generated THz radiation propagates an average distance of 3.5 mm through the Si prism, 59% of the generated THz radiation is being lost to absorption, which reduces ξ_{OR} and η_{OR} by the same amount. Therefore, implementing a lower THz radiation absorbing Si prism would permit a maximum $\xi_{OR}=54$ fJ and a maximum $\eta_{OR} = 2.7 \times 10^{-5}$. Importantly, this η_{OR} is comparable to Cherenkov waveguide THz radiation generation arrangements that utilize similar I_p , such as that in Ref. [120].

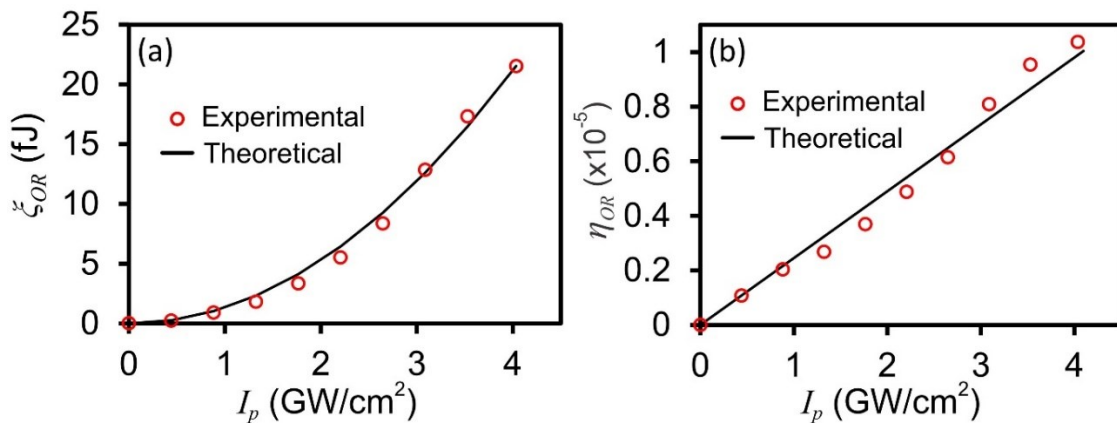


Fig. 6.21. (a) Energy and (b) conversion efficiency for the generated THz radiation. $\xi_{OR} \propto I_p^2$ and $\eta_{OR} \propto I_p$ are the theoretical equations describing this second-order nonlinear process.

6.5. Summary

Using the numerical FDTD techniques developed in Chapter 5, three unique planar LN waveguides are investigated for THz radiation generation via the second-order nonlinear processes of OR or DFG. The planar LN waveguide in Section 6.1 produced Cherenkov THz radiation that encompassed frequencies across the ultra-broad spectral range of 0.18-106 THz. The waveguide presented in Section 6.2 exhibited THz radiation generation enhancement near the LN phonon mode resonance, which allowed for THz radiation having a high central-frequency (i.e. 5.6 THz), a high electric field (i.e. kV/cm), and a high conversion efficiency (i.e. $\sim 10^{-4}$). Section 6.3 considered a planar waveguide that supported phase-matched THz radiation generation in the backwards direction (i.e. the generated THz radiation propagates in the direction opposite to the propagation direction of the excitation pulse). Such a waveguide was shown to produce narrowband (i.e. <100 GHz) THz radiation tunable between 2.4-3.2 THz. In Section 6.4, OR experiments were conducted using a planar LN waveguide, where the generated THz radiation was emitted into free-space as Cherenkov waves dependent on the excitation mode. The THz radiation encompassed frequencies up to ~ 3 THz and exhibited a conversion efficiency on the order of 10^{-5} . Upon scaling the length of the waveguide, we envision such structures being integrated as on-chip sources of THz radiation. Additionally, by utilizing excitation pulses with ultrashort pulse duration (i.e. $\lesssim 10$ fs), we foresee these waveguides being used to produce ultra-broadband THz radiation.

Chapter 7.

Generation of radiation in the near-IR and visible spectral regions

Second-order nonlinear optical phenomenon are not constrained to THz frequencies, since the physical principles driving the nonlinear interactions extend into other spectral regimes. Without any modification to the numerical approaches develop in Chapter 5, they can be used to explore generation in the near-IR and visible regions of the EM spectrum. Optical frequency-conversion in these spectral regions has become essential with advancements in optical communication [180,200,201], optical computing [202–204], and entangled photon generation for quantum computing [205,206]. In optical communication, all-optical frequency-conversion is necessary to implement wavelength division multiplexers for broadband data transfer [180,200,201]. These devices depend on frequency-conversion via the cascaded processes of SFG/DFG or SHG/DFG [180,200,201]. Additionally, developing the critical components of optical computing (e.g. the optical transistor and logic gates) rely upon all-optical nonlinear frequency-conversion processes [202–204]. Previously, optical NOT, AND, OR, NAND, NOR, XOR, and XNOR gates have been proposed, which require structures that convert the wavelength of light using the effects of SHG, SFG, DFG, and spontaneous parametric down conversion (SPDC) [202–204]. Regarding optical frequency-conversion for quantum photonics, cascaded SHG/SPDC or SFG/SPDC processes in waveguides are critical to the generation of polarization entangled photon pairs [205,206].

When considering on-chip applications, it is imperative that the optical frequency-conversion takes place in a compact footprint that is suitable for fabrication on the limited surface area of the chip. Both nanoscale and microscale structures are the primary means of achieving frequency-conversion in a small footprint, which has been observed in LN, AlN, GaN, and ZnSe waveguides [207–211], LN microresonators [212,213], and LN photonic crystal cavities [214,215]. Preferred arrangements for second-order nonlinear frequency-conversion are waveguides satisfying modal phase-matching or quasi-phase-matching, since both configurations allow for phase-matched operation, permit strong confinement of the fields, and have a small footprint compatible with on-chip applications. In this Chapter, SHG in LN and CSP waveguiding arrangements is numerically investigated (using the techniques developed in Chapter 5) for producing radiation in the near-IR and visible spectral regions. Subsequently, a planar LN waveguiding arrangement is experimentally-realized, which produces radiation in the visible spectral region via SHG. As discussed in Chapter 2, SHG, SFG, DFG, and OR are all second-order nonlinear processes capable of converting photons at certain frequencies to photons at other frequencies, such that this chapter emerges as a natural extension of investigating second-order nonlinear phenomena.

7.1. SHG in Au-LN-Au and LN hybrid-plasmonic waveguides¹³

Plasmonic effects are realized when an EM wave couples to the surface of a metal, resulting in the energy of the EM wave occupying a localized spatial region. Typically, higher peak intensities are realized when utilizing plasmonic confinement techniques, opposed to other confinement techniques (e.g. a dielectric waveguide of comparable dimensions). Since conversion efficiency is directly related to the peak intensity of the excitation pulse, plasmonic structures have received considerable attention in the area of nonlinear frequency-conversion. Herein, a metal-LN-metal (MLNM) nanoplasmonic waveguide and a LN hybrid-plasmonic (LNHP) waveguide are investigated for ultrashort electric field pulse generation occurring via the second-order nonlinear process of SHG.

7.1.1. Waveguiding structures

Figure 7.1(a) and 7.1(d) illustrate the MLNM nanoplasmonic and LNHP frequency-conversion waveguides, respectively, which are supported by a SiO₂ platform. The MLNM nanoplasmonic waveguiding structure is composed of a thin LN layer of thickness T , width W , and length L that is sandwiched between two 100 nm-thick gold film layers. Alternatively, the LNHP waveguide is composed of stacked gold, LN, and Si layers. Here, the LN width, thickness, and length are denoted as W , T , and L , respectively, the gold thickness is set to 100 nm, and the Si layer thickness is set as 123 nm. Since a substantial portion of the excitation

¹³A version of this section's work is published as B. N. Carnio and A. Y. Elezzabi, "Second harmonic generation in metal-LiNbO₃-metal and LiNbO₃ hybrid-plasmonic waveguides," *Opt. Express* **26**, 26283-26291 (2018).

and SHG modes are situated in the Si, this layer is used to adjust the effective refractive indices of these modes, where a Si thickness of 123 nm permits phase-matching. Notably, gold is chosen as the metal layer because it provides a stable chemical structure in air. This contrasts with silver, which is known to react with sulfur compounds in air and produce silver sulfide. In both waveguides, the c -axis of the LN is oriented along the z axis and the crystal's cross-section is cut along the (010) plane. The waveguides are excited by an electric field pulse having a central-wavelength of 1550 nm and a pulse duration of 100 fs. As such, the resulting excitation mode generates photons near a wavelength of 775 nm via SHG as it propagates along the LN waveguides. Importantly, very detailed analyses have been performed on coupling into these plasmonic waveguides [216–219]. For LN, the second-order nonlinear coefficient tensor is,

$$\bar{\bar{d}}_{LN} = \begin{bmatrix} 0 & 0 & 0 & 0 & d_{31} & -d_{22} \\ -d_{22} & d_{22} & 0 & d_{31} & 0 & 0 \\ d_{31} & d_{31} & d_{33} & 0 & 0 & 0 \end{bmatrix}, \quad (7.1)$$

where $d_{31}=4$ pm/V, $d_{22}=-2.4$ pm/V, and $d_{33}=20.6$ pm/V at an excitation wavelength of 1550 nm [189–191,220–222]. Notably, Eq. (7.1) utilizes the Kleinman symmetry condition, which is valid since dispersion is low across the relevant spectral regions [31]. The simulations implement the complete second-order nonlinear coefficient tensor of LN [i.e. Eq. (7.1)]. Furthermore, while nonlinear effects such as multi-photon absorption occur in LN at intensities >100 GW/cm² [186], the excited waveguide modes all have a peak intensity of 10 GW/cm², such that these nonlinear effects do not influence the SHG process. The ordinary and extraordinary refractive indices of the uniaxial LN crystal are obtained from Ref. [172], the linear optical properties of Si and SiO₂ are both taken from Ref. [182], and the linear optical data for gold is attained from Ref. [223].

Figure 7.1(a) illustrates the cross-section of the $W=400$ nm and $T=780$ nm MLNM nanoplasmonic waveguide. At these dimensions, the MLNM nanoplasmonic waveguide supports

the excitation mode and the quasi-TM₀₀ SHG mode displayed in Fig. 7.1(b) and 7.1(c), respectively. Notably, these modes exhibit significant spatial overlap and have the majority of their electric field polarization along the z axis, such that photons generated near 775 nm couple to the quasi-TM₀₀ SHG mode with a high efficiency. Similarly, the $W=400$ nm and $T=100$ nm LNHP waveguide [Fig. 7.1(d)] supports the excitation mode displayed in Fig. 7.1(e) and the SHG mode presented in Fig. 7.1(f). Again, since these modes occupy the same spatial region and both possess a significant z -directed electric field polarization component, photons generated near 775 nm couple to the SHG mode with high efficiency.

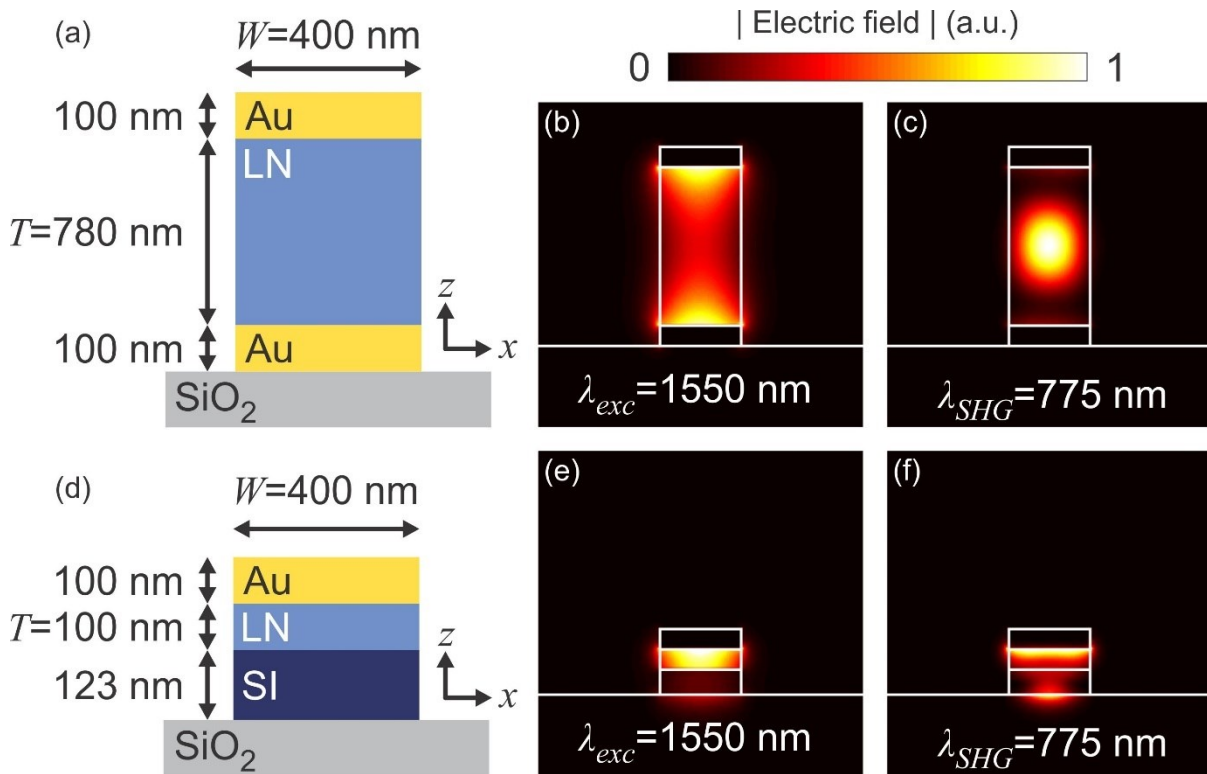


Fig. 7.1. (a) Cross-sectional schematic of the $W=400$ nm and $T=780$ nm MLNM nanoplasmic waveguide. (b) $\lambda_{exc}=1550$ nm and (c) $\lambda_{SHG}=775$ nm modal intensity distributions supported by the MLNM nanoplasmic waveguide. (d) Cross-section of the $W=400$ nm and $T=100$ nm LNHP waveguide. (e) $\lambda_{exc}=1550$ nm and (f) $\lambda_{SHG}=775$ nm modal intensity distributions supported by the LNHP waveguide.

7.1.2. SHG in MLNM nanoplasmonic and LNHP waveguides

The phase-matching condition is investigated for both the MLNM nanoplasmonic and LNHP waveguides. Figure 7.2(a) depicts the effective refractive indices of the modes, n_{eff}^m , for both waveguides over the wavelength ranges of $\lambda_{exc}=1450-1650$ nm and $\lambda_{SHG}=725-825$ nm. By choosing $T=780$ nm for the MLNM nanoplasmonic and $T=100$ nm for the LNHP waveguides, the excitation wavelength of $\lambda_{exc}=1550$ nm is phase-matched to the SHG wavelength of $\lambda_{SHG}=775$ nm. The SHG coherence length, L_c^{SHG} , is calculated from the relationship (see Section 2.3.2),

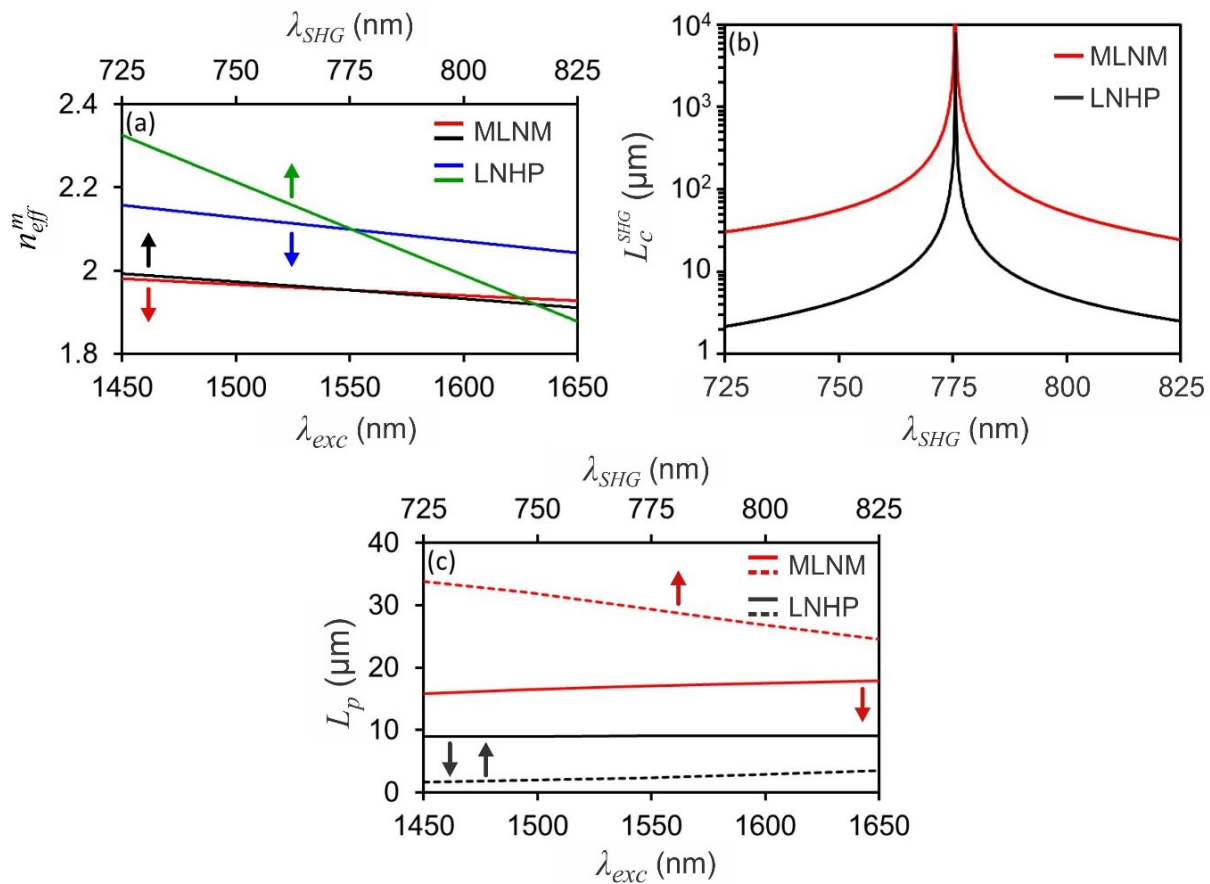


Fig. 7.2. (a) Effective refractive indices of the MLNM nanoplasmonic and LNHP modes, illustrating phase-matching between $\lambda_{exc}=1550$ nm and $\lambda_{SHG}=775$ nm. (b) Coherence length for the MLNM nanoplasmonic and LNHP waveguides. (c) Propagation lengths of the excitation and SHG wavelengths for the MLNM nanoplasmonic and LNHP waveguides.

$$L_c^{SHG}(\lambda_{SHG}) = \frac{\lambda_{SHG}}{2|n_{eff}^m(\lambda_{exc}) - n_{eff}^m(\lambda_{SHG})|}, \quad (7.2)$$

where $\lambda_{SHG} = \lambda_{exc}/2$. L_c^{SHG} is presented in Fig. 7.2(b), where the large peaks correspond to perfect phase-matching between $\lambda_{exc}=1550$ nm and $\lambda_{SHG}=775$ nm. Importantly, a large L_c^{SHG} is also obtained in the vicinity of $\lambda_{SHG}=775$ nm. For example, at a SHG wavelength of $\lambda_{SHG}=780$ nm, the MLNM nanoplasmonic and the LNHP waveguides have an L_c^{SHG} of 310 and 28 μm , respectively. Figure 7.2(c) shows the propagation length, L_p , of the excitation and SHG wavelengths. The small L_p values (i.e. <40 μm) observed in both waveguides are primarily due to loss introduced by the gold layers at both the excitation and SHG wavelengths. Clearly, the MLNM nanoplasmonic waveguide exhibits the largest L_p at the SHG wavelengths, since the associated quasi-TM₀₀ mode is mainly confined to the LN core and only a small portion of the electric field interacts with the gold layers. In both the MLNM nanoplasmonic and LNHP waveguide, $L_p < L_c^{SHG}$ near the central excitation and SHG wavelengths, such that absorption loss is the dominant mechanism limiting the length over which frequency-conversion can occur in these waveguides.

The time-averaged spatial distribution of the electric field magnitude at $\lambda_{SHG}=775$ nm is provided for the MLNM nanoplasmonic waveguide [Fig. 7.3(a)] and the LNHP waveguide [Fig. 7.3(b)]. For the MLNM nanoplasmonic waveguide [i.e. Fig. 7.3(a)], the electric field of the quasi-TM₀₀ SHG mode increases in magnitude with increasing propagation distance along the y axis. Since no electric field amplitude oscillations are observed, the MLNM nanoplasmonic waveguide does not support other phase-mismatched SHG modes. Furthermore, the quasi-TM₀₀ nature of this SHG mode would allow for efficient coupling into photonic waveguiding structures (e.g. a LN core). For the LNHP waveguide [i.e. Fig. 7.3(b)], the SHG mode has the highest electric field magnitude at a distance of $y=4-6$ μm from the input of the waveguide, such that the optimal

waveguide length of the LNHP waveguide is found to be between $y=4-6 \mu\text{m}$. Beyond this propagation distance, the SHG electric field decreases due to high loss at the excitation and SHG wavelengths. Clearly, part of the electric field propagates in the SiO_2 substrate layer. This is due to the height of the Si layer being 123 nm , which is less than the SHG wavelength in the Si layer (i.e. $\sim 200 \text{ nm}$). An interesting observation from Fig. 7.3(b) is the presence of electric field amplitude oscillations, where each electric field maximum is separated by a distance of $\sim 1.2 \mu\text{m}$.

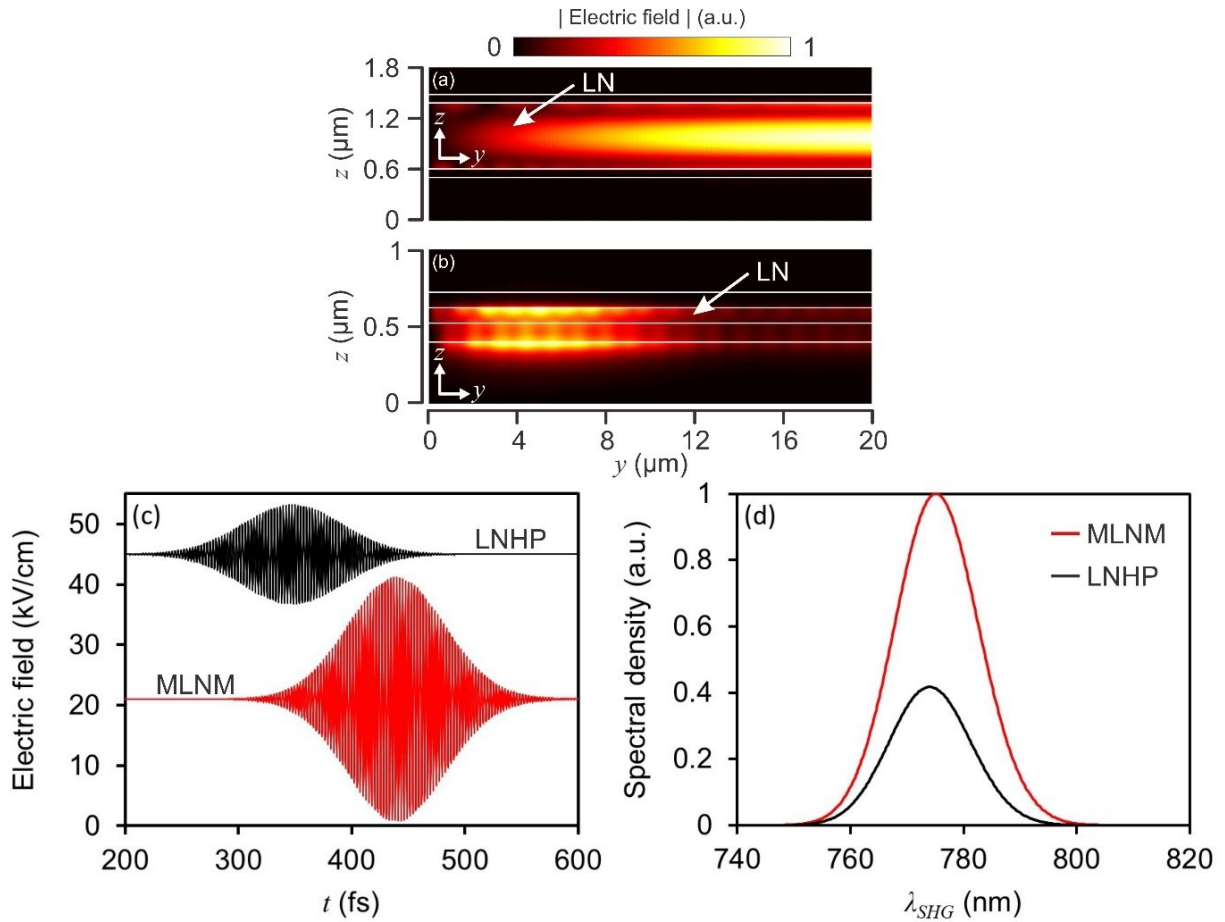


Fig. 7.3. Magnitude of the time-averaged spatial electric field distribution recorded at $\lambda_{\text{SHG}}=775 \text{ nm}$ for the (a) MLNM nanoplasmonic and (b) LNHP waveguides. (c) SHG time-domain electric field pulses and (d) SHG spectral density recorded in the waveguides near the positions of maximum electric fields.

This effect is due to a portion of the generated photons coupling to a phase-mismatched waveguide mode having an effective refractive index of 2.74 at $\lambda_{SHG}=775$ nm.

Figure 7.3(c) shows the SHG time-domain electric field signals recorded near the regions where the field is strongest. Notably, the electric field is very high in both the MLNM nanoplasmonic and LNHP waveguides, exhibiting peak-to-peak values of 40 and 16 kV/cm, respectively. For both the MLNM nanoplasmonic and LNHP waveguides, the SHG pulse durations are ~ 70 fs. Since SHG is dependent on the intensity of the excitation pulse, the SHG signals exhibit a shorter pulse duration than the 100 fs excitation pulse. As seen from Fig. 7.3(d), the spectral density of the SHG electric field pulses show uniform spectral distributions centered around ~ 775 nm. This is expected, since $L_p < L_c^{SHG}$ near 775 nm in the MLNM nanoplasmonic waveguide and the LNHP waveguides [see Figs. 7.2(b) and 7.2(c)]. From these spectral density plots, the SHG FWHM power bandwidths are calculated as 12 nm (i.e. 6 THz). Therefore, in terms of frequency, the SHG pulses have a larger bandwidth in comparison to the 4.4 THz FWHM power bandwidth associated with the 100 fs excitation pulse. Again, this is due to the SHG dependence on the excitation pulse intensity.

The performance of the phase-matched frequency-conversion plasmonic waveguides is studied by calculating the SHG conversion efficiency, η_{SHG} . Figure 7.4 demonstrates enhanced frequency-conversion obtained from the MLNM nanoplasmonic and LNHP waveguides in comparison to phase-matched Metal-LN (MLN) plasmonic and LN photonic waveguides. By choosing the LN photonic waveguide to have cross-sectional dimensions of $400 \text{ nm} \times 837 \text{ nm}$ (see Fig. 7.4 inset), phase-matching is achieved between the TM_{00} mode at $\lambda_{exc}=1550$ nm and the TM_{02} mode at $\lambda_{SHG}=775$ nm. Similarly, the cross-sectional dimensions of the MLN plasmonic waveguide are chosen as $400 \text{ nm} \times 509 \text{ nm}$, with a 100 nm-thick top gold layer (see Fig. 7.4 inset). This allows

phase-matching to be achieved between the plasmonic excitation mode at $\lambda_{exc}=1550$ nm and the quasi-TM₀₀ SHG mode at $\lambda_{SHG}=775$ nm. The MLN plasmonic waveguide exhibits the lowest conversion efficiency (i.e. $\eta_{SHG}<9\times 10^{-6}$) at nearly all investigated lengths. This is due to the plasmonic excitation mode being highly confined to the metal-LN interface, while the quasi-TM₀₀ SHG mode is primarily located in the LN central region, such that the spatial overlap of the electric fields is poor. Oscillations are evident in η_{SHG} of the LN photonic waveguide, which arise from generation of the phase-mismatched TM₀₀ SHG mode. From the effective refractive index of the TM₀₀ excitation mode ($n_{eff}^m=1.64$) and the TM₀₀ SHG mode ($n_{eff}^m=2$), the coherence length of these modes is calculated as $L_c^{SHG}=1.1$ μm at $\lambda_{SHG}=775$ nm. The power converted to a SHG mode is back-converted to the excitation mode after the distance of $2L_c^{SHG}$ [224] [see also Fig. 2.6(c) in Section 2.2.2]. This effect is clearly observed in Fig. 7.4, where the spatial oscillations have a period of $2L_c^{SHG}=2.2$ μm . Notably, in this photonic waveguide, coupling between the TM₀₀ excitation mode and the phase-mismatched TM₀₀ SHG mode is unavoidable because of the significant spatial overlap they exhibit.

The MLNM nanoplasmonic waveguide and the photonic LN waveguide are excited at the same peak intensity of 10 GW/cm², corresponding to excitation energies of 0.83 and 1 pJ, respectively. The $L=10$ μm MLNM nanoplasmonic waveguide has $\eta_{SHG}=6.5\times 10^{-5}$, which is 2.5 times higher than the value attained from the photonic LN waveguide. Furthermore, the $L=20$ μm MLNM nanoplasmonic waveguide reaches a high η_{SHG} of 1.1×10^{-4} , where this value is 1.15 times the value obtained from the photonic LN waveguide. Although the MLNM nanoplasmonic waveguide clearly exhibits the largest η_{SHG} at waveguide lengths between $L=4.7$ -20 μm , this comes at the expense of having a large footprint (i.e. large L). For lengths of $L=1.2$ -4.7 μm , the LNHP waveguide exhibits the highest conversion efficiencies, ranging from $\eta_{SHG}=0.5$ -2.3 $\times 10^{-5}$

and reaching its maximum value at $L=4.5 \mu\text{m}$. In comparison to the photonic LN waveguide of $L=2.1$ and $4.5 \mu\text{m}$, the LNHP waveguide exhibits an η_{SHG} that is 11 and 4 times higher, respectively. This dramatic enhancement is achieved despite the fact that the LNHP and photonic LN waveguides are being excited at the different energies of 0.22 and 1 pJ, respectively. This improvement in η_{SHG} is attained by confining the electric field to a smaller region in the LNHP waveguide in comparison to the LN photonic waveguide [225]. The $L>4.5 \mu\text{m}$ LNHP waveguides are strongly influenced by loss at the excitation and SHG wavelengths, such that η_{SHG} decreases to ~ 0 at $L\approx 20 \mu\text{m}$. Clearly, the LNHP waveguides are well-suited as miniaturized radiation sources for on-chip nano-optoelectronic applications.

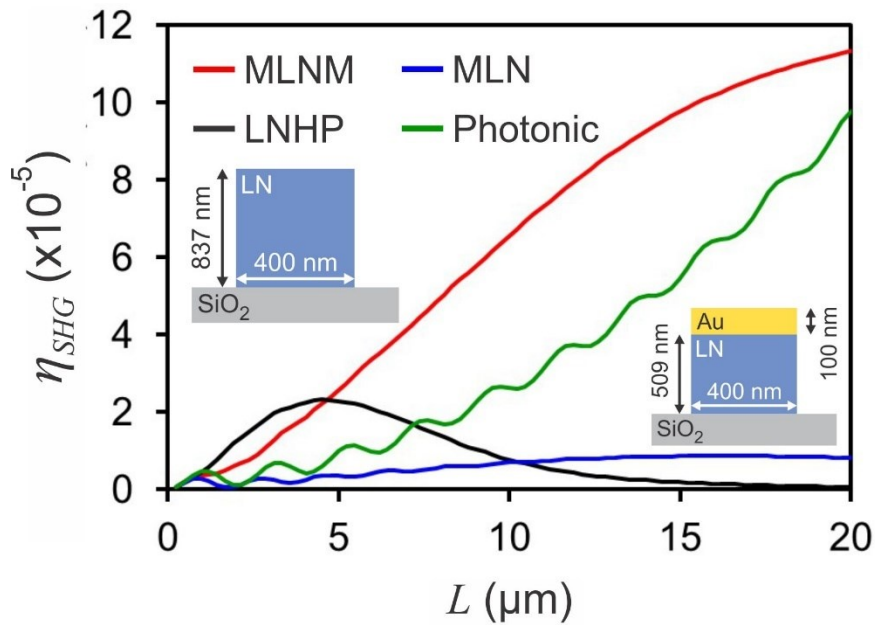


Fig. 7.4. Conversion efficiency for various lengths of the MLNM nanoplasmonic and LNHP waveguides. For comparison, the conversion efficiency is determined in a $400 \text{ nm} \times 509 \text{ nm}$ phase-matched MLN waveguide with a 100 nm thick gold layer situated on the LN, as well as a $400 \text{ nm} \times 837 \text{ nm}$ phase-matched LN photonic waveguide (see insets).

7.2. Optical frequency SHG in a CSP photonic waveguide¹⁴

As stated in Table 1.1, CSP has the key properties of a wide bandgap (i.e. 2.45 eV [37]) and a high second-order nonlinear coefficient (i.e. $d_{36}=84.5$ pm/V at an excitation wavelength of 4.6 μm [35]). Additionally, CSP exhibits a transparency range having a lower cut-off wavelength of 520 nm [35] [see Table 1.1]. In this section, nonlinear FDTD simulations are performed to investigate SHG near the wavelength of 775 nm in a CSP photonic waveguide, the results of which are compared to SHG from a LN photonic waveguide.

7.2.1. Waveguiding structure

The CSP and LN photonic waveguiding structure, having dimensions of $W \times T \times L$ and being situated on a low-index SiO_2 layer, is illustrated in Fig. 7.5. A 1550 nm central-wavelength electric field pulse having a duration of 100 fs is coupled into the CSP or LN region and propagates along the photonic waveguide. In such a frequency-conversion structure, SHG is the nonlinear process responsible for producing photons having wavelengths near 775 nm. To maximize frequency-conversion, the CSP photonic waveguide cross-section is cut along the (110) crystal plane and the LN photonic waveguide cross-section is cut along the (010) crystal plane, as shown in Fig. 7.5. Notably, both CSP and LN are uniaxial crystals with their optical axes along the c -axis. As such, z -directed electric field polarizations experience an extraordinary refractive index, while x and y -polarized electric fields experience an ordinary refractive index. When simulating the photonic

¹⁴A version of this section's work is published as B. N. Carnio and A. Y. Elezzabi, "Second harmonic generation in CdSiP_2 nanowires in the optical frequency regime," *IEEE Photonic Tech. Lett.* **30**, 1408-1411 (2018).

waveguides, the peak excitation pulse intensity is kept to values $<11.4 \text{ GW/cm}^2$, which is below the threshold for multi-photon absorption¹⁵ [186].

The uniaxial CSP and LN crystals are modeled using the linear optical data from Refs. [146] and [172], respectively, whereas the linear optical properties of the SiO_2 layer are taken from Ref. [182]. The comprehensive FDTD simulations implement the full second-order nonlinear tensor for both CSP and LN. Since CSP has $\bar{4}2m$ point group symmetry [226], it has a nonlinear tensor of the form [43],

$$\bar{\bar{d}}_{CSP} = \begin{bmatrix} 0 & 0 & 0 & d_{36} & 0 & 0 \\ 0 & 0 & 0 & 0 & d_{36} & 0 \\ 0 & 0 & 0 & 0 & 0 & d_{36} \end{bmatrix}, \quad (7.3)$$

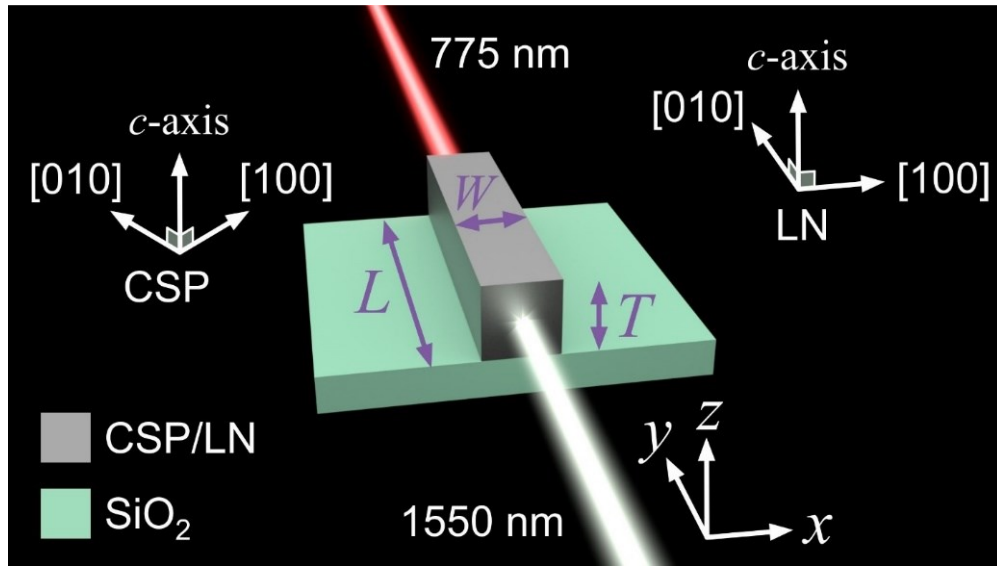


Fig. 7.5. Illustration of the CSP/LN photonic waveguide. A 1550 nm excitation pulse is converted to 775 nm via nonlinear effects in the photonic waveguides. The cross-sections of the photonic waveguides are cut along the (110) and (010) planes of the CSP and LN crystals, respectively.

¹⁵Using a 1550 nm, 84 fs pump pulse having a peak intensity between 0-20 GW/cm^2 , we experimentally observed intensity-independent transmission through the CSP crystal and a linear-dependence with SHG electric field generation in the CSP crystal.

where the Kleinman symmetry condition is utilized [31]. $d_{36}=105$ pm/V at the excitation wavelength of 1550 nm, which is calculated using Miller's rule with $d_{36}=84.5$ pm/V at a wavelength of 4.56 μm [226] and the CSP linear optical data in Ref. [146]. In reference to the coordinate system illustrated in Fig. 7.5, \bar{d}_{CSP} is used to ascertain the z -directed second-order nonlinear polarization,

$$P_{z,CSP}^{(2)} = 2\varepsilon_0 d_{36} E_x^2 - 2\varepsilon_0 d_{36} E_y^2, \quad (7.4)$$

where $E_{x,y}$ are the excitation electric fields polarized along the x and y axes, respectively. From Eq. (7.4) and the orientation of the CSP photonic waveguide shown in Fig. 7.5, it is evident that the excitation electric field should be largest along the x axis in order to generate the highest $P_{z,CSP}^{(2)}$. Alternatively, the LN crystal has $3m$ point group symmetry [173], the nonlinear tensor in Eq. (7.1), and $d_{31}=4$ pm/V, $d_{22}=-2.4$ pm/V, and $d_{33}=20.6$ pm/V at 1550 nm [173, 189, 231,232, 190, 220–222,227–230]. As such, the z -directed second-order nonlinear polarization is,

$$P_{z,LN}^{(2)} = 2\varepsilon_0 d_{31} E_x^2 + 2\varepsilon_0 d_{31} E_y^2 + 2\varepsilon_0 d_{33} E_z^2, \quad (7.5)$$

where E_z is the excitation electric field polarized along the z axis. Since d_{33} is ~ 5 times larger than d_{31} , the LN excitation mode should have the largest electric field contribution along the z axis to produce the highest $P_{z,LN}^{(2)}$.

7.2.2. SHG in CSP and LN photonic waveguides

The CSP and the LN photonic waveguides are set to have the same sub-micron width of $W=600$ nm, while the photonic waveguide thickness, T , is optimized to achieve phase-matching. The insets in Fig. 7.6(a) display the phase-matched modes supported by the $W=600$ nm and $T=650$ nm CSP photonic waveguide at the wavelengths of 1550 and 775 nm. Clearly, this photonic

waveguide supports the TE_{00} mode at 1550 nm and the TM_{20} mode at 775 nm. Figure 7.6(a) shows the effective refractive indices of the CSP mode, $n_{eff}^{m,CSP}$, at the excitation wavelengths and the SHG wavelengths, where $n_{eff}^{m,CSP}=2.68$ at $\lambda_{exc}=1550$ nm and $\lambda_{SHG}=775$ nm. The LN photonic waveguide of $W=600$ nm and $T=987$ nm supports the TM_{00} mode at 1550 nm and the TM_{02} mode at 775 nm, as shown in the insets of Fig. 7.6(b). The frequency-dependent effective refractive

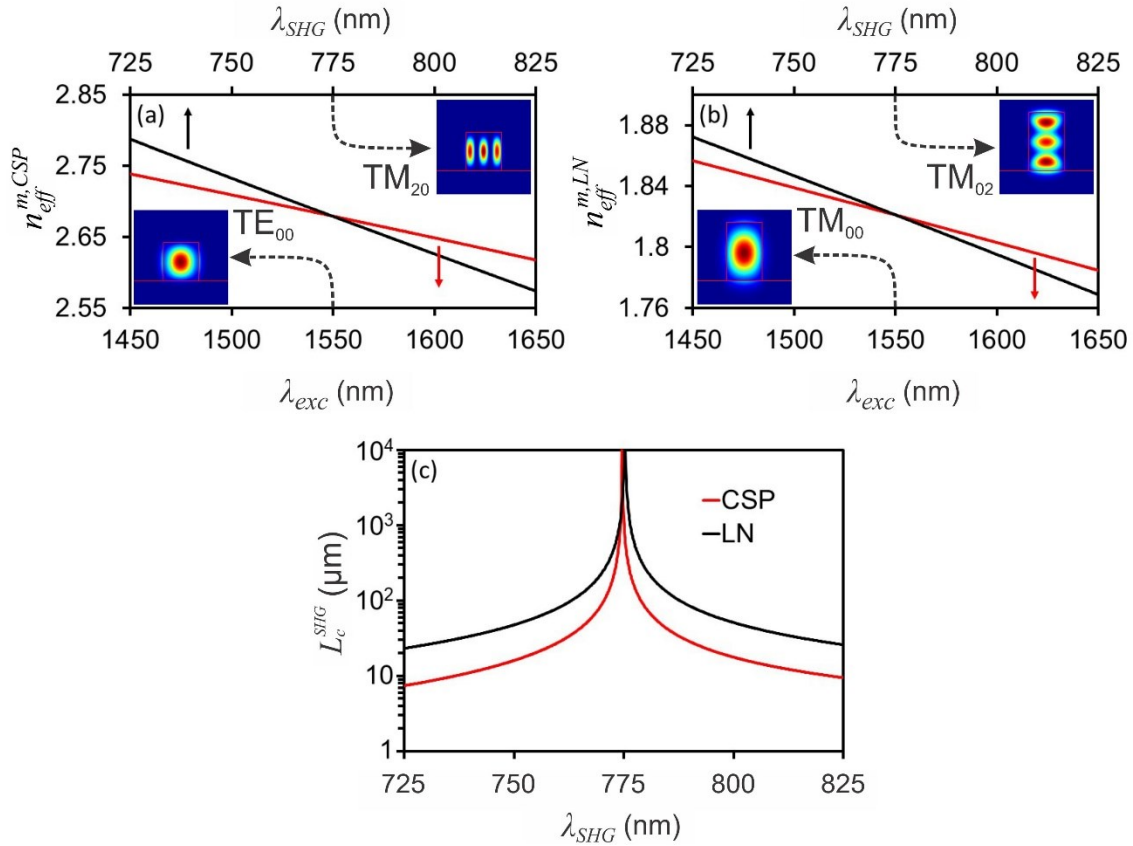


Fig. 7.6. (a) The effective refractive indices of the TE_{00} excitation mode and TM_{20} SHG mode for the $600 \text{ nm} \times 650 \text{ nm}$ CSP photonic waveguide. The insets depict the transverse mode profiles at wavelengths of $\lambda_{exc}=1550$ nm and $\lambda_{SHG}=775$ nm. (b) The effective refractive indices of the TM_{00} excitation mode and TM_{02} SHG mode for the $600 \text{ nm} \times 987 \text{ nm}$ LN photonic waveguide. The insets depict the $\lambda_{exc}=1550$ nm and $\lambda_{SHG}=775$ nm transverse mode profiles. (c) Coherence length between the excitation and SHG frequency components propagating along the CSP and LN photonic waveguides.

indices of the LN mode, $n_{eff}^{m, LN}$, at the excitation wavelengths and SHG wavelengths are shown in Fig. 7.6(b), where $n_{eff}^{m, LN}=1.82$ at $\lambda_{exc}=1550$ nm and $\lambda_{SHG}=775$ nm. The SHG coherence length, L_c^{SHG} , is calculated using Eq. (7.2). L_c^{SHG} is shown in Fig. 7.6(c) for the CSP and LN photonic waveguides, where L_c^{SHG} increases sharply near the SHG wavelength of 775 nm.

Figure 7.7(a) displays the SHG conversion efficiency, η_{SHG} , for both the phase-matched CSP and LN photonic waveguides at various lengths, L . In all of the photonic waveguides, the spatial oscillations observed in the conversion efficiency are due to the propagation of phase-mismatched modes. For an excitation pulse having an energy of $\xi_{exc}=786$ fJ, the LN photonic waveguide produces SHG radiation at $\eta_{SHG}<1.4\times 10^{-4}$ for all $L<30$ μm . In comparison, when exciting the CSP photonic waveguide at the same peak intensity of 5.8 GW/cm² (i.e. $\xi_{exc}=400$ fJ), η_{SHG} from the CSP photonic waveguide is higher by a factor of ~ 6 . More importantly, when the CSP and LN photonic waveguides are exciting at the same excitation energy of $\xi_{exc}=786$ fJ, η_{SHG} from the CSP photonic waveguide is higher by ~ 11 times. While the d_{36} coefficient of the CSP crystal is >5 times higher than the d_{33} coefficient of the LN crystal, η_{SHG} in the CSP photonic waveguide is also dictated by strength of the E_y electric field component. According to Eq. (7.4), this E_y component reduces the magnitude of $P_{z, CSP}^{(2)}$.

The time-averaged spatial distribution of the electric field at a wavelength of 775 nm is shown along the y - x plane [Fig. 7.7(b)] and the x - z plane [Fig. 7.7(c)] of the CSP photonic waveguide. Clearly, the generated radiation strength increases as the excitation pulse propagates along the CSP photonic waveguide, which is due to the generated radiation combining in-phase. Both electric field distributions show the three lobes of the phase-matched TM₂₀ SHG mode, while the y - x distribution displays alternating regions of high and low electric field magnitude in the

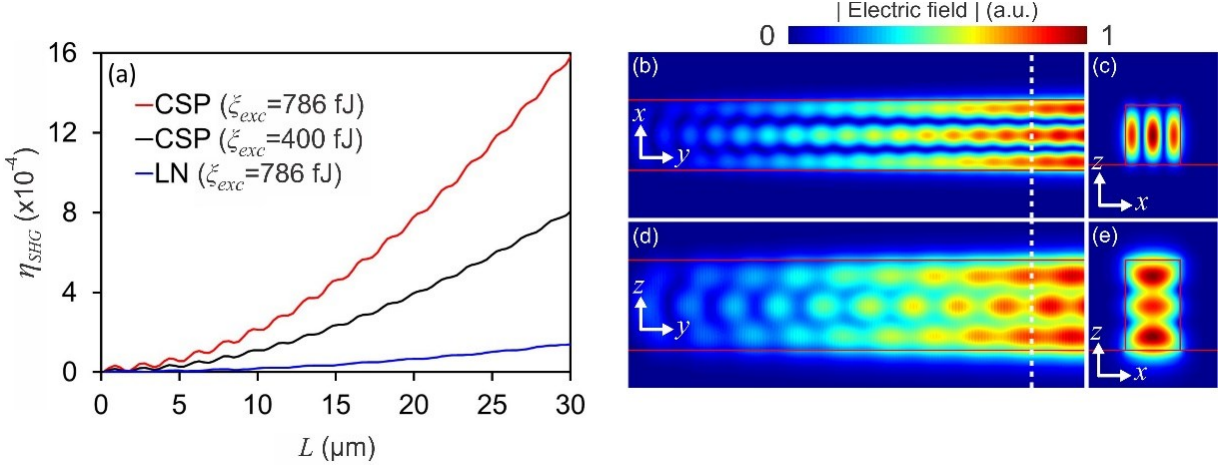


Fig. 7.7. (a) Conversion efficiency for various photonic waveguide lengths. Time-averaged spatial electric field distribution at $\lambda_{SHG}=775$ nm on the (b) y - x and (c) x - z planes of the $W=600$ nm \times $T=650$ nm \times $L=30$ μm CSP photonic waveguide. Time-averaged spatial electric field distribution at $\lambda_{SHG}=775$ nm on the (d) y - z and (e) x - z planes of the $W=600$ nm \times $H=987$ nm \times $L=30$ μm LN photonic waveguide. The transverse distributions in (c) and (e) are obtained along the dotted lines in (b) and (d), respectively.

direction of propagation. This mode beating effect indicates that the SHG electric field produced in the CSP photonic waveguide is a superposition of the phase-matched TM_{20} SHG mode and the phase-mismatched TM_{00} SHG mode. In these photonic waveguides, frequency-conversion between the TE_{00} excitation mode and the phase-mismatched TM_{00} SHG mode is unavoidable due to their significant spatial overlap. At $\lambda_{SHG}=775$ nm, the coherence length between the TE_{00} excitation mode and this phase-mismatched TM_{00} SHG mode is $L_c^{SHG}=0.88$ μm , such that the power converted to this TM_{00} SHG mode is back-converted [see Ref. [224] and Fig. 2.6(c) in Section 2.2.2] to the excitation mode at a distance of $2L_c^{SHG}=1.76$ μm . This back-conversion leads to the oscillations observed in Fig. 7.7(b), which clearly repeat every 1.76 μm . Similarly, the electric field distribution at a wavelength of 775 nm is shown along the y - z plane [Fig. 7.7(d)] and the x - z plane [Fig. 7.7(e)] for the LN photonic waveguide. The SHG radiation shows a modal

beating due to the LN photonic waveguide being influenced by the phase-mismatched TM_{00} SHG mode.

The SHG time-domain signals recorded near the output of the CSP and LN photonic waveguides (at the center of their cross-sections) are displayed in Fig. 7.8(a). The peak-to-peak electric field recorded in the LN photonic waveguide has an appreciable value of 23 kV/cm. Nonetheless, the CSP photonic waveguide excited at $\xi_{exc}=400$ and 786 fJ generates electric fields having peak-to-peak values 2.6 and 5 times higher, respectively. Figure 7.8(b) shows the spectral density of the time-domain signals recorded in the photonic waveguides. No phase-mismatching dips are observed in either the CSP or LN spectra, since the cross-sections of the photonic waveguides are optimized for excitation at a wavelength of $\lambda_{exc}=1550$ nm.

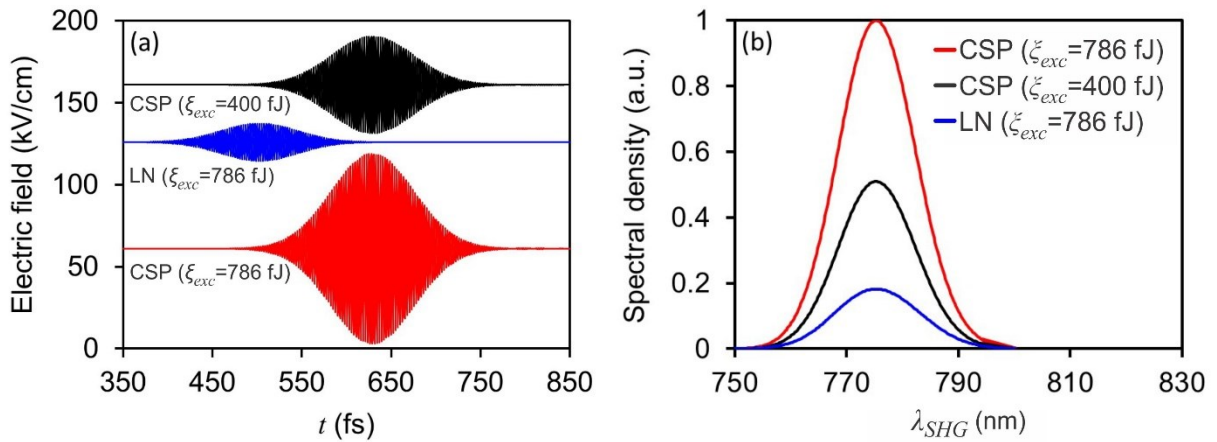


Fig. 7.8. (a) SHG time-domain electric field signals and (b) their associated spectral densities.

7.3. Phase-matched frequency-conversion in waveguides by means of transverse wavevector projections¹⁶

When considering nonlinear frequency-conversion in a waveguide, it is important to evaluate the phase-matching conditions, as well as the spatial overlap between the excitation mode and the generation mode. Although often discussed in far less detail, nonlinear frequency-conversion is equally dependent on the coupling arrangement of the excitation electric field. Quite obviously, if the excitation pulse does not couple into a given mode, then this particular mode cannot contribute to nonlinear frequency-conversion, even if it satisfies the phase-matching and spatial overlap requirements. A TEM_{00} free-space Gaussian electric field normally-incident on a dielectric waveguide does not couple into the odd-ordered modes, even when the incident electric field polarization is the same as the odd-ordered modes [89]. Alternatively, an off-normal-incidence TEM_{00} free-space Gaussian electric field can couple into both even-ordered and odd-ordered modes, given an incident electric field polarization matching that of the modes [89]. Such coupling is achieved by the angular-dependence introducing transverse wavevector projections on the cross-section of the waveguide [89]. In this section, FDTD simulations demonstrate the need to utilize the off-normal-incidence coupling arrangement to achieve phase-matched SHG from the TM_{10} and TM_{11} excitation modes in a LN waveguide.

¹⁶A version of this section's work is published as B. N. Carnio and A. Y. Elezzabi, "Phase-matched frequency-conversion in waveguides by means of transverse wavevector projections," *J. Opt. Soc. Am. B* **37**, 1140-1143 (2020).

7.3.1. Coupling arrangement

Figure 7.9 shows a schematic representation of the waveguiding geometry, which is composed of a SiO₂ substrate and a LN core (length L , thickness T , and width W) having its c -axis aligned with the z axis. The excitation electric field is taken to have a Gaussian spatial distribution, which couples into the waveguide at the arbitrary angles of θ_1 (directed towards the y - z plane) and θ_2 (directed towards the x - y plane). This excitation electric field has a pulse duration of 40 fs, a central-wavelength of 800 nm, a beam waist radius of 1 μm , and has its main polarization component oriented along the LN c -axis. The linear optical properties of the LN crystal and the SiO₂ platform are obtained from Refs. [172, 182,233], whereas the nonlinear optical properties of the LN crystal are taken from Ref. [190]. FDTD simulations are conducted, which model coupling of the excitation electric field into the waveguide and the SHG process occurring within the waveguide.

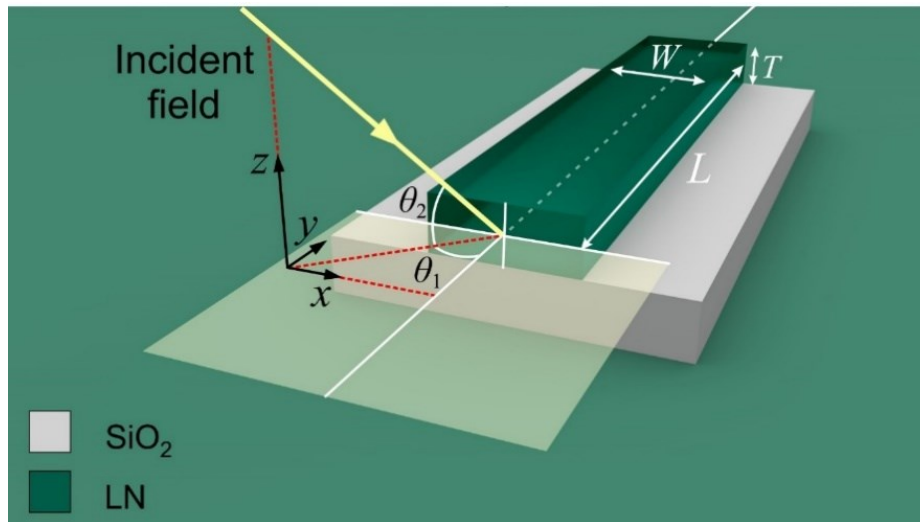


Fig. 7.9. Schematic of the coupling arrangement used to angularly excite the LN waveguide, where θ_1 is the coupling angle directed towards the y - z plane and θ_2 is the coupling angle directed towards the x - y plane.

7.3.2. SHG via off-normal-incidence coupling

To demonstrate the requirement of introducing a transverse wavevector projection to couple into the odd-ordered excitation modes, a waveguide is investigated having the dimensions of $W=670$ nm, $T=800$ nm, and $L=250$ μm . Although the waveguide supports several excitation and SHG modes, the modes important to the SHG process are those that simultaneously exhibit a non-zero spatial overlap integral [234], S , and have the same effective phase refractive index, n_{eff}^m . These conditions are satisfied by the TM_{10} mode at the excitation wavelength of $\lambda_{exc}=800$ nm [see Fig. 7.10(a)] and the TM_{40} mode at the SHG wavelength of $\lambda_{SHG}=400$ nm [see Fig. 7.10(b)], where

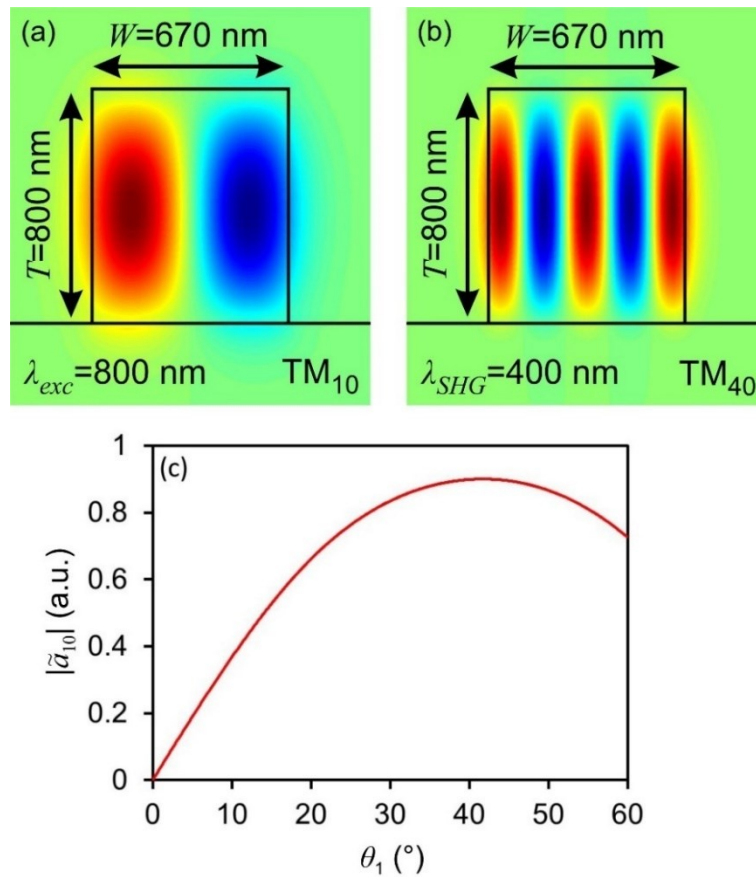


Fig. 7.10. (a) TM_{10} mode supported at the excitation wavelength of $\lambda_{exc}=800$ nm. (b) TM_{40} mode supported at the SHG wavelength of $\lambda_{SHG}=400$ nm. (c) Magnitude of the coupling coefficient for the TM_{10} excitation mode.

$\mathbb{S}=181 \text{ mm}^{-1}$ and $n_{eff}^m=1.88$. However, for any angle θ_2 , the excitation field can only couple into the TM_{10} waveguide mode provided that $\theta_1 \neq 0$, as this allows the incident electric field to satisfy the EM waveguide boundary conditions [89]. Figure 7.10(c) depicts the magnitude of the coupling coefficient for the TM_{10} mode, $|\tilde{a}_{10}|$, spanning the range of $\theta_1=0^\circ$ - 60° for $\theta_2=0^\circ$. Clearly, $|\tilde{a}_{10}|=0$ at $\theta_1=0^\circ$ and increases to a maximum value at $\theta_1 \approx 40^\circ$. Therefore, this waveguide is practical for the SHG process as it satisfies the phase-matching condition, exhibits a high spatial overlap between the excitation and SHG modes, and can achieve appreciable coupling efficiencies for the excitation electric field [89].

Figure 7.11(a) illustrates the SHG time-domain electric field obtained when $\theta_1=40^\circ$, calculated at the center of the waveguide's transverse profile (i.e. $x=z=0 \text{ }\mu\text{m}$). Clearly, the time-domain signal consists of two SHG pulses. A weak SHG signal is observed at $t=0.1 \text{ ps}$ and has the short-duration of $\sim 28 \text{ fs}$. Here, the free-space electric field couples to the TM_{00} mode and generates this signal through a phase-mismatched process. More importantly, a stronger SHG signal is observed having a long-duration of 0.8 ps . As expected, this is from the angularly-incident free-space electric field coupling into the TM_{10} mode, permitting SHG through phase-matching with the TM_{40} mode. As discussed in Ref. [235], the long duration of the generated signal is due to the phase-matched TM_{10} and the TM_{40} modes travelling at difference group velocities. This duration is expressed as,

$$\Delta t = \frac{L}{c} |n_{eff,g}^m(\lambda_{SHG}) - n_{eff,g}^m(\lambda_{exc})|, \quad (7.6)$$

where $n_{eff,g}^m$ is the effective group refractive index of the modes supported by the waveguide. $n_{eff,g}^m=3.6$ for the TM_{40} SHG mode and $n_{eff,g}^m=2.6$ for the TM_{10} excitation mode, such that $\Delta t=0.8 \text{ ps}$, in agreement with the duration observed in Fig. 7.11(a). Notably, even though $n_{eff,g}^m$

are not equal, phase-matching is satisfied because both the TM_{10} and the TM_{40} modes have the same $n_{eff}^m=1.88$. Figure 7.11(b) shows the SHG spectra produced at the angles of $\theta_1=0^\circ$ and $\theta_1=40^\circ$. At $\theta_1=0^\circ$, a weak SHG signal is obtained at the wavelength of $\lambda_{SHG}=405$ nm, which is due to phase-matching between the TM_{00} mode at the excitation wavelength and the TM_{22} mode at the SHG wavelength. At $\theta_1=40^\circ$, narrowband (i.e. 0.6 nm linewidth) SHG is observed at the wavelength of $\lambda_{SHG}=400$ nm, which is due to phase-matching between the TM_{10} mode at the excitation wavelength and the TM_{40} mode at the SHG wavelength. At this $\lambda_{SHG}=400$ nm, the spectral power for $\theta_1=40^\circ$ is >210 times higher than the spectral power for $\theta_1=0^\circ$. Interestingly, the SHG spectral power coupled to the TE_{ph} mode, $\mathcal{S}\mathcal{P}_{ph}^{SHG}$, is related to the coupling coefficient,

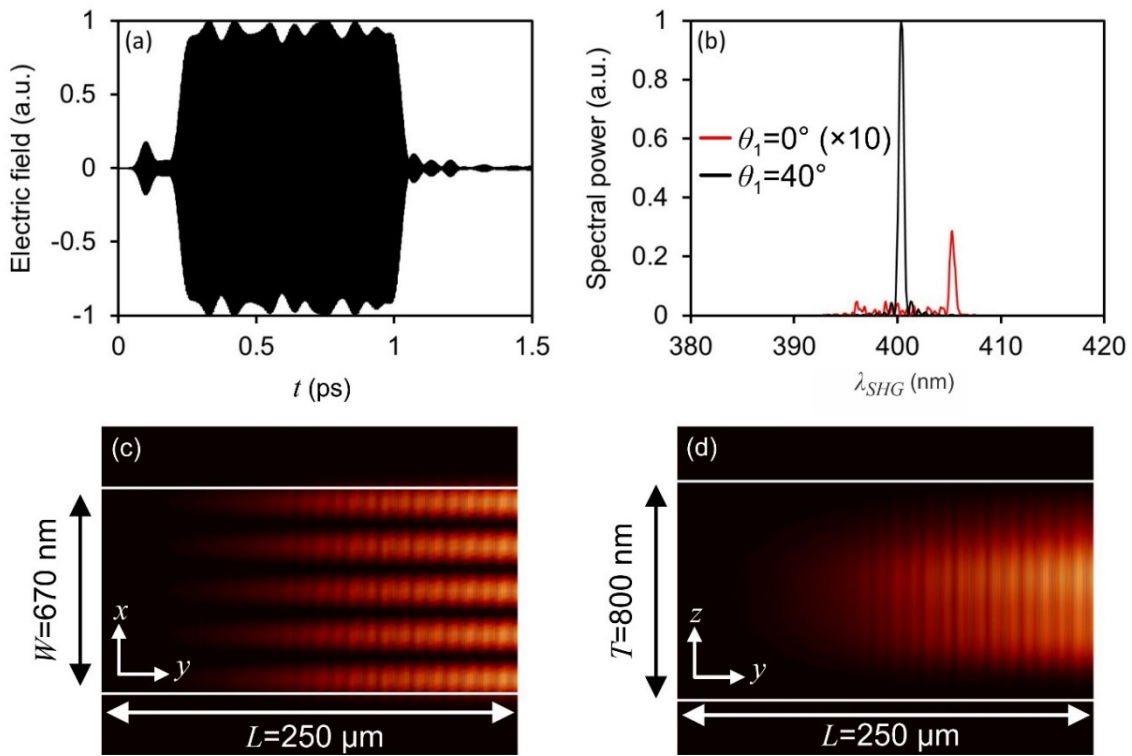


Fig. 7.11. (a) SHG time-domain signal produced from the $W=670$ nm, $T=800$ nm, and $L=250$ μm waveguide at $\theta_1=40^\circ$. (b) Spectral power of the SHG signal for $\theta_1=0^\circ$ and $\theta_1=40^\circ$. Time-averaged spatial power distributions at $\lambda_{SHG}=400$ nm along the (c) x - y plane and (d) z - y plane of the waveguide for $\theta_1=40^\circ$.

$$\mathcal{S}\mathcal{P}_{ph}^{SHG} \propto |\tilde{a}_{mv}^4|, \quad (7.7)$$

where \tilde{a}_{mv} is the complex coupling coefficient of the TE_{mv} mode at the excitation wavelength. As such, a change of $\theta_1=40^\circ$ (i.e. $|\tilde{a}_{10}|=0.9$) to $\theta_1=19^\circ$ (i.e. $|\tilde{a}_{10}|=0.64$) results in a reduction in this spectral power (i.e. $\mathcal{S}\mathcal{P}_{40}^{SHG}$) by a factor of 1/4. Figures 7.11(c) and 7.11(d) show the time-averaged spatial distribution of the power at $\lambda_{SHG}=400$ nm for $\theta_1=40^\circ$. Here, the SHG spatial power distribution is dominated by the TM_{40} mode, since the phase-matching condition is satisfied.

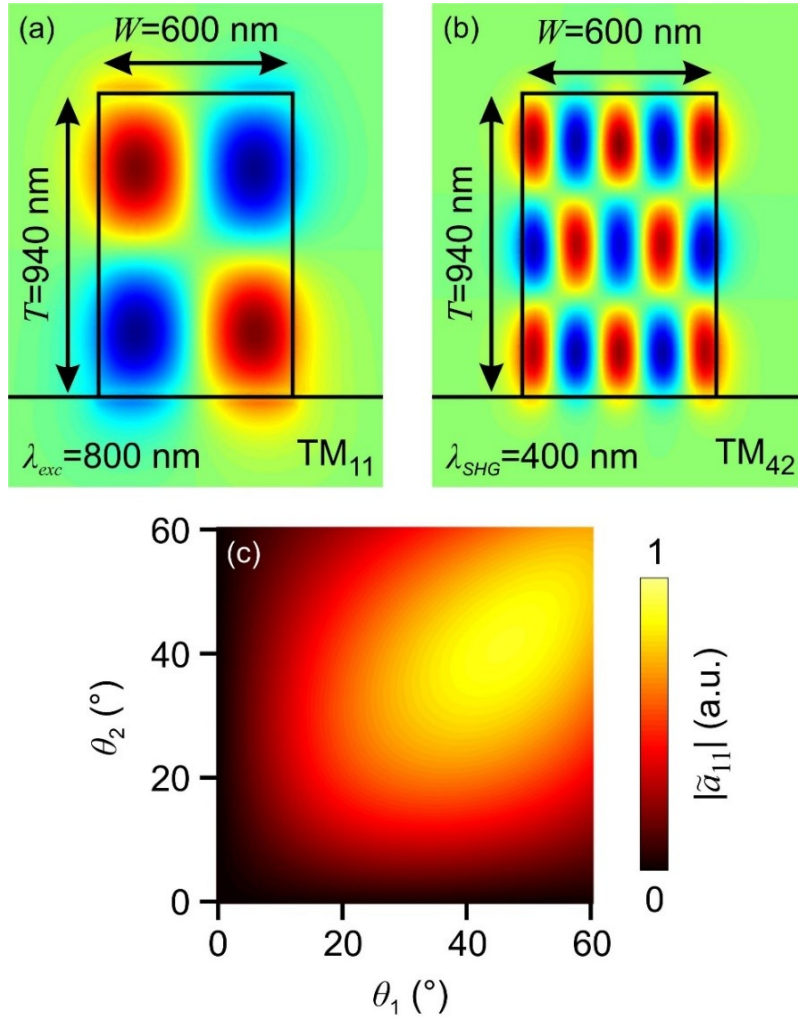


Fig. 7.12. (a) TM_{11} mode supported at the excitation wavelength of $\lambda_{exc}=800$ nm. (b) TM_{42} mode supported at the SHG wavelength of $\lambda_{SHG}=400$ nm. (c) Magnitude of the coupling coefficient for the TM_{11} mode.

In general, it is constructive to investigate the excitation of a mode that requires an off-normal-incidence angle in both transverse dimensions (i.e. $\theta_1 \neq 0^\circ$ and $\theta_2 \neq 0^\circ$). A waveguide having $W=600$ nm, $T=940$ nm, and $L=250$ μm supports the TM_{11} mode at the excitation wavelength of $\lambda_{exc}=800$ nm [see Fig. 7.12(a)] and the TM_{42} mode at the SHG wavelength of $\lambda_{SHG}=400$ nm [see Fig. 7.12(b)]. These modes satisfy perfect phase-matching, $n_{eff}^m=1.72$, and exhibit a spatial overlap integral of $S=69$ mm^{-1} . Figure 7.12(c) illustrates the magnitude of the coupling coefficient for the TM_{11} mode, $|\tilde{a}_{11}|$. As expected, $|\tilde{a}_{11}|=0$ if either $\theta_1=0^\circ$ or $\theta_2=0^\circ$; however, coupling reaches a maximum value at $\theta_1=\theta_2 \approx 40^\circ$. As such, this waveguide is practical for the SHG process, since it satisfies the phase-matching condition, exhibits a high spatial overlap between the modes, and achieves appreciable coupling efficiencies for the excitation electric field [89].

Figure 7.13(a) illustrates the SHG time-domain signal recorded at $x=z=0$ μm , where the waveguide is excited by an electric field incident at the angles of $\theta_1=\theta_2=40^\circ$. The signal observed at $t=0.1$ ps is due to a portion of the angularly-incident electric field coupling to the TM_{00} mode and producing phase-mismatched SHG. Similarly, the signal at $t=0.2$ ps occurs from a portion of the angularly-incident electric field coupling to the TM_{10} and TM_{01} modes, which produce phase-mismatched SHG. However, the signal between $t=0.4$ and 1.2 ps is due to the excitation electric field coupling to the TM_{11} mode and generating a SHG signal that is phase-matched to the TM_{42} mode [see Fig. 7.13(b) and 7.13(c)]. The duration of this time-domain signal (i.e. 0.8 ps) agrees with Eq. (7.6), where $n_{eff,g}^m=3.8$ for the TM_{42} SHG mode and $n_{eff,g}^m=2.8$ for the TM_{11} excitation mode. Here, the observed beating period is due to phase-matched SHG occurring at two distinct wavelengths within the investigate range. Figure 7.13(d) depicts the power spectra of the SHG signals produced by excitation electric fields incident at the angles of $\theta_1=\theta_2=0^\circ$ and $\theta_1=\theta_2=40^\circ$.

As expected, by exciting the waveguide at $\theta_1=\theta_2=40^\circ$, narrowband (i.e. 0.6 nm linewidth) SHG is produced at $\lambda_{SHG}=400$ nm. This spectral power is >10 times higher than the spectral power produced at $\theta_1=\theta_2=0^\circ$, since the TM_{11} mode is only excited by introducing a projection of the traverse wavevectors on the waveguide's cross-section (i.e. when $\theta_1 \neq 0^\circ$ and $\theta_2 \neq 0^\circ$). As seen from Eq. (7.7), when $\theta_1=\theta_2=40^\circ$ (i.e. $|\tilde{a}_{11}|=0.9$) is decreased to $\theta_1=\theta_2=24^\circ$ (i.e. $|\tilde{a}_{11}|=0.64$), the spectral density (i.e. $\mathcal{S}\mathcal{P}_{42}^{SH}$) is reduced by a factor of 1/4.

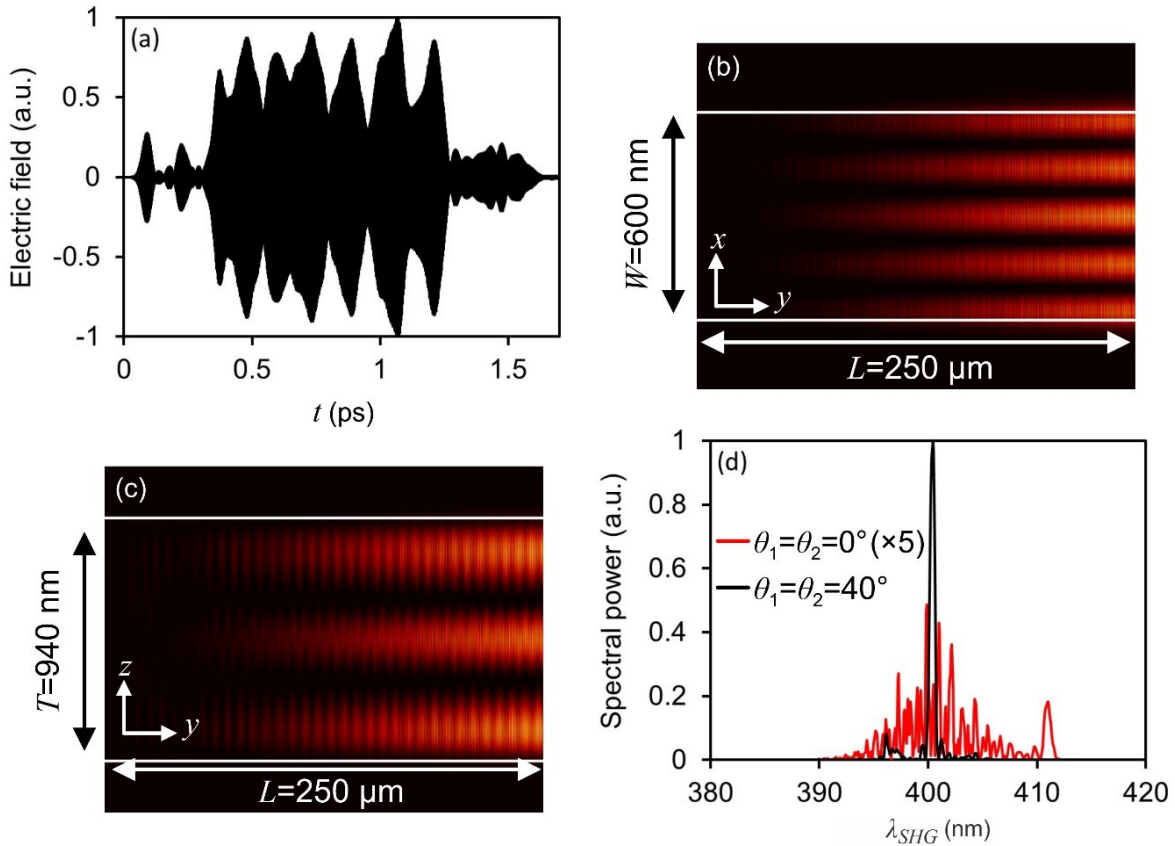


Fig. 7.13. (a) SHG time-domain signal produced from the $W=600$ nm, $T=940$ nm, and $L=250$ μm waveguide at $\theta_1=\theta_2=40^\circ$. Time-averaged spatial power distributions at $\lambda_{SHG}=400$ nm along the (b) x - y plane and (c) z - y plane of the waveguide for $\theta_1=\theta_2=40^\circ$. (d) Spectral power of the SHG signal for $\theta_1=\theta_2=0^\circ$ and $\theta_1=\theta_2=40^\circ$.

7.4. Off-normal-incidence coupling for phase-matched SHG in a sub-micron LN planar waveguide¹⁷

While the off-normal-incidence excitation technique and its impact on nonlinear frequency-conversion was numerically considered in Section 7.3, this section experimentally investigates off-normal-incidence coupling for SHG in a SiO₂-LN-air planar waveguide.

7.4.1. Experimental arrangement

The angular coupling arrangement being investigated is illustrated in Fig. 7.14, where a SiO₂-LN-air planar waveguide is the platform implemented to demonstrate SHG via off-normal-incidence excitation. The planar waveguide is 2.8 mm-long and the LN layer has a thickness of 775 nm. This structure is excited using a 5.1 MHz Ti:Sapphire oscillator producing electric field pulses having a duration of 50 fs, a central-wavelength of 790 nm, and nanojoule energies. These optical pulses are coupled into the waveguide at an incident angle of $\theta_i \approx 10^\circ$ [see Fig. 7.14]. Here,

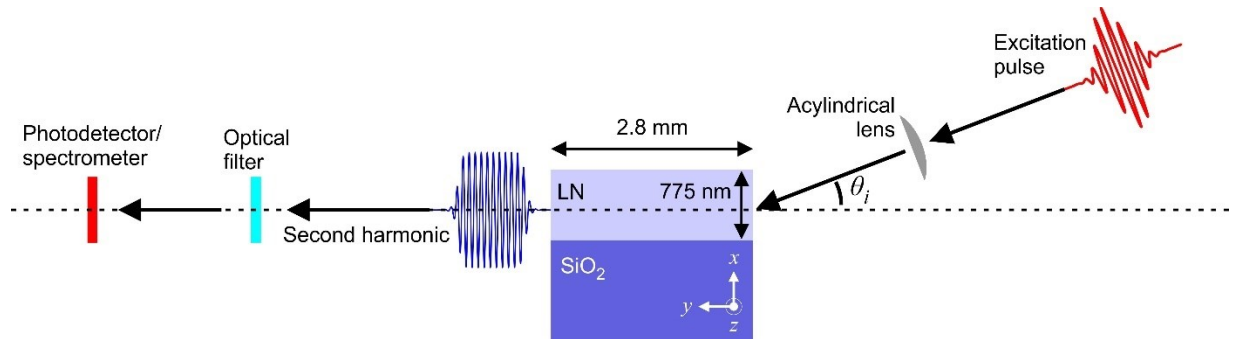


Fig. 7.14. Schematic of the experimental arrangement, which implements an acylindrical lens to couple the excitation pulse into the planar waveguide. The acylindrical lens is necessary to obtain the required line focus to couple the light into the planar waveguide.

¹⁷A version of this section's work is published as B. N. Carnio and A. Y. Elezzabi, "Off-normal incidence coupling for perfectly phase-matched second harmonic generation in a sub-micron LiNbO₃ planar waveguide," *J. Light. Technol.* **38**, 3959-3964 (2020).

a high NA (i.e. 0.49) acylindrical lens is used to focus the laser pulse and achieve a line focus of $\sim 4 \mu\text{m} \times 2.7 \text{ mm}$. The LN wafer used in the experiments is obtained from NANOLN. Their commercial fabrication technique implements He^+ ions into a bulk, single crystalline LN wafer, which is then flipped and bonded onto $2 \mu\text{m}$ of SiO_2 that is grown via plasma enhanced chemical vapour deposition on a $400 \mu\text{m}$ -thick Si wafer. After splitting the LN wafer along the He^+ ion implementation region, chemical mechanic polishing is used to obtain a sub-micron LN layer thickness.

7.4.2. Waveguide characteristics

Figure 7.15(a) shows a field emission scanning electron microscope (FESEM) image of the single-crystalline LN layer, which is cut along the (100) crystallographic plane and has a thickness of 775 nm . Since the d_{33} nonlinear coefficient of LN is the tensor element having the highest magnitude, an electric field polarized along the c -axis of the LN is used to generate a SHG electric field that is also polarized along the c -axis. In terms of planar waveguide notation, this means a TE mode at the excitation wavelength produces a TE mode at the SHG wavelength. To achieve high SHG conversion under these excitation conditions, it is important to first determine the excitation and SHG modes supported by the planar waveguide, as well as the conditions for perfect phase-matching and high spatial overlap. Figure 7.15(b) and 7.15(c) illustrate the TE electric field distributions supported by the LN planar waveguide at the representative excitation wavelength of $\lambda_{exc}=800 \text{ nm}$ and its SHG wavelength of $\lambda_{SHG}=400 \text{ nm}$, respectively. At $\lambda_{exc}=800 \text{ nm}$, the LN waveguide supports three excitation modes (i.e. TE_0 , TE_1 , and TE_2), whereas seven modes (i.e. TE_0 , TE_1 , TE_2 , TE_3 , TE_4 , TE_5 , and TE_6) are supported by the planar waveguide at $\lambda_{SHG}=400 \text{ nm}$.

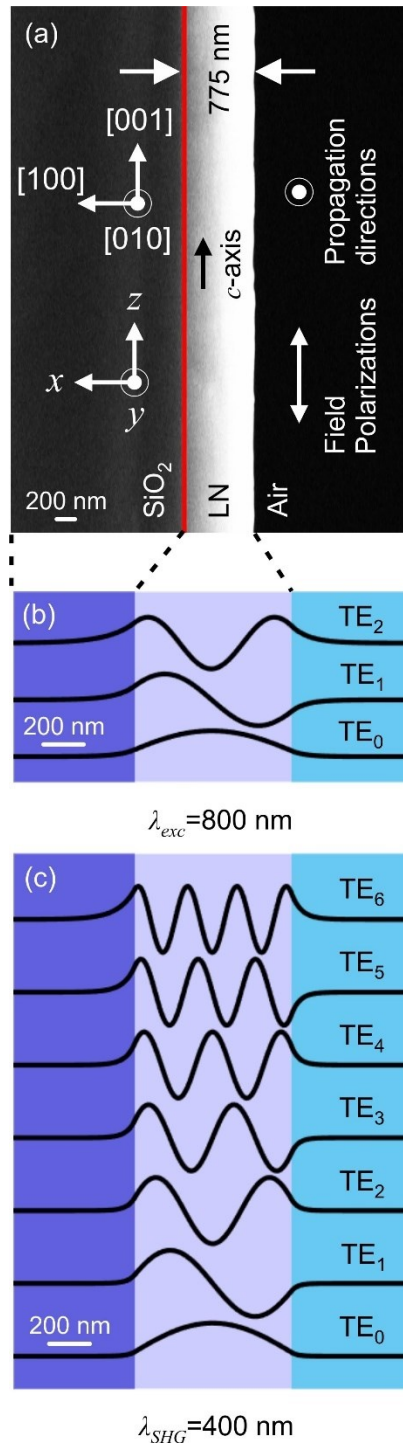


Fig. 7.15. (a) FESEM image showing the cross-section of the SiO₂-LN-air planar waveguide having a core thickness of 775 nm. Electric field distributions supported by the SiO₂-LN-air planar waveguide at (b) the excitation wavelength of $\lambda_{exc}=800$ nm and (c) its SHG wavelength of $\lambda_{exc}=400$ nm.

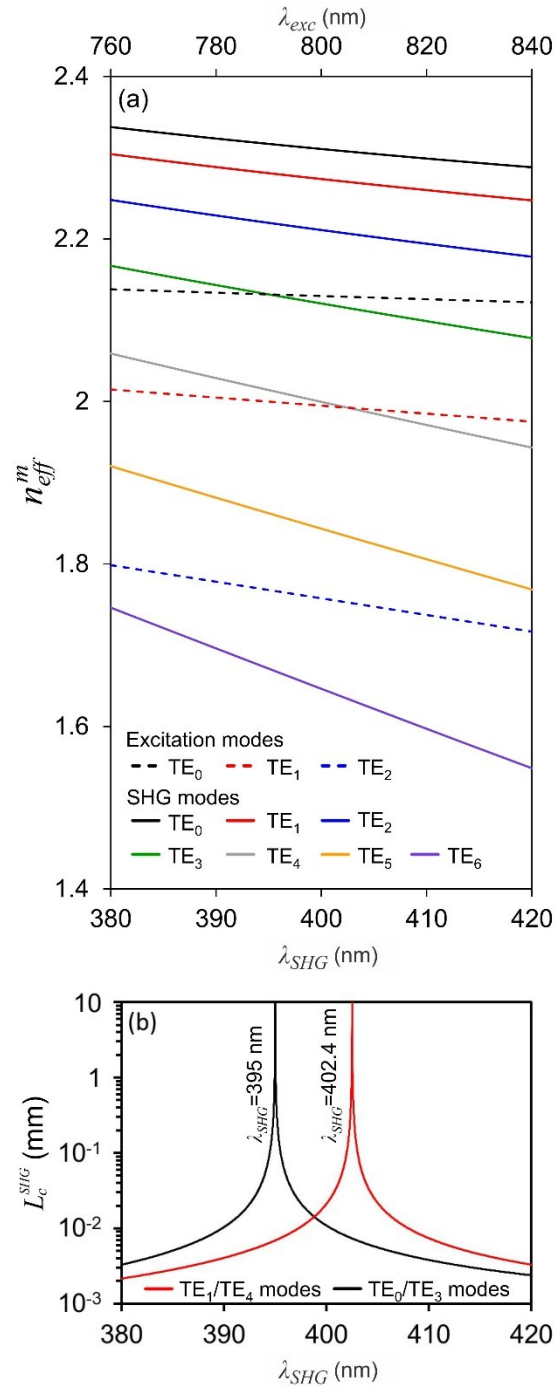


Fig. 7.16. (a) Effective refractive indices of the excitation and SHG modes, where perfect phase-matching is observed at the wavelengths of $\lambda_{SHG}=395$ nm and $\lambda_{SHG}=402.4$ nm. (b) Coherence length for the TE₀ excitation and TE₃ SHG modes, as well as the TE₁ excitation and TE₄ SHG modes.

Since the extraordinary refractive index of the LN crystal exhibits positive dispersion, perfect phase-matching can only occur between an excitation mode and a higher-order SHG mode. Calculations of the effective refractive indices of the waveguide modes, n_{eff}^m , are shown in Fig. 7.16(a). Clearly, over the SHG wavelength range of $\lambda_{SHG}=380-420$ nm, perfect phase-matching only occurs at two wavelengths. The TE₀ excitation mode at $\lambda_{exc}=790$ nm and the TE₃ SHG mode at $\lambda_{SHG}=395$ nm both have an $n_{eff}^m=2.13$. On the other hand, the TE₁ excitation mode at $\lambda_{exc}=804.8$ nm and the TE₄ SHG mode at $\lambda_{SHG}=402.4$ nm have an $n_{eff}^m=1.99$. As determined using Eq. (7.2), the coherence length, L_c^{SHG} , is infinite for these wavelengths [see Fig. 7.16(b)]. Nonetheless, the efficiency of the SHG process also depends on the spatial overlap between the excitation and SHG modes, which is characterized by the spatial overlap integral [234],

$$\mathbb{S} = \frac{1}{\sqrt{w_b}} \frac{|\int E_{exc}^2(x) E_{SHG}(x) dx|}{\int E_{exc}^2(x) dx \sqrt{\int E_{SHG}^2(x) dx}}, \quad (7.8)$$

where E_{exc} is the excitation electric field, E_{SHG} is the SHG electric field, and w_b ($=2.7$ mm) is the major-axis length of the focused laser beam. The numerator in Eq. (7.8) depends on the intensity of the excitation mode, which has an even spatial distribution across the SiO₂-LN-air layers, and on the electric field of the SHG mode, which can either have an even (e.g. TE₄) or odd (e.g. TE₃) spatial distribution across the SiO₂-LN-air layers. Consequently, for the TE₁ excitation and TE₄ SHG modes, $\mathbb{S}=2.6$ mm⁻¹, whereas $\mathbb{S}=0.05$ mm⁻¹ for the TE₀ excitation and TE₃ SHG modes. Indeed, the higher \mathbb{S} implies a higher SHG energy being produced in the frequency-conversion process.

7.4.3. Coupling characteristics

To facilitate phase-matched SHG between the TE_1 excitation and TE_4 SHG modes, the TE_1 excitation mode must be excited within the planar waveguide. Coupling into the odd-ordered waveguide modes can be achieved by angularly-exciting the waveguide [89]. By performing FDTD simulations, angular coupling and mode excitation are investigated using a 790 nm, 50 fs laser pulse focused onto the waveguide's input facet, where the beam is incident at an angle θ_i relative to the direction of normal incidence [see Fig. 7.14]. Figure 7.17(a) shows a snapshot of the time-domain electric field distribution after the planar waveguide is excited by end-coupling at $\theta_i=0^\circ$. Although the excitation field couples into the TE_0 and TE_2 excitation modes, it does not couple into the TE_1 excitation mode, such that phase-matched SHG cannot occur at $\theta_i=0^\circ$. Figure 7.17(b) shows a snapshot of the time-domain electric field distribution after the planar waveguide is excited at $\theta_i=10^\circ$. Clearly, the excitation field couples into the TE_1 excitation mode, thus permitting phase-matched SHG. Since the TE_0 , TE_1 , and TE_2 modes have different effective

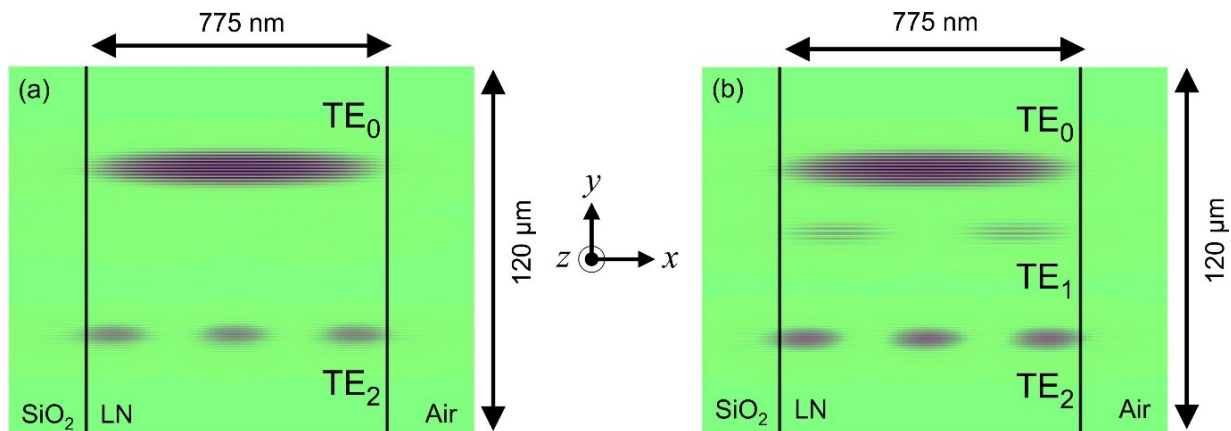


Fig. 7.17. (a) FDTD simulations showing the modes excited in the waveguide via coupling at the incident angles of (a) $\theta_i=0^\circ$ and (b) $\theta_i=10^\circ$. To excite the TE_1 mode necessary for phase-matched SHG, the optical excitation pulse must be coupled in at an off-normal-incidence angle. The $y:x$ spatial aspect ratio of these images is 155:1.

group refractive indices, they spatially separate as they propagate along the planar waveguide [see Fig. 7.17(b)].

7.4.4. Experimental measurements

Figure 7.18(a) depicts the SHG signal produced when the planar waveguide is excited at $\theta_i \approx 10^\circ$, which allows for a sufficiently high coupling efficiency of 2.6% into the TE_1 mode at $\lambda_{exc} = 804.8$ nm. The signal is detected at all positions along the planar waveguide, where SHG is clearly seen to originate at the entrance facet of the waveguide and is emitted into free-space at the waveguide's exit face. As shown in Fig. 7.18(b), this SHG signal has a wavelength of $\lambda_{SHG} = 402.4$ nm and a narrow linewidth of 1.5 nm. Although phase-mismatched SHG occurs across the entire $\lambda_{exc} = 770$ -840 nm bandwidth of the excitation pulse [see inset of Fig. 7.18(b)], this

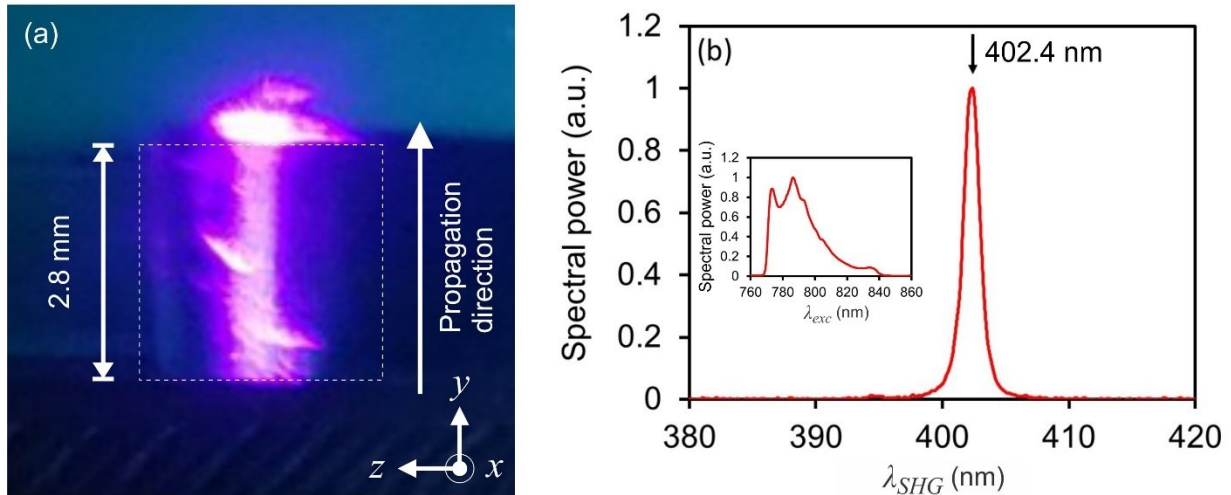


Fig. 7.18. (a) Image showing the perfectly phase-matched SHG light produced at all positions along the 2.8 mm-long planar waveguide having a LN layer thickness of 775 nm. (b) The SHG signal measured from the planar waveguide having a thickness of 775 nm, where phase-matched SHG occurs having a central-wavelength of $\lambda_{SHG} = 402.4$ nm and exhibiting the narrow linewidth of 1.5 nm. The inset shows the spectrum of the laser pulse that is exciting the planar waveguide, which encompasses wavelength components between $\lambda_{exc} = 770$ -840 nm.

process is negligible compared to the phase-matched SHG occurring at $\lambda_{SHG}=402.4$ nm. The measured SHG signal at $\lambda_{SHG}=402.4$ nm agrees well with the perfect phase-matching wavelength of the TE₁ excitation and TE₄ SHG modes [see Fig. 7.16(b)], which exhibits the high spatial overlap of $S=2.6$ mm⁻¹. Furthermore, the absence of the SHG signal at $\lambda_{SHG}=395$ nm confirms the negligible spatial overlap (i.e. $S=0.05$ mm⁻¹) between the TE₀ excitation and TE₃ SHG modes.

It is necessary to determine the energy of the SHG pulse, ξ_{SHG} , and the SHG conversion efficiency, η_{SHG} . Figure 7.19(a) shows ξ_{SHG} produced through the phase-matched SHG process, which is measured at various excitation pulse energies, ξ_{exc} . The highest SHG energy of $\xi_{SHG}=82$ fJ is achieved by exciting the waveguide at $\xi_{exc}=1.8$ nJ and the trend agrees with theory (i.e. $\xi_{SHG} \propto \xi_{exc}^2$). Figure 7.19(b) shows η_{SHG} for various ξ_{exc} , where the highest conversion efficiency of $\eta_{SHG}=4.6 \times 10^{-5}$ is obtained at $\xi_{exc}=1.8$ nJ and $\eta_{SHG} \propto \xi_{exc}$. Importantly, η_{SHG} could be improved by implementing several different approaches. While only 2.6% of the excitation pulse energy couples into the planar waveguide at $\theta_i=10^\circ$, 10% of the excitation pulse energy couples into the planar waveguide at $\theta_i=26^\circ$. Therefore, the measured $\eta_{SHG}=4.6 \times 10^{-5}$ at $\theta_i=10^\circ$ is estimated to increase to $\eta_{SHG}=1.8 \times 10^{-4}$ at $\theta_i=26^\circ$. In the experimental off-normal-incidence coupling arrangement, a broadband excitation field is used to achieve narrowband phase-matched SHG. However, by simply exciting the waveguide using a narrowband field at the wavelength of $\xi_{exc}=804.8$ nm, η_{SHG} is estimated to increase by approximately an order of magnitude. Furthermore, the pulse beam waist of 4 μ m is significantly larger than the LN thickness of 775 nm, which means η_{SHG} could be enhanced by reducing the pulse beam waist. The propagation lengths of the TE₁ excitation mode and the TE₄ SHG mode are both >10 cm, which is more than an order of magnitude longer than the investigated waveguide length of 2.8 mm. Therefore, η_{SHG} could be enhanced by simply increasing the length of the waveguide.

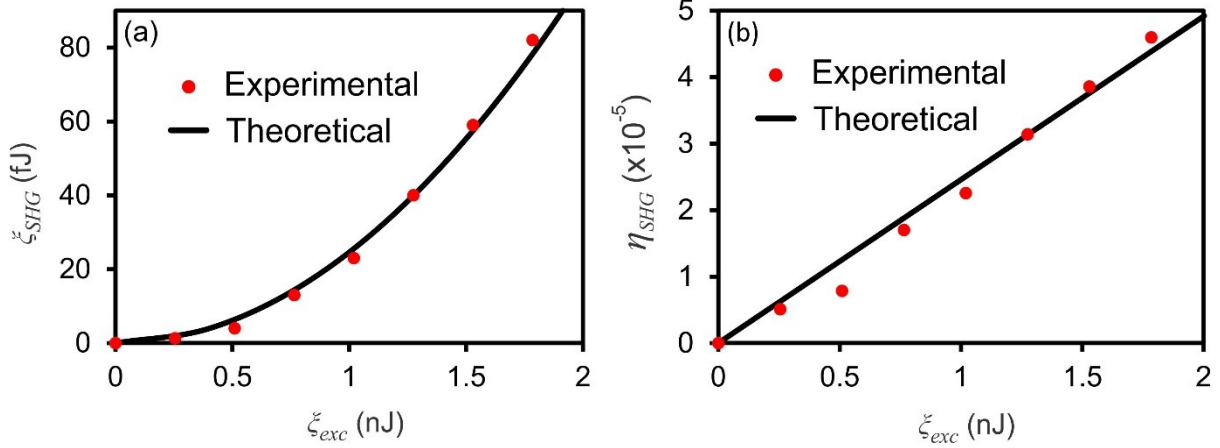


Fig. 7.19. (a) Energy of the SHG pulse and (b) SHG conversion efficiency with respect to the energy of the excitation pulse. As expected, $\xi_{SHG} \propto \xi_{exc}^2$ and $\eta_{SHG} \propto \xi_{exc}$.

7.5. Summary

Using the FDTD methods derived in Chapter 5, second-order nonlinear frequency-conversion is investigated in LN plasmonic waveguides, CSP photonic waveguides, and LN photonic waveguides for producing radiation in the near-IR and visible spectral regions. For waveguide lengths of a few microns to a few tens of microns, SHG occurred at a higher conversion efficiency in LN nanoplasmonic waveguides in comparison to a photonic LN waveguide having comparable dimensions. This conversion efficiency improvement is related to the plasmonic waveguiding structures confining the excitation electric field to a more localized spatial region than the photonic LN waveguide. A photonic waveguide comprised of the highly-nonlinear CSP crystal was shown to produce SHG radiation having a very high electric field (i.e. >100 kV/cm) and conversion efficiency (i.e. $>10^{-3}$), where the latter is 11 times higher than that achieved from a LN photonic waveguide. Odd-ordered excitation modes were considered for phase-matched SHG in a LN photonic waveguide, where SHG using these modes was only observed when the excitation electric field exhibited transverse wavevector projections on the waveguide's cross-

section. As was shown both numerically and experimentally, such a requirement was satisfied using an off-normal-incidence coupling scheme. Such investigations of nonlinear frequency-conversion in waveguides, as well as their coupling schemes, are key to advancing the areas of optical communication, optical computing, and entangled photon generation for quantum computing. Waveguiding geometries are ideal for on-chip applications, due to their compatibility with nanofabrication techniques and their ability to realize a small footprint.

Chapter 8.

Simultaneous generation of phase-matched radiation across multiple spectral bands

Multi-band photonic sources can be realized by satisfying the phase-matching requirements for several second-order nonlinear processes (e.g. SFG and DFG or SHG and OR) within the same structure, thus permitting generation within multiple spectral bands. As photonic technologies continue to advance, there is a need to increase the density of photonic devices on a single chip. Although miniaturization has been a highly successful approach for increasing the density of the photonic devices, this technique has been challenging when integrating nonlinear frequency-conversion photonic sources onto the same chip. Here, the strength of the converted radiation directly depends on the length of the photonic source; hence, there is a trade-off between miniaturization and the generated optical power. By combining the generation characteristics of two physical phenomena into a single platform, this limitation can be relaxed.

Multi-band generation would find use in the synchronous monitoring of nonlinear optical processes in photonic integrated circuits. In optical circuits that perform nonlinear processes for various applications (e.g. optical computing [203], optical communication [200], and entangled photon generation [206]), there is a need to non-invasively probe the efficiency of the frequency-conversion process during operation. Direct optical probing disturbs the nonlinear process by splitting and sampling a portion of the generated beam, which presents added difficulties when the

generated energy is confined to a waveguide. Instead, it is advantageous to monitor another nonlinear process that is occurring at the same time and from the same optical excitation. For instance, THz radiation produced through the process of OR is highly correlated to the radiation produced by the SHG process. Here, the SHG conversion efficiency, η_{SHG} , may be calibrated to the OR THz radiation conversion efficiency, η_{OR} . In the ideal scenario (e.g. no saturation of the generated radiation), the conversion efficiencies are correlated by the relationship $\eta_{SHG} \propto \eta_{OR}$. In a non-ideal system, other effects influence the second-order nonlinear generation processes. For example, temperature fluctuations lead to changes in the refractive indices of the nonlinear material. Interestingly, such fluctuations influence the emission wavelength at which SHG occurs, as well as the Cherenkov emission angle of the generated THz radiation, such that the SHG emission wavelength is correlated to the Cherenkov emission angle of the generated THz radiation. Additionally, in photonic circuits, temporal synchronization is important between the various optical components for addressing and clocking. As such, having THz radiation pulses, which can be converted into electrical signals, offers a means of synchronizing the nonlinear optical components with the optoelectronic devices on the same chip. Since Si is highly transparent to THz radiation, this hybrid integration is especially beneficial for Si-based photonic systems, where all the Si chip levels could be addressed simultaneously for clocking and parallel processing. Furthermore, since the THz radiation is broadband, selective device addressing can be realized via the incorporation of frequency-selective metasurfaces, where different nonlinear frequency-conversion structures are assigned a unique signature represented by a specific narrowband THz frequency.

In this chapter, multi-band generation via concurrent phase-matched second-order nonlinear processes is investigated both numerically and experimentally. Therefore, this chapter leverages

the physics connecting the various second-order nonlinear processes outlined in Chapter 2 (i.e. SHG, SFG, DFG, and OR) to simultaneously produce phase-matched radiation within multiple spectral bands. The numerical FDTD simulations conducted in this chapter incorporate the FDTD methods developed in Chapter 5.

8.1. Generation of mid-IR and visible radiation in a multi-band planar LN waveguide¹⁸

Numerous waveguiding geometries have been proposed and investigated for producing visible light via phase-matched SFG, as well as mid-IR radiation via phase-matched DFG. Since the conversion efficiencies associated with these frequency-conversion processes are typically small (e.g. <0.1%), much of the excitation pulse energy is not converted to new frequencies. Therefore, by constructing a single waveguiding structure to concurrently satisfy phase-matching for both of these nonlinear processes (i.e. SFG and DFG), the surplus energy of the excitation pulse can be used to simultaneously produce frequency components within multiple spectral bands. Here, a planar waveguide having a sub-micron LN core is considered, which produces multi-band radiation within the visible and mid-IR regions of the EM spectrum.

8.1.1. Waveguiding structure

Figure 8.1 shows a schematic of the planar waveguiding structure consisting of a LN core having thickness T , length L , and having its c -axis oriented along the z axis. The LN layer is

¹⁸A version of this section's work is published as B. N. Carnio and A. Y. Elezzabi, "Generation of mid-infrared and visible radiation in a multi-band phase-matched sub-wavelength LN waveguide," *J. Opt. Soc. Am. B* **36**, 1695-1699 (2019).

sandwiched between two SiO₂ cladding layers of thickness $T_c=500$ nm and two high-index 42° Si prisms. When exciting the planar waveguide with z -polarized femtosecond excitation pulses having the central angular frequencies of ω_1 and ω_2 , SFG and DFG produce the angular frequencies of $\Omega_{SFG} = \omega_1 + \omega_2$ and $\Omega_{DFG} = |\omega_1 - \omega_2|$, respectively. Figure 8.1 illustrates the emission directions of the generated radiation, where Ω_{SFG} is emitted along the planar waveguide and Ω_{DFG} is emitted at the Cherenkov angle. For the prism angle of 42°, Ω_{DFG} propagates nearly normal to the Si-air interface. The planar waveguide is numerically investigated by performing 2D FDTD simulations, where the refractive index and extinction coefficient data for LN, SiO₂, and Si are obtained from Refs. [172], [182], and [182], respectively. The LN second-order nonlinear susceptibility, $\chi_{33}^{(2)}(\Omega_{SFG,DFG}; \omega_1, \omega_2)$, is obtained using Refs. [38,190], and the LN multi-photon absorption threshold is acquired from Ref. [186]. $\chi_{33}^{(2)}(\Omega_{SFG,DFG}; \omega_1, \omega_2)$ [i.e. $\chi_{zzz}^{(2)}(\Omega_{SFG,DFG}; \omega_1, \omega_2)$ in non-contracted notation] is described by Eq. (5.58) with the parameters

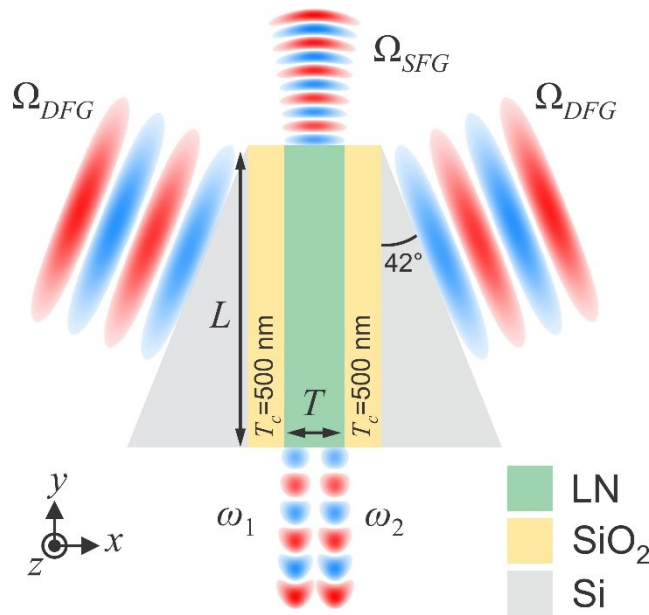


Fig. 8.1. Schematic of the multi-band generation planar waveguide producing Ω_{SFG} and Ω_{DFG} . The c -axis of the LN crystal is aligned along the z axis.

$\chi_E^{zzz}=19.8$ pm/V, $\Omega_1^{zzz}/(2\pi)=1360$ THz, $\Omega_2^{zzz}/(2\pi)=15.9$ THz, $\gamma_1^{zzz}/(2\pi)=0$ THz, $\gamma_2^{zzz}/(2\pi)=0$ THz, $C_1^{zzz}=1$, $C_2^{zzz}=4.1$, and $Q_{zzz}=2$.

8.1.2. SFG and DFG in a planar LN waveguide

In order to achieve the highest conversion efficiency for both Ω_{SFG} and Ω_{DFG} , the LN planar waveguide must satisfy phase-matching at both of these angular frequencies. However, since Ω_{SFG} and Ω_{DFG} cover different spectral regions, it would be unfeasible to confine the corresponding wavelengths within the LN core and achieve phase-matching via geometric manipulation. To overcome this challenge, we design a planar waveguide that exhibits Ω_{SFG} phase-matching but allows Ω_{DFG} to escape in the form of Cherenkov waves, which therefore add coherently outside the waveguide's LN core. In this manner, it is possible to achieve optimal generation efficiencies for both Ω_{SFG} and Ω_{DFG} , without the need to directly consider phase-matching of Ω_{DFG} . The coherence length, L_c^{SFG} , for the radiation generated via SFG (see Chapter 2) is,

$$L_c^{SFG}(\lambda_{SFG}) = \frac{1}{2 \left| \frac{n_{eff,1}^m}{\lambda_1} + \frac{n_{eff,2}^m}{\lambda_2} - \frac{n_{eff,SFG}^m}{\lambda_{SFG}} \right|}, \quad (8.1)$$

where $n_{eff,1}^m$ and $n_{eff,2}^m$ are the effective refractive indices of the excitation modes, $n_{eff,SFG}^m$ is the effective refractive index of the SFG mode, $\lambda_{1,2}$ are the free-space wavelengths of the excitation modes, and $\lambda_{SFG} = (1/\lambda_1 + 1/\lambda_2)^{-1}$ is the free-space wavelength of the SFG mode. For the planar waveguide being investigated, phase-matching is achieved between the TM_0 excitation modes [see Fig. 8.2(a) for the representative modes at $\lambda_1=806$ nm and $\lambda_2=1009$ nm] and the TM_2 SFG mode [see Fig. 8.2(b) for the representative mode at $\lambda_{SFG}=448$ nm]. Notably, phase-matching for the DFG wavelength, $\lambda_{DFG} = |1/\lambda_1 - 1/\lambda_2|^{-1}$, is inherently satisfied if the combined

thicknesses of the waveguide core and cladding are of sub-wavelength dimensions with respect to λ_{DFG} in the planar waveguide,

$$T + T_c \lesssim \frac{\lambda_{DFG}}{n_{eff,DFG}}, \quad (8.2)$$

where $n_{eff,DFG}$ is the effective refractive index of the DFG wavelength. Here, $n_{eff,DFG} = (n_{LN}T + n_c T_c)/(T + T_c)$, where n_{LN} and n_c are the refractive indices of the LN and SiO₂, respectively.

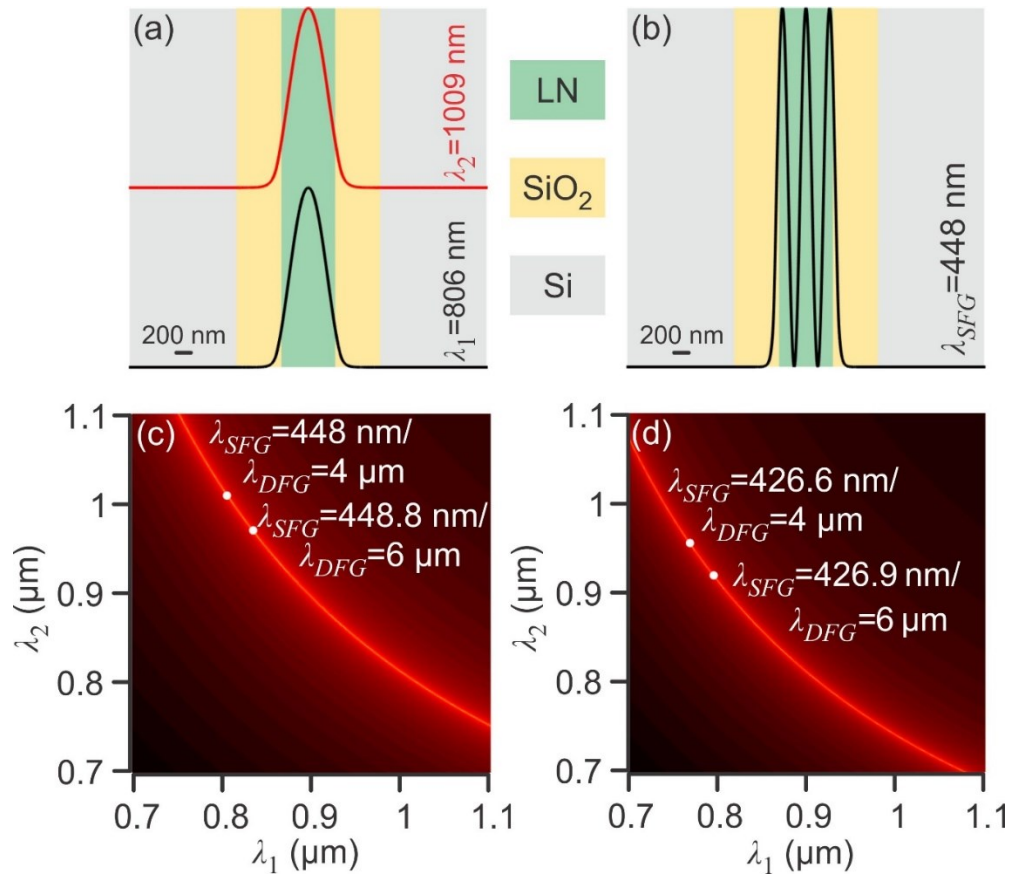


Fig. 8.2. (a) Intensity distribution of representative excitation modes at $\lambda_1=806$ nm and $\lambda_2=1009$ nm. (b) Intensity distribution of a representative SFG mode at $\lambda_{SFG}=448$ nm. The modal intensity distributions shown in (a) and (b) are calculated for the $T=700$ nm planar waveguide. The coherence length for the (c) $T=700$ nm and (d) $T=600$ nm planar waveguides.

Figure 8.2(c) shows L_c^{SFG} for the $T=700$ nm planar waveguide [calculated using Eq. (8.1)] at various excitation wavelengths. Perfect phase-matching (i.e. $L_c^{SFG} \rightarrow \infty$) is denoted by the distinct trend line. Here, $\lambda_{SFG} \approx 448$ nm at all positions along this phase-matching line and λ_{DFG} can vary over many spectral ranges. However, for the purpose of this study, we will only focus on $\lambda_{DFG} = 4\text{--}6$ μm (i.e. in the mid-IR spectral region), as represented by the annotated points in Fig. 8.2(c). The DFG phase-matching requirement is satisfied at both annotations because $\lambda_{DFG}/n_{eff,DFG} \geq 2.3$ μm , which is greater than $T + T_c = 1.2$ μm . Since phase-matching critically depends on T , we investigate L_c^{SHG} for a planar waveguide of $T=600$ nm [see Fig. 8.2(d)]. Similar to the L_c^{SFG} trend in Fig. 8.2(c), the annotations along the phase-matching line express that $\lambda_{SFG} \approx 427$ nm and $\lambda_{DFG} = 4\text{--}6$ μm . Evidently, for these representative planar waveguides, λ_{SFG} is dictated by the waveguide's core thickness and λ_{DFG} is determined by the excitation wavelengths. This feature allows for independent control over λ_{SFG} and λ_{DFG} .

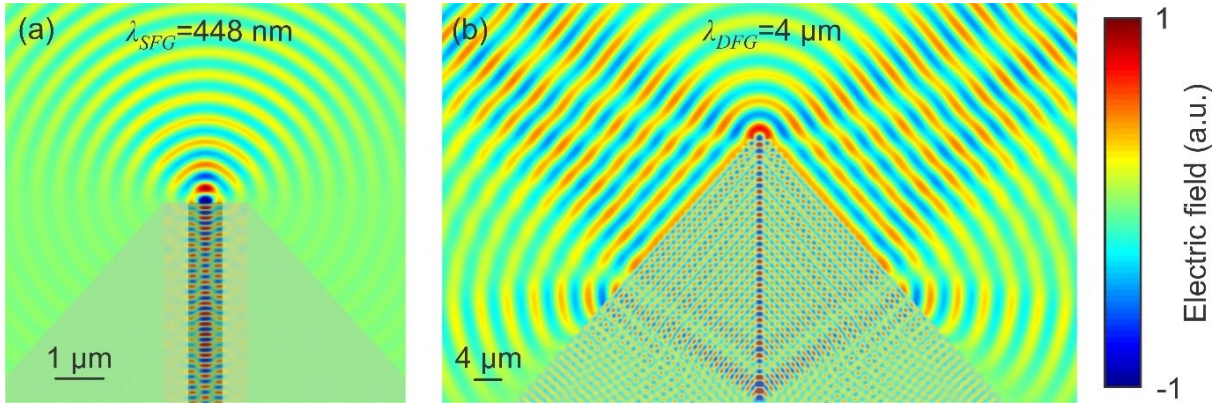


Fig. 8.3. Time-averaged spatial distribution of the electric field at the wavelengths of (a) $\lambda_{SFG} = 448$ nm and (b) $\lambda_{DFG} = 4$ μm .

An additional interesting feature of this planar waveguiding platform is the spatial distribution of the emitted wavelengths, λ_{SFG} and λ_{DFG} . This characteristic is investigated for the

$T=700$ nm and $L=40$ μm planar waveguide excited by pulses having durations of 200 fs, peak intensities of 90 GW/cm^2 , and central-wavelengths of $\lambda_1=806$ nm and $\lambda_2=1009$ nm. Figure 8.3(a) and 8.3(b) present the time-averaged spatial distribution of the electric field at $\lambda_{SFG}=448$ nm and $\lambda_{DFG}=4$ μm , respectively. Clearly, λ_{SFG} is emitted co-linearly from the planar waveguide output, while λ_{DFG} is emitted at the Cherenkov angle of $\sim 48^\circ$.

Figure 8.4(a) shows the SFG and DFG electric fields having peak-to-peak values of 15 and 1 kV/cm, respectively, which are considerably high given the short interaction length of $L=40$ μm . When considering the total radiation produced via SFG and DFG, the conversion efficiency is calculated to be 14×10^{-5} and 0.5×10^{-5} , respectively. This difference is due to the nonlinear polarization dipoles being more efficient emitters at higher frequencies, as discussed in Chapter 2. Additionally, due to the large refractive index difference of the Si and air regions, $\sim 30\%$ of the DFG radiation intensity is reflected from the Si-air interface. However, anti-reflective layers could be included to reduce this effect. Figures 8.4(b) and 8.4(c) show the SFG and DFG spectral powers, respectively. The SFG light is produced having a FWHM bandwidth of 2 nm (i.e. 3 THz), whereas that of the DFG radiation is 168 nm (i.e. 3.2 THz). Since phase-matching is satisfied across the entire bandwidths of the excitation pulses, no nulls are observed in either the SFG or DFG spectra. When using the planar waveguide cross-section to tune the refractive index of λ_{SFG} for phase-matching, an important issue to consider is the effect of waveguide and material dispersion on the generated SFG and DFG pulses. The time-frequency spectra presented in Fig. 8.4(d) and 8.4(e) show that all the frequencies encompassed in the electric field pulses arrive at the same time, such that both waveguide and material dispersion effects are negligible.

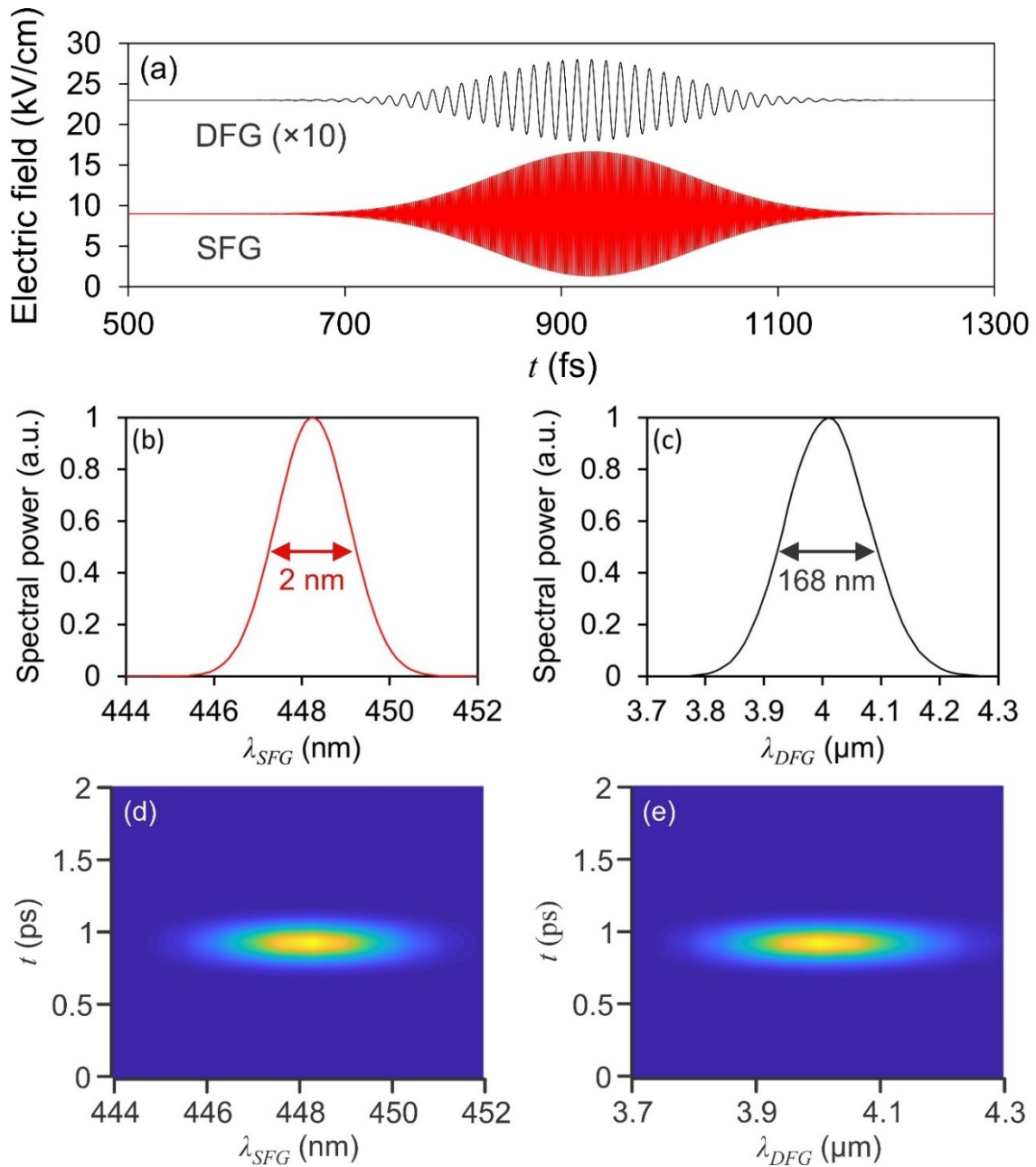


Fig. 8.4. (a) Time-domain electric fields of the SFG and DFG radiation after exiting the planar waveguide. Power spectra of the radiation produced through (b) SFG and (c) DFG. Time-frequency spectra for the (d) SFG and (e) DFG electric fields.

To show that λ_{SFG} is dictated by T and λ_{DFG} is controlled by $\lambda_{1,2}$, the planar waveguides are investigated for various excitation wavelengths and core thicknesses. The $T=700$ nm and $L=40$ μm

planar waveguide is excited using 200 fs pulses having central-wavelengths of $\lambda_1=806$ nm and $\lambda_2=1009$ nm, as well as $\lambda_1=835.2$ nm and $\lambda_2=970$ nm. It should be noted that both of these excitation wavelength sets allow for phase-matching of the generated SFG signal [see Fig. 8.2(c)]. As depicted in Fig. 8.5(a), the location of the SFG spectral bands are at ~ 448 nm, regardless of which excitation wavelengths are used. In contrast, Fig. 8.5(b) shows that $\lambda_{DFG}=4$ or 6 μm , highly dependent on the choice of excitation wavelengths. To demonstrate that λ_{SFG} can be altered through the choice of T , while maintaining the same λ_{DFG} of 4 and 6 μm , a $T=600$ nm planar waveguide is investigated. This waveguide is excited using 200 fs pulses having $\lambda_1=770.8$ nm and

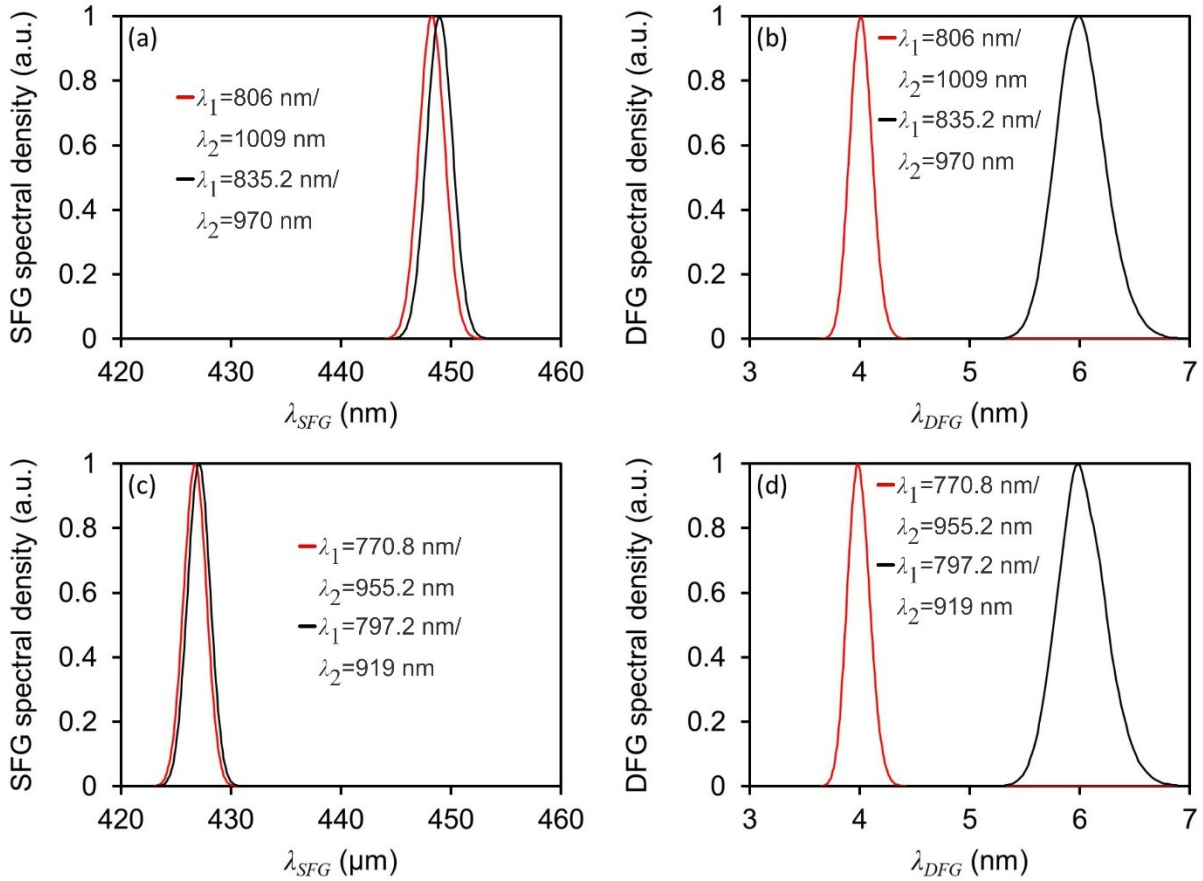


Fig. 8.5. (a) SFG and (b) DFG spectra showing the wavelength distribution for the $T=700$ nm planar waveguide. (c) SFG and (d) DFG spectra showing the wavelength distribution for the $T=600$ nm planar waveguide.

$\lambda_2=955.2$ nm, as well as $\lambda_1=797.2$ nm and $\lambda_2=919$ nm. As shown in Fig. 8.5(c) and 8.5(d), λ_{SFG} is shifted to ~ 427 nm and λ_{DFG} is maintained at 4 and 6 μm . Notably, although the wavelengths of 4 and 6 μm are used to represent the DFG process within the mid-IR region, the generated radiation is not restricted to these wavelengths. For example, by choosing the excitation wavelengths of $\lambda_1=849.6$ nm and $\lambda_2=950.8$ nm, the DFG process would produce radiation at the central-wavelength of $\lambda_{DFG}=7.9$ μm , whereas DFG radiation would be produced at the central-wavelength of $\lambda_{DFG}=10.1$ μm when $\lambda_1=859.2$ nm and $\lambda_2=940.4$ nm.

8.2. A multi-band planar LN waveguide for generating THz radiation and visible light¹⁹

While multi-band generation was numerically considered in Section 8.1, this section experimentally investigates multi-band generation in a SiO₂-LN-polymer planar waveguide via the second-order nonlinear processes of SHG and OR.

8.2.1. Waveguiding structure

The multi-band generation technique is investigated using the planar waveguide platform illustrated in Fig. 8.6(a), which consists of a LN core region, as well as SiO₂ and polymer cladding regions. A near-IR laser pulse couples into the planar waveguide, which produces modal phase-matched SHG light and THz radiation phase-matched via the Cherenkov emission technique. The near-IR excitation pulse has a central wavelength of $\lambda_c^{exc}=800$ nm, a pulse duration of 50 fs, and

¹⁹A version of this section's work is published as B. N. Carnio, E. Hopmann, B. Y. Shahriar, and A. Y. Elezzabi, "A Multi-Band Photonic Source by Means of Phase-Matched Nonlinear Generation Processes," *IEEE Photon. Technol. Lett.* **33**, 366-369 (2021).

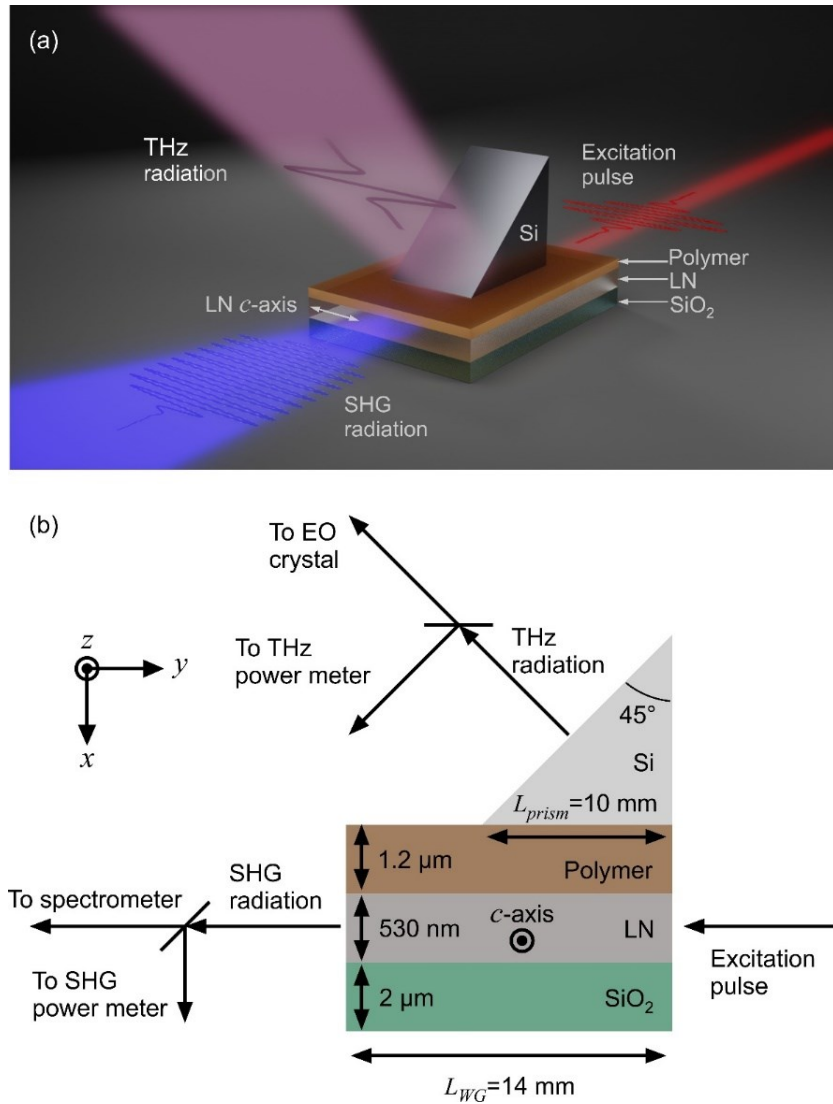


Fig. 8.6. (a) Planar waveguide depicting excitation by the near-IR pulse, as well as the SHG and THz radiation generation. (b) Schematic showing the planar waveguide, prism dimensions, and LN *c*-axis.

is focused onto the input facet of the planar waveguide using an acylindrical lens to achieve a beam waist size of $\sim 4 \mu\text{m}$. Although this beam waist size is much larger than the LN layer, it substantially relaxes coupling alignment while still permitting an excitation pulse peak intensity, I_p , of $2.4 \text{ GW}/\text{cm}^2$ to be coupled into the LN layer. Notably, the second-order nonlinear frequency-

conversion processes are expected to improve until the onset of limiting nonlinear effects (e.g. multi-photon absorption), observed at I_p of a few hundred GW/cm² [186]. The excitation pulse is polarized along the c -axis of the LN crystal, such that it produces SHG light and THz radiation having a polarization along the c -axis through the $\chi_{33}^{(2)}$ second-order nonlinear susceptibility tensor element. For the $\lambda_c^{exc}=800$ nm near-IR excitation pulse, $\chi_{33}^{(2)}\approx 50$ pm/V for generation in the SHG frequency regime and the $\chi_{33}^{(2)}$ magnitude is ~ 350 pm/V for generation in the THz frequency regime (i.e. $\lesssim 4$ THz), as presented in Ref. [190] and Fig. 5.3(a), respectively. Here, it is important to discuss the interrelatedness of the nonlinear processes. The nonlinear dipoles induced by the SHG process and the OR process both occupy the same spatial region (i.e. the LN layer) and are both induced by the same near-IR excitation pulse. These oscillating nonlinear dipoles simultaneously emit SHG light and THz radiation through the acceleration and deceleration of the bound electric charges. However, the SHG light is emitted from the waveguide output face and the generated THz radiation is out-coupled using a high-index Si prism (see Fig. 8.6). This presents an added benefit, as wavelength demultiplexing techniques would be required if the different wavelength were to occupy the same spatial region. Therefore, the SHG and THz radiation generation processes are integrated, whereas the output paths are advantageously decoupled.

The dimensions of the LN planar waveguide are shown in Fig. 8.6(b), where the SiO₂, LN, and polymer regions have thickness of 2 μ m, 530 nm, and 1.2 μ m, respectively. Notably, a range of polymer thicknesses are acceptable, provided it is sufficiently thick ($\gtrsim 500$ nm) to confine the near-IR excitation pulse to the LN layer and adequately thin ($\lesssim 5$ μ m) to permit the formation of Cherenkov THz radiation waves in the Si prism. The length of the waveguide is $L_{WG}=14$ mm, but the 45°-cut Si prism has a base length of $L_{prism}=10$ mm. As such, the phase-matched SHG light is

produced over a length of $L_{WG}=14$ mm, whereas the phase-matched THz radiation is being generated over the length of $L_{prism}=10$ mm. The SHG light is emitted co-linearly from the output facet of the planar waveguide, which is sent to a spectrometer and a power meter. The generated THz radiation is emitted near-normal to the Si prism hypotenuse face, where it is directed through the THz-TDS system [see Chapter 3] implementing a 500 μm -thick ZnTe EO crystal, as well as a THz power meter.

8.2.2. SHG visible-light generation

The modal phase-matching technique is used to obtain phase-matched SHG from the planar waveguide. Figure 8.7(a) depicts the effective refractive indices of the waveguide modes, n_{eff}^m (i.e. the TE₀, TE₁, and TE₂ excitation modes and the TE₀, TE₁, TE₂, TE₃, and TE₄ SHG modes). The TE₀ mode at the excitation wavelength of $\lambda_{exc}=806$ nm and the TE₂ mode at the SHG wavelength of $\lambda_{SHG}=403$ nm both have an $n_{eff}^m=2.09$, such that the modal phase-matching condition is satisfied. Here, the near-IR excitation pulse couples into the waveguide and propagates as the TE₀ mode [Fig. 8.7(b)], which subsequently produces SHG light that propagates along the waveguide as the TE₂ mode [Fig. 8.7(c)]. Notably, the SHG light is in-phase for all positions along the waveguide at $\lambda_{SHG}=403$ nm, but not at wavelengths far from $\lambda_{SHG}=403$ nm, such that modal phase-matching only occurs over a narrow wavelength range. When considering the $\lambda_{exc}=806$ nm TE₀ excitation and $\lambda_{SHG}=403$ nm TE₂ SHG modes, the spatial overlap integral is 2.5 mm^{-1} [234], such that these modes exhibit a good spatial overlap to support modal phase-matched SHG.

The SHG process is investigated for the planar waveguide being excited by the near-IR pulse. The SHG spectrum is shown in Fig. 8.8, which is centered at the SHG wavelength of $\lambda_c^{SHG}=403$ nm, in agreement with the calculated values of n_{eff}^m [see Fig. 8.7(a)]. Furthermore,

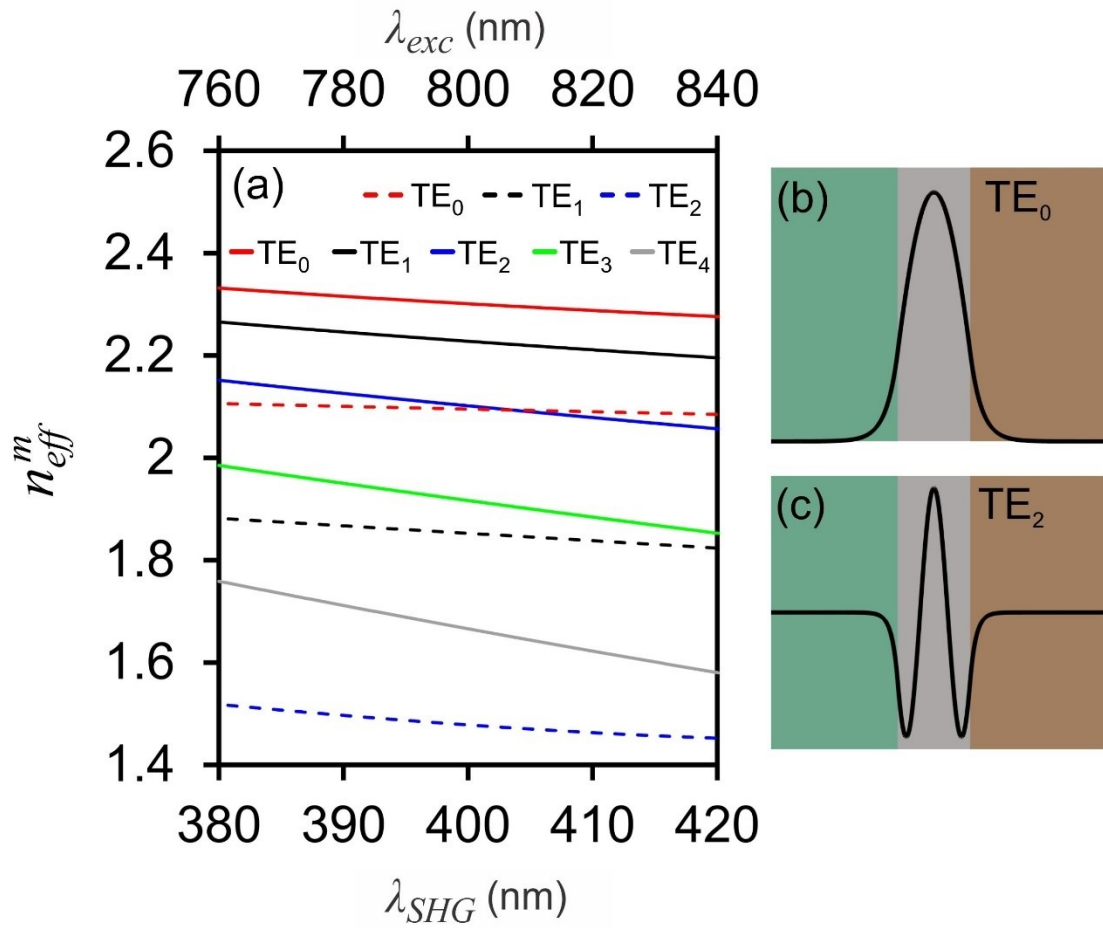


Fig. 8.7. (a) The effective refractive indices calculated for the excitation modes (dotted lines) and the SHG modes (solid lines) supported by the LN planar waveguide. (b) TE₀ mode electric field profile at $\lambda_{exc}=806$ nm and (c) TE₂ mode electric field profile at $\lambda_{SHG}=403$ nm.

despite the near-IR excitation pulse having the wide bandwidth of $\lambda_{exc} \approx 770\text{-}840$ nm, the SHG spectrum has a narrow FWHM linewidth of only 1.2 nm. This narrow linewidth, in conjunction with $\lambda_c^{SHG}=403$ nm, confirms that modal phase-matching between the TE₀ excitation mode and the TE₂ SHG mode is producing the SHG light within the linewidth of $\lambda_{SHG}=403 \pm 0.6$ nm. A narrow-bandwidth, and therefore long-duration, is critical to applications such as frequency comb generation, which has been observed in microresonators via cascaded second-order nonlinear

processes [236]. Interestingly, such frequency comb generation could be achieved by employing our multi-band generation technique in a microresonator structure. In this situation, SHG would be involved in producing the frequency combs, while the generated THz radiation could be used to monitor the frequency comb generation process, since the generated THz radiation is correlated to the SHG light. Using the measured SHG power, the SHG conversion efficiency, η_{SHG} , is calculated to be 3.7×10^{-4} , which is obtained by dividing the energy of the near-IR excitation pulse by the energy of the SHG light. Furthermore, we obtain $\eta_{SHG}/I_p = 1.5 \times 10^{-2} \text{ \%}/(\text{GW cm}^{-2})$, where this expression is expected to remain valid for I_p up to several hundreds of GW/cm^2 [186]. The observed η_{SHG}/I_p values are high, given the fact that a broadband excitation pulse (i.e. bandwidth of $\lambda_{exc} \approx 770\text{-}840 \text{ nm}$) is being converted to a narrowband SHG pulse (i.e. FWHM bandwidth of $\lambda_{SHG} = 403 \pm 0.6 \text{ nm}$). Additionally, the near-IR excitation beam waist size is much larger than the thickness of the LN layer, such that the SHG conversion efficiency could be improved by optimizing the near-IR excitation beam waist size for coupling into the TE_0 near-IR mode.

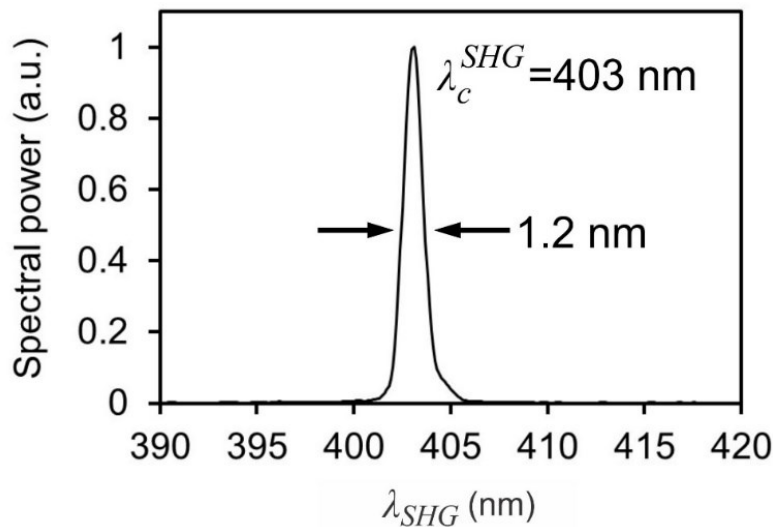


Fig. 8.8. SHG spectral power generated by the LN planar waveguide.

8.2.3. OR THz radiation generation

The Cherenkov emission technique is implemented to achieve phase-matched THz radiation generation from the LN planar waveguide. Cherenkov emission depends on the effective group refractive index of the near-IR excitation mode, $n_{eff,g}^m$, where $n_{eff,g}^m=2.31$ and 2.43 for the TE_0 and TE_1 near-IR excitation modes, respectively. Figure 8.9 illustrates the phase-matching Cherenkov emission angle, θ_c [calculated using Eq. (6.2)] for the TE_0 and TE_1 near-IR excitation modes. For $f \leq 4$ THz, $\theta_c \approx 47.6^\circ$ and 44.6° for the TE_0 and TE_1 near-IR excitation modes, respectively. Clearly, the Cherenkov angles weakly depend on the frequency of the generated THz radiation, due to the negligible dispersion in the Si prism, but strongly depend on $n_{eff,g}^m$.

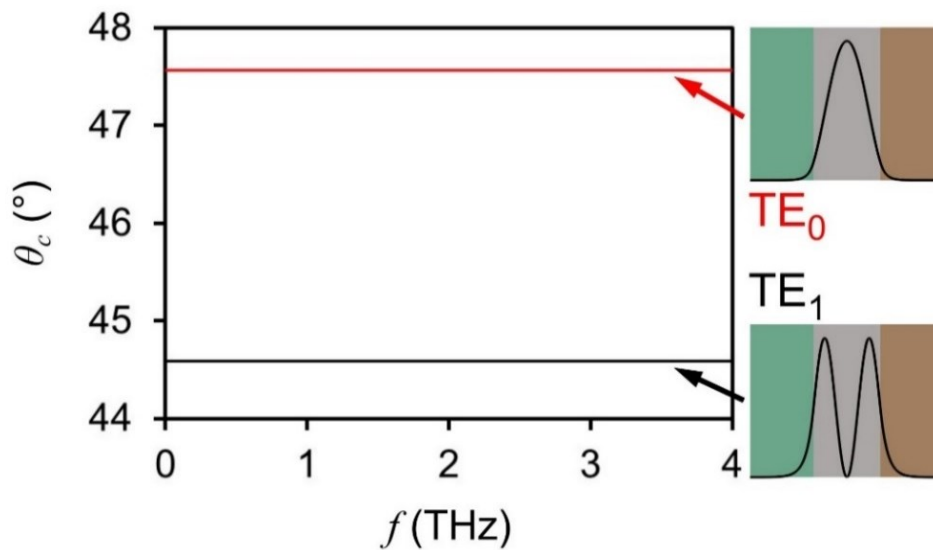


Fig. 8.9. The Cherenkov angle and intensity distributions for the near-IR excitation modes at $\lambda_c^{exc}=800$ nm.

THz radiation generation is investigated in the LN planar waveguide being excited by the near-IR excitation pulse. Figure 8.10(a) displays the THz time-domain signal transmitted through the Si prism, where the THz radiation pulses generated by the TE_0 and TE_1 near-IR excitation

modes arrive at different instances in time. Since the generated THz radiation pulses are emitted at different θ_c , they accumulate different path lengths as they propagate through the THz-TDS system, which manifests as the observed temporal delay. Although difficult to determine with high certainty, The THz radiation pulses at $t=4$ ps and $t=10$ ps are expected to result from the TE_0 and TE_1 near-IR excitation modes, respectively (see Section 6.4.2). It is also necessary to consider the emission characteristics of the THz radiation produced from the planar waveguide. The generated THz radiation is collimated upon exiting the Si prism, which is ideal for directing and manipulating the THz radiation beam. Nonetheless, free-space propagation could be avoided entirely in an on-chip arrangement by fabricating an integrated THz waveguide to collect the generated THz radiation and direct it to another region of the chip. Alternatively, a metasurface or plasmonic structure could be used in place of the Si prism, which would allow the generated THz radiation to be coupled out of the waveguide and directed into a THz waveguide. The spectral power of the THz time-domain pulses produced by the planar waveguide is shown in Fig. 8.10(b), where the bandwidths extend up to ~ 3.5 THz and have dynamic ranges >50 dB. Therefore, unlike

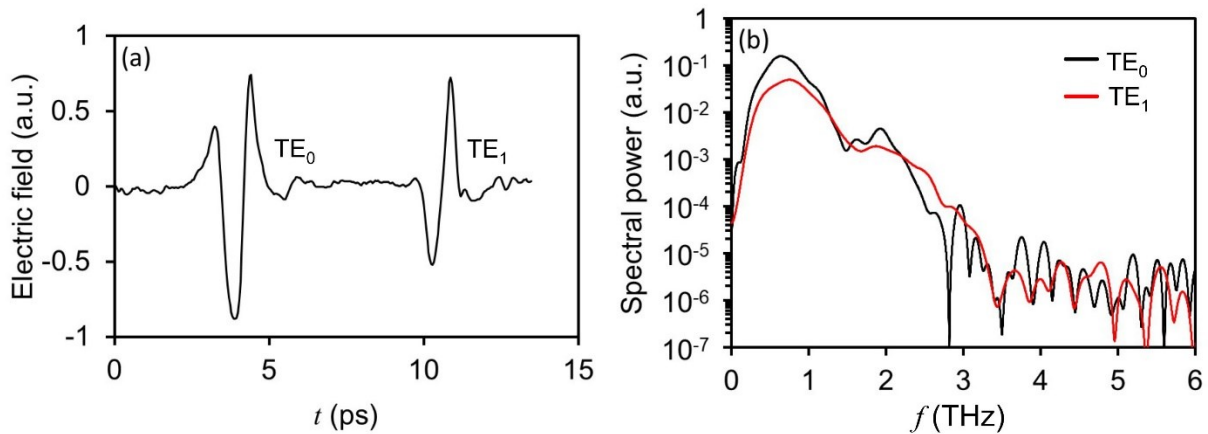


Fig. 8.10. (a) THz radiation pulses generated by the TE_0 and TE_1 near-IR modes and (b) their associated spectral powers. The generated THz radiation is sampled using a 500 μm -thick ZnTe EO crystal.

the narrowband SHG signal, which is simultaneously produced by the same waveguide, the generated THz radiation exhibits a wide bandwidth. Using the measured THz power, the OR conversion efficiency, η_{OR} , is calculated as 4.6×10^{-6} . $\eta_{OR}/I_p = 1.9 \times 10^{-4} \text{ \%}/(\text{GW}\cdot\text{cm}^{-2})$, which is expected to remain valid for I_p up to a few hundred GW/cm^2 [186]. Since the conversion efficiencies of both the SHG process and the OR THz radiation generation process are $\leq 3.7 \times 10^{-4}$, frequency-conversion is negligibly influenced by depletion of the excitation electric field.

8.3. Summary

Using a planar LN waveguide, multi-band generation was simultaneously achieved via the second-order nonlinear processes of SFG and DFG, which was observed by conducting numerical FDTD simulation incorporating the methods developed in Chapter 5. In this planar waveguiding arrangement, the phase-matched SFG wavelengths were emitted co-linearly from the output of the planar waveguide and the phase-matched DFG wavelengths were emitted at the Cherenkov angle. Subsequently, a planar LN waveguide was experimentally-realized for multi-band generation, where modal phase-matched SHG produced wavelengths at $403 \pm 0.6 \text{ nm}$ [conversion efficiency of $1.5 \times 10^{-2} \text{ \%}/(\text{GW}\cdot\text{cm}^{-2})$] and OR produced Cherenkov-emitted frequencies at $\lesssim 3.5 \text{ THz}$ [conversion efficiency of $1.9 \times 10^{-4} \text{ \%}/(\text{GW}\cdot\text{cm}^{-2})$]. We envision multi-band photonic sources based on phase-matched second-order nonlinear processes being integrated for use in on-chip applications.

Chapter 9.

Conclusion

The investigations commenced in this thesis explore THz radiation sources and detectors operating on the physical principles of second-order nonlinear phenomena. At its heart, this work examines novel crystals and waveguiding arrangements for THz radiation generation and/or detection.

By incorporating emerging pnictide and chalcogenide ternary crystals into a THz-TDS system, crystals from these classes are experimentally-investigated for second-order nonlinear THz radiation generation and detection. CSP and AGS crystals were both shown to provide better OR phase-matching in comparison to ZGP, where the AGS crystal exhibited the very long coherence length of $\sim 800 \mu\text{m}$ between 0.5-2.9 THz. A BGS crystal was shown to be a highly-efficient source of narrowband THz radiation, where the THz power generated from this crystal was higher than that from a ZnTe crystal within select spectral bands. Regarding THz radiation detection, a ZGP crystal was shown to provide phase-matched THz radiation EO detection across an exceptionally wide bandwidth, surpassing that of ZnTe.

Waveguiding arrangements were exploited for producing THz radiation through second-order nonlinear processes. Since numerical simulation techniques are in their infancy when it comes to modeling nonlinear optical interactions, two separate formalisms were developed to permit the incorporation of all 18 dispersive second-order nonlinear tensor elements into FDTD simulations. Although these nonlinear FDTD formalisms described second-order nonlinear interactions in arbitrary geometries, they are expected to provide the largest impact to on-chip

nonlinear frequency-conversion structures (e.g. waveguides). Using the developed nonlinear FDTD formalisms, LN planar waveguides were examined for second-order nonlinear THz radiation generation. Key highlights include ultra-broadband THz radiation generation (i.e. 0.18-106 THz), THz radiation generation enhancement near the LN phonon resonances, and phase-matched THz radiation produced in the backward direction (i.e. the direction opposite to the excitation electric field's propagation direction). A select LN planar waveguiding arrangement was incorporated into a THz-TDS system to experimentally realize THz radiation generation. The generated THz radiation was emitted into free-space as Cherenkov waves (dependent upon the excitation mode) and exhibited a conversion efficiency $>10^{-5}$.

The previously mentioned nonlinear FDTD formalisms are not constrained to the THz frequency regime, but extend to other spectral regimes, permitting second-order nonlinear interactions to be explored without boundaries. To make use of this marked opportunity, this thesis briefly devolved beyond the THz spectral regime to investigate second-order nonlinear phenomena for generation within the IR and visible spectral regimes. When compared to a LN photonic waveguide, a LN plasmonic waveguide and a CSP photonic waveguide provided up to an order of magnitude improvement in conversion efficiency. Additionally, a LN photonic waveguide was used as a platform to show that an off-normal-incident coupling angle was required to realize SHG incorporating odd-ordered excitation modes. A planar LN waveguide was utilized to experimentally-realize such an off-normal-incident coupling scheme, where phase-matching between the odd-ordered TE_1 excitation mode and the even-ordered TE_4 SHG mode produced radiation at 402 nm.

A new class of photonic sources was proposed based on multi-band radiation generation. By simultaneously satisfying the phase-matching conditions for SFG and DFG, visible-light and

mid-IR radiation were produced in a planar LN waveguide. To experimentally-realize such a multi-band source, a similar planar LN waveguide was exploited to concurrently satisfying the phase-matching conditions of SHG and OR, which produced spectral components at ~ 403 nm [conversion efficiency of 1.5×10^{-2} %/(GW cm⁻²)] and frequency components $\lesssim 3.5$ THz [conversion efficiency of 1.9×10^{-4} %/(GW cm⁻²)], respectively.

9.1. Future directions

Chapter 4 considered pnictide and chalcogenide ternary crystals for THz radiation generation and detection. Future investigations should continue to explore crystals within these classes for both generation and detection. Largely due to the fact that these crystal classes are up-and-coming THz sources and detectors, the incorporation of such crystals into waveguiding geometries for THz radiation generation and detection is non-existent, which should be the focus of future investigations.

In Chapter 5, nonlinear FDTD formalisms were developed to model all 18 second-order nonlinear tensor elements, allowing for dispersion of each element. Using the approach in Chapter 5 as a template, formalisms could be developed for third-order nonlinear effects, fourth-order nonlinear effects, etc.

In Section 6.1, a numerical investigation was conducted that showed ultra-broadband (i.e. 0.18-106 THz) THz radiation generation from a sub-wavelength LN waveguide. While such a waveguide was experimentally-realized (see Section 6.4), certain constraints prevented the investigation of THz frequencies $\gtrsim 3$ THz. Specifically, due to phase-mismatching in the 500 μm -thick EO crystal used in the THz-TDS system, the detected frequencies were limited to $\lesssim 3$ THz. As such, while the sub-wavelength LN waveguide was likely producing THz radiation

above this cut-off frequency, the THz-TDS system was unable to detect it. To address this concern, it is necessary to utilize an EO crystal capable of detecting high THz frequencies (e.g. GaSe [32,78]) or utilize a FTIR spectroscopy system, where the latter comes at the expense of losing the phase-information. Another factor limiting the THz radiation bandwidth is the duration of the excitation laser pulses, which was 50 fs in the experiments discussed in Section 6.4. Since the FWHM bandwidth of a 50 fs Gaussian pulse is 8.8 THz, OR is expected to be limited to a few tens of THz. Various Ti:Sapphire lasers are capable of producing electric field pulses having durations ≤ 10 fs, which could be utilized to resolve this issue. Additionally, the experimentally-realized LN planar waveguide had a length of 1 cm. THz radiation produced using a shorter-length (e.g. tens to hundreds of microns) waveguide would bring this waveguiding arrangement closer to being realized for on-chip applications. A LN planar waveguide was numerically studied for THz radiation generation enhancement near the LN phonon resonance (i.e. Section 6.2) and backward THz radiation generation (i.e. Section 6.3). These structures should be fabricated and incorporated into a THz-TDS system to experimentally-realize THz radiation generation.

Chapter 7 considered waveguides for generation in the near-IR and visible spectral regimes. LN plasmonic waveguides (Section 7.1) and a CSP photonic waveguide (Section 7.2) have been investigated numerically, such that the next step is to fabricate and test these structures experimentally.

Chapter 8 explored waveguiding arrangements to simultaneously generate radiation within multiple spectral bands. A centimeter-long multi-band LN planar waveguide was experimentally-investigated (section 8.2), such that preparing and testing a shorter-length (e.g. tens to hundreds of microns) waveguide would be the next step in preparing this multi-band waveguiding structure for on-chip applications.

9.2. Outlook

This thesis considered THz radiation generation and detection occurring through second-order nonlinear interactions, which have provided advancements to the field of nonlinear optics. THz sources and detectors were explored using the emerging classes of pnictide and chalcogenide ternary crystals. However, only a select few crystals were considered (i.e. ZGP, CSP, AGS, and BGS), such that this work serves as a launching pad for others to continue exploring these crystal classes within the THz spectral regime. In this thesis, several unique LN planar waveguiding geometries were investigated, which have the potential to bring THz radiation from being largely constrained to laboratory research environments and emerge into the realm of real-world applications. Going forward, we expect the integration of pnictide and chalcogenide ternary crystals into waveguiding arrangements to lead to breakthroughs within the domain of THz radiation technologies. Within the scope of this work, an entirely new class of multi-band photonic sources was proposed, which produced radiation within multiple spectral bands by simultaneously satisfying the phase-matching conditions for several second-order nonlinear processes. A novel discovery such as this has the potential to excite an endless number of future investigations. The work in this thesis sets the foundation for THz radiation generation and detection using novel crystals and/or waveguiding arrangements, which is one-day expected to allow THz radiation technologies to break-free from the constraints of laboratory environments and flourish in real-world applications.

References

- [1] A. Y. Pawar, D. D. Sonawane, K. B. Erande, and D. V. Derle, “Terahertz technology and its applications,” *Drug Inven. Today* **5**, 157–163 (2013).
- [2] D. J. Paul, “The progress towards terahertz quantum cascade lasers on silicon substrates,” *Laser Photonics Rev.* **4**, 610–632 (2010).
- [3] R. A. Lewis, “A review of terahertz sources,” *J. Phys. D Appl. Phys.* **47**, 374001 (2014).
- [4] S. Jablon and J. C. Bailar, “The contribution of ionizing radiation to cancer mortality in the United States,” *Prev. Med.* **9**, 219–226 (1980).
- [5] K. Krügener, J. Ornik, L. M. Schneider, A. Jäckel, C. L. Koch-Dandolo, E. Castro-Camus, N. Riedl-Siedow, M. Koch, and W. Viöl, “Terahertz inspection of buildings and architectural art,” *Appl. Sci.* **10**, 5166 (2020).
- [6] J. F. Federici, B. Schulkin, F. Huang, D. Gary, R. Barat, F. Oliveira, and D. Zimdars, “THz imaging and sensing for security applications—explosives, weapons and drugs,” *Semicond. Sci. Technol.* **20**, S266–S280 (2005).
- [7] J. A. Delgado-Notario, V. Clericò, E. Diez, J. E. Velázquez-Pérez, T. Taniguchi, K. Watanabe, T. Otsuji, and Y. M. Meziani, “Asymmetric dual-grating gates graphene FET for detection of terahertz radiations,” *APL Photonics* **5**, 066102 (2020).
- [8] B. Clough, J. Dai, and X.-C. Zhang, “Laser air photonics: Beyond the terahertz gap,” *Mater. Today* **15**, 50–58 (2012).
- [9] L. Zhang, M. Zhang, and A. S. Mujumdar, “Terahertz spectroscopy: A powerful technique for food drying research,” *Food Rev. Int.* **N/A**, 1–18 (2021).
- [10] L. Yang, T. Guo, X. Zhang, S. Cao, and X. Ding, “Toxic chemical compound detection by

- terahertz spectroscopy: A review,” *Rev. Anal. Chem.* **37**, 20170021 (2018).
- [11] A. J. Fitzgerald, B. E. Cole, and P. F. Taday, “Nondestructive analysis of tablet coating thicknesses using terahertz pulsed imaging,” *J. Pharm. Sci.* **94**, 177–183 (2005).
- [12] D. A. Crawley, C. Longbottom, V. P. Wallace, B. E. Cole, D. D. Arnone, and M. Pepper, “Three-dimensional terahertz pulse imaging of dental tissue,” *J. Biomed. Opt.* **8**, 303–307 (2003).
- [13] A. J. L. Adam, P. C. M. Planken, S. Meloni, and J. Dik, “TeraHertz imaging of hidden paint layers on canvas,” *Opt. Express* **17**, 3407–3416 (2009).
- [14] M. Picot, H. Ballacey, J. Guillet, Q. Cassar, and P. Mounaix, “Terahertz paint thickness measurements: From lab to automotive and aeronautics Industry,” in *15th Asia Pacific Conference for Non-Destructive Testing*, 1–8 (2017).
- [15] R. M. Woodward, V. P. Wallace, D. D. Arnone, E. H. Linfield, and M. Pepper, “Terahertz pulsed imaging of skin cancer in the time and frequency domain,” *J. Biol. Phys.* **29**, 257–261 (2003).
- [16] R. M. Woodward, B. E. Cole, V. P. Wallace, R. J. Pye, D. D. Arnone, E. H. Linfield, and M. Pepper, “Terahertz pulse imaging in reflection geometry of human skin cancer and skin tissue,” *Phys. Med. Biol.* **47**, 3853–3863 (2002).
- [17] M. Dutta, A. S. Bhalla, and R. Guo, “THz imaging of skin burn: Seeing the unseen—An Overview,” *Adv. Wound Care* **5**, 338–348 (2016).
- [18] I. F. Akyildiz, J. M. Jornet, and C. Han, “Terahertz band: Next frontier for wireless communications,” *Phys. Commun.* **12**, 16–32 (2014).
- [19] L. Afsah-Hejri, P. Hajeb, P. Ara, and R. J. Ehsani, “A comprehensive review on food applications of terahertz spectroscopy and imaging,” *Compr. Rev. Food Sci. Food Saf.* **18**,

- 1563–1621 (2019).
- [20] J.-S. Rieh, D. Yoon, and J. Yun, “An overview of solid-state electronic sources and detectors for terahertz imaging,” in *International Conference on Solid-State and Integrated Circuit Technology (ICSICT)*, 1–4 (2014).
- [21] T. Seifert, S. Jaiswal, U. Martens, J. Hannegan, L. Braun, P. Maldonado, F. Freimuth, A. Kronenberg, J. Henrizi, I. Radu, *et al.*, “Efficient metallic spintronic emitters of ultrabroadband terahertz radiation,” *Nat. Photonics* **10**, 483–488 (2016).
- [22] L. Zhang, Y. Wei, B. Wang, W. Shen, J. Xu, Y. Gong, and G.-S. Park, “Investigation of 0.38 THz backward-wave oscillator based on slotted sine waveguide and pencil electron beam,” *Phys. Plasmas* **23**, 033111 (2016).
- [23] F. Blanchard, G. Sharma, X. Ropagnol, L. Razzari, R. Morandotti, and T. Ozaki, “Improved terahertz two-color plasma sources pumped by high intensity laser beam,” *Opt. Express* **17**, 6044–6052 (2009).
- [24] F. Wang, J. Lee, D. J. Phillips, S. G. Holliday, S.-L. Chua, J. Bravo-Abad, J. D. Joannopoulos, M. Soljačić, S. G. Johnson, and H. O. Everitt, “A high-efficiency regime for gas-phase terahertz lasers,” *Proc. Natl. Acad. Sci.* **115**, 6614–6619 (2018).
- [25] N. Vinokurov, “Free electron lasers as a high-power terahertz sources,” *J. Infrared Millim. Terahertz Waves* **32**, 1123–1143 (2011).
- [26] B. S. Williams, “Terahertz quantum-cascade lasers,” *Nat. Photonics* **1**, 517–525 (2007).
- [27] N. M. Burford and M. O. El-Shenawee, “Review of terahertz photoconductive antenna technology,” *Opt. Eng.* **56**, 010901 (2017).
- [28] H. P. Piyathilaka, R. Sooriyagoda, V. Dewasurendra, M. B. Johnson, K. T. Zawilski, P. G. Schunemann, and A. D. Bristow, “Terahertz generation by optical rectification in

- chalcopyrite crystals ZnGeP₂, CdGeP₂ and CdSiP₂,” *Opt. Express* **27**, 16958–16965 (2019).
- [29] T. Zentgraf, R. Huber, N. C. Nielsen, D. S. Chemla, and R. A. Kaindl, “Ultrabroadband 50-130 THz pulses generated via phase-matched difference frequency mixing in LiIO₃,” *Opt. Express* **15**, 5775–5781 (2007).
- [30] R. W. Boyd, *Nonlinear Optics* (Academic Press, 1992).
- [31] R. L. Sutherland, *Handbook of Nonlinear Optics* (CRC Press, 2003).
- [32] K. Liu, J. Xu, and X.-C. Zhang, “GaSe crystals for broadband terahertz wave detection,” *Appl. Phys. Lett.* **85**, 863–865 (2004).
- [33] C. A. Baron and A. Y. Elezzabi, “A 360° angularly ranging time-domain terahertz spectroscopy system,” *Meas. Sci. Technol.* **19**, 065602 (2008).
- [34] B. J. Eggleton, B. Luther-Davies, and K. Richardson, “Chalcogenide photonics,” *Nat. Photonics* **5**, 141–148 (2011).
- [35] V. Petrov, F. Noack, I. Tunchev, P. Schunemann, and K. Zawilski, “The nonlinear coefficient d_{36} of CdSiP₂,” in *SPIE LASE: Lasers and Applications in Science and Engineering*, **7197**, 71970M (2009).
- [36] G. D. Boyd, E. Buehler, F. G. Storz, and J. H. Wernick, “Linear and nonlinear optical properties of ternary A^{II}B^{IV}C₂^V chalcopyrite semiconductors,” *IEEE J. Quantum Electron.* **8**, 419–426 (1972).
- [37] M. R. Ferdinandus, J. J. Gengler, K. L. Averett, K. T. Zawilski, P. G. Schunemann, and C. M. Liebig, “Nonlinear optical measurements of CdSiP₂ at near and mid-infrared wavelengths,” *Opt. Mater. Express* **10**, 2066–2074 (2020).
- [38] D. H. Auston and M. C. Nuss, “Electrooptic generation and detection of femtosecond electrical transients,” *IEEE J. Quantum Electron.* **24**, 184–197 (1988).

- [39] K. Zhong, C. Liu, M. Wang, J. Shi, B. Kang, Z. Yuan, J. Li, D. Xu, W. Shi, and J. Yao, “Linear optical properties of ZnGeP₂ in the terahertz range,” *Opt. Mater. Express* **7**, 3571–3579 (2017).
- [40] G. A. Medvedkin and V. G. Voevodin, “Magnetic and optical phenomena in nonlinear optical crystals ZnGeP₂ and CdGeP₂,” *J. Opt. Soc. Am. B* **22**, 1884–1898 (2005).
- [41] T. Yu, S. Wang, X. Zhang, C. Li, J. Qiao, N. Jia, B. Han, S.-Q. Xia, and X. Tao, “MnSiP₂: A new mid-IR ternary phosphide with strong SHG effect and ultrabroad transparency range,” *Chem. Mater.* **31**, 2010–2018 (2019).
- [42] K. V. Shportko, “Optical phonon behaviors in ZnGeP₂ single crystals from temperature dependent far-infrared reflectance spectra,” *Vib. Spectrosc.* **80**, 1–5 (2015).
- [43] P. N. Butcher and D. Cotter, *The Elements of Nonlinear Optics* (Cambridge University Press, 1990).
- [44] A. Miller and W. Clark, “Electrical properties of ZnGeP₂ and CdGeP₂,” *J. Phys. Colloquiums* **36**, C3-73–C3-75 (1975).
- [45] B. N. Carnio and A. Y. Elezzabi, “Analysis of electric field propagation in anisotropically absorbing and reflecting waveplates,” *J. Infrared Millim. Terahertz Waves* **39**, 313–325 (2018).
- [46] F. Li, K. Zhong, H. Qiao, K. Liu, X. Zhang, D. Xu, and J. Yao, “Efficient tunable terahertz generation via noncollinear phase matching in the ZnGeP₂ crystal,” *J. Opt. Soc. Am. B* **37**, 3857–3864 (2020).
- [47] N. Huang, H. Liu, Q. Sun, Z. Wang, S. Li, and J. Han, “Influence of absorption on stability of terahertz difference frequency generation,” *Appl. Opt.* **55**, 444–448 (2016).
- [48] Y. M. Andreev, A. A. Ionin, I. O. Kinyaevskiy, and Y. M. Klimachev, “Numerical study of

- multiline CO laser frequency conversion in a ZnGeP₂ crystal to the THz range,” *Bull. Russ. Acad. Sci. Phys.* **83**, 237–241 (2019).
- [49] D. Creedon, J. C. McCarthy, P. A. Ketteridge, T. Southward, P. G. Schunemann, J. J. Komiak, W. Dove, and E. P. Chicklis, “Compact fiber-pumped terahertz source based on difference frequency mixing in ZGP,” *IEEE J. Sel. Top. Quantum Electron.* **13**, 732–737 (2007).
- [50] P. Kumbhakar, T. Kobayashi, and G. C. Bhar, “Sellmeier dispersion for phase-matched terahertz generation in ZnGeP₂,” *Appl. Opt.* **43**, 3324–3328 (2004).
- [51] A. A. Sirotkin, N. N. Yudin, V. V. Dyomin, and A. I. Gribenyukov, “Tunable THz-radiation in a ZnGeP₂ single crystal pumped by dual-wavelength degenerate optical parametric oscillator,” *Laser Phys. Lett.* **17**, 035402 (2020).
- [52] W. Shi, Y. J. Ding, and P. G. Schunemann, “Coherent terahertz waves based on difference-frequency generation in an annealed zinc-germanium phosphide crystal: Improvements on tuning ranges and peak powers,” *Opt. Commun.* **233**, 183–189 (2004).
- [53] J. D. Rowley, J. K. Pierce, A. T. Brant, L. E. Halliburton, N. C. Giles, P. G. Schunemann, and A. D. Bristow, “Broadband terahertz pulse emission from ZnGeP₂,” *Opt. Lett.* **37**, 788–790 (2012).
- [54] J. D. Rowley, D. A. Bas, K. T. Zawilski, P. G. Schunemann, and A. D. Bristow, “Terahertz emission from ZnGeP₂: Phase-matching, intensity, and length scalability,” *J. Opt. Soc. Am. B* **30**, 2882–2888 (2013).
- [55] L. I. Isaenko and A. P. Yelissev, “Recent studies of nonlinear chalcogenide crystals for the mid-IR,” *Semicond. Sci. Technol.* **31**, 123001 (2016).
- [56] X. Zhang, J. Yao, W. Yin, Y. Zhu, Y. Wu, and C. Chen, “Determination of the nonlinear

- optical coefficients of the BaGa₄Se₇ crystal,” *Opt. Express* **23**, 552–558 (2015).
- [57] J. Chen, C. Lin, S. Yang, X. Jiang, S. Shi, Y. Sun, B. Li, S. Fang, and N. Ye, “Cd₄SiQ₆ (Q = S, Se): Ternary infrared nonlinear optical materials with mixed functional building motifs,” *Cryst. Growth Des.* **20**, 2489–2496 (2020).
- [58] W.-D. Cheng, C.-S. Lin, H. Zhang, and G.-L. Chai, “Theoretical evaluation on terahertz source generators from ternary metal chalcogenides of PbM₆Te₁₀ (M = Ga, In),” *J. Phys. Chem. C* **122**, 4557–4564 (2018).
- [59] S. M. Duguzhev, A. V. Makhin, V. A. Moshnikov, and A. I. Shelykh, “Doping of PbTe and Pb_{1-x}Sn_xTe with gallium and indium,” *Cryst. Res. Technol.* **25**, 145–149 (1990).
- [60] I. V. Kityk, O. Parasyuk, A. O. Fedorchuk, A. M. El-Naggar, A. A. Albassam, M. Piasecki, O. Y. Khyzhun, and I. Veremchuk, “PbGa₆Te₁₀ crystals for IR laser operated piezoelectricity,” *Mater. Res. Bull.* **100**, 131–137 (2018).
- [61] S. Avanesov, V. Badikov, A. Tyazhev, D. Badikov, V. Panyutin, G. Marchev, G. Shevyrdyaeva, K. Mitin, F. Noack, P. Vinogradova, *et al.*, “PbIn₆Te₁₀: New nonlinear crystal for three-wave interactions with transmission extending from 1.7 to 25 μm,” *Opt. Mater. Express* **1**, 1286–1291 (2011).
- [62] B. Zhou, W. Jie, T. Wang, Z. Kou, D. Zhao, L. Yin, F. Yang, S. Xi, G. Zha, and Z. Yin, “Observations on nanoscale Te precipitates in CdZnTe crystals grown by the traveling heater method using high resolution transmission electron microscopy,” *Crystals* **8**, 26 (2018).
- [63] T. L. Chu, S. S. Chu, C. Ferekides, and J. Britt, “Films and junctions of cadmium zinc telluride,” *J. Appl. Phys.* **71**, 5635–5640 (1992).
- [64] S. Prabakar, V. Balasubramanian, N. Suryanarayanan, and N. Muthukumarasamy, “Optical

- properties of copper indium diselenide thin films,” *Chalcogenide Lett.* **7**, 49–58 (2010).
- [65] G. E. Hallani, A. Ryah, N. Hassanain, M. Loghmarti, A. Mzerd, A. Arbaoui, N. Achargui, Y. Laaziz, N. Chahboun, and E. K. Hlil, “Optical properties of thin ternary semiconductor alloys CdZnTe prepared by hot wall evaporation technique,” in *Progress In Electromagnetics Research Symposium Proceedings*, 1897–1899 (2011).
- [66] J. Dong, Y. Xu, L. Ji, B. Xiao, B. Zhang, L. Guo, C. Zhang, C. Teichert, and W. Jie, “Enhanced terahertz response of diluted magnetic semiconductor $Zn_{1-x}Mn_xTe$ crystals,” *Opt. Mater. Express* **8**, 157–164 (2018).
- [67] M. Imamura, D. Tashima, J. Kitagawa, and H. Asada, “Magneto-optical properties of wider gap semiconductors ZnMnTe and ZnMnSe films prepared by MBE,” *J. Electron. Sci. Technol.* **18**, 100056 (2020).
- [68] X. Liu, U. Bindley, Y. Sasaki, and J. K. Furdyna, “Optical properties of epitaxial ZnMnTe and ZnMgTe films for a wide range of alloy compositions,” *J. Appl. Phys.* **91**, 2859–2865 (2002).
- [69] H. Qiao, K. Zhong, F. Li, X. Zhang, Z. Yuan, B. Kang, D. Xu, and J. Yao, “Temperature-dependent optical properties of AgGaS₂ in the terahertz range,” *Opt. Mater.* **119**, 111300 (2021).
- [70] Y. M. Andreev, V. V. Badikov, A. A. Ionin, I. O. Kinyaevskiy, Y. M. Klimachev, A. A. Kotkov, G. V. Lanskii, and V. A. Svetlichnyi, “Optical properties of PbIn₆Te₁₀ in the long-wave IR,” *Laser Phys. Lett.* **13**, 125405 (2016).
- [71] K. Takeya, Y. Takemoto, I. Kawayama, H. Murakami, T. Matsukawa, M. Yoshimura, Y. Mori, and M. Tonouchi, “Terahertz generation and optical properties of lithium ternary chalcogenide crystals,” *J. Infrared Millim. Terahertz Waves* **32**, 426–433 (2011).

- [72] Q. Liang, S. Wang, X. Tao, and T. Dekorsy, “Optical properties of LiInSe₂ in the THz frequency regime,” *Opt. Mater. Express* **4**, 1336–1344 (2014).
- [73] Q. Liang, S. Wang, X. Tao, and T. Dekorsy, “Temperature dependence of free carriers and optical phonons in LiInSe₂ in the terahertz frequency regime,” *Phys. Rev. B* **92**, 144303 (2015).
- [74] E. Yiwen, J. Yao, and L. Wang, “Propagation of terahertz waves in a monoclinic crystal BaGa₄Se₇,” *Sci. Rep.* **8**, 16229 (2018).
- [75] K. Takeya, Y. Takemoto, I. Kawayama, H. Murakami, T. Matsukawa, M. Yoshimura, Y. Mori, and M. Tonouchi, “Terahertz emission from coherent phonons in lithium ternary chalcopyrite crystals illuminated by 1560 nm femtosecond laser pulses,” *EPL* **91**, 20004 (2010).
- [76] M. Knorr, J. Raab, M. Tauer, P. Merkl, D. Peller, E. Wittmann, E. Riedle, C. Lange, and R. Huber, “Phase-locked multi-terahertz electric fields exceeding 13 MV/cm at a 190 kHz repetition rate,” *Opt. Lett.* **42**, 4367–4370 (2017).
- [77] I. Pupeza, D. Sánchez, J. Zhang, N. Lilienfein, M. Seidel, N. Karpowicz, T. Paasch-Colberg, I. Znakovskaya, M. Pescher, W. Schweinberger, *et al.*, “High-power sub-two-cycle mid-infrared pulses at 100 MHz repetition rate,” *Nat. Photonics* **9**, 721–724 (2015).
- [78] R. Huber, A. Brodschelm, F. Tauser, and A. Leitenstorfer, “Generation and field-resolved detection of femtosecond electromagnetic pulses tunable up to 41 THz,” *Appl. Phys. Lett.* **76**, 3191–3193 (2000).
- [79] C. Kübler, R. Huber, S. Tübel, and A. Leitenstorfer, “Ultrabroadband detection of multi-terahertz field transients with GaSe electro-optic sensors: Approaching the near infrared,” *Appl. Phys. Lett.* **85**, 3360 (2004).

- [80] F. Junginger, A. Sell, O. Schubert, B. Mayer, D. Brida, M. Marangoni, G. Cerullo, A. Leitenstorfer, and R. Huber, “Single-cycle multiterahertz transients with peak fields above 10 MV/cm,” *Opt. Lett.* **35**, 2645–2647 (2010).
- [81] Q. Liang, P. Qin, and N. Liu, “Terahertz generation and measurements with AgGaSe₂ crystal,” in *Asia Communications and Photonics Conference (ACP)*, 18355880 (2018).
- [82] M. Porer, J.-M. Ménard, and R. Huber, “Shot noise reduced terahertz detection via spectrally postfiltered electro-optic sampling,” *Opt. Lett.* **39**, 2435–2438 (2014).
- [83] A. Sell, A. Leitenstorfer, and R. Huber, “Phase-locked generation and field-resolved detection of widely tunable terahertz pulses with amplitudes exceeding 100 MV/cm,” *Opt. Lett.* **33**, 2767–2769 (2008).
- [84] H. S. Kang, H. I. Lee, and T. W. Kim, “Optical properties of terahertz wave emitter fabricated by using Cd_xZn_{1-x}Te single crystals,” *Jpn. J. Appl. Phys.* **43**, L1256–L1257 (2004).
- [85] K. Liu, H.-S. Kang, T.-K. Kim, and X.-C. Zhang, “Study of ZnCdTe crystals as terahertz wave emitters and detectors,” *Appl. Phys. Lett.* **81**, 4115–4117 (2002).
- [86] M. Yi, K. Jang, J. Ahn, I. Maeng, and J.-H. Son, “Optimal Cd molar fraction in Zn_{1-x}Cd_xTe terahertz emitters,” in *Quantum Electronics and Laser Science Conference (QEELS)*, JWA96 (2007).
- [87] H. S. Kang, H. I. Lee, and T. W. Kim, “Electrical and optical properties of Cd_xZn_{1-x}Te single crystals for applications as terahertz electro-optic sensors,” *J. Appl. Phys.* **96**, 1409–1412 (2004).
- [88] Y. Xu, J. Dong, H. Zheng, B. Xiao, L. Ji, Y. He, C. Zhang, B. Zhang, and W. Jie, “Improvement of the THz response of Zn_{1-x}Mn_xTe bulk crystals grown by a temperature

- gradient solution method,” *CrystEngComm* **19**, 3051–3057 (2017).
- [89] B. N. Carnio and A. Y. Elezzabi, “Theoretical formalism for off-normal angular coupling into selective and parity-dependent modes in a planar waveguide,” *Opt. Lett.* **45**, 948–951 (2020).
- [90] H. Hirori, A. Doi, F. Blanchard, and K. Tanaka, “Single-cycle terahertz pulses with amplitudes exceeding 1 MV/cm generated by optical rectification in LiNbO₃,” *Appl. Phys. Lett.* **98**, 091106 (2011).
- [91] S. B. Bodrov, M. I. Bakunov, and M. Hangyo, “Efficient Cherenkov emission of broadband terahertz radiation from an ultrashort laser pulse in a sandwich structure with nonlinear core,” *J. Appl. Phys* **104**, 093105 (2008).
- [92] G. Zhang, H. Ruan, X. Zhang, S. Wang, and X. Tao, “Vertical Bridgman growth and optical properties of CdSiP₂ crystals,” *CrystEngComm* **15**, 4255–4260 (2013).
- [93] A. Yelisseyev, P. Krinitsin, and L. Isaenko, “Spectroscopic features of nonlinear AgGaSe₂ crystals,” *J. Cryst. Growth* **387**, 41–47 (2014).
- [94] W. Zhu, A. Agrawal, H. Cao, and A. Nahata, “Generation of broadband radially polarized terahertz radiation directly on a cylindrical metal wire,” *Opt. Express* **16**, 8433–8439 (2008).
- [95] K. M. Schulz, A. G. C. Rusche, A. Y. Petrov, and M. Eich, “Integrated nonlinear waveguide optics for high-efficiency and wideband-tunable generation of THz radiation,” *ACS Photonics* **5**, 3779–3787 (2018).
- [96] I. Wilke and S. Sengupta, “Nonlinear optical techniques for terahertz pulse generation and detection-optical rectification and electrooptic sampling,” in *Terahertz Spectroscopy: Principles and Applications* (CRC Press, 2007).

- [97] J. L. Freeman, S. K. Diamond, H. Fong, and D. M. Bloom, “Electro-optic sampling of planar digital GaAs integrated circuits,” *Appl. Phys. Lett.* **47**, 1083–1084 (1985).
- [98] G. D. Boyd and M. A. Pollack, “Microwave nonlinearities in anisotropic dielectrics and their relation to optical and electro-optical nonlinearities,” *Phys. Rev. B* **7**, 5345–5359 (1973).
- [99] M. Vossebürger, M. Brucherseifer, G. C. Cho, H. G. Roskos, and H. Kurz, “Propagation effects in electro-optic sampling of terahertz pulses in GaAs,” *Appl. Opt.* **37**, 3368–3371 (1998).
- [100] T. Yang, S. Song, H. Dong, and R. Ba, “Waveguide structures for generation of terahertz radiation by electro-optical process in GaAs and ZnGeP₂ using 1.55 μm fiber laser pulses,” *Prog. Electromagn. Res. Lett.* **2**, 95–102 (2008).
- [101] L. Pálfalvi, J. A. Fülöp, and J. Hebling, “Absorption-reduced waveguide structure for efficient terahertz generation,” *Appl. Phys. Lett.* **107**, 233507 (2015).
- [102] K. L. Vodopyanov and Y. H. Avetisyan, “Optical terahertz wave generation in a planar GaAs waveguide,” *Opt. Lett.* **33**, 2314–2316 (2008).
- [103] K. Saito, T. Tanabe, and Y. Oyama, “Widely tunable terahertz-wave generation from planar GaP waveguides via difference frequency generation under collinear phase-matching condition,” *Jpn. J. Appl. Phys.* **53**, 102203 (2014).
- [104] K. Saito, T. Tanabe, and Y. Oyama, “Elliptically polarized THz-wave generation from GaP-THz planar waveguide via collinear phase-matched difference frequency mixing,” *Opt. Express* **20**, 26082–26088 (2012).
- [105] Y. Takushima, S. Y. Shin, and Y. C. Chung, “Design of a LiNbO₃ ribbon waveguide for efficient difference-frequency generation of terahertz wave in the collinear configuration,”

- Opt. Express* **15**, 14783–14792 (2007).
- [106] J.-I. Nishizawa, K. Suto, T. Tanabe, K. Saito, T. Kimura, and Y. Oyama, “THz generation from GaP rod-type waveguides,” *IEEE Photon. Technol. Lett.* **19**, 143–145 (2007).
- [107] K. Saito, T. Tanabe, Y. Oyama, K. Suto, and J. Nishizawa, “Terahertz-wave generation by GaP rib waveguides via collinear phase-matched difference-frequency mixing of near-infrared lasers,” *J. Appl. Phys.* **105**, 063102 (2009).
- [108] K. Saito, T. Tanabe, and Y. Oyama, “THz-Wave generation from GaP THz photonic crystal waveguides under difference-frequency mixing,” *Opt. Photonics J.* **2**, 201–205 (2012).
- [109] Y. Li, X. Hu, F. Liu, J. Li, Q. Xing, M. Hu, C. Lu, and C. Wang, “Terahertz waveguide emitters in photonic crystal fiber form,” *J. Opt. Soc. Am. B* **29**, 3114–3118 (2012).
- [110] H. Cao, R. A. Linke, and A. Nahata, “Broadband generation of terahertz radiation in a waveguide,” *Opt. Lett.* **29**, 1751–1753 (2004).
- [111] A. Marandi, T. E. Darcie, and P. P. M. So, “Design of a continuous-wave tunable terahertz source using waveguide-phase-matched GaAs,” *Opt. Express* **16**, 10427–10433 (2008).
- [112] K. Saito, T. Tanabe, and Y. Oyama, “Design of a GaP/Si composite waveguide for CW terahertz wave generation via difference frequency mixing,” *Appl. Opt.* **53**, 3587–3592 (2014).
- [113] T. Chen, J. Sun, L. Li, J. Tang, and Y. Zhou, “Design of a photonic crystal waveguide for terahertz-wave difference-frequency generation,” *IEEE Photon. Technol. Lett.* **24**, 921–923 (2012).
- [114] T. Chen, J. Sun, L. Li, and J. Tang, “Proposal for efficient terahertz-wave difference frequency generation in an AlGaAs photonic crystal waveguide,” *J. Light. Technol.* **30**, 2156–2162 (2012).

- [115] C. Staus, T. Kuech, and L. Mccaughan, “Continuously phase-matched terahertz difference frequency generation in an embedded-waveguide structure supporting only fundamental modes,” *Opt. Express* **16**, 13296–13303 (2008).
- [116] K. Suizu, K. Koketsu, T. Shibuya, T. Tsutsui, T. Akiba, and K. Kawase, “Extremely frequency-widened terahertz wave generation using Cherenkov-type radiation,” *Opt. Express* **17**, 6676–6681 (2009).
- [117] K. Takeya, K. Suizu, H. Sai, T. Ouchi, and K. Kawase, “Wide spectrum terahertz-wave generation from nonlinear waveguides,” *IEEE J. Sel. Top. Quantum Electron.* **19**, 8500212 (2013).
- [118] S. B. Bodrov, A. N. Stepanov, M. I. Bakunov, B. V. Shishkin, I. E. Ilyakov, and R. A. Akhmedzhanov, “Highly efficient optical-to-terahertz conversion in a sandwich structure with LiNbO₃ core,” *Opt. Express* **17**, 1871–1879 (2009).
- [119] S. B. Bodrov, I. E. Ilyakov, B. V. Shishkin, and M. I. Bakunov, “Highly efficient Cherenkov-type terahertz generation by 2- μ m wavelength ultrashort laser pulses in a prism-coupled LiNbO₃ layer,” *Opt. Express* **27**, 36059–36065 (2019).
- [120] M. I. Bakunov, E. A. Mashkovich, M. V. Tsarev, and S. D. Gorelov, “Efficient Cherenkov-type terahertz generation in Si-prism-LiNbO₃-slab structure pumped by nanojoule-level ultrashort laser pulses,” *Appl. Phys. Lett.* **101**, 151102 (2012).
- [121] S. B. Bodrov, I. E. Ilyakov, B. V. Shishkin, and A. N. Stepanov, “Efficient terahertz generation by optical rectification in Si-LiNbO₃-air-metal sandwich structure with variable air gap,” *Appl. Phys. Lett.* **100**, 201114 (2012).
- [122] M. I. Bakunov and S. B. Bodrov, “Si-LiNbO₃-air-metal structure for concentrated terahertz emission from ultrashort laser pulses,” *Appl. Phys. B* **98**, 1–4 (2010).

- [123] M. I. Bakunov, E. S. Efimenko, S. D. Gorelov, N. A. Abramovsky, and S. B. Bodrov, “Efficient Cherenkov-type optical-to-terahertz converter with terahertz beam combining,” *Opt. Lett.* **45**, 3533–3536 (2020).
- [124] S. Fan, H. Takeuchi, T. Ouchi, K. Takeya, and K. Kawase, “Broadband terahertz wave generation from a MgO:LiNbO₃ ridge waveguide pumped by a 1.5 μm femtosecond fiber laser,” *Opt. Lett.* **38**, 1654–1656 (2013).
- [125] K. Takeya, T. Minami, H. Okano, S. R. Tripathi, and K. Kawase, “Enhanced Cherenkov phase matching terahertz wave generation via a magnesium oxide doped lithium niobate ridged waveguide crystal,” *APL Photonics* **2**, 016102 (2017).
- [126] Y. Sasaki, Y. Suzuki, K. Suizu, H. Ito, S. Yamaguchi, and M. Imaeda, “Surface-emitted terahertz-wave difference-frequency generation in periodically poled lithium niobate ridge-type waveguide,” *Jpn. J. Appl. Phys.* **45**, L367–L369 (2006).
- [127] Y. Avetisyan, Y. Sasaki, and H. Ito, “Analysis of THz-wave surface-emitted difference-frequency generation in periodically poled lithium niobate waveguide,” *Appl. Phys. B* **73**, 511–514 (2001).
- [128] S. Coleman and D. Grischkowsky, “Parallel plate THz transmitter,” *Appl. Phys. Lett* **84**, 654–656 (2004).
- [129] G. Chang, C. J. Divin, J. Yang, M. A. Musheinish, S. L. Williamson, A. Galvanauskas, and T. B. Norris, “GaP waveguide emitters for high power broadband THz generation pumped by Yb- doped fiber lasers,” *Opt. Express* **15**, 16308–16315 (2007).
- [130] S. Xu, Y. Li, H. Cao, M. Hu, L. Chai, and C. Wang, “Terahertz wave generation in GaP waveguides by optical rectification with femtosecond bessel beam,” in *International Conference on Infrared, Millimeter, and Terahertz Waves, IRMMW-THz*, 1–2 (2016).

- [131] K.-H. Lin, C. A. Werley, and K. A. Nelson, “Generation of multicycle terahertz phonon-polariton waves in a planar waveguide by tilted optical pulse fronts,” *Appl. Phys. Lett.* **95**, 103304 (2009).
- [132] Y.-C. Huang, T.-D. Wang, Y.-H. Lin, C.-H. Lee, M.-Y. Chuang, Y.-Y. Lin, and F.-Y. Lin, “Forward and backward THz-wave difference frequency generations from a rectangular nonlinear waveguide,” *Opt. Express* **19**, 24577–24582 (2011).
- [133] D. J. Griffiths, *Introduction to Electrodynamics* (Prentice Hall, 1999).
- [134] C. Hooge, *BCIT Physics 0312 Textbook* (OpenStax, 2016).
- [135] M. Scalora, M. A. Vincenti, D. de Ceglia, V. Roppo, M. Centini, N. Akozbek, and M. J. Bloemer, “Second- and third-harmonic generation in metal-based structures,” *Phys. Rev. A* **82**, 043828 (2010).
- [136] Y. J. Ding, “Progress in terahertz sources based on difference-frequency generation [Invited],” *J. Opt. Soc. Am. B* **31**, 2696–2711 (2014).
- [137] C. Humbert, T. Noblet, L. Dalstein, B. Busson, and G. Barbillon, “Sum-frequency generation spectroscopy of plasmonic nanomaterials: A review,” *Materials (Basel)*. **12**, 836 (2019).
- [138] J. F. McGilp, “A review of optical second-harmonic and sum-frequency generation at surfaces and interfaces,” *J. Phys. D Appl. Phys.* **29**, 1812–1821 (1996).
- [139] B. E. Schmidt, P. Lassonde, G. Ernotte, M. Clerici, R. Morandotti, H. Ibrahim, and F. Légaré, “Decoupling Frequencies, Amplitudes and Phases in nonlinear optics,” *Sci. Rep.* **7**, 7861 (2017).
- [140] A. Tomasino, A. Parisi, S. Stivala, P. Livreri, A. C. Cino, A. C. Busacca, M. Peccianti, and R. Morandotti, “Wideband THz time domain spectroscopy based on optical rectification

- and electro-optic sampling,” *Sci. Rep.* **3**, 3116 (2013).
- [141] C. M. Lee, K. Kafle, Y. B. Park, and S. H. Kim, “Probing crystal structure and mesoscale assembly of cellulose microfibrils in plant cell walls, tunicate tests, and bacterial films using vibrational Sum Frequency Generation (SFG) spectroscopy,” *Phys. Chem. Chem. Phys.* **16**, 10844 (2014).
- [142] D. S. Sitnikov, S. A. Romashevskiy, A. V. Ovchinnikov, O. V. Chefonov, A. B. Savel’ev, and M. B. Agranat, “Estimation of THz field strength by an electro-optic sampling technique using arbitrary long gating pulses,” *Laser Phys. Lett.* **16**, 115302 (2019).
- [143] G. Ok, K. Park, H. J. Kim, H. S. Chun, and S.-W. Choi, “High-speed terahertz imaging toward food quality inspection,” *Appl. Opt.* **53**, 1406–1412 (2014).
- [144] M. Kawase, K. Yamamoto, K. Takagi, R. Yasuda, M. Ogawa, Y. Hatsuda, S. Kawanishi, Y. Hirotsu, M. Myotoku, Y. Urashima, *et al.*, “Non-destructive evaluation method of pharmaceutical tablet by terahertz-time-domain spectroscopy: Application to sound-alike medicines,” *J. Infrared Millim. Terahertz Waves* **34**, 566–571 (2013).
- [145] Y.-M. Ding, S. Gao, X. Shi, and H. Wu, “Analysis of inter-satellite terahertz communication link,” in *International Conference on Wireless Communication and Sensor Network (WCNS)*, 180–183 (2016).
- [146] K. T. Zawilski, P. G. Schunemann, T. C. Pollak, D. E. Zelmon, N. C. Fernelius, and F. Kenneth Hopkins, “Growth and characterization of large CdSiP₂ single crystals,” *J. Cryst. Growth* **312**, 1127–1132 (2010).
- [147] G. Gallot, J. Zhang, R. W. McGowan, T.-I. Jeon, and D. Grischkowsky, “Measurements of the THz absorption and dispersion of ZnTe and their relevance to the electro-optic detection of THz radiation,” *Appl. Phys. Lett.* **74**, 3450 (1999).

- [148] M. Unferdorben, Z. Szaller, I. Hajdara, J. Hebling, and L. Pálfalvi, “Measurement of refractive index and absorption coefficient of congruent and stoichiometric lithium niobate in the terahertz range,” *J. Infrared Millim. Terahertz Waves* **36**, 1203–1209 (2015).
- [149] C. M. Tu, S. A. Ku, W. C. Chu, C. W. Luo, J. C. Chen, and C. C. Chi, “Pulsed terahertz radiation due to coherent phonon-polariton excitation in <110> ZnTe crystal,” *J. Appl. Phys* **112**, 093110 (2012).
- [150] F. Blanchard, L. Razzari, H.-C. Bandulet, G. Sharma, R. Morandotti, J.-C. Kieffer, T. Ozaki, M. Reid, H. F. Tiedje, H. K. Haugen, *et al.*, “Generation of 1.5 μ J single-cycle terahertz pulses by optical rectification from a large aperture ZnTe crystal,” *Opt. Express* **15**, 13212–13220 (2007).
- [151] A. Schneider, M. Neis, M. Stillhart, B. Ruiz, R. U. A. Khan, and P. Günter, “Generation of terahertz pulses through optical rectification in organic DAST crystals: Theory and experiment,” *J. Opt. Soc. Am. B* **23**, 1822–1835 (2006).
- [152] P. G. Schunemann, S. D. Setzler, and T. M. Pollak, “Phase-matched crystal growth of AgGaSe₂ and AgGa_{1-x}In_xSe₂,” *J. Cryst. Growth* **211**, 257–264 (2000).
- [153] H. J. Bakker, G. C. Cho, H. Kurz, Q. Wu, and X.-C. Zhang, “Distortion of terahertz pulses in electro-optic sampling,” *J. Opt. Soc. Am. B* **15**, 1795–1801 (1998).
- [154] G. D. Boyd, H. M. Kasper, J. H. Mcfee, and F. G. Storz, “Linear and nonlinear optical properties of some ternary selenides,” *IEEE J. Quantum Electron.* **8**, 900–908 (1972).
- [155] X. Lin, G. Zhang, and N. Ye, “Growth and characterization of BaGa₄S₇: A new crystal for mid-IR nonlinear optics,” *Cryst. Growth Des.* **9**, 1186–1189 (2009).
- [156] V. Badikov, D. Badikov, G. Shevyrdyaeva, A. Tyazhev, G. Marchev, V. Panyutin, V. Petrov, and A. Kwasniewski, “Phase-matching properties of BaGa₄S₇ and BaGa₄Se₇: Wide-

- bandgap nonlinear crystals for the mid-infrared,” *Phys. Status Solidi RRL* **5**, 31–33 (2011).
- [157] S. P. Ong, W. D. Richards, A. Jain, G. Hautier, M. Kocher, S. Cholia, D. Gunter, V. L. Chevrier, K. A. Persson, and G. Ceder, “Python materials genomics (pymatgen): A robust, open-source python library for materials analysis,” *Comput. Mater. Sci.* **68**, 314–319 (2013).
- [158] Y. Yin, B. Wang, Y. E. J. Yao, L. Wang, X. Bai, and W. Liu, “Raman spectra and phonon structures of BaGa₄Se₇ crystal,” *Commun. Phys.* **3**, 1–6 (2020).
- [159] K. L. Vodopyanov, “Terahertz-wave generation with periodically inverted gallium arsenide,” *Laser Phys.* **19**, 305–321 (2009).
- [160] K. T. Zawilski, P. G. Schunemann, S. D. Setzler, and T. M. Pollak, “Large aperture single crystal ZnGeP₂ for high-energy applications,” *J. Cryst. Growth* **310**, 1891–1896 (2008).
- [161] M. Schall, M. Walther, and P. U. Jepsen, “Fundamental and second-order phonon processes in CdTe and ZnTe,” *Phys. Rev. B* **64**, 094301 (2001).
- [162] Y. S. Lee, *Principles of Terahertz Science and Technology* (Springer Science & Business Media, 2009).
- [163] M. Bettini and A. Miller, “Optical Phonons in ZnGeP₂ and CdGeP₂,” *Phys. Status Solidi B Basic Res.* **66**, 579–586 (1974).
- [164] S. V. Chuchupal, G. A. Komandin, E. S. Zhukova, A. S. Prokhorov, O. E. Porodinkov, I. E. Spektor, Y. A. Shakir, and A. I. Gribenyukov, “Mechanisms of loss formation in nonlinear optical crystals ZnGeP₂ in the terahertz frequency range,” *Phys. Solid State* **56**, 1391–1396 (2014).
- [165] A. Miller, G. D. Holah, and W. C. Clark, “Infrared dielectric dispersion of ZnGeP₂ and CdGeP₂,” *J. Phys. Chem. Solids* **35**, 685–693 (1974).

- [166] S. Casalbuoni, H. Schlarb, B. Schmidt, P. Schmüser, B. Steffen, and A. Winter, “Numerical studies on the electro-optic detection of femtosecond electron bunches,” *Phys. Rev. ST Accel. Beams* **11**, 072802 (2008).
- [167] A. Deneuve, D. Tanner, and P. H. Holloway, “Optical constants of ZnSe in the far infrared,” *Phys. Rev. B* **43**, 6544–6550 (1991).
- [168] H. H. Li, “Refractive index of ZnS, ZnSe, and ZnTe and its wavelength and temperature derivatives,” *J. Phys. Chem. Ref. Data* **13**, 103–150 (1984).
- [169] A. Taflove, *Computational Electrodynamics: The Finite-Difference Time-Domain Method* (Artech House Publishers, 1995).
- [170] M. C. Gupta and J. Ballato, *The Handbook of Photonics* (CRC Press, 2006).
- [171] S. Kojima, K. Kanehara, T. Hoshina, and T. Tsurumi, “Optical phonons and polariton dispersions of congruent LiNbO₃ studied by far-infrared spectroscopic ellipsometry and Raman scattering,” *Jpn. J. Appl. Phys.* **55**, 10TC02 (2016).
- [172] A. S. Barker and R. Loudon, “Dielectric Properties and Optical Phonons in LiNbO₃,” *Phys. Rev.* **158**, 433–445 (1967).
- [173] G. D. Boyd, R. C. Miller, K. Nassau, W. L. Bond, and A. Savage, “LiNbO₃: An efficient phase matchable nonlinear optical material,” *Appl. Phys. Lett.* **5**, 234–236 (1964).
- [174] G. D. Boyd, T. J. Bridges, M. A. Pollack, and E. H. Turner, “Microwave nonlinear susceptibilities due to electronic and ionic anharmonicities in acentric crystals,” *Phys. Rev. Lett.* **26**, 387–390 (1971).
- [175] N. Courjal, M.-P. Bernal, A. Caspar, G. Ulliac, F. Bassignot, L. Gauthier-Manuel, and M. Suarez, *Lithium niobate optical waveguides and microwaveguides* (IntechOpen, 2018).
- [176] W. L. Faust and C. H. Henry, “Mixing of visible and near-resonance infrared light in GaP,”

- Phys. Rev. Lett.* **17**, 1265–1268 (1966).
- [177] Y. J. Ding, “Efficient generation of high-frequency terahertz waves from highly lossy second-order nonlinear medium at polariton resonance under transverse-pumping geometry,” *Opt. Lett.* **35**, 262–264 (2010).
- [178] M. Cherchi, A. Taormina, A. C. Busacca, R. L. Oliveri, S. Bivona, A. C. Cino, S. Stivala, S. R. Sanseverino, and C. Leone, “Exploiting the optical quadratic nonlinearity of zinc-blende semiconductors for guided-wave terahertz generation: a material comparison,” *IEEE J. Quantum Electron.* **46**, 368–376 (2010).
- [179] D. E. Thompson and P. D. Coleman, “Step-tunable far infrared radiation by phase matched mixing in planar-dielectric waveguides,” *IEEE Trans. Microw. Theory Tech.* **22**, 995–1000 (1974).
- [180] Y. L. Lee, B.-A. Yu, C. Jung, Y.-C. Noh, J. Lee, and D.-K. Ko, “All-optical wavelength conversion and tuning by the cascaded sum- and difference frequency generation (cSFG/DFG) in a temperature gradient controlled Ti:PPLN channel waveguide,” *Opt. Express* **13**, 2988–2993 (2005).
- [181] H. Han, L. Cai, and H. Hu, “Optical and structural properties of single-crystal lithium niobate thin film,” *Opt. Mater.* **42**, 47–51 (2015).
- [182] E. D. Palik, *Handbook of Optical Constants of Solids: Volume 1* (Academic Press, 1998).
- [183] D. Chandler-Horowitz and P. M. Amirtharaj, “High-accuracy, midinfrared ($450\text{cm}^{-1} \leq \omega \leq 4000\text{cm}^{-1}$) refractive index values of silicon,” *J. Appl. Phys.* **97**, 123526 (2005).
- [184] *Lumerical* – www.lumerical.com
- [185] S. V. Mutilin and T. Khasanov, “The refractive index of homogeneous SiO₂ thin films,”

- Opt. Spectrosc.* **105**, 461–465 (2008).
- [186] X. Wu, S. Carbajo, K. Ravi, F. Ahr, G. Cirimi, Y. Zhou, O. D. Mücke, and F. X. Kärtner, “Terahertz generation in lithium niobate driven by Ti:sapphire laser pulses and its limitations,” *Opt. Lett.* **39**, 5403–5406 (2014).
- [187] Z. Su, Q. Meng, and B. Zhang, “Analysis on the damage threshold of MgO:LiNbO₃ crystals under multiple femtosecond laser pulses,” *Opt. Mater.* **60**, 443–449 (2016).
- [188] C.-C. Shih and A. Yariv, “A theoretical model of the linear electro-optic effect,” *J. Phys. C Solid State Phys.* **15**, 825–846 (1982).
- [189] I. Shoji, T. Kondo, A. Kitamoto, M. Shirane, and R. Ito, “Absolute scale of second-order nonlinear-optical coefficients,” *J. Opt. Soc. Am. B* **14**, 2268–2294 (1997).
- [190] R. Schiek and T. Pertsch, “Absolute measurement of the quadratic nonlinear susceptibility of lithium niobate in waveguides,” *Opt. Mater. Express* **2**, 126–139 (2012).
- [191] M. J. Weber, *Handbook of Optical Materials* (CRC Press, 2003).
- [192] T. D. Wang, S. T. Lin, Y. Y. Lin, A. C. Chiang, and Y. C. Huang, “Forward and backward Terahertz-wave difference-frequency generations from periodically poled lithium niobate,” *Opt. Express* **16**, 6471–6478 (2008).
- [193] R. Chen, G. Sun, G. Xu, Y. J. Ding, and I. B. Zotova, “Generation of high-frequency terahertz waves in periodically poled LiNbO₃ based on backward parametric interaction,” *Appl. Phys. Lett.* **101**, 111101 (2012).
- [194] G. Xu, X. Mu, Y. J. Ding, and I. B. Zotova, “Efficient generation of backward terahertz pulses from multiperiod periodically poled lithium niobate,” *Opt. Lett.* **34**, 995–997 (2009).
- [195] N. E. Yu, C. Jung, C.-S. Kee, Y. L. Lee, B.-A. Yu, D.-K. Ko, and J. Lee, “Backward terahertz generation in periodically poled lithium niobate crystal via difference frequency

- generation,” *Jpn. J. Appl. Phys.* **46**, 1501–1504 (2007).
- [196] K. Nawata, Y. Tokizane, Y. Takida, and H. Minamide, “Tunable backward terahertz-wave parametric oscillation,” *Sci. Rep.* **9**, 726 (2019).
- [197] Y. J. Ding, Y. Jiang, G. Xu, and I. B. Zotova, “Review of recent efforts on efficient generation of monochromatic THz pulses based on difference-frequency generation,” *Laser Phys.* **20**, 917–930 (2010).
- [198] R. M. Power and J. Huisken, “A guide to light-sheet fluorescence microscopy for multiscale imaging,” *Nat. Methods* **14**, 360–373 (2017).
- [199] J. Dai, J. Zhang, W. Zhang, and D. Grischkowsky, “Terahertz time-domain spectroscopy characterization of the far-infrared absorption and index of refraction of high-resistivity, float-zone silicon,” *J. Opt. Soc. Am. B* **21**, 1379–1386 (2004).
- [200] S. Gao, C. Yang, X. Xiao, Y. Tian, Z. You, and G. Jin, “Performance evaluation of tunable channel-selective wavelength shift by cascaded sum- and difference-frequency generation in periodically poled lithium niobate waveguides,” *J. Light. Technol.* **25**, 710–718 (2007).
- [201] H. Hu, R. Nouroozi, W. Wang, J. Yu, H. Suche, and W. Sohler, “Tunable all-optical wavelength conversion based on cascaded SHG/DFG in a Ti:PPLN waveguide using a single CW control laser,” *IEEE Photonics J.* **4**, 1396–1400 (2012).
- [202] J. Wang, J. Sun, and Q. Sun, “Experimental observation of a 1.5 μm band wavelength conversion and logic NOT gate at 40 Gbit/s based on sum-frequency generation,” *Opt. Lett.* **31**, 1711–1713 (2006).
- [203] K. Mukherjee, P. Ghosh, D. Kumbhakar, and A. K. Meikap, “A method of optical implementation of frequency encoded all optical logic gates based on multiphoton processes in non linear material,” *Opt. Quantum Electron.* **42**, 121–128 (2010).

- [204] F. A. Bovino, M. C. Larciprete, M. Giardina, A. Belardini, M. Centini, C. Sibilìa, M. Bertolotti, A. Passaseo, and V. Tasco, “Optical polarization based logic functions (XOR or XNOR) with nonlinear Gallium nitride nanoslab,” *Opt. Express* **17**, 19337–19344 (2009).
- [205] S. Arahira, N. Namekata, T. Kishimoto, H. Yaegashi, and S. Inoue, “Generation of polarization entangled photon pairs at telecommunication wavelength using cascaded $\chi^{(2)}$ processes in a periodically poled LiNbO₃ ridge waveguide,” *Opt. Express* **19**, 16032–16043 (2011).
- [206] S. Arahira, H. Murai, and H. Sasaki, “Generation of highly stable WDM time-bin entanglement by cascaded sum-frequency generation and spontaneous parametric downconversion in a PPLN waveguide device,” *Opt. Express* **24**, 19581–19591 (2016).
- [207] R. Luo, Y. He, H. Liang, M. Li, and Q. Lin, “Highly tunable efficient second-harmonic generation in a lithium niobate nanophotonic waveguide,” *Optica* **5**, 1006–1011 (2018).
- [208] M. R. Escalé, A. Sergeev, R. Geiss, and R. Grange, “Nonlinear mode switching in lithium niobate nanowaveguides to control light directionality,” *Opt. Express* **25**, 3013–3023 (2017).
- [209] W. H. P. Pernice, C. Xiong, C. Schuck, and H. X. Tang, “Second harmonic generation in phase matched aluminum nitride waveguides and micro-ring resonators,” *Appl. Phys. Lett.* **100**, 223501 (2012).
- [210] J. P. Long, B. S. Simpkins, D. J. Rowenhorst, and P. E. Pehrsson, “Far-field imaging of optical second-harmonic generation in single GaN nanowires,” *Nano Lett.* **7**, 831–836 (2007).
- [211] V. Barzda, R. Cisek, T. L. Spencer, U. Philipose, H. E. Ruda, and A. Shik, “Giant anisotropy of second harmonic generation for a single ZnSe nanowire,” *Appl. Phys. Lett.* **92**, 113111

- (2008).
- [212] R. Wu, J. Zhang, N. Yao, W. Fang, L. Qiao, Z. Chai, J. Lin, and Y. Cheng, “Lithium niobate micro-disk resonators of quality factors above 10^7 ,” *Opt. Lett.* **43**, 4116–4119 (2018).
- [213] R. Luo, H. Jiang, S. Rogers, H. Liang, Y. He, and Q. Lin, “On-chip second-harmonic generation and broadband parametric down-conversion in a lithium niobate microresonator,” *Opt. Express* **25**, 24531–24539 (2017).
- [214] S. Diziain, R. Geiss, M. Zilk, F. Schrepel, E.-B. Kley, A. Tünnermann, and T. Pertsch, “Second harmonic generation in free-standing lithium niobate photonic crystal L3 cavity,” *Appl. Phys. Lett.* **103**, 051117 (2013).
- [215] H. Jiang, H. Liang, R. Luo, X. Chen, Y. Chen, and Q. Lin, “Nonlinear frequency conversion in one dimensional lithium niobate photonic crystal nanocavities,” *Appl. Phys. Lett.* **113**, 021104 (2018).
- [216] Y. Song, J. Wang, Q. Li, M. Yan, and M. Qiu, “Broadband coupler between silicon waveguide and hybrid plasmonic waveguide,” *Opt. Express* **18**, 13173–13179 (2010).
- [217] M. Wu, Z. Han, and V. Van, “Conductor-gap-silicon plasmonic waveguides and passive components at subwavelength scale,” *Opt. Express* **18**, 11728–11736 (2010).
- [218] D. Kong and M. Tsubokawa, “Evaluation of slot-to-slot coupling between dielectric slot waveguides and metal-insulator-metal slot waveguides,” *Opt. Express* **23**, 19082–19091 (2015).
- [219] Z. Han, A. Y. Elezzabi, and V. Van, “Experimental realization of subwavelength plasmonic slot waveguides on a silicon platform,” *Opt. Lett.* **35**, 502–504 (2010).
- [220] R. S. Klein, G. E. Kugel, A. Maillard, K. Polgár, and A. Péter, “Absolute non-linear optical coefficients of LiNbO_3 for near stoichiometric crystal compositions,” *Opt. Mater.* **22**, 171–

- 174 (2003).
- [221] J. E. Bjorkholm, “Relative signs of the optical nonlinear coefficients d_{31} and d_{22} in LiNbO_3 ,” *Appl. Phys. Lett.* **13**, 36–37 (1968).
- [222] R. C. Miller, W. A. Nordland, and P. M. Bridenbaugh, “Dependence of second-harmonic-generation coefficients of LiNbO_3 on melt composition,” *J. Appl. Phys.* **42**, 4145–4147 (1971).
- [223] P. B. Johnson and R. W. Christy, “Optical constants of the noble metals,” *Phys. Rev. B* **6**, 4370–4379 (1972).
- [224] F. Träger, *Springer Handbook of Lasers and Optics* (Springer, 2012).
- [225] W. Fan, S. Zhang, N.-C. Panoiu, A. Abdenour, S. Krishna, R. M. Osgood Jr., K. J. Malloy, and S. R. J. Brueck, “Second harmonic generation from a nanopatterned isotropic nonlinear material,” *Nano Lett.* **6**, 1027–1030 (2006).
- [226] V. Kemlin, B. Boulanger, V. Petrov, P. Segonds, B. Ménaert, P. G. Schunneeman, and K. T. Zawilski, “Nonlinear, dispersive, and phase-matching properties of the new chalcopyrite CdSiP_2 [Invited],” *Opt. Mater. Express* **1**, 1292–1300 (2011).
- [227] R. C. Miller and W. A. Nordland, “Relative signs of nonlinear optical coefficients of polar crystals,” *Appl. Phys. Lett.* **16**, 174–176 (1970).
- [228] M. M. Choy and R. L. Byer, “Accurate second-order susceptibility measurements of visible and infrared nonlinear crystals,” *Phys. Rev. B* **14**, 1693–1706 (1976).
- [229] R. C. Eckardt, H. Masuda, Y. X. Fan, and R. L. Byer, “Absolute and relative nonlinear optical coefficients of KDP, KD^*P , BaB_2O_4 , LiIO_3 , $\text{MgO}:\text{LiNbO}_3$, and KTP measured by phase-matched second-harmonic generation,” *IEEE J. Quantum Electron.* **26**, 922–933 (1990).

- [230] R. C. Miller and A. Savage, “Temperature dependence of the optical properties of ferroelectric LiNbO_3 and LiTaO_3 ,” *Appl. Phys. Lett.* **9**, 169–171 (1966).
- [231] R. Kremer, A. Boudrioua, P. Moretti, and J. C. Loulergue, “Measurements of the non-linear d_{33} coefficients of light-ion implanted lithium niobate by second harmonic generation in total reflection geometry,” *Opt. Commun.* **219**, 389–393 (2003).
- [232] D. Xue, K. Betzler, and H. Hesse, “Dielectric properties of lithium niobate–tantalate crystals,” *Solid State Commun.* **115**, 581–585 (2000).
- [233] J. R. Schwesyg, M. C. C. Kajiyama, M. Falk, D. H. Jundt, K. Buse, and M. M. Fejer, “Light absorption in undoped congruent and magnesium-doped lithium niobate crystals in the visible wavelength range,” *Appl. Phys. B* **100**, 109–115 (2010).
- [234] C. Flueraru and C. P. Grover, “Overlap integral analysis for second-harmonic generation within inverted waveguide using mode dispersion phase match,” *IEEE Photon. Technol. Lett.* **15**, 697–699 (2003).
- [235] L. D. Noordam, H. J. Bakker, M. P. de Boer, and H. B. van L. van den Heuvell, “Second-harmonic generation of femtosecond pulses: observation of phase-mismatch effects,” *Opt. Lett.* **15**, 1464–1466 (1990).
- [236] J. Szabados, D. N. Puzyrev, Y. Minet, L. Reis, K. Buse, A. Villois, D. V. Skryabin, and I. Breunig, “Frequency comb generation via cascaded second-order nonlinearities in microresonators,” *Phys. Rev. Lett.* **124**, 203902 (2020).

Appendix A

Phase-matching in second-order nonlinear interactions

Second-order nonlinear frequency-conversion is illustrated in Fig. A1, with photons being used to represent electric fields within the crystal. As excitation electric fields at the angular frequencies of ω_1 (i.e. E_{ω_1}) and ω_2 (i.e. E_{ω_2}) propagate through a non-centrosymmetric crystal, they continuously generate an electric field at the angular frequency of $\omega_3 = \omega_1 + \omega_2$ (i.e. E_{ω_3}). However, to obtain an intuitive understanding of phase-matching, generation can be considered at the discrete positions of x_i (where $i=1, 2$, or 3) within the crystal. The excitation electric fields at position x_i (i.e. $E_{\omega_1}^{x_i}$ and $E_{\omega_2}^{x_i}$) produce an electric field at position x_i , denoted as $E_{\omega_3}^{x_i:x_i}$. $E_{\omega_3}^{x_1:x_1}$ and $E_{\omega_3}^{x_2:x_2}$ continue to propagate along the crystal and are denoted as $E_{\omega_3}^{x_3:x_1}$ and $E_{\omega_3}^{x_3:x_2}$ at position x_3 , respectively. The total electric field at x_3 , $E_{\omega_3}^{x_3}$, is the superposition of the various electric field contributions, such that $E_{\omega_3}^{x_3} = E_{\omega_3}^{x_3:x_1} + E_{\omega_3}^{x_3:x_2} + E_{\omega_3}^{x_3:x_3}$. Phase-matching is achieved when $E_{\omega_3}^{x_3:x_1}$, $E_{\omega_3}^{x_3:x_2}$, and $E_{\omega_3}^{x_3:x_3}$ constructively interfere, while phase-mismatching occurs when $E_{\omega_3}^{x_3:x_1}$, $E_{\omega_3}^{x_3:x_2}$, and $E_{\omega_3}^{x_3:x_3}$ exhibit destructive interference. The conditions leading to phase-matching are discussed in Chapter 2. Notably, the aforementioned discussion pertains to: (i) SHG when $\omega_1 \rightarrow \omega_1$ and $\omega_2 \rightarrow \omega_1$ or $\omega_1 \rightarrow \omega_2$ and $\omega_2 \rightarrow \omega_2$, (ii) SFG when $\omega_1 \rightarrow \omega_1$ and $\omega_2 \rightarrow \omega_2$, and (iii) DFG when $\omega_1 \rightarrow \omega_1$ and $\omega_2 \rightarrow -\omega_2$. Additionally, phase-matching in OR is similar to the aforementioned discussion, where phase-matching occurs when the electric fields generated at various positions within the crystal exhibit constructive interference.

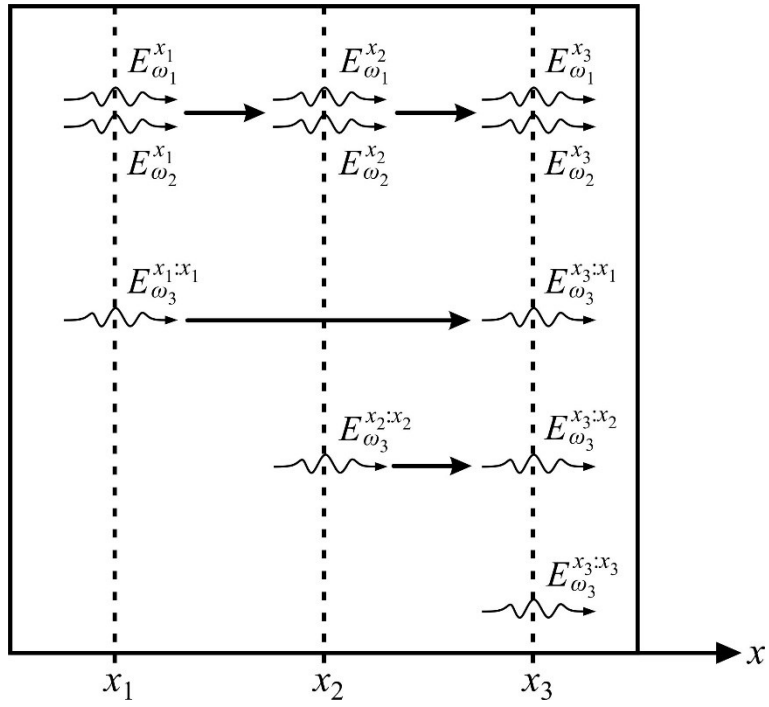


Fig. A1. Frequency-conversion occurring within a non-centrosymmetric crystal due to second-order nonlinear interactions. The various generation events are vertically offset.